

On the Effective Behavior, Microstructure Evolution, and Macroscopic Stability of Elastomeric Composites

OSCAR LOPEZ-PAMIES

A Dissertation
in

MECHANICAL ENGINEERING AND APPLIED MECHANICS

Presented to the Faculty of the University of Pennsylvania
in Partial Fulfillment of the Requirements for the
Degree of Doctor of Philosophy.
2006

PROFESSOR P. PONTE CASTAÑEDA
Supervisor of Dissertation

PROFESSOR P. PONTE CASTAÑEDA
Graduate Group Chairperson

To my parents and E.D.T.

ACKNOWLEDGMENTS

Many thanks are in order to Professor Tony Farquhar for introducing me to Professor Pedro Ponte Castañeda. In a sense, that was the “spark” that started the work presented in this thesis.

More importantly, I would like to record my particular gratitude to my Ph.D. advisor, Professor Pedro Ponte Castañeda. In addition to introducing me to the subject of homogenization and—more broadly—guiding me to grow in mechanics, Professor Pedro Ponte Castañeda has been an inspiring and extraordinary person to work with during the entire span of this thesis. Plainly put, he has been a great mentor.

I gratefully thank Professor John Bassani and Professor Vaclav Vitek, who, in the midst of their activity, accepted to be members of my dissertation committee. Special thanks go to Professor John Bassani for his advice in technical and professional matters.

Many thanks go in particular to Professor Nick Triantafyllidis for his expert advice in technical issues. More importantly, I am much indebted to Professor Nick Triantafyllidis for his guidance and energetic support.

Special thanks go to my fellow Ph.D. student and close friend Martin Idiart for our great scientific and philosophical discussions. Martin, it has been a pleasure working with you.

Finally, I would also like to record my gratitude to my fellow colleagues Kostas Danas and Michele Brun for our scientific (and not-so-scientific) debates, which were certainly enriching.

Financial support for this research was provided by NSF Grant DMS-0204617 and DOE Grant DE-FG02-04ER46110.

ABSTRACTON THE EFFECTIVE BEHAVIOR, MICROSTRUCTURE EVOLUTION,
AND MACROSCOPIC STABILITY OF ELASTOMERIC COMPOSITES

Oscar Lopez-Pamies

Pedro Ponte Castañeda

Elastomeric composites are currently used in numerous commercial applications and have shown great promise for utilization in new technologies. This raises the practical—as well as theoretical—need to understand the connection between the underlying microstructure of elastomeric composites and their mechanical and physical properties, and how the latter may be enhanced with changes in the former. In this connection, the principal aim of this thesis is the development of an analytical, nonlinear *homogenization* framework for determining the overall response of elastomeric composites subjected to finite deformations. The framework accounts for the evolution of the underlying microstructure, which results from the finite changes in geometry induced by the applied loading. This point is essential as the evolution of the microstructure can have a significant geometric softening (or stiffening) effect on the overall response of the material, which, in turn, may lead to the possible development of macroscopic instabilities. The main concept behind the proposed nonlinear homogenization method is the construction of suitable variational principles utilizing the idea of a “linear comparison composite,” which ultimately allow for the conversion of available linear homogenization estimates into analytical estimates for the large-deformation overall response of the nonlinear elastomeric composites. This thesis includes applications of the proposed theory to various classes of reinforced and porous elastomers with random and periodic microstructures. A comprehensive analysis of the effective behavior, the microstructure evolution, and the development of macroscopic instabilities is provided for all these applications.

Contents

Acknowledgements	iii
Abstract	iv
List of Figures	ix
1 Introduction	1
2 Theory	11
2.1 Hyperelastic composites and effective behavior	11
2.1.1 Hyperelastic materials	11
2.1.2 Effective behavior	13
2.1.3 Constitutive hypotheses	15
2.1.4 Macroscopic and microscopic instabilities	19
2.2 Bounds and estimates	21
2.3 Second-order homogenization method	22
2.3.1 On the specific choice of the variables $\mathbf{F}^{(r)}$ and $\mathbf{L}^{(r)}$ for isotropic phases	27
2.4 Effective behavior of two-phase hyperelastic composites with “particulate” microstructures	29
2.4.1 Classical bounds	29
2.4.2 The linear comparison composite	31
2.4.3 Second-order homogenization estimates: compliant particles	34
2.4.4 Second-order homogenization estimates: porous elastomers	37
2.4.5 Second-order homogenization estimates: rigid particles	38
2.5 Microstructure evolution	40
2.5.1 Range of validity of the HS-type second-order estimates	46
2.6 Macroscopic stability	47
2.7 Concluding remarks	49
2.8 Appendix I. Overall objectivity of \widetilde{W}	51
2.9 Appendix II. On the relation $\widetilde{\mathbf{S}} = \partial\widetilde{W}/\partial\overline{\mathbf{F}}$	52
2.10 Appendix III. Microscopic and macroscopic instabilities in periodic elastomers	52
2.11 Appendix IV. On the limit of $\widetilde{\mathbf{L}}$ as $\overline{\mathbf{F}} \rightarrow \mathbf{I}$	57

2.12	Appendix V. Earlier versions of the second-order homogenization method	60
2.12.1	Tangent second-order estimates	61
2.12.2	Second-order estimates with fluctuations: $\mathbf{F}^{(r)} = \bar{\mathbf{F}}^{(r)}$	62
2.13	Appendix VI. The tensor \mathbf{P} for cylindrical fibers and laminates	63
3	Porous elastomers: cylindrical voids, random microstructure	66
3.1	Plane-strain loading of transversely isotropic, random porous elastomers	67
3.1.1	Second-order homogenization estimates	68
3.1.2	Tangent second-order homogenization estimates	73
3.1.3	Comparisons with exact results	76
3.1.4	Loss of strong ellipticity	78
3.2	Results for plane-strain loading: random porous elastomers	79
3.2.1	Hydrostatic loading	79
3.2.2	Uniaxial loading	82
3.2.3	Pure shear loading	84
3.2.4	Failure surfaces	86
3.3	Concluding remarks	88
3.4	Appendix I. In-plane components of the tensor \mathbf{P} for cylindrical inclusions with circular cross-section	91
3.5	Appendix II. Second-order estimates for transversely isotropic porous elastomers with incompressible Neo-Hookean matrix phase	92
3.6	Appendix III. Coefficients associated with the incompressible limit for the second-order estimate of Neo-Hookean porous elastomers	96
3.7	Appendix IV. Tangent second-order estimates for transversely isotropic porous elastomers with incompressible Neo-Hookean matrix phase	97
4	Porous elastomers: cylindrical voids, periodic microstructure	100
4.1	Plane-strain loading of periodic porous elastomers	100
4.1.1	Second-order homogenization estimates	102
4.1.2	Loss of strong ellipticity	105
4.2	Results for plane-strain loading: periodic porous elastomers	106
4.2.1	Hydrostatic loading	107
4.2.2	Aligned uniaxial loading	109
4.2.3	Failure surfaces	112
4.3	Concluding remarks	118
4.4	Appendix I. Expressions for the microstructural tensor \mathbf{P}	120
4.5	Appendix II. Onset of percolation	120

5	Porous elastomers: spherical voids	122
5.1	Overall behavior of isotropic porous elastomers	123
5.1.1	Earlier estimates	124
5.1.2	Second-order homogenization estimates	126
5.1.3	Small-strain elastic moduli	130
5.1.4	Exact evolution of porosity	130
5.1.5	Loss of strong ellipticity	131
5.2	Results and discussion	132
5.2.1	Axisymmetric loadings	133
5.2.2	Plane-strain loadings	150
5.3	Concluding remarks	157
5.4	Appendix I. Second-order estimates for isotropic porous elastomers with compressible matrix phases	159
5.5	Appendix II. Second-order estimates for isotropic porous elastomers with incompressible matrix phases	163
6	Hyperelastic laminates	169
6.1	Effective behavior of hyperelastic laminates	170
6.1.1	Tangent second-order homogenization estimates	171
6.1.2	Microstructure evolution	177
6.2	Plane-strain loading of Neo-Hookean laminates	178
6.3	Results and discussion	180
6.3.1	Aligned pure shear	180
6.3.2	Pure shear at an angle	182
6.4	Concluding remarks	186
7	Reinforced elastomers: cylindrical fibers, random microstructure	187
7.1	Plane-strain loading of fiber-reinforced, random elastomers	187
7.1.1	Second-order homogenization estimates: compliant fibers	190
7.1.2	Second-order homogenization estimates: rigid fibers	193
7.1.3	Loss of strong ellipticity	198
7.2	Results for plane-strain loading: random reinforced elastomers	201
7.2.1	Pure shear: circular rigid fibers and incompressible matrix	201
7.2.2	Aligned pure shear: rigid fibers and incompressible matrix	206
7.2.3	Pure shear at an angle: rigid fibers and incompressible matrix	209
7.2.4	Aligned pure shear: compliant fibers and compressible matrix	215
7.2.5	Simple shear: rigid fibers and incompressible matrix	218
7.3	Concluding remarks	220
7.4	Appendix I. Incompressibility limit for rigidly reinforced elastomers: cylindrical fibers	222

8 Reinforced elastomers: cylindrical fibers, periodic microstructure	226
8.1 Overall behavior of periodic, fiber-reinforced elastomers	226
8.1.1 Voigt bound	228
8.1.2 Second-order homogenization estimates	228
8.2 Results and discussion	235
8.2.1 Axisymmetric shear	236
8.2.2 In-plane pure shear	240
8.2.3 In-plane simple shear	248
8.2.4 Out-of-plane pure shear	250
8.3 Concluding remarks	253
8.4 Appendix I. The microstructural tensor \mathbf{P}	255
9 Closure	256
Appendices	262
A Second-order homogenization estimates incorporating field fluctuations in finite elasticity¹	263
A.1 Hyperelastic composites and effective behavior	264
A.2 The second-order variational procedure	268
A.3 Application to particle-reinforced elastomers	272
A.3.1 Lower bounds	273
A.3.2 Second-order estimates	274
A.4 Plane strain loading of transversely isotropic, fiber-reinforced Neo-Hookean composites	277
A.4.1 Formulation	277
A.4.2 Results	281
A.5 Concluding remarks	286
Bibliography	293

List of Figures

2.1	Schematic representation of the “particulate” microstructures considered in this work. (a) Ellipsoidal particles distributed <i>randomly</i> with “ellipsoidal symmetry;” the solid ellipsoids denote the inclusions, and the dashed ellipsoids, their distribution. (b) Ellipsoidal particles distributed <i>periodically</i> ; the solid ellipsoids denote the inclusions, and the dashed parallelepipeds, their distribution.	30
2.2	Schematic representation of two-phase, “particulate” composites in the undeformed configuration identifying the initial state of the various microstructural variables. (a) Random, ellipsoidal distribution. (b) Periodic distribution.	42
2.3	Schematic representation of the evolution, from the undeformed to the deformed configuration, of the microstructure in two-phase, “particulate” composites. Part (a) shows the evolution of a typical inclusion (denoted by the color ellipsoid)—as determined by $\bar{\mathbf{F}}^{(2)}$ —and of its <i>random</i> , ellipsoidal distribution (denoted by the dashed ellipsoid)—as determined by $\bar{\mathbf{F}}$. Part (b) shows analogous results for the periodic distribution.	46
3.1	Reference configuration depiction of the random, isotropic arrangement of circular voids.	67
3.2	Comparisons of the second-order estimates (Version 1 and 3) with the exact results for the effective response of a porous rubber subjected to in-plane hydrostatic loading ($\bar{\lambda}_2 = \bar{\lambda}_1 = \bar{\lambda}$). The results correspond to an incompressible ¹ Neo-Hookean matrix phase with various initial concentrations f_0 of aligned cylindrical voids, and are shown as a function of the logarithmic strain $\bar{e} = \ln(\bar{\lambda})$. (a) The stored-energy function $\widehat{\Phi}^I$; and (b) the corresponding stresses $\bar{S} = \partial\widehat{\Phi}^I/\partial\bar{\lambda}_1 = \partial\widehat{\Phi}^I/\partial\bar{\lambda}_2$	80
3.3	In-plane hydrostatic loading ($\bar{\lambda}_2 = \bar{\lambda}_1 = \bar{\lambda}$) of a porous rubber with an incompressible, Neo-Hookean matrix phase with various initial concentrations f_0 of aligned cylindrical voids. (a) The evolution of porosity f as predicted by Versions 1 and 3 of the second-order method compared with the exact result as a function of the logarithmic strain $\bar{e} = \ln(\bar{\lambda})$. (b) The critical stretches $\bar{\lambda}_{crit}$ at which the loss of strong ellipticity of the homogenized elastomer takes place as a function of initial porosity f_0 . (This last plot also includes the critical loads for the first two buckling modes ($n = 2$, and 3) of a cylindrical shell (Wang and Ertepinar, 1972).)	81

3.4	Version 1 and 3 estimates of the second-order method for the effective response of a porous rubber subjected to uniaxial loading ($\bar{\lambda}_2 = 1$ and $\bar{\lambda}_1 = \bar{\lambda}$). The results correspond to an incompressible Neo-Hookean matrix phase with various initial concentrations f_0 of aligned cylindrical voids, and are shown as a function of the logarithmic strain $\bar{e} = \ln(\bar{\lambda})$. (a) The stress component $\bar{S}_{11} = \partial\hat{\Phi}^I/\partial\bar{\lambda}_1$. (b) The stress component $\bar{S}_{22} = \partial\hat{\Phi}^I/\partial\bar{\lambda}_2$	83
3.5	Version 1 and 3 estimates of the second-order method for the effective response of a porous rubber subjected to uniaxial loading ($\bar{\lambda}_2 = 1$ and $\bar{\lambda}_1 = \bar{\lambda}$). The results correspond to an incompressible Neo-Hookean matrix phase with various initial concentrations f_0 of aligned cylindrical voids, and are shown as a function of the logarithmic strain $\bar{e} = \ln(\bar{\lambda})$. (a) The evolution of the porosity f compared with the exact result. (b) The evolution of the average aspect ratio of the voids ω	84
3.6	Version 3 estimates of the second-order method for the effective response of a porous rubber subjected to pure shear loading ($\bar{\lambda}_1 = 1/\bar{\lambda}_2 = \bar{\lambda}$). The results correspond to an incompressible Gent matrix phase with given initial porosity $f_0 = 0.1$ and various values of the material parameter J_m , and are shown as a function of the logarithmic strain $\bar{e} = \ln(\bar{\lambda})$. (a) The effective stored-energy function $\hat{\Phi}^I$ compared with the Voigt upper bound. (b) The evolution of the aspect ratio ω	85
3.7	Version 3 estimates of the second-order method for the effective response of a porous rubber subjected to pure shear loading ($\bar{\lambda}_1 = 1/\bar{\lambda}_2 = \bar{\lambda}$). The results correspond to an incompressible Gent matrix phase with given initial porosity $f_0 = 0.1$ and various values of the material parameter J_m , and are shown as a function of the logarithmic strain $\bar{e} = \ln(\bar{\lambda})$. (a) The stress component $\bar{S}_{11} = \partial\hat{\Phi}^I/\partial\bar{\lambda}_1$. (b) The stress component $\bar{S}_{22} = \partial\hat{\Phi}^I/\partial\bar{\lambda}_2$	86
3.8	Domains of strong ellipticity on the $(\bar{e}_1 - \bar{e}_2)$ -plane for a porous elastomer with incompressible, Neo-Hookean, matrix phase and various levels of initial concentrations f_0 of aligned cylindrical voids, as determined by Version 1 and 3 of the second-order variational procedure. The dotted lines denote the boundary at which the level of zero porosity has been reached upon compressive deformation. (a) Comparisons between the Version 1 and 3 estimates; and (b) Version 3 estimates for low initial porosity.	87
4.1	Reference configuration depiction of the various microgeometries investigated: (a) periodic square, and (b) periodic hexagonal arrangement of circular voids.	101
4.2	Comparisons of the effective response, as predicted by the second-order estimate (SOE), with FEM calculations of a porous elastomer with compressible Neo-Hookean matrix phase subjected to hydrostatic compression ($\bar{\lambda}_1 = \bar{\lambda}_2 = \bar{\lambda} \leq 1$). Results are shown for a periodic square (SQ) distribution of voids and various values of initial porosity f_0 , as a function of the logarithmic strain $\bar{e} = \ln \bar{\lambda}$. (a) The macroscopic stress $\bar{S} = \partial\widehat{W}/\partial\bar{F}_{11} = \partial\widehat{W}/\partial\bar{F}_{22} = \partial\widehat{W}/\partial\bar{F}_{33}$. (b) The evolution of the porosity f	107

- 4.3 Comparisons of the effective response, as predicted by the second-order estimate (SOE), with FEM calculations of a porous elastomer with compressible Neo-Hookean matrix phase subjected to hydrostatic compression ($\bar{\lambda}_1 = \bar{\lambda}_2 = \bar{\lambda} \leq 1$). Results are shown for a periodic hexagonal (HX) distribution of voids and various values of initial porosity f_0 , as a function of the logarithmic strain $\bar{e} = \ln \bar{\lambda}$. (a) The macroscopic stress $\bar{S} = \partial \widehat{W} / \partial \bar{F}_{11} = \partial \widehat{W} / \partial \bar{F}_{22} = \partial \widehat{W} / \partial \bar{F}_{33}$. (b) The evolution of the porosity f 108
- 4.4 Comparisons of the effective response, as predicted by the second-order estimate, with FEM calculations of a porous elastomer with compressible Neo-Hookean matrix phase subjected to aligned uniaxial compression ($\bar{\lambda}_1 = \bar{\lambda}$, $\bar{\lambda}_2 = 1$, $\bar{\theta} = 0$). Results are shown for a periodic square (SQ) distribution of voids and various values of initial porosity f_0 , as a function of the logarithmic strain $\bar{e} = \ln \bar{\lambda}$. (a) The macroscopic stress $\bar{S}_{11} = \partial \widehat{W} / \partial \bar{F}_{11}$. (b) The macroscopic stress $\bar{S}_{22} = \partial \widehat{W} / \partial \bar{F}_{22}$ 109
- 4.5 Aligned uniaxial compression ($\bar{\lambda}_1 = \bar{\lambda}$, $\bar{\lambda}_2 = 1$, $\bar{\theta} = 0$) of a porous elastomer with compressible Neo-Hookean matrix phase and various values of initial porosity f_0 . The results are shown for a periodic square (SQ) distribution of voids, as a function of the logarithmic strain $\bar{e} = \ln \bar{\lambda}$. Comparisons between the second-order estimates and FEM calculations for (a) the evolution of the porosity f ; and (b) the evolution of the average aspect ratio of the pores ω 110
- 4.6 Comparisons of the effective response, as predicted by the second-order estimate, with FEM calculations of a porous elastomer with compressible Neo-Hookean matrix phase subjected to aligned uniaxial compression ($\bar{\lambda}_1 = \bar{\lambda}$, $\bar{\lambda}_2 = 1$, $\bar{\theta} = 0$). Results are shown for a periodic hexagonal (HX) distribution of voids and various values of the initial porosity f_0 as a function of the logarithmic strain $\bar{e} = \ln \bar{\lambda}$. (a) The macroscopic stress $\bar{S}_{11} = \partial \widehat{W} / \partial \bar{F}_{11}$. (b) The macroscopic stress $\bar{S}_{22} = \partial \widehat{W} / \partial \bar{F}_{22}$ 111
- 4.7 Aligned uniaxial compression ($\bar{\lambda}_1 = \bar{\lambda}$, $\bar{\lambda}_2 = 1$, $\bar{\theta} = 0$) of a porous elastomer with compressible Neo-Hookean matrix phase and various values of initial porosity f_0 . The results are shown for a periodic hexagonal (HX) distribution of voids as a function of the logarithmic strain $\bar{e} = \ln \bar{\lambda}$. Comparisons between the second-order estimates and FEM calculations for (a) the evolution of the porosity f ; and (b) the evolution of the average aspect ratio of the pores ω 112
- 4.8 Macroscopic onset-of-failure surface, as determined by the loss of strong ellipticity of the second-order estimate and FEM calculations, for a porous elastomer with periodic square (SQ) arrangement of voids and compressible Neo-Hookean matrix phase. (a) The results in the \bar{e}_1 - \bar{e}_2 plane in strain space; and (b) the corresponding results in stress space. . . . 113
- 4.9 Macroscopic onset-of-failure surface, as determined by the loss of strong ellipticity of the second-order estimate and FEM calculations, for a porous elastomer with periodic hexagonal (HX) arrangement of voids and compressible Neo-Hookean matrix phase. (a) The results in the \bar{e}_1 - \bar{e}_2 plane in strain space; and (b), the corresponding results in stress space. 114

-
- 4.10 Macroscopic onset-of-failure surface, as determined by the loss of strong ellipticity of the second-order estimate and FEM calculations, for a porous elastomer with periodic square (SQ) arrangement of voids and compressible Neo-Hookean matrix phase. The results are shown in principal strain space \bar{e}_1 – \bar{e}_2 . The onset of percolation, as predicted by the second-order estimate, has also been included in the figure for completeness. 115
- 4.11 Macroscopic onset-of-failure surface, as determined by the loss of strong ellipticity of the second-order estimate, for a porous elastomer with periodic hexagonal (HX) arrangement of voids and compressible Neo-Hookean matrix phase. The results are shown in principal strain space \bar{e}_1 – \bar{e}_2 . The onset of percolation and pore closure, as predicted by the second-order estimate, have also been included in the figure for completeness. 116
- 4.12 Macroscopic onset-of-failure surface, as determined by the loss of strong ellipticity of the second-order estimate, for a porous elastomer with random, isotropic distribution of voids and compressible Neo-Hookean matrix phase. The results are shown in principal strain space \bar{e}_1 – \bar{e}_2 . The boundary at which the porosity vanishes, as predicted by the second-order estimate, has also been included in the figure for completeness. 117
- 4.13 Loading orientation influence on the macroscopic onset-of-failure surfaces, in principal logarithmic strain space, for a Neo-Hookean elastomer with an initial square (SQ) distribution of pores subjected to macroscopic loadings that are aligned ($\bar{\theta} = 0$) and at an angle ($\bar{\theta} = 10^\circ$) with respect to the principal axes of the microstructure. 118
- 5.1 Comparisons of the effective response, as predicted by the second-order estimate (SOE) (5.16), with the exact results (Hashin, 1985), of a porous elastomer with incompressible matrix phase subjected to hydrostatic tension and compression ($\bar{\lambda}_1 = \bar{\lambda}_2 = \bar{\lambda}_3 = \bar{\lambda}$). The results correspond to a material with Neo-Hookean matrix phase and various values of initial porosity f_0 , and are shown as a function of the logarithmic strain $\bar{e} = \ln \bar{\lambda}$. (a) The normalized macroscopic stress $\bar{S}/\mu = \mu^{-1} \partial \hat{\Phi}^I / \partial \bar{\lambda}_1 = \mu^{-1} \partial \hat{\Phi}^I / \partial \bar{\lambda}_2 = \mu^{-1} \partial \hat{\Phi}^I / \partial \bar{\lambda}_3$. (b) The evolution of the porosity f 133
- 5.2 Effective response, as predicted by the second-order estimate (SOE) (13) and the DPB model (5.12), of a porous elastomer with incompressible matrix phase subjected to hydrostatic loading ($\bar{\lambda}_1 = \bar{\lambda}_2 = \bar{\lambda}_3 = \bar{\lambda}$). The results correspond to a material with Neo-Hookean matrix phase and initial porosity of $f_0 = 30\%$, and are shown as a function of the logarithmic strain $\bar{e} = \ln \bar{\lambda}$. (a) The non-zero components ($i, j \in \{1, 2, 3\}$, $i \neq j$, no summation) of the effective incremental modulus $\hat{\mathcal{L}}$ —written with respect to the Lagrangian principal axes—for hydrostatic compression ($\bar{\lambda} \leq 1$). (b) The corresponding results for hydrostatic tension ($\bar{\lambda} \geq 1$). 135

- 5.3 Hydrostatic compression ($\bar{\lambda}_1 = \bar{\lambda}_2 = \bar{\lambda}_3 = \bar{\lambda} \leq 1$) of a porous elastomer with incompressible, Neo-Hookean matrix phase. (a) The critical stretch $\bar{\lambda}_{crit}$ at which the second-order estimate (5.16) loses strong ellipticity as a function of initial porosity f_0 . (b) The associated normalized critical stress \bar{S}_{crit}/μ . The isolated data points in the plots correspond to experimental results for the critical buckling of spherical shells under hydrostatic compression (Wesolowski, 1967). 137
- 5.4 Effective response, as predicted by the second-order estimate (5.16), of a porous rubber subjected to biaxial tension and compression ($\bar{\lambda}_2 = \bar{\lambda}_3 = \bar{\lambda}$, $\bar{S}_{11} = \partial\hat{\Phi}^I/\partial\bar{\lambda}_1 = 0$), as a function of the logarithmic strain $\bar{e} = \ln\bar{\lambda}$. The results correspond to a material with incompressible, Gent matrix with lock-up parameter $J_m = 50$ and various values of initial porosity f_0 . (a) The normalized macroscopic stress $\bar{S}_{bi}/\mu = \mu^{-1}\partial\hat{\Phi}^I/\partial\bar{\lambda}_2 = \mu^{-1}\partial\hat{\Phi}^I/\partial\bar{\lambda}_3$. (b) The lateral strain $\bar{e}_{lat} = \ln\bar{\lambda}_1$ 140
- 5.5 Biaxial tension and compression ($\bar{\lambda}_2 = \bar{\lambda}_3 = \bar{\lambda}$, $\bar{S}_{11} = \partial\hat{\Phi}^I/\partial\bar{\lambda}_1 = 0$) of a porous elastomer with incompressible, Gent matrix phase with lock-up parameter $J_m = 50$ and various values of initial porosity f_0 . (a) The evolution of porosity f , as predicted by the second-order estimate (5.16), compared with the exact result. (b) The evolution of the aspect ratios ω_1 and ω_2 as predicted by the second-order estimate (5.16). 141
- 5.6 Effective response, as predicted by the second-order estimate (13), of a porous elastomer with incompressible matrix phase subjected to biaxial tension and compression ($\bar{\lambda}_2 = \bar{\lambda}_3 = \bar{\lambda}$, $\bar{S}_{11} = \partial\hat{\Phi}^I/\partial\bar{\lambda}_1 = 0$). The results correspond to a material with Gent matrix phase ($J_m = 50$) and initial porosity of $f_0 = 30\%$, and are shown as a function of the logarithmic strain $\bar{e} = \ln\bar{\lambda}$. The normal and shear principal components of the effective incremental modulus $\hat{\mathcal{L}}$ for: (a) biaxial compression ($\bar{\lambda} \leq 1$), and (b) biaxial tension ($\bar{\lambda} \geq 1$). 142
- 5.7 Biaxial tension and compression ($\bar{\lambda}_2 = \bar{\lambda}_3 = \bar{\lambda}$, $\bar{S}_{11} = \partial\hat{\Phi}^I/\partial\bar{\lambda}_1 = 0$) of a porous elastomer with incompressible, Neo-Hookean matrix phase with various values of initial porosity f_0 . (a) The critical stretch $\bar{\lambda}_{crit}$ at which the second-order estimate (5.16) loses strong ellipticity as a function of initial porosity f_0 . (b) The corresponding critical stress \bar{S}_{crit}/μ . 144
- 5.8 Effective response, as predicted by the second-order estimate (5.16), of a porous rubber subjected to uniaxial tension and compression ($\bar{\lambda}_1 = \bar{\lambda}$, $\bar{S}_{22} = \partial\hat{\Phi}^I/\partial\bar{\lambda}_2 = \bar{S}_{33} = \partial\hat{\Phi}^I/\partial\bar{\lambda}_3 = 0$), as a function of the logarithmic strain $\bar{e} = \ln\bar{\lambda}$. The results correspond to a material with incompressible, Gent matrix phase with $J_m = 50$ and various values of initial porosity f_0 . (a) The normalized macroscopic stress $\bar{S}_{uni}/\mu = \mu^{-1}\partial\hat{\Phi}^I/\partial\bar{\lambda}_1$. (b) The lateral strain $\bar{e}_{lat} = \ln\bar{\lambda}_2 = \ln\bar{\lambda}_3$ 145
- 5.9 Uniaxial tension and compression ($\bar{\lambda}_1 = \bar{\lambda}$, $\bar{S}_{22} = \partial\hat{\Phi}^I/\partial\bar{\lambda}_2 = \bar{S}_{33} = \partial\hat{\Phi}^I/\partial\bar{\lambda}_3 = 0$) of a porous elastomer with incompressible, Gent matrix phase with $J_m = 50$ and various values of initial porosity f_0 . (a) The evolution of porosity f , as predicted by the second-order estimate (5.16), compared with the exact result. (b) The evolution of the aspect ratios ω_1 and ω_2 as predicted by second-order estimate (5.16). 146

- 5.10 Macroscopic onset-of-failure surface, as determined by the loss of strong ellipticity of the second-order estimate (5.16), for a porous elastomer with incompressible, Neo-Hookean matrix phase and various values of initial porosity. Part (a) illustrates the results for applied axisymmetric deformations ($\bar{e}_3 = \bar{e}_2$) in the \bar{e}_1 - \bar{e}_2 -plane in strain space. Part (b) shows corresponding results for applied axisymmetric stresses ($\bar{S}_{33} = \bar{S}_{22}$) in the \bar{S}_{11} - \bar{S}_{22} -plane in dimensionless stress space. 147
- 5.11 Macroscopic onset-of-failure surface, as determined by the loss of strong ellipticity of the second-order estimates (5.13) and (5.16), for a porous elastomer with Neo-Hookean matrix phase and two values of compressibility ratio of the matrix phase. Part (a) illustrates the results for applied axisymmetric deformations ($\bar{e}_3 = \bar{e}_2$) in the \bar{e}_1 - \bar{e}_2 -plane in strain space. Part (b) shows corresponding results for applied axisymmetric stresses ($\bar{S}_{33} = \bar{S}_{22}$) in the \bar{S}_{11} - \bar{S}_{22} -plane in dimensionless stress space. 149
- 5.12 Effective response of a porous rubber with an incompressible, Gent matrix phase subjected to pure shear ($\bar{\lambda}_1 = \bar{\lambda}$, $\bar{\lambda}_2 = \bar{\lambda}^{-1}$, $\bar{\lambda}_3 = 1$), as a function of the logarithmic strain $\bar{e} = \ln \bar{\lambda}$. (a) The normalized effective stored-energy function $\hat{\Phi}^I/\mu$ as predicted by the second-order estimate (5.16) and the Voigt bound (5.7). (b) The evolution of the aspect ratios of the underlying pores, ω_1 and ω_2 . Part (b) also includes the aspect ratios as predicted by the DPB model (5.12). 150
- 5.13 Effective response of a porous rubber with an incompressible Gent matrix phase subjected to pure shear ($\bar{\lambda}_1 = \bar{\lambda}$, $\bar{\lambda}_2 = \bar{\lambda}^{-1}$, $\bar{\lambda}_3 = 1$), as a function of the logarithmic strain $\bar{e} = \ln \bar{\lambda}$. (a) The normalized macroscopic stress \bar{S}_{11}/μ . (b) The normalized macroscopic stress \bar{S}_{22}/μ . 151
- 5.14 Effective response of a porous rubber subjected to plane-strain tension ($\bar{\lambda}_1 = \bar{\lambda} \geq 1$, $\bar{S}_{22} = \partial\hat{\Phi}^I/\partial\bar{\lambda}_2 = 0$, $\bar{\lambda}_3 = 1$), as a function of the logarithmic strain $\bar{e} = \ln \bar{\lambda}$. Comparisons between the SOE predictions, the Danielsson-Parks-Boyce model (DPB), and FEM results for a material with incompressible, Neo-Hookean matrix phase and various values of initial porosity f_0 . (a) The normalized macroscopic Cauchy stress $\bar{T}/\mu = \mu^{-1}(1/\bar{\lambda}_2)\partial\hat{\Phi}^I/\partial\bar{\lambda}_1$. (b) The lateral strain $\bar{e}_{lat} = \ln \bar{\lambda}_2$ 152
- 5.15 Effective response of a porous rubber subjected to plane-strain compression ($\bar{\lambda}_1 = \bar{\lambda} \leq 1$, $\bar{S}_{22} = \partial\hat{\Phi}^I/\partial\bar{\lambda}_2 = 0$, $\bar{\lambda}_3 = 1$), as a function of the logarithmic strain $\bar{e} = \ln \bar{\lambda}$. Comparisons between the SOE and the Danielsson-Parks-Boyce (DPB) predictions for a material with incompressible, Neo-Hookean matrix phase and various values of initial porosity f_0 . (a) The normalized macroscopic Cauchy stress $\bar{T}/\mu = \mu^{-1}(1/\bar{\lambda}_2)\partial\hat{\Phi}^I/\partial\bar{\lambda}_1$. (b) The lateral strain $\bar{e}_{lat} = \ln \bar{\lambda}_2$ 154
- 5.16 Plane-strain tension and compression ($\bar{\lambda}_1 = \bar{\lambda}$, $\bar{S}_{22} = \partial\hat{\Phi}^I/\partial\bar{\lambda}_2 = 0$, $\bar{\lambda}_3 = 1$) of a porous elastomer with incompressible, Neo-Hookean matrix phase with various values of initial porosity f_0 . Comparisons between the SOE and the Danielsson-Parks-Boyce (DPB) predictions for: (a) the evolution of porosity f , and (b) the evolution of the aspect ratios ω_1 and ω_2 155

5.17	Macroscopic onset-of-failure surface, as determined by the loss of strong ellipticity of the second-order estimate (5.16), for a porous elastomer with incompressible, Neo-Hookean matrix phase and various values of initial porosity under plane-strain loading ($\bar{e}_3 = 0$). (a) Failure surface in strain space. (b) The corresponding failure surface in dimensionless stress space.	156
6.1	Reference configuration depiction of a laminate with lamination direction $\mathbf{N} = \mathbf{e}_1$ relative to the fixed laboratory frame of reference $\{\mathbf{e}_i\}$	170
6.2	Schematic representation of the evolution of the direction of lamination along a loading path with macroscopic deformation gradient $\bar{\mathbf{F}}$	178
6.3	Schematic representation of: (a) the applied boundary conditions, and (b) the evolution of the lamination direction. In (b), the colored rectangle represents a typical layer with normal \mathbf{N} in the undeformed configuration; the dashed rectangle corresponds to the same layer in the deformed configuration, with current lamination direction \mathbf{n}	179
6.4	Effective behavior of a hyperelastic laminate with compressible Neo-Hookean phases subjected to aligned pure shear loading ($\bar{\theta} = 90^\circ$). (a) The macroscopic stress $d\widehat{W}/d\bar{\lambda}$ for various values of initial volume fraction of the stiffer phase, c_0 , as a function of the logarithmic strain $\bar{e} = \ln \bar{\lambda}$. (b) The critical stretch, $\bar{\lambda}_{crit}$, at which the homogenized laminate loses strong ellipticity for various values of the contrast $t = \mu^{(2)}/\mu^{(1)} = \kappa^{(2)}/\kappa^{(1)}$, as a function of the initial volume fraction c_0	180
6.5	Effective behavior of a hyperelastic laminate subjected to pure shear loading at various angles $\bar{\theta}$ (in the <i>large</i> deformation regime). The results correspond to compressible Neo-Hookean phases with contrast $t = \mu^{(2)}/\mu^{(1)} = \kappa^{(2)}/\kappa^{(1)} = 20$, initial volume fraction of the stiffer phase $c_0 = 30\%$, and are shown as a function of the macroscopic stretch $\bar{\lambda}$. (a) The macroscopic stress $d\widehat{W}/d\bar{\lambda}$. (b) The angle of rotation of layers ϕ	182
6.6	Effective behavior of a hyperelastic laminate subjected to pure shear loading at various angles $\bar{\theta}$ (in the <i>small</i> deformation regime). The results correspond to compressible Neo-Hookean phases with contrast $t = \mu^{(2)}/\mu^{(1)} = \kappa^{(2)}/\kappa^{(1)} = 20$, initial volume fraction of the stiffer phase $c_0 = 30\%$, and are shown as a function of the macroscopic stretch $\bar{\lambda}$. (a) The macroscopic stress $d\widehat{W}/d\bar{\lambda}$. (b) The angle of rotation of layers ϕ	184
6.7	Pure shear loading of Neo-Hookean laminates. (a) The critical stretch, $\bar{\lambda}_{crit}$, at which loss of strong ellipticity takes place for various values of the contrast $t = \mu^{(2)}/\mu^{(1)} = \kappa^{(2)}/\kappa^{(1)}$, as a function of the loading angle $\bar{\theta}$. (b) The corresponding results for $\bar{\lambda}_{crit}$ for various values of the loading angle $\bar{\theta}$, as a function of the contrast t	185

- 7.1 Schematic representation of the microstructure of a fiber-reinforced elastomer, depicting the applied loading and the various microstructural variables. (a) The 1-2 cross section of the composite together with the applied loading conditions. (b) The shaded ellipse represents the 1-2 cross section of a typical fiber with initial aspect ratio $\omega_0 = z_2^0/z_1^0$ in the reference configuration; the dashed ellipse corresponds to the 1-2 cross-section of the same fiber in the deformed configuration, with current aspect ratio $\omega = z_2/z_1$ and current orientation relative to the fixed laboratory frame given by ϕ 189
- 7.2 Effective response, as predicted by the second-order (SOE) and the exact result for sequentially laminated materials (deBotton), of a rigidly reinforced elastomer subjected to *pure shear* loading. The results correspond to an incompressible Neo-Hookean matrix phase and various values of the reinforcement concentration c , and are shown as a function of the principal macroscopic stretch $\bar{\lambda}$. (a) The effective stored-energy function \widehat{W} . (b) The corresponding stress $\bar{S} = d\widehat{W}/d\bar{\lambda}$ 202
- 7.3 Second-order estimates for the effective behavior of elastomers reinforced with rigid fibers of circular cross section subjected to *pure shear* loading. The results correspond to an incompressible Gent matrix phase with given matrix lock-up parameter $J_m = 50$ and various values of the fiber concentration c , and are shown as a function of the principal macroscopic stretch $\bar{\lambda}$. (a) The effective stored-energy function \widehat{W} . (b) The corresponding stress $\bar{S} = d\widehat{W}/d\bar{\lambda}$ 203
- 7.4 Second-order estimates for the effective behavior of elastomers reinforced with rigid fibers of circular cross section subjected to *pure shear* loading. The results correspond to an incompressible Gent matrix phase with $c = 30\%$ and various values of the matrix lock-up parameter J_m , and are shown as a function of the principal macroscopic stretch $\bar{\lambda}$. (a) The effective stored-energy function \widehat{W} . (b) The corresponding stress $\bar{S} = d\widehat{W}/d\bar{\lambda}$ 204
- 7.5 Second-order estimates for the macroscopic stretch $\bar{\lambda}_{lock}$ at which an (in-plane) isotropic rigidly reinforced incompressible Gent elastomer locks up. (a) $\bar{\lambda}_{lock}$ as a function of fiber concentration c for various values of the matrix lock-up parameter J_m . (b) $\bar{\lambda}_{lock}$ as a function of J_m for various values of c 205
- 7.6 Second-order estimates for the effective behavior of rigidly reinforced elastomers subjected to aligned pure shear loading ($\bar{\theta} = 0^\circ$). The results correspond to an incompressible, Neo-Hookean matrix phase with given fiber concentration $c = 30\%$, and various values of the fiber aspect ratio ω , and are shown as a function of the principal macroscopic stretch $\bar{\lambda}$. (a) The effective stored-energy function \widehat{W} . (b) The corresponding stress $\bar{S} = d\widehat{W}/d\bar{\lambda}$. . . 206
- 7.7 Aligned pure shear loading ($\bar{\theta} = 0^\circ$) of a rigidly reinforced, incompressible, Neo-Hookean elastomer. (a) The critical stretch $\bar{\lambda}_{crit}$ at which loss of strong ellipticity of the homogenized elastomer takes place for various fiber concentrations as a function of the aspect ratio of the fibers ω . (b) The critical stretch $\bar{\lambda}_{crit}$ for various aspect ratios as a function of the concentration of fibers c 207

- 7.8 Aligned pure shear loading ($\bar{\theta} = 0^\circ$) of rigidly reinforced elastomers. (a) The critical stretch $\bar{\lambda}_{crit}$ at which loss of strong ellipticity of a rigidly reinforced, incompressible, Gent elastomer takes place for various values of the lock-up parameter J_m as a function of the aspect ratio of the fibers ω . (b) The corresponding critical stretch $\bar{\lambda}_{crit}$ for a rigidly reinforced, compressible, Neo-Hookean elastomer, at various values of the bulk modulus $\kappa^{(1)}$, as a function of the aspect ratio of the fibers ω 209
- 7.9 Second-order estimates for the effective behavior of rigidly reinforced elastomer subjected to pure shear loading at a fixed angle ($\bar{\theta} = 20^\circ$). The results correspond to an incompressible, Neo-Hookean, matrix phase with given fiber concentration $c = 30\%$, and various values of the fiber aspect ratio ω , and are shown as a function of the principal macroscopic stretch $\bar{\lambda}$. (a) The effective stress $\bar{S} = d\widehat{W}/d\bar{\lambda}$. (b) The angle of rotation of the fibers ϕ 210
- 7.10 Second-order estimates for the effective behavior of rigidly reinforced elastomer subjected to pure shear loading at various angles $\bar{\theta}$ (in the large deformation regime). The results correspond to an incompressible, Neo-Hookean matrix phase with given fiber concentration $c = 30\%$ and aspect ratio $\omega = 2$, and are shown as a function of the principal macroscopic stretch $\bar{\lambda}$. (a) The effective stress $\bar{S} = d\widehat{W}/d\bar{\lambda}$. (b) The average angle of rotation of the fibers ϕ 211
- 7.11 Second-order estimates for the effective behavior of rigidly reinforced elastomer subjected to pure shear loading at various angles $\bar{\theta}$ (in the small deformation regime). The results correspond to an incompressible, Neo-Hookean matrix phase with given fiber concentration $c = 30\%$ and aspect ratio $\omega = 2$, and are shown as a function of the principal macroscopic stretch $\bar{\lambda}$. (a) The effective stress $\bar{S} = d\widehat{W}/d\bar{\lambda}$. (b) The average angle of rotation of the fibers ϕ 213
- 7.12 Pure shear loading of rigidly reinforced elastomers. (a) The critical stretch $\bar{\lambda}_{crit}$ at which loss of strong ellipticity of a rigidly reinforced, incompressible, Neo-Hookean elastomer takes place for various loading angles $\bar{\theta}$, as a function of the aspect ratio of the fibers ω . (b) The corresponding results for $\bar{\lambda}_{crit}$ for various values of the aspect ratio of the fiber as a function of the angle of loading $\bar{\theta}$ 214
- 7.13 Second-order estimates for the effective behavior of reinforced elastomers subjected to aligned pure shear loading ($\bar{\theta} = 0^\circ$). The results correspond to a compressible, Neo-Hookean matrix reinforced with an initial volume fraction of 30% of stiffer, Neo-Hookean fibers of initially elliptical cross section. (a) The effective stress $\bar{S} = d\widehat{W}/d\bar{\lambda}$ for contrasts of $t = \mu^{(2)}/\mu^{(1)} = \kappa^{(2)}/\kappa^{(1)} = 10$ and various aspect ratios, as a function of the applied stretch $\bar{\lambda}$. (b) The critical stretch $\bar{\lambda}_{crit}$ at which loss of strong ellipticity of the homogenized reinforced elastomer takes place for various fiber aspect ratios, as a function of the contrast t . 215

- 7.14 Aligned pure shear loading ($\bar{\theta} = 0^\circ$) of a compressible, Neo-Hookean elastomer reinforced with stiffer Neo-Hookean fibers of initially elliptical cross section. Results are shown for a contrast of $t = \mu^{(2)}/\mu^{(1)} = \kappa^{(2)}/\kappa^{(1)} = 10$, various initial fiber aspect ratios, and initial fiber concentration of 30%, as a function of the applied stretch $\bar{\lambda}$. (a) The evolution of the volume fraction of the fibers. (b) The evolution of the aspect ratio of the fibers. 217
- 7.15 Second-order estimates for the effective behavior of rigidly reinforced elastomers subjected to simple shear “perpendicular” to the fibers. The results correspond to an incompressible, Neo-Hookean, matrix phase with fiber concentration $c = 30\%$ and various values of the fiber aspect ratio ω , and are shown as a function of the applied macroscopic shear $\bar{\gamma}$. (a) The effective stress $\bar{\tau} = d\widehat{W}/d\bar{\gamma}$. (b) The average angle of rotation of the fibers ϕ 218
- 7.16 Second-order estimates for the effective behavior of rigidly reinforced elastomers subjected to simple shear “parallel” to the fibers. The results correspond to an incompressible Neo-Hookean matrix phase with fiber concentration $c = 30\%$ and various values of the fiber aspect ratio ω , and are shown as a function of the applied macroscopic shear $\bar{\gamma}$. (a) The effective stress $\bar{\tau} = d\widehat{W}/d\bar{\gamma}$. (b) The average angle of rotation of the fibers ϕ 219
- 8.1 Undeformed configuration depiction of: (a) periodic square and (b) periodic hexagonal arrangement of circular fibers. 229
- 8.2 Effective response, as predicted by the second-order estimate (SOE) and the Voigt bound, of a fiber-reinforced elastomer subjected to “tensile” axisymmetric shear: $\bar{\mathbf{F}} = \bar{\lambda}_1 \mathbf{e}_1 \otimes \mathbf{e}_1 + \bar{\lambda}_2 \mathbf{e}_2 \otimes \mathbf{e}_2 + \bar{\lambda}_3 \mathbf{e}_3 \otimes \mathbf{e}_3$ with $\bar{\lambda}_3 = \bar{\lambda} \geq 1$ and $\bar{\lambda}_1 = \bar{\lambda}_2 = \bar{\lambda}^{-1/2}$. The results correspond to Gent phases with compressibility ratios $\kappa^{(1)}/\mu^{(1)} = \kappa^{(2)}/\mu^{(2)} = 50$, contrast $t = \mu^{(2)}/\mu^{(1)} = 20$, and various values of initial volume fraction of fibers c_0 , and are shown as a function of the logarithmic strain $\bar{e} = \ln \bar{\lambda}$. (a) The normalized effective stored-energy function $\widehat{W}/\mu^{(1)}$. (b) The normalized stress component $\bar{S}_{33}/\mu^{(1)} = (1/\mu^{(1)})\partial\widehat{W}/\partial\bar{F}_{33}$ 236
- 8.3 Effective response of a fiber-reinforced elastomer subjected to “compressive” axisymmetric shear: $\bar{\mathbf{F}} = \bar{\lambda}_1 \mathbf{e}_1 \otimes \mathbf{e}_1 + \bar{\lambda}_2 \mathbf{e}_2 \otimes \mathbf{e}_2 + \bar{\lambda}_3 \mathbf{e}_3 \otimes \mathbf{e}_3$ with $\bar{\lambda}_3 = \bar{\lambda} \leq 1$ and $\bar{\lambda}_1 = \bar{\lambda}_2 = \bar{\lambda}^{-1/2}$. The results correspond to Gent phases with compressibility ratios $\kappa^{(1)}/\mu^{(1)} = \kappa^{(2)}/\mu^{(2)} = 50$, contrast $t = \mu^{(2)}/\mu^{(1)} = 20$, and various values of initial volume fraction of fibers c_0 , and are shown as a function of the logarithmic strain $\bar{e} = \ln \bar{\lambda}$. (a) The normalized effective stored-energy function $\widehat{W}/\mu^{(1)}$. (b) The normalized stress component $\bar{S}_{33}/\mu^{(1)} = (1/\mu^{(1)})\partial\widehat{W}/\partial\bar{F}_{33}$. 237
- 8.4 Axisymmetric shear ($\bar{\mathbf{F}} = \bar{\lambda}^{-1/2} \mathbf{e}_1 \otimes \mathbf{e}_1 + \bar{\lambda}^{-1/2} \mathbf{e}_2 \otimes \mathbf{e}_2 + \bar{\lambda} \mathbf{e}_3 \otimes \mathbf{e}_3$) of a Gent elastomer reinforced with aligned, cylindrical Gent fibers distributed periodically in a hexagonal arrangement (HA). (a) The critical strain $\bar{e}_{crit} = \ln \bar{\lambda}_{crit}$ at which the homogenized fiber-reinforced elastomer loses strong ellipticity for two values of the contrast $t = \mu^{(2)}/\mu^{(1)}$, as a function of the initial volume fraction of fibers c_0 . (b) The critical strain \bar{e}_{crit} for various values of the compressibility ratios $\kappa^{(1)}/\mu^{(1)} = \kappa^{(2)}/\mu^{(1)}$, as a function of the contrast t 239

- 8.5 In-plane pure shear (aligned $\bar{\mathbf{F}} = \bar{\lambda} \mathbf{e}_1 \otimes \mathbf{e}_1 + \bar{\lambda}^{-1} \mathbf{e}_2 \otimes \mathbf{e}_2 + \mathbf{e}_3 \otimes \mathbf{e}_3$ and at a 45° angle $\bar{\mathbf{F}} = (\bar{\lambda} + \bar{\lambda}^{-1})/2(\mathbf{e}_1 \otimes \mathbf{e}_1 + \mathbf{e}_2 \otimes \mathbf{e}_2) + (\bar{\lambda} - \bar{\lambda}^{-1})/2(\mathbf{e}_1 \otimes \mathbf{e}_2 + \mathbf{e}_2 \otimes \mathbf{e}_1) + \mathbf{e}_3 \otimes \mathbf{e}_3$) of a fiber-reinforced elastomer. The results, which are given for periodic square (SA and SA_{45}) and hexagonal (HA) arrangement of fibers, correspond to Gent phases with compressibility ratios $\kappa^{(1)}/\mu^{(1)} = 50$ and $\kappa^{(2)}/\mu^{(2)} = 30$, contrast $t = \mu^{(2)}/\mu^{(1)} = 50$, and fiber volume fraction $c_0 = 25\%$, and are shown as a function of the logarithmic strain $\bar{e} = \ln \bar{\lambda}$. (a) The normalized effective stored-energy function $\widehat{W}/\mu^{(1)}$. (b) The normalized stress components $\bar{S}_{11}/\mu^{(1)}$, $\bar{S}_{22}/\mu^{(1)}$, $\bar{S}_{33}/\mu^{(1)}$ written with respect to the macroscopic Lagrangian principal axes. 241
- 8.6 In-plane aligned pure shear ($\bar{\mathbf{F}} = \bar{\lambda} \mathbf{e}_1 \otimes \mathbf{e}_1 + \bar{\lambda}^{-1} \mathbf{e}_2 \otimes \mathbf{e}_2 + \mathbf{e}_3 \otimes \mathbf{e}_3$) of a fiber-reinforced Gent elastomer with an initially hexagonal arrangement (HA) of fibers. The results correspond to compressibility ratios $\kappa^{(1)}/\mu^{(1)} = 50$, $\kappa^{(2)}/\mu^{(2)} = 30$, contrast $t = \mu^{(2)}/\mu^{(1)} = 50$, and initial volume fractions $c_0 = 15, 25$ and 35% . The normalized stress components $\bar{S}_{11}/\mu^{(1)}$, $\bar{S}_{22}/\mu^{(1)}$, $\bar{S}_{33}/\mu^{(1)}$ for: (a) pure shear compression $\bar{e} \leq 0$, and (b) pure shear tension $\bar{e} \geq 0$. 244
- 8.7 In-plane aligned pure shear ($\bar{\mathbf{F}} = \bar{\lambda} \mathbf{e}_1 \otimes \mathbf{e}_1 + \bar{\lambda}^{-1} \mathbf{e}_2 \otimes \mathbf{e}_2 + \mathbf{e}_3 \otimes \mathbf{e}_3$) of a fiber-reinforced Gent elastomer with an initially hexagonal arrangement (HA) of fibers. The results correspond to compressibility ratios $\kappa^{(1)}/\mu^{(1)} = 50$, $\kappa^{(2)}/\mu^{(2)} = 30$, initial volume fraction $c_0 = 0.25$ and shear contrasts $t = \mu^{(2)}/\mu^{(1)} = 5, 50, 150$. The normalized stress components $\bar{S}_{11}/\mu^{(1)}$, $\bar{S}_{22}/\mu^{(1)}$, $\bar{S}_{33}/\mu^{(1)}$ for: (a) pure shear compression $\bar{e} \leq 0$, and (b) pure shear tension $\bar{e} \geq 0$. 245
- 8.8 In-plane aligned pure shear ($\bar{\mathbf{F}} = \bar{\lambda} \mathbf{e}_1 \otimes \mathbf{e}_1 + \bar{\lambda}^{-1} \mathbf{e}_2 \otimes \mathbf{e}_2 + \mathbf{e}_3 \otimes \mathbf{e}_3$) of fiber-reinforced Gent elastomers with initially square (SA) and hexagonal (HA) arrangements of fibers. (a) The critical strain $\bar{e}_{crit} = \ln \bar{\lambda}_{crit}$ at which the homogenized fiber-reinforced elastomer loses strong ellipticity, as a function of the initial volume fraction of fibers c_0 . (b) The critical strain \bar{e}_{crit} as a function of the shear contrast $t = \mu^{(2)}/\mu^{(1)}$. The results are given for various values of compressibility ratios $\kappa^{(1)}/\mu^{(1)}$ and $\kappa^{(2)}/\mu^{(2)}$ 247
- 8.9 In-plane simple shear ($\bar{\mathbf{F}} = \mathbf{e}_1 \otimes \mathbf{e}_1 + \mathbf{e}_2 \otimes \mathbf{e}_2 + \mathbf{e}_3 \otimes \mathbf{e}_3 + \bar{\gamma} \mathbf{e}_1 \otimes \mathbf{e}_2$) of a fiber-reinforced elastomer. The results, which are given for periodic square (SA) and hexagonal (HA) distributions of fibers, correspond to Gent phases with compressibility ratios $\kappa^{(1)}/\mu^{(1)} = 50$ and $\kappa^{(2)}/\mu^{(2)} = 30$. The normalized effective shear stress $\bar{S}_{12}/\mu^{(1)} = (1/\mu^{(1)})\partial\widehat{W}/\partial\bar{\gamma}$, as a function of the amount of shear $\bar{\gamma}$ for: (a) contrast $t = \mu^{(2)}/\mu^{(1)} = 50$ and various initial volume fractions c_0 , and (b) for initial volume fraction $c_0 = 25\%$ and various values of the contrast t 248

- 8.10 In-plane pre-compressed simple shear ($\bar{\mathbf{F}} = \mathbf{e}_1 \otimes \mathbf{e}_1 + 3/5\mathbf{e}_2 \otimes \mathbf{e}_2 + \mathbf{e}_3 \otimes \mathbf{e}_3 + \bar{\gamma}\mathbf{e}_1 \otimes \mathbf{e}_2$) of a fiber-reinforced elastomer. The results, which are given for periodic square (*SA*) and hexagonal (*HA*) distributions of fibers, correspond to Gent phases with compressibility ratios $\kappa^{(1)}/\mu^{(1)} = 5$ and $\kappa^{(2)}/\mu^{(2)} = 30$, contrast $t = 50$, and initial volume fraction of fibers $c_0 = 11$ and 25%. (a) The normalized effective shear stress $\bar{S}_{12}/\mu^{(1)} = (1/\mu^{(1)})\partial\widehat{W}/\partial\bar{\gamma}$, as a function of the applied amount of shear $\bar{\gamma}$. (b) Schematic representation of the evolution of the distribution of fibers upon loading. 249
- 8.11 Effective response of Gent fiber-reinforced elastomers subjected to “tensile” out-of-plane pure shear: $\bar{\mathbf{F}} = \bar{\lambda}_1 \mathbf{e}_1 \otimes \mathbf{e}_1 + \bar{\lambda}_2 \mathbf{e}_2 \otimes \mathbf{e}_2 + \bar{\lambda}_3 \mathbf{e}_3 \otimes \mathbf{e}_3$ with $\bar{\lambda}_3 = \bar{\lambda} \geq 1$, $\bar{\lambda}_1 = \bar{\lambda}^{-1}$, and $\bar{\lambda}_2 = 1$. Results are shown for compressibility ratios $\kappa^{(1)}/\mu^{(1)} = \kappa^{(2)}/\mu^{(2)} = 50$, contrast $t = \mu^{(2)}/\mu^{(1)} = 20$, and various values of initial volume fraction of fibers c_0 , as a function of the logarithmic strain $\bar{e} = \ln \bar{\lambda}$. (a) The normalized effective stored-energy function $\widehat{W}/\mu^{(1)}$. (b) The normalized stress components $\bar{S}_{11}/\mu^{(1)}$, $\bar{S}_{22}/\mu^{(1)}$, $\bar{S}_{33}/\mu^{(1)}$ 251
- 8.12 Effective response of Gent fiber-reinforced elastomers subjected to “compressive” out-of-plane pure shear: $\bar{\mathbf{F}} = \bar{\lambda}_1 \mathbf{e}_1 \otimes \mathbf{e}_1 + \bar{\lambda}_2 \mathbf{e}_2 \otimes \mathbf{e}_2 + \bar{\lambda}_3 \mathbf{e}_3 \otimes \mathbf{e}_3$ with $\bar{\lambda}_3 = \bar{\lambda} \leq 1$, $\bar{\lambda}_1 = \bar{\lambda}^{-1}$, and $\bar{\lambda}_2 = 1$. Results are shown for compressibility ratios $\kappa^{(1)}/\mu^{(1)} = \kappa^{(2)}/\mu^{(2)} = 50$, contrast $t = \mu^{(2)}/\mu^{(1)} = 20$, and various values of initial volume fraction of fibers c_0 , as a function of the logarithmic strain $\bar{e} = \ln \bar{\lambda}$. (a) The normalized effective stored-energy function $\widehat{W}/\mu^{(1)}$. (b) The normalized stress components $\bar{S}_{11}/\mu^{(1)}$, $\bar{S}_{22}/\mu^{(1)}$, $\bar{S}_{33}/\mu^{(1)}$ 252
- A.1 (a) Sketch of the *nonlinear* constitutive relation (continuous stress S vs. stretch F curve) and of its *linear approximation* (dashed line). (b) Schematic comparison of the “secant” ($\mathbf{L}_s^{(r)}$), “tangent” ($\mathbf{L}_t^{(r)}$) and *new* “generalized secant” ($\mathbf{L}_0^{(r)}$) approximations. 270
- A.2 New second-order and other estimates and bounds for the effective stored energy of a *compressible* Neo-Hookean rubber reinforced with a fixed concentration ($c = 0.3$) of aligned rigid fibers, as functions of the applied stretch λ . (a) Pure shear loading with $\bar{\lambda}_1 = \lambda$ and $\bar{\lambda}_2 = 1/\lambda$; and (b) loading with $\bar{\lambda}_1 = \lambda$ and $\bar{\lambda}_2$ such that $\bar{J}^{(1)} = 1$. The labels $\tilde{\Phi}_{HS}^{(+)}$ and $\tilde{\Phi}_{HS}^{(-)}$ correspond to the “positive” and “negative” roots of the new Hashin-Shtrikman second-order estimates, and the labels $\tilde{\Phi}_{OHS}$, $\tilde{\Phi}_R$, and $\tilde{\Phi}_{PC}$ correspond respectively to the old version (Ponte Castañeda and Tiberio, 2000) of the second-order HS estimates, the Reuss estimate and the polyconvex lower bound, respectively. 281
- A.3 Plots of the phase fluctuation measures $\hat{F}_{11}^{(1)} - \bar{F}_{11}^{(1)}$, $\hat{F}_{22}^{(1)} - \bar{F}_{22}^{(1)}$ and $\hat{J}^{(1)} - \bar{J}^{(1)}$, versus the stretch λ for the same reinforced, compressible, Neo-Hookean rubbers considered in the context of Figure A.2. (a) Pure shear loading with $\bar{\lambda}_1 = \lambda$ and $\bar{\lambda}_2 = 1/\lambda$; and (b) loading with $\bar{\lambda}_1 = \lambda$ and $\bar{\lambda}_2$ such that $\bar{J}^{(1)} = 1$ 283

A.4	Plots of the new (positive-root only) and old second-order predictions for the effective response of an <i>incompressible</i> Neo-Hookean rubber reinforced with various concentrations c of aligned rigid fibers, and loaded in pure shear with $\bar{\lambda}_1 = \lambda$ and $\bar{\lambda}_2 = 1/\lambda$. (a) The stored-energy functions $\tilde{\Phi}_{HS}^I$ and $\tilde{\Phi}_{OHS}^A$; and (b) the corresponding stresses $S = d\tilde{\Phi}_{HS}^I/d\lambda$ and $d\tilde{\Phi}_{OHS}^A/d\lambda$, both as functions of the applied stretch λ	284
A.5	Plots of the phase fluctuations variable $\hat{\mathbf{F}}^{(1)}$ versus the stretch λ for an <i>incompressible</i> Neo-Hookean rubber reinforced with $c = 0.3$ concentration of aligned rigid fibers, and loaded in pure shear with $\bar{\lambda}_1 = \lambda$ and $\bar{\lambda}_2 = 1/\lambda$. (a) The four non-zero components of $\hat{\mathbf{F}}^{(1)}$, as well as $\hat{J}^{(1)}$; and (b) the normalized field fluctuations variables $\hat{F}_{11}^{(1)} - \bar{F}_{11}^{(1)}$, $\hat{F}_{22}^{(1)} - \bar{F}_{22}^{(1)}$ and $\hat{J}^{(1)} - \bar{J}^{(1)}$	285
A.6	Plot of μ^* as a function of the stretch λ for various concentrations c of aligned rigid fibers under pure shear loading $\bar{\lambda}_1 = \lambda$ and $\bar{\lambda}_2 = 1/\lambda$	291

Chapter 1

Introduction

Elastomeric materials are used pervasively in industry. Applications include rubber tires, shoes, flexible tubes and catheters, cable coatings, conveyor and transmission belts, balloons, shock absorbers, floatation devices, insulators, fire retardants, packaging and cushioning materials, noise abating structures, etc. In many of these applications, the elastomers are reinforced with particles and/or fibers to improve their mechanical properties and, in particular, their overall stiffness. In contrast, there are also numerous situations in which light weight and high compliance are desirable. The elastomeric materials used for such applications are then weakened with voids or softer materials.

The standard example of a reinforced elastomer is that of a rubber tire, which derives its black color from the presence of carbon-black particles that are distributed randomly in a matrix of a synthetic rubber (see, for instance, the monograph by Mark *et al.*, 2005 and the references therein). At a larger length scale, rubber tires are also reinforced with steel or other types of fibers. Other commonly used micron- and nano-sized fillers include silica, mica, talc, clay, calcium carbonate particles, as well as carbon nanotubes. In addition, there is a large class of thermoplastic polymers, which exhibit rubber-like behavior, namely, thermoplastic elastomers (TPEs). These materials are block copolymers where the “hard” glassy blocks self-aggregate into an “inclusion” phase that is embedded in a “matrix” of the “soft” rubbery blocks, thus leading to a “particulate” microstructure with an overall rubbery response (Honeker and Thomas, 1996). The hard blocks, which can appear in the form of particles (Prasman and Thomas, 1998), fibers (Honeker *et al.*, 2000), interconnected networks (Dair *et al.*, 1999), or layers (Cohen *et al.*, 2000), are distributed in a periodic arrangement, and play the role of the reinforcing phase. They are increasingly being used in industry—where they are replacing standard cross-linked rubbers in many technological

applications—due to their superior mechanical and recycling properties.

The standard example of a weakened elastomer is that of (elastomeric) foams (see the monograph by Gibson and Ashby, 1997 and the references therein). These materials are essentially made out of an elastomeric matrix in which there is a distribution—usually random—of vacuous or gas-filled inclusions. Foams can be found in an “open cell” form, in which the (vacuous) inclusions are interconnected, as in an absorbent sponge, or in a “closed cell” form, in which all the inclusions are completely surrounded by matrix phase, as in a car seat. In addition to the just-described foams, in which the vacuous or gas-filled inclusions are deliberately introduced in elastomers as part of the manufacturing process, there also other elastomeric materials in which a significant amount of porosity may be introduced unintentionally via defects or forming processes.

In many of the above-mentioned applications, the composite elastomers are subjected to large deformations. It is therefore of practical—as well as of theoretical—interest to develop constitutive models for the mechanical behavior of elastomeric composites under such loading conditions. Ideally, these models should be accurate and relatively simple, so that they are amenable to direct implementation into standard finite element packages for solving structural problems of interest. This presents a substantial challenge for at least three reasons. First, there is the strong material nonlinearity that is present in constitutive models for pure, or “neat” elastomers. Second, the mechanical behavior of elastomeric composites is known to depend critically on their underlying initial microstructure, which is by and large very complex. Indeed, more often than not, the distribution of the constituents (e.g., particles, fibers, voids) is *random*. Also, depending on the application, the relative proportions of the various phases may range from very small to very large, which evidently leads to a vast range of diverse behaviors. Finally, there is the additional complication of the evolution of the microstructure due to the finite changes in geometry induced during loading. Presumably because of the technical difficulties associated with modeling this complex behavior, most of the work in the literature to date has been based on empirical or *ad hoc* models. In the next two paragraphs, we briefly enumerate previous attempts to model the effective behavior of reinforced and porous elastomers. The list is by no means exhaustive, but merely aims to provide an overview of available methods.

In the context of reinforced elastomers, most of the modeling work has been focused on “particulate” microstructures where the reinforcing phases are *particles* of various shapes, or long cylindrical *fibers*. *Micromechanics-based* approaches for *particle* reinforced elastomers include, for

instance, models that make use of the notion of a strain-amplification factor (Mullins and Tobin, 1965; Treloar, 1975; Meinecke and Taftaf, 1988; Govindjee and Simo, 1991, Bergström and Boyce, 1999). More specifically, these models make use of the idea that the average strain in the elastomeric matrix phase of filled elastomers is larger than the applied macroscopic strain in the composite (simply because the fillers are much stiffer than the elastomeric matrix). Having selected a strain measure and determined a phenomenological amplification factor to multiply it with, the model for the reinforced elastomer is then given essentially by that of the corresponding matrix phase evaluated at the selected amplified strain. There are also recent two-dimensional (2D) *numerical simulations* based on unit-cell computations (Lahellec *et al.*, 2004), or for systems with more complex microstructures (Govindjee, 1997; Bergström and Boyce, 1999). In addition, also in the context of 2D *numerical simulations*, there is the recent work of Triantafyllidis *et al.* (2006) which—based on earlier work of Triantafyllidis and co-workers (see, e.g., Triantafyllidis and Maker, 1985; Geymonat *et al.*, 1993)—provides an in-depth analysis of the stability of reinforced elastomers at a microscopic, as well as at a macroscopic level. In connection with the above simulations, it is important to emphasize that, on one hand, they correspond to rigorous results, but that, on the other hand, they are computationally very intensive. In terms of approaches based on *homogenization*, there is the Voigt-type upper bound (Ogden, 1978), as well as some non-trivial Reuss-type lower bounds (Ponte Castañeda, 1989). Unfortunately, these bounds are microstructure-independent, and therefore not very useful in general. An *exact* result has been generated recently (deBotton, 2005) for hyperelastic composites with a very special type of microstructure known as sequentially laminated microstructures. The drawback of this result is that it is not clear whether, or not, it corresponds to filled elastomers with more realistic types of microstructures. For *fiber* reinforced elastomers, there is a voluminous literature on *phenomenological* constitutive models. In a pioneering contribution, Spencer (1972) idealized fibers as *inextensible* material line elements to develop a simple theory for *incompressible* fiber-reinforced materials that permitted the analytical treatment of numerous boundary value problems. Other (less idealized) phenomenological models are based on the idea of augmenting existing isotropic stored-energy functions with additional terms—which depend on the invariants associated with the fiber direction (Spencer, 1984)—that penalize deformation in a particular direction (see, e.g., Qiu and Pence, 1997; Merodio and Ogden, 2005; Horgan and Saccomandi, 2005). The main appeal of these phenomenological models is that they are simple. In addition, they can be “calibrated” to become

macroscopically unstable—via loss of strong ellipticity—for loading conditions where such instabilities are expected to occur from physical experience (Triantafyllidis and Abeyaratne, 1983). In spite of these desirable features, the predictive capabilities of phenomenological models for the general response of actual fiber-reinforced elastomers remain limited. Following a *micromechanics* approach, Guo *et al.* (2006) have recently proposed a hyperelastic model with incompressible Neo-Hookean matrix phases. In addition, there is also a number of *numerical* studies based on (2D) periodic microstructures which include the stability analyses of these materials (Triantafyllidis and Maker, 1985; Triantafyllidis and Nestorvić, 2005). In terms of *homogenization-based* methods, in addition, of course, to the microstructure-independent Voigt-type (Ogden, 1978) and Reuss-type (Ponte Castañeda, 1989) bounds, there is a recent estimate due to deBotton *et al.* (2006) for fiber-reinforced elastomers with incompressible Neo-Hookean phases and the *Composite Cylinder Assemblage* (CCA) microstructure of Hashin (1962). One of the strengths of this model is that it is exact for axisymmetric and out-of-plane shear loading conditions. Moreover, it should be recorded that He *et al.* (2006) have recently provided a set of non-trivial conditions—in terms of the local material properties and the applied loading conditions—for which the Voigt-type bound is attained in fiber-reinforced elastomers. Finally, it should be mentioned that constitutive models for hyperelastic solids with orthotropic material symmetry have also been developed (Bischoff *et al.*, 2002) from a *statistical mechanics* approach.

In the context of porous elastomers, most of the modeling efforts have been devoted to high-porosity elastomers (or low-density foams). Indeed, ever since the pioneering work of Gent and Thomas (1959), there have been numerous contributions concerning the modeling of the mechanical behavior of low-density foams under large deformations (see Gibson and Ashby, 1997 and the references therein). In contrast, the study of porous elastomers with low to moderate levels of porosity has not been pursued to nearly the same extent. *Phenomenological* approaches for this class of materials include, for instance, the model of Blatz and Ko (1962), which was motivated by experimental work on polyurethane rubber with a random and isotropic distribution of pores of about 40μ in diameter and an approximate volume fraction of about 50%. The predictive capabilities of this model for the response of actual porous elastomers is limited. However, the Blatz-Ko material does have a very appealing physical property: it loses strong ellipticity at sufficiently large compressive deformations (Knowles and Sternberg, 1975). This property is in

agreement with experimental evidence, as well as with *numerical* results (Abeyaratne and Triantafyllidis, 1984), suggesting that porous elastomers can develop macroscopic bands of *strain localization* at sufficiently large deformations, which correspond to buckling of the matrix ligaments at the micro scale. *Homogenization* approaches include the microstructure-independent Voigt-type bound (Ogden, 1978), some rigorous estimates for special microstructures and loading conditions (Hashin, 1985), and various *ad hoc* approximations (Feng and Christensen, 1982; Levin *et al.*, 2000). There is also a recently proposed estimate by Danielsson *et al.* (2004) for isotropic porous elastomers with incompressible, isotropic matrix phases. In fact, this estimate—as it will be discussed in Chapter 5—can be shown to be a rigorous *upper bound* for porous elastomers with incompressible matrix phases and the *Composite Sphere Assemblage* (CSA) microstructure (Hashin, 1962). In this regard, it should be noted that—admittedly a very special class of microstructure—the CSA can be considered as a fair approximation to actual microstructures in actual porous elastomers.

In this thesis, our proposal for generating homogenization estimates in finite elasticity is based on an appropriate extension of the “second-order” homogenization method proposed by Pedro Ponte Castañeda (2001; 2002a) in the context of nonlinear dielectrics and viscoplastic materials. This technique has the capability to incorporate statistical information about the microstructure beyond the volume fraction of the phases and can be applied to *large classes* of elastomeric composites, including reinforced and porous elastomers, as well as other heterogeneous elastomeric systems, such as the TPEs introduced above. The main concept behind the second-order method is the construction of suitable variational principles utilizing the idea of a “linear comparison composite.” The first attempt along these lines for hyperelastic composites was carried out by Ponte Castañeda and Tiberio (2000) (see also Willis, 2000 and Lahellec *et al.*, 2004), who made use of the so-called “tangent” second-order variational procedure, initially proposed for viscoplastic materials by Ponte Castañeda (1996). While the resulting estimates certainly had some desirable properties, such as the ability to account for the stiffness of the phases, their shape, concentration and distribution, they also had some shortcomings. Thus, for example, they were able to recover only approximately the overall incompressibility constraint associated with rigidly reinforced elastomers with an incompressible matrix phase (typical of rubbers). In retrospect, this was not too surprising

in view of the strong nonlinearity associated with the incompressibility constraint on the determinant of the deformation. Here, use will be made of an improved second-order method, also—as already stated—first developed in the context of viscoplastic composites (Ponte Castañeda, 2002a), which makes use of the local field fluctuations in the determination of the relevant linear comparison composite. An application of a preliminary extension of this method to particle-reinforced rubbers with isotropic microstructures was carried out by Lopez-Pamies and Ponte Castañeda (2004a). It was found to provide much more accurate estimates satisfying exactly the overall incompressibility constraint for rigidly reinforced elastomers with an incompressible matrix phase. In this work, we will develop a full extension of the “second-order” homogenization method to general elastomeric composites. For simplicity, we will ignore hysteresis, temperature and rate-dependent effects, which can be important for these materials (Bergström and Boyce, 1998; Khan and Lopez-Pamies, 2002), as well as particle/matrix interface effects (Ramier, 2004) and the possible development of damage, through particle debonding at interfaces. However, it should be emphasized that the methods to be developed here apply to elastomeric composites with general microstructures and arbitrary hyperelastic constituents. In addition, it is believed that a suitably generalized version of the methods to be developed in this work could incorporate dependence on all of the above-mentioned effects, as discussed further in the closure of this thesis.

This thesis is organized into chapters whose main contents correspond to articles that have been published, or are in preparation to be submitted for publication. For convenience, the list of such articles is provided at the end of this introduction. Next, a brief description of the main contents of each chapter is provided.

The next chapter (Chapter 2), which corresponds to references 1, 2 and 4 in the list of publications, deals with the theoretical aspects regarding the overall behavior of elastomeric composites. In particular, the mathematical formulation of *effective properties* for hyperelastic composites is introduced. This includes the definitions of suitably selected macroscopic variables, as well as the definitions of *microscopic* and *macroscopic* instabilities. Having set the problem on a solid mathematical foundation, the notions of bounds and estimates are then presented. This is followed by the main result of this thesis, namely, the derivation of the “second-order” homogenization method for hyperelastic composites. In this connection, it is emphasized that a preliminary attempt to generate such method was carried out by Lopez-Pamies and Ponte Castañeda (2004a). For completeness, this article has been included as Appendix A. Within the general second-order

formulation—motivated by experimental findings evidencing that rubber-like solids are isotropic relative to the undistorted state—special attention is dedicated to hyperelastic composites with *isotropic* phases. For such a class of composites, sufficient conditions are provided for the second-order estimates to satisfy overall *objectivity* and *material symmetry* requirements. In addition, for such a class of composites, further specialization of the second-order estimates is provided for the case of two-phase composites with “particulate” (random and periodic) microstructures—the motivation for such specialization being practical interest. Chapter 2 finally presents the consistent identification of microstructural variables, as well as the required formulae to estimate their evolution along a given macroscopic loading path.

Chapter 3, which corresponds to reference 3 in the list of publications, is the first of three chapters dealing with the application of the theoretical framework developed in Chapter 2 to *porous* elastomers. The specific problem that is addressed in Chapter 3 is that of the in-plane effective behavior of a porous elastomer consisting of aligned cylindrical voids with initially circular cross section that are distributed *randomly* and *isotropically* in the undeformed configuration. As it turns out, this is a very useful model problem that includes all the main features concerning the mechanical response of porous elastomers subjected to finite deformations, and, at the same time, is amenable to a more transparent mathematical treatment. In this chapter, second-order estimates are generated for materials with *compressible* and *incompressible*, isotropic matrix phases. In particular, it should be emphasized that the estimates generated for porous elastomers with incompressible matrix phases are ultimately given in closed form. Corresponding estimates derived with the earlier “tangent” second-order method of Ponte Castañeda and Tiberio (2000) are also generated for comparison purposes. The chapter concludes with the presentation and discussion of representative results for the effective stress-strain relation, microstructure evolution, and macroscopic instabilities of porous elastomers for a wide range of loading conditions and values of initial porosity.

Chapter 4 corresponds to reference 6 and is—in a sense—a natural continuation of Chapter 3. The problem of interest in this chapter is also that of the in-plane effective behavior of porous elastomers consisting of aligned cylindrical voids with initially circular cross section, but the distribution of the voids here is *periodic* (as opposed to *random*). In particular, two types of periodic microstructures are considered: (i) square and (ii) hexagonal arrangements of pores. The interest

to consider such microstructures is essentially twofold. First, it provides the means to assess the accuracy of the second-order method through comprehensive comparisons with more accurate FEM calculations available for periodic microstructures. Second, it allows to study the influence of the initial distribution of pores on the overall behavior and stability of porous elastomers.

Chapter 5, which corresponds to references 7 and 8, is concerned with the application of the theoretical framework developed in Chapter 2 to generate a homogenization-based constitutive model for porous elastomers consisting of a *random* and *isotropic* distribution of initially spherical, polydisperse pores in an isotropic, elastomeric matrix. Unlike the microstructures considered in Chapters 3 and 4, this microstructure—though idealized—can be considered as a fair approximation to actual microstructures in real porous elastomers. For comparison purposes, a brief review is provided at the beginning of the chapter summarizing earlier estimates available for the effective behavior of overall isotropic porous elastomers. This is followed by the derivation of the second-order estimates for porous elastomers with *compressible* and *incompressible* matrix phases. Finally, illustrative results are presented and discussed for the effective stress-strain relation, microstructure evolution, and onset-of-failure surfaces—in stress and strain space—for a wide range of loading conditions and values of initial porosity.

Chapters 6, 7, and 8—in contrast to Chapters 3 through 5, which deal with porous elastomers—are concerned with the application of the theory developed in Chapter 2 to *reinforced* elastomers. In particular, Chapter 6, which corresponds to reference 10 in the list of publications, deals with the effective behavior of reinforced elastomers with a very special class of microstructures: laminates. This microstructure has repeatedly proved of great theoretical importance, especially in the context of the classical theory of linear elasticity (see Chapter 9 in Milton, 2002 and the references therein). In addition, laminates are also of increasing practical interest, as they have been observed to appear in a number of elastomeric systems such as thermoplastic elastomers. To date, the effective behavior and stability of hyperelastic composites with layered microstructures have been studied in relative depth (see, e.g., Triantafyllidis and Maker, 1985; Triantafyllidis and Nestorvić, 2005). However, it seems that no connection has been ever made between the evolution of the underlying microstructure (induced by the applied finite deformations) and the effective behavior and stability of these materials. To establish this connection is precisely one of the main aims of Chapter 6. In addition, being a limiting-type microgeometry, the results for laminates will be used in the following chapter to validate the results for more general microstructures.

Chapter 7, which corresponds to reference 5, addresses the problem of in-plane effective behavior of elastomers reinforced with aligned cylindrical fibers of elliptical cross section distributed *randomly*—with *elliptical symmetry*—in the undeformed configuration. The main results of this chapter include *closed-form, analytical* expressions for the homogenized stored-energy function of an *incompressible* rubber reinforced by *rigid* fibers, as well as corresponding expressions for the in-plane rotation of the fibers, under general plane-strain conditions. The transparency of these expressions allows to gain precious insight regarding the subtle interplay between the evolution of the underlying microstructure and the overall behavior and stability of fiber-reinforced elastomers, which is comprehensively studied in this chapter.

Chapter 8 corresponds to reference 9 and provides the application of the theoretical framework developed in Chapter 2 to generate a homogenization-based constitutive model for fiber-reinforced elastomers with periodic microstructures subjected to general finite deformations. The primary applications of models based on these (constitutive and geometric) hypotheses are the aforementioned class of thermoplastic elastomers, as well as tires. Complementing the analysis of Chapter 7, Chapter 8 includes results for a wide range of three-dimensional loading conditions.

Finally, Chapter 9 provides a brief summary of the main findings of this work together with some concluding remarks, as well as some prospects for future work.

List of publications that resulted from this dissertation work

1. Lopez-Pamies, O., Ponte Castañeda, P., 2003. Second-order estimates for the large deformation response of particle-reinforced rubber. *Comptes Rendus Mecanique* 331, 1–8.
2. Lopez-Pamies, O., Ponte Castañeda, P., 2004. Second-order homogenization estimates incorporating field fluctuations in finite elasticity. *Mathematics and Mechanics of Solids* 9, 243–270.
3. Lopez-Pamies, O., Ponte Castañeda, P., 2004. Second-order estimates for the macroscopic response and loss of ellipticity in porous rubbers at large deformations. *Journal of Elasticity* 76, 247–287.
4. Lopez-Pamies, O., Ponte Castañeda, P., 2006. On the overall behavior, microstructure evolution, and macroscopic stability in reinforced rubbers at large deformations. I—Theory. *Journal of the Mechanics and Physics of Solids* 54, 807–830.
5. Lopez-Pamies, O., Ponte Castañeda, P., 2006. On the overall behavior, microstructure evolution, and macroscopic stability in reinforced rubbers at large deformations. II—Application to cylindrical fibers. *Journal of the Mechanics and Physics of Solids* 54, 831–863.
6. Michel, J.-C., Lopez-Pamies, O., Ponte Castañeda, P., Triantafyllidis, N., 2007. Microscopic and macroscopic instabilities in finitely strained porous elastomers. *Journal of the Mechanics and Physics of Solids*. 55, 900-938
7. Lopez-Pamies, O., Ponte Castañeda, P., 2007. Homogenization-based constitutive models for porous elastomers and implications for macroscopic instabilities: I—Analysis. *Journal of the Mechanics and Physics of Solids* 55, 1677-1701
8. Lopez-Pamies, O., Ponte Castañeda, P., 2007. Homogenization-based constitutive models for porous elastomers and implications for macroscopic instabilities: II—Results. *Journal of the Mechanics and Physics of Solids* 55, 1702-1728.
9. Brun, M., Lopez-Pamies, O., Ponte Castañeda, P., 2007. Homogenization estimates for fiber-reinforced elastomers with periodic microstructures. *International Journal of Solids and Structures* 44, 5953-5979.

Chapter 2

Theory

This chapter deals with the development of an analytical framework for determining the overall constitutive response of elastomeric composites subjected to finite deformations, with special interest in two-phase elastomers with “particulate” microstructures. The framework accounts for the evolution of the underlying microstructure, which results from the finite changes in geometry that are induced by the applied loading. This point is essential, as the evolution of the microstructure provides geometric softening/hardening mechanisms that may have a very significant effect on the overall behavior and stability of elastomeric composites. The theory is founded on a recently developed “second-order” homogenization method (Ponte Castañeda, 2002a), which is based on the construction of suitable variational principles utilizing the idea of a “linear comparison composite.” The theory developed in this chapter will be applied in subsequent chapters to elastomeric systems of theoretical and practical interest, including various classes of reinforced and porous elastomers.

2.1 Hyperelastic composites and effective behavior

2.1.1 Hyperelastic materials

Consider a material made up of N different (homogeneous) phases that are distributed, either randomly or periodically, in a specimen occupying a volume Ω_0 , with boundary $\partial\Omega_0$, in the reference configuration, in such a way that the characteristic length of the inhomogeneities (*e.g.*, voids, particles, etc.) is assumed to be much smaller than the size of the specimen and the scale of variation of the applied loading.

Material points in the solid are identified by their initial position vector \mathbf{X} in the reference

configuration Ω_0 , while the current position vector of the same point in the deformed configuration Ω is given by

$$\mathbf{x} = \boldsymbol{\chi}(\mathbf{X}). \quad (2.1)$$

The deformation gradient tensor \mathbf{F} at \mathbf{X} , a quantity that measures the deformation in the neighborhood of \mathbf{X} , is defined as:

$$\mathbf{F}(\mathbf{X}) = \frac{\partial \boldsymbol{\chi}}{\partial \mathbf{X}}(\mathbf{X}). \quad (2.2)$$

Note that \mathbf{F} is not necessarily continuous across interphase boundaries in the composite, but in this work we assume that the various phases are perfectly bonded so that $\boldsymbol{\chi}$ is everywhere continuous. Furthermore, in order to satisfy *global* material impenetrability, the mapping $\boldsymbol{\chi}$ is required to be one-to-one on Ω_0 . Thus, for all points \mathbf{X} and $\mathbf{X}' \in \Omega_0$,

$$\boldsymbol{\chi}(\mathbf{X}') = \boldsymbol{\chi}(\mathbf{X}) \quad \text{if and only if} \quad \mathbf{X}' = \mathbf{X}. \quad (2.3)$$

The *local* form of (2.3) is

$$\det \mathbf{F}(\mathbf{X}) \neq 0 \quad \forall \quad \mathbf{X} \in \Omega_0. \quad (2.4)$$

However, in this work we are interested in physically plausible deformation paths with starting point $\mathbf{F}(\mathbf{X}) = \mathbf{I} \quad \forall \quad \mathbf{X} \in \Omega_0$, where \mathbf{I} denotes the identity operator in the space of second-order tensors. Thus, by continuity, it follows from (2.4) that

$$\det \mathbf{F}(\mathbf{X}) > 0 \quad \forall \quad \mathbf{X} \in \Omega_0. \quad (2.5)$$

Note that this condition would be automatically satisfied for incompressible materials, where $\det \mathbf{F}$ is required to be identically 1.

The constitutive behavior of the phases is characterized by stored-energy functions $W^{(r)}$ ($r = 1, \dots, N$), which are taken to be *non-convex* functions of the deformation gradient tensor \mathbf{F} . Thus, the *local* stored-energy function of the hyperelastic composite is expressible as:

$$W(\mathbf{X}, \mathbf{F}) = \sum_{r=1}^N \chi^{(r)}(\mathbf{X}) W^{(r)}(\mathbf{F}), \quad (2.6)$$

where the characteristic functions $\chi^{(r)}$, equal to 1 if the position vector \mathbf{X} is inside phase r (*i.e.*, $\mathbf{X} \in \Omega_0^{(r)}$) and zero otherwise, describe the distribution of the phases (*i.e.*, the microstructure) in the reference configuration. Note that in the case of periodic distributions, the dependence of $\chi^{(r)}$ on \mathbf{X} is completely determined once a unit cell D_0 has been specified. In contrast, for random

distributions, the dependence of $\chi^{(r)}$ on \mathbf{X} is not known precisely, and the microstructure is only partially defined in terms of n -point statistics. The stored-energy functions of the phases are, of course, taken to be *objective*, in the sense that

$$W^{(r)}(\mathbf{Q}\mathbf{F}) = W^{(r)}(\mathbf{F}) \quad (2.7)$$

for all proper orthogonal \mathbf{Q} and all deformation gradients \mathbf{F} . Making use of the right polar decomposition $\mathbf{F} = \mathbf{R}\mathbf{U}$, where \mathbf{R} is the macroscopic rotation tensor and \mathbf{U} denotes the right stretch tensor, it follows, in particular, that $W^{(r)}(\mathbf{F}) = W^{(r)}(\mathbf{U})$. Moreover, to try to ensure material impenetrability, the domain of $W^{(r)}$ is taken to be the set of all second-order tensors with positive determinant: $\{\mathbf{F} \mid \det \mathbf{F} > 0\}$. Further, $W^{(r)}$ are assumed to satisfy the condition:

$$W^{(r)}(\mathbf{F}) \rightarrow \infty \quad \text{if} \quad \det \mathbf{F} \rightarrow 0^+. \quad (2.8)$$

It is thus seen that $W^{(r)}$ are indeed non-convex functions of \mathbf{F} since their domain, $\{\mathbf{F} \mid \det \mathbf{F} > 0\}$, is not convex.¹

Assuming sufficient smoothness for W on \mathbf{F} , it is now useful to define the *local* constitutive functions

$$\mathcal{S}(\mathbf{X}, \mathbf{F}) = \frac{\partial W}{\partial \mathbf{F}}(\mathbf{X}, \mathbf{F}) \quad \text{and} \quad \mathcal{S}^{(r)}(\mathbf{F}) = \frac{\partial W^{(r)}}{\partial \mathbf{F}}(\mathbf{F}), \quad (2.9)$$

as well as

$$\mathcal{L}(\mathbf{X}, \mathbf{F}) = \frac{\partial^2 W}{\partial \mathbf{F} \partial \mathbf{F}}(\mathbf{X}, \mathbf{F}) \quad \text{and} \quad \mathcal{L}^{(r)}(\mathbf{F}) = \frac{\partial^2 W^{(r)}}{\partial \mathbf{F} \partial \mathbf{F}}(\mathbf{F}). \quad (2.10)$$

It then follows that the *local* or microscopic constitutive relation for the composite is given by:

$$\mathbf{S}(\mathbf{X}) = \mathcal{S}(\mathbf{X}, \mathbf{F}), \quad (2.11)$$

where \mathbf{S} denotes the first Piola-Kirchhoff stress tensor². Furthermore, note that the *local* elasticity, or tangent modulus tensor of the material is given by $(2.10)_1$.

2.1.2 Effective behavior

Following Hill (1972) and Hill and Rice (1973), under the hypothesis of *statistical uniformity* and the above-mentioned *separation of length scales*, the *effective stored-energy function* \widetilde{W} of the

¹This is easy to check by constructing an example where the sum of two distinct second-order tensors \mathbf{F} and \mathbf{F}' , with $\det \mathbf{F} > 0$ and $\det \mathbf{F}' > 0$, does not have positive determinant (see, e.g., Chapter 31 in Milton, 2002).

²Recall that \mathbf{S} is related to the Cauchy stress tensor \mathbf{T} by $\mathbf{S} = \det(\mathbf{F}) \mathbf{T} \mathbf{F}^{-T}$.

hyperelastic composite is defined by:

$$\widetilde{W}(\overline{\mathbf{F}}) = \min_{\mathbf{F} \in \mathcal{K}(\overline{\mathbf{F}})} \langle W(\mathbf{X}, \mathbf{F}) \rangle = \min_{\mathbf{F} \in \mathcal{K}(\overline{\mathbf{F}})} \sum_{r=1}^N c_0^{(r)} \langle W^{(r)}(\mathbf{F}) \rangle^{(r)}, \quad (2.12)$$

where \mathcal{K} denotes the set of kinematically admissible deformation gradients:

$$\mathcal{K}(\overline{\mathbf{F}}) = \{\mathbf{F} \mid \exists \mathbf{x} = \boldsymbol{\chi}(\mathbf{X}) \text{ with } \mathbf{F} = \text{Grad } \boldsymbol{\chi}(\mathbf{X}) \text{ in } \Omega_0, \mathbf{x} = \overline{\mathbf{F}}\mathbf{X} \text{ on } \partial\Omega_0\}. \quad (2.13)$$

In the above expressions, the brackets $\langle \cdot \rangle$ and $\langle \cdot \rangle^{(r)}$ denote volume averages—in the undeformed configuration—over the composite (Ω_0) and over the phase r ($\Omega_0^{(r)}$), respectively, so that the scalars $c_0^{(r)} = \langle \chi^{(r)} \rangle$ represent the initial volume fractions of the given phases. Note that \widetilde{W} physically represents the average elastic energy stored in the composite when subjected to an affine displacement boundary condition that is consistent with $\langle \mathbf{F} \rangle = \overline{\mathbf{F}}$. Note further that, from the definition (2.12) and the objectivity of $W^{(r)}$, it follows that \widetilde{W} is objective, and hence that $\widetilde{W}(\overline{\mathbf{F}}) = \widetilde{W}(\overline{\mathbf{U}})$. (For completeness, the proof of this result is given in Appendix I.) Here, $\overline{\mathbf{U}}$ represents the macroscopic right stretch tensor associated with the macroscopic polar decomposition $\overline{\mathbf{F}} = \overline{\mathbf{R}} \overline{\mathbf{U}}$, with $\overline{\mathbf{R}}$ denoting the macroscopic rotation tensor (of course, $\langle \mathbf{U} \rangle \neq \overline{\mathbf{U}}$ and $\langle \mathbf{R} \rangle \neq \overline{\mathbf{R}}$).

In analogy with the *local* expressions (2.9) and (2.10), and assuming sufficient smoothness for \widetilde{W} on $\overline{\mathbf{F}}$, it is convenient to define the following *effective* quantities:

$$\widetilde{\mathbf{S}}(\overline{\mathbf{F}}) = \frac{\partial \widetilde{W}}{\partial \overline{\mathbf{F}}}(\overline{\mathbf{F}}), \quad (2.14)$$

and

$$\widetilde{\mathcal{L}}(\overline{\mathbf{F}}) = \frac{\partial^2 \widetilde{W}}{\partial \overline{\mathbf{F}} \partial \overline{\mathbf{F}}}(\overline{\mathbf{F}}). \quad (2.15)$$

It then follows that the *global* or macroscopic constitutive relation for the composite—that is, the relation between the macroscopic first Piola-Kirchhoff stress and the macroscopic deformation gradient tensor—is given by (see Appendix II):

$$\overline{\mathbf{S}} = \widetilde{\mathbf{S}}(\overline{\mathbf{F}}), \quad (2.16)$$

where $\overline{\mathbf{S}} = \langle \mathbf{S} \rangle$ is the *average first Piola-Kirchhoff stress* in the composite. Furthermore, the *effective* tangent modulus tensor is given by (2.15).

Having defined the *local* and *effective* behavior of hyperelastic composites, it is now in order to make pertinent remarks regarding the *existence* and *uniqueness* of minimizers for $W(\mathbf{X}, \mathbf{F})$ in the definition (2.12) for the effective stored-energy function \widetilde{W} .

2.1.3 Constitutive hypotheses

As is well known, imposing the constitutive requirement that $W(\mathbf{X}, \mathbf{F})$ be *strictly convex* in \mathbf{F} for all $\mathbf{X} \in \Omega_0$, namely,

$$W(\mathbf{X}, t\mathbf{F} + (1-t)\mathbf{F}') < tW(\mathbf{X}, \mathbf{F}) + (1-t)W(\mathbf{X}, \mathbf{F}') \quad (2.17)$$

for all $t \in [0, 1]$ and all pairs \mathbf{F} and \mathbf{F}' , together with suitable smoothness and growth conditions, ensures that the solution of the Euler-Lagrange equations associated with the variational problem (2.12) exists, is unique, and gives the minimum energy (see, e.g., Hill, 1957; Beju, 1971). However, as explicitly stated above, $W(\mathbf{X}, \mathbf{F})$ has been taken to be non-convex with respect to \mathbf{F} and cannot satisfy (2.17). This is because—motivated by material impenetrability requirements—the domain $\{\mathbf{F} | \det \mathbf{F} > 0\}$ of $W(\mathbf{X}, \mathbf{F})$ is not convex, and further, $W(\mathbf{X}, \mathbf{F})$ is required to satisfy the condition (2.8). Moreover, motivated by experimental evidence, it is also recognized that $W(\mathbf{X}, \mathbf{F})$ needs to be non-convex in \mathbf{F} in order not to rule out bifurcation phenomena such as buckling. In short, some other constitutive condition on W —less restrictive than *convexity*—is required to guarantee the existence of minimizers in (2.12) without necessarily guaranteeing the uniqueness of the associated Euler-Lagrange equations.

Ball showed in his celebrated paper in 1977 that if the stored-energy function $W(\mathbf{X}, \mathbf{F})$ is (strictly) *polyconvex*, namely,

$$W(\mathbf{X}, \mathbf{F}) = f(\mathbf{X}, \mathbf{F}, \mathbf{F}^{adj}, \det \mathbf{F}) \quad (2.18)$$

with $f(\mathbf{X}, \cdot, \cdot, \cdot)$ (strictly) convex for each \mathbf{X} and $\mathbf{F}^{adj} = \det(\mathbf{F})\mathbf{F}^{-T}$, and if certain growth hypotheses are satisfied, then there exist minimizers for (2.12). Ball's remarkable existence theorem applies to *compressible* materials that satisfy the physical condition (2.8), as well as to *incompressible* materials, which require the constraint $\det \mathbf{F} = 1$ (which also poses technical difficulties). It should be noted that even though the constitutive restriction of polyconvexity (2.18) has yet to be given strict physical meaning, is general enough as to include many of the more commonly used hyperelastic stored-energy functions such as the Neo-Hookean, Gent, Arruda-Boyce, Mooney-Rivlin, and Ogden materials.

A less restrictive constitutive condition than polyconvexity is that of *quasiconvexity*, which was introduced by Morrey in 1952. In this celebrated article, Morrey provided (see also Acerbi and Fusco, 1984) a theorem for the existence of minimizers in problems of the type (2.12) by

making use of the constitutive hypothesis of quasiconvexity together with certain growth conditions. Unfortunately, the growth hypotheses are too stringent and prohibit the condition (2.8). Thus, as they stand, the existence theorems for minimizers of integrals of general quasiconvex functions do not apply to finite elasticity (Ball, 2002). However, it has been suggested (see, e.g., Ball and Murat, 1984 and Ball, 2002) that quasiconvexity might be the more appropriate constitutive requirement—less restrictive than polyconvexity—for existence of energy minimizers in finite elasticity. That such suggestion is actually correct remains a fundamental open problem in finite elasticity. A key difficulty in proving this result is that there is no known useful characterization of quasiconvexity, other than its definition, which is *nonlocal*.

Finally, it is fitting to spell out an even less restrictive constitutive condition than quasiconvexity, namely, *rank-one convexity*. Thus, the stored-energy function $W(\mathbf{X}, \mathbf{F})$ is said to be rank-one convex if it satisfies the *Legendre-Hadamard* condition, namely, if it satisfies:

$$B(\mathbf{X}, \mathbf{F}) \equiv \min_{\|\mathbf{m}\|=\|\mathbf{N}\|=1} \{m_i N_j \mathcal{L}_{ijkl}(\mathbf{X}, \mathbf{F}) m_k N_l\} \geq 0, \quad (2.19)$$

where it is recalled that \mathcal{L} is given by (2.10)₁ and indicial notation has been used to indicate precisely the products involved. (In the absence of explicit notice to the contrary, Latin indices range from 1 to 3, and the usual summation convention is employed). Note that the strict inequality in (2.19) (*i.e.*, strict rank-one convexity) corresponds to strong ellipticity, whose physical meaning is that the hyperelastic composite never admits solutions with discontinuous deformation gradients within the given phases (see, e.g., Knowles and Sternberg, 1977; Hill, 1979). In this connection, it is important to remark that other types of singular solutions, such as cavitation, are not precluded by strong ellipticity. The interested reader is referred to Ball (1982) for a detailed discussion of such material instabilities. On the practical side, for many of the cases considered in this work, it should be mentioned that void nucleation is not expected to occur (Ball, 1982).

The conditions of convexity, polyconvexity, quasiconvexity, and rank-one convexity introduced above satisfy the following chain of implications (see, e.g., Dacorogna, 1989):

$$\text{Convexity} \Rightarrow \text{Polyconvexity} \Rightarrow \text{Quasiconvexity} \Rightarrow \text{Rank-One Convexity}. \quad (2.20)$$

As explained above, convexity is not a valid assumption for materials in finite elasticity. On the other hand, polyconvexity, for which Ball's existence theorems apply, is valid for many common non-linear elastic materials. In addition, polyconvexity—as opposed to quasiconvexity and rank-one convexity—is a relatively easy assumption to impose in practice (at least for isotropic

materials). Hence, in this work we will adopt the constitutive assumption of polyconvexity for the local behavior of hyperelastic materials. More specifically, we will insist in local *strict* polyconvexity. In this connection, it is convenient to record that (see, e.g., Marsden and Hughes, 1983)

$$\text{Strict Convexity} \Rightarrow \text{Strict Polyconvexity} \Rightarrow \text{Strict Rank-One Convexity}. \quad (2.21)$$

This chain of implications, together with (2.20), entails that *strictly* polyconvex hyperelastic materials are also *quasiconvex* and *strongly elliptic*. In this regard, it is important to make the following remark. In spite of the fact that the local behavior is assumed to be *locally* strongly elliptic, the effective stored-energy function \widetilde{W} may lose strong ellipticity. This can be seen by recognizing that \widetilde{W} , as defined by (2.12), is quasiconvex and therefore—according to (2.20)—rank-one convex, but *not* necessarily strictly so (Geymonat *et al.*, 1993). One of the issues of interest in this work is establishing under what conditions the overall behavior of the composite can lose *strict* rank-one convexity, that is, under what conditions

$$\widetilde{B}(\overline{\mathbf{F}}) \equiv \min_{\|\mathbf{m}\|=\|\mathbf{N}\|=1} \{m_i N_j \widetilde{\mathcal{L}}_{ijkl}(\overline{\mathbf{F}}) m_k N_l\} > 0 \quad (2.22)$$

ceases to hold true. Recall that in this last expression $\widetilde{\mathcal{L}}$ is given by (2.15).

Specific stored-energy functions for the phases

In subsequent chapters dealing with applications to specific material systems, we will restrict attention to a special class of stored-energy functions $W^{(r)}$ for the phases of hyperelastic composites. In particular, motivated by experimental evidence indicating that elastomers are normally isotropic with respect to the undistorted state, special attention will be given to *isotropic* stored-energy functions $W^{(r)}$.

Recall that the restriction of *isotropy* (together with that of objectivity) implies that the stored-energy functions $W^{(r)}$ of the material constituents can be expressed as functions of the principal invariants of the right Cauchy-Green deformation tensor $\mathbf{C} = \mathbf{F}^T \mathbf{F}$:

$$\begin{aligned} I_1 &= \text{tr} \mathbf{C} = \lambda_1^2 + \lambda_2^2 + \lambda_3^2, \\ I_2 &= \frac{1}{2} [(\text{tr} \mathbf{C})^2 - \text{tr} \mathbf{C}^2] = \lambda_1^2 \lambda_2^2 + \lambda_2^2 \lambda_3^2 + \lambda_3^2 \lambda_1^2, \\ I_3 &= \sqrt{\det \mathbf{C}} = \lambda_1 \lambda_2 \lambda_3, \end{aligned} \quad (2.23)$$

or, equivalently, as symmetric functions of the principal stretches $\lambda_1, \lambda_2, \lambda_3$ associated with \mathbf{F} .

Namely, $W^{(r)}$ may be written as:

$$W^{(r)}(\mathbf{F}) = \varphi^{(r)}(I_1, I_2, I_3) = \Phi^{(r)}(\lambda_1, \lambda_2, \lambda_3), \quad (2.24)$$

where $\Phi^{(r)}$ are symmetric. A fairly general (and relatively simple) class of stored-energy functions (2.24), which has been found to provide good agreement with experimental data for rubberlike materials, is given by:

$$W^{(r)}(\mathbf{F}) = g^{(r)}(I) + h^{(r)}(J) + \frac{\kappa^{(r)}}{2}(J - 1)^2, \quad (2.25)$$

where $I \equiv I_1$ and $J \equiv I_3$ have been introduced for convenience. The parameter $\kappa^{(r)}$ corresponds to the three-dimensional³ bulk modulus of phase r at zero strain, and $g^{(r)}$ and $h^{(r)}$ are twice-differentiable, material functions that satisfy the conditions: $g^{(r)}(3) = h^{(r)}(1) = 0$, $g_I^{(r)}(3) = \mu^{(r)}/2$, $h_J^{(r)}(1) = -\mu^{(r)}$, and $4g_{II}^{(r)}(3) + h_{JJ}^{(r)}(1) = \mu^{(r)}/3$. Here, $\mu^{(r)}$ denotes the shear modulus of phase r at zero strain, and the subscripts I and J indicate differentiation with respect to these invariants. Note that when these conditions are satisfied $W^{(r)}(\mathbf{F}) = (1/2)(\kappa^{(r)} - 2/3\mu^{(r)})(\text{tr}\boldsymbol{\varepsilon})^2 + \mu^{(r)}\text{tr}\boldsymbol{\varepsilon}^2 + o(\boldsymbol{\varepsilon}^3)$, where $\boldsymbol{\varepsilon}$ is the infinitesimal strain tensor, as $\mathbf{F} \rightarrow \mathbf{I}$, so that the stored-energy function (2.25) linearizes properly. Furthermore, note that to recover incompressible behavior in (2.25), it suffices to make the parameter $\kappa^{(r)}$ tend to infinity (in which case $W^{(r)}(\mathbf{F}) = g^{(r)}(I)$ together with the incompressibility constraint $J = 1$).

Experience suggests that “neat” elastomers normally do not admit *localized* deformations. Within the context of the material model (2.25), this property can be easily enforced by simply insisting that $g(I)$ and $h(J) + \frac{\kappa}{2}(J - 1)^2$ be strictly convex functions of their arguments, which renders the stored-energy function (2.25) *strictly polyconvex*, and in turn—according to (2.21)—*strongly elliptic*. Note also that the stored-energy function (2.25) is an extension of the so-called generalized Neo-Hookean (or I_1 -based) materials to account for compressibility. It includes constitutive models widely used in the literature such as the Neo-Hookean, Arruda-Boyce 8-chain (Arruda and Boyce, 1993), Yeoh (Yeoh, 1993), and Gent (Gent, 1996) models.

In the sequel, we will consider a number of applications in the context of plane-strain deformations. For this type of loading conditions, the problems at hand will be essentially two-dimensional (2D). In this regard, for such problems, it will prove more helpful to work with the 2D form of (2.25) rather than with (2.25) itself. Thus, by fixing—without loss generality— $\lambda_3 = 1$ and defining

³In terms of the Lamé moduli, $\mu^{(r)}$ and $\mu^{(r)}$, $\kappa^{(r)} = \mu^{(r)} + 2/3\mu^{(r)}$.

the *in-plane* principal invariants of $\mathbf{C} = \mathbf{F}^T \mathbf{F}$ as:

$$\check{I} = \lambda_1^2 + \lambda_2^2, \quad \text{and} \quad \check{J} = \lambda_1 \lambda_2, \quad (2.26)$$

the stored-energy function (2.25) under plane-strain conditions can be conveniently rewritten as:

$$W^{(r)}(\mathbf{F}) = \check{g}^{(r)}(\check{I}) + \check{h}^{(r)}(\check{J}) + \frac{\check{\kappa}^{(r)} - \mu^{(r)}}{2}(\check{J} - 1)^2, \quad (2.27)$$

where now the parameter $\check{\kappa}^{(r)}$ corresponds to the two-dimensional⁴ bulk modulus of phase r at zero strain, and $\check{g}^{(r)}$ and $\check{h}^{(r)}$ are such that: $\check{g}^{(r)}(2) = \check{h}^{(r)}(1) = 0$, $\check{g}^{(r)}_I(2) = \mu^{(r)}/2$, $\check{h}^{(r)}_J(1) = -\mu^{(r)}$, and $4\check{g}^{(r)}_{II}(2) + \check{h}^{(r)}_{JJ}(1) = \mu^{(r)}$. Here, similar to (2.25), the subscripts \check{I} and \check{J} indicate differentiation with respect to these invariants. Further, the above conditions make the stored-energy function (2.27) linearized correctly in the limit of small deformations. In the sequel, the above-utilized check mark “ $\check{\cdot}$ ” to denote 2D quantities will be dropped if there is no potential for confusion.

2.1.4 Macroscopic and microscopic instabilities

Next, it is important to recall that more mathematically precise definitions of the effective energy \widetilde{W} , other than (2.12), have been given by Braides (1985) and Müller (1987) for *periodic* microstructures. Such definitions generalize the classical definition of the effective energy for periodic media with convex energies (Marcellini, 1978), by accounting for the fact that, in the non-convex case, it is not sufficient to consider one-cell periodic solutions, as solutions involving interactions between several unit cells may lead to lower overall energies. Physically, this corresponds to the possible development of “microscopic” instabilities in the composite at sufficiently large deformation (see Appendix III for a more precise definition of microscopic instabilities). In this connection, it is important to remark that Geymonat *et al.* (1993), following earlier work by Triantafyllidis and Maker (1985) for laminated materials, have shown rigorously that loss of strong ellipticity in the homogenized behavior of the composite corresponds to the development of long-wavelength (*i.e.*, “macroscopic”) instabilities in the form of localized shear/compaction bands. Furthermore, the “failure surfaces” defined by the loss of strong ellipticity condition of this homogenized behavior provide upper bounds for the onset of other types of instabilities.

In view of the difficulties associated with the computation of the microscopic instabilities mentioned in the previous paragraph, especially for composites with random microstructures, a more

⁴In terms of the Lamé moduli, $\mu^{(r)}$ and $\mu^{(r)}$, $\check{\kappa}^{(r)} = \mu^{(r)} + \mu^{(r)}$.

pragmatic approach will be followed here. By assuming—for consistency with the classical theory of linear elasticity—that $W^{(r)} = \frac{1}{2}\boldsymbol{\varepsilon} \cdot \mathbf{L}_{lin}^{(r)}\boldsymbol{\varepsilon} + o(\boldsymbol{\varepsilon}^3)$ as $\mathbf{F} \rightarrow \mathbf{I}$, where $\boldsymbol{\varepsilon}$ denotes the infinitesimal strain tensor and $\mathbf{L}_{lin}^{(r)}$ are positive-definite⁵, constant, fourth-order tensors, it is expected (except for very special cases) that, at least in a neighborhood of $\bar{\mathbf{F}} = \mathbf{I}$, the solution of the Euler-Lagrange equations associated with the variational problem (2.12) is unique, and gives the minimum energy. As the deformation progresses into the nonlinear range, the composite material may reach a point at which this “principal” solution bifurcates into lower-energy solutions. This point corresponds to the onset of a *microscopic* instability beyond which the applicability of the “principal” solution becomes questionable. However, it is still possible to extract useful information from the principal solution by computing the associated *macroscopic* instabilities from the loss of strong ellipticity of the homogenized behavior. This means that, in practice, we will estimate the effective stored-energy function (2.12) by means of the *stationary* variational statement:

$$\widehat{W}(\bar{\mathbf{F}}) = \underset{\mathbf{F} \in \mathcal{K}(\bar{\mathbf{F}})}{\text{stat}} \sum_{r=1}^N c_0^{(r)} \langle W^{(r)}(\mathbf{F}) \rangle^{(r)}, \quad (2.28)$$

where it is emphasized that the energy is evaluated at the above-described “principal” solution of the relevant Euler-Lagrange equations. From its definition, it is clear that $\widetilde{W}(\bar{\mathbf{F}}) = \widehat{W}(\bar{\mathbf{F}})$ up to the onset of the first *microscopic* instability. Beyond this point, and up to the onset of the first *macroscopic* instability, $\widetilde{W}(\bar{\mathbf{F}}) \leq \widehat{W}(\bar{\mathbf{F}})$. The point is that while the microscopic instabilities are difficult to compute, the macroscopic instabilities are easy to estimate from $\widehat{W}(\bar{\mathbf{F}})$. Furthermore, it is often the case (Geymonat *et al.*, 1993; Triantafyllidis *et al.*, 2006) that the first instability is indeed a long-wavelength instability, in which case $\widetilde{W}(\bar{\mathbf{F}}) = \widehat{W}(\bar{\mathbf{F}})$ all the way up to the development of a macroscopic instability, as characterized by the loss of strong ellipticity of the homogenized moduli associated with $\widehat{W}(\bar{\mathbf{F}})$. More generally, the first instability is of finite wavelength (*i.e.*, small compared to the size of the specimen), but even in this case, it so happens, as we have already mentioned, that the loss of strong ellipticity of the homogenized energy $\widehat{W}(\bar{\mathbf{F}})$ provides an upper bound for the development of microscopic instabilities. In other words, the composite material will become unstable before reaching the “failure surface” defined by the macroscopic instabilities. Furthermore, recent work (Michel *et al.*, 2007) suggests that the macroscopic instabilities may be the more relevant ones for random systems, since many of the microscopic instabilities in periodic systems tend to disappear as the periodicity of the microstructure is broken down.

⁵This condition can be relaxed to include composites with voids, in which case $\mathbf{L}_{lin}^{(r)} = \mathbf{0}$.

2.2 Bounds and estimates

Following up on the preceding framework, the primary objective of this work is to generate estimates for the effective stored-energy function \widehat{W} of hyperelastic composites subjected to finite deformations. A second objective is to study the evolution of the underlying microstructure, as well as the possible onset of macroscopic instabilities—as measured by loss of strong ellipticity of the homogenized behavior—in these materials. This is an extremely difficult problem, because it amounts to solving a set of highly nonlinear partial differential equations with oscillatory coefficients. As a consequence, there are precious few *analytical* estimates for \widehat{W} . Ogden (1978) noted that use of the trial field $\mathbf{F} = \overline{\mathbf{F}}$ in the definition (2.12) for \widehat{W} leads to an upper bound analogous to the well-known Voigt upper bound (Voigt, 1889) in linear elasticity, namely

$$\widehat{W}(\overline{\mathbf{F}}) \leq \widetilde{W}_V(\overline{\mathbf{F}}) \doteq \sum_{r=1}^N c_0^{(r)} W^{(r)}(\overline{\mathbf{F}}). \quad (2.29)$$

Note that this rigorous upper bound depends only on the initial volume fractions of the phases, and contains no dependence on higher-order statistical information about the microstructure. Under appropriate hypotheses on W , ensuring the existence of a principle of minimum complementary energy, Ogden (1978) also proposed a generalization of the Reuss lower bound (Reuss, 1929). However, the required constitutive hypothesis on W was too strong and excluded the majority of physically sound hyperelastic materials used in the literature. For this reason, Ponte Castañeda (1989) proposed an alternative generalization of the Reuss lower bound, exploiting the polyconvexity hypothesis. For polyconvex materials of the type:

$$W(\mathbf{X}, \mathbf{F}) = f(\mathbf{X}, \mathbf{F}, \mathbf{F}^{adj}, \det \mathbf{F}), \quad (2.30)$$

where f is convex in \mathbf{F} , $\mathbf{F}^{adj} (= \det \mathbf{F} \mathbf{F}^{-T})$, and $\det \mathbf{F}$, this lower bound takes the form:

$$\widehat{W}(\overline{\mathbf{F}}) \geq \widetilde{W}_{PC}(\overline{\mathbf{F}}) \doteq (\overline{f^*})^*(\overline{\mathbf{F}}, \overline{\mathbf{F}}^{adj}, \det \overline{\mathbf{F}}). \quad (2.31)$$

Note that—due to the lack of convexity of the function W —this lower bound is much sharper (see Ponte Castañeda, 1989) than the bound that would be obtained by means of the standard Legendre-Fenchel transform applied directly to the function W , which would lead to a bound of the type $(\overline{W^*})^*(\overline{\mathbf{F}})$. Note further that, similar to (2.29), the rigorous lower bound (2.31) is microstructure independent (but see Ponte Castañeda, 1989 to incorporate higher-order statistical information).

As stated in the Introduction, there are also numerous estimates for special microstructures and special loading conditions, as well as empirically based and *ad hoc* estimates for various special systems, including the cases of reinforced rubbers (see, e.g., Mullins and Tobin, 1965; Treloar, 1975; Meinecke and Taftaf, 1988; Govindjee and Simo, 1991; Bergström and Boyce, 1999; deBotton, 2005; deBotton *et al.*, 2006) and porous elastomers (see, e.g., Gent and Thomas, 1959; Feng and Christensen, 1982; Hashin, 1985; Danielsson *et al.*, 2004). Our aim here is to develop a general class of *analytical estimates* that are based on homogenization theory and that are applicable to large classes of composite systems, including reinforced rubbers, porous elastomers and other heterogeneous elastomeric systems, such as TPEs. Such estimates should allow for the incorporation of statistical information beyond the phase volume fractions, thus allowing for a more precise characterization of the influence of microstructure on effective behavior. Some progress along these lines has already been accomplished (Ponte Castañeda and Tiberio, 2000; Lahellec *et al.*, 2004) with the extension of the “tangent” second-order nonlinear homogenization technique (Ponte Castañeda, 1996) to finite elasticity.

2.3 Second-order homogenization method

Our proposal for generating homogenization estimates in finite elasticity is based on an appropriate extension of the “second-order” homogenization procedure that has been recently developed by Ponte Castañeda (2001; 2002a) in the context of nonlinear dielectrics and viscous composites with convex, nonlinear potentials. This new method is in turn a generalization of the “linear comparison” variational method of Ponte Castañeda (1991) in a way that incorporates many of the desirable features of an earlier version of the second-order method (Ponte Castañeda, 1996; Ponte Castañeda and Willis, 1999), including the fact that the estimates generated should be exact to second order in the heterogeneity contrast (Suquet and Ponte Castañeda, 1993). It is relevant to mention in this context that earlier works (e.g., Talbot & Willis 1985, Ponte Castañeda 1991) delivered bounds that are exact *only to first* order in the contrast. Next we give the description of the proposed method. For completeness, the descriptions of (relevant) earlier versions of the method have been included in Appendix V.

The main idea behind the second-order homogenization theory is the construction of a *fictitious* linear comparison composite (LCC) with the same microstructure as the nonlinear composite (*i.e.*,

the same $\chi^{(r)}$. Thus, the local stored-energy function of the LCC may be written as:

$$W_T(\mathbf{X}, \mathbf{F}) = \sum_{r=1}^N \chi^{(r)}(\mathbf{X}) W_T^{(r)}(\mathbf{F}), \quad (2.32)$$

where the quadratic functions $W_T^{(r)}$ are given by the second-order Taylor approximations of the nonlinear stored-energy functions $W^{(r)}$ about some reference deformation gradients $\mathbf{F}^{(r)}$:

$$W_T^{(r)}(\mathbf{F}) = W^{(r)}(\mathbf{F}^{(r)}) + \mathcal{S}^{(r)}(\mathbf{F}^{(r)}) \cdot (\mathbf{F} - \mathbf{F}^{(r)}) + \frac{1}{2}(\mathbf{F} - \mathbf{F}^{(r)}) \cdot \mathbf{L}^{(r)}(\mathbf{F} - \mathbf{F}^{(r)}). \quad (2.33)$$

Here, it is recalled that $\mathcal{S}^{(r)}$ are given by expression (2.9)₂, and the $\mathbf{L}^{(r)}$ are fourth-order tensors with major symmetry to be determined later. Note that, in general, $\mathbf{L}^{(r)} \neq \mathcal{L}^{(r)}$.

Next, ‘‘corrector’’ functions $V^{(r)}$ are introduced such that:

$$V^{(r)}(\mathbf{F}^{(r)}, \mathbf{L}^{(r)}) = \text{stat}_{\hat{\mathbf{F}}^{(r)}} \left[W^{(r)}(\hat{\mathbf{F}}^{(r)}) - W_T^{(r)}(\hat{\mathbf{F}}^{(r)}) \right]. \quad (2.34)$$

These functions, which are multiple-valued depending on the parameters $\mathbf{F}^{(r)}$ and $\mathbf{L}^{(r)}$, serve to measure the nonlinearity of the phases of the original material, so that, under appropriate hypotheses (essentially, when the functions $V^{(r)}$ are smooth with respect to the moduli $\mathbf{L}^{(r)}$), the local stored-energy functions of the phases of the nonlinear composite may be written as:

$$W^{(r)}(\mathbf{F}) = \text{stat}_{\mathbf{L}^{(r)}} \left\{ W_T^{(r)}(\mathbf{F}) + V^{(r)}(\mathbf{F}^{(r)}, \mathbf{L}^{(r)}) \right\}, \quad (2.35)$$

for any choice of the reference deformations $\mathbf{F}^{(r)}$. In connection with this expression, it should be emphasized that the appropriate branches of the functions $V^{(r)}$ must be chosen in order to recover the equality. Note that this relation may still be used in an *approximate* sense, even when the local potentials are such that the equality in relation (2.35) does not hold strictly.

Now, by making use of (2.35) in expression (2.28), it follows that the effective stored-energy function \widehat{W} of the nonlinear composite may be expressed as:

$$\widehat{W}(\bar{\mathbf{F}}) = \text{stat}_{\mathbf{F} \in \mathcal{K}} \text{stat}_{\mathbf{L}^{(s)}(\mathbf{X})} \sum_{r=1}^N c_0^{(r)} \left\langle W_T^{(r)}(\mathbf{F}) + V^{(r)}(\mathbf{F}^{(r)}, \mathbf{L}^{(r)}) \right\rangle^{(r)}, \quad (2.36)$$

which after interchanging the stationarity operations with respect to \mathbf{F} and $\mathbf{L}^{(r)}$ may be recast as

$$\widehat{W}(\bar{\mathbf{F}}) = \text{stat}_{\mathbf{L}^{(s)}(\mathbf{X})} \left\{ \widehat{W}_T(\bar{\mathbf{F}}; \mathbf{F}^{(s)}, \mathbf{L}^{(s)}) + \sum_{r=1}^N c_0^{(r)} \left\langle V^{(r)}(\mathbf{F}^{(r)}, \mathbf{L}^{(r)}) \right\rangle^{(r)} \right\}. \quad (2.37)$$

In this last expression, use has been made of the fact that the corrector functions $V^{(r)}$ do not depend on $\mathbf{F}(\mathbf{X})$, and

$$\widehat{W}_T(\bar{\mathbf{F}}; \mathbf{F}^{(s)}, \mathbf{L}^{(s)}) = \text{stat}_{\mathbf{F} \in \mathcal{K}} \langle W_T(\mathbf{X}, \mathbf{F}) \rangle = \text{stat}_{\mathbf{F} \in \mathcal{K}} \sum_{r=1}^N c_0^{(r)} \left\langle W_T^{(r)}(\mathbf{F}) \right\rangle^{(r)} \quad (2.38)$$

is the effective stored-energy function associated with the LCC defined by relations (2.32) and (2.33).

It is important to emphasize at this point that expression (2.37) provides a variational principle for the effective stored-energy function \widehat{W} of the elastomeric composite, where the relevant trial fields are the modulus tensors $\mathbf{L}^{(s)}(\mathbf{X})$ of the N phases in the LCC. The main advantage of this variational principle over the original form (2.28) is that the trial fields $\mathbf{L}^{(s)}(\mathbf{X})$ do not need to satisfy any differential constraints, such as the compatibility requirement. Of course, for the resulting estimates to make sound physical sense, the compatibility requirement must be, and indeed is, enforced through the use of the LCC with effective stored-energy function \widehat{W}_T given by (2.38). In this context, it is natural to exploit the variational structure of (2.37) by restricting our attention to *constant-per-phase* trial fields $\mathbf{L}^{(s)}$ in order to generate the following estimate for \widehat{W} :

$$\widehat{W}(\overline{\mathbf{F}}) \approx \text{stat}_{\mathbf{L}^{(s)}} \left\{ \widehat{W}_T(\overline{\mathbf{F}}; \mathbf{F}^{(s)}, \mathbf{L}^{(s)}) + \sum_{r=1}^N c_0^{(r)} V^{(r)}(\mathbf{F}^{(r)}, \mathbf{L}^{(r)}) \right\}, \quad (2.39)$$

where the stat(ionary) condition in this last expression is now over constant-per-phase, fourth-order tensors $\mathbf{L}^{(s)}$.

Next, it is relevant to spell out the stationarity conditions in expressions (2.34) and (2.39). They read as follows:

$$\mathcal{S}^{(r)}(\widehat{\mathbf{F}}^{(r)}) - \mathcal{S}^{(r)}(\mathbf{F}^{(r)}) = \mathbf{L}^{(r)}(\widehat{\mathbf{F}}^{(r)} - \mathbf{F}^{(r)}), \quad (2.40)$$

and

$$\frac{\partial \widehat{W}_T}{\partial \mathbf{L}^{(r)}} + c_0^{(r)} \frac{\partial V^{(r)}}{\partial \mathbf{L}^{(r)}} = \mathbf{0}, \quad (2.41)$$

respectively. But using the facts that:

$$\left. \frac{\partial \widehat{W}_T}{\partial \mathbf{L}^{(r)}} \right|_{\mathbf{F}^{(r)}} = \frac{c_0^{(r)}}{2} \langle (\mathbf{F} - \mathbf{F}^{(r)}) \otimes (\mathbf{F} - \mathbf{F}^{(r)}) \rangle^{(r)}, \quad (2.42)$$

and

$$\left. \frac{\partial V^{(r)}}{\partial \mathbf{L}^{(r)}} \right|_{\mathbf{F}^{(r)}} = -\frac{1}{2} (\widehat{\mathbf{F}}^{(r)} - \mathbf{F}^{(r)}) \otimes (\widehat{\mathbf{F}}^{(r)} - \mathbf{F}^{(r)}), \quad (2.43)$$

where the notation $\left. \cdot \right|_{\mathbf{F}^{(r)}}$ has been used to emphasize that the derivatives with respect to $\mathbf{L}^{(r)}$ are taken with $\mathbf{F}^{(r)}$ fixed, the stationary condition (2.41) can be rewritten in the form:

$$\langle (\mathbf{F} - \mathbf{F}^{(r)}) \otimes (\mathbf{F} - \mathbf{F}^{(r)}) \rangle^{(r)} = (\widehat{\mathbf{F}}^{(r)} - \mathbf{F}^{(r)}) \otimes (\widehat{\mathbf{F}}^{(r)} - \mathbf{F}^{(r)}), \quad (2.44)$$

or, equivalently, as:

$$\mathbf{C}_{\mathbf{F}}^{(r)} = (\widehat{\mathbf{F}}^{(r)} - \mathbf{F}^{(r)}) \otimes (\widehat{\mathbf{F}}^{(r)} - \mathbf{F}^{(r)}) - (\overline{\mathbf{F}}^{(r)} - \mathbf{F}^{(r)}) \otimes (\overline{\mathbf{F}}^{(r)} - \mathbf{F}^{(r)}), \quad (2.45)$$

where $\overline{\mathbf{F}}^{(r)} \doteq \langle \mathbf{F} \rangle^{(r)}$ and $\mathbf{C}_{\mathbf{F}}^{(r)} \doteq \langle (\mathbf{F} - \overline{\mathbf{F}}^{(r)}) \otimes (\mathbf{F} - \overline{\mathbf{F}}^{(r)}) \rangle^{(r)}$ have been introduced to denote the average and covariance tensor of the fluctuations of the deformation gradient over phase r in the linear comparison composite. Thus, expression (2.45) can be seen to provide a set of conditions on the fluctuations of the deformation-gradient fields in the phases of the LCC. It is important to realize that these conditions are overly constraining, in general, as they would require that the fourth-order tensors $\langle (\mathbf{F} - \overline{\mathbf{F}}^{(r)}) \otimes (\mathbf{F} - \overline{\mathbf{F}}^{(r)}) \rangle^{(r)}$ be of rank 2. This suggests that it may not be possible to optimize with respect to completely general tensors $\mathbf{L}^{(r)}$ in the variational statement (2.39). As will be discussed in more detail in the next subsection, one possible way out of this problem is to optimize with respect to suitably chosen *subclasses* of tensors $\mathbf{L}^{(r)}$. In this case, the optimality conditions with respect to the $\mathbf{L}^{(r)}$ would still be of the form (2.41), where the derivatives would be taken with respect to the appropriate components of the $\mathbf{L}^{(r)}$ in the relevant subclass. But the form (2.45) of these conditions would need to be replaced by suitable traces of these expressions, depending on the specific form selected for the $\mathbf{L}^{(r)}$.

By making use of conditions (2.40) and (2.41), the general second-order estimate (2.39) may be shown to reduce to:

$$\widehat{W}(\overline{\mathbf{F}}) = \sum_{r=1}^N c_0^{(r)} \left[W^{(r)}(\hat{\mathbf{F}}^{(r)}) - \mathcal{S}^{(r)}(\mathbf{F}^{(r)}) \cdot (\hat{\mathbf{F}}^{(r)} - \overline{\mathbf{F}}^{(r)}) \right]. \quad (2.46)$$

It is interesting to remark that relation (2.46) depends directly on the average deformation gradients $\overline{\mathbf{F}}^{(r)}$ in the phases of the LCC. In addition, expression (2.46) also exhibits an explicit dependence on the variables $\hat{\mathbf{F}}^{(r)}$, which are associated with the field fluctuations of the deformation fields in the phases of the LCC through relations of the type (2.45). Moreover, the estimate (2.46) can be shown to be exact to second order in the heterogeneity contrast, provided that the corresponding estimates for the LCC are also taken to be exact to second order in the contrast, and that the reference variables $\mathbf{F}^{(r)}$ be assumed to tend to the macroscopic average $\overline{\mathbf{F}}$ in the small-contrast limit.

In connection with the general second-order estimate (2.46), it should be emphasized that this estimate is, in principle, valid for any choice of the reference deformation gradients $\mathbf{F}^{(r)}$, which suggests optimizing with respect to these variables. However, it has been found (Lopez-Pamies and Ponte Castañeda, 2004a) that the result of such an optimization appears to be inconsistent with conditions of the type (2.45) on the field fluctuations. As a consequence, it becomes necessary to appeal to other physically based considerations to make a choice for the variables $\mathbf{F}^{(r)}$. Among such considerations is the requirement of *objectivity* of the effective stored-energy function \widehat{W} . Indeed,

this is a non-trivial requirement in the context of the second-order variational estimate (2.46), which makes use of a LCC with local stored-energy functions $W_T^{(r)}$, defined by (2.33), that are *a priori* not objective (*i.e.*, $W_T^{(r)}(\mathbf{Q}\mathbf{F}) \neq W_T^{(r)}(\mathbf{F})$, for all proper orthogonal \mathbf{Q}). However, remarking that the reference variables $\mathbf{F}^{(r)}$, as well as the modulus tensors $\mathbf{L}^{(r)}$, ultimately depend on the macroscopic deformation gradient $\bar{\mathbf{F}}$, it follows that these tensors must be objective quantities in order to ensure the objectivity of the effective stored-energy function: $\widehat{W}(\bar{\mathbf{Q}}\bar{\mathbf{F}}) = \widehat{W}(\bar{\mathbf{F}})$ for all proper orthogonal tensors $\bar{\mathbf{Q}}$. Therefore, it will be required here that the tensors $\mathbf{F}^{(r)}$ and $\mathbf{L}^{(r)}$ satisfy the following invariance relations under the change of observer (frame) defined by the rotation tensor $\bar{\mathbf{Q}}$:

$$F_{ij}^{(r)} \longrightarrow \bar{Q}_{ik} F_{kj}^{(r)}, \quad \text{and} \quad L_{ijkl}^{(r)} \longrightarrow \bar{Q}_{ip} \bar{Q}_{kq} L_{pqjl}^{(r)}, \quad (2.47)$$

where indicial notation has been used to indicate precisely the products involved in the second relation for the $\mathbf{L}^{(r)}$. Parenthetically, it is interesting to remark that, under conditions (2.47), the effective stored-energy function \widehat{W}_T of the LCC can also be shown to be an objective scalar function of $\bar{\mathbf{F}}$, even though, again, the constituent phases $W_T^{(r)}$ are locally *not* objective.

Similarly, the stored-energy function \widehat{W} of the composite must satisfy the overall symmetry requirements of the system, that is, $\widehat{W}(\bar{\mathbf{F}}\bar{\mathbf{K}}) = \widehat{W}(\bar{\mathbf{F}})$ for all orthogonal, second-order tensors $\bar{\mathbf{K}}$ belonging to the symmetry group of the material, \mathcal{G} . For instance, for a composite with isotropic constituents and an isotropic distribution of the phases, the symmetry group \mathcal{G} would correspond to the full orthogonal group. In this work, attention will be focused on composite elastomers with isotropic phases, but with *anisotropic* distribution of the phases. For this class of materials, it can be shown that requiring the variables $\mathbf{F}^{(r)}$ and $\mathbf{L}^{(r)}$ to be invariant under each of the transformations (changes of reference configuration defined by) $\bar{\mathbf{K}} \in \mathcal{G}$ leads to estimates (2.46) for the stored-energy function that satisfy the overall symmetry requirements of the material. Hence, it will be required here that the tensors $\mathbf{F}^{(r)}$ and $\mathbf{L}^{(r)}$ satisfy the following invariance relations:

$$F_{ij}^{(r)} \longrightarrow F_{ik}^{(r)} \bar{K}_{kj}, \quad \text{and} \quad L_{ijkl}^{(r)} \longrightarrow L_{ipkq}^{(r)} \bar{K}_{pj} \bar{K}_{ql}, \quad (2.48)$$

for all symmetry transformations defined by orthogonal, second-order tensors $\bar{\mathbf{K}} \in \mathcal{G}$.

In essence, conditions (2.47) and (2.48) provide general invariance requirements that must be satisfied by the reference deformation gradients $\mathbf{F}^{(r)}$ and the modulus tensors $\mathbf{L}^{(r)}$ in the phases of the LCC. In practice, however, enforcing conditions (2.47) and (2.48) is not a simple matter because of the implicit manner in which $\mathbf{F}^{(r)}$ and $\mathbf{L}^{(r)}$ enter the stationary conditions (2.40) and

(2.41). In the next subsection, we provide specific choices (motivated by the local isotropy of the phases) for $\mathbf{F}^{(r)}$ and $\mathbf{L}^{(r)}$ that satisfy the invariance requirements (2.47) and (2.48).

2.3.1 On the specific choice of the variables $\mathbf{F}^{(r)}$ and $\mathbf{L}^{(r)}$ for isotropic phases

It is clear from the expressions (2.33) for the stored-energy functions $W_T^{(r)}$ of the phases in the LCC that requiring the variables $\mathbf{F}^{(r)}$ and $\mathbf{L}^{(r)}$ be isotropic functions of the *local* deformation gradient \mathbf{F} would be sufficient to ensure the isotropy of these linear phases. However, given the approximation (2.39) for \widehat{W} , the variables $\mathbf{F}^{(r)}$ and $\mathbf{L}^{(r)}$ are constant per phase, and therefore it is not possible to choose them in this manner. On the other hand, recalling that the “generalized secant” tensors $\mathbf{L}^{(r)}$ provide a generalization of the tangent moduli tensors $\mathcal{L}^{(r)}(\mathbf{F}^{(r)})$, it is sensible to require $\mathbf{L}^{(r)}$ to satisfy the same objectivity and material symmetry restrictions, with respect to $\mathbf{F}^{(r)}$, as those satisfied by $\mathcal{L}^{(r)}(\mathbf{F}^{(r)})$. In the particular context of phases that are characterized by *objective* and *isotropic* stored-energy functions $W^{(r)}$, the corresponding tangent moduli tensors $\mathcal{L}^{(r)}(\mathbf{F}^{(r)})$ must satisfy the following conditions:

$$\mathcal{L}_{ijkl}^{(r)}(\mathbf{Q}\mathbf{F}^{(r)}\mathbf{Q}') = Q_{im}Q_{kn}\mathcal{L}_{mpnq}^{(r)}(\mathbf{F}^{(r)})Q'_{pj}Q'_{ql}, \quad (2.49)$$

for all proper orthogonal, second-order tensors \mathbf{Q} and \mathbf{Q}' . In other words, the $\mathcal{L}^{(r)}(\mathbf{F}^{(r)})$ are objective and isotropic tensor functions of the variables $\mathbf{F}^{(r)}$.

Next, note that the “reference” deformation gradient tensors $\mathbf{F}^{(r)}$ may be expressed in the form:

$$\mathbf{F}^{(r)} = \mathbf{R}^{(r)}\mathbf{U}^{(r)} = \mathbf{R}^{(r)}\mathbf{Q}^{(r)}\mathbf{D}^{(r)}(\mathbf{Q}^{(r)})^T, \quad (2.50)$$

where $\mathbf{R}^{(r)}$ and $\mathbf{U}^{(r)}$ correspond, respectively, to the “rotation” and the “right stretch” tensors associated with the polar decomposition of $\mathbf{F}^{(r)}$, $\mathbf{D}^{(r)}$ is a symmetric, second-order tensor with matrix representation (relative to the laboratory frame of reference) $D^{(r)} = \text{diag}(\lambda_1^{(r)}, \lambda_2^{(r)}, \lambda_3^{(r)})$, with $\lambda_1^{(r)}$, $\lambda_2^{(r)}$, and $\lambda_3^{(r)}$ denoting the principal stretches of $\mathbf{U}^{(r)}$, and $(\mathbf{Q}^{(r)})^T$ is the proper orthogonal, second-order tensor describing the orientation of the principal axes of $\mathbf{U}^{(r)}$ relative to the laboratory frame of reference. It then follows from conditions (2.49) that:

$$\mathcal{L}_{ijkl}^{(r)}(\mathbf{F}^{(r)}) = Q_{rm}^{(r)}Q_{jn}^{(r)}Q_{sp}^{(r)}Q_{lq}^{(r)}R_{ir}^{(r)}R_{ks}^{(r)}\mathcal{L}_{mnpq}^{(r)}(\mathbf{D}^{(r)}), \quad (2.51)$$

where it is noted that $\mathcal{L}_{mnpq}^{(r)}(\mathbf{D}^{(r)})$ will exhibit orthotropic symmetry—characterized by 12 independent principal components⁶—with respect to the laboratory frame of reference. Since, as already stated, the generalized moduli tensors $\mathbf{L}^{(r)}$ are expected to also be objective and isotropic tensor functions of $\mathbf{F}^{(r)}$, it is reasonable to prescribe the following requirement for the functional dependence of the moduli tensors $\mathbf{L}^{(r)}$ on the variables $\mathbf{F}^{(r)}$:

$$L_{ijkl}^{(r)}(\mathbf{F}^{(r)}) = Q_{rm}^{(r)} Q_{jn}^{(r)} Q_{sp}^{(r)} Q_{lq}^{(r)} R_{ir}^{(r)} R_{ks}^{(r)} L_{mnpq}^{(r)}(\mathbf{D}^{(r)}), \quad (2.52)$$

where the $\mathbf{L}^{*(r)} \doteq \mathbf{L}^{(r)}(\mathbf{D}^{(r)})$ will be assumed to be orthotropic, fourth-order tensors with respect to the laboratory frame of reference. Thus, since $\mathbf{R}^{(r)}$ and $\mathbf{Q}^{(r)}$ can be readily determined from $\mathbf{F}^{(r)}$, it is seen that prescription (2.52) reduces the number of independent components of $\mathbf{L}^{(r)}$ from 45 to only 12, namely, the 12 independent components of the orthotropic tensor $L_{mnpq}^{*(r)}$. At this stage it is useful to note that relation (2.44) (or (2.45)) can be thought of as a set of equations for the 9 components of the second-order tensor $\hat{\mathbf{F}}^{(r)}$ (for each $r = 1, \dots, N$). Therefore, the simplest way to generate a *consistent* system of equations out of relation (2.44) is to further reduce the number of independent components of $L_{mnpq}^{*(r)}$ to 9. (Recall that our objective in the present work is not to obtain the best possible results.) In this case, only 9 equations will be generated by differentiating with respect to these 9 independent components, which will involve only certain traces of the fluctuations tensors $\mathbf{C}_{\mathbf{F}}^{(r)}$, as will be seen below. Prescriptions of the type (2.52), as it will be seen in more detail in the applications presented in the sequel, turn out to be consistent with the physical requirements of objectivity (2.47)₂ and overall material symmetry (2.48)₂.

Having established the result (2.52) for the modulus tensors $\mathbf{L}^{(r)}$ for composite elastomers with isotropic phases, it remains to establish a consistent prescription for the variables $\mathbf{F}^{(r)}$. The simplest prescription satisfying the objectivity and overall material symmetry requirements, (2.47)₁ and (2.48)₁, as well as the requirement that the reference variables $\mathbf{F}^{(r)}$ tend to the macroscopic average $\bar{\mathbf{F}}$ in the small-contrast limit, is, of course,

$$\mathbf{F}^{(r)} = \bar{\mathbf{F}}, \quad (2.53)$$

An alternative prescription, also satisfying these requirements, would be to set $\mathbf{F}^{(r)} = \bar{\mathbf{F}}^{(r)}$, as initially proposed by Lopez-Pamies and Ponte Castañeda (2004a).⁷ However, it has been shown

⁶Recall that an orthotropic fourth-order tensor with only major symmetry has 15 independent principal components. However, tangent modulus tensors derived from isotropic stored-energy functions contain only 12 independent principal components.

⁷This article has been included as Appendix A at the end of this thesis.

that for certain limiting cases, the prescriptions $\mathbf{F}^{(r)} = \overline{\mathbf{F}}^{(r)}$ lead to inconsistencies (see Appendix VI). For this reason, in this work, dealing with general elastomeric systems, use will be made of the prescription (2.53), which has been found to lead to more physically consistent results. However, it should be re-emphasized that it is not yet known what the best prescription for the reference variables $\mathbf{F}^{(r)}$ is.

In the next section, we will make use of conditions (2.53) for the $\mathbf{F}^{(r)}$ and of conditions (2.52) for the $\mathbf{L}^{(r)}$ to specialize the general second-order estimate (2.46) to the case of two-phase elastomeric composites with “particulate” microstructures, where both the matrix and the inclusion phase will be taken to be isotropic.

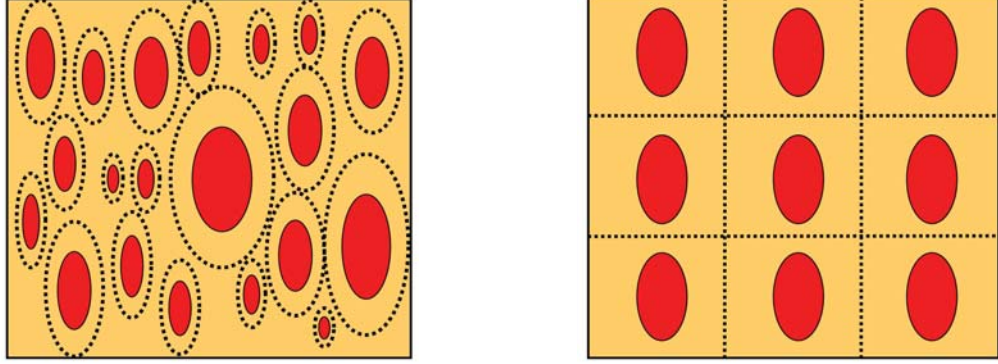
2.4 Effective behavior of two-phase hyperelastic composites with “particulate” microstructures

In this section, we specialize the general second-order estimate (2.46) for the effective stored-energy function \widehat{W} to the specific case of two-phase composites consisting of ellipsoidal particles,⁸ with given initial volume fraction $c_0^{(2)} = c_0$ and characterized by the *isotropic* stored-energy function $W^{(2)}$, which are distributed either *randomly* with “ellipsoidal symmetry” (Willis, 1977; Ponte Castañeda and Willis, 1995) or *periodically* (Nemat-Nasser *et al.*, 1982; Suquet, 1990) in a compressible elastomeric matrix with *isotropic* stored-energy function $W^{(1)}$ (see Fig. 2.1).

2.4.1 Classical bounds

Before proceeding with the specialization of the second-order estimates, it is important to make certain remarks with regard to the classical Voigt upper bound (2.29) and the Reuss-type polyconvex lower bound (2.31), which depend only on the initial volume fractions of the phases. (The specializations of these bounds to the case of two-phase elastomers with hyperelastic matrix phase $W^{(1)}$ and inclusion phase $W^{(2)}$ are straightforward and therefore will not be detailed here.) First, note that in the limit when the inclusion phase is made *rigid*, the Voigt upper bound becomes infinite. Although rigorously an upper bound, the Voigt estimate is physically unrealistic in this limiting case, as it would suggest that the addition of any fraction (even infinitesimal) of rigid

⁸This assumption could be relaxed to admit other particle shapes, but, for conciseness, this will not be done here.



(a)

(b)

Figure 2.1: Schematic representation of the “particulate” microstructures considered in this work. (a) Ellipsoidal particles distributed *randomly* with “ellipsoidal symmetry;” the solid ellipsoids denote the inclusions, and the dashed ellipsoids, their distribution. (b) Ellipsoidal particles distributed *periodically*; the solid ellipsoids denote the inclusions, and the dashed parallelepipeds, their distribution.

reinforcement into an elastomeric matrix would result in a rigid material, which is in contradiction with experimental evidence. On the other hand, the polyconvex lower bound remains finite in this limit, and therefore it can be of use. However, it should be recalled that this bound does not linearize properly (Ponte Castañeda, 1989), *i.e.*, it does not reduce to the classical Reuss lower bound for infinitesimal deformations. Second, note that in the limit when the inclusion phase becomes *vacuous* (*i.e.*, $W^{(2)} = 0$) and the matrix phase is *incompressible* (typical of rubbers), the Voigt bound becomes unbounded for all loadings, except for isochoric deformations. That is, the Voigt bound suggests that a porous elastomer with incompressible matrix phase is itself incompressible, which is in contradiction with experience. Moreover, the polyconvex lower bound vanishes identically in the limit when the inclusion phase becomes vacuous. The corresponding failures of the Voigt upper bound and the polyconvex lower bound can be used as motivation for generating the new type of estimates that we propose to develop in this work. Although, they are less rigorous in the sense that they are not bounds, they will be much more accurate, providing more realistic predictions, especially, for cases when the inclusion phase is significantly stiffer or softer than the matrix phase.

2.4.2 The linear comparison composite

The computation of the second-order estimates for two-phase elastomeric composites requires the determination of the effective stored-energy function associated with a *fictitious* linear comparison composite (LCC) with the same microstructure as the original elastomer, as well as the corresponding phase averages $\bar{\mathbf{F}}^{(r)}$ and fluctuations $\mathbf{C}_{\mathbf{F}}^{(r)}$ ($r = 1, 2$). It is remarked that the LCC problem at hand involves non-symmetric measures of “stress” and “strain” and hence a suitable generalization of the classical problem is required. This generalization is straightforward and it was carried out by Ponte Castañeda and Tiberio (2000) in the broader context of N -phase “thermoelastic” composites. The general expressions will not be repeated here, instead, only the relevant results specialized to two-phase systems will be considered. In this regard, it is recalled that great simplification of the general relations for thermoelastic composites is available for the special class of two-phase composites. Thus, making use of an appropriate generalization of the Levin relations (Levin, 1967), the effective stored-energy function \widehat{W}_T for the two-phase LCC may be written simply as:

$$\widehat{W}_T(\bar{\mathbf{F}}) = \tilde{f} + \tilde{\mathbf{T}} \cdot \bar{\mathbf{F}} + \frac{1}{2} \bar{\mathbf{F}} \cdot \tilde{\mathbf{L}} \bar{\mathbf{F}}, \quad (2.54)$$

where $\tilde{f} = \bar{f} + \frac{1}{2} (\Delta \mathbf{L})^{-1} \Delta \mathbf{T} \cdot (\tilde{\mathbf{L}} - \bar{\mathbf{L}}) (\Delta \mathbf{L})^{-1} \Delta \mathbf{T}$, $\tilde{\mathbf{T}} = \bar{\mathbf{T}} + (\tilde{\mathbf{L}} - \bar{\mathbf{L}}) (\Delta \mathbf{L})^{-1} \Delta \mathbf{T}$ are effective “specific-heat” and “thermal stress” quantities, depending on the effective modulus tensor $\tilde{\mathbf{L}}$, which is characterized in more detail further below. Also, in these expressions, $f^{(r)} = W^{(r)}(\mathbf{F}^{(r)}) - \mathbf{T}^{(r)} \cdot \mathbf{F}^{(r)} - \frac{1}{2} \mathbf{F}^{(r)} \cdot \mathbf{L}^{(r)} \mathbf{F}^{(r)}$, $\mathbf{T}^{(r)} = \mathcal{S}^{(r)}(\mathbf{F}^{(r)}) - \mathbf{L}^{(r)} \mathbf{F}^{(r)}$ ($r = 1, 2$), and $\Delta \mathbf{L} = \mathbf{L}^{(1)} - \mathbf{L}^{(2)}$, $\Delta \mathbf{T} = \mathbf{T}^{(1)} - \mathbf{T}^{(2)}$. Furthermore, \bar{f} , $\bar{\mathbf{T}}$, and $\bar{\mathbf{L}}$ are the volume averages of f , \mathbf{T} , and \mathbf{L} . Note that the effective stored-energy function \widehat{W}_T is completely determined in terms of $\tilde{\mathbf{L}}$.

In the above relations, $\tilde{\mathbf{L}}$ is the effective modulus tensor of the two-phase, *linear-elastic* comparison composite with modulus tensors $\mathbf{L}^{(1)}$ and $\mathbf{L}^{(2)}$, and the same microstructure, in its undeformed configuration, as the nonlinear hyperelastic composite. A reasonably good estimate for the type of “particulate” microstructures considered in this section is the generalized estimate of the Hashin-Shtrikman (HS) type (Willis, 1977):

$$\tilde{\mathbf{L}} = \mathbf{L}^{(1)} + c_0 [(1 - c_0) \mathbf{P} - (\Delta \mathbf{L})^{-1}]^{-1}. \quad (2.55)$$

Here, \mathbf{P} is a microstructural tensor that depends on the size, shape and orientation of the inclusions, as well as on their spatial distribution. In particular, the tensor \mathbf{P} depends on whether the distribution of the inclusions is *random* (Willis, 1977; Ponte Castañeda and Willis, 1995), or

periodic (Nemat-Nasser *et al.*, 1982; Suquet, 1990). In passing, it is appropriate to remark that the HS-type estimate (2.55) reduces to the classical result in the limit of small deformations (see Appendix IV for details). Furthermore, the estimate (2.55) is known to be accurate for small to moderate initial volume fractions of inclusions, c_0 , and that it may become inaccurate for large c_0 , when the interactions among the particles become especially strong. Since the volume fraction of inclusions, as well as their shape, orientation, and distribution, in a elastomeric composite can evolve (see Section 2.5) as a function of finite deformation histories, this has the practical implication that the second-order estimates of the HS type may become inaccurate once the volume fraction, or other relevant microstructural variables, reach values approaching the percolation limit (as explained in detail in Section 2.5). However, it should be emphasized that the second-order estimates (2.46) could still be used beyond this range, provided that a more sophisticated estimate was used for the LCC. Next, we provide explicit expressions for \mathbf{P} for the *random* and *periodic* microstructures considered in this work.

For a *random*, “*ellipsoidal*” distribution of ellipsoidal inclusions, the microstructural tensor \mathbf{P} can be written as (Willis, 1977; 1982):

$$\mathbf{P} = \frac{1}{4\pi \det(\mathbf{Z}_0)} \int_{|\boldsymbol{\xi}|=1} \mathbf{H}(\boldsymbol{\xi}) (\mathbf{Z}_0^{-1}\boldsymbol{\xi} \cdot \mathbf{Z}_0^{-1}\boldsymbol{\xi})^{-3/2} dS. \quad (2.56)$$

In this relation, $H_{ijkl}(\boldsymbol{\xi}) = K_{ik}^{-1} \xi_j \xi_l$, with $K_{ik} = L_{ijkl}^{(1)} \xi_j \xi_l$, and the symmetric second-order tensor \mathbf{Z}_0 serves to characterize the “ellipsoidal symmetry” of the microstructure in the reference configuration. More specifically, the tensor \mathbf{Z}_0 serves to define the shape and orientation of the ellipsoidal particles, as well as the “shape” and “orientation” of their two-point correlation function, which are assumed to be initially identical to those of the particles. (This assumption could be relaxed by allowing the shapes and orientations of the particles and of their distribution functions to be different (Ponte Castañeda and Willis, 1995), but this is not done here as it would necessitate the use of two different \mathbf{P} tensors.) For later use, it will prove convenient to spell out three limiting cases of practical interest in expression (2.56). The first one corresponds to an isotropic distribution of *spherical particles*, and is simply obtained by setting $\mathbf{Z}_0 = \mathbf{I}$ in (2.56). The second limiting case corresponds to aligned *cylindrical fibers* distributed with “elliptical” symmetry in the plane transverse to the fiber direction, and can be obtained by setting $\mathbf{Z}_0 = \text{diag}(1/z_1^0, 1/z_2^0, \epsilon)$ in (2.56) and taking the limit $\epsilon \rightarrow 0$. The analysis of this limit is given in Appendix V, but the final

expression for the tensor \mathbf{P} can be written as follows:

$$P_{ijkl} = \frac{\omega_0}{2\pi} \int_{\xi_1^2 + \xi_2^2 = 1} \frac{H_{ijkl}(\xi_1, \xi_2, \xi_3 = 0)}{\xi_1^2 + \omega_0^2 \xi_2^2} dS. \quad (2.57)$$

Here, it should be noted that the components in (2.57) are relative to the principal axes of \mathbf{Z}_0 , as defined by the rectangular Cartesian basis $\{\mathbf{e}_i\}$. Moreover, in expression (2.57), $\omega_0 = z_2^0/z_1^0$ and the fibers have been aligned—without loss of generality—in the \mathbf{e}_3 direction. Finally, the third limiting case corresponds to *layers* forming a laminate, and can be obtained by setting $Z_0 = \text{diag}(1/z_1^0, \epsilon, \epsilon)$ in (2.56) and taking the limit $\epsilon \rightarrow 0$, or, equivalently, by taking the limit $\omega_0 \rightarrow \infty$ (or $\omega_0 \rightarrow 0$) in (2.57). The analysis of this limit is also included in Appendix V, but the corresponding final expression for the tensor \mathbf{P} characterizing a laminate microstructure reads as follows:

$$\mathbf{P} = \mathbf{H}(\mathbf{N}), \quad (2.58)$$

where \mathbf{N} denotes the direction of lamination in the undeformed configuration.

For a *periodic* distribution of ellipsoidal inclusions, the microstructural tensor \mathbf{P} can be written as (Suquet, 1990):

$$\mathbf{P} = \frac{c_0}{1 - c_0} \sum_{\boldsymbol{\xi} \in \mathcal{R}^* - \{\mathbf{0}\}} \mathbf{H}(\boldsymbol{\xi}) G_I(-\boldsymbol{\xi}) G_I(\boldsymbol{\xi}), \quad (2.59)$$

where $\mathbf{H}(\boldsymbol{\xi})$ has already been defined above, $G_I(\boldsymbol{\xi}) = 3(\sin \eta - \eta \cos \eta)/\eta^3$ with $\eta = (\mathbf{Z}_0^{-1} \boldsymbol{\xi} \cdot \mathbf{Z}_0^{-1} \boldsymbol{\xi})^{1/2}$, and \mathcal{R}^* denotes the reciprocal periodic lattice (*i.e.*, in Fourier space). Note that here, similar to (2.56), the tensor \mathbf{Z}_0 characterizes the shape and orientation of the ellipsoidal particles in the undeformed configuration. On the other hand, the initial distribution of the (center of the) particles is *completely* characterized by \mathcal{R}^* (see, e.g. Chapter 2 in Kittel (1968)). Finally, it is worth noticing that the computation of (both, (2.56) and (2.59), tensors) \mathbf{P} depends on the anisotropy of the modulus $\mathbf{L}^{(1)}$, which in turn depends on the functional form of the potential $W^{(1)}$, as well as the particular type of loading, as determined by $\bar{\mathbf{F}}$.

Next, it can be shown (see, for example, Ponte Castañeda and Suquet, 1998) that the average deformations $\bar{\mathbf{F}}^{(1)}$ and $\bar{\mathbf{F}}^{(2)}$ in the matrix and inclusion phase of the LCC can be conveniently determined from the overall average deformation condition, together with the stored-energy function (2.54), through the relations:

$$\bar{\mathbf{F}}^{(1)} = \frac{1}{1 - c_0} \left(\bar{\mathbf{F}} - c_0 \bar{\mathbf{F}}^{(2)} \right), \quad \text{and} \quad \bar{\mathbf{F}}^{(2)} = \frac{1}{c_0} \left. \frac{\partial(\widehat{W}_T - \bar{f})}{\partial \mathbf{T}^{(2)}} \right|_{\mathbf{L}^{(2)}}, \quad (2.60)$$

respectively. Note that the derivative of $\widehat{W}_T - \bar{f}$ with respect to $\mathbf{T}^{(2)}$ in the second of relation (2.60) must be carried out with $\mathbf{L}^{(2)}$ held fixed.

Furthermore, the fluctuations $\mathbf{C}_{\mathbf{F}}^{(1)}$ and $\mathbf{C}_{\mathbf{F}}^{(2)}$ in the matrix and inclusion phase of the LCC can be readily determined through the relations:

$$\mathbf{C}_{\mathbf{F}}^{(1)} = \frac{2}{1 - c_0} \left. \frac{\partial \widehat{W}_T}{\partial \mathbf{L}^{(1)}} \right|_{\mathbf{F}^{(1)} = \bar{\mathbf{F}}^{(1)}}, \quad \text{and} \quad \mathbf{C}_{\mathbf{F}}^{(2)} = \mathbf{0}, \quad (2.61)$$

respectively. Note that the derivative of \widehat{W}_T with respect to $\mathbf{L}^{(1)}$ in the RHS of (2.61)₁ must be carried out with $\mathbf{F}^{(1)}$ held fixed. Moreover, the vanishing of the fluctuations in the inclusions, as stated by (2.61)₂, is a direct consequence of the use of the HS-type estimates (2.55) in the homogenization process.

2.4.3 Second-order homogenization estimates: compliant particles

In this subsection, we specialize the general second-order estimate (2.46) to the case of the two-phase, particulate, elastomeric composites introduced above. For later use, it is convenient to present the development for a general reference deformation gradient $\mathbf{F}^{(1)}$. On the other hand, in view of the fact that the fluctuations associated with the HS-type estimate for the LCC vanish identically in phase 2, it proves computationally simpler to set the reference deformation gradient $\mathbf{F}^{(2)} = \bar{\mathbf{F}}^{(2)}$. It is emphasized that any other prescription (satisfying the conditions of objectivity (2.47)₁ and overall material symmetry (2.48)₁) for $\mathbf{F}^{(2)}$ would lead to exactly the same second-order estimate (as a consequence of the use of the HS-type estimates (2.55) for the LCC). Thus, the second-order estimate for two-phase elastomeric materials simplifies to:

$$\widehat{W}(\bar{\mathbf{F}}) = (1 - c_0) \left[W^{(1)}(\hat{\mathbf{F}}^{(1)}) - \mathcal{S}^{(1)}(\mathbf{F}^{(1)}) \cdot (\hat{\mathbf{F}}^{(1)} - \bar{\mathbf{F}}^{(1)}) \right] + c_0 W^{(2)}(\bar{\mathbf{F}}^{(2)}). \quad (2.62)$$

Here, $\bar{\mathbf{F}}^{(1)}$, $\bar{\mathbf{F}}^{(2)}$, $\hat{\mathbf{F}}^{(1)}$, $\hat{\mathbf{F}}^{(2)}$, together with the modulus tensors $\mathbf{L}^{(1)}$ and $\mathbf{L}^{(2)}$, need to be made explicit. To this end, it is important to realize that by setting $\mathbf{F}^{(2)} = \bar{\mathbf{F}}^{(2)}$ it follows (from the appropriate specialization of equations (2.40) and (2.41)) that $\hat{\mathbf{F}}^{(2)} = \bar{\mathbf{F}}^{(2)}$, and that the modulus tensor of the inclusion phase in the LCC reduces to $\mathbf{L}^{(2)} = \partial^2 W^{(2)}(\bar{\mathbf{F}}^{(2)}) / \partial \mathbf{F}^2$. Next, it is noted that the average deformation gradient $\bar{\mathbf{F}}^{(1)}$ in the matrix phase of the relevant LCC is determined, in terms of the applied macroscopic loading $\bar{\mathbf{F}}$ and the average deformation gradient $\bar{\mathbf{F}}^{(2)}$ in the inclusion phase of the LCC, from the overall average deformation condition (2.60)₁.

Now, with the above simplifications, equation (2.60)₂ leads to:

$$\bar{\mathbf{F}}^{(2)} = \bar{\mathbf{F}} - \frac{1}{c_0} (\Delta \mathbf{L})^{-1} (\tilde{\mathbf{L}} - \bar{\mathbf{L}}) (\Delta \mathbf{L})^{-1} \left[\Delta \mathbf{S} + \mathbf{L}^{(1)} (\bar{\mathbf{F}} - \mathbf{F}^{(1)}) - \mathbf{L}^{(2)} (\bar{\mathbf{F}} - \bar{\mathbf{F}}^{(2)}) \right], \quad (2.63)$$

where $\Delta \mathbf{S} = \mathbf{S}^{(1)}(\mathbf{F}^{(1)}) - \mathbf{S}^{(2)}(\bar{\mathbf{F}}^{(2)})$. Making use of the HS estimate (2.55), this expression can be shown to simplify to:

$$\bar{\mathbf{F}} - \bar{\mathbf{F}}^{(2)} = (1 - c_0) \mathbf{P} \left[\mathbf{L}^{(1)} (\mathbf{F}^{(1)} - \bar{\mathbf{F}}^{(2)}) - \mathbf{S}^{(1)}(\mathbf{F}^{(1)}) + \mathbf{S}^{(2)}(\bar{\mathbf{F}}^{(2)}) \right], \quad (2.64)$$

which can be seen to constitute a system of 9 nonlinear algebraic equations for the 9 components of the average deformation gradient $\bar{\mathbf{F}}^{(2)}$. Note that these equations depend directly on the modulus tensor $\mathbf{L}^{(1)}$ of the matrix phase, but, remarkably, *not* on the modulus tensor $\mathbf{L}^{(2)}$ of the inclusion phase.

Next, the generalized secant condition (2.40) for the matrix phase provides an equation for the variable $\hat{\mathbf{F}}^{(1)}$, which is given by:

$$\mathbf{S}^{(1)}(\hat{\mathbf{F}}^{(1)}) - \mathbf{S}^{(1)}(\mathbf{F}^{(1)}) = \mathbf{L}^{(1)}(\hat{\mathbf{F}}^{(1)} - \mathbf{F}^{(1)}). \quad (2.65)$$

This relation can be interpreted as a set of 9 nonlinear algebraic equations for the 9 components of $\hat{\mathbf{F}}^{(1)}$.

As discussed in the previous section, the modulus tensor $\mathbf{L}^{(1)}$ for the *isotropic* matrix phase will be taken to be of the form (2.52), which is now written as:

$$L_{ijkl}^{(1)} = Q_{rm}^{(1)} Q_{jn}^{(1)} Q_{sp}^{(1)} Q_{lq}^{(1)} R_{ir}^{(1)} R_{ks}^{(1)} L_{mnpq}^*, \quad (2.66)$$

where the notation $L_{ijkl}^* = L_{ijkl}^{(1)}(\mathbf{D}^{(1)})$ has been introduced for convenience. It is recalled that \mathbf{L}^* should be assumed to have orthotropic symmetry relative to the laboratory frame of reference. In order to avoid the potential inconsistencies associated with equation (2.45) for the second moments of the deformation gradient field in the matrix phase of the LCC, the tensors \mathbf{L}^* will be chosen here to have only 9 independent components, instead of the 12 components that would normally be associated with orthotropic symmetry (for fourth-order tangent modulus tensors derived from isotropic stored-energy functions). As it will be seen in the applications to follow, the choice of the 9 independent components of \mathbf{L}^* is somewhat arbitrary, and depends on the specific constitutive behavior of the hyperelastic matrix phase. However, at this stage, it is only important to recognize

that the restriction to 9 independent components for \mathbf{L}^* will translate into internal constraints among the 12 standard components of the orthotropic tensor \mathbf{L}^* . Then, denoting by ℓ_α^* ($\alpha = 1, 2, \dots, 9$) the 9 independent components of \mathbf{L}^* , and repeating the procedure that led from the stationarity condition (2.41) to expression (2.44) now gives:

$$\left(\hat{\mathbf{F}}^{(1)} - \mathbf{F}^{(1)}\right) \cdot \frac{\partial \mathbf{L}^{(1)}}{\partial \ell_\alpha^*} \left(\hat{\mathbf{F}}^{(1)} - \mathbf{F}^{(1)}\right) = \frac{2}{1 - c_0} \left. \frac{\partial \widehat{W}_T}{\partial \ell_\alpha^*} \right|_{\mathbf{F}^{(1)}}. \quad (2.67)$$

In this expression, \widehat{W}_T is the stored-energy function of the relevant LCC given by (2.54) with $\mathbf{F}^{(2)} = \overline{\mathbf{F}}^{(2)}$, and $\mathbf{L}^{(2)} = \partial^2 W^{(2)}(\overline{\mathbf{F}}^{(2)})/\partial \mathbf{F}^2$. Thus, the right-hand side of this equation can be computed by performing the indicated derivatives with respect to the moduli ℓ_α^* . The resulting expressions, which involve suitable traces of the fluctuation tensor $\mathbf{C}_{\mathbf{F}}^{(1)}$, are rather complicated, but can be simplified dramatically by repeated use of the expression (2.64) for $\overline{\mathbf{F}}^{(2)}$. In the end, the equations (2.67) can be rewritten in the simple form:

$$\begin{aligned} \left(\hat{\mathbf{F}}^{(1)} - \mathbf{F}^{(1)}\right) \cdot \frac{\partial \mathbf{L}^{(1)}}{\partial \ell_\alpha^*} \left(\hat{\mathbf{F}}^{(1)} - \mathbf{F}^{(1)}\right) &= \frac{1}{1 - c_0} \left(\overline{\mathbf{F}} - \mathbf{F}^{(1)}\right) \cdot \frac{\partial \mathbf{L}^{(1)}}{\partial \ell_\alpha^*} \left(\overline{\mathbf{F}} - \mathbf{F}^{(1)}\right) \\ &\quad - \frac{c_0}{1 - c_0} \left(\mathbf{F}^{(1)} - \overline{\mathbf{F}}^{(2)}\right) \cdot \frac{\partial \mathbf{L}^{(1)}}{\partial \ell_\alpha^*} \left(\mathbf{F}^{(1)} - \overline{\mathbf{F}}^{(2)}\right) \\ &\quad - \frac{c_0}{(1 - c_0)^2} \left(\overline{\mathbf{F}} - \overline{\mathbf{F}}^{(2)}\right) \cdot \mathbf{P}^{-1} \frac{\partial \mathbf{P}}{\partial \ell_\alpha^*} \mathbf{P}^{-1} \left(\overline{\mathbf{F}} - \overline{\mathbf{F}}^{(2)}\right). \end{aligned} \quad (2.68)$$

They constitute a system of 9 scalar equations for the 9 scalar variables ℓ_α^* , which, remarkably, are also independent of the modulus tensor $\mathbf{L}^{(2)}$ of the inclusion phase. (Recall that $\overline{\mathbf{F}}^{(2)}$, as determined by equation (2.64), is independent of $\mathbf{L}^{(2)}$.)

The only variable that remains to be specified is the reference deformation gradient $\mathbf{F}^{(1)}$, which in this work will be set equal to $\overline{\mathbf{F}}$ (*i.e.*, $\mathbf{F}^{(1)} = \overline{\mathbf{F}}$). Therefore, in conclusion, equations (2.64), (2.65), and (2.68) constitute a closed system of 27 nonlinear algebraic equations for the 27 scalar unknowns formed by the 9 components of $\overline{\mathbf{F}}^{(2)}$, the 9 components of $\hat{\mathbf{F}}^{(1)}$, and the 9 independent components of $\mathbf{L}^{(1)}$ (*i.e.*, the 9 independent components of \mathbf{L}^* , denoted by ℓ_α^*), which, in general, must be solved numerically. Having computed the values of all the components of $\overline{\mathbf{F}}^{(2)}$, $\hat{\mathbf{F}}^{(1)}$, and $\mathbf{L}^{(1)}$ for a given loading $\overline{\mathbf{F}}$, the values of the components of $\overline{\mathbf{F}}^{(1)}$ can be readily determined using relation (2.60)₁. In turn, the second-order estimate for the effective stored-energy function \widehat{W} for two-phase, particulate, elastomeric composites can now be computed, from relation (2.62), using these results. It should be emphasized that the resulting estimate is objective, as will be seen in more detail in subsequent chapters of this work.

To conclude, it is interesting to remark that the just-defined system of equations defining the effective stored-energy function \widehat{W} for a general, two-phase, hyperelastic composite with particulate microstructure does *not* depend explicitly on the modulus tensor $\mathbf{L}^{(2)}$ of the inclusion phase (although, of course, it does depend on the behavior of the hyperelastic inclusion phase through the energy function $W^{(2)}$). This unexpected result is a consequence of the use of the HS-type estimate (2.55), which implies vanishing fluctuations in the inclusion phase of the LCC. In any event, the independence of the second-order estimate (2.62) (together with expressions (2.64), (2.65), and (2.68)) on $\mathbf{L}^{(2)}$ will greatly facilitate the computation of the limiting cases of vacuous inclusions and rigid particles, which are considered next.

2.4.4 Second-order homogenization estimates: porous elastomers

The specialization of the second-order estimate (2.62) for general two-phase elastomers with particulate microstructures to porous elastomers can be simply obtained by setting $W^{(2)} = 0$. The result reads as follows:

$$\widehat{W}(\overline{\mathbf{F}}) = (1 - f_0) \left[W^{(1)}(\hat{\mathbf{F}}^{(1)}) - \mathcal{S}^{(1)}(\overline{\mathbf{F}}) \cdot (\hat{\mathbf{F}}^{(1)} - \overline{\mathbf{F}}^{(1)}) \right], \quad (2.69)$$

where $f_0 = c_0$ for consistency with later chapters, and the variables $\overline{\mathbf{F}}^{(1)}$, $\hat{\mathbf{F}}^{(1)}$, and $\mathbf{L}^{(1)}$ are determined by suitably specializing the relations (2.60)₁, (2.64), (2.65), and (2.68), and eliminating the variable $\overline{\mathbf{F}}^{(2)}$ in these equations in favor of $\overline{\mathbf{F}}^{(1)}$. Thus, having set $\mathbf{F}^{(1)} = \overline{\mathbf{F}}$, the resulting equations are (2.65), which does not change, the following *explicit* equation for the average deformation gradient $\overline{\mathbf{F}}^{(1)}$ in the matrix phase:

$$\overline{\mathbf{F}}^{(1)} = \overline{\mathbf{F}} - f_0 \left(\mathbf{E}^{(1)} \right)^{-1} \mathcal{S}^{(1)}(\overline{\mathbf{F}}), \quad (2.70)$$

where

$$\mathbf{E}^{(1)} = \mathbf{P}^{-1} - (1 - f_0)\mathbf{L}^{(1)} \quad (2.71)$$

is a fourth-order tensor with major symmetry depending only on $\mathbf{L}^{(1)}$, and the field-fluctuations equation:

$$(\hat{\mathbf{F}}^{(1)} - \overline{\mathbf{F}}) \cdot \frac{\partial \mathbf{L}^{(1)}}{\partial \ell_\alpha^*} (\hat{\mathbf{F}}^{(1)} - \overline{\mathbf{F}}) = \frac{1}{f_0} \left(\overline{\mathbf{F}} - \overline{\mathbf{F}}^{(1)} \right) \cdot \frac{\partial \mathbf{E}^{(1)}}{\partial \ell_\alpha^*} \left(\overline{\mathbf{F}} - \overline{\mathbf{F}}^{(1)} \right). \quad (2.72)$$

In short, equations (2.65) and (2.72) constitute a closed system of 18 nonlinear, algebraic equations for the 18 unknowns formed by the 9 components of $\hat{\mathbf{F}}^{(1)}$ and the 9 independent components of $\mathbf{L}^{(1)}$ (*i.e.*, the parameters ℓ_α^*). Having computed all the components of $\hat{\mathbf{F}}^{(1)}$ and $\mathbf{L}^{(1)}$, for a given

loading $\overline{\mathbf{F}}$ and initial microstructure, the components of $\overline{\mathbf{F}}^{(1)}$ can be readily obtained from (2.70). In turn, these results can be used to finally compute the second-order estimate (2.69)

Finally, it is worth mentioning that the above-developed expressions are equivalent to those given in Section 4.3 of Lopez-Pamies and Ponte Castañeda (2004b) (for version 3 of the second-order estimates) for porous elastomers, but the expressions given here are more explicit (and therefore easier to implement).

2.4.5 Second-order homogenization estimates: rigid particles

In this subsection, we specialize further the general second-order estimate (2.62) to the limiting case when the particles are taken to be *rigid*. To this end, for simplicity and without loss of generality, the following choice is made for the stored-energy function of the inclusion phase:

$$W^{(2)}(\mathbf{F}) = \frac{\mu^{(2)}}{2} (\mathbf{F} \cdot \mathbf{F} - 3) - \mu^{(2)} \ln(\det \mathbf{F}) \quad (2.73)$$

where the shear modulus $\mu^{(2)}$ will be taken to tend to infinity in order to model rigid behavior. Note that this form for $W^{(2)}$ is objective and consistent with the requirement that the deformation gradient \mathbf{F} within the particles should tend to an orthogonal tensor \mathbf{R} (*i.e.*, the particles should undergo a rigid body rotation) in the limit $\mu^{(2)} \rightarrow \infty$. Based on this choice for the stored-energy function of the inclusion phase, an expansion for the average deformation gradient $\overline{\mathbf{F}}^{(2)}$ in the particles of the LCC is attempted in the limit as $\mu^{(2)} \rightarrow \infty$ of the following form:

$$\overline{\mathbf{F}}^{(2)} = \overline{\mathbf{R}}^{(2)} + \epsilon \overline{\mathbf{F}}_1^{(2)} + O(\epsilon^2), \quad (2.74)$$

where $\epsilon = 1/\mu^{(2)}$ is a small parameter, and $\overline{\mathbf{R}}^{(2)}$ and $\overline{\mathbf{F}}_1^{(2)}$ are second-order tensors to be determined from the asymptotic analysis that follows. As suggested by (2.73), $\overline{\mathbf{R}}^{(2)}$ is assumed to be orthogonal. It is now relevant to spell out the asymptotic expansions for the stored-energy function $W^{(2)}$, as well as for the associated stress $\mathcal{S}^{(2)}$, evaluated at the average deformation gradient (2.74) in the limit as $\epsilon \rightarrow 0$. The results read as follows:

$$W^{(2)}(\overline{\mathbf{F}}^{(2)}) = 0 + O(\epsilon), \quad \mathcal{S}^{(2)}(\overline{\mathbf{F}}^{(2)}) = \frac{\partial W^{(2)}}{\partial \mathbf{F}}(\overline{\mathbf{F}}^{(2)}) = \mathcal{S}_o^{(2)} + O(\epsilon), \quad (2.75)$$

where the second-order tensor $\mathcal{S}_o^{(2)}$ is given by:

$$\mathcal{S}_o^{(2)} = \overline{\mathbf{F}}_1^{(2)} + \overline{\mathbf{R}}^{(2)} (\overline{\mathbf{F}}_1^{(2)})^T \overline{\mathbf{R}}^{(2)}. \quad (2.76)$$

We remark, for later use, that

$$(\overline{\mathbf{R}}^{(2)})^T \mathcal{S}_o^{(2)} = (\mathcal{S}_o^{(2)})^T \overline{\mathbf{R}}^{(2)}. \quad (2.77)$$

Although this identity can be easily verified algebraically, it is a simple consequence of the objectivity of the stored-energy function (2.73).

Now, using $\mathbf{F}^{(1)} = \overline{\mathbf{F}}$ for the reference deformation, it follows from the above asymptotic results that the leading-order term in equation (2.64) can be written in the form:

$$\mathbf{E}^{(1)}(\overline{\mathbf{F}} - \overline{\mathbf{R}}^{(2)}) + (1 - c_0) \left[\mathcal{S}^{(1)}(\overline{\mathbf{F}}) - \mathcal{S}_o^{(2)} \right] = \mathbf{0}, \quad (2.78)$$

where $\mathbf{E}^{(1)}$ and $\mathcal{S}_o^{(2)}$ are given, respectively, by expressions (2.71) and (2.76).

The expression (2.78), which is a *full* second-order tensorial relation (*i.e.*, it contains 9 independent scalar equations), can be used to generate an equation for the rotation tensor $\overline{\mathbf{R}}^{(2)}$, which has only 3 independent components, by first left-multiplying expression (2.78) by $(\overline{\mathbf{R}}^{(2)})^T$, extracting the skew-symmetric part of this expression, and making use of the identity (2.77). The resulting equation for the average rigid rotation $\overline{\mathbf{R}}^{(2)}$ of the particles may be written in the form:

$$\begin{aligned} & (\overline{\mathbf{R}}^{(2)})^T \left[\mathbf{E}^{(1)}(\overline{\mathbf{F}} - \overline{\mathbf{R}}^{(2)}) \right] - \left[\mathbf{E}^{(1)}(\overline{\mathbf{F}} - \overline{\mathbf{R}}^{(2)}) \right]^T \overline{\mathbf{R}}^{(2)} \\ & + (1 - c_0) \left[(\overline{\mathbf{R}}^{(2)})^T \mathcal{S}^{(1)}(\overline{\mathbf{F}}) - (\mathcal{S}^{(1)}(\overline{\mathbf{F}}))^T \overline{\mathbf{R}}^{(2)} \right] = \mathbf{0}, \end{aligned} \quad (2.79)$$

which provides a set of 3 independent equations for the 3 components of $\overline{\mathbf{R}}^{(2)}$. It should be clear from the derivation that this equation is independent of the form of the constitutive behavior (2.73) assumed for the inclusion phase, since the only property that we have really used is the objectivity of $W^{(2)}$.

Having determined $\overline{\mathbf{R}}^{(2)}$ from equation (2.79), it is now a simple matter to obtain $\overline{\mathbf{F}}^{(1)}$ with the help of relation (2.60)₁. The result is:

$$\overline{\mathbf{F}}^{(1)} = \frac{1}{1 - c_0} \left(\overline{\mathbf{F}} - c_0 \overline{\mathbf{R}}^{(2)} \right) + O(\epsilon). \quad (2.80)$$

The generalized secant modulus expression (2.65) remains unchanged in the limit as $\epsilon \rightarrow 0$, but the expression (2.68) involving the field fluctuations can be easily shown to reduce to:

$$\left(\hat{\mathbf{F}}^{(1)} - \overline{\mathbf{F}} \right) \cdot \frac{\partial \mathbf{L}^{(1)}}{\partial \ell_\alpha^*} \left(\hat{\mathbf{F}}^{(1)} - \overline{\mathbf{F}} \right) = \frac{c_0}{(1 - c_0)^2} \left(\overline{\mathbf{F}} - \overline{\mathbf{R}}^{(2)} \right) \cdot \frac{\partial \mathbf{E}^{(1)}}{\partial \ell_\alpha^*} \left(\overline{\mathbf{F}} - \overline{\mathbf{R}}^{(2)} \right). \quad (2.81)$$

Finally, making use of expressions (2.75)₁ and (2.80) in (2.62), it is easy to show that the second-order estimate for the effective behavior of elastomers reinforced with *rigid* particles reduces to:

$$\widehat{W}(\overline{\mathbf{F}}) = (1 - c_0) W^{(1)}(\hat{\mathbf{F}}^{(1)}) + \mathcal{S}^{(1)}(\overline{\mathbf{F}}) \cdot \left[\overline{\mathbf{F}} - c_0 \overline{\mathbf{R}}^{(2)} - (1 - c_0) \hat{\mathbf{F}}^{(1)} \right]. \quad (2.82)$$

In summary, equations (2.65), (2.79) and (2.81) constitute a closed system of 21 nonlinear algebraic equations for the 21 scalar unknowns formed by the 3 components of $\overline{\mathbf{R}}^{(2)}$, the 9 components of $\hat{\mathbf{F}}^{(1)}$, and the 9 components of $\mathbf{L}^{(1)}$ (*i.e.*, the independent components ℓ_{α}^*), which, in general, must be solved numerically. Having computed all the components of $\overline{\mathbf{R}}^{(2)}$, $\hat{\mathbf{F}}^{(1)}$, and $\mathbf{L}^{(1)}$, for a given loading $\overline{\mathbf{F}}$ and initial microstructure, the second-order estimate (2.82) for the effective stored-energy function \widehat{W} of the rigidly reinforced elastomers can be readily obtained.

In passing, it is noted that the above results for rigidly reinforced elastomers provide a generalization of the earlier results of Ponte Castañeda and Tiberio (2000) and Lopez-Pamies and Ponte Castañeda (2004a), where, on account of the considered isotropic symmetry of the microstructure, it was sufficient to set the average rigid rotations for the rigid inclusions equal to the identity (*i.e.*, $\overline{\mathbf{R}}^{(2)} = \mathbf{I}$).

2.5 Microstructure evolution

When a composite material is subjected to finite deformations on its boundary, its microstructure will not remain fixed, but instead will evolve at every step of the deformation. In general, the problem of characterizing the evolution of the microstructure in a detailed manner is a hopelessly difficult task, due to the large number of microstructural variables that would be involved. However, for special classes of microstructures, such as the “particulate” microstructures discussed above, it is possible to develop consistent models for the evolution of suitably chosen microstructural variables. For viscoplastic composites, such types of models have been proposed by Kailasam and Ponte Castañeda (1998), the central idea being that the evolution of the size, shape and orientation of the inclusions should be controlled—on the average—by the average strain-rate and spin fields in the inclusion phase, essentially generalizing notions introduced by Eshelby (1957) for linearly viscous composite systems with dilute concentrations of inclusions. Thus, for the viscoplastic composites with particulate microstructures, the relevant microstructural variables were identified to be the volume fraction of the inclusion phase, and the average aspect ratios and orientation angles of the inclusions, and evolution laws for these variables were generated combining basic kinematics principles with nonlinear homogenization estimates for the average strain-rate and spin fields in the inclusion phase. For non-dilute systems, additional microstructural variables were also identified (Ponte Castañeda and Willis, 1995) serving to characterize the “distribution” of the

inclusions in the matrix phase, and evolution laws for these variables have also been proposed (Kailasam *et al.*, 1997).

For the viscoplastic composites mentioned in the previous paragraph, the development of evolution laws for the relevant microstructural variables was *essential* to be able to describe the constitutive response of these materials under *finite-deformation* histories. Given that the constitutive behavior of these materials is most naturally characterized by means of a Eulerian description of the kinematics, the relevant homogenization procedure is carried out by taking a snapshot of the microstructure at the current instant of time and generating an estimate for the instantaneous constitutive response of the material. This means that this snapshot homogenization process must be supplemented by appropriate laws serving to characterize the evolution of the microstructure from one instant to another instant in time.

In the present work, the interest is on hyperelastic composites, which are characterized, as we have seen, by a Lagrangian description of the kinematics. This means that—unlike the example of viscoplastic composites—the evolution of the microstructure resulting from the finite changes in geometry is already accounted for in the homogenized constitutive description, given by equations (2.16) with (2.12) for these materials. In other words, it is not necessary to obtain *additional* equations to characterize the evolution of the microstructure in these systems. Indeed, the minimizing solution in expression (2.12) for the effective stored-energy function of the composite elastomer contains implicitly all the necessary information to describe how every point in the specimen moves, and therefore, also how the microstructure evolves. Nevertheless, even if it is not necessary to know how the microstructure evolves in order to determine the effective behavior of a composite elastomer, it is still of interest to have access to this information, as it will be useful to develop a better understanding of the constitutive response of composite elastomers. As will be seen in the context of the applications in the sequel, the evolution of the microstructure plays a critical role in the determination of the overall response of composite elastomers, in general, and of their macroscopic stability, in particular.

For simplicity, the focus here will be on composite elastomers with the “particulate” microstructures described in the preceding section. These are two-phase composite systems comprised of an elastomeric matrix phase reinforced (or weakened) with ellipsoidal inclusions, which are all taken to be identical in shape and orientation, and are described by a “characteristic ellipsoid”

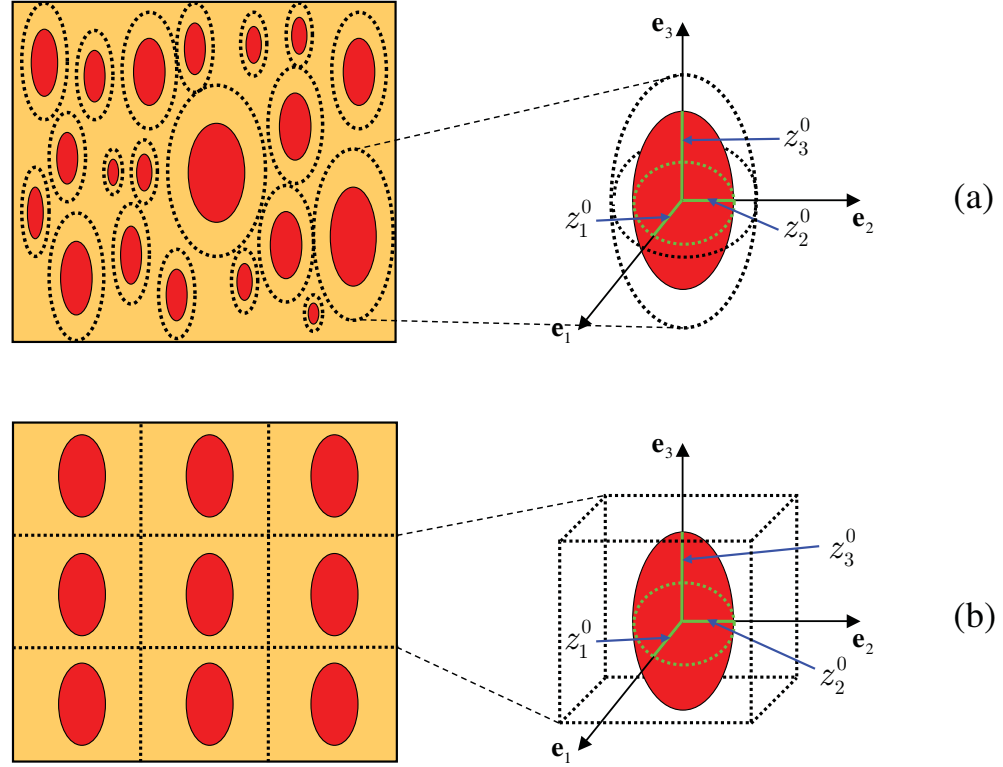


Figure 2.2: Schematic representation of two-phase, “particulate” composites in the undeformed configuration identifying the initial state of the various microstructural variables. (a) Random, ellipsoidal distribution. (b) Periodic distribution.

$E_0 = \{\mathbf{X} \mid \mathbf{X} \cdot (\mathbf{Z}_0^T \mathbf{Z}_0) \mathbf{X} \leq 1\}$ in the *reference* configuration. The symmetric second-order tensor $\mathbf{Z}_0^T \mathbf{Z}_0$ has principal values $1/(z_1^0)^2$, $1/(z_2^0)^2$, and $1/(z_3^0)^2$, defining two initial aspect ratios $\omega_1^0 = z_3^0/z_1^0$ and $\omega_2^0 = z_3^0/z_2^0$, and principal directions defining a rectangular Cartesian basis $\{\mathbf{e}_i\}$. In addition, the inclusions are assumed to be distributed either *randomly* or *periodically* (see Fig. 2.2). In the former case, it is further assumed that the inclusions are distributed with “ellipsoidal symmetry” with the same aspect ratio and orientation as the inclusions in the reference configuration, hence the use of only one microstructural tensor \mathbf{P} in (2.56) (see Ponte Castañeda and Willis, 1995).

Given the significant nonlinearities involved in these hyperelastic composites, the deformation-gradient field \mathbf{F} will *not* be uniform inside the inclusions, even for dilute concentrations ($c_0 \ll 1$). This means that the initially ellipsoidal inclusions will deform into inclusions with shapes that will not, except in the small-deformation domain, continue to be ellipsoidal. However, consistent with

the general aims of homogenization, where the interest is not in the details of the deformation fields, but only on average information on these fields, our objective here will be to characterize the evolution of the “average” size, shape and orientation of the inclusions, as determined by the *average deformation gradient* $\overline{\mathbf{F}}^{(2)}$ in the inclusion phase. It is important to mention in this context that this approximation is entirely consistent with the use of the estimates of the HS-type described in the previous section, since the deformation gradient field \mathbf{F} in this type of approximation turns out to be constant inside the inclusions, and therefore, such that $\mathbf{F}(\mathbf{X}) = \overline{\mathbf{F}}^{(2)}$ for $\mathbf{X} \in \Omega_0^{(2)}$.

Under these hypotheses, the material inside an inclusion centered at \mathbf{X}^c in the undeformed configuration, which is defined by the ellipsoid:

$$E_0^c = \{\mathbf{X} \mid (\mathbf{X} - \mathbf{X}^c) \cdot \mathbf{Z}_0^T \mathbf{Z}_0 (\mathbf{X} - \mathbf{X}^c) \leq 1\}, \quad (2.83)$$

will deform according to: $\mathbf{x} - \mathbf{x}^c = \overline{\mathbf{F}}^{(2)}(\mathbf{X} - \mathbf{X}^c)$, where \mathbf{x}^c denotes the center of the inclusion in the deformed configuration. It then follows that the inclusion defined by (2.83) evolves into the ellipsoid:

$$E^c = \{\mathbf{x} \mid (\mathbf{x} - \mathbf{x}^c) \cdot \mathbf{Z}^T \mathbf{Z} (\mathbf{x} - \mathbf{x}^c) \leq 1\}, \quad (2.84)$$

in the deformed configuration, where $\mathbf{Z} = \mathbf{Z}_0(\overline{\mathbf{F}}^{(2)})^{-1}$. The symmetric, second-order tensor $\mathbf{Z}^T \mathbf{Z}$ has principal values $1/(z_1)^2$, $1/(z_2)^2$, and $1/(z_3)^2$, which serve to define the two *current* aspect ratios $\omega_1 = z_3/z_1$ and $\omega_2 = z_3/z_2$ for the inclusions (in the deformed configuration). Similarly, the principal directions of $\mathbf{Z}^T \mathbf{Z}$, denoted here by the rectangular Cartesian basis $\{\mathbf{e}'_i\}$, define the principal directions of the inclusion in the *deformed* configuration. The evolution of the average shape and orientation of the inclusions can thus be characterized—through the tensor \mathbf{Z} —from the knowledge of the average deformation gradient $\overline{\mathbf{F}}^{(2)}$ in the inclusion phase, together with the initial shape and orientation of the inclusions in the reference configuration, as determined by \mathbf{Z}_0 .

Next, note that the *current* volume fraction of the inclusions in the *deformed* configuration is given by:

$$c \doteq \frac{\int_{\Omega^{(2)}} dv}{\int_{\Omega} dv} = \frac{\int_{\Omega_0^{(2)}} \det \mathbf{F} dV}{\int_{\Omega_0} \det \mathbf{F} dV} = \frac{\langle \det \mathbf{F} \rangle^{(2)}}{\langle \det \mathbf{F} \rangle} c_0 = \frac{\langle \det \mathbf{F} \rangle^{(2)}}{\det \overline{\mathbf{F}}} c_0, \quad (2.85)$$

where Ω and $\Omega^{(2)}$ denote the volume of the specimen and inclusion phase in the *deformed* configuration, respectively, and use has been made of the fact that $\det \mathbf{F}$ is a null-Lagrangian. Now, recalling that within the context of the HS-type estimates (2.55), used in the homogenization process for the above-described composites, the fields in the inclusion phase are constant, it follows that $\langle \det \mathbf{F} \rangle^{(2)} = \det \langle \mathbf{F} \rangle^{(2)} = \det \overline{\mathbf{F}}^{(2)}$, so that the current volume fraction of the inclusions in the

deformed configuration can be written as:

$$c = \frac{\det \overline{\mathbf{F}}^{(2)}}{\det \overline{\mathbf{F}}} c_0, \quad (2.86)$$

which may be readily computed in terms of the available estimate, $\overline{\mathbf{F}}^{(2)}$, for the average deformation gradient in the inclusion phase, and the known, initial volume fraction, c_0 , of the inclusions in the reference configuration.

The above results simplify considerably for the case when the particles are taken to be *rigid*. In this case, the inclusions are constrained to undergo an average rigid rotation $\overline{\mathbf{F}}^{(2)} = \overline{\mathbf{R}}^{(2)}$. This implies that $\det \overline{\mathbf{F}}^{(2)} = 1$, so that the current volume fraction of particles in the deformed configuration simplifies to:

$$c = \frac{c_0}{\det \overline{\mathbf{F}}}. \quad (2.87)$$

When the matrix phase is further assumed to be incompressible, $\det \overline{\mathbf{F}} = 1$, the expression (2.87) for the current value of the volume fraction of the inclusion phase further reduces to $c = c_0$, as expected on physical grounds. Moreover, in this case, the tensor $\mathbf{Z}^T \mathbf{Z}$ characterizing the shape and orientation of the particles in the deformed configuration reduces to:

$$\mathbf{Z}^T \mathbf{Z} = \overline{\mathbf{R}}^{(2)} \mathbf{Z}_0^T \mathbf{Z}_0 (\overline{\mathbf{R}}^{(2)})^T. \quad (2.88)$$

From this result, it is evident that for rigid particles the principal values of $\mathbf{Z}^T \mathbf{Z}$ are equal to those of $\mathbf{Z}_0^T \mathbf{Z}_0$. This implies that the shape of the particles will remain fixed upon deformation (*i.e.*, $\omega_1 = \omega_1^0$ and $\omega_2 = \omega_2^0$), which is, of course, consistent with the particles being rigid. On the other hand, the rotation tensor $\overline{\mathbf{R}}^{(2)}$ serves to characterize the reorientation of the principal axes of $\mathbf{Z}^T \mathbf{Z}$ with respect to those of $\mathbf{Z}_0^T \mathbf{Z}_0$.

In short, it has been shown that the evolution of the volume fraction, the *average* shape, and the *average* orientation of the inclusions in the type of reinforced elastomers considered in this work can be consistently estimated from the knowledge of the average deformation gradient $\overline{\mathbf{F}}^{(2)}$ in the particles, which, in turn, can be readily obtained from the homogenization estimates of the previous section.

Next, we address the evolution of the *distribution* of the inclusions (*i.e.*, the relative motion of the center of the underlying particles) as a function of the applied deformation $\overline{\mathbf{F}}$. For (simple) *periodic* microgeometries, it can be shown rigorously that the relative motion of the centers of the underlying inclusions are governed by the macroscopic deformation gradient $\overline{\mathbf{F}}$ (and not by

the average field $\bar{\mathbf{F}}^{(2)}$ in the inclusion phase), at least up to the onset of the first instability. On the other hand, for composite elastomers with *random* microstructures, the situation is less clear. Indeed, the author is not aware of any rigorous result regarding the evolution of the distribution of the underlying inclusions in elastomers with this type of microgeometries. However, it has been suggested (Lopez-Pamies and Ponte Castañeda, 2006a) that in this case the inclusions might also move—on the average—with the macroscopic flow, as determined by $\bar{\mathbf{F}}$. Accordingly, for all microgeometries studied in this work (periodic, as well as random), the evolution of the distribution of the inclusions is taken to be controlled by the macroscopic deformation gradient $\bar{\mathbf{F}}$. In particular, this implies that an inclusion centered at \mathbf{X}^c in the undeformed configuration will move according to: $\mathbf{x}^c = \bar{\mathbf{F}} \mathbf{X}^c$.

At this stage, it proves useful to illustrate the above-stated results pictorially. Fig. 2.3 shows a schematic representation of a typical inclusion and of its distribution with the various microstructural variables, before and after deformation. Part (a) illustrates the random microstructure, and part (b), the periodic one. (Note that, for clarity, the periodic microstructure has been depicted as a simple cubic distribution; however, it is emphasized that use could have been made of *any* other periodic distribution.) Fig. 2.3(a) depicts how a typical, initially ellipsoidal inclusion deforms into another ellipsoid, with *current* aspect ratios $\omega_1 = z_1/z_3$, $\omega_2 = z_2/z_3$, and with *current* orientation characterized by the three Euler angles ϕ_1, ϕ_2, ϕ_3 , as determined by $\bar{\mathbf{F}}^{(2)}$. This figure also illustrates how the initially ellipsoidal distribution of inclusions in the undeformed configuration evolves to another ellipsoidal distribution—controlled by $\bar{\mathbf{F}}$ —in the deformed configuration. Fig. 2.3(b) shows analogous features for the periodic microstructure. Thus, similar to Fig. 2.3(a), Fig. 2.3(b) shows the evolution of the initially ellipsoidal particle into another ellipsoid, as determined by $\bar{\mathbf{F}}^{(2)}$. Moreover, this figure illustrates how the initially periodic cubic distribution of inclusions in the undeformed configuration evolves to a parallelepiped distribution—controlled by $\bar{\mathbf{F}}$ —in the deformed configuration.

We conclude this section by making an important connection between the microstructure evolution results discussed in this section, and the Hashin-Shtrikman (HS) estimates (2.55) used in the context of the linear comparison composite (2.54) associated with the second-order estimate (2.62).

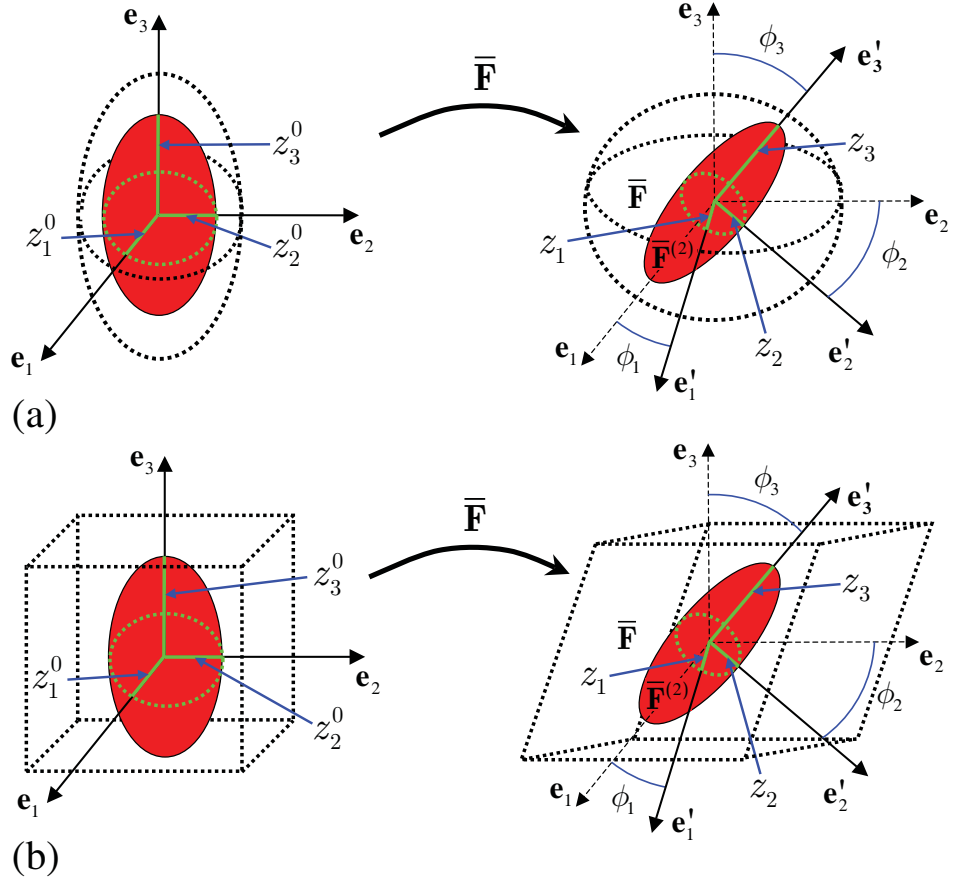


Figure 2.3: Schematic representation of the evolution, from the undeformed to the deformed configuration, of the microstructure in two-phase, “particulate” composites. Part (a) shows the evolution of a typical inclusion (denoted by the color ellipsoid)—as determined by $\bar{\mathbf{F}}^{(2)}$ —and of its *random*, ellipsoidal distribution (denoted by the dashed ellipsoid)—as determined by $\bar{\mathbf{F}}$. Part (b) shows analogous results for the periodic distribution.

2.5.1 Range of validity of the HS-type second-order estimates

Recall from Section 2.4.2 that the Hashin-Shtrikman (HS) estimates (2.55) have been established to be accurate for small to moderate volume fractions of inclusions, but that they become increasingly inaccurate and ultimately meaningless near the percolation limit, when the interactions among the inclusions become especially strong. By combining this fact together with the above discussion on microstructure evolution, it is plain that the second-order estimates of the HS type (2.62) may not be used once the relevant microstructural variables (which evolve along the loading path of choice) reach values approaching the percolation limit.

For the *random* microgeometry, following Ponte Castañeda and Willis (1995), the HS-type

second-order estimates utilized in this work are taken to become unsound whenever the underlying inclusions penetrate the “security” distributional ellipsoids surrounding them. More precisely, making contact with Fig. 2.3(a), the HS-type second-order estimates for two-phase, particulate, composite elastomers with the random “ellipsoidal” microgeometry first become invalid whenever the deformed ellipsoidal inclusion comes into contact with the surrounding “ellipsoid” serving to characterize the distribution of the inclusions in the deformed configuration. In line with this definition of rigorous validity, it is important to note that the second-order estimates of the HS type for the random microgeometry become invalid before percolation (*i.e.*, before adjacent ellipsoids coming into contact lead to a percolating network of inclusions) actually takes place, in general.

For the *periodic* microgeometry, similar to the random one, the HS-type second-order estimates become unsound whenever the underlying inclusions penetrate the distributional shapes surrounding them. For instance, making contact with Fig. 2.3(b), the HS-type second-order estimates for two-phase, particulate, composite elastomers with the periodic cubic microgeometry first become invalid whenever the deformed ellipsoidal inclusion comes into contact with the surrounding parallelepiped serving to characterize the distribution of the inclusions in the deformed configuration. Again, it should be noted that, consistently with the above definition of rigorous validity, the second-order estimates of the HS type for the periodic microgeometry become invalid before percolation actually takes place, in general.

2.6 Macroscopic stability

As already stated in Section 2.1, a comprehensive analysis of the development of instabilities in the type of composite elastomers under investigation in this work is exceedingly complicated, especially for composite elastomers with *random* microstructures (see Appendix III for composites with *periodic* microstructures). Nevertheless, following Geymonat *et al.* (1993), it is possible to identify the onset of *macroscopic* instabilities (*i.e.*, instabilities with wavelengths comparable to the size of the specimen) with the *loss of strong ellipticity* of the homogenized constitutive relation for the composite elastomer, which can be efficiently estimated by means of the second-order method developed in Section 2.3. In this connection, we state next the conditions for strong ellipticity of the second-order estimate (2.46) for \widehat{W} . Thus, a homogenized elastomeric composite characterized by the effective stored-energy function \widehat{W} is said to be strongly elliptic if and only if its associated

acoustic tensor is positive definite, namely, if and only if

$$\widehat{K}_{ik}m_im_k = \widehat{\mathcal{L}}_{ijkl}N_jN_lm_im_k > 0, \quad (2.89)$$

for all $\mathbf{m} \otimes \mathbf{N} \neq \mathbf{0}$. Here, $\widehat{K}_{ik} = \widehat{\mathcal{L}}_{ijkl}N_jN_l$ is the effective acoustic tensor and $\widehat{\mathcal{L}} = \partial^2\widehat{W}/\partial\bar{\mathbf{F}}^2$ is the effective incremental elastic modulus characterizing the overall incremental response of the material. Note that when condition (2.89) is satisfied, the associated macroscopic equilibrium equations form a system of strongly elliptic partial differential equations.

In connection with the condition (2.89), it should be remarked that, in general, $\widehat{\mathcal{L}} \neq \widetilde{\mathbf{L}}$. That is, the incremental elastic modulus associated with the effective stored-energy function \widehat{W} of the elastomeric composite does not correspond exactly to the effective modulus of the auxiliary linear comparison composite (LCC). This raises the possibility that the LCC may lose strong ellipticity before the actual nonlinear composite. Given that the LCC is a *fictitious* material whose main role is to allow the estimation of the effective behavior of the actual nonlinear composite, in this work, we will insist on strong ellipticity of the incremental modulus $\widehat{\mathcal{L}}$, and not on strong ellipticity of the effective modulus $\widetilde{\mathbf{L}}$ of the LCC. In passing, it is recalled that the condition of ellipticity requires the acoustic tensor to be merely non-singular and not necessarily positive definite. Hence, strong ellipticity implies ellipticity, but the converse is not true in general. However, the interest here is in the determination of the loss of strong ellipticity of homogenized materials that are strictly convex, and therefore strongly elliptic, for infinitesimal deformations. Then, elliptic regions containing the point $\bar{\mathbf{F}} = \mathbf{I}$, by continuity, will necessarily also be strongly elliptic. Thus, for the cases of interest here, the elliptic and strongly elliptic regions coincide.

In general, the detection of loss of strong ellipticity requires a tedious, but straightforward, scanning process (*i.e.*, a numerical search of unit vectors \mathbf{N} and \mathbf{m} for which condition (2.89) ceases to hold true). Incidentally, for certain particular cases, including when \widehat{W} is objective and isotropic (*i.e.*, $\widehat{W}(\bar{\mathbf{Q}}'\bar{\mathbf{F}}\bar{\mathbf{Q}}) = \widehat{W}(\bar{\mathbf{F}})$ for all $\bar{\mathbf{F}}$, and all proper, orthogonal, second-order tensors $\bar{\mathbf{Q}}'$, $\bar{\mathbf{Q}}$), it is possible to write *necessary* and *sufficient* conditions for the strong ellipticity of \widehat{W} exclusively in terms of the material properties (*i.e.*, in terms of the components of $\widehat{\mathcal{L}}$). The relevant specific conditions will be spell out in the subsequent chapters as needed. For studies on sufficient and necessary conditions for strong ellipticity see Knowles and Sternberg (1977), Hill (1979), Simpson and Spector (1983), Zee and Sternberg (1983), Silhavy (1999), and Dacorogna (2001).

2.7 Concluding remarks

In this chapter, we have developed a homogenization-based framework for estimating the macroscopic behavior of general elastomeric composites subjected to finite deformations. The main idea behind the framework—which is based on an appropriate extension of the “second-order” homogenization method developed by Ponte Castañeda (2002a) in the context of viscoplastic materials—is the construction of suitable variational principles utilizing the concept of “linear comparison composite” (LCC). Ultimately, this allows the conversion of available linear homogenization estimates into analytical estimates for the large-deformation overall response of elastomeric composites. Motivated by most applications of practical interest, special attention has been given to elastomers with isotropic phases and “particulate” microstructures. For this class of materials, estimates have also been derived for the evolution of suitably identified microstructural variables. In addition, the proposed estimates for the overall behavior, which were enforced to satisfy overall objectivity, can also be used to obtain estimates—in a rather efficient manner—for the onset of macroscopic instabilities, through loss of ellipticity of the effective incremental moduli of the composite (Geymonat *et al.*, 1993).

In this chapter, specific results have been provided for non-dilute concentrations of aligned ellipsoidal particles of arbitrary shape and compliance dispersed randomly or periodically in an elastomeric matrix with general isotropic, hyperelastic constitutive behavior. However, more general micro-geometries could be easily considered, including multiple families of aligned inclusions, as well as randomly oriented fibers, by exploiting more general versions of the Willis (Ponte Castañeda and Willis, 1995) and Suquet (Suquet, 1990) estimates for the LCC.

The limiting cases of vacuum and ideally rigid inclusions, which are of particular practical importance to model porous and reinforced rubbers, were also considered in detail, and it was found that the resulting estimates simplified considerably. In particular, it was found that for the rigid case, the deformation of the inclusions reduced to a pure rotation, as expected on physical grounds. This is a remarkable result that bodes well for the power of the method: even though the homogenization is carried out at the level of a *linear* (comparison) composite, the method has the capability of accounting for the *nonlinear* kinematics involved in the actual behavior of the composite elastomer. Another example of the strength of the method developed in this work will be discussed in subsequent chapters, where estimates will be obtained for rigidly reinforced and porous elastomers with *incompressible* matrix phases. For the case of rigidly reinforced elastomers, the

incompressibility of both phases, which translates into a kinematical constraint on the *determinant* of the local deformation, dictates overall incompressibility for the composite. Thus, it will be seen in Chapters 6–7 that the method is indeed able to recover overall incompressibility for the composite (at least for the particular cases considered), in spite of the strong nonlinearity associated with the local incompressibility constraint for the phases. For the case of porous elastomers, the incompressibility of the matrix phase dictates the evolution of the porosity. As it will be seen in Chapters 3–5, the method is also able to recover (exactly in 2D and approximately in 3D) the evolution of porosity. Furthermore, in the sequel, it will also be seen that the method is able to predict macroscopic instabilities of the shear/compaction-band type for elastomeric composites, even when the behavior of the constituent phases is itself strongly elliptic, and therefore excludes such types of instabilities at the local level.

Finally, it should be emphasized that the method proposed here for composite elastomers is still not fully optimized. In particular, it is not yet clear what the best choice is for the reference deformation variables $\mathbf{F}^{(r)}$, nor it is yet known what the optimal form is for the modulus tensors $\mathbf{L}^{(r)}$ of the LCC. But, as it will be demonstrated in the chapters that follow, even at its current stage of development, the method is already capable of providing physically meaningful estimates for a large class of composite elastomers in the finite-deformation regime. To the best of the author’s knowledge, there are no other analytical methods available in the literature with comparable capabilities in terms of accuracy and generality.

2.8 Appendix I. Overall objectivity of \widetilde{W}

In this appendix we show that the stored-energy function \widetilde{W} , as defined by

$$\widetilde{W}(\overline{\mathbf{F}}) = \min_{\mathbf{F} \in \mathcal{K}(\overline{\mathbf{F}})} \langle W(\mathbf{X}, \mathbf{F}) \rangle = \min_{\mathbf{F} \in \mathcal{K}(\overline{\mathbf{F}})} \sum_{r=1}^N c_0^{(r)} \langle W^{(r)}(\mathbf{F}) \rangle^{(r)}, \quad (2.90)$$

with the kinematically admissible set \mathcal{K} given by:

$$\mathcal{K}(\overline{\mathbf{F}}) = \{\mathbf{F} \mid \exists \mathbf{x} = \mathbf{x}(\mathbf{X}) \text{ with } \mathbf{F} = \text{Grad } \mathbf{x} \text{ in } \Omega_0, \mathbf{x} = \overline{\mathbf{F}}\mathbf{X} \text{ on } \partial\Omega_0\}, \quad (2.91)$$

and objective local phases:

$$W^{(r)}(\mathbf{Q}\mathbf{F}) = W^{(r)}(\mathbf{F}) \quad \forall \quad \mathbf{Q} \in \text{Orth}^+, \quad (2.92)$$

is objective. In this last expression, Orth^+ denotes the proper orthogonal group.

First, let us consider the slightly different problem

$$\widetilde{W}(\overline{\mathbf{Q}}\overline{\mathbf{F}}) = \min_{\mathbf{F} \in \mathcal{K}(\overline{\mathbf{Q}}\overline{\mathbf{F}})} \sum_{r=1}^N c_0^{(r)} \langle W^{(r)}(\mathbf{F}) \rangle^{(r)}, \quad (2.93)$$

with

$$\mathcal{K}(\overline{\mathbf{Q}}\overline{\mathbf{F}}) = \{\mathbf{F} \mid \exists \mathbf{x} = \mathbf{x}(\mathbf{X}) \text{ with } \mathbf{F} = \text{Grad } \mathbf{x} \text{ in } \Omega_0, \mathbf{x} = \overline{\mathbf{Q}}\overline{\mathbf{F}}\mathbf{X} \text{ on } \partial\Omega_0\}, \quad (2.94)$$

where $\overline{\mathbf{Q}}$ is an arbitrary, proper orthogonal, second-order tensor. Now, by introducing the following change of variables:

$$\mathbf{x} = \overline{\mathbf{Q}}\mathbf{x}', \quad (2.95)$$

it follows that

$$\mathbf{F} = \frac{\partial \mathbf{x}}{\partial \mathbf{X}} = \overline{\mathbf{Q}} \frac{\partial \mathbf{x}'}{\partial \mathbf{X}} = \overline{\mathbf{Q}}\mathbf{F}'. \quad (2.96)$$

In turn, by exploiting local objectivity, it follows that

$$W^{(r)}(\mathbf{F}) = W^{(r)}(\overline{\mathbf{Q}}\mathbf{F}') = W^{(r)}(\mathbf{F}'). \quad (2.97)$$

Finally, by making use of (2.95)–(2.97), the problem (2.93) can be rewritten as:

$$\widetilde{W}(\overline{\mathbf{Q}}\overline{\mathbf{F}}) = \min_{\mathbf{F}' \in \mathcal{K}(\overline{\mathbf{F}})} \sum_{r=1}^N c_0^{(r)} \langle W^{(r)}(\mathbf{F}') \rangle^{(r)}, \quad (2.98)$$

with the kinematically admissible set \mathcal{K} given by:

$$\mathcal{K}(\overline{\mathbf{F}}) = \{\mathbf{F}' \mid \exists \mathbf{x}' = \mathbf{x}'(\mathbf{X}) \text{ with } \mathbf{F}' = \text{Grad } \mathbf{x}' \text{ in } \Omega_0, \mathbf{x}' = \overline{\mathbf{F}}\mathbf{X} \text{ on } \partial\Omega_0\}. \quad (2.99)$$

It is then concluded that

$$\widetilde{W}(\overline{\mathbf{Q}}\overline{\mathbf{F}}) = \widetilde{W}(\overline{\mathbf{F}}) \quad \forall \quad \overline{\mathbf{Q}} \in \text{Orth}^+. \quad (2.100)$$

2.9 Appendix II. On the relation $\bar{\mathbf{S}} = \partial\widetilde{W}/\partial\bar{\mathbf{F}}$

In this appendix, we provide a proof for the relation

$$\bar{\mathbf{S}} \doteq \langle \mathbf{S} \rangle = \widetilde{\mathbf{S}}(\bar{\mathbf{F}}) \doteq \frac{\partial\widetilde{W}}{\partial\bar{\mathbf{F}}} \quad (2.101)$$

Here, it is recalled that \mathbf{S} denotes the first Piola-Kirchhoff stress tensor in the hyperelastic composite, $\bar{\mathbf{F}}$ denotes the applied macroscopic deformation gradient tensor, and \widetilde{W} stands for the effective stored-energy function of the composite, as defined by expression (2.12) in the main body of the text.

The proof is as follows (in component form).

$$\begin{aligned} \frac{\partial\widetilde{W}}{\partial\bar{F}_{ij}} &= \frac{1}{|\Omega_0|} \int_{\Omega_0} \frac{\partial W}{\partial F_{kl}} \frac{\partial F_{kl}}{\partial\bar{F}_{ij}} dV \quad (\text{by the Chain Rule}) \\ &= \frac{1}{|\Omega_0|} \int_{\Omega_0} S_{kl} \frac{\partial^2 x_k}{\partial\bar{F}_{ij} \partial X_l} dV \\ &= \frac{1}{|\Omega_0|} \int_{\partial\Omega_0} S_{kl} \frac{\partial x_k}{\partial\bar{F}_{ij}} N_l dS \quad (\text{by the Divergence Theorem and Equilibrium}) \\ &= \frac{1}{|\Omega_0|} \int_{\partial\Omega_0} S_{il} X_j N_l dS \quad (\text{from the Boundary Conditions}) \\ &= \frac{1}{|\Omega_0|} \int_{\Omega_0} \frac{\partial(S_{il} X_j)}{\partial X_l} dV \quad (\text{by the Divergence Theorem}) \\ &= \frac{1}{|\Omega_0|} \int_{\Omega_0} S_{ij} dV \quad (\text{from the Equilibrium Equations}) \\ &= \langle S_{ij} \rangle. \end{aligned} \quad (2.102)$$

2.10 Appendix III. Microscopic and macroscopic instabilities in periodic elastomers

In this appendix, following the work of Triantafyllidis and co-workers (see, e.g., Triantafyllidis and Maker, 1985; Geymonat *et al.*, 1993; Triantafyllidis *et al.*, 2006; Michel *et al.*, 2007), we recall the precise definitions of *microscopic* and *macroscopic* instabilities in *periodic*, hyperelastic composites subjected to finite deformations, and detail their connection.

Consider an elastomeric composite whose periodic, stress-free state is used as the undeformed reference configuration. Without loss of generality, the solid can be thought as resulting by periodic repetition along each coordinate direction of a fundamental building block D_0 (with boundary

∂D_0), which is termed the *unit cell*. Without loss of generality D_0 is assumed to be a parallelepiped of dimension L_i in the direction \mathbf{e}_i . Then, the distribution of the material is characterized by D_0 -periodic characteristic functions

$$\chi^{(r)}(X_1, X_2, X_3) = \chi^{(r)}(X_1 + k_1 L_1, X_2 + k_2 L_2, X_3 + k_3 L_3), \quad (2.103)$$

where k_1, k_2, k_3 are arbitrary integers, and L_1, L_2, L_3 , the unit cell dimensions.

For hyperelastic composites with periodic microstructure, it is known (Braides, 1985; Müller, 1987) that the computation of the effective stored-energy function \widetilde{W} , as determined by relation (2.12) in the main body of the text, cannot be simplified further, as a consequence of the lack of convexity of the local stored-energy function W . (Recall that, for a periodic medium, the computation of the effective stored-energy function \widetilde{W} , as determined by relation (2.12), can be reduced to a computation on the unit cell, provided that the local stored-energy function W be convex (Marcellini, 1978).) However, as will be discussed in further detail below, it is still useful in this context to define the *one-cell effective energy* function $\widehat{W}_\#$ via the expression:

$$\widehat{W}_\#(\overline{\mathbf{F}}) = \min_{\mathbf{u}' \in D_\#} \left\{ \frac{1}{|D_0|} \int_{D_0} W(\mathbf{X}, \overline{\mathbf{F}} + \nabla \mathbf{u}') d\mathbf{X} \right\}, \quad (2.104)$$

where by $D_\#$ is denoted the set of all D_0 -periodic fluctuation functions \mathbf{u}' with $\int_{D_0} \nabla \mathbf{u}' d\mathbf{X} = \mathbf{0}$. Note that, since the macroscopic deformation gradient is given by $\overline{\mathbf{F}}$, the local fluctuation field is given in terms of the deformation field by: $\mathbf{u}' = \mathbf{x} - \overline{\mathbf{F}}\mathbf{X}$. Attention is focused only on macroscopic deformations $\overline{\mathbf{F}}$ for which such a fluctuation field, denoted by $\mathbf{u}'_{\overline{\mathbf{F}}}$, exists and corresponds to a stable equilibrium solution of the unit-cell deformation problem:

$$\int_{D_0} \frac{\partial W}{\partial F_{ij}}(\mathbf{X}, \overline{\mathbf{F}} + \nabla \mathbf{u}'_{\overline{\mathbf{F}}}) \delta u_{i,j} d\mathbf{X} = 0, \quad (2.105)$$

$$\beta_{D_0} \equiv \min_{\mathbf{u}' \in D_\#} \left\{ \int_{D_0} \frac{\partial^2 W}{\partial F_{ij} \partial F_{kl}}(\mathbf{X}, \overline{\mathbf{F}} + \nabla \mathbf{u}'_{\overline{\mathbf{F}}}) u'_{i,j} u'_{k,l} d\mathbf{X} / \int_{D_0} u'_{i,j} u'_{i,j} d\mathbf{X} \right\} > 0, \quad (2.106)$$

where $\delta \mathbf{u}$ is any arbitrary D_0 -periodic fluctuation field. The first of the above equations indicates that $\mathbf{u}'_{\overline{\mathbf{F}}}$ is an extremum of the unit-cell energy $\widehat{W}_\#(\overline{\mathbf{F}})$, and the second that it corresponds to a local minimum of this energy.

Although—by assumption—the material is at each point strongly elliptic, this property does not usually hold for the homogenized solid. The search for the macroscopic deformations $\overline{\mathbf{F}}$ for which the homogenized solid characterized by $\widehat{W}_\#(\overline{\mathbf{F}})$ loses its strict rank-one convexity is addressed

next. To this end, one needs to investigate the one-cell homogenized moduli tensor $\widehat{\mathcal{L}}_{\#}(\bar{\mathbf{F}})$, which is defined by

$$\widehat{\mathcal{L}}_{\#}(\bar{\mathbf{F}}) \equiv \frac{\partial^2 \widehat{W}_{\#}}{\partial \bar{\mathbf{F}} \partial \bar{\mathbf{F}}}(\bar{\mathbf{F}}), \quad \widehat{W}_{\#}(\bar{\mathbf{F}}) = \frac{1}{|D_0|} \int_{D_0} W(\mathbf{X}, \bar{\mathbf{F}} + \nabla \mathbf{u}'_{\bar{\mathbf{F}}}) d\mathbf{X}. \quad (2.107)$$

When an explicit expression for $\widehat{W}_{\#}$ exists, the homogenized moduli are calculated by taking the second derivative with respect to $\bar{\mathbf{F}}$ of $\widehat{W}_{\#}$ given in (2.107). For the case of regular microgeometries where the unit-cell problem — as defined in (2.105) — is solved numerically using an F.E.M. technique, a different calculation strategy, which is based on the interchange between the homogenization and linearization steps, is employed.

Thus, for a solid with a linearized response characterized by its tangent moduli $\mathcal{L}(\mathbf{X})$, where \mathcal{L} is a D_0 -periodic function of \mathbf{X} , the homogenized tangent modulus tensor \mathcal{L}^H is uniquely defined by:

$$G_{ij} \mathcal{L}_{ijkl}^H G_{kl} = \min_{\mathbf{u}' \in D_{\#}} \left\{ \frac{1}{|D_0|} \int_{D_0} \mathcal{L}_{ijkl}(\mathbf{X}) (G_{ij} + u'_{i,j}) (G_{kl} + u'_{k,l}) d\mathbf{X} \right\}, \quad (2.108)$$

where \mathbf{G} is an arbitrary second-order tensor. A formal calculation based on (2.108) shows that the components of the homogenized tangent moduli are given by:

$$\mathcal{L}_{pqrs}^H = \frac{1}{|D_0|} \int_{D_0} \mathcal{L}_{ijkl}(\mathbf{X}) (\delta_{ip} \delta_{jq} + \chi_{i,j}^{pq}) (\delta_{kr} \delta_{ls} + \chi_{k,l}^{rs}) d\mathbf{X}, \quad (2.109)$$

where the characteristic functions $\chi^{pq} \in D_{\#}$ are D_0 -periodic fluctuations defined by:

$$\int_{D_0} \mathcal{L}_{ijkl}(\mathbf{X}) (\delta_{ip} \delta_{jq} + \chi_{i,j}^{pq}) \delta u_{k,l} d\mathbf{X} = 0, \quad (2.110)$$

for arbitrary variations $\delta \mathbf{u} \in D_{\#}$. A formal calculation of $\widehat{\mathcal{L}}_{\#}$ based on (2.107), which makes use of (2.105), shows that the above-defined linearization and homogenization operations commute, and therefore,

$$\widehat{\mathcal{L}}_{\#} = \mathcal{L}^H. \quad (2.111)$$

It also follows that the characteristic functions χ^{pq} (defined in (2.110)) involved in the determination of \mathcal{L}^H are the $\bar{\mathbf{F}}$ derivatives of the fluctuation functions $\mathbf{u}'_{\bar{\mathbf{F}}}$, namely,

$$\chi^{pq} = \frac{\partial \mathbf{u}'_{\bar{\mathbf{F}}}}{\partial F_{pq}}. \quad (2.112)$$

By definition, the one-cell homogenized energy $\widehat{W}_{\#}$ (of course) requires minimization of the energy over a single unit cell. However, it is possible that, by minimizing the energy over larger

domains containing several unit cells, a lower value can be found for the energy per volume of these larger samples. The corresponding fluctuation fields are periodic over much larger (possibly infinite) domains $\mathbf{k}D_0$, where $\mathbf{k}D_0$ denotes a *super-cell* of dimensions $k_i L_i$ in each direction. Hence, a fully consistent definition (see Müller, 1987) of the homogenized energy \widetilde{W} requires the consideration of fluctuations \mathbf{u}' that are $\mathbf{k}D_0$ -periodic. Thus, for a periodic hyperelastic medium, the general expression (2.12) specializes to:

$$\widetilde{W}(\overline{\mathbf{F}}) \equiv \inf_{\mathbf{k} \in N^3} \left\{ \min_{\mathbf{u}' \in \mathbf{k}D_{\#}} \left\{ \frac{1}{|\mathbf{k}D_0|} \int_{\mathbf{k}D_0} W(\mathbf{X}, \overline{\mathbf{F}} + \nabla \mathbf{u}') d\mathbf{X} \right\} \right\}, \quad (2.113)$$

From the definitions in (2.104) and (2.113), one can easily conclude that $\widetilde{W}(\overline{\mathbf{F}}) \leq \widehat{W}_{\#}(\overline{\mathbf{F}})$. The equality holds when the infimum is a minimum occurring at $\mathbf{k} = (1, 1, 1)$, *i.e.*, when the one-cell minimizing fluctuation displacement $\mathbf{u}'_{\overline{\mathbf{F}}}$ is also the minimizing fluctuation displacement for any super-cell $\mathbf{k}D_0$.

For small strains (near $\overline{\mathbf{F}} = \mathbf{I}$), one expects that $\widetilde{W}(\overline{\mathbf{F}}) = \widehat{W}_{\#}(\overline{\mathbf{F}})$, but as the macroscopic strain increases, eventually, $\widetilde{W}(\overline{\mathbf{F}}) < \widehat{W}_{\#}(\overline{\mathbf{F}})$. It is always possible to calculate, exactly, as well as approximately, the one-cell homogenized energy $\widehat{W}_{\#}(\overline{\mathbf{F}})$ and the corresponding macroscopic moduli $\widehat{\mathcal{L}}_{\#}(\overline{\mathbf{F}})$. However, it is practically impossible to calculate the correct homogenized energy $\widetilde{W}(\overline{\mathbf{F}})$, in view of the infinity of the required domain of its definition ($\mathbf{k}D_0$ with $\|\mathbf{k}\| \rightarrow \infty$). Therefore, it is important to establish the region of macroscopic strain space where the one-cell homogenized energy is the correct one ($\widehat{W}_{\#}(\overline{\mathbf{F}}) = \widetilde{W}(\overline{\mathbf{F}})$). To this end, and in an analogous way to (2.106), one can define the coercivity constant $\beta(\overline{\mathbf{F}})$ for the infinite domain ($\Omega_0 = R^3$):

$$\begin{aligned} \beta(\overline{\mathbf{F}}) &\equiv \inf_{\mathbf{k} \in N^3} \beta_{\mathbf{k}D_0}(\overline{\mathbf{F}}), \\ \beta_{\mathbf{k}D_0}(\overline{\mathbf{F}}) &\equiv \min_{\mathbf{u}' \in \mathbf{k}D_{\#}} \left\{ \int_{\mathbf{k}D_0} \frac{\partial^2 W}{\partial F_{ij} \partial F_{kl}}(\mathbf{X}, \overline{\mathbf{F}} + \nabla \mathbf{u}'_{\overline{\mathbf{F}}}) u'_{i,j} u'_{k,l} d\mathbf{X} / \int_{\mathbf{k}D_0} u'_{i,j} u'_{i,j} d\mathbf{X} \right\}. \end{aligned} \quad (2.114)$$

As shown by Geymonat *et al.* (1993), a necessary condition for $\widetilde{W}(\overline{\mathbf{F}}) = \widehat{W}_{\#}(\overline{\mathbf{F}})$ is that $\beta(\overline{\mathbf{F}}) > 0$. Fortunately, unlike the computation of $\widetilde{W}(\overline{\mathbf{F}})$, the determination of the coercivity constant $\beta(\overline{\mathbf{F}})$ requires only calculations on the unit cell D_0 , as will be seen next. Thus, using the Bloch-wave representation theorem (Bloch, 1928), it was proved by Geymonat *et al.* (1993) that the eigenmode \mathbf{v} corresponding to $\beta(\overline{\mathbf{F}})$ can always be put in the form:

$$\begin{aligned} \mathbf{v}(\mathbf{X}) &= \mathbf{u}'(\mathbf{X}) \exp(i\omega_k X_k), \quad \mathbf{u}' \in D_{\#}; \\ \boldsymbol{\omega} &\equiv (\omega_1, \omega_2, \omega_3), \quad 0 \leq \omega_1 L_1, \omega_2 L_2, \omega_3 L_3 < 2\pi, \end{aligned} \quad (2.115)$$

and hence that the coercivity constant $\beta(\bar{\mathbf{F}})$ is determined from:

$$\beta(\bar{\mathbf{F}}) \equiv \inf_{\boldsymbol{\omega}} \left\{ \min_{\mathbf{u}' \in D_{\#}} \left\{ \int_{D_0} \frac{\partial^2 W}{\partial F_{ij} \partial F_{kl}}(\mathbf{X}, \bar{\mathbf{F}} + \nabla \mathbf{u}'_{\bar{\mathbf{F}}}) v_{i,j}^* v_{k,l} d\mathbf{X} / \int_{D_0} v_{i,j}^* v_{i,j} d\mathbf{X} \right\} \right\}, \quad (2.116)$$

with \mathbf{v} given by (2.115). Here, \mathbf{v}^* is the complex conjugate of the field \mathbf{v} . Of particular interest here is $\beta_0(\bar{\mathbf{F}})$, the long-wavelength limit ($\boldsymbol{\omega} \rightarrow 0$) of the above expression (2.116), defined as:

$$\beta_0(\bar{\mathbf{F}}) \equiv \liminf_{\boldsymbol{\omega} \rightarrow 0} \left\{ \min_{\mathbf{u}' \in D_{\#}} \left\{ \int_{D_0} \frac{\partial^2 W}{\partial F_{ij} \partial F_{kl}}(\mathbf{X}, \bar{\mathbf{F}} + \nabla \mathbf{u}'_{\bar{\mathbf{F}}}) v_{i,j}^* v_{k,l} d\mathbf{X} / \int_{D_0} v_{i,j}^* v_{i,j} d\mathbf{X} \right\} \right\}, \quad (2.117)$$

which, as will be subsequently discussed, when it vanishes, signals the loss of strict rank-one convexity of the one-cell homogenized stored energy $\widehat{W}_{\#}(\bar{\mathbf{F}})$.

The use of $\liminf_{\boldsymbol{\omega} \rightarrow 0}$ in the above expression merits further explanation. As seen from (2.115) two different types of eigenmodes exist in the neighborhood of $\boldsymbol{\omega} = 0$; the strictly D_0 -periodic ones, for which $\boldsymbol{\omega} = 0$, and the long-wavelength modes, for which $\boldsymbol{\omega} \rightarrow 0$. Depending on the case, the lowest value of the integral can occur for long wavelength modes, in which case the limit $\boldsymbol{\omega} \rightarrow 0$ is a singular one depending on the ratio of the $\boldsymbol{\omega}$ components, thus justifying the notation used in (2.117).

Finally, and in analogy with the effective coercivity constant defined in (2.22), a macroscopic one-cell coercivity constant $\widehat{B}_{\#}$ is defined by:

$$\widehat{B}_{\#}(\bar{\mathbf{F}}) \equiv \min_{\|\mathbf{m}\|=\|\mathbf{N}\|=1} \{m_i N_j \widehat{\mathcal{L}}_{\#ijkl}(\bar{\mathbf{F}}) m_k N_l\}. \quad (2.118)$$

With the definition of the three coercivity (also, and equivalently, termed ‘‘stability constants’’), $\widehat{B}_{\#}(\bar{\mathbf{F}})$, $\beta_0(\bar{\mathbf{F}})$ and $\beta(\bar{\mathbf{F}})$, for the macroscopic loading $\bar{\mathbf{F}}$, the stage has been set for discussing the stability of the porous solid at that load level. It follows from the definitions of these three coercivity constants (see Geymonat *et al.*, 1993) that the following relation holds for arbitrary vectors \mathbf{m} and \mathbf{N} :

$$m_i N_j \widehat{\mathcal{L}}_{\#ijkl}(\bar{\mathbf{F}}) m_k N_l \geq \beta_0(\bar{\mathbf{F}}) \|\mathbf{m}\|^2 \|\mathbf{N}\|^2 \geq \beta(\bar{\mathbf{F}}) \|\mathbf{m}\|^2 \|\mathbf{N}\|^2 \implies \widehat{B}_{\#}(\bar{\mathbf{F}}) \geq \beta_0(\bar{\mathbf{F}}) \geq \beta(\bar{\mathbf{F}}). \quad (2.119)$$

More specifically, the above relations indicate that when the one-cell based homogenized energy is the correct one (*i.e.*, $\beta(\bar{\mathbf{F}}) > 0$ in which case $\widehat{W}(\bar{\mathbf{F}}) = \widehat{W}_{\#}(\bar{\mathbf{F}})$), the homogenized energy function is *strictly* rank-one convex. Moreover, microscopic stability ($\beta(\bar{\mathbf{F}}) > 0$, which means from (2.117), that the solid is stable to bounded perturbations of arbitrary wavelength $\boldsymbol{\omega}$) implies macroscopic stability ($\widehat{B}_{\#}(\bar{\mathbf{F}}) > 0$, which means that the corresponding one-cell based homogenized moduli $\widehat{\mathcal{L}}_{\#}$ are also strongly elliptic).

Finding the domain in macroscopic strain ($\bar{\mathbf{F}}$) space for which the material is locally stable, *i.e.*, $\beta(\bar{\mathbf{F}}) > 0$, although feasible thanks to (2.116), requires tedious and time consuming calculations since one has to scan using a fine grid the $(0, 2\pi) \times (0, 2\pi) \times (0, 2\pi)$ domain in Fourier ($\boldsymbol{\omega}$) space. On the other hand, finding the larger domain in the same macroscopic strain ($\bar{\mathbf{F}}$) space for which the one-cell homogenized solid $\widehat{W}_{\#}(\bar{\mathbf{F}})$ is macroscopically stable, *i.e.*, $\widehat{B}_{\#}(\bar{\mathbf{F}}) > 0$, is a rather straightforward calculation since it only requires the determination of the homogenized moduli $\widehat{\mathcal{L}}_{\#}(\bar{\mathbf{F}})$ at each macroscopic deformation $\bar{\mathbf{F}}$.

An interesting observation about the loss of macroscopic stability is in order at this stage. It has been shown by Geymonat *et al.* (1993) that $\widehat{B}_{\#}(\bar{\mathbf{F}})$ and $\beta_0(\bar{\mathbf{F}})$ always vanish simultaneously, *i.e.*, if $\beta_0(\bar{\mathbf{F}}) = 0$, then it implies that $\widehat{B}_{\#}(\bar{\mathbf{F}}) = 0$. This means from (2.119) that the onset of a long-wavelength instability ($\boldsymbol{\omega} \rightarrow 0$ — the wavelength of the eigenmode is much larger compared to the cell size) is always detectable as a loss of strong ellipticity of the homogenized moduli. Therefore, the following remark can be made about the first (in a monotonic loading process) loss of microscopic stability ($\beta(\bar{\mathbf{F}}_c) = 0$) in a microstructured elastic solid at some critical macroscopic deformation $\bar{\mathbf{F}}_c$: if $\beta_0(\bar{\mathbf{F}}_c) = \beta(\bar{\mathbf{F}}_c)$, the wavelength of the first instability encountered is much larger than the unit cell size and hence the instability can be macroscopically detected as a loss of strong ellipticity of the homogenized moduli $\widehat{\mathcal{L}}_{\#}$ since $\widehat{B}_{\#}(\bar{\mathbf{F}}_c) = 0$. For the case when $\beta_0(\bar{\mathbf{F}}_c) > \beta(\bar{\mathbf{F}}_c) = 0$, the first instability encountered in the loading process has a finite wavelength, and from that point on the one-cell homogenization is no longer adequate and $\widehat{W}_{\#}$ cannot provide any useful information about the solid. Henceforth a tedious numerical process that follows the bifurcated equilibrium solutions is required to determine the response of the solid under the macroscopic strains in the neighborhood of $\bar{\mathbf{F}}_c$ and beyond.

2.11 Appendix IV. On the limit of $\widetilde{\mathbf{L}}$ as $\bar{\mathbf{F}} \rightarrow \mathbf{I}$

In this appendix, we show that—in the context of two-phase, particulate composites consisting of ellipsoidal particles distributed (randomly with ellipsoidal symmetry or periodically) in an elastomeric phase—the expression (2.55) for the effective modulus tensor $\widetilde{\mathbf{L}}$ of the LCC auxiliary problem, repeated here for convenience:

$$\widetilde{\mathbf{L}} = \mathbf{L}^{(1)} + c_0 [(1 - c_0)\mathbf{P} - (\Delta\mathbf{L})^{-1}]^{-1}, \quad (2.120)$$

reduces to the classical result—with major and minor symmetries—in the limit of small deformations (i.e., in the limit as $\bar{\mathbf{F}} \rightarrow \mathbf{I}$).

First, recall from Section 2.4 that the modulus tensors $\mathbf{L}^{(1)}$ and $\mathbf{L}^{(2)}$ (and therefore the microstructural tensor \mathbf{P} , as defined by (2.56) and (2.59)) are ultimately functions of the macroscopic deformation gradient tensor $\bar{\mathbf{F}}$. In particular, in the limit as $\bar{\mathbf{F}} \rightarrow \mathbf{I}$, these tensors are of the form:

$$\mathbf{L}^{(r)} = \mathbf{L}_0^{(r)} + \epsilon \mathbf{L}_1^{(r)} + o(\epsilon^2) \quad (2.121)$$

($r = 1, 2$) and

$$\mathbf{P} = \mathbf{P}_0 + \epsilon \mathbf{P}_1 + o(\epsilon^2), \quad (2.122)$$

where $\epsilon = \|\bar{\mathbf{F}} - \mathbf{I}\|$ is a small parameter. The leading-order terms in expressions (2.121) have both, major (i.e., $L_{0ijkl}^{(r)} = L_{0klij}^{(r)}$) and minor (i.e., $L_{0ijkl}^{(r)} = L_{0jikl}^{(r)} = L_{0ijlk}^{(r)}$) symmetries. On the other hand, the leading-order term in expression (2.122) for the expansion of the microstructural tensor \mathbf{P} —as determined by (2.56) and (2.59)—has major, but *not* minor symmetry.

Next, recall that the *inverse* operation in expression (2.120) is defined by

$$A_{ijmn} A_{mnkl}^{-1} = A_{ijmn}^{-1} A_{mnkl} = \mathcal{I}_{ijkl} = \delta_{ik} \delta_{jl}; \quad (\mathbf{A} \mathbf{A}^{-1} = \mathbf{A}^{-1} \mathbf{A} = \mathcal{I}), \quad (2.123)$$

where \mathbf{A} is an arbitrary fourth-order tensor and \mathbf{A}^{-1} denotes its inverse. (For convenience, the symbol \mathcal{I} has been introduced in (2.123) to denote the identity operator in the space of fourth-order tensors.)

Having spelled out the asymptotic behavior of $\mathbf{L}^{(1)}$, $\mathbf{L}^{(2)}$, and \mathbf{P} , as well as having recalled the precise definition of the inverse operation, we turn next to compute the limit of (2.120) for $\tilde{\mathbf{L}}$ as $\bar{\mathbf{F}} \rightarrow \mathbf{I}$. To this end, we first consider the term $(\Delta \mathbf{L})^{-1}$, needed in the computation of (2.120). In this regard, it is important to recognize that—because $\mathbf{L}_0^{(r)}$ does have minor symmetries—the leading-order term of $\Delta \mathbf{L}$: $\Delta \mathbf{L}_0 \doteq \mathbf{L}_0^{(1)} - \mathbf{L}_0^{(2)}$ is singular in the sense of (2.123) (i.e., there is no fourth-order tensor $(\Delta \mathbf{L}_0)^{-1}$ such that $\Delta \mathbf{L}_0 (\Delta \mathbf{L}_0)^{-1} = (\Delta \mathbf{L}_0)^{-1} \Delta \mathbf{L}_0 = \mathcal{I}$). To better understand “how singular” $\Delta \mathbf{L}_0$ is, it proves useful to compute its null space; that is, the set of second-order tensors that $\Delta \mathbf{L}_0$ maps to the zero (second-order) tensor:

$$\text{null } \Delta \mathbf{L}_0 = \{\mathbf{G} \mid \Delta \mathbf{L}_0 \mathbf{G} = \mathbf{0}\}. \quad (2.124)$$

Thus, by solving

$$\Delta \mathbf{L}_0 \mathbf{G} = \mathbf{0} \quad (2.125)$$

for \mathbf{G} it is seen that

$$\text{null } \Delta \mathbf{L}_0 = \text{span}\{\mathbf{W}_1, \mathbf{W}_2, \mathbf{W}_3\}, \quad (2.126)$$

where $\{\mathbf{W}_1, \mathbf{W}_2, \mathbf{W}_3\}$ denotes an orthogonal basis for the set of skew-symmetric second-order tensors. To be precise, $\mathbf{W}_i + \mathbf{W}_i^T = \mathbf{0}$ ($i = 1, 2, 3$) and $\mathbf{W}_i \cdot \mathbf{W}_j = \mathbf{0}$ ($i \neq j$). Now, by making use of (2.126), together with the definition of inverse (2.123), we have that in the limit as $\bar{\mathbf{F}} \rightarrow \mathbf{I}$:

$$(\Delta \mathbf{L})^{-1} = \epsilon^{-1} \Delta \mathbf{M}_\epsilon + \Delta \mathbf{M}_0 + o(\epsilon), \quad (2.127)$$

where

$$\Delta \mathbf{M}_\epsilon = \sum_{i=1}^3 \frac{1}{\mathbf{W}_i \cdot \Delta \mathbf{L}_1 \mathbf{W}_i} \mathbf{W}_i \otimes \mathbf{W}_i. \quad (2.128)$$

Further, $\Delta \mathbf{M}_\epsilon$ and $\Delta \mathbf{M}_0$ satisfy the following conditions:

$$\Delta \mathbf{L}_0 \Delta \mathbf{M}_\epsilon = \Delta \mathbf{M}_\epsilon \Delta \mathbf{L}_0 = \mathbf{0} \quad (2.129)$$

and

$$\Delta \mathbf{L}_0 \Delta \mathbf{M}_0 + \Delta \mathbf{L}_1 \Delta \mathbf{M}_\epsilon = \Delta \mathbf{M}_0 \Delta \mathbf{L}_0 + \Delta \mathbf{M}_\epsilon \Delta \mathbf{L}_1 = \mathcal{I}. \quad (2.130)$$

In these last expressions, $\Delta \mathbf{L}_1 = \mathbf{L}_1^{(1)} - \mathbf{L}_1^{(2)}$ has been introduced to denote the second-order term in the expansion of $\Delta \mathbf{L}$ in the limit as $\bar{\mathbf{F}} \rightarrow \mathbf{I}$.

Having specified the expansion of $(\Delta \mathbf{L})^{-1}$, we next consider the expansion of the term $[(1 - c_0)\mathbf{P} - (\Delta \mathbf{L})^{-1}]^{-1}$, also needed in the computation of (2.120). Thus, by making use of the preceding development, it follows that in the limit as $\bar{\mathbf{F}} \rightarrow \mathbf{I}$:

$$\begin{aligned} [(1 - c_0)\mathbf{P} - (\Delta \mathbf{L})^{-1}]^{-1} &= [-\epsilon^{-1} \Delta \mathbf{M}_\epsilon + (1 - c_0)\mathbf{P}_0 - \Delta \mathbf{M}_0 + o(\epsilon)]^{-1} \\ &= \mathbf{N}_0 + \epsilon \mathbf{N}_1 + o(\epsilon^2), \end{aligned} \quad (2.131)$$

where \mathbf{N}_0 and \mathbf{N}_1 satisfy the following relations:

$$\Delta \mathbf{M}_\epsilon \mathbf{N}_0 = \mathbf{N}_0 \Delta \mathbf{M}_\epsilon = \mathbf{0} \quad (2.132)$$

and

$$((1 - c_0)\mathbf{P}_0 - \Delta \mathbf{M}_0) \mathbf{N}_0 - \Delta \mathbf{M}_\epsilon \mathbf{N}_1 = \mathbf{N}_0 ((1 - c_0)\mathbf{P}_0 - \Delta \mathbf{M}_0) - \mathbf{N}_1 \Delta \mathbf{M}_\epsilon = \mathcal{I}. \quad (2.133)$$

Note that equation (2.132) simply states that \mathbf{N}_0 must be a fourth-order tensor with major and minor symmetries. The complete determination of \mathbf{N}_0 requires some more work. Thus, by right

multiplying relation (2.133) with $\Delta\mathbf{L}_0$, noticing from (2.130) that $\Delta\mathbf{M}_0\Delta\mathbf{L}_0 = \mathcal{I} - \Delta\mathbf{M}_\epsilon\Delta\mathbf{L}_1$, and making use of (2.132), can be shown to lead to the following equation for \mathbf{N}_0 :

$$(1 - c_0)\mathbf{N}_0\mathbf{P}_0\Delta\mathbf{L}_0 - \mathbf{N}_0 = \Delta\mathbf{L}_0. \quad (2.134)$$

At this point, it is useful to exploit the fact that \mathbf{N}_0 and $\Delta\mathbf{L}_0$ have major and minor symmetries, so that relation (2.134) can be rewritten as:

$$\mathbf{N}_0 [(1 - c_0)\mathbf{P}_0^{sym}\Delta\mathbf{L}_0 - \mathcal{I}^{sym}] = \Delta\mathbf{L}_0, \quad (2.135)$$

where \mathbf{P}_0^{sym} is the symmetric part of \mathbf{P}_0 :

$$P_{0ijkl}^{sym} = \frac{1}{4} (P_{0ijkl} + P_{0jikl} + P_{0ijlk} + P_{0jilk}) \quad (2.136)$$

and \mathcal{I}^{sym} is the identity operator in the space of fourth-order tensors with minor symmetries:

$$\mathcal{I}_{ijkl}^{sym} = \frac{1}{2} (\delta_{ik}\delta_{jl} + \delta_{jk}\delta_{il}). \quad (2.137)$$

Equation (2.135) can now be readily solved for \mathbf{N}_0 to render:

$$\mathbf{N}_0 = \left[(1 - c_0)\mathbf{P}_0^{sym} - (\Delta\mathbf{L}_0)^{-1^{sym}} \right]^{-1^{sym}}. \quad (2.138)$$

Here, the symbol “ -1^{sym} ” denotes the inverse operation in the space of fourth-order tensors with minor symmetries:

$$B_{ijmn}B_{mnkl}^{-1^{sym}} = B_{ijmn}^{-1^{sym}}B_{mnkl} = \mathcal{I}_{ijkl}^{sym}; \quad (\mathbf{B}\mathbf{B}^{-1^{sym}} = \mathbf{B}^{-1^{sym}}\mathbf{B} = \mathcal{I}^{sym}), \quad (2.139)$$

where \mathbf{B} is an arbitrary fourth-order tensor with minor symmetries (i.e., $B_{ijkl} = B_{jikl} = B_{ijlk}$).

Finally, by making use of the above results, it is easy to see that in the limit as $\bar{\mathbf{F}} \rightarrow \mathbf{I}$:

$$\tilde{\mathbf{L}} = \mathbf{L}_0^{(1)} + c_0 \left[(1 - c_0)\mathbf{P}_0^{sym} - (\Delta\mathbf{L}_0)^{-1^{sym}} \right]^{-1^{sym}} + o(\epsilon), \quad (2.140)$$

which is precisely the classical result in the context of linear elasticity where the effective modulus tensor $\tilde{\mathbf{L}}$ has both, major and minor symmetries.

2.12 Appendix V. Earlier versions of the second-order homogenization method

In this appendix, we provide a brief outline of earlier versions of the second-order method. For more general treatments see Ponte Castañeda (1996), Ponte Castañeda and Willis (1999), Ponte

Castañeda and Tiberio (2000), Lopez-Pamies and Ponte Castañeda (2003), and Lopez-Pamies and Ponte Castañeda (2004a). Recall that this last reference has been included as Appendix A at the end of this thesis for completeness.

2.12.1 Tangent second-order estimates

As stated in Section 2.3 in the main body of the text, relations (2.33) and (2.34) can be combined to approximate the local stored-energy functions of the phases of the hyperelastic composite. To be precise,

$$W^{(r)}(\mathbf{F}) \approx W_T^{(r)}(\mathbf{F}) + V^{(r)}(\mathbf{F}^{(r)}, \mathbf{L}^{(r)}). \quad (2.141)$$

By making use of (2.141), the effective stored-energy function (2.28) of the nonlinear composite may be correspondingly approximated as

$$\widehat{W}(\overline{\mathbf{F}}) \approx \widehat{W}_T(\overline{\mathbf{F}}; \mathbf{F}^{(s)}, \mathbf{L}^{(s)}) + \sum_{r=1}^N c_0^{(r)} V^{(r)}(\mathbf{F}^{(r)}, \mathbf{L}^{(r)}), \quad (2.142)$$

where \widehat{W}_T , which denotes the effective stored-energy function associated with the linear comparison composite (LCC) defined by relations (2.32) and (2.33), is given by expression (2.38) in the main body of the text.

Note that the approximation (2.142) is valid for any reference deformation gradients $\mathbf{F}^{(r)}$ and modulus tensors $\mathbf{L}^{(r)}$, which suggests its optimization with respect to these variables. In fact, the solution of this optimization problem for the variables $\mathbf{F}^{(r)}$ and $\mathbf{L}^{(r)}$ in the estimate (2.142) for \widehat{W} depends on the solution of the stationary problems (2.34) defining the “corrector” functions $V^{(r)}$. In this regard, it is recalled from Section 2.3 that the stationarity with respect to the variables $\widehat{\mathbf{F}}^{(r)}$ in (2.34) leads to the conditions:

$$\mathcal{S}^{(r)}(\widehat{\mathbf{F}}^{(r)}) - \mathcal{S}^{(r)}(\mathbf{F}^{(r)}) = \mathbf{L}^{(r)}(\widehat{\mathbf{F}}^{(r)} - \mathbf{F}^{(r)}), \quad (2.143)$$

which can be trivially satisfied by letting $\widehat{\mathbf{F}}^{(r)}$ tend to $\mathbf{F}^{(r)}$. Note that this choice makes the corrector functions $V^{(r)}$ vanish identically. In this connection, optimality of the reference deformations $\mathbf{F}^{(r)}$ in (2.142) leads to the prescriptions:

$$\mathbf{F}^{(r)} = \overline{\mathbf{F}}^{(r)} = \langle \mathbf{F} \rangle^{(r)}, \quad (2.144)$$

where, for convenience, it has been recalled that $\overline{\mathbf{F}}^{(r)}$ denotes the average deformation gradient field over phase r in the LCC. As shown by Ponte Castañeda and Tiberio (2000), under the above

conditions, the general estimate (2.142) leads to the following *tangent second-order estimate*:

$$\widehat{W}(\overline{\mathbf{F}}) = \sum_{r=1}^N c_0^{(r)} \left[W^{(r)}(\overline{\mathbf{F}}^{(r)}) + \frac{1}{2} \mathcal{S}^{(r)}(\overline{\mathbf{F}}^{(r)}) \cdot (\overline{\mathbf{F}} - \overline{\mathbf{F}}^{(r)}) \right]. \quad (2.145)$$

A key disadvantage of the estimate (2.145) is that by setting $\hat{\mathbf{F}}^{(r)} = \mathbf{F}^{(r)}$, the optimality conditions for the moduli $\mathbf{L}^{(r)}$ in expression (2.142), which for this case specialize to:

$$\langle (\mathbf{F} - \mathbf{F}^{(r)}) \otimes (\mathbf{F} - \mathbf{F}^{(r)}) \rangle^{(r)} = \mathbf{0}, \quad (2.146)$$

where it is recalled that $\mathbf{F} = \mathbf{F}(\mathbf{X})$ is the solution of the LCC problem (2.38), cannot be satisfied in general (Ponte Castañeda and Willis, 1999). Parenthetically, it is interesting to remark that condition (2.146) is actually *exact* for laminate microstructures. For this reason, as it will be shown more explicitly in Chapter 6, the tangent second-order estimate (2.145) is able to recover the exact effective stored-energy function for hyperelastic laminates (with constant deformation gradients in the phases). Thus, instead of insisting on (2.146), the physically motivated prescription:

$$\mathbf{L}^{(r)} = \mathcal{L}^{(r)}(\overline{\mathbf{F}}^{(r)}) = \frac{\partial^2 W^{(r)}}{\partial \mathbf{F} \partial \mathbf{F}}(\overline{\mathbf{F}}^{(r)}), \quad (2.147)$$

which is entirely consistent with the limit $\hat{\mathbf{F}}^{(r)} \rightarrow \mathbf{F}^{(r)}$ in (2.143), is imposed to close the problem.

It is important to remark here that while the resulting *tangent second-order estimate* (2.145) certainly has some desirable properties, such as the ability to account for the stiffness, concentration, and distribution of the given phases in a hyperplastic composite, it also has some shortcomings. Thus, for example, the tangent second-order estimate (2.145) is able to recover only approximately the overall incompressibility constraint associated with rigidly reinforced elastomers with an incompressible matrix phase (typical of rubbers) (see, e.g., Ponte Castañeda and Tiberio, 2000; Lahellec *et al.*, 2004). Furthermore, for porous elastomers with incompressible matrix phases, the estimate (2.145) fails to recover the exact evolution of the porosity (see Lopez-Pamies and Ponte Castañeda, 2004b and Chapter 3). The new second-order estimates derived in Section 2.3 will be shown—in the subsequent chapters—to circumvent such shortcomings.

2.12.2 Second-order estimates with fluctuations: $\mathbf{F}^{(r)} = \overline{\mathbf{F}}^{(r)}$

As already discussed in Section 2.3 in the text, the general second-order estimate (2.46) is valid for any choice of the reference deformation $\mathbf{F}^{(r)}$. Lopez-Pamies and Ponte Castañeda (2004a) originally proposed to set

$$\mathbf{F}^{(r)} = \overline{\mathbf{F}}^{(r)} = \langle \mathbf{F} \rangle^{(r)}. \quad (2.148)$$

This prescription has the advantage that it makes stationary (with respect to $\mathbf{F}^{(r)}$) the stored energy \widetilde{W}_T , given by expression (2.38), of the LCC. Making use of (2.148) in (2.46) leads to the following second-order estimate:

$$\widetilde{W}(\overline{\mathbf{F}}) = \sum_{r=1}^N c^{(r)} \left[W^{(r)}(\hat{\mathbf{F}}^{(r)}) - \mathcal{S}^{(r)}(\overline{\mathbf{F}}^{(r)}) \cdot (\hat{\mathbf{F}}^{(r)} - \overline{\mathbf{F}}^{(r)}) \right]. \quad (2.149)$$

The estimate (2.149) has been found to be superior to the earlier tangent second-order estimate (2.145). In particular, in the context of (2D) reinforced elastomers, it has been shown by Lopez-Pamies and Ponte Castañeda⁹ (2004a) that (2.149), unlike (2.145), does recover the exact incompressibility constraint in the limit as the composite becomes incompressible. In spite of the improvement over earlier estimates, (2.149) has been shown to lead to inconsistencies for certain limiting cases. For instance, when applied to (2D) porous elastomers with incompressible matrix phases, the second-order estimate (2.149) ceases to be well defined for hydrostatic loading (unpublished work). More specifically, in this case, the computation of (2.149) reduces to solving a system of two distinct equations for only one unknown, which is, of course, ill posed.

2.13 Appendix VI. The tensor \mathbf{P} for cylindrical fibers and laminates

This Appendix deals with the computation of the tensor \mathbf{P} , defined by expression (2.56), in the limit as the ellipsoidal inclusions, as characterized by the tensor \mathbf{Z}_0 , tend to cylindrical fibers and layers.

To obtain cylindrical fibers we set, without loss of generality, $Z_0 = \text{diag}(1/z_1^0, 1/z_2^0, \epsilon)$ in the general expression (2.56) and take the limit $\epsilon \rightarrow 0$. Here, $\epsilon = 1/z_3^0$, where z_3^0 denotes the length of the principal semi-axis of the ellipsoidal inclusion in the \mathbf{e}_3 direction, so that $\epsilon \rightarrow 0$ corresponds to the inclusion becoming infinitely long in that direction. Thus, writing the components of (2.56), with respect to the principal axes of the ellipsoidal inclusion, in polar cylindrical coordinates:

$$\xi_1 = \sqrt{1-z^2} \cos \theta, \quad \xi_2 = \sqrt{1-z^2} \sin \theta, \quad \xi_3 = z, \quad (2.150)$$

leads to

$$P_{ijkl} = \frac{z_1^0 z_2^0 \epsilon^{-1}}{4\pi} \int_0^{2\pi} \int_{-1}^1 \frac{H_{ijkl}(\xi_1, \xi_2, \xi_3)}{[(1-z^2)((z_1^0)^2 \cos^2 \theta + (z_2^0)^2 \sin^2 \theta) + \epsilon^{-2} z^2]^{3/2}} dz d\theta. \quad (2.151)$$

⁹Recall that this article has been included as Appendix A at the end of this thesis.

By changing variables to

$$z' = \frac{z}{\epsilon} \quad (2.152)$$

we can rewrite the integral (2.151) as

$$P_{ijkl} = \frac{z_1^0 z_2^0}{4\pi} \int_0^{2\pi} \int_{-1/\epsilon}^{1/\epsilon} \frac{H_{ijkl}(\xi_1, \xi_2, \epsilon z)}{[(1 - \epsilon^2 z'^2) ((z_1^0)^2 \cos^2 \theta + (z_2^0)^2 \sin^2 \theta) + z'^2]^{3/2}} dz' d\theta. \quad (2.153)$$

Carrying out now the limit $\epsilon \rightarrow 0$ in (2.153) leads to

$$P_{ijkl} = \frac{z_1^0 z_2^0}{4\pi} \int_0^{2\pi} \int_{-\infty}^{\infty} \frac{H_{ijkl}(\xi_1, \xi_2, 0)}{[(z_1^0)^2 \cos^2 \theta + (z_2^0)^2 \sin^2 \theta + z'^2]^{3/2}} dz' d\theta, \quad (2.154)$$

which upon integrating in z' yields finally

$$P_{ijkl} = \frac{z_2^0}{2\pi z_1^0} \int_0^{2\pi} \frac{H_{ijkl}(\xi_1, \xi_2, 0)}{\cos^2 \theta + (z_2^0/z_1^0)^2 \sin^2 \theta} d\theta. \quad (2.155)$$

Note that the integral in (2.155) is nothing more than an integral over the unit circle, so that it can be rewritten more generally as expression (2.57) in the main body of the text.

To generate layers, we start out from (2.155) and take the limit as the length z_2^0 of the principal semi-axis of the cylindrical fibers in the \mathbf{e}_2 direction tends to infinity. (Note that taking the limit $z_1^0 \rightarrow \infty$ would lead exactly to the same final result, but with the lamination direction parallel to the \mathbf{e}_2 direction as opposed to the \mathbf{e}_1 .) In this case, it proves more convenient to use Cartesian coordinates. Thus, rewriting (2.155) in Cartesian coordinates:

$$\xi_1 = \begin{cases} \xi_1^+ = \sqrt{1-y^2} & \text{if } 0 \leq \theta \leq \pi/2 \text{ and } 3\pi/2 \leq \theta \leq 2\pi \\ \xi_1^- = -\sqrt{1-y^2} & \text{if } \pi/2 \leq \theta \leq 3\pi/2 \end{cases}, \quad \xi_2 = y, \quad (2.156)$$

can be shown to lead to

$$\begin{aligned} P_{ijkl} &= \frac{z_1^0 z_2^0}{2\pi} \int_0^1 \frac{H_{ijkl}(\xi_1^+, \xi_2, 0) + H_{ijkl}(\xi_1^-, \xi_2, 0)}{(z_1^0)^2(1-y^2) + (z_2^0)^2 y^2} \frac{1}{\sqrt{1-y^2}} dy \\ &+ \frac{z_1^0 z_2^0}{2\pi} \int_0^1 \frac{H_{ijkl}(\xi_1^+, -\xi_2, 0) + H_{ijkl}(\xi_1^-, -\xi_2, 0)}{(z_1^0)^2(1-y^2) + (z_2^0)^2 y^2} \frac{1}{\sqrt{1-y^2}} dy. \end{aligned} \quad (2.157)$$

By defining $\Delta \doteq 1/z_2^0$ and changing variables to

$$y' = \frac{y}{\Delta}, \quad (2.158)$$

the integrals (2.157) can be rewritten as follows

$$\begin{aligned} P_{ijkl} &= \frac{z_1^0}{2\pi} \int_0^{1/\Delta} \frac{H_{ijkl}(\xi_1', \Delta y', 0) + H_{ijkl}(-\xi_1', \Delta y', 0)}{(z_1^0)^2(1 - \Delta^2 y'^2) + y'^2} \frac{1}{\sqrt{1 - \Delta^2 y'^2}} dy' \\ &+ \frac{z_1^0}{2\pi} \int_0^{1/\Delta} \frac{H_{ijkl}(\xi_1', -\Delta y', 0) + H_{ijkl}(-\xi_1', -\Delta y', 0)}{(z_1^0)^2(1 - \Delta^2 y'^2) + y'^2} \frac{1}{\sqrt{1 - \Delta^2 y'^2}} dy', \end{aligned} \quad (2.159)$$

where $\xi'_1 = \sqrt{1 - \Delta^2 y'^2}$. Carrying out now the limit $\Delta \rightarrow 0$ in (2.159) leads to

$$P_{ijkl} = \frac{z_1^0}{\pi} \int_0^\infty \frac{H_{ijkl}(1, 0, 0) + H_{ijkl}(-1, 0, 0)}{(z_1^0)^2 + y'^2} dy'. \quad (2.160)$$

which upon integrating in y' finally renders

$$P_{ijkl} = H_{ijkl}(1, 0, 0). \quad (2.161)$$

Thus, in the limit as the ellipsoidal inclusions become layers, the microstructural tensor \mathbf{P} simply reduces to $\mathbf{H}(\mathbf{N})$, where \mathbf{N} denotes the direction of lamination in the undeformed configuration.

Chapter 3

Porous elastomers: cylindrical voids, random microstructure

In the preceding chapter, we developed a homogenization framework for determining the overall behavior, the evolution of the underlying microstructure, and the onset of macroscopic instabilities in hyperelastic composites subjected to finite deformations, with special interest in two-phase, particulate microstructures. In the present and subsequent chapters, we make use of this framework to study the behavior of specific material systems.

This is the first of two chapters dealing with the overall behavior of porous elastomers consisting of aligned cylindrical voids in an isotropic elastomeric matrix phase subjected to *plane-strain* loading conditions. This application proves general enough to contain all the essential features of the problem, including the subtle interplay between the evolution of the underlying microstructure and the effective behavior and stability of porous elastomers. At the same time, this application is simple enough to allow for a transparent mathematical analysis—to the extent that it leads to *analytical* solutions. In particular, explicit results are provided for the case when the cylindrical voids are distributed *randomly* and *isotropically* in the plane of deformation and the isotropic elastomeric matrix is taken to be incompressible and strongly elliptic. In spite of the strong ellipticity of the matrix phase, the homogenized second-order estimates for the overall behavior of the porous elastomer are found to lose strong ellipticity at sufficiently large *compressive* deformations corresponding to the possible development of shear-band type instabilities. The reasons for this result are linked to the evolution of the microstructure, which, under appropriate loading conditions, can induce geometric softening leading to overall loss of strong ellipticity.

3.1 Plane-strain loading of transversely isotropic, random porous elastomers

In this chapter, as already stated above, we study the problem of *plane-strain* loading of porous elastomers, with initial porosity f_0 , consisting of cylindrical voids with initially circular cross-section, and aligned in the \mathbf{e}_3 direction. In addition, the in-plane distribution of the pores is *random* and *isotropic* (see Fig. 3.1).

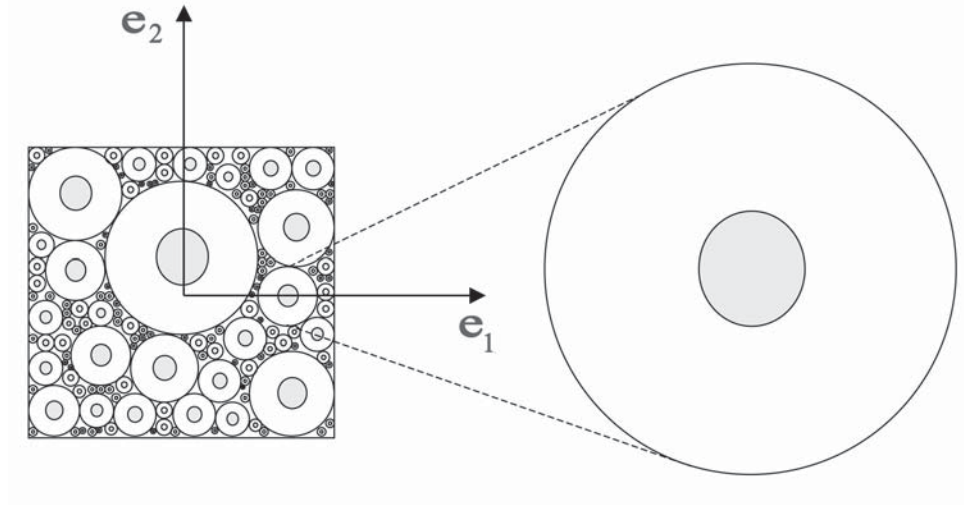


Figure 3.1: Reference configuration depiction of the random, isotropic arrangement of circular voids.

Following Section 2.1.3, the elastomeric matrix phase is taken to be characterized by the (2D) isotropic stored-energy function:

$$W^{(1)}(\mathbf{F}) = W(\mathbf{F}) = \Phi(\lambda_1, \lambda_2) = g(I) + h(J) + \frac{\kappa - \mu}{2}(J - 1)^2, \quad (3.1)$$

where the superscript “(1),” denoting matrix phase quantities, has been dropped for ease of notation, and it is recalled that g and h are material functions of their arguments: $I = \lambda_1^2 + \lambda_2^2$ and $J = \lambda_1 \lambda_2$. Furthermore, κ denotes the two-dimensional bulk modulus of the material at zero strain, while μ denotes the corresponding shear modulus. A relatively simple model of the general type (3.1), which captures the limiting chain extensibility of elastomers, is the Gent model (Gent, 1996):

$$W(\mathbf{F}) = -\frac{\mu J_m}{2} \ln \left[1 - \frac{I - 2}{J_m} \right] - \mu \ln J + \left(\frac{\kappa - \mu}{2} - \frac{\mu}{J_m} \right) (J - 1)^2, \quad (3.2)$$

where the parameter J_m is the limiting value for $I - 2$ at which the material locks up. Note that

(3.2) reduces to the compressible Neo-Hookean material:

$$W(\mathbf{F}) = \frac{\mu}{2}(I - 2) - \mu \ln J + \frac{\kappa - \mu}{2}(J - 1)^2, \quad (3.3)$$

upon taking the limit $J_m \rightarrow \infty$. It is important to recall here from Section 2.1.3 that most stored-energy functions of the form (3.1) describe best the actual behavior of elastomers when “calibrated” to be strongly elliptic. For example, the compressible Gent material, characterized by the stored-energy function (3.2), is strongly elliptic under plane-strain deformations if (but not only if) $\mu > 0$, $J_m > 0$, and $\kappa > 2\mu/J_m + \mu$. Note that for a Neo-Hookean elastomer, these sufficient conditions simplify to $\mu > 0$ and $\kappa > \mu$. In fact, for realistic elastomers, $\mu > 0$, $J_m > 0$, and κ is several orders of magnitude larger than μ , namely, $\kappa/\mu \approx 10^4$. Consequently, the Gent elastomers utilized in this work to model the matrix behavior of the porous elastomers will be assumed to be strongly elliptic for all deformations. As a parenthetical remark, it is worth mentioning that having strict convexity in the linearized region, *i.e.*, $\mu > 0$ and $\kappa > 0$ in the limit $\lambda_1 \rightarrow 1$ and $\lambda_2 \rightarrow 1$, does not ensure strong ellipticity of a Gent material for all deformations. The analysis to be developed below will be carried out for general stored-energy functions of the form (3.1). However, for definiteness, results will be illustrated for porous elastomers with matrix phase characterized by the stored-energy functions (3.2) and (3.3).

By virtue of the overall *objectivity* and in-plane *isotropy* of the porous elastomers at hand, it suffices to confine attention to (in-plane) *diagonal* pure stretch loadings. Thus, making contact with the decompositions $\bar{\mathbf{F}} = \bar{\mathbf{R}}\bar{\mathbf{U}}$ and $\bar{\mathbf{U}} = \bar{\mathbf{Q}}\bar{\mathbf{D}}\bar{\mathbf{Q}}^T$ used in the context of expression (2.66), we will consider:

$$\bar{\mathbf{F}} = \bar{\mathbf{D}} = \text{diag}(\bar{\lambda}_1, \bar{\lambda}_2) \quad \text{and} \quad \bar{\mathbf{R}} = \bar{\mathbf{Q}} = \mathbf{I}, \quad (3.4)$$

where $\bar{\lambda}_1$ and $\bar{\lambda}_2$ denote the principal stretches of the macroscopic right stretch tensor $\bar{\mathbf{U}}$.

Having specified the initial microstructure, local constitutive behavior, and loading conditions, we next spell out the specialization of the second-order estimates (2.69) to the class of porous elastomers of interest in this chapter.

3.1.1 Second-order homogenization estimates

Compressible matrix

In order to carry out the computation for the HS-type second-order estimates (2.69) for porous elastomers with matrix phase (3.1) under plane strain conditions, it suffices to confine the analysis

to in-plane quantities. Thus, it suffices to consider the in-plane components of the modulus tensor $\mathbf{L}^{(1)} = \mathbf{L}$ of the matrix phase of the LCC, defined by expression (2.66). Making use of the applied conditions (3.4)₂, it follows from (2.66) that $\mathbf{L} = \mathbf{L}^*$, where it is recalled that \mathbf{L}^* is taken to be orthotropic. Therefore, the relevant in-plane components of the modulus tensor \mathbf{L} of the matrix phase of the linear comparison composite can be expediently represented as a matrix in $\Re^{4 \times 4}$ as follows:

$$\begin{bmatrix} L_{1111}^* & L_{1122}^* & 0 & 0 \\ L_{1122}^* & L_{2222}^* & 0 & 0 \\ 0 & 0 & L_{1212}^* & L_{1221}^* \\ 0 & 0 & L_{1221}^* & L_{2121}^* \end{bmatrix}, \quad (3.5)$$

where use has been made of major symmetry (*i.e.*, $L_{ijkl} = L_{klij}$) and it is emphasized that \mathbf{L} possesses 6 independent components, namely, $L_{1111}^*, L_{1122}^*, L_{2222}^*, L_{1212}^*, L_{1221}^*$, and L_{2121}^* . For simplicity, guided by the fact that the tensor $\hat{\mathbf{F}}^{(1)}$ has at most 4 independent components ($\hat{F}_{11}^{(1)}, \hat{F}_{22}^{(1)}, \hat{F}_{12}^{(1)}, \hat{F}_{21}^{(1)}$), it is expedient to reduce the number of independent components of (3.5) to just 4, with respect to which $\mathbf{E}^{(1)} = \mathbf{E}$ will be differentiated in (2.72) to generate 4 consistent equations for the components of $\hat{\mathbf{F}}^{(1)}$. Thus, the following constraints are imposed among the components of \mathbf{L} :

$$L_{2121}^* = L_{1212}^*, \quad \text{and} \quad L_{1221}^* = \sqrt{(L_{1111}^* - L_{1212}^*)(L_{2222}^* - L_{1212}^*)} - L_{1122}^*. \quad (3.6)$$

The motivation for the choices (3.6) is twofold: (i) the components of the tangent modulus of a Neo-Hookean material, expressed relative to the corresponding Lagrangian principal axes, satisfy¹ (3.6); and (ii) the conditions (3.6) simplify significantly the computations involved. In particular, they simplify the expressions for the microstructural tensor \mathbf{P} (see Appendix I).

Now, using the facts that $\bar{F} = \bar{D} = \text{diag}(\bar{\lambda}_1, \bar{\lambda}_2)$ and $\mathbf{L} = \mathbf{L}^*$, it follows from (2.70) that the average deformation gradient in the matrix phase of the LCC, needed in the computation of the second-order estimate (2.69) for \widehat{W} , is of the form $\bar{F}^{(1)} = \text{diag}(\bar{\lambda}_1^{(1)}, \bar{\lambda}_2^{(1)})$, where the average principal stretches $\bar{\lambda}_1^{(1)}$ and $\bar{\lambda}_2^{(1)}$ in the matrix phase are given explicitly by:

$$\begin{aligned} \bar{\lambda}_1^{(1)} &= \bar{\lambda}_1 - f_0 A_{1111} [2\bar{g}_I \bar{\lambda}_1 + (\bar{h}_J + (\kappa - \mu)(\bar{J} - 1)) \bar{\lambda}_2] \\ &\quad - f_0 A_{1122} [2\bar{g}_I \bar{\lambda}_2 + (\bar{h}_J + (\kappa - \mu)(\bar{J} - 1)) \bar{\lambda}_1], \\ \bar{\lambda}_2^{(1)} &= \bar{\lambda}_2 - f_0 A_{1122} [2\bar{g}_I \bar{\lambda}_1 + (\bar{h}_J + (\kappa - \mu)(\bar{J} - 1)) \bar{\lambda}_2] \\ &\quad - f_0 A_{2222} [2\bar{g}_I \bar{\lambda}_2 + (\bar{h}_J + (\kappa - \mu)(\bar{J} - 1)) \bar{\lambda}_1]. \end{aligned} \quad (3.7)$$

¹In fact, (3.6)₁ is consistent with the tangent modulus of any isotropic hyperelastic material of the form (3.1).

In these expressions, $\bar{g}_I = g_I(\bar{I})$, $\bar{h}_J = h_J(\bar{J})$ have been introduced for convenience, and $\mathbf{A} = \mathbf{E}^{-1}$ where it is recalled from Eq. (2.71) in Section 2.4.4 that $\mathbf{E} = \mathbf{P}^{-1} - (1 - f_0)\mathbf{L}$. The explicit expressions for the relevant components of the microstructural tensor \mathbf{P} are given in Appendix I.

Having determined $\bar{\mathbf{F}}^{(1)}$, we proceed next to compute the variable $\hat{\mathbf{F}}^{(1)}$, also needed in the computation of \widehat{W} . Thus, with the choice (3.6) for the components (3.5) of $\mathbf{L} = \mathbf{L}^*$, and making use of the identifications $\ell_1^* = L_{1111}^*$, $\ell_2^* = L_{2222}^*$, $\ell_3^* = L_{1212}^*$, and $\ell_4^* = L_{1122}^*$, Eq. (2.72) can be seen to reduce to 4 consistent equations for the 4 in-plane components of $\hat{\mathbf{F}}^{(1)}$, which are of the form:

$$\begin{aligned} \left(\hat{F}_{11}^{(1)} - \bar{\lambda}_1\right)^2 + 2f_1\hat{F}_{12}^{(1)}\hat{F}_{21}^{(1)} &= k_1, \\ \left(\hat{F}_{22}^{(1)} - \bar{\lambda}_2\right)^2 + 2f_2\hat{F}_{12}^{(1)}\hat{F}_{21}^{(1)} &= k_2, \\ \left(\hat{F}_{12}^{(1)}\right)^2 + \left(\hat{F}_{21}^{(1)}\right)^2 + 2f_3\hat{F}_{12}^{(1)}\hat{F}_{21}^{(1)} &= k_3, \\ \left(\hat{F}_{11}^{(1)} - \bar{\lambda}_1\right)\left(\hat{F}_{22}^{(1)} - \bar{\lambda}_2\right) - \hat{F}_{12}^{(1)}\hat{F}_{21}^{(1)} &= k_4. \end{aligned} \quad (3.8)$$

Here, $f_1 = \partial L_{1221}^*/\partial L_{1111}^*$, $f_2 = \partial L_{1221}^*/\partial L_{2222}^*$, $f_3 = \partial L_{1221}^*/\partial L_{1212}^*$, and

$$\begin{aligned} k_1 &= \frac{1}{f_0} \left(\bar{\mathbf{D}} - \bar{\mathbf{F}}^{(1)}\right) \cdot \frac{\partial \mathbf{E}}{\partial L_{1111}^*} \left(\bar{\mathbf{D}} - \bar{\mathbf{F}}^{(1)}\right), \\ k_2 &= \frac{1}{f_0} \left(\bar{\mathbf{D}} - \bar{\mathbf{F}}^{(1)}\right) \cdot \frac{\partial \mathbf{E}}{\partial L_{2222}^*} \left(\bar{\mathbf{D}} - \bar{\mathbf{F}}^{(1)}\right), \\ k_3 &= \frac{1}{f_0} \left(\bar{\mathbf{D}} - \bar{\mathbf{F}}^{(1)}\right) \cdot \frac{\partial \mathbf{E}}{\partial L_{1212}^*} \left(\bar{\mathbf{D}} - \bar{\mathbf{F}}^{(1)}\right), \\ k_4 &= \frac{1}{2f_0} \left(\bar{\mathbf{D}} - \bar{\mathbf{F}}^{(1)}\right) \cdot \frac{\partial \mathbf{E}}{\partial L_{1122}^*} \left(\bar{\mathbf{D}} - \bar{\mathbf{F}}^{(1)}\right). \end{aligned} \quad (3.9)$$

Although nonlinear, equations (3.8) can be solved in closed form to yield two distinct solutions for $\hat{F}_{11}^{(1)}$ and $\hat{F}_{22}^{(1)}$, in terms of which $\hat{F}_{12}^{(1)}$ and $\hat{F}_{21}^{(1)}$ may be determined. Note, however, that the variables $\hat{F}_{12}^{(1)}$ and $\hat{F}_{21}^{(1)}$ only enter the equations through the combinations $\hat{F}_{12}^{(1)}\hat{F}_{21}^{(1)}$ and $(\hat{F}_{12}^{(1)})^2 + (\hat{F}_{21}^{(1)})^2$, and hence, only these combinations will be determined from (3.8). The two solutions for $\hat{F}_{11}^{(1)}$ and $\hat{F}_{22}^{(1)}$ are as follows:

$$\hat{F}_{11}^{(1)} - \bar{\lambda}_1 = \pm \frac{2f_1k_4 + k_1}{\sqrt{4f_1^2k_2 + 4f_1k_4 + k_1}}, \quad \hat{F}_{22}^{(1)} - \bar{\lambda}_2 = \pm \frac{2f_1k_2 + k_4}{\sqrt{4f_1^2k_2 + 4f_1k_4 + k_1}}, \quad (3.10)$$

where it must be emphasized that the positive (and negative) signs in the roots for $\hat{F}_{11}^{(1)}$ and $\hat{F}_{22}^{(1)}$ go together. The corresponding solution for the remaining combinations are given by:

$$\hat{F}_{12}^{(1)}\hat{F}_{21}^{(1)} = (\hat{F}_{11}^{(1)} - \bar{\lambda}_1)(\hat{F}_{22}^{(1)} - \bar{\lambda}_2) - k_4, \quad \left(\hat{F}_{12}^{(1)}\right)^2 + \left(\hat{F}_{21}^{(1)}\right)^2 = k_3 - 2f_3\hat{F}_{12}^{(1)}\hat{F}_{21}^{(1)}. \quad (3.11)$$

Next, each of the two distinct roots of (3.10) can be substituted into the generalized secant condition (2.65) to obtain a system of 4 equations for the 4 unknowns L_{1111}^* , L_{2222}^* , L_{1122}^* , and L_{1212}^* , which must be solved numerically. Having computed the values of all the components of \mathbf{L} for a given initial porosity (f_0), given material behavior (g, h, κ , and μ), and given loading ($\bar{\lambda}_1$ and $\bar{\lambda}_2$), the values of the components of $\bar{\mathbf{F}}^{(1)}$ and $\hat{\mathbf{F}}^{(1)}$ can be readily determined using relations (3.7) and (3.10), respectively. In turn, the second-order estimate (2.69) for the effective stored-energy function $\widehat{W} = \widehat{\Phi}$ for (in-plane) isotropic porous elastomers can be computed using these results. At this point, it should be noted that the two above roots lead to very similar results for the effective behavior of the porous elastomer when small values of κ are considered (*i.e.*, for κ of the order of μ). However, for larger values of κ , the estimates produced by the two distinct roots are very different. In fact, as explained in more detail in the following subsection, it can be shown that for large values of κ only one of the two roots provides physically meaningful results. Consequently, this is the root that should be chosen to compute the effective behavior of the porous elastomer.

We conclude this subsection by spelling out the evolution of the relevant microstructural variables associated with the second-order estimate (2.69) developed here. Following Section 2.5, the appropriate microstructural variables in the present context are the current porosity, f , and the current average aspect ratio of the pores, ω —as determined by the average deformation gradient in the porous phase $\bar{\mathbf{F}}^{(2)}$, by means of the tensor $\mathbf{Z} = \bar{\mathbf{F}}^{(2)-1}$. (No reference is made here to the evolution of the orientation and distribution of the pores since they can be readily computed from the macroscopic deformation $\bar{\mathbf{F}}$). In short, within the present context, the current porosity and current average aspect ratio of the voids in the deformed configuration are given, respectively, by:

$$f = \frac{\bar{\lambda}_1^{(2)} \bar{\lambda}_2^{(2)}}{\bar{\lambda}_1 \bar{\lambda}_2} f_0 \quad \text{and} \quad \omega = \frac{\bar{\lambda}_1^{(2)}}{\bar{\lambda}_2^{(2)}}, \quad (3.12)$$

where $\bar{\lambda}_1^{(2)} = (\bar{\lambda}_1 - (1 - f_0)\bar{\lambda}_1^{(1)})/f_0$ and $\bar{\lambda}_2^{(2)} = (\bar{\lambda}_2 - (1 - f_0)\bar{\lambda}_2^{(1)})/f_0$ denote the principal stretches associated with $\bar{\mathbf{F}}^{(2)}$, and it is recalled that the variables $\bar{\lambda}_1^{(1)}$ and $\bar{\lambda}_2^{(1)}$ are given by expression (3.7).

Incompressible matrix

The above expressions can be simplified considerably in the limit of incompressibility of the matrix phase (*i.e.*, $\kappa \rightarrow \infty$). As already stated, this limit is interesting from a practical perspective, given that actual elastomers exhibit a nearly incompressible behavior (*i.e.*, they usually exhibit a ratio

between the bulk and shear moduli of the order of 10^4). In this regard, it is important to realize that the asymptotic behavior of one of the two above roots leads to nonphysical predictions in the limit as κ becomes unbounded. More specifically, for deformations satisfying $\bar{e}_1 + \bar{e}_2 \leq 0$ only the “positive” (+) root provides physically reasonable predictions, whereas for deformations with $\bar{e}_1 + \bar{e}_2 \geq 0$, only the “negative” (−) root has the physically plausible asymptotic behavior; here, the logarithmic strains $\bar{e}_1 = \ln(\bar{\lambda}_1)$ and $\bar{e}_2 = \ln(\bar{\lambda}_2)$ have been introduced for convenience. Taking this observation into account, it can be shown that the second-order estimate (2.69) for the effective stored-energy function of a porous elastomer with an incompressible isotropic matrix phase may be written as:

$$\widehat{W}^I(\bar{\mathbf{F}}) = \widehat{\Phi}^I(\bar{\lambda}_1, \bar{\lambda}_2) = (1 - f_0)g(\hat{I}^{(1)}), \quad (3.13)$$

where $\hat{I}^{(1)} = \hat{I}^{(1)}(\alpha, \beta, \gamma)$, and α, β, γ are the solution to three nonlinear algebraic equations, not shown here for their bulkiness, which can be solved for in terms of the initial porosity f_0 , given material behavior g , and given loading $\bar{\lambda}_1$ and $\bar{\lambda}_2$. In general, it is not possible to solve these equations in closed form. However, for the particular case of a porous elastomer with an incompressible Neo-Hookean matrix phase, the general estimate (3.13) can be shown (see Appendix II) to reduce to:

$$\widehat{\Phi}^I(\bar{\lambda}_1, \bar{\lambda}_2) = \frac{(1 - f_0)\mu}{2} \left[\frac{p_4 v^4 + p_3 v^3 + p_2 v^2 + p_1 v + p_0}{(q_2 v^2 + q_1 v + q_0)^2} - 2 \right], \quad (3.14)$$

where v is the solution of the quartic polynomial:

$$r_4 v^4 + r_3 v^3 + r_2 v^2 + r_1 v + r_0 = 0, \quad (3.15)$$

Here, the coefficients $p_0, p_1, p_2, p_3, p_4, q_0, q_1, q_2, r_0, r_1, r_2, r_3$ and r_4 , which depend on $f_0, \mu, \bar{\lambda}_1$ and $\bar{\lambda}_2$, are given in explicit form in Appendix III. Since the estimate (3.14) depends effectively on the solution of the *quartic* polynomial equation (3.15), it may be written in closed form. However, for all practical purposes, it is simpler to solve (3.15) numerically. In this regard, it is emphasized that only one of the 4 roots² of (3.15) gives the correct linearized behavior for the effective response of porous materials; this is indeed the root that should be chosen.

It is useful, for comparison purposes, to spell out the simplification of the second-order estimate (3.14) for the case of in-plane hydrostatic loading, *i.e.*, $\bar{\lambda}_1 = \bar{\lambda}_2 = \bar{\lambda}$. The result reads as follows:

$$\widehat{\Phi}^I(\bar{\lambda}, \bar{\lambda}) = \frac{2\mu}{1 - f_0} \left[(1 + f_0)\bar{\lambda}^2 + f_0 - 1 - 2\bar{\lambda}\sqrt{f_0(\bar{\lambda}^2 + f_0 - 1)} \right]. \quad (3.16)$$

²The correct root linearizes as $v = 2\mu + O(\bar{\lambda}_1 - 1) + O(\bar{\lambda}_2 - 1)$.

For later use, it is noted that the average deformation field in the matrix phase associated with the stored-energy function (3.16) is given by:

$$\overline{\mathbf{F}}^{(1)} = \overline{\lambda}^I \mathbf{I}, \quad (3.17)$$

where

$$\overline{\lambda}^I = \frac{\sqrt{f_0(\overline{\lambda}^2 + f_0 - 1)} - \overline{\lambda}}{f_0 - 1}. \quad (3.18)$$

Finally, it is emphasized that the result (3.18) holds true, not only for a porous elastomer with incompressible Neo-Hookean matrix, but in fact for a porous elastomer with general incompressible isotropic matrix phase.

3.1.2 Tangent second-order homogenization estimates

In this section, for comparison purposes, we make use of the tangent second-order method of Ponte Castañeda and Tiberio (2000) to generate estimates for the above-defined type of porous elastomers. It should be remarked that tangent second-order estimates have already been computed for reinforced elastomers by a number of authors (see, e.g., Ponte Castañeda and Tiberio, 2000 and Lahellec *et al.*, 2004), but no such results have been generated so far for porous elastomers.

Compressible matrix

Under the given plane-strain loading conditions and matrix material behavior (3.1), the *tangent second-order estimate* (see Section 3.1 in Lopez-Pamies and Ponte Castañeda, 2004b) for the effective stored-energy function \widehat{W} of the type of porous elastomers defined above can be written as follows:

$$\widehat{W}(\overline{\mathbf{F}}) = \widehat{\Phi}(\overline{\lambda}_1, \overline{\lambda}_2) = (1 - f_0) \left[W(\overline{\mathbf{F}}^{(1)}) + \frac{1}{2} \mathcal{S}(\overline{\mathbf{F}}^{(1)}) \cdot (\overline{\mathbf{F}} - \overline{\mathbf{F}}^{(1)}) \right], \quad (3.19)$$

where the nontrivial components of the average deformation gradient $\overline{F}_{11}^{(1)} = \overline{\lambda}_1^{(1)}$, $\overline{F}_{22}^{(1)} = \overline{\lambda}_2^{(1)}$ (the other in-plane components are identically zero) of the average deformation $\overline{\mathbf{F}}^{(1)}$ in the matrix phase of the relevant linear comparison composite are the solution to the following system of nonlinear,

algebraic equations:

$$\begin{aligned}
& f_0(\bar{\lambda}_2^{(1)} - \bar{\lambda}_2)(L_{1122}P_{1111} + L_{2222}P_{1122}) + \\
& + (\bar{\lambda}_1^{(1)} - \bar{\lambda}_1)[(L_{1122}P_{1122} - 1)(1 + (f_0 - 1)L_{1122}P_{1122}) - \\
& - (f_0 - 1)(L_{2222} + L_{1122}^2P_{1111} - L_{1111}L_{2222}P_{1111})P_{2222} + \\
& + L_{1111}(P_{1111} - (f_0 - 1)L_{2222}P_{1122}^2)] \\
& - f_0(P_{1111} - (f_0 - 1)L_{2222}P_{1122}^2 + (f_0 - 1)L_{2222}P_{1111}P_{2222})\bar{\mathcal{S}}_{11}^{(1)} - \\
& - f_0(P_{1122} + (f_0 - 1)L_{1122}P_{1122}^2 - (f_0 - 1)L_{1122}P_{1111}P_{2222})\bar{\mathcal{S}}_{22}^{(1)} = 0,
\end{aligned}$$

$$\begin{aligned}
& f_0(\bar{\lambda}_1^{(1)} - \bar{\lambda}_1)(L_{1122}P_{2222} + L_{1111}P_{1122}) + \\
& + (\bar{\lambda}_2^{(1)} - \bar{\lambda}_2)[(L_{1122}P_{1122} - 1)(1 + (f_0 - 1)L_{1122}P_{1122}) - \\
& - (f_0 - 1)(L_{1111} + L_{1122}^2P_{2222} - L_{2222}L_{1111}P_{2222})P_{1111} + \\
& + L_{2222}(P_{2222} - (f_0 - 1)L_{1111}P_{1122}^2)] \\
& - f_0(P_{2222} - (f_0 - 1)L_{1111}P_{1122}^2 + (f_0 - 1)L_{1111}P_{2222}P_{1111})\bar{\mathcal{S}}_{22}^{(1)} - \\
& - f_0(P_{1122} + (f_0 - 1)L_{1122}P_{1122}^2 - (f_0 - 1)L_{1122}P_{2222}P_{1111})\bar{\mathcal{S}}_{11}^{(1)} = 0.
\end{aligned}$$

(3.20)

In these equations, $\bar{\mathcal{S}}_{ij}^{(1)} = \partial W(\bar{\mathbf{F}}^{(1)})/\partial F_{ij}$ and $L_{ijkl} = \partial^2 W(\bar{\mathbf{F}}^{(1)})/\partial F_{ij}\partial F_{kl}$, so that

$$\begin{aligned}
\bar{\mathcal{S}}_{11}^{(1)} &= 2\bar{g}_I^{(1)}\bar{\lambda}_1^{(1)} + \bar{h}_J^{(1)}\bar{\lambda}_2^{(1)} + (\kappa - \mu)(\bar{\lambda}_1^{(1)}\bar{\lambda}_2^{(1)} - 1)\bar{\lambda}_2^{(1)}, \\
\bar{\mathcal{S}}_{22}^{(1)} &= 2\bar{g}_I^{(1)}\bar{\lambda}_2^{(1)} + \bar{h}_J^{(1)}\bar{\lambda}_1^{(1)} + (\kappa - \mu)(\bar{\lambda}_1^{(1)}\bar{\lambda}_2^{(1)} - 1)\bar{\lambda}_1^{(1)},
\end{aligned}$$

and

$$\begin{aligned}
L_{1111} &= 2\bar{g}_I^{(1)} + 4(\bar{\lambda}_1^{(1)})^2\bar{g}_{II}^{(1)} + (\bar{h}_{JJ}^{(1)} + \kappa - \mu)(\bar{\lambda}_2^{(1)})^2, \\
L_{2222} &= 2\bar{g}_I^{(1)} + 4(\bar{\lambda}_2^{(1)})^2\bar{g}_{II}^{(1)} + (\bar{h}_{JJ}^{(1)} + \kappa - \mu)(\bar{\lambda}_1^{(1)})^2, \\
L_{1122} &= \bar{h}_J^{(1)} - (\kappa - \mu) + (4\bar{g}_{II}^{(1)} + \bar{h}_{JJ}^{(1)} + 2(\kappa - \mu))\bar{\lambda}_1^{(1)}\bar{\lambda}_2^{(1)}.
\end{aligned}$$

Here, use has been made of the notation $\bar{g}^{(1)} = g(\bar{I}^{(1)})$ and $\bar{h}^{(1)} = h(\bar{J}^{(1)})$, where $\bar{I}^{(1)} = (\bar{\lambda}_1^{(1)})^2 + (\bar{\lambda}_2^{(1)})^2$ and $\bar{J}^{(1)} = \bar{\lambda}_1^{(1)}\bar{\lambda}_2^{(1)}$ denote the principal invariants associated with $\bar{\mathbf{F}}^{(1)}$. Furthermore, the explicit expressions for P_{1111} , P_{2222} , and P_{1122} are given—in terms of the in-plane components of the modulus tensor \mathbf{L} —by expression (3.36) in Appendix I.

Incompressible matrix

The limit when the matrix phase is made incompressible (*i.e.*, $\kappa \rightarrow \infty$) in (3.19) is considered next. Due to the cumbersomeness of the final expressions, the asymptotic analysis of the incompressible limit involving the general stored-energy function (3.1) will not be included here. Instead, for illustrative purposes, only the particular case of a Neo-Hookean matrix phase will be discussed. The details of the relevant asymptotic analysis are given in Appendix IV, but the final expression for the *tangent second-order estimate* for the effective stored-energy function of a porous elastomer with incompressible Neo-Hookean matrix phase may be written as:

$$\widehat{W}^I(\overline{\mathbf{F}}) = \widehat{\Phi}^I(\overline{\lambda}_1, \overline{\lambda}_2) = \frac{(1-f_0)}{2u} \mu \left[(u^2-1)(\overline{\lambda}_1 - \overline{\lambda}_2) + \frac{(1+u^2)(\overline{\lambda}_2 u^2 - 2u + \overline{\lambda}_1)((1+f_0)u^2 + (\overline{\lambda}_2 - \overline{\lambda}_1)u - 1 - f_0)}{u(\overline{\lambda}_1 - \overline{\lambda}_2 u^2)} \right]. \quad (3.21)$$

In this expression, u is the solution of the equation:

$$\begin{aligned} & \left(\overline{\lambda}_2^2 + f_0^2 - 1 \right) u^4 + 2(\overline{\lambda}_1 + (f_0 - 1)\overline{\lambda}_2) u^3 + \left(\overline{\lambda}_2^2 - \overline{\lambda}_1^2 \right) u^2 \\ & - 2((f_0 - 1)\overline{\lambda}_1 + \overline{\lambda}_2) u + 1 - f_0^2 - \overline{\lambda}_1^2 = 0, \end{aligned} \quad (3.22)$$

which can be determined explicitly as a function of f_0 , μ , $\overline{\lambda}_1$, and $\overline{\lambda}_2$. Note that (3.22) is a *quartic* polynomial equation and hence it may be solved in closed form. However, for practical purposes, it proves helpful to solve (3.22) numerically. In this regard, it is emphasized that only one of the 4 roots³ of (3.22) gives the correct linearized behavior for the effective response of porous materials; this is indeed the root that should be chosen.

For the special case of in-plane hydrostatic loading, *i.e.*, $\overline{\lambda}_1 = \overline{\lambda}_2 = \overline{\lambda}$, the second-order estimate (3.21) can be shown to further reduce to:

$$\widehat{\Phi}^I(\overline{\lambda}, \overline{\lambda}) = 2\mu \frac{(1-f_0)(\overline{\lambda}-1)^2}{f_0 + \overline{\lambda} - 1}. \quad (3.23)$$

For later use, it is also noted that the average deformation field in the matrix phase associated with the stored-energy function (3.23) is given by:

$$\overline{\mathbf{F}}^{(1)} = \mathbf{I}. \quad (3.24)$$

³The correct root linearizes as $u = 1 + O(\overline{\lambda}_1 - 1) + O(\overline{\lambda}_2 - 1)$.

Finally, it is noted that the result (3.24) holds true, not only for a porous elastomer with incompressible Neo-Hookean matrix, but for a porous elastomer with a general incompressible isotropic matrix phase.

3.1.3 Comparisons with exact results

Hydrostatic Loading

With regard to porous elastomers subjected to finite deformations, there are very few exact results available. For the special case of hydrostatic loading, Hashin (1985) obtained an *exact* equilibrium solution by making use of the idea of the *Composite Spheres Assemblage*. Following that work, it is straightforward to show that an *exact* result for the effective stored-energy function of a porous elastomer with *incompressible*, isotropic matrix $W(\mathbf{F}) = \Phi(\lambda_1, \lambda_2)$ and the *Composite Cylinder Assemblage* (CCA) microstructure subjected to in-plane hydrostatic loading ($\bar{\lambda}_1 = \bar{\lambda}_2 = \bar{\lambda}$) is given by:

$$\widehat{W}^I(\bar{\mathbf{F}}) = \widehat{\Phi}^I(\bar{\lambda}, \bar{\lambda}) = 2 \int_{\sqrt{f_0}}^1 \Phi(\lambda, \lambda^{-1}) R \, dR, \quad (3.25)$$

where

$$\lambda = \sqrt{1 + \frac{\bar{\lambda}^2 - 1}{R^2}}. \quad (3.26)$$

The corresponding *exact* average deformation in the matrix phase reads as:

$$\bar{\mathbf{F}}^{(1)} = \bar{\lambda}^I \mathbf{I}, \quad (3.27)$$

with

$$\bar{\lambda}^I = \frac{\sqrt{f_0(\bar{\lambda}^2 + f_0 - 1)} - \bar{\lambda}}{f_0 - 1}, \quad (3.28)$$

where $\bar{\lambda}$ must be greater than $\sqrt{1 - f_0}$.

In general, the integral in (3.25) cannot be computed analytically; however, for the particular case of a porous elastomer with incompressible Neo-Hookean matrix phase, the *exact* stored-energy function may be expressed as:

$$\widehat{\Phi}^I(\bar{\lambda}, \bar{\lambda}) = \frac{\mu}{2} (\bar{\lambda}^2 - 1) \left[\ln \left(\frac{\bar{\lambda}^2 + f_0 - 1}{f_0} \right) - \ln(\bar{\lambda}^2) \right] \quad (3.29)$$

It can thus be seen that the two versions of the second-order estimates, as defined by (3.16) and (3.23), do not recover the exact result (3.29) for the effective stored-energy function of porous

elastomers with incompressible Neo-Hookean matrix phase subjected to general in-plane hydrostatic finite deformations. Nonetheless, both estimates can be shown to be exact to *third order* in the infinitesimal strain (*i.e.*, up to $O(\bar{\lambda} - 1)^3$). For larger finite deformations, however, the behavior of both estimates is very different. As it will be seen in the following section, whereas the expression (3.16), which takes into account the field fluctuations, provides estimates that are in very good agreement with the exact result, the corresponding tangent expression (3.23) delivers estimates that deviate drastically from (3.29). This disparity is mainly due to the difference in the prediction of the evolution of the microstructure. In fact, while the average deformation gradient in the matrix phase (3.24) predicted by the tangent second-order theory is exactly equal to the identity, the corresponding $\bar{\mathbf{F}}^{(1)}$ (3.17) predicted by the second-order method with fluctuations is consistent with the exact result (3.27). This is a remarkable result. Indeed, by taking into account the fluctuations, the second-order estimate (2.69) is able to improve on the earlier tangent second-order estimate (3.19) in that it recovers the exact average deformation fields in a porous elastomer with an incompressible isotropic matrix under finite in-plane hydrostatic loading.

General Loading

For more general loadings, there are no other known exact solutions for the finite deformation of porous elastomers. However, for incompressible matrix phase materials, a simple kinematical argument allows for the determination of the exact evolution of the porosity f as a function of deformation. The result is as follows:

$$f = \frac{\langle \det \mathbf{F} \rangle^{(2)}}{\langle \det \mathbf{F} \rangle} f_0 = \frac{\langle \det \mathbf{F} \rangle - (1 - f_0) \langle \det \mathbf{F} \rangle^{(1)}}{f_0 \langle \det \mathbf{F} \rangle} f_0 = 1 - \frac{1 - f_0}{\det \bar{\mathbf{F}}}, \quad (3.30)$$

where use has been made of the fact that $\det \mathbf{F}$ is a null Lagrangian. It can be shown that the estimate for the porosity associated with the second-order estimate (3.13) for porous elastomers with incompressible isotropic matrix phases is in exact agreement with the exact result (3.30). The proof of this is sketched out for the particular case of a Neo-Hookean porous material at the end of Appendix II. On the other hand, the corresponding estimate for the porosity arising from the tangent second-order estimate (3.21) deviates radically from (3.30) for large deformations, as will be shown explicitly in the next section.

In summary, the second-order estimate (3.13), unlike the tangent second-order estimate (3.21), is able to predict the exact evolution of the porosity for general finite loading, and consequently the exact average deformation fields for hydrostatic loading, for a porous elastomer with incompressible

isotropic matrix phase. This is a nontrivial result, since the actual fields in a deformed porous elastomer are highly heterogeneous. However, it appears that the “generalized secant” linearization together with the incorporation of field fluctuations leads to improved approximations capable of capturing better the heterogeneity of these fields in order to deliver the exact results mentioned above.

3.1.4 Loss of strong ellipticity

For the particular case of plane-strain deformations at hand, the general strong ellipticity condition (2.89) can be written more explicitly, especially in the context of in-plane isotropic materials. In fact, under plane-strain deformations, *necessary* and *sufficient* conditions for strong ellipticity of the effective constitutive behavior of the class of (in-plane) isotropic porous systems considered here can be shown (Knowles and Sternberg, 1977; Hill, 1979) to reduce to:

$$\widehat{\mathcal{L}}_{1111} > 0, \quad \widehat{\mathcal{L}}_{2222} > 0, \quad \widehat{\mathcal{L}}_{1212} > 0, \quad \widehat{\mathcal{L}}_{2121} > 0, \quad \text{and}$$

$$\widehat{\mathcal{L}}_{1111}\widehat{\mathcal{L}}_{2222} + \widehat{\mathcal{L}}_{1212}\widehat{\mathcal{L}}_{2121} - (\widehat{\mathcal{L}}_{1122} + \widehat{\mathcal{L}}_{1221})^2 > -2\sqrt{\widehat{\mathcal{L}}_{1111}\widehat{\mathcal{L}}_{2222}\widehat{\mathcal{L}}_{1212}\widehat{\mathcal{L}}_{2121}}, \quad (3.31)$$

where

$$\begin{aligned} \widehat{\mathcal{L}}_{iijj} &= \frac{\partial^2 \widehat{\Phi}}{\partial \bar{\lambda}_i \partial \bar{\lambda}_j}, \\ \widehat{\mathcal{L}}_{ijij} &= \frac{1}{\bar{\lambda}_i^2 - \bar{\lambda}_j^2} \left(\bar{\lambda}_i \frac{\partial \widehat{\Phi}}{\partial \bar{\lambda}_i} - \bar{\lambda}_j \frac{\partial \widehat{\Phi}}{\partial \bar{\lambda}_j} \right) \quad i \neq j, \\ \widehat{\mathcal{L}}_{ijji} &= \frac{1}{\bar{\lambda}_i^2 - \bar{\lambda}_j^2} \left(\bar{\lambda}_j \frac{\partial \widehat{\Phi}}{\partial \bar{\lambda}_i} - \bar{\lambda}_i \frac{\partial \widehat{\Phi}}{\partial \bar{\lambda}_j} \right) \quad i \neq j, \end{aligned} \quad (3.32)$$

$(i, j = 1, 2)$ are the components of the modulus $\widehat{\mathcal{L}}$ written in the Lagrangian principal axes. Note that the third and fourth conditions in (3.31) are equivalent and that for loadings with $\bar{\lambda}_i = \bar{\lambda}_j$ ($i \neq j$), suitable limits must be taken for some of the components in (3.32). In particular, equations (3.32)₂ and (3.32)₃ transform into:

$$\begin{aligned} \widehat{\mathcal{L}}_{ijij} &= \frac{1}{2} \left(\widehat{\mathcal{L}}_{iiii} - \widehat{\mathcal{L}}_{iijj} + \frac{1}{\bar{\lambda}_i} \frac{\partial \widehat{\Phi}}{\partial \bar{\lambda}_i} \right) \quad i \neq j, \\ \widehat{\mathcal{L}}_{ijji} &= \frac{1}{2} \left(\widehat{\mathcal{L}}_{iiii} - \widehat{\mathcal{L}}_{iijj} - \frac{1}{\bar{\lambda}_i} \frac{\partial \widehat{\Phi}}{\partial \bar{\lambda}_i} \right) \quad i \neq j, \end{aligned} \quad (3.33)$$

respectively.

In the next section, the second-order estimates developed in this chapter will be used to generate predictions for the strongly elliptic domains of *random* porous elastomers with incompressible Gent and Neo-Hookean matrix phases subjected to plane-strain deformations. It will be shown that even though the behavior of the matrix phase is strongly elliptic, the homogenized behavior of the porous elastomer can lose strong ellipticity. This is consistent with the earlier observations of Abeyaratne and Triantafyllidis (1984) for porous elastomers with *periodic* microstructures.

3.2 Results for plane-strain loading: random porous elastomers

This section presents results associated with the second-order estimates developed in the preceding sections for the in-plane hydrostatic, uniaxial, and pure shear loading of porous elastomers with incompressible Gent and Neo-Hookean matrix phases. Henceforth, for consistency with (Lopez-Pamies and Ponte Castañeda, 2004b), the second-order estimates (3.14) will be denoted as Version 3, and the tangent second-order estimates (3.21), as Version 1. Results are given for $\mu = 1$ and various levels of initial porosity f_0 , and were computed up to the point at which the effective incremental moduli were found to lose strong ellipticity, or truncated at some sufficiently large strain if no such loss was found. For clarity, the points at which loss of strong ellipticity occurred are denoted with the symbols “□” and “○” for Version 1 and 3, respectively. The characterization of the strongly elliptic domains is given in the last subsection. It is further noted that exact results and bounds are presented when available.

3.2.1 Hydrostatic loading

Figure 3.2 presents the comparison between the effective behavior as predicted by Version 1 (HS1) and 3 (HS3) of the second-order method and the “exact” result (for CCA microstructures), for a Neo-Hookean porous elastomer with incompressible matrix phase ($\kappa \rightarrow \infty$) under hydrostatic loading with $\bar{\lambda}_2 = \bar{\lambda}_1 = \bar{\lambda}$. Results are shown for initial porosities of 30, 50, and 70% as a function of the logarithmic strain $\bar{\epsilon} = \ln(\bar{\lambda})$ for both: (a) the effective stored-energy function $\widehat{\Phi}^I$; and (b) the associated stress $\bar{S} = \partial \widehat{\Phi}^I / \partial \bar{\lambda}_1 = \partial \widehat{\Phi}^I / \partial \bar{\lambda}_2$. Recall that closed-form expressions for the effective stored-energy functions shown in Figure 3.2(a) are given by (3.16), (3.23), and (3.29) for Version

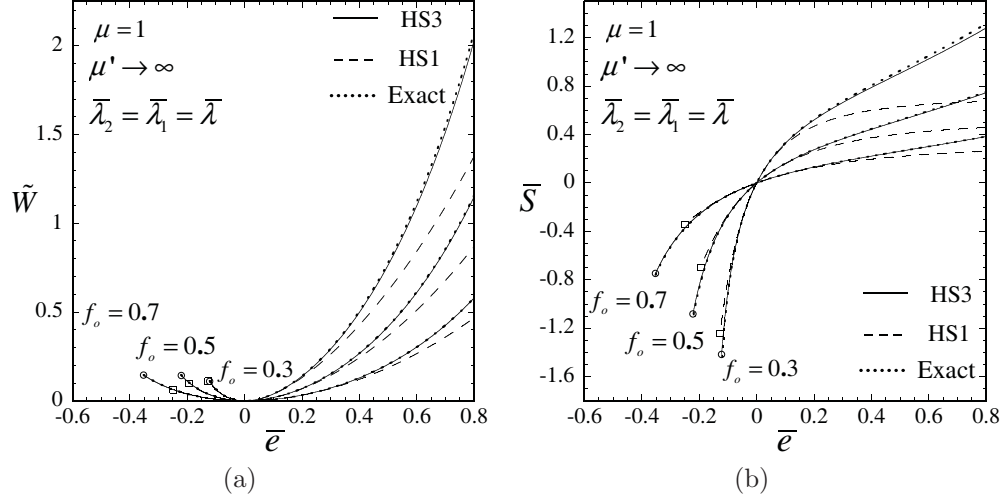


Figure 3.2: Comparisons of the second-order estimates (Version 1 and 3) with the exact results for the effective response of a porous rubber subjected to in-plane hydrostatic loading ($\bar{\lambda}_2 = \bar{\lambda}_1 = \bar{\lambda}$). The results correspond to an incompressible¹ Neo-Hookean matrix phase with various initial concentrations f_0 of aligned cylindrical voids, and are shown as a function of the logarithmic strain $\bar{e} = \ln(\bar{\lambda})$. (a) The stored-energy function $\tilde{\Phi}^I$; and (b) the corresponding stresses $\bar{S} = \partial\tilde{\Phi}^I/\partial\bar{\lambda}_1 = \partial\tilde{\Phi}^I/\partial\bar{\lambda}_2$.

3, Version 1, and the exact result, respectively.

The main observation that can be made from Figure 3.2 is that Version 3 of the second-order variational procedure provides estimates for the effective constitutive behavior which are in excellent agreement with the exact result. Version 1 also delivers estimates that compare reasonably well with the exact result for compressive loadings. However, the predictions by Version 1 deviate significantly from the exact behavior for large tensile deformations. It is also seen that both versions of the second-order method predict loss of strong ellipticity of the homogenized porous elastomer under in-plane hydrostatic compression, while no such behavior is observed under in-plane hydrostatic tension. Moreover, both second-order estimates for the effective behavior exhibit a better agreement with the exact result for higher values of f_0 . Finally, it is interesting to note from Figure 3.2(b) that the overall constitutive behavior of the composite consistently exhibits hardening under compression and softening under tension. This feature will be shown shortly to be due partially to a geometric effect caused by the evolution of the porosity.

Figure 3.3 provides plots associated with the results shown in Figure 3.2 for: (a) the porosity as a function of the logarithmic strain $\bar{e} = \ln(\bar{\lambda})$; and (b) the critical stretch $\bar{\lambda}_{crit}$ at which the loss of strong ellipticity of the homogenized elastomer takes place, as a function of initial porosity f_0 .

¹For consistency with Lopez-Pamies and Ponte Castañeda (2004b), $\mu' \rightarrow \infty$, as opposed to $\kappa \rightarrow \infty$, is used in all figures in this chapter to indicate the incompressibility of the matrix phase.

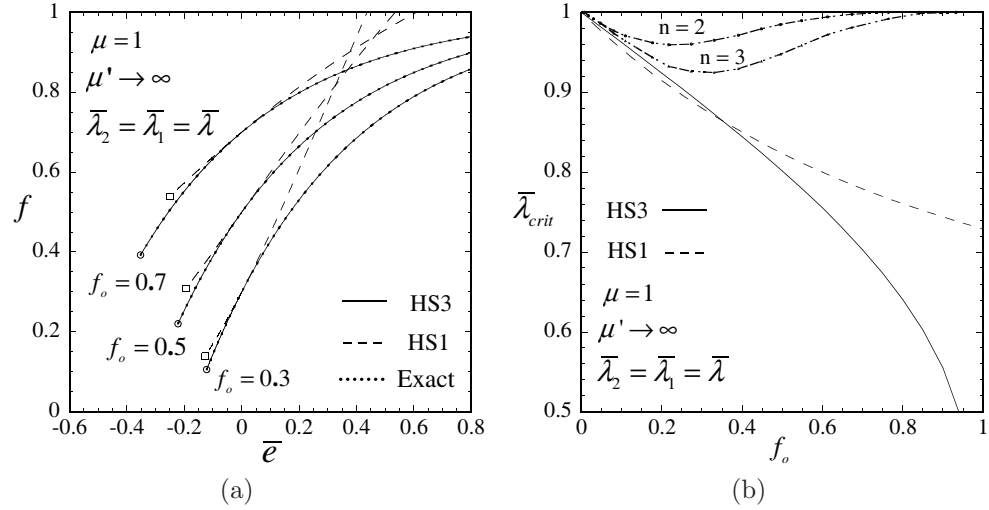


Figure 3.3: In-plane hydrostatic loading ($\bar{\lambda}_2 = \bar{\lambda}_1 = \bar{\lambda}$) of a porous rubber with an incompressible, Neo-Hookean matrix phase with various initial concentrations f_0 of aligned cylindrical voids. (a) The evolution of porosity f as predicted by Versions 1 and 3 of the second-order method compared with the exact result as a function of the logarithmic strain $\bar{e} = \ln(\bar{\lambda})$. (b) The critical stretches $\bar{\lambda}_{crit}$ at which the loss of strong ellipticity of the homogenized elastomer takes place as a function of initial porosity f_0 . (This last plot also includes the critical loads for the first two buckling modes ($n = 2$, and 3) of a cylindrical shell (Wang and Ertepinar, 1972).)

First, a key point to be drawn from Figure 3.3(a) is that the porosity decreases for compressive deformations and increases for tensile ones. This entails a geometric hardening/softening on the overall response of the porous elastomer which is entirely consistent with the hardening/softening exhibited by the effective constitutive behavior observed in Figure 3.2(b). Moreover, the porosity predicted by Version 3 of the second-order method reduces to the exact result, as already pointed out in the previous section (see expressions (3.17) and (3.27)). On the other hand, the porosity delivered by Version 1 deviates from the exact evolution for large finite deformations, especially for tensile hydrostatic loading. In fact, under hydrostatic tension, Version 1, which does not take into account information about the field fluctuations, predicts unrealistic values for the porosity (*i.e.*, greater than unity). This explains the extremely soft effective constitutive behavior observed in Figure 3.2 for Version 1 of the second-order method under hydrostatic tension. Also, in accordance with the trend discerned from Figure 3.2, it appears that the porosity evolution predicted by Version 1 gets worse with decreasing initial porosity.

The main observation with regard to Figure 3.3(b) is the somewhat counterintuitive result that the porous material becomes more stable ($\bar{\lambda}_{crit}$ smaller) with increasing initial values of the porosity. In this connection, it is relevant to remark that while exact results are available for

the effective stored-energy function and porosity evolution for the in-plane hydrostatic loading of composite cylinders (with incompressible matrix phase), the exact loss of strong ellipticity of these structures has not been studied. However, Wang and Ertepinar (1972) did study the stability of an isolated cylindrical Neo-Hookean shell under in-plane hydrostatic loading. Of course, the buckling behavior of an isolated shell cannot be rigorously identified with the buckling instabilities that would take place in an actual composite cylinder system, except possibly in the dilute limit, when no interaction among pores is expected. In this connection, we have included in Figure 3.3(b) the results of Wang and Ertepinar (1972) for the buckling flexural modes $n = 2$, which corresponds to the collapse to an oval shape, and $n = 3$, for reference purposes. Remarkably, these results are in good agreement with the second-order estimates in the small porosity regime, where the comparisons may be relevant. In addition, for large initial porosities it is noted that the second-order predictions bound the buckling modes for an isolated cylindrical shell. Figure 3.3(b) also shows that for the interval $0 < f_0 < 0.4$ the $\bar{\lambda}_{crit}$ predicted by Version 3 is slightly smaller than the one obtained from Version 1. In contrast, for initial porosities higher than 0.4, the prediction of $\bar{\lambda}_{crit}$ by Version 1 becomes smaller than the one computed from Version 3. The difference between the results of these two versions becomes more pronounced in the limit $f_0 \rightarrow 1$, where $\bar{\lambda}_{crit} \rightarrow 0.73$ and $\bar{\lambda}_{crit} \rightarrow 0$ for Versions 1 and 3, respectively. We expect the estimate for the critical stretch associated with Version 3 to be more accurate, but we do not have an explanation for its relatively low values at high porosities. However, it should be kept in mind that it is expected that other (smaller wavelength) instabilities would take place before reaching the loss of ellipticity condition.

3.2.2 Uniaxial loading

In Figure 3.4, plots for the effective stress-strain behavior associated with Versions 1 and 3 are presented for a Neo-Hookean porous elastomer with incompressible matrix phase ($\kappa \rightarrow \infty$) under uniaxial loading with $\bar{\lambda}_2 = 1$, $\bar{\lambda}_1 = \bar{\lambda}$. The results for the stress components $\bar{S}_{11} = \partial \hat{\Phi}^I / \partial \bar{\lambda}_1$ and $\bar{S}_{22} = \partial \hat{\Phi}^I / \partial \bar{\lambda}_2$ are presented in parts (a) and (b), respectively, for values of $f_0 = 30, 50$, and 70%, as functions of the logarithmic strain $\bar{e} = \ln(\bar{\lambda})$. Similar to the case of in-plane hydrostatic loading, the results for compressive (tensile) deformations shown in Figure 3.4 exhibit a clear hardening (softening) behavior with increasing deformation, but less pronounced than the corresponding results for in-plane hydrostatic loading. From Figure 3.4(a) it is seen that the effective constitutive behavior for \bar{S}_{11} obtained from Version 1 is significantly softer than the one obtained from Version

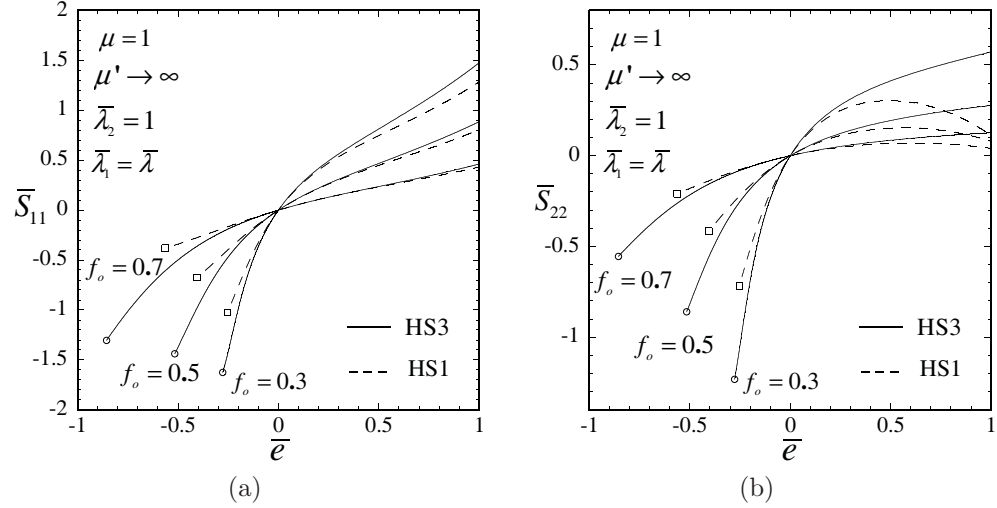


Figure 3.4: Version 1 and 3 estimates of the second-order method for the effective response of a porous rubber subjected to uniaxial loading ($\bar{\lambda}_2 = 1$ and $\bar{\lambda}_1 = \bar{\lambda}$). The results correspond to an incompressible Neo-Hookean matrix phase with various initial concentrations f_0 of aligned cylindrical voids, and are shown as a function of the logarithmic strain $\bar{e} = \ln(\bar{\lambda})$. (a) The stress component $\bar{S}_{11} = \partial \hat{\Phi}^I / \partial \bar{\lambda}_1$. (b) The stress component $\bar{S}_{22} = \partial \hat{\Phi}^I / \partial \bar{\lambda}_2$.

3. This is also the case for the component \bar{S}_{22} as shown by Figure 3.4(b). In fact, the prediction for this component of the stress by Version 1 is not only much softer than the corresponding stress predicted by Version 3, but it even decreases for tensile loadings reaching negative values, which is physically unrealistic. This suggests that the predictions of Version 1 could be too soft for large finite deformations, especially for tensile loadings. Furthermore, as it was the case for hydrostatic loadings, loss of ellipticity was found for compressive loadings but not for tensile ones.

Figure 3.5 provides corresponding results for: (a) the porosity f ; and (b) the average aspect ratio of the pores ω , as function of the logarithmic strain $\bar{e} = \ln(\bar{\lambda})$. Recall from (3.12)₂ that the aspect ratio has been defined as $\omega = \bar{\lambda}_1^{(2)} / \bar{\lambda}_2^{(2)}$, with $\bar{\lambda}_1^{(2)}$ and $\bar{\lambda}_2^{(2)}$ denoting the principal stretches associated with the average deformation gradient tensor of the vacuous phase $\bar{\mathbf{F}}^{(2)}$, so that $\omega > (<)1$ correspond to an oblate (prolate) average shape of the pores. As it was the case for hydrostatic loading, it is seen from Figure 3.5(a) that the porosity decreases for compressive deformations and increases for tensile ones. In turn, this can be related to the aforementioned hardening/softening trend exhibited by the effective stress-strain behavior in Figure 3.4. As already anticipated in Section 5.1.4, Figure 3.5(a) also shows that the prediction for the evolution of the porosity by Version 3 of the second-order method is in agreement with the exact result, whereas the prediction by Version 1 deviates from the correct behavior for large deformations. This deviation, which

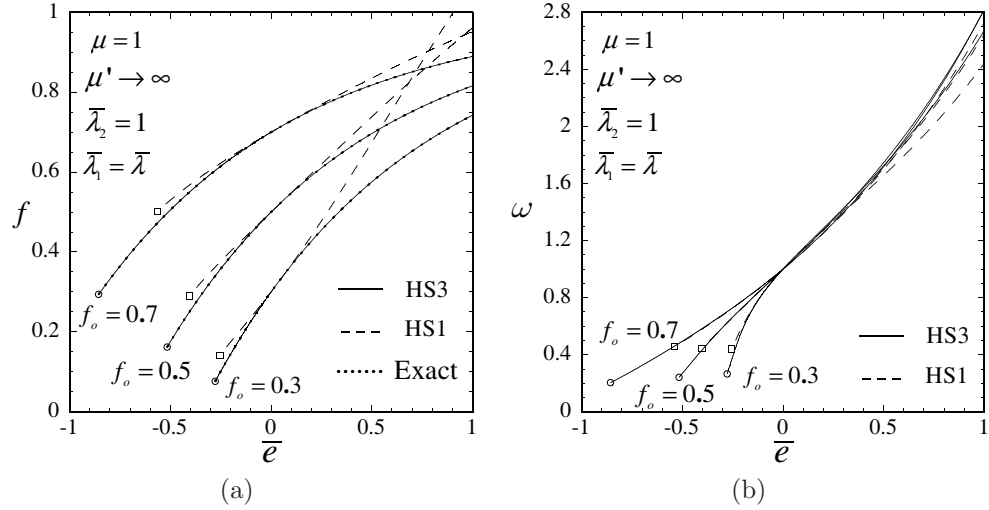


Figure 3.5: Version 1 and 3 estimates of the second-order method for the effective response of a porous rubber subjected to uniaxial loading ($\bar{\lambda}_2 = 1$ and $\bar{\lambda}_1 = \bar{\lambda}$). The results correspond to an incompressible Neo-Hookean matrix phase with various initial concentrations f_0 of aligned cylindrical voids, and are shown as a function of the logarithmic strain $\bar{e} = \ln(\bar{\lambda})$. (a) The evolution of the porosity f compared with the exact result. (b) The evolution of the average aspect ratio of the voids ω .

is much more drastic for tensile loadings and lower values of f_0 , helps explain the unphysical behavior observed in Figure 3.4(b) for \bar{S}_{22} . In particular, it is seen that \bar{S}_{22} tends to negative values whenever f approaches one. Figure 3.5(b) shows that both versions of the second-order method give similar predictions for the average aspect ratio of the pores. Note that in compression the changes in aspect ratio are more rapid for smaller f_0 .

It is concluded from the observations made in the context of these figures for uniaxial stretch, as well as the earlier figures for hydrostatic deformation, that Version 3 of the second-order method leads to more consistent predictions for the overall behavior and microstructure evolution of the porous elastomers, and therefore it should be preferred over Version 1. For this reason, in the following sections only results associated with Version 3 will be presented.

3.2.3 Pure shear loading

Figure 3.6 provides Version 3 second-order estimates for a Gent porous elastomer with incompressible matrix phase under pure shear ($\bar{\lambda}_1 = 1/\bar{\lambda}_2 = \bar{\lambda}$). Results are shown for an initial porosity of 10% and values of the lock-up parameter $J_m = 42, 100$, and $J_m \rightarrow \infty$ as functions of the logarithmic strain $\bar{e} = \ln(\bar{\lambda})$ for: (a) the effective stored-energy function $\hat{\Phi}^I$ compared with the Voigt upper bound; and (b) the evolution of the aspect ratio ω . First, it is observed from Figure 3.6(a) that

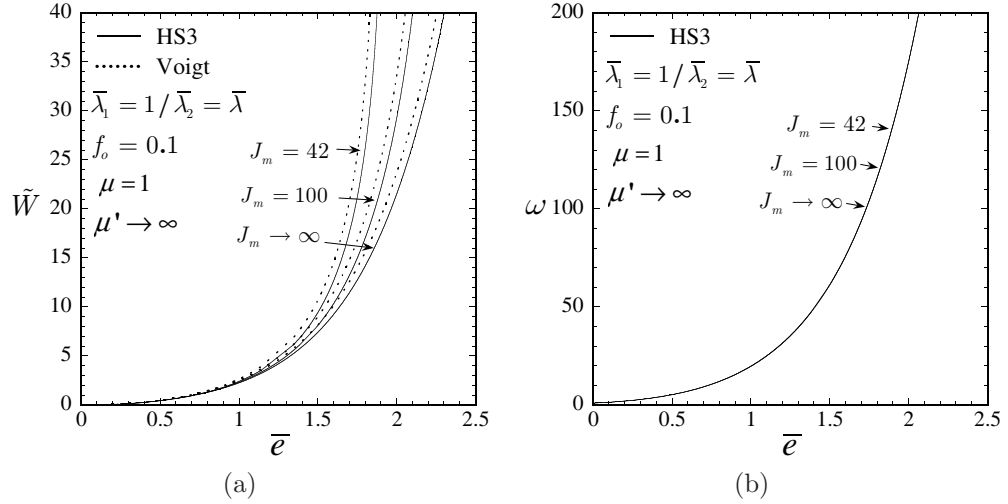


Figure 3.6: Version 3 estimates of the second-order method for the effective response of a porous rubber subjected to pure shear loading ($\bar{\lambda}_1 = 1/\bar{\lambda}_2 = \bar{\lambda}$). The results correspond to an incompressible Gent matrix phase with given initial porosity $f_o = 0.1$ and various values of the material parameter J_m , and are shown as a function of the logarithmic strain $\bar{e} = \ln(\bar{\lambda})$. (a) The effective stored-energy function $\hat{\Phi}^I$ compared with the Voigt upper bound. (b) The evolution of the aspect ratio ω .

the Version 3 estimates for the effective stored-energy function satisfy the rigorous Voigt upper bound. It is emphasized again that this bound is only helpful when considering isochoric loadings, like the one considered in this section, since it becomes unbounded otherwise. Note that no loss of ellipticity was detected at any level of deformation. In connection with the evolution of the microstructure, it is remarked that the porosity does not evolve under pure shear deformations. On the other hand, as clearly shown by Figure 3.6(b), the aspect ratio of the pores does increase fairly rapidly with increasing strains. Furthermore, note that ω appears to be insensitive to the value of the material parameter J_m .

Figure 3.7 presents plots of the corresponding results for the stress components: (a) \bar{S}_{11} ; and (b) \bar{S}_{22} . One of the main points that can be drawn from Figure 3.7 is the strong dependence of the effective stress-strain relation of the porous rubber on the lock-up parameter J_m of the matrix phase. Interestingly, it can also be deduced from these figures that the evolution of the aspect ratio appears to have little effect on the effective constitutive behavior of the porous elastomer under pure shear.

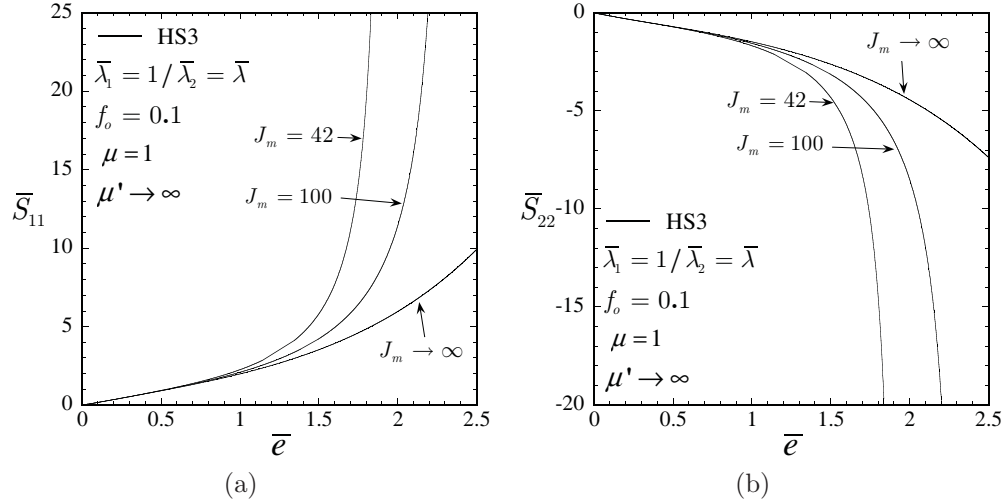


Figure 3.7: Version 3 estimates of the second-order method for the effective response of a porous rubber subjected to pure shear loading ($\bar{\lambda}_1 = 1/\bar{\lambda}_2 = \bar{\lambda}$). The results correspond to an incompressible Gent matrix phase with given initial porosity $f_o = 0.1$ and various values of the material parameter J_m , and are shown as a function of the logarithmic strain $\bar{e} = \ln(\bar{\lambda})$. (a) The stress component $\bar{S}_{11} = \partial\hat{\Phi}^I/\partial\bar{\lambda}_1$. (b) The stress component $\bar{S}_{22} = \partial\hat{\Phi}^I/\partial\bar{\lambda}_2$.

3.2.4 Failure surfaces

Figure 3.8 displays the strongly elliptic (and non-elliptic) domains for the 2-D porous elastomer with incompressible Neo-Hookean matrix phase, subjected to in-plane deformations. The results are shown in the plane $(\bar{e}_1 - \bar{e}_2)$ for: (a) Version 1 and 3 estimates for initial porosities $f_o = 30, 50$, and 70%; and for (b) Version 3 estimates for initial porosities $f_o = 10, 20$, and 30%. In order to aid the discussion of the results, the boundary at which the porosity vanishes has also been included in Figure 3.8. Note that once the zero-porosity boundary is reached, further compressive deformation (with $\bar{J} < 1$) of the material is not possible.

An interesting observation that can be made from Figure 3.8 is that the loci of points describing loss of strong ellipticity satisfy $\bar{e}_2 + \bar{e}_1 < 0$, which implies that a necessary condition for loss of strong ellipticity to occur is the existence of a compressive component in the state of deformation. Also, note that the predictions from both versions of the second-order method have roughly the same qualitative behavior; however, the results of Version 1 appear to be more restrictive than those of Version 3 for all initial values of porosity and loadings, with the exception of cases satisfying $f_o < 0.3$, $\bar{e}_1 < 0$, and $\bar{e}_2 < 0$, for which the onset of loss of strong ellipticity of Version 3 precedes that one of Version 1. Furthermore, it is interesting to note that the strongly elliptic (and non-elliptic) domains shown in Figure (3.8) are similar to the results obtained by Abeyaratne and

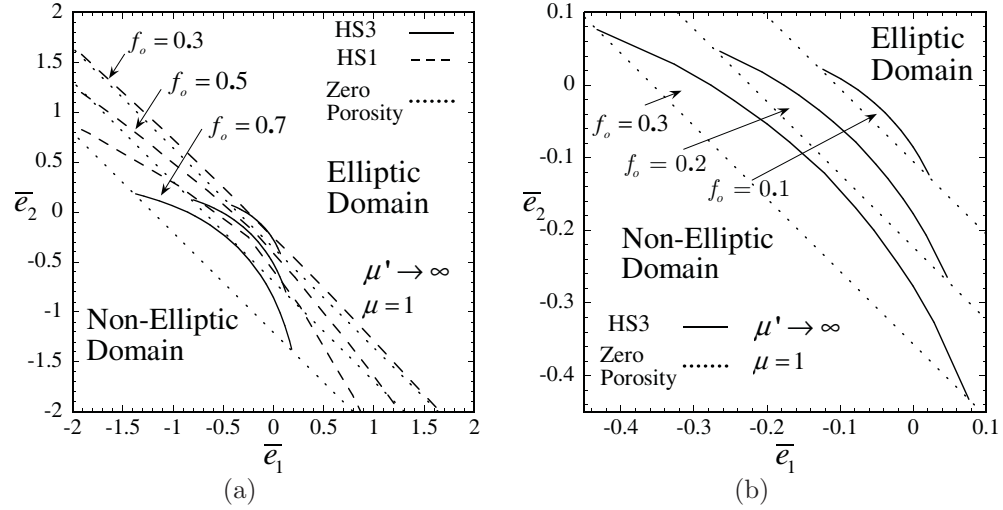


Figure 3.8: Domains of strong ellipticity on the $(\bar{e}_1 - \bar{e}_2)$ -plane for a porous elastomer with incompressible, Neo-Hookean, matrix phase and various levels of initial concentrations f_0 of aligned cylindrical voids, as determined by Version 1 and 3 of the second-order variational procedure. The dotted lines denote the boundary at which the level of zero porosity has been reached upon compressive deformation. (a) Comparisons between the Version 1 and 3 estimates; and (b) Version 3 estimates for low initial porosity.

Triantafyllidis (1984) for the loss of strong ellipticity of *periodic* porous elastomers with a nearly incompressible Neo-Hookean matrix phase. However, their results appear to be more restrictive than the ones obtained here. In particular, these investigators did find loss of strong ellipticity for deformations with $\bar{e}_2 + \bar{e}_1 > 0$, which includes pure shear loading. These discrepancies seem to be consistent with their periodic microstructure, as it is more susceptible to instabilities than the random microstructure utilized in this work. This point will be elaborated further in the next chapter, where we will consider porous elastomers with periodic microstructures in full detail. Another important point that deserves further comment is the trend followed by the onset of loss of ellipticity as a function of initial porosity. In effect, Figure 3.8 suggests that a Neo-Hookean porous elastomer with random and isotropic microstructure becomes more stable with increasing values of initial porosity. This is in contrast to the behavior followed in stress space—not shown here for conciseness—where higher values of initial porosity do lead to smaller critical stresses at loss of strong ellipticity. For convenience, a detailed discussion of this intricate behavior will not be given here, but, instead, it will be postponed until Chapter 5. Finally it is interesting to remark that it was through the failure of the third (and equivalently fourth) condition of (3.31) that the porous elastomer with incompressible Neo-Hookean matrix phase lost strong ellipticity systematically. Indeed, whereas the evolution of the microstructure for compressive loadings led to

the already-mentioned hardening of some of the components of the effective incremental modulus, it also led to the softening of the shear component $\widehat{\mathcal{L}}_{1212}$, which resulted in the overall loss of ellipticity of the porous elastomer.

For completeness, it is noted that the corresponding domains of strong ellipticity for porous elastomers with incompressible Gent matrix phases are essentially identical to those shown in Figure 3.8. Indeed, the results predicted by the second-order theory indicate that the value of the lock-up parameter J_m does not play a major role in estimating the onset of loss of ellipticity of porous elastomers with random and isotropic microstructures. This is consistent with the fact that loss of strong ellipticity takes place under compressive deformations at which the lock-up effect, as characterized by J_m , is not “felt.”

In summary, the second-order estimates for the homogenized constitutive behavior of porous elastomers with isotropic, strongly elliptic, matrix phases have been found to admit loss of strong ellipticity at reasonable levels of deformation. This behavior has been linked to the evolution of the microstructure under finite deformations, which, depending on the specific loading conditions, was found to induce hardening or softening behavior resulting in the loss of strong ellipticity for the porous elastomer.

3.3 Concluding remarks

In this chapter, *analytical* estimates have been derived for the in-plane effective behavior of transversely isotropic porous elastomers with *random* microstructures subjected to finite deformations, by means of the homogenization framework developed in Chapter 2.

As already discussed in the preceding chapter, a key ingredient in the general framework of the second-order variational procedure proposed in this work is the scheme employed for the linearization of the constitutive relation of the hyperelastic phases in the composite. Thus, while the earlier tangent linearization proposed by Ponte Castañeda and Tiberio (2000) results in estimates for the effective constitutive behavior which depend exclusively on the average fields of the constituent phases, the estimates associated with the generalized secant linearization scheme proposed here not only depend on the average fields, but also exhibit a direct dependence on the field fluctuations. The difference between these two approaches has already been shown to be significant in the context of reinforced incompressible elastomers, where the incorporation of field fluctuations

proved necessary to obtain the correct overall incompressibility constraint for these materials (see Lopez-Pamies and Ponte Castañeda, 2004a). Within the richer class of porous elastomers presented in this chapter, the direct incorporation of field fluctuations into the computation of the effective behavior has turned out to be essential as well.

Thus, by incorporating field fluctuations, the second-order method has been shown to lead to the exact evolution of the porosity in porous elastomers with incompressible, isotropic, matrix phases, under general plane strain loading. This is a remarkable result in view of the strong nonlinearity of the problem. Furthermore, for the particular case of hydrostatic loading, the effective constitutive estimates exhibit excellent agreement with the available exact result. This can be related to the correct prediction of the porosity evolution. Unfortunately, no other exact results are available for the effective constitutive behavior of porous elastomers. However, based on the comparisons presented, it seems plausible that the second-order variational procedure should be also able to deliver accurate estimates for the homogenized behavior of porous elastomers for more general loading conditions. In the next chapter, where second-order estimates will be compared with FEM calculations, this will be shown to be indeed the case.

On the contrary, the tangent second-order method, which only makes use of the average fields, delivers predictions for the evolution of the microstructure that deviate rapidly from the expected behavior for finite deformations, especially for tensile loadings. The negative consequences of this deviation were put in evidence by the comparisons with the exact result for hydrostatic loading, where the tangent second-order estimates, even though exact to third order in the infinitesimal strain, break down under large tensile deformations.

A major result of this work is the strong influence of the microstructure evolution on the overall behavior of porous elastomers, in particular, through geometric hardening/softening mechanisms arising as a consequence of the evolution of the pore microstructure during a finite-deformation history. Indeed, it was seen that the decrease of the porosity during compressive deformations results in a significant hardening of the effective constitutive behavior of the porous elastomer. On the other hand, the increase of the porosity associated with tensile deformations leads to a pronounced softening.

Finally, it has been shown that loss of strong ellipticity, corresponding to the possible development of shear-band instabilities, can take place in porous elastomers with *random* microstructures at physically realistic levels of compressive deformation. This is consistent with earlier findings by

Abeyaratne and Triantafyllidis (1984) for porous systems with *periodic* microstructures. Indeed, in this work, we have been able to relate softening mechanisms associated with the evolution of the microstructure under finite deformations with the possible onset of macroscopic instabilities, even for materials with strongly elliptic matrix phases.

3.4 Appendix I. In-plane components of the tensor \mathbf{P} for cylindrical inclusions with circular cross-section

In this appendix, we provide explicit expressions for the (relevant) in-plane components of the tensor \mathbf{P} associated with a random and isotropic distribution of aligned cylindrical fibers with circular cross section in a matrix material with orthotropic modulus tensor \mathbf{L} , with matrix representation

$$\begin{bmatrix} L_{1111} & L_{1122} & 0 & 0 \\ L_{1122} & L_{2222} & 0 & 0 \\ 0 & 0 & L_{1212} & L_{1221} \\ 0 & 0 & L_{1221} & L_{1212} \end{bmatrix}. \quad (3.34)$$

In this case, having set the initial aspect ratio of the pores $\omega_0 = 1$, the general expression (2.57) for \mathbf{P} simplifies to:

$$P_{ijkl} = \frac{1}{2\pi} \int_0^{2\pi} (L_{imkn} \xi_m \xi_n)^{-1} \xi_j \xi_l \, d\theta, \quad (3.35)$$

where $\xi_1 = \cos \theta$, $\xi_2 = \sin \theta$, and $\xi_3 = 0$. Carrying out the appropriate integrals leads to the following expressions:

$$\begin{aligned} P_{1111} &= \frac{(L_{1122} + L_{1221})^2 + (L_{2222} - L_{1212}) \left(Q_2 - \sqrt{\frac{L_{1111}}{L_{1212}}} \sqrt{Q_1} \right)}{\sqrt{\frac{L_{1111}}{L_{1212}}} Q_3}, \\ P_{2222} &= \frac{(L_{1122} + L_{1221})^2 + (L_{1111} - L_{1212}) \left(Q_2 - \sqrt{\frac{L_{2222}}{L_{1212}}} \sqrt{Q_1} \right)}{\sqrt{\frac{L_{2222}}{L_{1212}}} Q_3}, \\ P_{1122} &= \frac{(L_{1122} + L_{1221}) (\sqrt{Q_1} - \sqrt{L_{1111} L_{1212}} - \sqrt{L_{1212} L_{2222}})}{Q_3}, \end{aligned} \quad (3.36)$$

where

$$\begin{aligned} Q_1 &= \left(\sqrt{L_{1111} L_{2222} + L_{1212}} \right)^2 - (L_{1122} + L_{1221})^2, \\ Q_2 &= L_{1212} + \sqrt{L_{1111} L_{2222}}, \\ Q_3 &= \left((L_{1122} + L_{1221})^2 - (L_{1111} - L_{1212})(L_{2222} - L_{1212}) \right) \sqrt{Q_1}. \end{aligned} \quad (3.37)$$

At this point, it should be remarked that no allusion is made to the remaining non-zero, in-plane components of the tensor \mathbf{P} : P_{1212} , P_{2121} , and P_{1221} , simply because they do not enter in the homogenization process of the plane-strain loading of transversely isotropic elastomeric composites.

Next, we spell out the simplification of expressions (3.36) when specialized to a modulus \mathbf{L} that satisfies the constraints (3.6) given in the main body of the text. Note that under such constraints

$Q_3 = 0$, so that suitable limits must be taken in relations (3.36). The final expressions read as follows:

$$\begin{aligned}
P_{1111} &= \frac{1 + \frac{L_{2222}}{L_{1212}} + 2\sqrt{\frac{L_{2222}}{L_{1111}}}}{2L_{1111} \left(1 + \sqrt{\frac{L_{2222}}{L_{1111}}}\right)^2}, \\
P_{2222} &= \frac{1 + \frac{L_{1111}}{L_{1212}} + 2\sqrt{\frac{L_{1111}}{L_{2222}}}}{2L_{1111} \left(1 + \sqrt{\frac{L_{2222}}{L_{1111}}}\right)^2}, \\
P_{1122} &= \frac{-(L_{1221} + L_{1122})}{2L_{1111}L_{1212} \left(1 + \sqrt{\frac{L_{2222}}{L_{1111}}}\right)^2}.
\end{aligned} \tag{3.38}$$

3.5 Appendix II. Second-order estimates for transversely isotropic porous elastomers with incompressible Neo-Hookean matrix phase

In this appendix, a brief outline of the asymptotic analysis corresponding to the incompressibility limit associated with the second-order estimate (2.69) for a transversely isotropic porous elastomer with a Neo-Hookean matrix phase is presented. As discussed in the main body of the text, only one of the roots derivable from the second-order method has a physically consistent asymptotic behavior in the limit of incompressibility. The limit associated with this root is the one presented here. It is noted that the results obtained from the following asymptotic analysis have been checked to be in agreement with the full numerical solution.

Based on numerical evidence from the results for general κ , an expansion for the unknowns in this problem, *i.e.*, L_{1111}^* , L_{2222}^* , L_{1122}^* , L_{1212}^* , is attempted in the limit as $\kappa \rightarrow \infty$ of the following form:

$$\begin{aligned}
L_{1111}^* &= \frac{a_1}{\Delta} + a_2 + a_3\Delta + O(\Delta^2), \\
L_{2222}^* &= \frac{b_1}{\Delta} + b_2 + b_3\Delta + O(\Delta^2), \\
L_{1122}^* &= \frac{c_1}{\Delta} + c_2 + c_3\Delta + O(\Delta^2), \\
L_{1212}^* &= d_2 + O(\Delta),
\end{aligned} \tag{3.39}$$

where, $\Delta \doteq 1/\kappa$ is a small parameter and a_1 , a_2 , a_3 , b_1 , b_2 , b_3 , c_1 , c_2 , c_3 , and d_2 are unknown coefficients that ultimately depend on the applied loading $\bar{\lambda}_1$, $\bar{\lambda}_2$, the initial concentration of voids

f_0 , and the material parameter μ . For later use, it proves helpful to spell out the corresponding expansion for the constrained component L_{1221}^* in the limit as $\kappa \rightarrow \infty$. Thus, introducing (3.39) in (3.6) can be shown to lead to:

$$L_{1221}^* = \frac{\sqrt{a_1 b_1} - c_1}{\Delta} + \frac{a_2 b_1 + a_1 b_2 - (a_1 + b_1)\mu}{2\sqrt{a_1 b_1}} - c_2 + O(\Delta). \quad (3.40)$$

Now, it is important to remark that for the particular case of a Neo-Hookean matrix phase one of the generalized secant equations (2.65) can be solved exactly for the variable L_{1212}^* in terms of the other components of the modulus \mathbf{L} . This can be shown to result into the following simplifications:

$$L_{1212}^* = d_2 = \mu. \quad (3.41)$$

Next, introducing relations (3.39)—(3.41) in the general expressions (3.10) and (3.11) for the components of $\hat{\mathbf{F}}^{(1)} - \bar{\mathbf{F}}$ can be shown to lead to the following expansions:

$$\begin{aligned} \hat{F}_{11}^{(1)} - \bar{\lambda}_1 &= x_1 + x_2 \Delta + O(\Delta^2), \\ \hat{F}_{22}^{(1)} - \bar{\lambda}_2 &= y_1 + y_2 \Delta + O(\Delta^2), \\ \hat{F}_{12}^{(1)} \hat{F}_{21}^{(1)} &= p_1 + p_2 \Delta + O(\Delta^2), \\ (\hat{F}_{12}^{(1)})^2 + (\hat{F}_{21}^{(1)})^2 &= s_1 + s_2 \Delta + O(\Delta^2). \end{aligned} \quad (3.42)$$

The explicit expressions for the coefficients of these expansions have not been included here for their bulkiness; however, it is useful to spell out their dependence on the variables introduced in (3.39). Thus, the coefficients of first order x_1 , y_1 , p_1 , and s_1 exhibit dependence on a_1 , b_1 , c_1 , a_2 , b_2 , and c_2 , whereas, the second order terms x_2 , y_2 , p_2 , and s_2 are functions of a_1 , b_1 , c_1 , a_2 , b_2 , c_2 , a_3 , b_3 , and c_3 .

In connection with relations (3.42), it is necessary to clarify that the asymptotic expressions for the combinations $\hat{F}_{12}^{(1)} \hat{F}_{12}^{(1)}$ and $(\hat{F}_{12}^{(1)})^2 + (\hat{F}_{12}^{(1)})^2$ have been specified in (3.42), rather than those for the independent components $\hat{F}_{12}^{(1)}$ and $\hat{F}_{12}^{(1)}$, since, as discussed previously, they are the relevant variables in this problem.

Now, by introducing expressions (3.39), (3.40), and (3.42) into the three reduced (recall that $L_{1212}^* = d_2 = \mu$) generalized secant equations (2.65), a hierarchical system of equations is obtained for the remaining unknown coefficients introduced in (3.39). Thus, the equations of first-order

$O(\Delta^{-1})$ lead to the following results:

$$\begin{aligned} b_1 &= \frac{\bar{\lambda}_1^2}{\bar{\lambda}_2} a_1, \\ c_1 &= \frac{\bar{\lambda}_1}{\bar{\lambda}_2} a_1, \end{aligned} \quad (3.43)$$

whereas the equations of second-order $O(\Delta^0)$, by making use of (3.43), can be shown to render the following relations:

$$b_2 = \frac{\bar{\lambda}_1^2}{\bar{\lambda}_2} a_2 - \frac{(\bar{\lambda}_1 - \bar{\lambda}_2)(\bar{\lambda}_1 + \bar{\lambda}_2)}{\bar{\lambda}_2} \mu, \quad (3.44)$$

$$a_1 = \frac{\bar{\lambda}_2(\bar{\lambda}_1 \bar{\lambda}_2 - 1)(q_2 n_2^2 + q_1 n_2 + q_0)}{2f_0 \bar{\lambda}_1 (z_2 n_2^2 + z_1 n_2 + z_0)}, \quad (3.45)$$

$$r_4 n_2^4 + r_3 n_2^3 + r_2 n_2^2 + r_1 n_2 + r_0 = 0, \quad (3.46)$$

where $n_2 = \bar{\lambda}_1 a_2 - \bar{\lambda}_2 c_2$,

$$\begin{aligned} z_2 &= (f_0 - 1)\bar{\lambda}_1, \\ z_1 &= \mu \left[(3 - 2f_0)\bar{\lambda}_1^2 + 2\bar{\lambda}_1 \bar{\lambda}_2 + \bar{\lambda}_2^2 \right], \\ z_0 &= \mu^2 (\bar{\lambda}_1 + \bar{\lambda}_2) \left[(f_0 - 2)\bar{\lambda}_1^2 - (1 + f_0)\bar{\lambda}_1 \bar{\lambda}_2 - \bar{\lambda}_2^2 \right], \end{aligned} \quad (3.47)$$

and $q_2, q_1, q_0, r_4, r_3, r_2, r_1$, and r_0 have been given in Appendix III.

Prescriptions (3.43) through (3.47) can be shown to be sufficient to fully determine the first-order terms of all of the components of $\hat{\mathbf{F}}^{(1)} - \bar{\mathbf{F}}$ and $\bar{\mathbf{F}}^{(1)}$. The final expressions may be written as:

$$\begin{aligned} x_1 &= -\frac{\bar{\lambda}_1}{\bar{\lambda}_2} y_1 - \frac{(\bar{J} - 1)\bar{\lambda}_2}{a_1}, \\ y_1 &= -\frac{\bar{\lambda}_2 \left[a_1 f_0 \mu (\bar{\lambda}_2^2 - \bar{\lambda}_1^2) + \bar{\lambda}_2 (\bar{\lambda}_1 \bar{\lambda}_2 - 1) ((f_0 - 1)n_2 + 2\mu(\bar{\lambda}_1 + \bar{\lambda}_2)) \right]}{a_1 \left[2(f_0 - 1)n_2 \bar{\lambda}_1 - \mu(\bar{\lambda}_1 + \bar{\lambda}_2) ((f_0 - 3)\bar{\lambda}_1 - (1 + f_0)\bar{\lambda}_2) \right]}, \\ p_1 &= x_1 y_1 + \bar{\lambda}_2 x_1 + \bar{\lambda}_1 y_1 + \bar{\lambda}_1 \bar{\lambda}_2 - 1, \\ s_1 &= \frac{\mu(\bar{\lambda}_1 - \bar{\lambda}_2)^2 (\bar{\lambda}_1 + \bar{\lambda}_2)^2}{a_1^2 f_0 \bar{\lambda}_1 \left[2(f_0 - 1)n_2 \bar{\lambda}_1 - \mu(\bar{\lambda}_1 + \bar{\lambda}_2) ((f_0 - 3)\bar{\lambda}_1 - (1 + f_0)\bar{\lambda}_2) \right]^2} \\ &\times (a_1 f_0 \mu (\bar{\lambda}_1 + \bar{\lambda}_2)^2 + (f_0 - 1)\bar{\lambda}_2 (\bar{\lambda}_1 \bar{\lambda}_2 - 1)(n_2 - \mu(\bar{\lambda}_1 + \bar{\lambda}_2))) \\ &\times \left(2a_1 f_0 \bar{\lambda}_1 + \bar{\lambda}_2 (1 + f_0 - (1 + f_0)\bar{\lambda}_1 \bar{\lambda}_2) \right) + \left(\frac{\bar{\lambda}_1}{\bar{\lambda}_2} + \frac{\bar{\lambda}_2}{\bar{\lambda}_1} \right) p_1, \end{aligned} \quad (3.48)$$

and

$$\begin{aligned} \bar{\lambda}_1^{(1)} &= x_1 + \bar{\lambda}_1 + O(\Delta), \\ \bar{\lambda}_2^{(1)} &= y_1 + \bar{\lambda}_2 + O(\Delta). \end{aligned} \quad (3.49)$$

At this point, it is important to remark that relations (3.48) and (3.49), by means of (3.45), ultimately depend on the variable n_2 , which can be determined in closed form by solving the fourth-order polynomial equation (3.46). This is precisely the same equation as (3.15) given in the main body of text, where for clarity of notation n_2 was relabelled as v . Under the above development, it is then straightforward to show that the leading order term of the expansion of the second-order estimate (2.69) in the limit of incompressibility may be expressed in closed form, as it ultimately depends on the coefficient n_2 . The final explicit expression (in terms of the variable $n_2 = v$) is given by (3.14) in the text.

Next, it is shown that the porosity associated with the second-order estimate (3.14) for a porous elastomer with an incompressible Neo-Hookean matrix phase reduces to the exact result (3.30). Given that a HS-type approximation is utilized in the homogenization process, the fields in the porous phase are assumed constant. This implies that the average change in volume of the porous phase is simply given by:

$$\begin{aligned}\bar{J}^{(2)} &= \langle \det \mathbf{F} \rangle^{(2)} \\ &= \det(\mathbf{F})^{(2)} \\ &= \frac{(f_0 \bar{\lambda}_1 - (1 - f_0)x_1)(f_0 \bar{\lambda}_2 - (1 - f_0)y_1)}{f_0^2},\end{aligned}\tag{3.50}$$

where use has been made of the relation $\bar{\mathbf{F}} = (1 - f_0)\bar{\mathbf{F}}^{(1)} + f_0\bar{\mathbf{F}}^{(2)}$. Expression (3.50) can now be used to compute the porosity associated with the second-order estimate (3.14) through the relation:

$$f = \frac{\bar{J}^{(2)}}{J} f_0,\tag{3.51}$$

which, after some simplification, can be shown to reduce to the exact result (3.30). Finally it should be emphasized that this result has been proven to hold not only for Neo-Hookean porous elastomers, but more generally, for porous elastomers with incompressible isotropic matrix phases.

3.6 Appendix III. Coefficients associated with the incompressible limit for the second-order estimate of Neo-Hookean porous elastomers

This appendix provides, in terms of $\bar{\lambda}_1, \bar{\lambda}_2, f_0$, and μ , the explicit expressions for the coefficients introduced in relations (3.14) and (3.15). They read as follows:

$$\begin{aligned}
p_4 &= (f_0 - 1)^2(1 + f_0)\bar{\lambda}_1^2(\bar{\lambda}_1^2 + \bar{\lambda}_2^2), \\
p_3 &= -4(f_0 - 1)\mu\bar{\lambda}_1^2\left((-1 + f_0^2)\bar{\lambda}_1^3 - (1 + f_0)\bar{\lambda}_1^2\bar{\lambda}_2 + \right. \\
&\quad \left. + (-1 + (f_0 - 4)f_0)\bar{\lambda}_1\bar{\lambda}_2^2 - (1 + f_0)\bar{\lambda}_2^3\right), \\
p_2 &= 2\mu^2\bar{\lambda}_1\left(3(f_0 - 1)^2(1 + f_0)\bar{\lambda}_1^5 + (5 + (4 - 7f_0)f_0)\bar{\lambda}_1^4\bar{\lambda}_2 + \right. \\
&\quad \left. + 2(2 + f_0(13 + (-12 + f_0)f_0))\bar{\lambda}_1^3\bar{\lambda}_2^2 + 4(1 - 2(-2 + f_0)f_0)\bar{\lambda}_1^2\bar{\lambda}_2^3 - \right. \\
&\quad \left. - (1 + f_0)(-1 + (f_0 - 4)f_0)\bar{\lambda}_1\bar{\lambda}_2^4 - (1 + (f_0 - 4)f_0)\bar{\lambda}_2^5\right), \\
p_1 &= -4\mu^3\bar{\lambda}_1(\bar{\lambda}_1 + \bar{\lambda}_2)\left((f_0 - 1)^2(1 + f_0)\bar{\lambda}_1^5 - (-1 + f_0(-5 + \right. \\
&\quad \left. + f_0(3 + f_0))\bar{\lambda}_1^4\bar{\lambda}_2 + (f_0 - 4)(-3 + f_0)f_0\bar{\lambda}_1^3\bar{\lambda}_2^2 - (f_0 - 4)f_0 \times \right. \\
&\quad \left. \times (1 + f_0)\bar{\lambda}_1^2\bar{\lambda}_2^3 + (-1 + 3f_0)\bar{\lambda}_1\bar{\lambda}_2^4 + (f_0 - 1)\bar{\lambda}_2^5\right), \\
p_0 &= \mu^4(\bar{\lambda}_1 + \bar{\lambda}_2)^2\left((f_0 - 1)^2(1 + f_0)\bar{\lambda}_1^6 - 2f_0(-5 + f_0(2 + f_0))\bar{\lambda}_1^5\bar{\lambda}_2 + \right. \\
&\quad \left. + (-1 + f_0(11 + 2(f_0 - 1)f_0))\bar{\lambda}_1^4\bar{\lambda}_2^2 - 2f_0(-2 + (-3 + f_0)f_0)\bar{\lambda}_1^3\bar{\lambda}_2^3 + \right. \\
&\quad \left. + (-1 + f_0(5 + (f_0 - 1)f_0))\bar{\lambda}_1^2\bar{\lambda}_2^4 + 2f_0(1 + f_0)\bar{\lambda}_1\bar{\lambda}_2^5 + (1 + f_0)\bar{\lambda}_2^6\right), \\
q_2 &= (f_0 - 1)^2\bar{\lambda}_1, \\
q_1 &= 2(f_0 - 1)\mu\bar{\lambda}_1(\bar{\lambda}_1 - f_0\bar{\lambda}_1 + \bar{\lambda}_2), \\
q_0 &= \mu^2\left((f_0 - 1)^2\bar{\lambda}_1^3 - (1 + f_0)^2\bar{\lambda}_1\bar{\lambda}_2^2 - (1 + f_0)\bar{\lambda}_2^3 + \bar{\lambda}_1^2(\bar{\lambda}_2 - 3f_0\bar{\lambda}_2)\right), \\
r_4 &= -(-1 + f_0)^3\bar{\lambda}_1^2(-1 + f_0 + \bar{\lambda}_1\bar{\lambda}_2), \\
r_3 &= -4(-1 + f_0)^2\mu\bar{\lambda}_1^2(\bar{\lambda}_1 - f_0\bar{\lambda}_1 + \bar{\lambda}_2)(-1 + f_0 + \bar{\lambda}_1\bar{\lambda}_2), \\
r_2 &= -2(-1 + f_0)\mu^2\bar{\lambda}_1\left(3(-1 + f_0)^3\bar{\lambda}_1^3 + (-1 + f_0)\bar{\lambda}_1^2(5 - 7f_0 + \right. \\
&\quad \left. + 3(-1 + f_0)\bar{\lambda}_1^2)\bar{\lambda}_2 - \bar{\lambda}_1(1 - 3f_0 + f_0^2 + f_0^3 + (-5 + 7f_0)\bar{\lambda}_1^2)\bar{\lambda}_2^2 - \right. \\
&\quad \left. - (-1 + f_0^2 + (-1 + f_0(4 + f_0))\bar{\lambda}_1^2)\bar{\lambda}_2^3 - (1 + f_0)\bar{\lambda}_1\bar{\lambda}_2^4\right),
\end{aligned}$$

$$\begin{aligned}
r_1 &= 4\mu^3 \bar{\lambda}_1 (\bar{\lambda}_1 + \bar{\lambda}_2) \left((-1 + f_0)^3 \bar{\lambda}_1^4 \bar{\lambda}_2 + \bar{\lambda}_1 \bar{\lambda}_2^2 (-1 + f_0^2 + (1 + f_0 + f_0^2) \bar{\lambda}_2^2) + \right. \\
&\quad + \bar{\lambda}_1^3 ((-1 + f_0)^4 - (1 + f_0(-4 + f_0 + f_0^2)) \bar{\lambda}_2^2) + \bar{\lambda}_2^3 (-1 + f_0(f_0 + \bar{\lambda}_2^2)) + \\
&\quad \left. + \bar{\lambda}_1^2 \bar{\lambda}_2 (1 + \bar{\lambda}_2^2 - f_0(4 - 4f_0 + f_0^3 + (-3 + f_0) \bar{\lambda}_2^2)) \right), \\
r_0 &= -\mu^4 (\bar{\lambda}_1 + \bar{\lambda}_2)^2 \left((-1 + f_0)^4 \bar{\lambda}_1^4 - (-1 + f_0)^2 \bar{\lambda}_1^3 (2f_0(1 + f_0) - \right. \\
&\quad - (-1 + f_0) \bar{\lambda}_1^2 \bar{\lambda}_2 + \bar{\lambda}_1^2 (-2 + f_0(2 + 3f_0 + f_0^3 - 2(-3 + f_0^2) \bar{\lambda}_1^2)) \bar{\lambda}_2^2 + \\
&\quad + \bar{\lambda}_1 (2f_0(1 + f_0)^2 + (2 + f_0(4 + f_0 + f_0^2)) \bar{\lambda}_1^2) \bar{\lambda}_2^3 + \\
&\quad \left. + (1 + f_0)(1 + f_0 + 2f_0 \bar{\lambda}_1^2) \bar{\lambda}_2^4 + (-1 + f_0) \bar{\lambda}_1 \bar{\lambda}_2^5 \right).
\end{aligned}$$

3.7 Appendix IV. Tangent second-order estimates for transversely isotropic porous elastomers with incompressible Neo-Hookean matrix phase

In this appendix some details are presented concerning the incompressibility limit associated with the tangent second-order estimate (3.19) for a porous elastomer with Neo-Hookean matrix. The asymptotic solution resulting from this heuristic derivation has been checked to be in agreement with the full numerical results.

Motivated by the observed properties of the numerical solution for general κ , an expansion for the unknowns in this problem, *i.e.*, $\bar{\lambda}_1^{(1)}$ and $\bar{\lambda}_2^{(1)}$, is attempted in the limit as $\kappa \rightarrow \infty$ of the following form:

$$\begin{aligned}
\bar{\lambda}_1^{(1)} &= \alpha_1 + \alpha_2 \Delta + \alpha_3 \Delta^2 + O(\Delta^3), \\
\bar{\lambda}_2^{(1)} &= \beta_1 + \beta_2 \Delta + \beta_3 \Delta^2 + O(\Delta^3),
\end{aligned} \tag{3.52}$$

where, $\Delta \doteq 1/\kappa$ is a small parameter, and $\alpha_1, \alpha_2, \alpha_3, \beta_1, \beta_2$, and β_3 are unknown coefficients which ultimately depend on the applied loading $\bar{\lambda}_1, \bar{\lambda}_2$, the initial concentration of voids f_0 , and the material parameter μ .

By making use of expressions (3.52) in relation (3.20), a hierarchical system of equations is obtained for the coefficients $\alpha_1, \alpha_2, \alpha_3, \beta_1, \beta_2$, and β_3 . The leading order terms $O(\Delta^{-1})$ of these equations can be shown to lead to the following relationship:

$$\beta_1 = 1/\alpha_1, \tag{3.53}$$

which implies that the determinant of $\overline{\mathbf{F}}^{(1)}$, denoted by $\overline{J}^{(1)}$, is exactly equal to one in the incompressible limit.

Next, under condition (3.53), the equations of order $O(\Delta^0)$ yield the relationship:

$$\alpha_2 + \alpha_1^2 \beta_2 = \frac{(1 + \alpha_1^2)(-1 - f_0 + (1 + f_0)\alpha_1^2 + (\overline{\lambda}_2 - \overline{\lambda}_1)\alpha_1)\mu}{\overline{\lambda}_1 - \alpha_1^2 \overline{\lambda}_2}, \quad (3.54)$$

which determines the combination $\alpha_2 + \alpha_1^2 \beta_2$ in terms of α_1 .

Finally, the equations of order $O(\Delta)$ derived from (3.20) are considered. Making use of relations (3.53) and (3.54) in these equations can be shown to lead to the following expressions:

$$\alpha_3 + G_1(\alpha_1, \alpha_2)\beta_3 = G_2(\alpha_1, \alpha_2), \quad (3.55)$$

and

$$\begin{aligned} & \left(\overline{\lambda}_2^2 + f_0^2 - 1\right) \alpha_1^4 + 2(\overline{\lambda}_1 + (f_0 - 1)\overline{\lambda}_2) \alpha_1^3 + \left(\overline{\lambda}_2^2 - \overline{\lambda}_1^2\right) \alpha_1^2 \\ & - 2((f_0 - 1)\overline{\lambda}_1 + \overline{\lambda}_2) \alpha_1 + 1 - f_0^2 - \overline{\lambda}_1^2 = 0, \end{aligned} \quad (3.56)$$

where G_1 and G_2 are (known functions of their arguments) too cumbersome to be included here.

It is noted that (3.55) establishes a linear relationship between β_3 and α_3 analogous to the one established by equation (3.54) between β_2 and α_2 . More importantly, (3.56) provides a fourth-order polynomial equation for the coefficient α_1 in terms of the initial concentration of pores f_0 , the material parameter μ , and the applied loading as determined by $\overline{\lambda}_1$ and $\overline{\lambda}_2$. This equation is precisely the equation (3.22) given in the main body of the text, where for clarity of notation α_1 was denoted as u . It turns out that the leading order term of the effective energy (3.19) in the limit of incompressibility may eventually be characterized entirely in terms of the coefficient α_1 . The final result is given by expression (3.21) in the text, where, as already pointed out, u must be identified with α_1 .

It is noted that for the particular case of hydrostatic loading, *i.e.* $\overline{\lambda}_2 = \overline{\lambda}_1 = \overline{\lambda}$, a suitable limit must be taken in the above expressions. For this type of deformation, it is straightforward to show that $\overline{\lambda}_2^{(1)} = \overline{\lambda}_1^{(1)}$, and hence that, $\beta_1 = \alpha_1$, $\beta_2 = \alpha_2$, and $\beta_3 = \alpha_3$. Now, making use of these relations together with the equation of order $O(\Delta^{-1})$ given by (3.53) leads to $\alpha_1 = 1$. In turn, this result for α_1 makes the equation (of order $O(\Delta^0)$) (3.54) be satisfied trivially, whereas

the one of order $O(\Delta^1)$ can be shown to render the following identities:

$$\begin{aligned}\alpha_2 &= \frac{\bar{\lambda} - 1}{\bar{\lambda} + f_0 - 1} \mu, \\ \alpha_3 &= \frac{(\bar{\lambda} - 1) \left(3 - 5f_0 + 2f_0^2 + (7f_0 - 6)\bar{\lambda} + 3\bar{\lambda}^2 \right)}{2(\bar{\lambda} + f_0 - 1)^3} \mu^2.\end{aligned}\tag{3.57}$$

Recognizing now that under expression (3.52), hydrostatic loading, and $\alpha_1 = 1$, the expansion of the second-order estimate (3.19) in the incompressibility limit can be written, to first order, as:

$$\widehat{W}^I(\bar{\mathbf{F}}) = \widehat{\Phi}^I(\bar{\lambda}, \bar{\lambda}) = 2(1 - f_0) (\bar{\lambda} - 1) \alpha_2 + O(\Delta),\tag{3.58}$$

together with (3.57)₁, leads to the final result (3.23).

Chapter 4

Porous elastomers: cylindrical voids, periodic microstructure

This chapter—as the preceding one—is concerned with the overall, *plane-strain* behavior of porous elastomers consisting of aligned cylindrical voids in an isotropic elastomeric matrix subjected to finite deformations. Unlike in Chapter 3, however, the distribution of the pores here is taken to be *periodic*. This provides the means to achieve the two main objectives of this chapter: (i) to assess the accuracy of the second-order estimates through comprehensive comparisons with more accurate FEM calculations available for periodic microstructures, and (ii) to study the influence of the initial microgeometry of porous elastomers on the overall behavior and stability of these materials.

It is noted that the FEM results presented in this chapter are due to Jean-Claude Michel (LMA, Marseille) and Nicolas Triantafyllidis (University of Michigan, Ann Arbor) in the context of a NSF–CNRS international collaboration. For a detailed description of the FEM calculations the reader is referred to Triantafyllidis *et al.* (2006) and Michel *et al.* (2007).

4.1 Plane-strain loading of periodic porous elastomers

In the present chapter, as already stated above, we study the problem of plane-strain loading of porous elastomers consisting of cylindrical voids perpendicular to the plane of deformation and aligned in the \mathbf{e}_3 axis direction. The voids are taken to have initially circular cross section and initial volume fraction f_0 . Moreover, two types of pore distributions—in the reference configuration—are considered: (a) periodic square and (b) periodic hexagonal arrangements, as depicted in Figure

4.1.

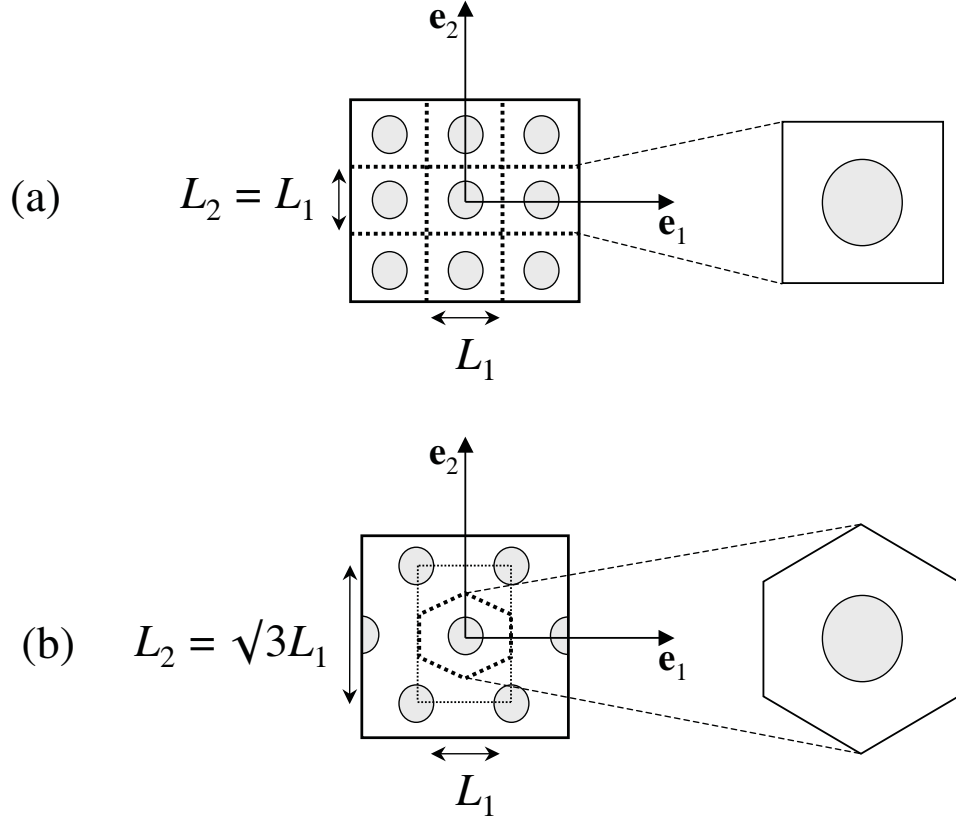


Figure 4.1: Reference configuration depiction of the various microgeometries investigated: (a) periodic square, and (b) periodic hexagonal arrangement of circular voids.

For definiteness, the elastomeric matrix phase is taken to be characterized by the (2D) compressible Neo-Hookean material with stored-energy function (3.3), repeated here for convenience:

$$W(\mathbf{F}) = \frac{\mu}{2}(I - 2) - \mu \ln J + \frac{\kappa - \mu}{2}(J - 1)^2. \quad (4.1)$$

Recall that in this expression, $I = \lambda_1^2 + \lambda_2^2$, $J = \lambda_1 \lambda_2$, and μ and κ denote, respectively, the shear and bulk modulus of the material at zero strain.

In contrast to the in-plane isotropic distribution of voids considered in Chapter 3, the pore distributions studied in this chapter are *anisotropic*. As a result, the overall in-plane response of the class of porous elastomers considered here is *anisotropic*. In this regard, attention cannot be restricted only to pure stretch diagonal loadings, as it was done in Chapter 3, but, instead, general in-plane loadings need to be considered. Thus, by exploiting the objectivity of \widehat{W} —namely, by

setting $\bar{\mathbf{R}} = \mathbf{I}$ —and by making use of the decomposition $\bar{\mathbf{U}} = \bar{\mathbf{Q}} \bar{\mathbf{D}} \bar{\mathbf{Q}}^T$, we will consider (in-plane) macroscopic deformation gradients $\bar{\mathbf{F}}$ of the form¹:

$$\bar{F}_{ij} = \bar{U}_{ij} = \begin{bmatrix} \cos \bar{\theta} & -\sin \bar{\theta} \\ \sin \bar{\theta} & \cos \bar{\theta} \end{bmatrix} \begin{bmatrix} \bar{\lambda}_1 & 0 \\ 0 & \bar{\lambda}_2 \end{bmatrix} \begin{bmatrix} \cos \bar{\theta} & \sin \bar{\theta} \\ -\sin \bar{\theta} & \cos \bar{\theta} \end{bmatrix}. \quad (4.2)$$

In this last expression, $\bar{\lambda}_1$ and $\bar{\lambda}_2$ denote the in-plane macroscopic principal stretches, and $\bar{\theta}$ serves to characterize the orientation (in the anticlockwise sense relative to the fixed laboratory frame of reference) of the macroscopic, in-plane, Lagrangian principal axes (*i.e.*, the principal axes of $\bar{\mathbf{U}}$). For convenience, the coordinates $\{\mathbf{e}_i\}$ defining the solid's axes of orthotropy in the reference configuration (see Fig. 4.1) will be identified here as the fixed laboratory frame of reference. In the sequel, the components of any tensorial quantity will be referred to $\{\mathbf{e}_i\}$.

Having specified the initial microstructure, the constitutive behavior of the matrix phase, and the applied loading conditions, we next detail the specialization of the second-order estimate (2.69) to the class of porous elastomers of interest in this chapter.

4.1.1 Second-order homogenization estimates

The computation of the second-order estimate (2.69) for the class of periodic porous elastomers defined above, though similar, is considerably more involved—due to the anisotropic distribution of the pores—than that of random, isotropic porous elastomers given in Section 3.1.1. First, following similar arguments to those given in Section 3.1.1, it suffices to consider the in-plane components of the modulus tensor $\mathbf{L}^{(1)} = \mathbf{L}$ of the matrix phase of the linear comparison composite, which may be conveniently expressed as a matrix in $\Re^{4 \times 4}$:

$$\begin{bmatrix} L_{1111} & L_{1122} & L_{1112} & L_{1121} \\ L_{1122} & L_{2222} & L_{2212} & L_{2221} \\ L_{1112} & L_{2212} & L_{1212} & L_{1221} \\ L_{1121} & L_{2221} & L_{1221} & L_{2121} \end{bmatrix}, \quad (4.3)$$

where, once again, for notational simplicity, the superscript ‘(1)’ has been suppressed for $\mathbf{L}^{(1)}$ and its components, and use has been made of major symmetry (*i.e.*, $L_{ijkl} = L_{klij}$). Further, recalling

¹Here and subsequently in this chapter, Latin indices range from 1 to 2.

that \mathbf{L}^* has been taken to be orthotropic, it follows that it may be written in the form:

$$\begin{bmatrix} L_{1111}^* & L_{1122} & 0 & 0 \\ L_{1122}^* & L_{2222}^* & 0 & 0 \\ 0 & 0 & L_{1212}^* & L_{1221}^* \\ 0 & 0 & L_{1221}^* & L_{2121}^* \end{bmatrix}. \quad (4.4)$$

Since $\overline{\mathbf{R}}$ and $\overline{\mathbf{Q}}$ are known quantities, the prescription (2.66), together with (4.4), entails that \mathbf{L} possesses 6 independent components, namely, L_{1111}^* , L_{2222}^* , L_{1122}^* , L_{1212}^* , L_{2121}^* , and L_{1221}^* . Following similar arguments to those given in Section 3.1.1—namely, guided by the fact that under plane-strain conditions the tensor $\hat{\mathbf{F}}^{(1)}$ has at most 4 independent components ($\hat{F}_{11}^{(1)}$, $\hat{F}_{22}^{(1)}$, $\hat{F}_{12}^{(1)}$, $\hat{F}_{21}^{(1)}$) which should be determined from equation (2.72)—it is expedient to reduce the independent components of (4.4) from 6 to just 4. To this end, we impose the constraints (3.6), repeated here for convenience:

$$L_{2121}^* = L_{1212}^*, \quad \text{and} \quad L_{1221}^* = \sqrt{(L_{1111}^* - L_{1212}^*)(L_{2222}^* - L_{1212}^*)} - L_{1122}^*, \quad (4.5)$$

among the components of (4.4). Recall that the motivation for the choices (4.5) is twofold: (i) the principal components of the tangent modulus of a Neo-Hookean material satisfy (3.6); and (ii) the conditions (4.5) simplify considerably the computations involved.

Now, making use of the above results, the average deformation gradient $\overline{\mathbf{F}}^{(1)}$ in the matrix phase of the LCC, needed in the computation of \widehat{W} , can be readily computed from (2.70) in terms of the applied loading $\overline{\mathbf{F}}$, the initial porosity f_0 , the matrix material parameters μ , κ , and the 4 unknowns L_{1111}^* , L_{2222}^* , L_{1122}^* , and L_{1212}^* . Note from the RHS of (2.70) that $\overline{\mathbf{F}}^{(1)}$ depends also on whether the underlying pores are distributed with square (see Fig. 4.1(a)) or hexagonal (see Fig. 4.1(b)) arrangement, since it depends directly on the microstructural tensor \mathbf{P} , via $\mathbf{E}^{(1)} = \mathbf{E} = \mathbf{P}^{-1} - (1 - f_0)\mathbf{L}$. In this connection, it is noted that the explicit expressions for the components of the tensor \mathbf{P} for the two types of periodic microstructures considered in this chapter are given in Appendix I.

Having specified the variable $\overline{\mathbf{F}}^{(1)}$, we next turn to determining $\hat{\mathbf{F}}^{(1)}$, also needed in the computation of \widehat{W} . With conditions (4.5) for the components (4.4) of \mathbf{L}^* , and making use of the identifications $\ell_1^* = L_{1111}^*$, $\ell_2^* = L_{2222}^*$, $\ell_3^* = L_{1212}^*$, and $\ell_4^* = L_{1122}^*$, the equations (2.72) can be seen to reduce to 4 consistent equations for the 4 components of $\hat{\mathbf{F}}^{(1)}$. These equations are more

conveniently expressed in terms of the variable \mathbf{Y} :

$$\mathbf{Y} = \bar{\mathbf{Q}}^T \bar{\mathbf{R}}^T \left(\hat{\mathbf{F}}^{(1)} - \bar{\mathbf{F}} \right) \bar{\mathbf{Q}}, \quad (4.6)$$

which leads to the expressions:²

$$\begin{aligned} (Y_{11})^2 + 2f_1 Y_{12} Y_{21} &= k_1, \\ (Y_{22})^2 + 2f_2 Y_{12} Y_{21} &= k_2, \\ (Y_{12})^2 + (Y_{21})^2 + 2f_3 Y_{12} Y_{21} &= k_3, \\ Y_{11} Y_{22} - Y_{12} Y_{21} &= k_4, \end{aligned} \quad (4.7)$$

where $f_1 = \partial L_{1221}^* / \partial L_{1111}^*$, $f_2 = \partial L_{1221}^* / \partial L_{2222}^*$, $f_3 = \partial L_{1221}^* / \partial L_{1212}^*$, and

$$\begin{aligned} k_1 &= \frac{1}{f_0} \left(\bar{\mathbf{D}} - \check{\mathbf{F}}^{(1)} \right) \cdot \frac{\partial \mathbf{E}^*}{\partial L_{1111}^*} \left(\bar{\mathbf{D}} - \check{\mathbf{F}}^{(1)} \right), \\ k_2 &= \frac{1}{f_0} \left(\bar{\mathbf{D}} - \check{\mathbf{F}}^{(1)} \right) \cdot \frac{\partial \mathbf{E}^*}{\partial L_{2222}^*} \left(\bar{\mathbf{D}} - \check{\mathbf{F}}^{(1)} \right), \\ k_3 &= \frac{1}{f_0} \left(\bar{\mathbf{D}} - \check{\mathbf{F}}^{(1)} \right) \cdot \frac{\partial \mathbf{E}^*}{\partial L_{1212}^*} \left(\bar{\mathbf{D}} - \check{\mathbf{F}}^{(1)} \right), \\ k_4 &= \frac{1}{2f_0} \left(\bar{\mathbf{D}} - \check{\mathbf{F}}^{(1)} \right) \cdot \frac{\partial \mathbf{E}^*}{\partial L_{1122}^*} \left(\bar{\mathbf{D}} - \check{\mathbf{F}}^{(1)} \right). \end{aligned} \quad (4.8)$$

In relations (4.8), $\check{\mathbf{F}}^{(1)} = \bar{\mathbf{Q}}^T \bar{\mathbf{R}}^T \bar{\mathbf{F}}^{(1)} \bar{\mathbf{Q}}$ and $\mathbf{E}^* = (\mathbf{P}^*)^{-1} - (1 - f_0) \mathbf{L}^*$ with \mathbf{P}^* such that

$$P_{ijkl} = \bar{Q}_{rm} \bar{Q}_{jn} \bar{Q}_{sp} \bar{Q}_{lq} \bar{R}_{ir} \bar{R}_{ks} P_{mnpq}^*, \quad (4.9)$$

have been introduced for ease of notation.

In spite of the fact that equations (4.7) are nonlinear, they can be solved in closed form to yield two distinct solutions for Y_{11} and Y_{22} and the combinations $Y_{12} Y_{21}$ and $(Y_{12})^2 + (Y_{21})^2$. The two solutions are as follows:

$$\begin{aligned} Y_{11} &= \pm \frac{2f_1 k_4 + k_1}{\sqrt{4f_1^2 k_2 + 4f_1 k_4 + k_1}}, & Y_{22} &= \pm \frac{2f_1 k_2 + k_4}{\sqrt{4f_1^2 k_2 + 4f_1 k_4 + k_1}}, \\ Y_{12} Y_{21} &= Y_{11} Y_{22} - k_4, & Y_{12}^2 + Y_{21}^2 &= k_3 - 2f_3 Y_{12} Y_{21}, \end{aligned} \quad (4.10)$$

where it must be emphasized that the positive (and negative) signs must be chosen to go together in the roots for Y_{11} and Y_{22} .

Next, using the relation $\hat{\mathbf{F}}^{(1)} = \bar{\mathbf{R}} \bar{\mathbf{Q}} \mathbf{Y} \bar{\mathbf{Q}}^T + \bar{\mathbf{F}}$, each of the two distinct roots for \mathbf{Y} may be substituted into expression (2.65). The resulting relation forms a system of 4 nonlinear algebraic

²Note that the algebraic system of equations (4.7) is mathematically equivalent to (3.8) (which appeared in the context of the random, isotropic microstructure).

equations for the 4 scalar unknowns L_{1111}^* , L_{2222}^* , L_{1122}^* , and L_{1212}^* , which must be solved numerically. It is worth mentioning that by exploiting the objectivity and isotropy of the Neo-Hookean stored-energy function (4.1), the equations obtained from (2.65) may be finally cast into a rather simple form. Having computed the values of all the components of \mathbf{L} for a given initial porosity f_0 , given material parameters μ and κ , and given loading $\bar{\mathbf{F}}$, the values of the components of $\bar{\mathbf{F}}^{(1)}$ and $\hat{\mathbf{F}}^{(1)}$ can be readily determined using relations (2.70) and (4.10), respectively. In turn, these results may be used to compute the second-order estimate (2.69) for the effective stored-energy function \widehat{W} of the porous elastomers. In this connection, it should be noted that, similar to the random case discussed in the previous chapter, there is only one root, between the two possible choices in (4.10), that leads to physically sound, superior estimates for \widehat{W} . The criterion is as follows: (i) the “positive” (+) root in (4.10) should be selected for deformations satisfying $\bar{e}_1 + \bar{e}_2 \leq 0$; (ii) the “negative” (−) root in (4.10) should be selected for deformations satisfying $\bar{e}_1 + \bar{e}_2 \geq 0$, where it is recalled that $\bar{e}_i = \ln \bar{\lambda}_i$.

To conclude this section, it proves expedient for later use to write down the evolution of the relevant microstructural variables in this problem. Thus, following Section 2.5, the current porosity and current average aspect ratio of the underlying pores in the deformed configuration are given, respectively, by:

$$f = \frac{\bar{\lambda}_1^{(2)} \bar{\lambda}_2^{(2)}}{\bar{\lambda}_1 \bar{\lambda}_2} f_0 \quad \text{and} \quad \omega = \frac{\bar{\lambda}_1^{(2)}}{\bar{\lambda}_2^{(2)}}. \quad (4.11)$$

In these expressions, $\bar{\lambda}_1^{(2)}$ and $\bar{\lambda}_2^{(2)}$ denote the principal stretches associated with the average deformation gradient tensor $\bar{\mathbf{F}}^{(2)}$ in the porous phase, which can be readily computed from knowledge of $\bar{\mathbf{F}}^{(1)}$, by making use of the macroscopic average condition: $\bar{\mathbf{F}}^{(2)} = 1/f_0(\bar{\mathbf{F}} - (1 - f_0)\bar{\mathbf{F}}^{(1)})$.

4.1.2 Loss of strong ellipticity

As already stated in the preceding chapter, the general strong ellipticity condition (2.89) can be written down more explicitly for the particular case of plane-strain deformations. Indeed, it can be shown that, under plane-strain conditions, loss of strong ellipticity is first attained along a given loading path (with origin at $\bar{\mathbf{F}} = \mathbf{I}$) whenever the fourth-order polynomial equation:

$$\det \left[\hat{\mathcal{L}}_{i_1 k_1} \left(\frac{N_1}{N_2} \right)^2 + (\hat{\mathcal{L}}_{i_1 k_2} + \hat{\mathcal{L}}_{i_2 k_1}) \frac{N_1}{N_2} + \hat{\mathcal{L}}_{i_2 k_2} \right] = 0 \quad (4.12)$$

admits one or more real roots N_1/N_2 . In this expression, it should be recalled that N_1 and N_2 denote the direction cosines of the normal \mathbf{N} to the characteristic direction in the undeformed

configuration, and that $\widehat{\mathcal{L}} = \partial^2 \widehat{W} / \partial \overline{\mathbf{F}}^2$. Explicit (but cumbersome) conditions on the components of $\widehat{\mathcal{L}}$ may be written down in order for the quartic equation (4.12) to possess complex roots. However, in general, it is simpler to determine the loss of strong ellipticity by monitoring the 4 roots of (4.12), which are known in closed form, along the loading path of interest, and detecting at which point at least one of these 4 roots becomes real.

For later use, it proves helpful to record here the simplification of condition (4.12) for the cases in which the loading is aligned with the microstructure (*i.e.*, for $\bar{\theta} = 0$ and $\bar{\theta} = \pi/2$ in (4.2)). For such cases, (4.12) can be shown to reduce to

$$\begin{aligned} & \widehat{\mathcal{L}}_{1111} \widehat{\mathcal{L}}_{2121} \left(\frac{N_1}{N_2} \right)^4 + \left(\widehat{\mathcal{L}}_{1111} \widehat{\mathcal{L}}_{2222} + \widehat{\mathcal{L}}_{1212} \widehat{\mathcal{L}}_{2121} - (\widehat{\mathcal{L}}_{1122} + \widehat{\mathcal{L}}_{1221})^2 \right) \left(\frac{N_1}{N_2} \right)^2 \\ & + \widehat{\mathcal{L}}_{2222} \widehat{\mathcal{L}}_{1212} = 0. \end{aligned} \quad (4.13)$$

Interestingly, the conditions on the components of $\widehat{\mathcal{L}}$ for (4.13) to have complex roots—as opposed to those needed for the more general polynomial (4.12)—are rather simple. They read as follows:

$$\widehat{\mathcal{L}}_{1111} > 0, \quad \widehat{\mathcal{L}}_{2222} > 0, \quad \widehat{\mathcal{L}}_{1212} > 0, \quad \widehat{\mathcal{L}}_{2121} > 0, \quad \text{and}$$

$$\widehat{\mathcal{L}}_{1111} \widehat{\mathcal{L}}_{2222} + \widehat{\mathcal{L}}_{1212} \widehat{\mathcal{L}}_{2121} - (\widehat{\mathcal{L}}_{1122} + \widehat{\mathcal{L}}_{1221})^2 > -2 \sqrt{\widehat{\mathcal{L}}_{1111} \widehat{\mathcal{L}}_{2222} \widehat{\mathcal{L}}_{1212} \widehat{\mathcal{L}}_{2121}}. \quad (4.14)$$

Note that conditions (4.14) are identical to those encountered for porous elastomers with random, isotropic microstructures, given by (3.31) in Chapter 3. However, it should be remarked that while the third and fourth conditions in (3.31) are equivalent to each other—due to the fact that for isotropic materials $\widehat{\mathcal{L}}_{2121} = \widehat{\mathcal{L}}_{1212}$ —the third and fourth conditions in (4.14) are not correlated.

4.2 Results for plane-strain loading: periodic porous elastomers

In this section, the above-developed second-order estimates are compared with FEM calculations for the effective stress-strain, the microstructure evolution, and the macroscopic stability of *periodic* porous elastomers with compressible Neo-Hookean matrix phases subjected to various types of finite plane-strain deformations. Special attention is given to *hydrostatic* and aligned (*i.e.*, $\bar{\theta} = 0$ in (4.2)) *uniaxial* loading conditions, as well as to macroscopic failure surfaces—as determined by

loss of strong ellipticity—in both, strain and stress space. Results are given for $\mu = 1$, $\kappa = 10$, and various values of initial porosity f_0 , and are computed up to the point at which either the effective behavior is found to lose strong ellipticity, or, alternatively, the porosity vanishes or percolation takes place. The computation of the latter phenomenon is explained in Appendix II.

4.2.1 Hydrostatic loading

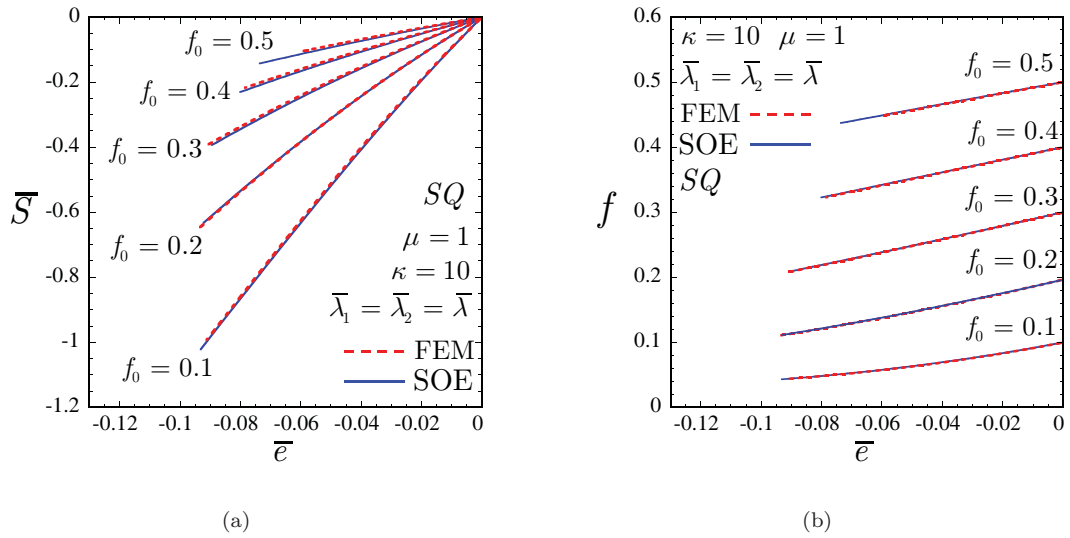


Figure 4.2: Comparisons of the effective response, as predicted by the second-order estimate (SOE), with FEM calculations of a porous elastomer with compressible Neo-Hookean matrix phase subjected to hydrostatic compression ($\bar{\lambda}_1 = \bar{\lambda}_2 = \bar{\lambda} \leq 1$). Results are shown for a periodic square (SQ) distribution of voids and various values of initial porosity f_0 , as a function of the logarithmic strain $\bar{e} = \ln \bar{\lambda}$. (a) The macroscopic stress $\bar{S} = \partial \widehat{W} / \partial \bar{F}_{11} = \partial \widehat{W} / \partial \bar{F}_{22} = \partial \widehat{W} / \partial \bar{F}_{33}$. (b) The evolution of the porosity f .

Figures 4.2 and 4.3 present comparisons between the second-order estimate (SOE) and FEM calculations for the effective behavior of periodic porous elastomers subjected to in-plane hydrostatic compression ($\bar{\lambda}_1 = \bar{\lambda}_2 = \bar{\lambda} \leq 1$). Figure 4.2 displays results for an initial square (SQ) arrangement of pores with initial porosities of 10, 20, 30, 40, and 50% as a function of the logarithmic strain $\bar{e} = \ln \bar{\lambda}$, while Figure 4.3 displays corresponding results for an initial hexagonal (HX) arrangement of pores with initial porosities of 10, 30, and 50%. Parts (a) show the macroscopic stress $\bar{S} = \partial \widehat{W} / \partial \bar{F}_{11} = \partial \widehat{W} / \partial \bar{F}_{22} = \partial \widehat{W} / \partial \bar{F}_{33}$, and parts (b), the evolution of the porosity f .

The main observation from Figures 4.2 and 4.3 is that the second-order estimates are in excellent agreement with the FEM results for all values of initial porosity f_0 considered. It is also interesting

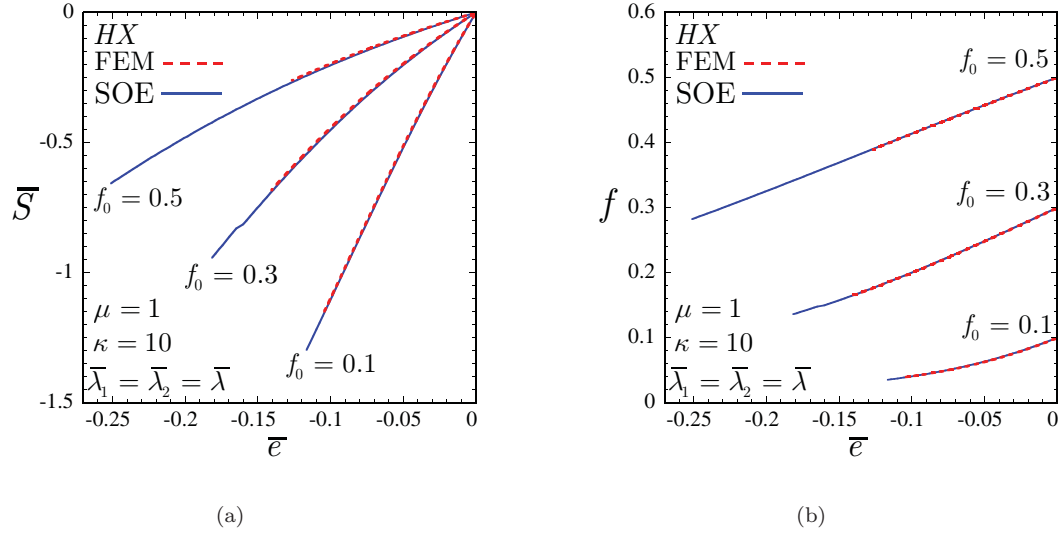


Figure 4.3: Comparisons of the effective response, as predicted by the second-order estimate (SOE), with FEM calculations of a porous elastomer with compressible Neo-Hookean matrix phase subjected to hydrostatic compression ($\bar{\lambda}_1 = \bar{\lambda}_2 = \bar{\lambda} \leq 1$). Results are shown for a periodic hexagonal (HX) distribution of voids and various values of initial porosity f_0 , as a function of the logarithmic strain $\bar{e} = \ln \bar{\lambda}$. (a) The macroscopic stress $\bar{S} = \partial \widehat{W} / \partial \bar{F}_{11} = \partial \widehat{W} / \partial \bar{F}_{22} = \partial \widehat{W} / \partial \bar{F}_{33}$. (b) The evolution of the porosity f .

to remark that both microgeometries, SQ and HX , lead to very similar results for the stress-strain relations as well as for the evolution of the porosity. This suggests that the initial distribution of pores does not play a major role in the overall behavior of porous elastomers. In fact, as it will be shown more explicitly further below, this is partially true. More precisely, the initial pore distribution will be shown to have a “mild” influence on the effective stress-strain response of porous elastomers. However, it will be seen that it does play a major role in the development of instabilities in these materials. Next, it is noted that—in accord with the results found in the preceding chapter dealing with random, isotropic porous elastomers—the effective behavior of the porous elastomer is softer for higher values of f_0 . Note further that the porosity decreases with increasing compressive strain, which induces geometrical hardening on the overall response of the material. Finally, it should be remarked that, both, the SOE and the FEM predictions lose strong ellipticity at finite levels of compressive strain. A quantitative comparison between both these predictions will be carried out at the end of this section.

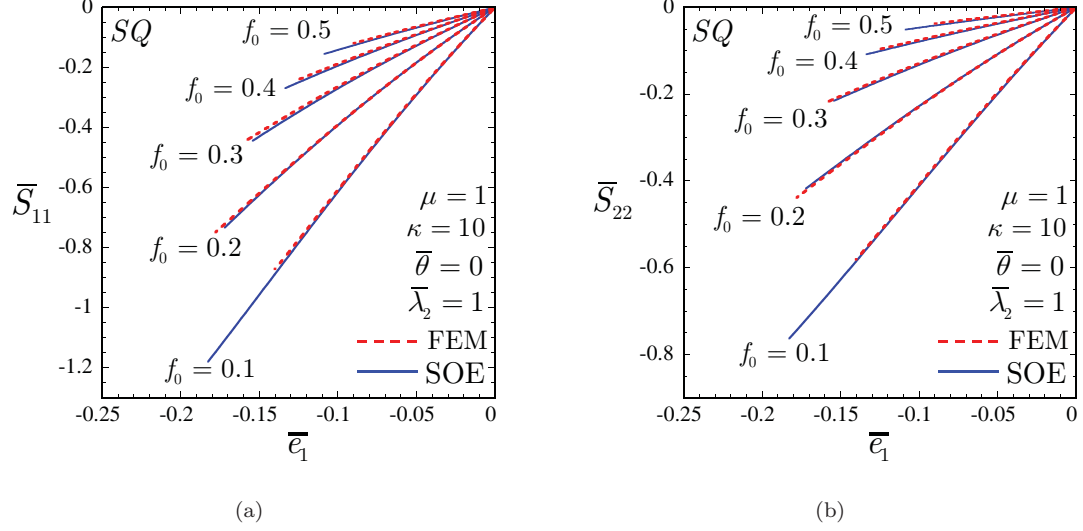


Figure 4.4: Comparisons of the effective response, as predicted by the second-order estimate, with FEM calculations of a porous elastomer with compressible Neo-Hookean matrix phase subjected to aligned uniaxial compression ($\bar{\lambda}_1 = \bar{\lambda}$, $\bar{\lambda}_2 = 1$, $\bar{\theta} = 0$). Results are shown for a periodic square (SQ) distribution of voids and various values of initial porosity f_0 , as a function of the logarithmic strain $\bar{e} = \ln \bar{\lambda}$. (a) The macroscopic stress $\bar{S}_{11} = \partial \widehat{W} / \partial \bar{F}_{11}$. (b) The macroscopic stress $\bar{S}_{22} = \partial \widehat{W} / \partial \bar{F}_{22}$.

4.2.2 Aligned uniaxial loading

Figure 4.4 provides comparisons between the second-order estimate (SOE) and FEM calculations for the effective behavior of periodic porous elastomers subjected to aligned ($\bar{\theta} = 0$) uniaxial compression ($\bar{\lambda}_2 = 1$, $\bar{\lambda}_1 \leq 1$). Results are shown for a square (SQ) arrangement of pores with initial porosities of 10, 20, 30, 40, and 50% as a function of the logarithmic strain $\bar{e}_1 = \ln \bar{\lambda}_1$. Part (a) shows the macroscopic stress component $\bar{S}_{11} = \partial \widehat{W} / \partial \bar{F}_{11}$, and part (b), the stress component $\bar{S}_{22} = \partial \widehat{W} / \partial \bar{F}_{22}$. As for the previous case dealing with hydrostatic compression, the second-order estimates are in excellent agreement with the FEM results for all values of initial porosity f_0 considered. In addition, and also similar to hydrostatic compression, the effective response of the porous elastomer is seen to be softer for higher values of f_0 . Finally, note that the SOE and FEM results lose strong ellipticity under uniaxial compression.

Figure 4.5 provides comparisons between the second-order estimate (SOE) and FEM calculations for the evolution of the microstructural variables associated with the results shown in Figure 4.4. Part (a) shows the evolution of porosity f , and part (b), the evolution of the average aspect ratio of the pores ω . Again, note that the agreement between the SOE and FEM predictions is

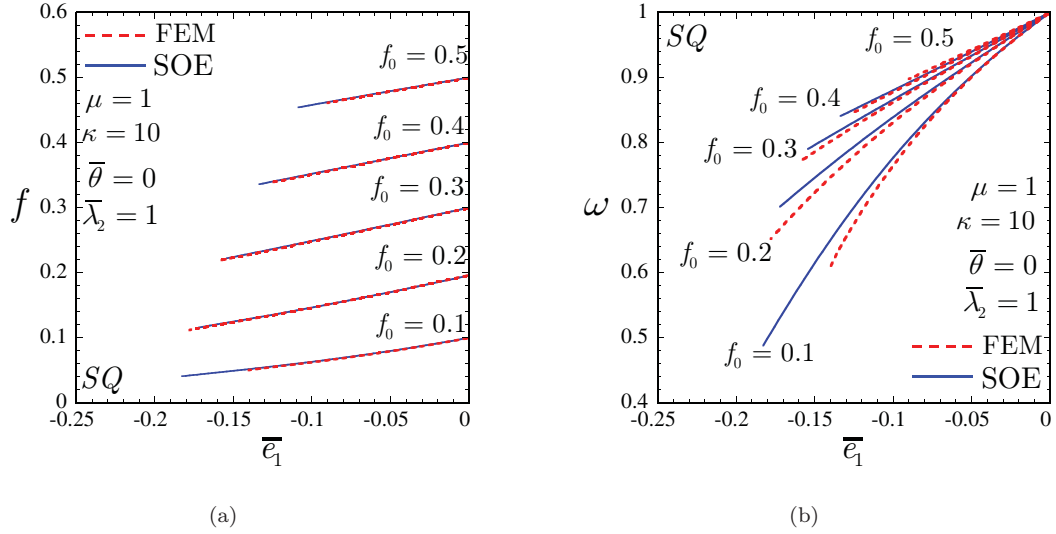


Figure 4.5: Aligned uniaxial compression ($\bar{\lambda}_1 = \bar{\lambda}$, $\bar{\lambda}_2 = 1$, $\bar{\theta} = 0$) of a porous elastomer with compressible Neo-Hookean matrix phase and various values of initial porosity f_0 . The results are shown for a periodic square (SQ) distribution of voids, as a function of the logarithmic strain $\bar{e} = \ln \bar{\lambda}$. Comparisons between the second-order estimates and FEM calculations for (a) the evolution of the porosity f ; and (b) the evolution of the average aspect ratio of the pores ω .

good, especially for f . The SOE predictions for ω tend to slightly overestimate the corresponding FEM results. As expected on physical grounds, Figure 4.5(a) illustrates that the porosity decreases with increasing compressive strain. In addition, it is seen from Figure 4.5(b) that the aspect ratio decreases with the applied loading, which implies that the initially circular pores evolve—on average—into elliptical pores with the semi-minor axes aligned with the direction of applied compression.

Figures 4.6 and 4.7 illustrate analogous results to those shown in Figures 4.4 and 4.5 for a hexagonal (HX)—as opposed to square—arrangement of the pores. The agreement between the SOE and FEM predictions is very good. This is particularly true for the two smallest initial porosities (*i.e.*, for $f_0 = 10$ and 30%). For $f_0 = 50\%$, the agreement is good but it gets worse progressively with increasing compressive strain. This is consistent with the fact that the Hashin-Shtrikman estimate (2.55) utilized in the computation of the second-order estimates is expected to become more inaccurate for higher values of f_0 . Furthermore, as for the SQ microgeometry, the SOE and FEM results shown in Figures 4.6 and 4.7 lose strong ellipticity. Finally, note that the HX results shown in Figures 4.6 and 4.7 are very similar (quantitatively) to the corresponding

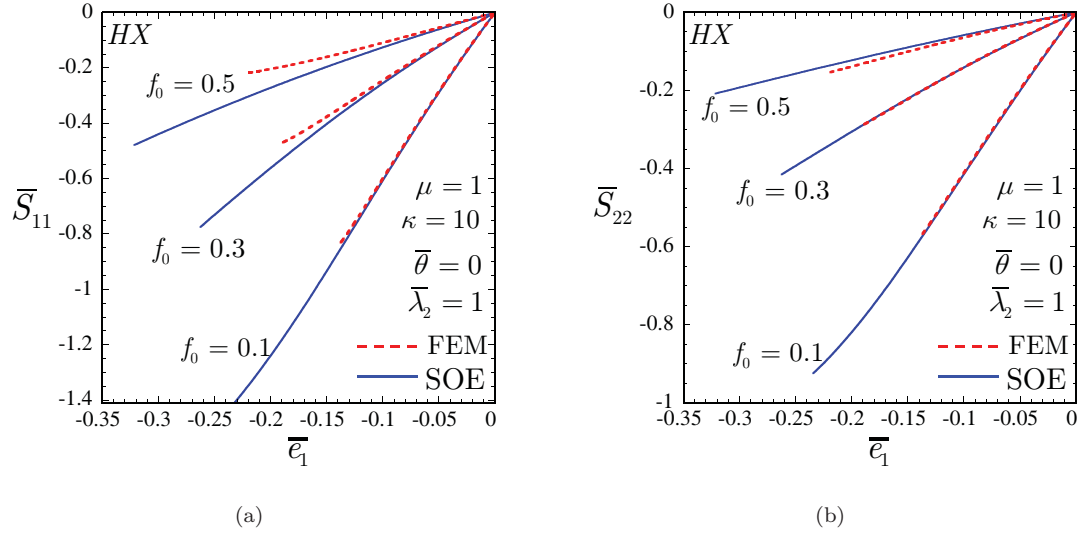


Figure 4.6: Comparisons of the effective response, as predicted by the second-order estimate, with FEM calculations of a porous elastomer with compressible Neo-Hookean matrix phase subjected to aligned uniaxial compression ($\bar{\lambda}_1 = \bar{\lambda}$, $\bar{\lambda}_2 = 1$, $\bar{\theta} = 0$). Results are shown for a periodic hexagonal (HX) distribution of voids and various values of the initial porosity f_0 as a function of the logarithmic strain $\bar{e} = \ln \bar{\lambda}$. (a) The macroscopic stress $\bar{S}_{11} = \partial \bar{W} / \partial \bar{F}_{11}$. (b) The macroscopic stress $\bar{S}_{22} = \partial \bar{W} / \partial \bar{F}_{22}$.

SQ results shown in Figures 4.4 and 4.5. This fact corroborates the above-stated remark that the initial distribution of pores does not affect significantly the overall stress-strain relation and microstructural evolution of porous elastomers.

In summary, the above results indicate that the second-order method provides remarkably accurate estimates for the effective stress-strain relation and the microstructure evolution of periodic porous elastomers with small to moderate levels of initial porosity. It should be noted, however, that all the results presented above correspond to compressive deformations, under which the porosity decreases. As explained in Section 2.5.1, this has the direct implication that the (Hashin-Shtrikman-type) second-order estimates become more accurate with the applied deformation. Comparisons between the SOE predictions and FEM calculations for tensile deformation—under which the porosity increases—have been also carried out, but the results will not be included here for brevity. For such tensile deformations, the SOE results compare well with the FEM calculations for small to moderate deformations, but, as expected, they deteriorate significantly for very large deformations, when the porosity reaches values near percolation. In this regard, it should be re-emphasized that this failure is due to the use of the HS estimates (2.55) for the LCC, and

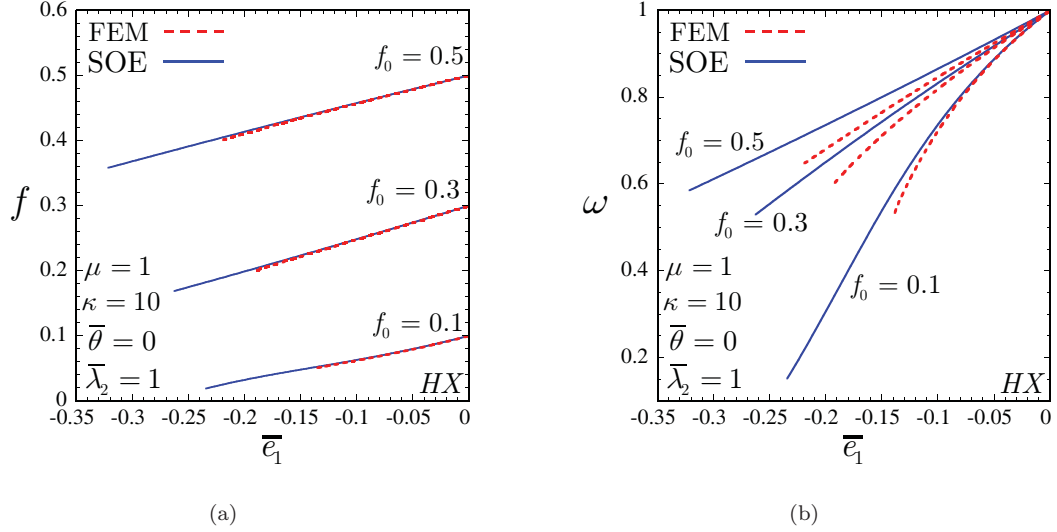


Figure 4.7: Aligned uniaxial compression ($\bar{\lambda}_1 = \bar{\lambda}$, $\bar{\lambda}_2 = 1$, $\bar{\theta} = 0$) of a porous elastomer with compressible Neo-Hookean matrix phase and various values of initial porosity f_0 . The results are shown for a periodic hexagonal (HX) distribution of voids as a function of the logarithmic strain $\bar{\epsilon} = \ln \bar{\lambda}$. Comparisons between the second-order estimates and FEM calculations for (a) the evolution of the porosity f ; and (b) the evolution of the average aspect ratio of the pores ω .

not to the second-order method itself. As pointed out in Section 2.5.1, this problem could be circumvented by using a more accurate estimate for the effective behavior of the linear comparison composite.

4.2.3 Failure surfaces

This subsection presents results for the macroscopic onset-of-failure surfaces (Triantafyllidis *et al.*, 2006)—as determined by loss of strong ellipticity—for the class of *periodic* porous elastomers under consideration in this chapter. Results are provided in both, strain and stress space. In addition, special attention is given to aligned (*i.e.*, $\bar{\theta} = 0$) loading conditions, but some representative results are also presented for “misaligned” deformations (*i.e.*, $\bar{\theta} \neq 0$).

Figure 4.8 illustrates the macroscopic failure surfaces, as determined by the second-order estimate (SOE) and FEM calculations, for a porous elastomer with an initially periodic square (SQ) distribution of circular voids and initial porosities of $f_0 = 10, 30$, and 50%. The results correspond to aligned (*i.e.*, $\bar{\theta} = 0$) plane-strain deformations. Part (a) shows failure surfaces in the III-quadrant (*i.e.*, $\bar{e}_1 \leq 0$ and $\bar{e}_2 \leq 0$) in strain space, and part (b), the corresponding failure

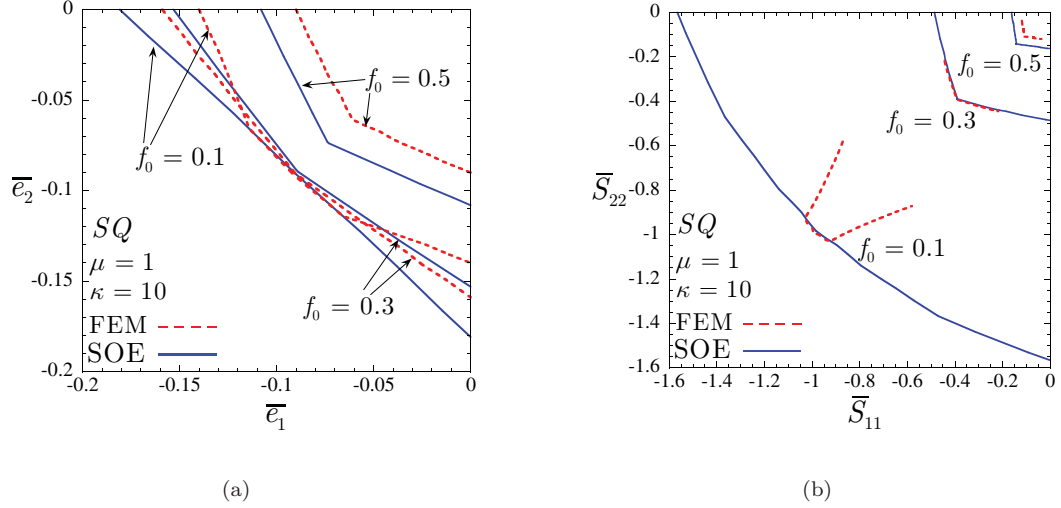


Figure 4.8: Macroscopic onset-of-failure surface, as determined by the loss of strong ellipticity of the second-order estimate and FEM calculations, for a porous elastomer with periodic square (SQ) arrangement of voids and compressible Neo-Hookean matrix phase. (a) The results in the \bar{e}_1 – \bar{e}_2 plane in strain space; and (b) the corresponding results in stress space.

surfaces in stress space. First, it is observed from Figure 4.8 that the SOE predictions are in remarkably good agreement with the FEM results near hydrostatic compression (*i.e.*, near $\bar{e}_2 = \bar{e}_1$), especially for $f_0 = 10$ and 30%. For the remaining loadings in the III-quadrant, the agreement between the SOE and FEM results remains excellent for the case of $f_0 = 30\%$ but deteriorates considerably for $f_0 = 10\%$. For $f_0 = 50\%$, the SOE predictions can be seen to be qualitatively identical to the corresponding FEM results, but quantitatively more stable—in the sense that the SOE onset of instability occurs at larger compressive strains and stresses. Interestingly, the FEM results shown in Figure 4.8(a) indicate that the porous elastomer with $f_0 = 10\%$ is more unstable than the one with $f_0 = 30\%$ near hydrostatic compression in strain space (since loss of strong ellipticity occurs at smaller compressive strains). For loadings near uniaxial compression (*i.e.*, near $\bar{e}_1 = 0$ and $\bar{e}_2 = 0$), higher values of f_0 lead consistently to a more unstable behavior. In contrast, Figure 4.8(b) shows that in stress space, higher values of initial porosity systematically lead to more unstable behavior, regardless of the loading conditions.

Figure 4.9 provides analogous results to those given in Figure 4.8 for a hexagonal (HX)—as opposed to square—distribution of pores. In this case, the comparisons between the SOE predictions and the FEM calculations are less favorable than those found in Figure 4.8 (for the

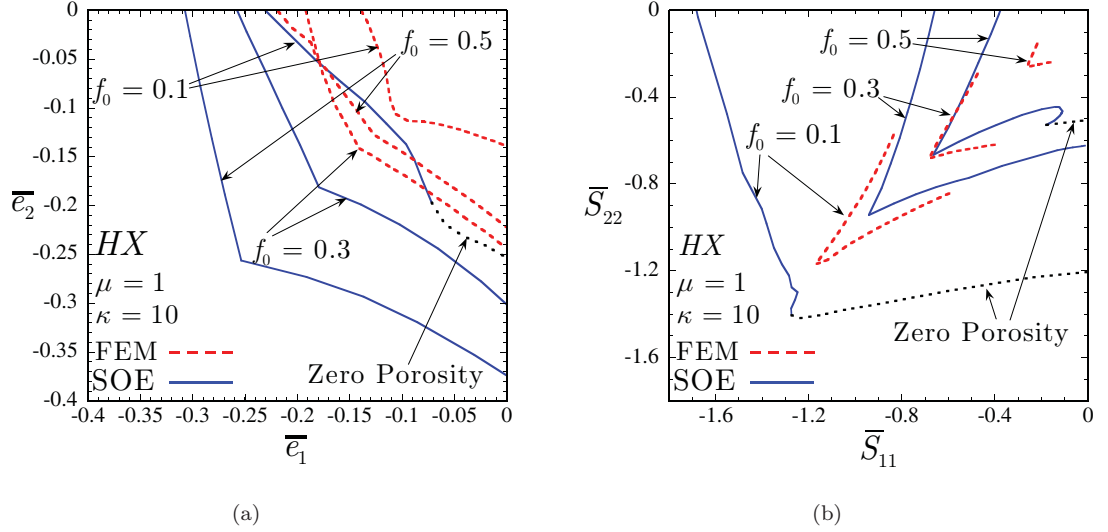


Figure 4.9: Macroscopic onset-of-failure surface, as determined by the loss of strong ellipticity of the second-order estimate and FEM calculations, for a porous elastomer with periodic hexagonal (HX) arrangement of voids and compressible Neo-Hookean matrix phase. (a) The results in the \bar{e}_1 - \bar{e}_2 plane in strain space; and (b), the corresponding results in stress space.

square pore distribution). The reasons for this disparity are not entirely clear, but they might be associated with the fact that certain shear moduli of the HS estimate (2.55) turn out to be less accurate for the hexagonal distribution than for the square one. In any case, the SOE predictions are qualitatively similar to the FEM results. In quantitative terms, it is seen that the second-order estimates lose strong ellipticity at larger compressive strains and stresses. Interestingly, Figure 4.9(a) shows that both, the SOE and FEM results, indicate that the porous elastomer is more stable with increasing initial porosity in strain space, provided that $f_0 \leq 50\%$. In stress space, on the other hand, the porous elastomer is seen to be more unstable—systematically—for higher values of f_0 . Thus, combining this result together with the corresponding results shown in Figures 4.8 (for square pore distribution) and 3.8 (for random, isotropic distribution), we conclude that, regardless of the initial distributions of the pores, porous elastomers are more unstable in stress space—in the sense that they lose of strong ellipticity at smaller stresses—for higher values of initial porosity f_0 . In contrast, in strain space, there is no such monotonicity and the trend followed by the failures surfaces with increasing f_0 depends very critically on the initial distribution of pores. In particular, the results presented here suggest that as the distribution of the pores tends to be more random and isotropic (*i.e.*, $SQ \rightarrow HX \rightarrow random$), the porous elastomer tends to lose strong

ellipticity at larger strains for higher values of initial porosity.

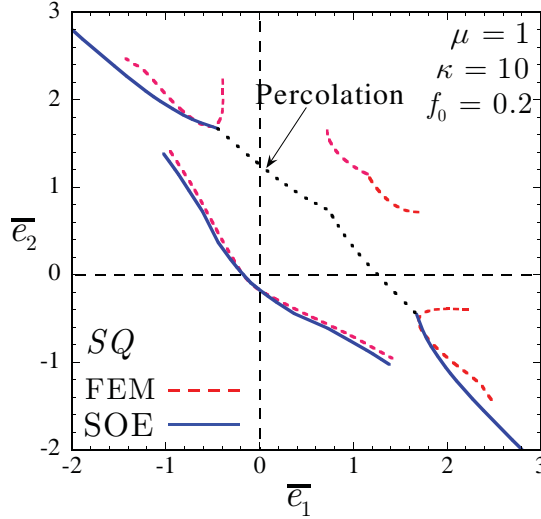


Figure 4.10: Macroscopic onset-of-failure surface, as determined by the loss of strong ellipticity of the second-order estimate and FEM calculations, for a porous elastomer with periodic square (*SQ*) arrangement of voids and compressible Neo-Hookean matrix phase. The results are shown in principal strain space \bar{e}_1 – \bar{e}_2 . The onset of percolation, as predicted by the second-order estimate, has also been included in the figure for completeness.

Figure 4.10 illustrates the macroscopic failure surfaces, as determined by the second-order estimate (SOE) and FEM calculations, for a porous elastomer with an initially periodic *square* (*SQ*) distribution of circular voids and initial porosity of $f_0 = 20\%$. The results correspond to aligned (*i.e.*, $\bar{\theta} = 0$) plane-strain deformations and are displayed in the entire strain space. The onset of percolation (dotted line), as predicted by the second-order estimate (see Appendix II), has also been included in the figure for completeness. The main observation from Figure 4.10 is the overall excellent agreement between the SOE and the FEM results, even at extremely large deformations (recall that \bar{e}_i are *logarithmic* strains). The sole region that the second-order estimates fail to predict accurately corresponds to loadings near hydrostatic tension (*i.e.*, near $\bar{e}_1 = \bar{e}_2 > 0$). This is due to the fact that for hydrostatic tensile deformations the porosity increases the fastest and hence—as already remarked above—the use of the HS estimate (2.55) for the linear comparison composite problem result in inaccurate second-order estimates. Another important observation from Figure 4.10 is that loss of strong ellipticity is more susceptible to occur under *compressive* strains.

Figure 4.11 provides analogous results to those shown by Figure 4.10 for an initially *hexagonal* (*HX*) distribution of pores. Unfortunately, no FEM results were available for this case, and

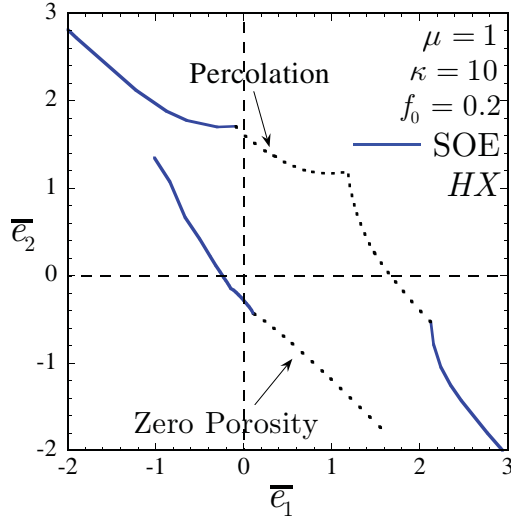


Figure 4.11: Macroscopic onset-of-failure surface, as determined by the loss of strong ellipticity of the second-order estimate, for a porous elastomer with periodic hexagonal (HX) arrangement of voids and compressible Neo-Hookean matrix phase. The results are shown in principal strain space \bar{e}_1 - \bar{e}_2 . The onset of percolation and pore closure, as predicted by the second-order estimate, have also been included in the figure for completeness.

hence attention has been restricted to second-order estimates. First, note that the results shown in Figure 4.11 are not symmetric around the line $\bar{e}_2 = \bar{e}_1$. The reasons for this asymmetry are due to the evolution of the underlying microstructure. To be precise, the porous elastomer with hexagonal microgeometry considered here is *isotropic* in the small deformation regime, but because the underlying microstructure itself is *not* isotropic, different loading conditions lead to different microstructure evolutions, which, in turn, lead to overall anisotropic behavior, as manifested in Figure 4.11. Interestingly, Figure 4.11 also indicates that porous elastomers with HX pore distribution are more stable than those with SQ distribution (see Figure 4.10).

To try to complete the understanding of the effect of the initial distribution of pores on the onset-of-failure surfaces of porous elastomers, Figure 4.12 illustrates the corresponding results to those shown in Figures 4.10 and 4.11 for an initially *random, isotropic* distribution of pores. (Note that the results shown in Figure 4.12 correspond to a compressible Neo-Hookean matrix phase (with $\kappa = 10$), whereas the results given in Figure 3.8 in the preceding chapter correspond to an incompressible matrix phase (with $\kappa = \infty$.) An important conclusion to be drawn from Figure 4.12 is that loss of strong ellipticity persists even when the microstructure is random. In addition, the results shown in Figure 4.12 also confirm the tendency of porous elastomers to be more stable whenever the periodicity of the microstructure is broken down.

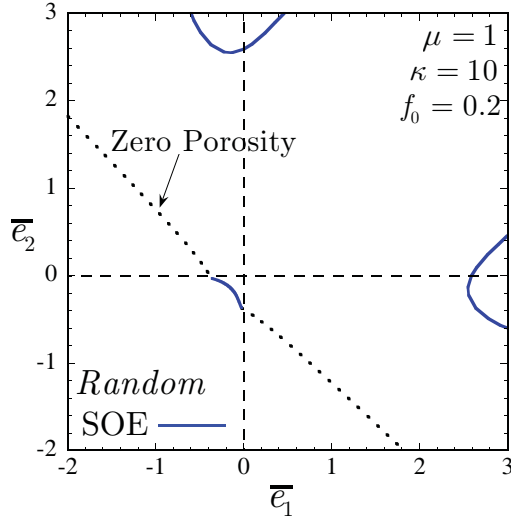


Figure 4.12: Macroscopic onset-of-failure surface, as determined by the loss of strong ellipticity of the second-order estimate, for a porous elastomer with random, isotropic distribution of voids and compressible Neo-Hookean matrix phase. The results are shown in principal strain space \bar{e}_1 - \bar{e}_2 . The boundary at which the porosity vanishes, as predicted by the second-order estimate, has also been included in the figure for completeness.

All the results up to this point have been concerned with loading conditions where the macroscopic Lagrangian principal axes are coaxial with the axes of orthotropy ($\bar{\theta} = 0$) of the material. In order to acquire a representative notion of the effect of loading orientation on the development of instabilities in porous elastomers, Figure 4.13 compares the macroscopic failure surfaces for macroscopic loadings with principal strain axes aligned ($\bar{\theta} = 0$) and at an angle ($\bar{\theta} = 10^\circ$) with respect to the initial axes of orthotropy. The results correspond to a porous elastomer with Neo-Hookean matrix phase, an initially periodic *square* (*SQ*) distribution of circular voids, and initial porosity of $f_0 = 20\%$. The onset of pore closure and of percolation (dotted line), as predicted by the second-order estimate, have also been included in the figure for completeness.

Note that outside the biaxial compression range (III-quadrant), a slight change in the orientation of the loading has a very significant effect on the stability of the porous elastomer. In particular, the loss of strong ellipticity in the II and IV quadrant almost disappears, leading to a more stable behavior. On the other hand, in the III-quadrant, the change in the orientation of the loading appears to have no effect on the development of instabilities.

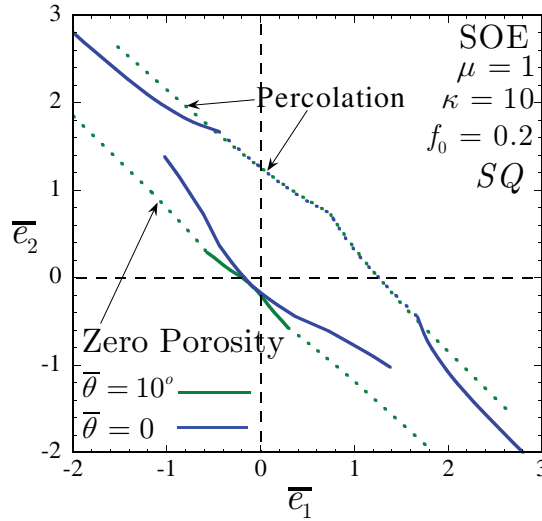


Figure 4.13: Loading orientation influence on the macroscopic onset-of-failure surfaces, in principal logarithmic strain space, for a Neo-Hookean elastomer with an initial square (SQ) distribution of pores subjected to macroscopic loadings that are aligned ($\bar{\theta} = 0$) and at an angle ($\bar{\theta} = 10^\circ$) with respect to the principal axes of the microstructure.

4.3 Concluding remarks

In this chapter, second-order estimates have been generated and compared with FEM calculations for the in-plane effective behavior of porous elastomers with two types of *periodic* microstructures subjected to finite deformations.

The second-order estimates have been shown to compare remarkably well—qualitatively as well as quantitatively—with the FEM results not only for the effective stress-strain relation of porous elastomers under various types of loading conditions, but also for the evolution of the underlying microstructure, as well as the development of macroscopic instabilities in these materials. In view of the strong geometric and constitutive nonlinearities inherent in the problem, this, indeed, is a remarkable result. Further, it indicates that the proposed second-order method proves extremely promising as a first order approximation for modeling the complex behavior of elastomeric composites in general.

The second main conclusion of this chapter is that while the initial distribution of pores plays a minor role in the overall stress-strain relations of porous elastomers, it does have, however, a dramatic influence on the development of macroscopic instabilities in these materials. In particular, it has been shown that as the periodicity of the microstructure is broken down, the stability of porous elastomers improves. This is consistent with the fact that by breaking down the periodicity

of the system, we are effectively reducing the number of symmetries that can be broken, and, hence, reducing the number of potential instabilities that might develop.

4.4 Appendix I. Expressions for the microstructural tensor

P

In this appendix, we provide explicit expressions for the in-plane components of the tensor \mathbf{P} , which serves to characterize the two types of microstructures (in the reference configuration) considered in this work: (i) periodic square, and (ii) periodic hexagonal distribution of aligned cylindrical pores with initial circular cross section.

Periodic square distribution

The microstructural tensor \mathbf{P} for the square distribution of cylindrical fibers with circular cross section may be written as (see Suquet, 1990):

$$P_{ijkl} = \frac{1}{\pi(1-f_0)} \sum_{\substack{p=-\infty \\ -\{p=q=0\}}}^{+\infty} \sum_{q=-\infty}^{+\infty} (L_{imkn} \xi_m \xi_n)^{-1} \xi_j \xi_l \frac{J_1^2 \left(2\sqrt{\pi f_0} \sqrt{p^2 + q^2} \right)}{p^2 + q^2}, \quad (4.15)$$

where $\xi_1 = p$, $\xi_2 = q$, and $J_1(\cdot)$ is the Bessel function of first kind.

Periodic hexagonal distribution

The microstructural tensor \mathbf{P} for the hexagonal distribution of cylindrical fibers with circular cross section may be written as (see Suquet, 1990):

$$P_{ijkl} = \frac{\sqrt{3}}{2\pi(1-f_0)} \sum_{\substack{p=-\infty \\ -\{p=q=0\}}}^{+\infty} \sum_{q=-\infty}^{+\infty} (L_{imkn} \xi_m \xi_n)^{-1} \xi_j \xi_l \frac{J_1^2 \left(\frac{2^{3/2}}{3^{1/4}} \sqrt{\pi f_0} \sqrt{p^2 - pq + q^2} \right)}{p^2 - pq + q^2}, \quad (4.16)$$

where $\xi_1 = p$, $\xi_2 = \sqrt{3}/3(2q - p)$, and $J_1(\cdot)$ is the Bessel function of first kind.

4.5 Appendix II. Onset of percolation

In this appendix, we provide explicit conditions, in terms of the current porosity f and current average aspect ratio ω , under which the underlying pores in the type of porous elastomers considered in this chapter first come in contact when subjected to aligned loading conditions (*i.e.*, for $\bar{\theta} = 0$ and $\bar{\theta} = \pi/2$ in (4.2)). In this connection, it should be recalled from Section 2.5.1 that, in general, the Hashin-Shtrikman-type second-order estimates (2.69) utilized here are expected to

become unsound before percolation actually takes place. However, it is not difficult to check that, for periodic square and hexagonal microgeometries (see Fig. 4.1) and aligned loading conditions, percolation coincides identically with the limit of validity of the second-order estimates.

Periodic square distribution

Percolation, as predicted by the HS-type second-order estimates, in porous elastomers with the *periodic square* microgeometry subjected to aligned loading conditions first takes place whenever one of the following equalities holds:

$$(i) f = \frac{\pi}{4\omega} \frac{\bar{\lambda}_1}{\bar{\lambda}_2}, \quad (ii) f = \frac{\pi\omega}{4} \frac{\bar{\lambda}_2}{\bar{\lambda}_1}. \quad (4.17)$$

For clarity, it is recalled here that $\omega = \bar{\lambda}_1^{(2)}/\bar{\lambda}_2^{(2)}$, where $\bar{\lambda}_i^{(2)}$ ($i = 1, 2$) denote the principal stretches associated with $\bar{\mathbf{F}}^{(2)}$. It is interesting to note that in the undeformed configuration (*i.e.*, for $\bar{\lambda}_1 = \bar{\lambda}_2 = 1$) $\omega = 1$ and percolation occurs at a porosity of $f = f_0 = \pi/4$ (which agrees with the *exact* result).

Periodic hexagonal distribution

Percolation, as predicted by the HS-type second-order estimates, in porous elastomers with the *periodic hexagonal* microgeometry subjected to aligned loading conditions first takes place whenever one of the following equalities holds:

$$(i) f = \frac{\pi}{2\sqrt{3}} \frac{\bar{\lambda}_1}{\bar{\lambda}_2} \omega^{-1}, \quad (ii) f = \frac{\pi}{8\sqrt{3}} \left(3\omega \frac{\bar{\lambda}_2}{\bar{\lambda}_1} + \frac{\bar{\lambda}_1}{\bar{\lambda}_2} \omega^{-1} \right), \quad (4.18)$$

where ω is defined as above. Similar to the previous case, it is noted that in the undeformed configuration percolation take place at a porosity of $f = f_0 = \pi/(2\sqrt{3})$ (which agrees with the *exact* result).

Chapter 5

Porous elastomers: spherical voids

The preceding two chapters, Chapters 3 and 4, have provided much insight regarding the overall behavior of porous elastomers subjected to finite deformations. Indeed, even though two-dimensional (2D), the applications presented in those chapters were general enough as to contain all the essential features concerning porous elastomers, including the subtle interplay between the evolution of the underlying microstructure and the effective behavior and stability of these materials. The results presented in Chapters 3 and 4 have also served to establish the accuracy of the second-order homogenization method, which has been shown to deliver accurate estimates not only for the macroscopic constitutive behavior, but also for the more sensitive information on the possible development of macroscopic instabilities in porous elastomers with *random* and *periodic* microstructures. These encouraging results for 2D microstructures strongly suggest that the second-order theory should also be able to deliver accurate estimates for the effective behavior, as well as for the onset of macroscopic instabilities, of porous elastomers with more realistic, three-dimensional (3D) microstructures. The objective of this chapter pertains precisely to the application of the second-order homogenization method to porous elastomers consisting of *random* and *isotropic* distribution of polydisperse pores in an isotropic, elastomeric matrix phase. This microstructure—though idealized—can be considered as a fair approximation to actual microstructures in real porous elastomers. In this connection, it should be remarked that while for 3D periodic microstructures results can be computed *numerically* (in spite of intensive computations), for the random case this approach would be exceedingly intensive from a computational point of view, and the analytical approach proposed here—though approximate—is perhaps more appropriate.

5.1 Overall behavior of isotropic porous elastomers

In this chapter, we make use of the second-order estimate (2.69) to develop a homogenization-based constitutive model for the effective mechanical response of isotropic porous elastomers subjected to finite deformations. More specifically, the type of porous elastomers of interest are made up of initially spherical, polydisperse, vacuous inclusions distributed *randomly* and *isotropically*—in the undeformed configuration—in an isotropic elastomeric matrix. In particular, following Section 2.1.3, the elastomeric matrix phase is taken to be characterized by stored-energy functions of the form:

$$W^{(1)}(\mathbf{F}) = W(\mathbf{F}) = g(I) + h(J) + \frac{\kappa}{2}(J - 1)^2, \quad (5.1)$$

where the superscript “(1)” has been dropped for ease of notation, and it is recalled that g and h are material functions of their arguments: $I = \lambda_1^2 + \lambda_2^2 + \lambda_3^2$, $J = \lambda_1\lambda_2\lambda_3$. Furthermore, κ denotes the three-dimensional bulk modulus of the material at zero strain. The analysis to be developed below will be carried out for general stored-energy functions of the form (5.1). However, for definiteness, results will be illustrated for porous elastomers with specific matrix phases. In particular, we will make use of the three dimensional version of the Gent material (3.2) utilized in Chapter 3, which can be written as:

$$W(\mathbf{F}) = -\frac{J_m \mu}{2} \ln \left[1 - \frac{I - 3}{J_m} \right] - \mu \ln J + \left(\frac{\kappa}{2} - \frac{J_m + 3}{3 J_m} \mu \right) (J - 1)^2. \quad (5.2)$$

In this expression, it is recalled that μ denotes the shear modulus of the material at zero strain and the parameter J_m indicates the limiting value for $I - 3$ at which the elastomer locks up. Note that the stored-energy function (5.2) is strongly elliptic for all deformations provided that $\mu > 0$, $J_m > 0$, and $\kappa > 2\mu/J_m + 2/3\mu$, which will be assumed here. Note further that upon taking the limit $J_m \rightarrow \infty$ in (5.2), the Gent material reduces to the compressible Neo-Hookean solid:

$$W(\mathbf{F}) = \frac{\mu}{2} (I - 3) - \mu \ln J + \left(\frac{\kappa}{2} - \frac{\mu}{3} \right) (J - 1)^2. \quad (5.3)$$

Moreover, in order to recover incompressible behavior in (5.2), it suffices to take the limit $\kappa \rightarrow \infty$, in which case (5.2) reduces to:

$$W(\mathbf{F}) = -\frac{J_m \mu}{2} \ln \left[1 - \frac{I - 3}{J_m} \right], \quad (5.4)$$

together with the incompressibility constraint $J = 1$.

By virtue of the overall objectivity and isotropy of the porous elastomers at hand, it suffices to confine attention to diagonal pure stretch loadings. Thus, making contact with the decompositions $\bar{\mathbf{F}} = \bar{\mathbf{R}}\bar{\mathbf{U}}$ and $\bar{\mathbf{U}} = \bar{\mathbf{Q}}\bar{\mathbf{D}}\bar{\mathbf{Q}}^T$ used in the context of expression (2.66), this implies that:

$$\bar{F} = \bar{D} = \text{diag}(\bar{\lambda}_1, \bar{\lambda}_2, \bar{\lambda}_3) \quad \text{and} \quad \bar{\mathbf{R}} = \bar{\mathbf{Q}} = \mathbf{I}, \quad (5.5)$$

where $\bar{\lambda}_1, \bar{\lambda}_2, \bar{\lambda}_3$ denote the principal stretches of the right stretch tensor $\bar{\mathbf{U}}$.

Having specified the initial microstructure, the constitutive behavior for the elastomeric matrix phase, and the loading conditions, we next spell out the specialization of the second-order estimates (2.69) to the class of porous elastomers of interest in this chapter. Before proceeding with the second-order estimates, however, it proves useful, for comparison purposes, to recall earlier estimates for the effective behavior of porous elastomers. For clarity, this will be done only in the context of Gent matrix phases (5.2) and (5.4) (and not more generally for stored-energy functions (5.1)).

5.1.1 Earlier estimates

Voigt bound

As pointed out in Chapters 1 and 2, there are very few homogenization-based estimates for the effective behavior of porous elastomers subjected to finite deformations. The most basic one is the Voigt upper bound due to Ogden (1978). When specialized to porous elastomers with initial porosity f_0 and Gent matrix phases of the form (5.2), this bound leads to:

$$\begin{aligned} \widehat{W}(\bar{\mathbf{F}}) = \widehat{\Phi}(\bar{\lambda}_1, \bar{\lambda}_2, \bar{\lambda}_3) &= (f_0 - 1) \left[\frac{J_m \mu}{2} \ln \left[1 - \frac{\bar{I} - 3}{J_m} \right] + \mu \ln \bar{J} \right. \\ &\quad \left. - \left(\frac{\kappa}{2} - \frac{J_m + 3}{3 J_m} \mu \right) (\bar{J} - 1)^2 \right], \end{aligned} \quad (5.6)$$

where $\bar{I} = \text{tr}(\bar{\mathbf{F}}^T \bar{\mathbf{F}}) = \bar{\lambda}_1^2 + \bar{\lambda}_2^2 + \bar{\lambda}_3^2$, and $\bar{J} = \det \bar{\mathbf{F}} = \bar{\lambda}_1 \bar{\lambda}_2 \bar{\lambda}_3$ stand for, respectively, the first and third invariants associated with the macroscopic deformation gradient tensor $\bar{\mathbf{F}}$. The rigorous upper bound (5.6) depends only on the initial value of the porosity, f_0 , and contains no dependence on higher-order statistical information about the microstructure. Moreover, in the limit when the elastomeric matrix phase becomes incompressible (*i.e.*, for $\kappa \rightarrow \infty$), expression (5.6) can be seen to become infinite for all deformations, except for isochoric loading paths (*i.e.*, for loading paths with $\bar{J} = 1$), for which it reduces to:

$$\widehat{W}^I(\bar{\mathbf{F}}) = \widehat{\Phi}^I(\bar{\lambda}_1, \bar{\lambda}_2, \bar{\lambda}_3) = (f_0 - 1) \frac{J_m \mu}{2} \ln \left[1 - \frac{\bar{I} - 3}{J_m} \right]. \quad (5.7)$$

In other words, the Voigt bound suggests that a porous elastomer with incompressible matrix phase is itself incompressible, which is in contradiction with experimental evidence. Finally, it is interesting to remark that—also in disagreement with experience—the Voigt bounds (5.6) and (5.7) remain strongly elliptic for all deformations, provided that $\mu > 0$, $J_m > 0$, and $\kappa > 2\mu/J_m + 2/3\mu$, which has been assumed here.

Hashin estimate

In addition, an *exact* result has been given by Hashin (1985) for *hydrostatic loading* ($\bar{\lambda}_1 = \bar{\lambda}_2 = \bar{\lambda}_3 = \bar{\lambda}$) of porous elastomers with *incompressible*, isotropic matrix phase and the *Composite Sphere Assemblage* (CSA) microstructure (Hashin, 1962). When specialized to porous elastomers with incompressible Gent matrix phases of the form (5.4), the result reads as follows:

$$\widehat{W}^I(\bar{\mathbf{F}}) = \widehat{\Phi}^I(\bar{\lambda}, \bar{\lambda}, \bar{\lambda}) = -\frac{3J_m\mu}{2} \int_{f_0^{1/3}}^1 \ln \left[1 - \frac{I-3}{J_m} \right] R^2 dR, \quad (5.8)$$

where $I = 2\lambda^2 + \lambda^{-4}$ with $\lambda = (1 + (\bar{\lambda}^3 - 1)/R^3)^{1/3}$. The integral (5.8) can be computed analytically, but the final expression is too cumbersome to be included here. Instead, for illustrative purposes, we include the specialization of (5.8) to the simpler, limiting case of Neo-Hookean matrix phase (*i.e.*, $J_m \rightarrow \infty$):

$$\begin{aligned} \widehat{W}^I(\bar{\mathbf{F}}) &= \frac{3\mu}{2} \left(f_0 - 1 - \bar{\lambda}^{-1} + 2\bar{\lambda}^2 + f_0^{4/3}(\bar{\lambda}^3 + f_0 - 1)^{-1/3} \right. \\ &\quad \left. - 2f_0^{1/3}(\bar{\lambda}^3 + f_0 - 1)^{2/3} \right). \end{aligned} \quad (5.9)$$

The Danielsson-Parks-Boyce model

Finally, Danielsson *et al.* (2004) have recently provided a model, henceforth referred to as the DPB model, for isotropic porous elastomers with *incompressible*, isotropic matrix phases. When specialized to porous elastomers with incompressible Gent matrix phases of the form (5.4), the DPB estimate reads as follows:

$$\widehat{W}^I(\bar{\mathbf{F}}) = -\frac{3J_m\mu}{8\pi} \int_{f_0^{1/3}}^1 \int_0^{2\pi} \int_0^\pi \ln \left[1 - \frac{I-3}{J_m} \right] R^2 \sin \Theta d\Theta d\Psi dR. \quad (5.10)$$

In this expression,

$$I = \frac{1}{J^{2/3}} \left[\psi^2 \bar{I} + \frac{1}{R^2} \left(\bar{\lambda}_1^2 X_1^2 + \bar{\lambda}_2^2 X_2^2 + \bar{\lambda}_3^2 X_3^2 \right) \left(\frac{1}{\psi^4} - \psi^2 \right) \right], \quad (5.11)$$

where \bar{I} and \bar{J} have already been defined above, $\psi = (1 + (\bar{J} - 1)/R^3)^{1/3}$, and $X_1 = R \sin \Theta \sin \Psi$, $X_2 = R \sin \Theta \cos \Psi$, and $X_3 = R \cos \Theta$. In the limiting case of Neo-Hookean matrix phases (*i.e.*, $J_m \rightarrow \infty$), it is possible to integrate (5.10) in closed form. Following Danielsson *et al.* (2004) (Section 3.2), the corresponding final expression can be written as follows:

$$\widehat{W}^I(\bar{\mathbf{F}}) = \frac{\mu}{2} \left(2 - \frac{1}{\bar{J}} - \frac{f_0 + 2(\bar{J} - 1)}{\bar{J}^{2/3} \eta^{1/3}} \right) \bar{I} - \frac{3}{2}(1 - f_0)\mu, \quad (5.12)$$

where $\eta = 1 + (\bar{J} - 1)/f_0$.

At this point, it is important to remark that the DPB model is in fact a generalization of both, the Voigt bound and the Hashin estimate, in the sense that it reduces to the Voigt bound for isochoric deformations and it recovers Hashin's exact solution for hydrostatic loading. This can be verified directly from relation (5.10). Indeed, it is easy to check that for $\bar{J} = \bar{\lambda}_1 \bar{\lambda}_2 \bar{\lambda}_3 = 1$, the DPB estimate (5.10) reduces to the Voigt bound (5.7), and for $\bar{\lambda}_1 = \bar{\lambda}_2 = \bar{\lambda}_3 = \bar{\lambda}$, to the Hashin estimate (5.8). For more general loadings, the DPB estimate can be shown to be actually a *rigorous upper bound* for porous elastomers with incompressible matrix phases and the *Composite Sphere Assemblage* (CSA) microstructure. The reasons for this result rely on the fact that the DPB model is constructed by making use of a *kinematically admissible* field in a spherical volume element (Danielsson *et al.*, 2004). Then, by well known arguments (Hashin, 1962; Herve *et al.*, 1991), it follows that the resulting estimate is an upper bound for porous elastomers with the CSA microstructure, much like the Gurson model (Gurson, 1977) is an upper bound for porous metals with ideally plastic matrix phase and the CSA microstructure. In conclusion, the DPB model is expected to be too “stiff”—given that it is an upper bound for the CSA microstructure—for general loading conditions, with the exception of hydrostatic loading, for which it should be very accurate (in fact, it is exact for the CSA microstructure).

5.1.2 Second-order homogenization estimates

Compressible matrix

In this subsection, we specialize the second-order estimate (2.69) for the effective stored-energy function \widehat{W} to porous elastomers with initial porosity f_0 and *compressible*, isotropic, elastomeric matrix phase characterized by the stored-energy function (5.1). In addition, we spell out the expressions for the evolution of the associated microstructural variables. The detailed derivation of the results is given in Appendix I, but the final expression for the effective stored-energy function

may be written as:

$$\begin{aligned}
\widehat{W}(\overline{\mathbf{F}}) &= \widehat{\Phi}(\bar{\lambda}_1, \bar{\lambda}_2, \bar{\lambda}_3) \\
&= (1 - f_0) \left[g(\hat{I}^{(1)}) + h(\hat{J}^{(1)}) + \frac{\kappa}{2} (\hat{J}^{(1)} - 1)^2 \right. \\
&\quad - \left(\hat{F}_{11}^{(1)} - \bar{\lambda}_1^{(1)} \right) (2\bar{g}_I \bar{\lambda}_1 + \bar{h}_J \bar{\lambda}_2 \bar{\lambda}_3 + \kappa(\bar{J} - 1) \bar{\lambda}_2 \bar{\lambda}_3) \\
&\quad - \left(\hat{F}_{22}^{(1)} - \bar{\lambda}_2^{(1)} \right) (2\bar{g}_I \bar{\lambda}_2 + \bar{h}_J \bar{\lambda}_1 \bar{\lambda}_3 + \kappa(\bar{J} - 1) \bar{\lambda}_1 \bar{\lambda}_3) \\
&\quad \left. - \left(\hat{F}_{33}^{(1)} - \bar{\lambda}_3^{(1)} \right) (2\bar{g}_I \bar{\lambda}_3 + \bar{h}_J \bar{\lambda}_1 \bar{\lambda}_2 + \kappa(\bar{J} - 1) \bar{\lambda}_1 \bar{\lambda}_2) \right], \tag{5.13}
\end{aligned}$$

where $\bar{g}_I = g_I(\bar{I})$, $\bar{h}_J = h_J(\bar{J})$ have been introduced for convenience, and it is recalled that $\bar{I} = \bar{\lambda}_1^2 + \bar{\lambda}_2^2 + \bar{\lambda}_3^2$, and $\bar{J} = \bar{\lambda}_1 \bar{\lambda}_2 \bar{\lambda}_3$.

Further, in the estimate (5.13), the variables $\bar{\lambda}_1^{(1)}$, $\bar{\lambda}_2^{(1)}$, $\bar{\lambda}_3^{(1)}$, which correspond to the principal stretches associated with the phase average deformation gradient $\overline{\mathbf{F}}^{(1)}$ defined by expression (2.70), are given *explicitly* by expression (5.31) in Appendix I. They depend ultimately on the applied loading, $\bar{\lambda}_1$, $\bar{\lambda}_2$, $\bar{\lambda}_3$, the initial porosity, f_0 , the constitutive functions, g , h , κ , characterizing the elastomeric matrix phase, as well as on the 7 variables ℓ_α^* ($\alpha = 1, 2, \dots, 7$) that are the solution of the nonlinear system of equations (5.36) in Appendix I. Similarly, the variables $\hat{F}_{11}^{(1)}$, $\hat{F}_{22}^{(1)}$, $\hat{F}_{33}^{(1)}$, given *explicitly* by (5.34), as well as the variables $\hat{I}^{(1)}$ and $\hat{J}^{(1)}$, given *explicitly* by (5.38), can be seen to depend ultimately on the applied loading, $\bar{\lambda}_1$, $\bar{\lambda}_2$, $\bar{\lambda}_3$, the initial porosity, f_0 , the constitutive functions, g , h , κ , and the 7 variables ℓ_α^* ($\alpha = 1, 2, \dots, 7$).

Thus, in essence, the computation of the second-order estimate (5.13) amounts to solving a system of 7 nonlinear, algebraic equations—provided by relations (5.36). In general, these equations must be solved numerically, but, depending on the functional character of g and h , and the applied loading conditions, possible simplifications may be carried out.

Next, we spell out the expressions for the evolution of the relevant microstructural variables associated with the second-order estimate (5.13). To this end, recall from Section 2.5 that the appropriate microstructural variables in the present context are the current porosity, f , the current average aspect ratios, ω_1 , ω_2 , and the current orientation of the underlying voids in the deformed configuration—as determined from the average deformation gradient in the porous phase $\overline{\mathbf{F}}^{(2)}$, by means of the tensor $\mathbf{Z} = \overline{\mathbf{F}}^{(2)-1}$ defined by (2.84). (No reference is made here to the evolution of the distribution of pores, since it is assumed to be controlled by the applied macroscopic deformation $\overline{\mathbf{F}}$.) Recall as well that, by employing overall objectivity and isotropy arguments, attention has been restricted (without loss of generality) to diagonal loadings (5.5). It then follows that within

the framework of the second-order estimate (5.13), the current porosity and current average aspect ratios of the voids in the deformed configuration are given, respectively, by:

$$f = \frac{\bar{\lambda}_1^{(2)} \bar{\lambda}_2^{(2)} \bar{\lambda}_3^{(2)}}{\bar{\lambda}_1 \bar{\lambda}_2 \bar{\lambda}_3} f_0, \quad (5.14)$$

and

$$\omega_1 = \frac{\bar{\lambda}_1^{(2)}}{\bar{\lambda}_3^{(2)}}, \quad \omega_2 = \frac{\bar{\lambda}_2^{(2)}}{\bar{\lambda}_3^{(2)}}, \quad (5.15)$$

where $\bar{\lambda}_i^{(2)} = (\bar{\lambda}_i - (1 - f_0)\bar{\lambda}_i^{(1)})/f_0$ ($i = 1, 2, 3$) denote the principal stretches associated with $\bar{\mathbf{F}}^{(2)}$ and the variables $\bar{\lambda}_i^{(1)}$ are given by expression (5.31) in Appendix I. In the context of relations (5.14) and (5.15), it is important to recognize that $\bar{\lambda}_i^{(2)}$ ($i = 1, 2, 3$) depend ultimately on the same variables that the stored-energy function (5.13).

Finally, it remains to point out that under the applied, diagonal, loading conditions (5.5), the average orientation of the pores does not evolve with the deformation, but instead it remains fixed. In this connection, it is important to remark that in the present context the average deformation gradient in the pores, $\bar{\mathbf{F}}^{(2)}$, can be shown to be an objective and isotropic tensor function of the applied deformation gradient $\bar{\mathbf{F}}$ (*i.e.*, $\bar{\mathbf{F}}^{(2)}(\bar{\mathbf{K}}\bar{\mathbf{F}}\bar{\mathbf{K}}') = \bar{\mathbf{K}}\bar{\mathbf{F}}^{(2)}(\bar{\mathbf{F}})\bar{\mathbf{K}}'$ for all $\bar{\mathbf{F}}$, and all proper, orthogonal, second-order tensors $\bar{\mathbf{K}}, \bar{\mathbf{K}}'$). As a result, from the general loading $\bar{\mathbf{F}} = \bar{\mathbf{R}}\bar{\mathbf{Q}}\bar{\mathbf{D}}\bar{\mathbf{Q}}^T$ used in the context of expression (2.66), it follows that $\bar{\mathbf{F}}^{(2)}(\bar{\mathbf{F}}) = \bar{\mathbf{R}}\bar{\mathbf{Q}}\bar{\mathbf{F}}^{(2)}(\bar{\mathbf{D}})\bar{\mathbf{Q}}^T$. In turn, it follows that the tensor $\mathbf{Z}^T \mathbf{Z}$ in (2.84) can be simply written as $\mathbf{Z}^T \mathbf{Z} = \mathbf{H} \mathbf{A} \mathbf{H}^T$, where $\mathbf{A} = \text{diag}(\bar{\lambda}_1^{(2)-2}, \bar{\lambda}_2^{(2)-2}, \bar{\lambda}_3^{(2)-2})$ in the frame of reference of choice and $\mathbf{H} = \bar{\mathbf{R}}\bar{\mathbf{Q}}$. In essence, this result reveals that for a general applied deformation $\bar{\mathbf{F}}$, the current, average orientation of the pores is characterized *explicitly* by $\mathbf{H} = \bar{\mathbf{R}}\bar{\mathbf{Q}}$, where it is recalled that $\bar{\mathbf{R}}$ is the macroscopic rotation tensor in the polar decomposition of $\bar{\mathbf{F}}$, and $\bar{\mathbf{Q}}$ is the proper-orthogonal, second-order tensor describing the orientation of the macroscopic Lagrangian principal axes.

Incompressible matrix

As already stated through this work, elastomers are known to be essentially incompressible, since they usually exhibit a ratio between the bulk and shear moduli of the order of 10^4 . Accordingly, it is of practical interest to generate estimates for the effective behavior of porous elastomers with *incompressible* matrix phases. This can be efficiently accomplished by taking the limit $\kappa \rightarrow \infty$ in the second-order estimate (5.13). The corresponding asymptotic analysis has been included in Appendix II, but the final result for the effective stored-energy function \widehat{W}^I for the class of

porous elastomers considered in this work, with elastomeric matrix phase characterized by the stored-energy function (5.1) (with $\kappa = \infty$), reduces to the form:

$$\widehat{W}^I(\overline{\mathbf{F}}) = \widehat{\Phi}^I(\overline{\lambda}_1, \overline{\lambda}_2, \overline{\lambda}_3) = (1 - f_0)g(\hat{I}^{(1)}), \quad (5.16)$$

where $\hat{I}^{(1)}$ is given by expression (5.52) in Appendix II. Here, it should be emphasized that $\hat{I}^{(1)}$ depends ultimately on the applied loading, $\overline{\lambda}_1, \overline{\lambda}_2, \overline{\lambda}_3$, the initial porosity, f_0 , the constitutive function, g , as well as on the 7 variables u_α ($\alpha = 1, 2, \dots, 7$) defined by (5.50), that are the solution of the system of 7 nonlinear equations formed by relations (5.47) and (5.48) in Appendix II. Thus, similar to its compressible counterpart (5.13), the computation of the second-order estimate (5.16) for the effective stored-energy function of porous elastomers with incompressible matrix phases amounts to solving a system of 7 nonlinear, algebraic equations.

In general, it is not possible to solve these equations in closed form. However, for certain applied deformations, the estimate (5.16) may be written down more explicitly. For instance, for the case of hydrostatic loading $\overline{\lambda}_1 = \overline{\lambda}_2 = \overline{\lambda}_3 = \overline{\lambda}$, the expression (5.52) for $\hat{I}^{(1)}$ can be shown to simplify to:

$$\hat{I}^{(1)} = \frac{\overline{\lambda}^2 \left[9u^2 f_0 - 6u f_0 \overline{\lambda} (\overline{\lambda}^3 - 1) + (2 + f_0) \overline{\lambda}^2 (\overline{\lambda}^3 - 1)^2 \right]}{3u^2 f_0}, \quad (5.17)$$

where the variable u satisfies the following condition:

$$\begin{aligned} 27f_0^{\frac{3}{2}}u^3 - 27f_0^{\frac{3}{2}}\overline{\lambda}^4 u^2 + 9(f_0 - 1)\sqrt{f_0}(\overline{\lambda}^3 - 1)\overline{\lambda}^5 u - \\ (\sqrt{f_0} - 1)^2 (2 + \sqrt{f_0}) (\overline{\lambda}^3 - 1)^2 \overline{\lambda}^6 = 0. \end{aligned} \quad (5.18)$$

Of course, the solution to the cubic equation (5.18) may be worked out in closed form. However, for all practical purposes, it is simpler to solve (5.18) numerically. In this regard, it is emphasized that only 1 of the 3 roots¹ of (5.18) leads to the correct linearized behavior; hence, this is the root that should be selected.

We conclude this subsection by noticing that expressions (5.14) and (5.15) continue to apply for determining the current porosity, f , and the current aspect ratios, ω_1, ω_2 , of the underlying voids in porous elastomers with *incompressible* matrix phases, provided that the leading-order terms in expression (5.42) in Appendix II be used for the stretches $\overline{\lambda}_i^{(1)}$ ($i = 1, 2, 3$). In this light, f, ω_1, ω_2 , are seen to depend ultimately on the same variables as the effective stored-energy function (5.16).

¹The correct root linearizes as $u = 1 + (1 + 3f_0)/f_0(\overline{\lambda} - 1) + O(\overline{\lambda} - 1)^2$.

5.1.3 Small-strain elastic moduli

In the limit of small strains, the estimates (5.13) and (5.16) linearize properly, and therefore recover the classical Hashin-Shtrikman (HS) upper bounds for the effective shear and bulk moduli of the composite. To be precise, the estimate (5.13) with *compressible* matrix phases linearizes to $\widehat{W}(\overline{\mathbf{F}}) = 1/2(\tilde{\kappa} - 2/3\tilde{\mu})(\text{tr}\overline{\boldsymbol{\varepsilon}})^2 + \tilde{\mu}\text{tr}\overline{\boldsymbol{\varepsilon}}^2 + o(\overline{\boldsymbol{\varepsilon}}^3)$, as $\overline{\mathbf{F}} \rightarrow \mathbf{I}$, where $\overline{\boldsymbol{\varepsilon}} = \frac{1}{2}(\overline{\mathbf{F}} + \overline{\mathbf{F}}^T - 2\mathbf{I})$ is the macroscopic, infinitesimal strain tensor, and

$$\tilde{\mu} = \frac{(1-f_0)(9\kappa+8\mu)\mu}{(9+6f_0)\kappa+4(2+3f_0)\mu}, \quad \tilde{\kappa} = \frac{4(1-f_0)\kappa\mu}{3f_0\kappa+4\mu}, \quad (5.19)$$

are the effective shear and bulk moduli, respectively. Similarly, the estimate (5.16) with *incompressible* matrix phases linearizes to $\widehat{W}^I(\overline{\mathbf{F}}) = 1/2(\tilde{\kappa}^I - 2/3\tilde{\mu}^I)(\text{tr}\overline{\boldsymbol{\varepsilon}})^2 + \tilde{\mu}^I\text{tr}\overline{\boldsymbol{\varepsilon}}^2 + o(\overline{\boldsymbol{\varepsilon}}^3)$, as $\overline{\mathbf{F}} \rightarrow \mathbf{I}$, where

$$\tilde{\mu}^I = \frac{3(1-f_0)}{3+2f_0}\mu, \quad \tilde{\kappa}^I = \frac{4(1-f_0)}{3f_0}\mu. \quad (5.20)$$

It should be recalled that the HS effective moduli (5.19) and (5.20) are actually *exact* results in the limit of dilute concentration of spherical voids (*i.e.*, for $f_0 \rightarrow 0$). Moreover, the effective moduli (5.19) and (5.20) are known to correlate well with experimental results for the elastic constants of isotropic porous rubbers with small and moderate initial porosities (see, e.g., O'Rourke *et al.* (1997)).

5.1.4 Exact evolution of porosity

For later use, we recall that for porous elastomers with *incompressible* matrix phase, it is possible to compute—from a simple kinematical argument—the exact evolution of the porosity in terms of the applied macroscopic deformation. The result—already stated in Chapter 3—is repeated here for convenience:

$$f = 1 - \frac{1-f_0}{\det \overline{\mathbf{F}}}. \quad (5.21)$$

In contrast to its two-dimensional counterpart (3.12)₁, the specialization of the second-order estimate (5.14) for f to porous elastomers with incompressible matrix phases does not recover the exact result (5.21). Nonetheless, expression (5.14), when specialized to incompressible matrix phases, can be shown to be exact up to second order in the strain (*i.e.*, up to $O(\overline{\boldsymbol{\varepsilon}}^2)$). For larger finite deformations, as shown in the results section, relation (5.14) provides estimates that are in very good agreement with the exact result (5.21), except for the limiting case of large hydrostatic tension together with small initial porosities.

5.1.5 Loss of strong ellipticity

In general, the detection of loss of strong ellipticity in three dimensions requires a tedious, but straightforward, scanning process (*i.e.*, a numerical search of unit vectors \mathbf{N} and \mathbf{m} for which condition (2.89) ceases to hold true). Incidentally, for the particular case when \widehat{W} is objective and isotropic (*i.e.*, $\widehat{W}(\overline{\mathbf{Q}}' \overline{\mathbf{F}} \overline{\mathbf{Q}}) = \widehat{W}(\overline{\mathbf{F}})$ for all $\overline{\mathbf{F}}$, and all proper, orthogonal, second-order tensors $\overline{\mathbf{Q}}'$, $\overline{\mathbf{Q}}$), it is possible to write *necessary* and *sufficient* conditions for the strong ellipticity of $\widehat{W}(\overline{\mathbf{F}}) = \widehat{\Phi}(\bar{\lambda}_1, \bar{\lambda}_2, \bar{\lambda}_3)$ exclusively in terms of the material properties (*i.e.*, in terms of the components of $\widehat{\mathcal{L}}$). These conditions, first provided in 3 dimensions by Simpson and Spector (1983) (see also Zee and Sternberg, 1983 and Dacorogna, 2001), may be written as follows:

$$\widehat{\mathcal{L}}_{iii} > 0, \quad i = 1, 2, 3, \quad (5.22)$$

$$\widehat{\mathcal{L}}_{ijij} > 0, \quad 1 \leq i < j \leq 3, \quad (5.23)$$

$$\widehat{\mathcal{L}}_{iii} \widehat{\mathcal{L}}_{jjjj} + \widehat{\mathcal{L}}_{ijij}^2 - \left(\widehat{\mathcal{L}}_{iijj} + \widehat{\mathcal{L}}_{ijji} \right)^2 + 2 \widehat{\mathcal{L}}_{ijij} \sqrt{\widehat{\mathcal{L}}_{iii} \widehat{\mathcal{L}}_{jjjj}} > 0, \quad 1 \leq i < j \leq 3, \quad (5.24)$$

and either

$$m_{12}^\delta \sqrt{\widehat{\mathcal{L}}_{3333}} + m_{13}^\delta \sqrt{\widehat{\mathcal{L}}_{2222}} + m_{23}^\delta \sqrt{\widehat{\mathcal{L}}_{1111}} + \sqrt{\widehat{\mathcal{L}}_{1111} \widehat{\mathcal{L}}_{2222} \widehat{\mathcal{L}}_{3333}} \geq 0 \quad (5.25)$$

or

$$\det M^\delta > 0 \quad (5.26)$$

where $M^\delta = (m_{ij}^\delta)$ is symmetric and

$$m_{ij}^\delta = \begin{cases} \widehat{\mathcal{L}}_{iii} & \text{if } i = j \\ \widehat{\mathcal{L}}_{ijij} + \delta_i \delta_j \left(\widehat{\mathcal{L}}_{iijj} + \widehat{\mathcal{L}}_{ijji} \right) & \text{if } i \neq j \end{cases} \quad (5.27)$$

for any choice of $\delta_i \in \{\pm 1\}$.

Here,

$$\begin{aligned} \widehat{\mathcal{L}}_{iijj} &= \frac{\partial^2 \widehat{\Phi}}{\partial \bar{\lambda}_i \partial \bar{\lambda}_j}, \\ \widehat{\mathcal{L}}_{ijij} &= \frac{1}{\bar{\lambda}_i^2 - \bar{\lambda}_j^2} \left(\bar{\lambda}_i \frac{\partial \widehat{\Phi}}{\partial \bar{\lambda}_i} - \bar{\lambda}_j \frac{\partial \widehat{\Phi}}{\partial \bar{\lambda}_j} \right) \quad i \neq j, \\ \widehat{\mathcal{L}}_{ijji} &= \frac{1}{\bar{\lambda}_i^2 - \bar{\lambda}_j^2} \left(\bar{\lambda}_j \frac{\partial \widehat{\Phi}}{\partial \bar{\lambda}_i} - \bar{\lambda}_i \frac{\partial \widehat{\Phi}}{\partial \bar{\lambda}_j} \right) \quad i \neq j, \end{aligned} \quad (5.28)$$

$(i, j = 1, 2, 3)$ are the components of the effective incremental elastic modulus $\widehat{\mathcal{L}}$ written with respect to the macroscopic Lagrangian principal axis (*i.e.*, the principal axis of $\overline{\mathbf{U}}$). Note that for loadings with $\overline{\lambda}_i = \overline{\lambda}_j$ ($i \neq j$), suitable limits must be taken for the shear components in (5.28), namely, equations (5.28)₂–(5.28)₃ reduce to

$$\begin{aligned}\widehat{\mathcal{L}}_{ijij} &= \frac{1}{2} \left(\widehat{\mathcal{L}}_{iiii} - \widehat{\mathcal{L}}_{iijj} + \frac{1}{\overline{\lambda}_i} \frac{\partial \widehat{\Phi}}{\partial \overline{\lambda}_i} \right) \quad i \neq j, \\ \widehat{\mathcal{L}}_{ijji} &= \frac{1}{2} \left(\widehat{\mathcal{L}}_{iiii} - \widehat{\mathcal{L}}_{iijj} - \frac{1}{\overline{\lambda}_i} \frac{\partial \widehat{\Phi}}{\partial \overline{\lambda}_i} \right) \quad i \neq j,\end{aligned}\tag{5.29}$$

respectively. Furthermore, note that there are 3 conditions in (5.22), 3 in (5.23), 3 in (5.24), and, due to all possible signs, 4 in (5.25) or in (5.26). Thus, there is a total of 13 conditions.

In the next section, it will be shown that even in the case when the behavior of the elastomeric matrix phase is chosen to be strongly elliptic, the homogenized behavior of the porous elastomer can lose strong ellipticity. This result for 3D, *random*, porous elastomers parallels those previously found for porous elastomers with 2D *periodic* (Abeyaratne and Triantafyllidis, 1984; Michel *et al.*, 2007) and 2D *random* (Lopez-Pamies and Ponte Castañeda, 2004b) microstructures.

5.2 Results and discussion

In this section, the constitutive models (5.13) and (5.16) are used to study the effective stress-strain response, the microstructure evolution, and the macroscopic stability of porous elastomers with Gent matrix phases under different types of finite deformations. Results are given for various values of the compressibility ratio κ/μ and lock-up parameter J_m , as well as various values of initial porosity f_0 , and are computed up to the point at which either the associated effective incremental modulus is found to lose strong ellipticity, or, alternatively, the porosity is found to vanish. If neither of these phenomena occurs, the results are truncated at some sufficiently large value of the deformation. For clarity, the points at which the homogenized material loses strong ellipticity are indicated with the symbol “o” in the figures, whereas the symbol “◇” is utilized to indicate the vanishing of the porosity.

The results presented in this section are organized as follows. First, we address the effective response of Gent porous elastomers subjected to *axisymmetric loading conditions*. Special attention is given to *hydrostatic*, *biaxial*, and *uniaxial* tension/compression loadings, which, beyond providing comprehensive physical insight and contributing to establish the accuracy of the

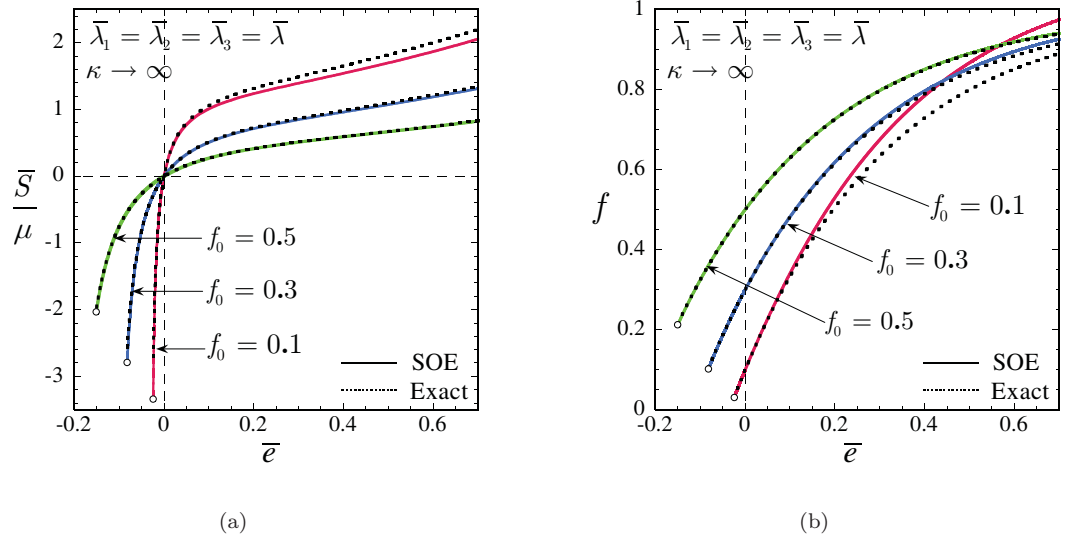


Figure 5.1: Comparisons of the effective response, as predicted by the second-order estimate (SOE) (5.16), with the exact results (Hashin, 1985), of a porous elastomer with incompressible matrix phase subjected to hydrostatic tension and compression ($\bar{\lambda}_1 = \bar{\lambda}_2 = \bar{\lambda}_3 = \bar{\lambda}$). The results correspond to a material with Neo-Hookean matrix phase and various values of initial porosity f_0 , and are shown as a function of the logarithmic strain $\bar{e} = \ln \bar{\lambda}$. (a) The normalized macroscopic stress $\bar{S}/\mu = \mu^{-1} \partial \hat{\Phi}^I / \partial \bar{\lambda}_1 = \mu^{-1} \partial \hat{\Phi}^I / \partial \bar{\lambda}_2 = \mu^{-1} \partial \hat{\Phi}^I / \partial \bar{\lambda}_3$. (b) The evolution of the porosity f .

proposed models through comparisons with the available exact results, happen to correspond to actual loading conditions easily achievable with standard experimental equipment. Following the axisymmetric subsection, we provide representative results for the overall behavior of Gent porous elastomers subjected to *plane-strain loading conditions*. In particular, we focus on *pure shear* and *in-plane uniaxial* tension/compression loadings. The corresponding macroscopic failure surfaces, as determined by the loss of strong ellipticity of the homogenized behavior of the material, are presented—in principal strain and stress spaces—and discussed for the axisymmetric, as well as for the plane-strain loading conditions.

5.2.1 Axisymmetric loadings

Hydrostatic tension/compression

Figure 5.1 presents the comparison between the effective behavior as predicted by the second-order estimate (SOE) (5.16) and the “exact” (Hashin, 1985) estimate (5.9) for a porous elastomer with incompressible Neo-Hookean matrix phase under hydrostatic loading ($\bar{\lambda}_1 = \bar{\lambda}_2 = \bar{\lambda}_3 = \bar{\lambda}$). Recall

that the DPB model (5.12) coincides identically with the exact result (5.9) in this case. Results are shown for initial porosities of 10, 30, and 50% as a function of the logarithmic strain $\bar{\epsilon} = \ln(\bar{\lambda})$. Part (a) shows the normalized macroscopic stress $\bar{S}/\mu = \mu^{-1}\partial\widehat{\Phi}^I/\partial\bar{\lambda}_1 = \mu^{-1}\partial\widehat{\Phi}^I/\partial\bar{\lambda}_2 = \mu^{-1}\partial\widehat{\Phi}^I/\partial\bar{\lambda}_3$, and part (b), the associated evolution of the porosity f . It is observed from Fig. 5.1(a) that the SOE predictions are in very good agreement with the exact result. Note that the agreement improves for higher values of initial porosity f_0 . It is also discerned from Fig. 5.1(a) that the effective behavior of the material is softer for higher values of f_0 , as expected on physical grounds. Interestingly, it is further recognized from Fig. 5.1(a) that the overall response of the porous elastomer under hydrostatic compression exhibits very significant stiffening, but that, under hydrostatic tension, the behavior gets more compliant with increasing strain. In this connection, we note from Fig. 5.1(b) that the porosity decreases for compressive deformations and increases for tensile ones. This entails a *geometric* stiffening/softening mechanism that is entirely consistent with the stress-strain results shown in Fig. 5.1(a). With regard to the remaining microstructural variables, it should be realized that they do not evolve under hydrostatic loading, that is, the initially spherical shape and distribution of the underlying pores remain—on average—spherical for all applied hydrostatic deformations. Turning back to Fig. 5.1(b), we remark that the predictions for the evolution of the porosity f as determined by the SOE are in very good agreement with the exact result (5.21) for the cases of 30 and 50 % initial porosity. The agreement between the prediction and the exact result for the case of $f_0 = 10\%$ is excellent for hydrostatic compression, but it deteriorates appreciably for tensile hydrostatic deformations larger than $\bar{\epsilon} = \ln\bar{\lambda} = 0.2$. This has the effect of slightly exaggerating the geometric softening in tension for $f_0 = 10\%$, leading to slightly softer predictions than the Hashin estimate. Finally, it should be noticed from Fig. 5.1 that the homogenized response of the porous elastomer, as predicted by the SOE, becomes unstable—through loss of strong ellipticity—under hydrostatic compression (denoted by the symbol “o”), while it remains strongly elliptic under hydrostatic tension. This result is investigated in more detail in the context of the next two figures.

Figure 5.2 provides results associated with those shown in Fig. 5.1 for the components² of the normalized effective incremental modulus $\widehat{\mathcal{L}} = \mu^{-1}\partial^2\widehat{W}^I/\partial\bar{\mathbf{F}}^2$ of a porous elastomer with incompressible, Neo-Hookean matrix phase and initial porosity of 30% under hydrostatic loading ($\bar{\lambda}_1 = \bar{\lambda}_2 = \bar{\lambda}_3 = \bar{\lambda}$). Part (a) shows results for hydrostatic compression ($\bar{\lambda} \leq 1$), and part (b),

²Here and subsequently, the components of the effective incremental modulus $\widehat{\mathcal{L}}$ are referred to the macroscopic Lagrangian principal axes, i.e., the principal axes of $\bar{\mathbf{F}}^T\bar{\mathbf{F}}$.

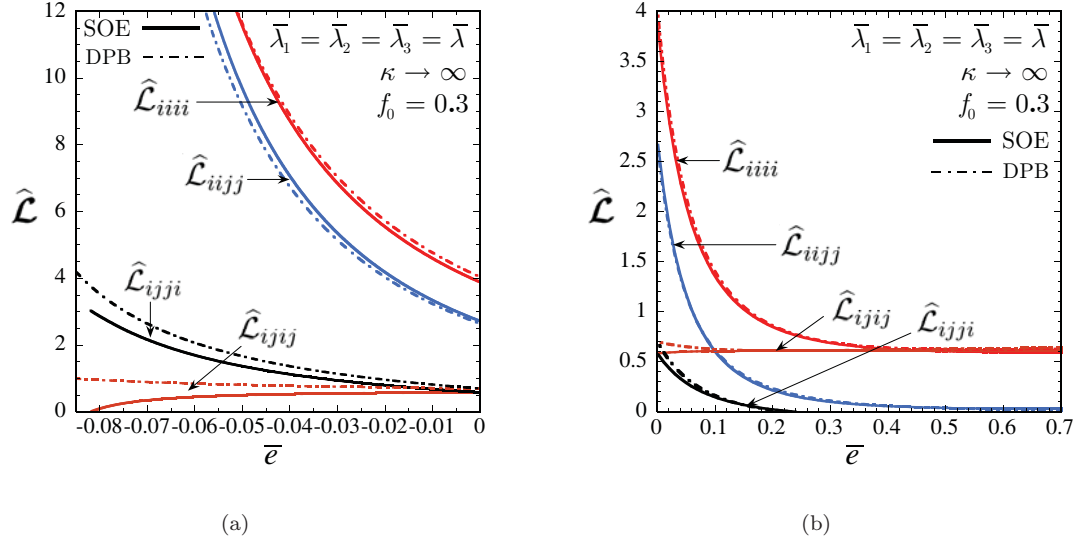


Figure 5.2: Effective response, as predicted by the second-order estimate (SOE) (13) and the DPB model (5.12), of a porous elastomer with incompressible matrix phase subjected to hydrostatic loading ($\bar{\lambda}_1 = \bar{\lambda}_2 = \bar{\lambda}_3 = \bar{\lambda}$). The results correspond to a material with Neo-Hookean matrix phase and initial porosity of $f_0 = 30\%$, and are shown as a function of the logarithmic strain $\bar{\epsilon} = \ln \bar{\lambda}$. (a) The non-zero components ($i, j \in \{1, 2, 3\}, i \neq j$, no summation) of the effective incremental modulus $\hat{\mathcal{L}}$ —written with respect to the Lagrangian principal axes—for hydrostatic compression ($\bar{\lambda} \leq 1$). (b) The corresponding results for hydrostatic tension ($\bar{\lambda} \geq 1$).

for hydrostatic tension ($\bar{\lambda} \geq 1$). Fig. 5.2(a) illustrates that—in accord with the stress-strain results shown in Fig. 5.1(a)—the normal components $\hat{\mathcal{L}}_{1111}$, $\hat{\mathcal{L}}_{2222}$, and $\hat{\mathcal{L}}_{3333}$, as predicted by the second-order estimate (SOE) (5.16), increase rapidly with the applied compressive strain. That is, the porous elastomer *stiffens* very significantly in the “direction” of the applied loading. On the other hand, the effective incremental shear response of the porous elastomer, as measured³ by $\hat{\mathcal{L}}_{1212}$, $\hat{\mathcal{L}}_{1313}$, and $\hat{\mathcal{L}}_{2323}$, is seen to *soften* with the applied hydrostatic compression to the point that $\hat{\mathcal{L}}_{1212} = \hat{\mathcal{L}}_{1313} = \hat{\mathcal{L}}_{2323} = 0$ at some critical finite stretch $\bar{\lambda}_{crit}$. This critical stretch corresponds to the point at which the porous elastomer loses strong ellipticity. In this connection, it should be remarked that the combinations $\hat{\mathcal{L}}_{iiii}\hat{\mathcal{L}}_{jjjj} + \hat{\mathcal{L}}_{ijij}^2 - (\hat{\mathcal{L}}_{iiij} + \hat{\mathcal{L}}_{ijji})^2 + 2\hat{\mathcal{L}}_{ijij}\sqrt{\hat{\mathcal{L}}_{iiii}\hat{\mathcal{L}}_{jjjj}}$ ($i, j \in \{1, 2, 3\}, i \neq j$, no summation) also vanish at $\bar{\lambda}_{crit}$. Thus, making contact with Section 5.1.5, this means that conditions (5.23) and (5.24) cease to hold true. Physically, this implies that the porous elastomer may develop localized deformations in planar zones with arbitrary normals \mathbf{N} . Furthermore, the deformation in these zones localizes in shear, since $\mathbf{m} \perp \mathbf{N}$. (Recall from

³Recall that for isotropic materials $\hat{\mathcal{L}}_{ijij} = \hat{\mathcal{L}}_{jiji}$ ($i, j \in \{1, 2, 3\}, i \neq j$, no summation).

Section 2.6 in Chapter 2 that \mathbf{m} denotes the eigenvector corresponding to the zero eigenvalue of the acoustic tensor associated with \mathbf{N} , so that it characterizes the type of deformation within the localized band.) This remarkable behavior predicted by the SOE is consistent with numerical simulations (Michel *et al.*, 2007), as well as with physical evidence (see, e.g., Kinney *et al.*, 2001; Gong and Kyriakides, 2005). Indeed, local buckling of matrix ligaments is anticipated to occur in porous elastomers subjected to *compressive* states of deformation. In turn, connected networks of buckled ligaments that extend throughout the entire specimen correspond to bands of *localized deformation* at the macroscopic level. The development of these macroscopic bands of localized deformation corresponds precisely to the loss of strong ellipticity of the homogenized behavior of the material (Geymonat *et al.*, 1993). Comparing now the SOE with the DPB predictions in Fig. 5.2(a), it is observed that the normal components $\widehat{\mathcal{L}}_{1111}$, $\widehat{\mathcal{L}}_{2222}$, and $\widehat{\mathcal{L}}_{3333}$ of both models are in very good agreement. In contrast, the effective incremental shear moduli $\widehat{\mathcal{L}}_{1212}$, $\widehat{\mathcal{L}}_{1313}$, and $\widehat{\mathcal{L}}_{2323}$ predicted by the DPB model are much stiffer than the corresponding SOE results. In fact, they exhibit different trends: while the SOE shear moduli decrease with the applied loading, the DPB shear moduli increase, which ultimately entails that the DPB model remains strongly elliptic for all applied hydrostatic compression (in disagreement with numerical results and physical experience). Turning now to Fig. 5.2(b), it is noticed that—in accord with the stress-strain results shown in Fig. 5.1(a)—the normal components $\widehat{\mathcal{L}}_{1111}$, $\widehat{\mathcal{L}}_{2222}$, and $\widehat{\mathcal{L}}_{3333}$ decrease very distinctly with the applied hydrostatic tension. That is, the porous elastomer *softens* in the “direction” of loading with the applied tensile strain. Conversely, the effective incremental shear moduli $\widehat{\mathcal{L}}_{1212}$, $\widehat{\mathcal{L}}_{1313}$, and $\widehat{\mathcal{L}}_{2323}$ are seen to increase—though very slightly. Furthermore, Fig. 5.2(b) also shows more explicitly the fact (already mentioned above) that there is no loss of strong ellipticity for hydrostatic tension. Note that—as opposed to hydrostatic compression—the SOE and DPB predictions in Fig. 5.2(b) are in very good agreement for the normal, as well as for the shear effective moduli. Note finally that the results shown in Fig. 5.2 for $f_0 = 0.3$ are representative for all values of initial porosity, since the trends followed by the components of $\widehat{\mathcal{L}}$ for all values of f_0 are similar to those displayed in Fig. 5.2. The precise effect of f_0 on the effective incremental behavior and stability of porous elastomers subjected to hydrostatic loading will be addressed in detail in the context of the next figure.

In short, Fig. 5.2 puts into evidence the subtle influence of the evolution of the underlying microstructure on the effective behavior and stability of porous elastomers subjected to finite

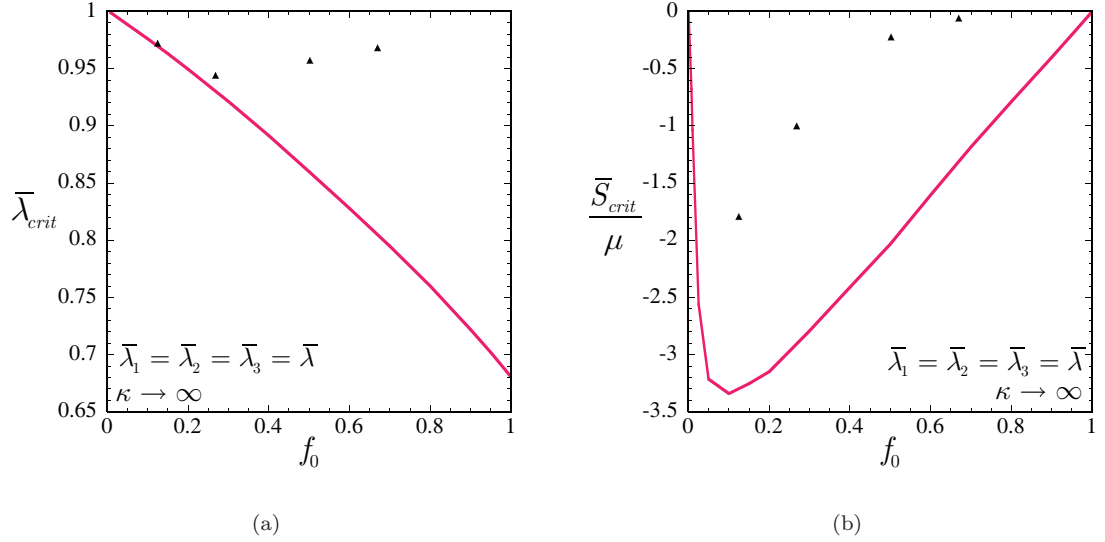


Figure 5.3: Hydrostatic compression ($\bar{\lambda}_1 = \bar{\lambda}_2 = \bar{\lambda}_3 = \bar{\lambda} \leq 1$) of a porous elastomer with incompressible, Neo-Hookean matrix phase. (a) The critical stretch $\bar{\lambda}_{crit}$ at which the second-order estimate (5.16) loses strong ellipticity as a function of initial porosity f_0 . (b) The associated normalized critical stress \bar{S}_{crit}/μ . The isolated data points in the plots correspond to experimental results for the critical buckling of spherical shells under hydrostatic compression (Wesolowski, 1967).

deformations. Indeed, the *stiffening* of the effective incremental normal response of the porous elastomer—as measured by $\hat{\mathcal{L}}_{1111}$, $\hat{\mathcal{L}}_{2222}$, and $\hat{\mathcal{L}}_{3333}$ —when subjected to hydrostatic compression (see Fig. 5.2(a)) is entirely consistent with the decrease of porosity illustrated in Fig. 5.1(b). However, as shown in Fig. 5.2(a), the decrease of porosity does also lead to the geometric *softening* of the effective incremental shear response of the material—as measured by $\hat{\mathcal{L}}_{1212}$, $\hat{\mathcal{L}}_{1313}$, and $\hat{\mathcal{L}}_{2323}$ —which eventually leads to the loss of strong ellipticity of the porous elastomer at some finite stretch (in spite of the fact that the elastomeric matrix phase is strongly elliptic). Analogously, the *softening* of the effective incremental normal response of the porous elastomer when subjected to hydrostatic tension (see Fig. 5.2(b)) is entirely consistent with the increase of porosity illustrated in Fig. 5.1(b). Further, the increase of porosity does also lead to the (slight) geometric *stiffening* of the effective incremental shear response of the material, which, in some sense, prevents the porous elastomer from losing stability.

Figure 5.3 provides plots associated with the results shown in Figs. 5.1 and 5.2 for: (a) the critical stretch, $\bar{\lambda}_{crit}$, and (b) the normalized critical stress, \bar{S}_{crit}/μ , at which the second-order estimate (5.16) loses strong ellipticity under hydrostatic compression as a function of the

initial porosity f_0 . Fig. 5.3 exhibits two distinct regimes: the “dilute,” or small-porosity regime ($0 < f_0 < 0.1$), and the “finite,” or large-porosity regime ($0.1 < f_0 < 1$). Interestingly, for $0 < f_0 < 0.1$, Fig. 5.3 shows that the porous elastomer becomes more stable, in both, strain and stress space, with increasing initial porosity. That is, in the small-porosity regime, the material loses strong ellipticity at smaller stretches $\bar{\lambda}_{crit}$ (larger compressive strains) and larger compressive stresses \bar{S}_{crit}/μ , for higher values of the initial porosity f_0 . In passing, we remark that this rather counterintuitive result has already been observed in 2D porous elastomers with random and periodic microstructures (Lopez-Pamies and Ponte Castañeda, 2004b; Michel *et al.*, 2007). In contrast, for $0.1 < f_0 < 1$, the porous elastomer continues to improve its stability with increasing porosity in strain space; however, in stress space, the trend is reversed and the material is seen to become more unstable for higher values of f_0 . The fact that for the range of initial porosities $0.1 < f_0 < 1$ the critical stretch $\bar{\lambda}_{crit}$ exhibits a different trend than \bar{S}_{crit}/μ can be understood by recognizing that the stress-strain relation of the porous elastomer under hydrostatic compression softens drastically with increasing f_0 in this regime (see Fig. 5.1(a)). This implies that even though $|\bar{S}_{crit}/\mu|$ decreases with increasing f_0 , the corresponding stretches $\bar{\lambda}_{crit}$ required to reach such critical stresses may, and in fact do, decrease with increasing f_0 . In connection with the results shown in Fig. 5.3, it is important to recall that, unlike for small and moderate values of porosity, the SOE predictions are not expected to be accurate—except for the CSA microstructure—for very large f_0 , as discussed in Section 2.5.1. Whatever the case may be, it is interesting to note that, according to the SOE results, $\bar{S}_{crit}/\mu \rightarrow 0$ as $f_0 \rightarrow 1$, as it may be expected on physical grounds.

At this stage, it is important to remark that while the work of Hashin (1985) provides exact results for the effective stored-energy function, \widehat{W} , and the porosity evolution, f , for the hydrostatic loading of porous elastomers with incompressible, isotropic matrix phase and the *Composite Sphere Assemblage* (CSA) microstructure, it contains essentially no information about the macroscopically stability of these materials. This is simply due to the fact that the exact results of Hashin are given for a *fixed* loading path—namely, $\bar{\lambda}_1 = \bar{\lambda}_2 = \bar{\lambda}_3$ —and therefore, the corresponding effective incremental modulus $\widehat{\mathcal{L}}$, needed for detecting loss of strong ellipticity, cannot be computed. On the other hand, it is possible to compute the effective incremental modulus associated with the DPB model (5.12), which as already stated agrees with the Hashin estimate for hydrostatic loading,

and check for loss of strong ellipticity. It turns out, however, that—unlike the second-order estimate (5.16)—the DPB model (5.12) remains strongly elliptic for all hydrostatic deformations, in contradiction with physical experience. More precisely, under this type of loading conditions—as illustrated in Fig. 5.2—the effective incremental modulus $\widehat{\mathcal{L}}$ associated with the DPB model not only remains strongly elliptic, but stiffens significantly with increasing strain. This overly stiff behavior seems to be consistent with the fact that the DPB model is a rigorous upper bound for CSA microstructures. Finally, it is fitting to mention that there have been a number of experimental and analytical studies (see, e.g., Wesolowski, 1967; Wang and Ertepinar, 1972) on the stability of isolated spherical shells under hydrostatic loading. Of course, the buckling instabilities of an isolated shell cannot be identified with the buckling instabilities that would take place in an actual porous elastomer with the CSA microstructure, except possibly in the dilute limit, when no interaction is expected among the pores. In this connection, we have included in Fig. 5.3 the experimental findings of Wesolowski (1967) comprising the critical stretches and pressures at which a Neo-Hookean, thick-walled, spherical shell first buckles as function of initial porosity (i.e., the cube of the ratio of inner to outer radius of the shell in the undeformed state). Remarkably, the experimental results of Wesolowski (1967) in strain space agree extremely well with the SOE predictions in the small-porosity regime, where the comparisons between the isolated shell and the porous elastomer may be relevant. For large values of initial porosity, it is interesting to observe that the SOE results provide a bound for the experimental “failure surface” characterized by the stretches and stresses at which the isolated shell first buckles.

Biaxial tension/compression

Figure 5.4 presents the SOE predictions for the effective response of a porous elastomer with incompressible Gent matrix phase under biaxial loading ($\bar{\lambda}_2 = \bar{\lambda}_3 = \bar{\lambda}$, $\bar{S}_{11} = \partial\widehat{\Phi}^I/\partial\bar{\lambda}_1 = 0$). Results are shown for a matrix lock-up parameter of $J_m = 50$ and initial porosities of $f_0 = 0, 10, 30$ and 50% as a function of the logarithmic strain $\bar{e} = \ln \bar{\lambda}$. Part (a) shows the normalized macroscopic “biaxial” stress $\bar{S}_{bi}/\mu = \mu^{-1}\partial\widehat{\Phi}^I/\partial\bar{\lambda}_2 = \mu^{-1}\partial\widehat{\Phi}^I/\partial\bar{\lambda}_3$, and part (b), the associated “lateral” strain $\bar{e}_{lat} = \ln \bar{\lambda}_1$. Similar to hydrostatic loading and as expected on physical grounds, Fig. 5.4(a) shows that the effective response of the porous elastomer is softer for higher values of the initial porosity f_0 . Furthermore, for biaxial tension, as well as for compression, the material is seen to stiffen very significantly with increasing strain. In spite of this similarity, the porous elastomer is seen to

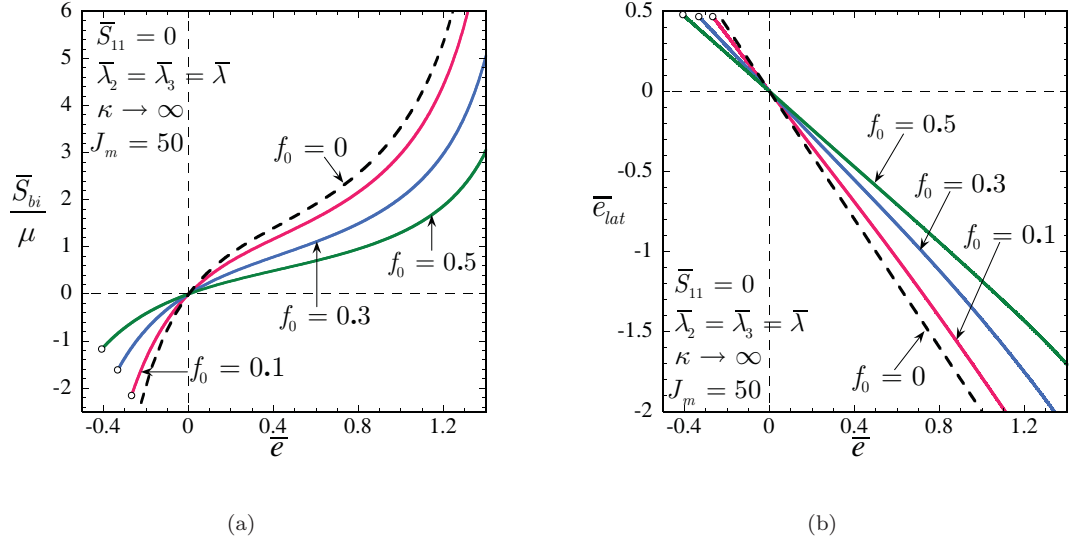


Figure 5.4: Effective response, as predicted by the second-order estimate (5.16), of a porous rubber subjected to biaxial tension and compression ($\bar{\lambda}_2 = \bar{\lambda}_3 = \bar{\lambda}$, $\bar{S}_{11} = \partial\hat{\Phi}^I/\partial\bar{\lambda}_1 = 0$), as a function of the logarithmic strain $\bar{e} = \ln \bar{\lambda}$. The results correspond to a material with incompressible, Gent matrix with lock-up parameter $J_m = 50$ and various values of initial porosity f_0 . (a) The normalized macroscopic stress $\bar{S}_{bi}/\mu = \mu^{-1}\partial\hat{\Phi}^I/\partial\bar{\lambda}_2 = \mu^{-1}\partial\hat{\Phi}^I/\partial\bar{\lambda}_3$. (b) The lateral strain $\bar{e}_{lat} = \ln \bar{\lambda}_1$.

become unstable—through loss of strong ellipticity—under biaxial compression, while it remains stable under biaxial tension. This disparity will be shown shortly to be due to differences in the evolution of the underlying microstructure. Turning now to Fig. 5.4(b), we notice that the volume of the porous elastomer increases (decreases) when subjected to biaxial tension (compression), that is, $\ln(\det \bar{\mathbf{F}}) = \bar{e}_{lat} + 2\bar{e} > (<) 0$. Since the elastomeric matrix phase is incompressible, this has the direct implication that the porosity increases (decreases) with the applied tensile (compressive) deformation. In this connection, it is interesting to remark further from Fig. 5.4(b) that for biaxial tension (compression) the porous elastomer undergoes a larger volume increase (decrease) for higher values of initial porosity f_0 .

Figure 5.5 provides corresponding results for: (a) the evolution of the porosity f ; and (b) the evolution of the average aspect ratios ω_1 and ω_2 . Fig. 5.5(a) shows that the SOE predictions for the evolution of the porosity f virtually coincide with the “exact” result for all values of initial porosities considered. In this regard, we should make the following parenthetical clarification. As discussed in Section 5.1.4, the evolution of porosity in porous elastomers with incompressible matrix phase can be computed exactly through expression (5.21), provided that the determinant of the macroscopic

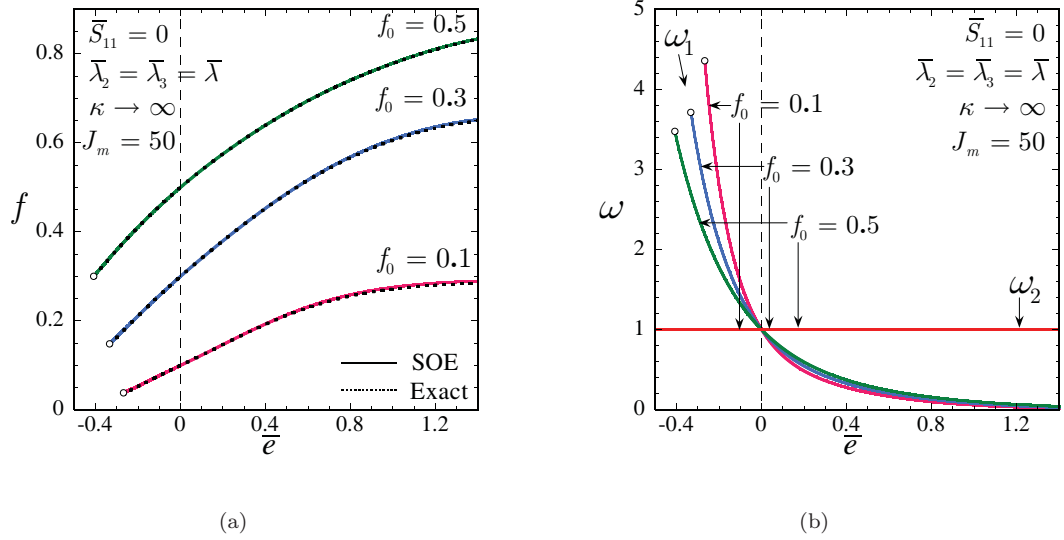


Figure 5.5: Biaxial tension and compression ($\bar{\lambda}_2 = \bar{\lambda}_3 = \bar{\lambda}$, $\bar{S}_{11} = \partial\hat{\Phi}^I/\partial\bar{\lambda}_1 = 0$) of a porous elastomer with incompressible, Gent matrix phase with lock-up parameter $J_m = 50$ and various values of initial porosity f_0 . (a) The evolution of porosity f , as predicted by the second-order estimate (5.16), compared with the exact result. (b) The evolution of the aspect ratios ω_1 and ω_2 as predicted by the second-order estimate (5.16).

deformation gradient, $\det \bar{\mathbf{F}}$, is known. For displacement boundary conditions, $\det \bar{\mathbf{F}}$ is of course known since it is prescribed. On the other hand, for traction and mixed boundary conditions, such as the one considered in this subsection, $\det \bar{\mathbf{F}}$ is not known a priori and must be computed from the material response. In this connection, we remark that what we have denoted by “exact” porosity in Fig. 5.5 corresponds to the porosity generated by expression (5.21) evaluated at the $\det \bar{\mathbf{F}}$ predicted by the second-order estimate (5.16). Having clarified this point we next note that Fig. 5.5(a) illustrates explicitly the fact already pointed out in Fig. 5.4(b) that the porosity increases for tensile loadings and decreases for compressive ones. The former mechanism induces geometric softening and the latter, stiffening. With regard to the evolution of the aspect ratios, we first notice from Fig. 5.5(b) that the average aspect ratio ω_2 remains identically equal to one throughout the entire loading process, as a result of the imposed macroscopic biaxial state of deformation (*i.e.*, $\bar{\lambda}_2 = \bar{\lambda}_3$). On the other hand, the aspect ratio ω_1 is seen to decrease (increase) very significantly for tensile (compressive) loadings, entailing that the pores evolve on average into oblate (prolate) spheroids. In short, the pore ovalization resulting from the applied biaxial compression induces geometric softening on the overall stress-strain relation of the porous elastomer, while the development of

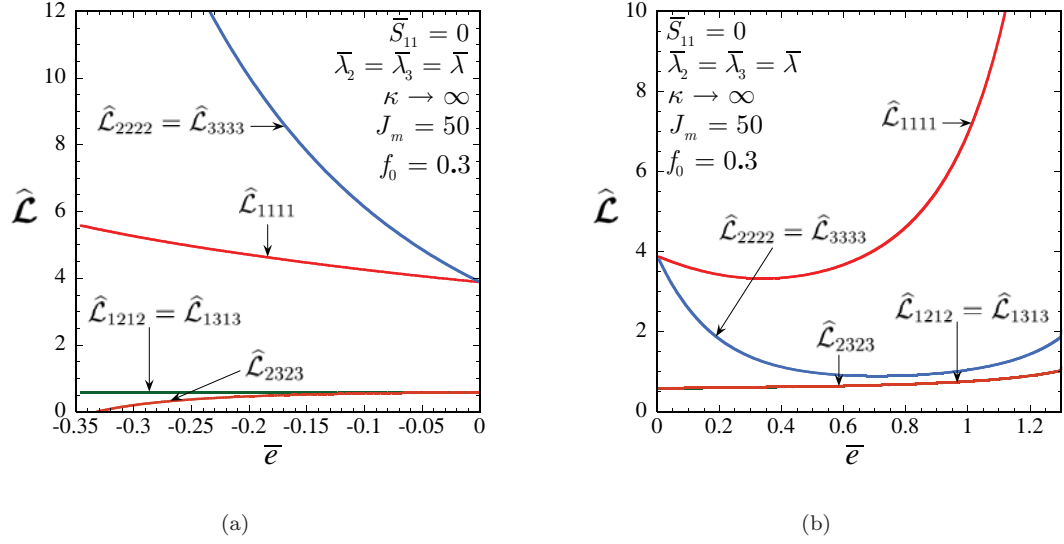


Figure 5.6: Effective response, as predicted by the second-order estimate (13), of a porous elastomer with incompressible matrix phase subjected to biaxial tension and compression ($\bar{\lambda}_2 = \bar{\lambda}_3 = \bar{\lambda}$, $\bar{S}_{11} = \partial\hat{\Phi}^I/\partial\bar{\lambda}_1 = 0$). The results correspond to a material with Gent matrix phase ($J_m = 50$) and initial porosity of $f_0 = 30\%$, and are shown as a function of the logarithmic strain $\bar{e} = \ln \bar{\lambda}$. The normal and shear principal components of the effective incremental modulus $\hat{\mathcal{L}}$ for: (a) biaxial compression ($\bar{\lambda} \leq 1$), and (b) biaxial tension ($\bar{\lambda} \geq 1$).

“pancake” shapes for the pores resulting from tension induces geometric stiffening. Thus, in summary, the results illustrated in Fig. 5.5 make it plain that the evolution of the underlying microstructure is very different for biaxial compression than for tension. This is consistent with the fact that the porous elastomer loses strong ellipticity under biaxial compression and *not* under biaxial tension.

In order to gain further insight on the results shown in Figs. 5.4 and 5.5, Fig. 5.6 provides results for the normal ($\hat{\mathcal{L}}_{1111}$, $\hat{\mathcal{L}}_{2222}$, $\hat{\mathcal{L}}_{3333}$) and shear ($\hat{\mathcal{L}}_{1212}$, $\hat{\mathcal{L}}_{1313}$, $\hat{\mathcal{L}}_{2323}$) components of the normalized effective incremental modulus $\hat{\mathcal{L}} = \mu^{-1} \partial^2 \widehat{W}^I / \partial \bar{\mathbf{F}}^2$ of a porous elastomer with Gent matrix phase ($J_m = 50$) and initial porosity of 30% under biaxial loading ($\bar{\lambda}_2 = \bar{\lambda}_3 = \bar{\lambda}$, $\bar{S}_{11} = \partial\hat{\Phi}^I/\partial\bar{\lambda}_1 = 0$). Part (a) shows results for biaxial compression ($\bar{\lambda} \leq 1$), and part (b), for biaxial tension ($\bar{\lambda} \geq 1$). Fig. 5.6(a) shows that—in agreement with the stress-strain results shown in Fig. 5.4(a)—the normal components $\hat{\mathcal{L}}_{2222} = \hat{\mathcal{L}}_{3333}$ increase monotonically with the applied compressive strain. Note also that the normal component $\hat{\mathcal{L}}_{1111}$ increases monotonically as well. In contrast, the effective shear moduli $\hat{\mathcal{L}}_{1212}$, $\hat{\mathcal{L}}_{1313}$, $\hat{\mathcal{L}}_{2323}$ are seen to decrease with increasing biaxial compression, especially $\hat{\mathcal{L}}_{2323}$ which vanishes at some critical finite stretch $\bar{\lambda}_{crit}$. This stretch corresponds precisely to the

point at which the material loses strong ellipticity. In this connection, similar to the hydrostatic loading case, it should be noted that the combination $\widehat{\mathcal{L}}_{2222}\widehat{\mathcal{L}}_{3333} + \widehat{\mathcal{L}}_{2323}^2 - (\widehat{\mathcal{L}}_{2233} + \widehat{\mathcal{L}}_{2332})^2 + 2\widehat{\mathcal{L}}_{2323}\sqrt{\widehat{\mathcal{L}}_{2222}\widehat{\mathcal{L}}_{3333}}$ does also vanish at $\bar{\lambda}_{crit}$. Making contact with Section 5.1.5, this means that conditions (5.23)₃ and (5.24)₃ cease to hold true. This implies that the porous elastomer may develop localized deformations in bands with normals $\mathbf{N} \in \text{Span}\{\mathbf{u}_2, \mathbf{u}_3\}$, where \mathbf{u}_2 and \mathbf{u}_3 denote the unit vectors defining the macroscopic Lagrangian principal axes associated with the principal stretches $\bar{\lambda}_2$ and $\bar{\lambda}_3$, respectively. Moreover, the vector \mathbf{m} associated with a given \mathbf{N} is such that $\mathbf{m} \perp \mathbf{N}$, so that the deformation localizes in shear within the bands. In other words, when subjected to biaxial compression, the porous elastomer may become infinitesimally soft under incremental shear deformations in planes with normals defined by the Lagrangian principal axes associated with the smallest principal stretches (which correspond to the largest compressive strains). As for the hydrostatic loading case, it should be emphasized that this behavior is rather subtle. Indeed, Fig. 5.5(a) shows that, under biaxial compression, the porous elastomer *stiffens* in the “direction” of the applied loading (i.e., $\widehat{\mathcal{L}}_{2222} = \widehat{\mathcal{L}}_{3333}$ increase with the applied stretch). However, its incremental shear response (in the \mathbf{u}_2 – \mathbf{u}_3 –plane) *softens* to the point that the material loses strong ellipticity at some finite critical stretch $\bar{\lambda}_{crit}$ (at which $\widehat{\mathcal{L}}_{2323} = \widehat{\mathcal{L}}_{3232} = \widehat{\mathcal{L}}_{2222}\widehat{\mathcal{L}}_{3333} + \widehat{\mathcal{L}}_{2323}^2 - (\widehat{\mathcal{L}}_{2233} + \widehat{\mathcal{L}}_{2332})^2 + 2\widehat{\mathcal{L}}_{2323}\sqrt{\widehat{\mathcal{L}}_{2222}\widehat{\mathcal{L}}_{3333}} = 0$). Turning now to Fig. 5.6(b), it is observed that—in accord with the stress-strain results shown in Fig. 5.4(a)—the incremental normal moduli $\widehat{\mathcal{L}}_{2222} = \widehat{\mathcal{L}}_{3333}$ initially decrease and then increase, as a function of the applied biaxial strain. On the other hand, the effective incremental shear moduli $\widehat{\mathcal{L}}_{1212}, \widehat{\mathcal{L}}_{1313}, \widehat{\mathcal{L}}_{2323}$ increase monotonically with the applied tensile strain, improving the stability of the porous elastomer. Even though the results illustrated in Fig. 5.6 correspond to $f_0 = 0.3$, they are representative of results for porous elastomers with any value of initial porosity f_0 . A more detailed investigation of the effect of f_0 on the effective incremental behavior and stability of porous elastomers subjected to biaxial loading will be addressed in the context of the next figure. As a final remark, it is appropriate to emphasize that the DPB model (5.12) (with Neo-Hookean matrix phase) can be shown to remain strongly elliptic for all biaxial tension/compression loading. This implies that the corresponding DPB estimate with Gent matrix phase (5.10) remains strongly elliptic for all biaxial tension/compression loading as well. This is easy to check by realizing that a Gent material is a stiffer than a Neo-Hookean material for all modes of deformation.

Figure 5.7 presents plots associated with the results shown in Figs. 5.4, 5.5, 5.6 for: (a)

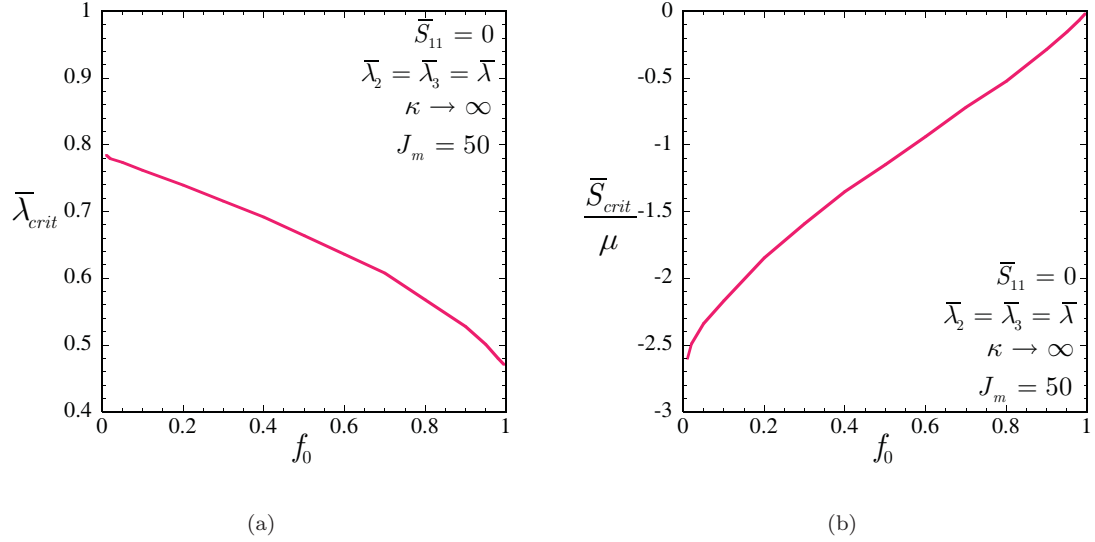


Figure 5.7: Biaxial tension and compression ($\bar{\lambda}_2 = \bar{\lambda}_3 = \bar{\lambda}$, $\bar{S}_{11} = \partial\hat{\Phi}^I/\partial\bar{\lambda}_1 = 0$) of a porous elastomer with incompressible, Neo-Hookean matrix phase with various values of initial porosity f_0 . (a) The critical stretch $\bar{\lambda}_{crit}$ at which the second-order estimate (5.16) loses strong ellipticity as a function of initial porosity f_0 . (b) The corresponding critical stress \bar{S}_{crit}/μ .

the critical stretch, $\bar{\lambda}_{crit}$, and (b) the normalized critical stress, \bar{S}_{crit}/μ , at which the second-order estimate (5.16) loses strong ellipticity under biaxial compression as a function of the initial porosity f_0 . Fig. 5.7(a) illustrates that the stability of the porous material improves in strain space with increasing initial porosity, in accord with the results found for hydrostatic compression (see Fig. 5.3(a)). Notice, however, that the stretches $\bar{\lambda}_{crit}$ in Fig. 5.7(a) are significantly smaller than those in Fig. 5.3(a). In particular, it is observed that $\bar{\lambda}_{crit} \rightarrow \bar{\lambda}_{crit}^0$ with $\bar{\lambda}_{crit}^0 \approx 0.78$ as $f_0 \rightarrow 0$ for biaxial compression, whereas, for hydrostatic compression, $\bar{\lambda}_{crit} \rightarrow 1$ as $f_0 \rightarrow 0$. This implies that for biaxial compression $\bar{\lambda}_{crit}$ has a discontinuity at $f_0 = 0$, since for this type of loading $\bar{\lambda}_{crit} = 0$ at $f_0 = 0$ (due to the fact that the matrix phase is strongly elliptic for all isochoric deformations). Physically, this result suggests that the addition of even a small proportion of pores can have a dramatic effect on the overall stability of porous elastomers with incompressible, strongly elliptic matrix phases under certain type of finite deformations. In contrast to the results found for hydrostatic compression, Fig. 5.7(b) shows that, in stress space, the porous elastomer becomes more unstable with increasing initial porosity throughout the entire physical domain $0 < f_0 < 1$. That is, $|\bar{S}_{crit}|$ decreases *monotonically* with increasing f_0 .

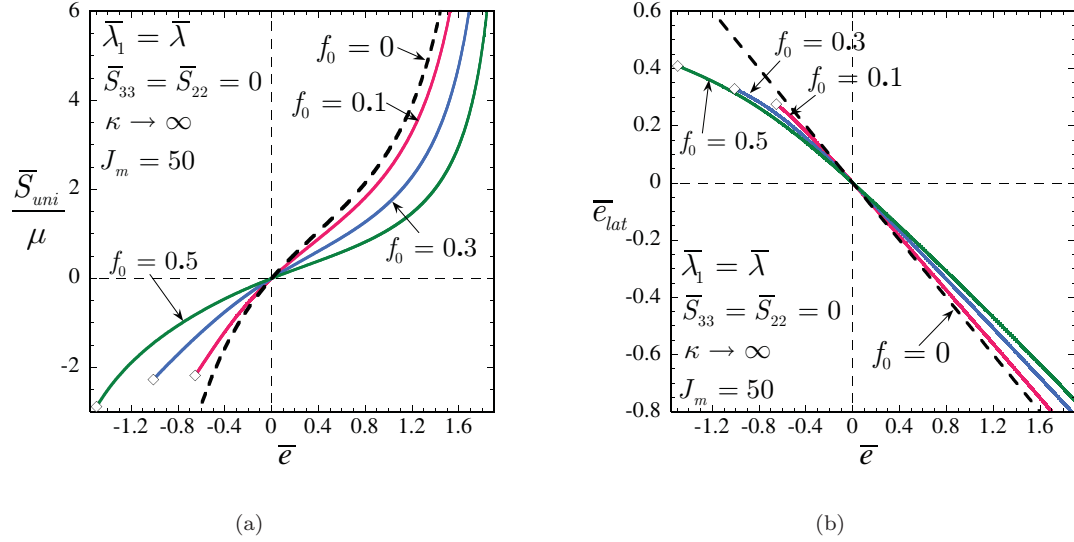


Figure 5.8: Effective response, as predicted by the second-order estimate (5.16), of a porous rubber subjected to uniaxial tension and compression ($\bar{\lambda}_1 = \bar{\lambda}$, $\bar{S}_{22} = \partial\hat{\Phi}^I/\partial\bar{\lambda}_2 = \bar{S}_{33} = \partial\hat{\Phi}^I/\partial\bar{\lambda}_3 = 0$), as a function of the logarithmic strain $\bar{e} = \ln \bar{\lambda}$. The results correspond to a material with incompressible, Gent matrix phase with $J_m = 50$ and various values of initial porosity f_0 . (a) The normalized macroscopic stress $\bar{S}_{uni}/\mu = \mu^{-1}\partial\hat{\Phi}^I/\partial\bar{\lambda}_1$. (b) The lateral strain $\bar{e}_{lat} = \ln \bar{\lambda}_2 = \ln \bar{\lambda}_3$.

Uniaxial tension/compression

Figure 5.8 shows the SOE predictions for the effective response of a porous elastomer with incompressible Gent matrix phase under uniaxial loading ($\bar{\lambda}_1 = \bar{\lambda}$, $\bar{S}_{22} = \partial\hat{\Phi}^I/\partial\bar{\lambda}_2 = \bar{S}_{33} = \partial\hat{\Phi}^I/\partial\bar{\lambda}_3 = 0$). Results are depicted for a matrix lock-up parameter of $J_m = 50$ and initial porosities of $f_0 = 0, 10, 30$ and 50% as a function of the logarithmic strain $\bar{e} = \ln \bar{\lambda}$. Part (a) shows the normalized macroscopic “uniaxial” stress $\bar{S}_{uni}/\mu = \mu^{-1}\partial\hat{\Phi}^I/\partial\bar{\lambda}_1$, and part (b), the associated “lateral” strain $\bar{e}_{lat} = \ln \bar{\lambda}_2 = \ln \bar{\lambda}_3$. A glance at Fig. 5.8 suffices to remark its many similarities with Fig. 5.4 (for biaxial loading). Indeed, Fig. 5.8 shows that the effective stress-strain behavior of the porous elastomer is softer for higher values of the initial porosity f_0 and exhibits a very substantial stiffening for tension as well as compression. Additionally, the volume of the porous elastomer increases under uniaxial tension and decreases under uniaxial compression. That is, in the present context, $\ln(\det \bar{\mathbf{F}}) = 2\bar{e}_{lat} + \bar{e} > 0$ for $\bar{e} > 0$ and $2\bar{e}_{lat} + \bar{e} < 0$ for $\bar{e} < 0$. There are, however, two major differences worth of notice. First, we remark that while for biaxial tension (compression) the underlying pores evolve into oblate (prolate) spheroids, the opposite is true for uniaxial tension (compression). This has an important effect on the overall behavior and, especially, on the stability

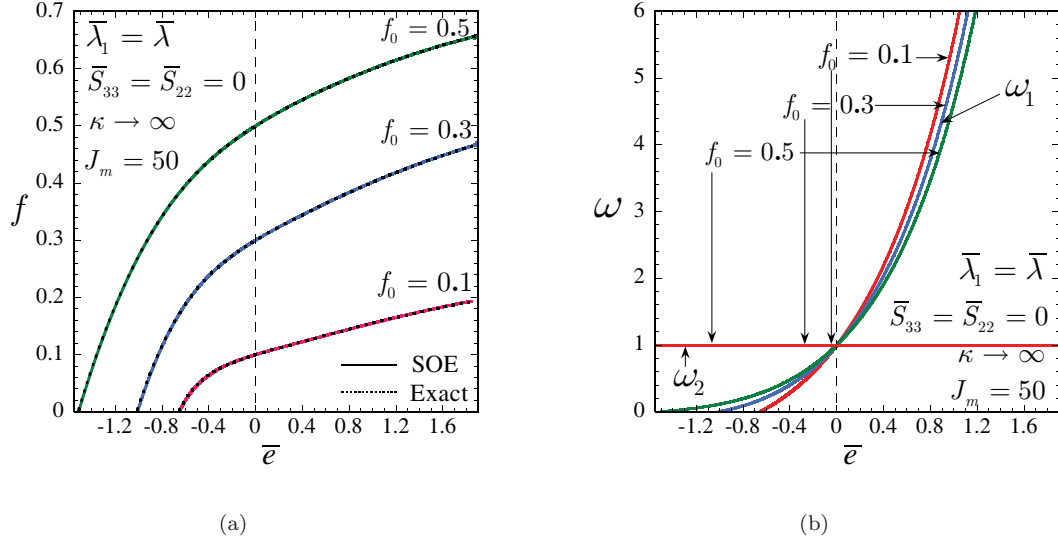


Figure 5.9: Uniaxial tension and compression ($\bar{\lambda}_1 = \bar{\lambda}$, $\bar{S}_{22} = \partial\hat{\Phi}^I/\partial\bar{\lambda}_2 = \bar{S}_{33} = \partial\hat{\Phi}^I/\partial\bar{\lambda}_3 = 0$) of a porous elastomer with incompressible, Gent matrix phase with $J_m = 50$ and various values of initial porosity f_0 . (a) The evolution of porosity f , as predicted by the second-order estimate (5.16), compared with the exact result. (b) The evolution of the aspect ratios ω_1 and ω_2 as predicted by second-order estimate (5.16).

of the porous elastomer. In this connection, we note that, as opposed to biaxial compression, no loss of strong ellipticity takes place under uniaxial compression. In fact, the SOE predicts that for uniaxial compression the porosity will vanish at some finite stretch (denoted with the symbol “ \diamond ” in the plots) before any macroscopic instabilities take place.

For completeness, Fig. 5.9 illustrates the evolution of the relevant microstructural variables associated with the results shown in Fig. 5.8. Part (a) shows the evolution of the porosity f and part (b), the evolution of the aspect ratios ω_1 and ω_2 , as a function of the logarithmic strain $\bar{e} = \ln \bar{\lambda}$. First, note that the porosity f , as predicted by the second-order estimate (5.16), is in excellent agreement with the “exact” result (as computed from expression (5.21) evaluated at the $\det \bar{\mathbf{F}}$ predicted by (5.16)). Note further that the aspect ratio ω_2 is identically equal to one throughout the entire loading process, as a consequence of the resulting macroscopic uniaxial state of deformation (*i.e.*, $\bar{\lambda}_3 = \bar{\lambda}_2$ since $\bar{S}_{33} = \bar{S}_{22}$). On the other hand, $\omega_1 > (<)1$ for $\bar{e} > (<)0$, so that the initially spherical pores deform on average into prolate (oblate) spheroids under uniaxial tension (compression), corroborating the comments in the previous paragraph. In summary, the above-presented results for uniaxial loading induce similar geometric stiffening/softening effects to those found for biaxial loading. Namely, under uniaxial tension, the increase of porosity induces

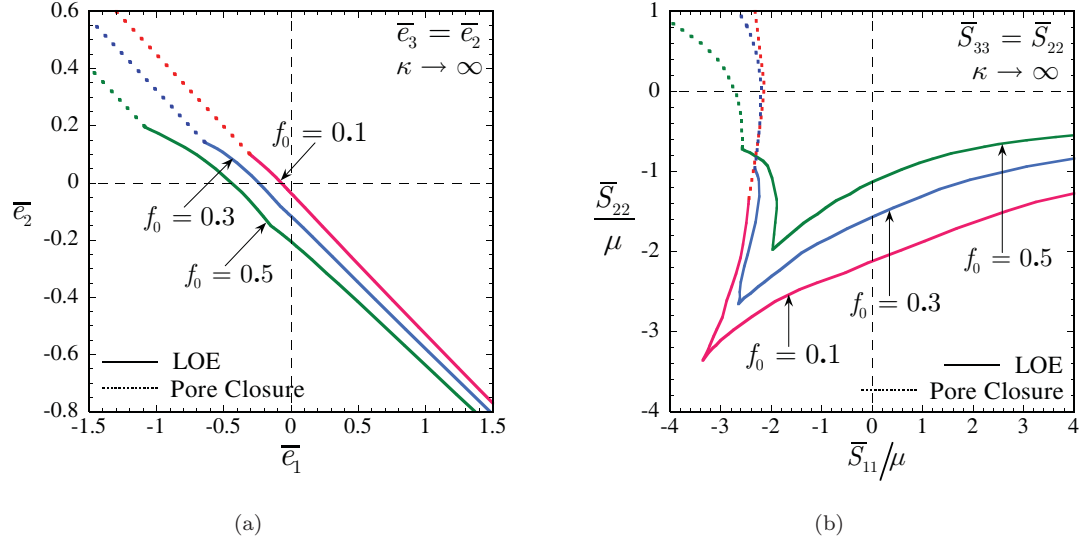


Figure 5.10: Macroscopic onset-of-failure surface, as determined by the loss of strong ellipticity of the second-order estimate (5.16), for a porous elastomer with incompressible, Neo-Hookean matrix phase and various values of initial porosity. Part (a) illustrates the results for applied axisymmetric deformations ($\bar{e}_3 = \bar{e}_2$) in the \bar{e}_1 - \bar{e}_2 -plane in strain space. Part (b) shows corresponding results for applied axisymmetric stresses ($\bar{S}_{33} = \bar{S}_{22}$) in the \bar{S}_{11} - \bar{S}_{22} -plane in dimensionless stress space.

geometric softening and the pore ovalization, stiffening. Conversely, under uniaxial compression, the decrease of porosity induces geometric stiffening and the pore ovalization, softening.

Macroscopic failure surfaces

Figure 5.10 illustrates the macroscopic failure surfaces, as determined by the loss of strong ellipticity of the second-order estimate (5.16) (denoted by LOE in the plots). Results are given for a porous elastomer with incompressible Neo-Hookean matrix phase and initial porosities of $f_0 = 10, 30$, and 50%. Part (a) shows failure surfaces for applied axisymmetric deformations ($\bar{e}_3 = \bar{e}_2$) in strain space, and part (b), for applied axisymmetric stresses ($\bar{S}_{33} = \bar{S}_{22}$) in stress space. For completeness, the boundary at which the porosity vanishes has also been included (dotted lines) in Fig. 5.10. Note that once the pore-closure boundary is reached, no further compressive (with $\bar{J} < 1$) deformation is possible.

Before proceeding with the bulk of the discussion, it is helpful to identify in Fig. 5.10 the loading paths considered in the three previous subsections. Thus, we note that the line $\bar{e}_2 = \bar{e}_1$ in Fig. 5.10(a), as well as the line $\bar{S}_{22} = \bar{S}_{11}$ in Fig. 5.10(b), correspond precisely to hydrostatic

loading, which was considered in detail in Figs. 5.1–5.3. Moreover, the lines $\bar{S}_{11} = 0$ and $\bar{S}_{22} = 0$ in Fig. 5.10(b), correspond to biaxial and uniaxial tension/compression, respectively. These loading paths were considered in detail in Figs. 5.4–5.7 and Figs. 5.8–5.9.

A key feature to remark from Fig. 5.10(a) is that the loci of points at which loss of strong ellipticity occurs satisfy the condition: $\ln(\det \bar{\mathbf{F}}) = \bar{e}_1 + \bar{e}_2 + \bar{e}_3 = \bar{e}_1 + 2\bar{e}_2 < 0$. Thus, according to the second-order estimate (5.16), loss of strong ellipticity occurs necessarily under volume-reducing deformations. Or, in other words, the development of macroscopic instabilities may take place exclusively at “sufficiently” large *compressive* deformations. Another interesting point that deserves further comment is the trend followed by the onset of loss of strong ellipticity as a function of the initial porosity f_0 . In effect, the porous elastomer becomes more stable—in the sense that it loses strong ellipticity at larger strains—with increasing initial porosity. Recall that this behavior has already been observed in the context of hydrostatic and biaxial compression (see Fig. 5.3(a) and Fig. 5.7(a)). Fig. 5.10(a) illustrates, thus, that this counterintuitive trend applies more broadly to general axisymmetric loading conditions.

In parallel with Fig. 5.10(a), Fig. 5.10(b) shows that a necessary condition for loss of strong ellipticity to occur is the existence of a *compressive* component in the state of stress. Fig. 5.10(b) also illustrates that the porous elastomer becomes more unstable—in the sense that it loses strong ellipticity at smaller stresses—with increasing initial porosity f_0 . This trend is in contrast to that one observed in strain space. The explanation for such disparity follows that one given in the context of Fig. 5.3 (for hydrostatic compression). That is, given the drastically softer stress-strain relations of the porous elastomer for larger values of initial porosity, the strains required to reach the critical stresses happen to be larger for larger initial porosities.

Figure 5.11 provides analogous results to those shown in Fig. 5.10 for a porous elastomer with an initial porosity of $f_0 = 30\%$ and Neo-Hookean matrix phase with compressibility ratios $\kappa/\mu = 10$ and $\kappa \rightarrow \infty$. Part (a) shows the macroscopic failure surfaces for applied axisymmetric deformations ($\bar{e}_3 = \bar{e}_2$) in strain space, and part (b), for applied axisymmetric stresses ($\bar{S}_{33} = \bar{S}_{22}$) in stress space. The main observation that can be made from Fig. 5.11 is that the effect of compressibility of the matrix phase, as measured by the bulk modulus κ , on the overall stability of porous elastomers is opposite to that of the initial porosity f_0 . Namely, in strain space, the porous elastomer loses strong ellipticity at smaller strains for larger bulk modulus. On the other hand, in stress space, the porous elastomer loses strong ellipticity at larger stresses for larger bulk modulus.

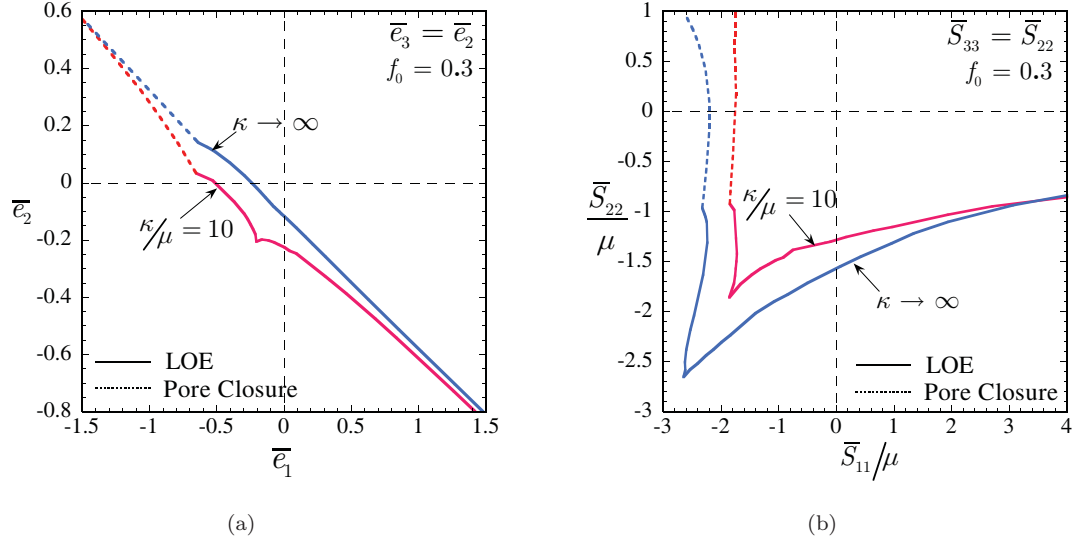


Figure 5.11: Macroscopic onset-of-failure surface, as determined by the loss of strong ellipticity of the second-order estimates (5.13) and (5.16), for a porous elastomer with Neo-Hookean matrix phase and two values of compressibility ratio of the matrix phase. Part (a) illustrates the results for applied axisymmetric deformations ($\bar{e}_3 = \bar{e}_2$) in the \bar{e}_1 - \bar{e}_2 -plane in strain space. Part (b) shows corresponding results for applied axisymmetric stresses ($\bar{S}_{33} = \bar{S}_{22}$) in the \bar{S}_{11} - \bar{S}_{22} -plane in dimensionless stress space.

In this regard, we notice that by increasing the bulk modulus of the matrix phase we are effectively *constraining* the matrix material to deform isochorically. This results in an overall stiffening of the matrix phase, and therefore, also of the porous elastomer. In turn, the critical stresses at which the material loses strong ellipticity increase, while the corresponding critical strains decrease, with increasing κ .

Finally, it is appropriate to mention that the Neo-Hookean results shown in Figs. 5.10 and 5.11 are representative of results for Gent porous elastomers with any value of the material lock-up parameter J_m . Indeed, according to the SOE predictions, the lock-up parameter J_m has virtually no effect on the onset of loss of strong ellipticity. This is consistent with the fact that loss of strong ellipticity occurs mostly at compressive states of deformation, at which the effect of J_m is not “felt”.

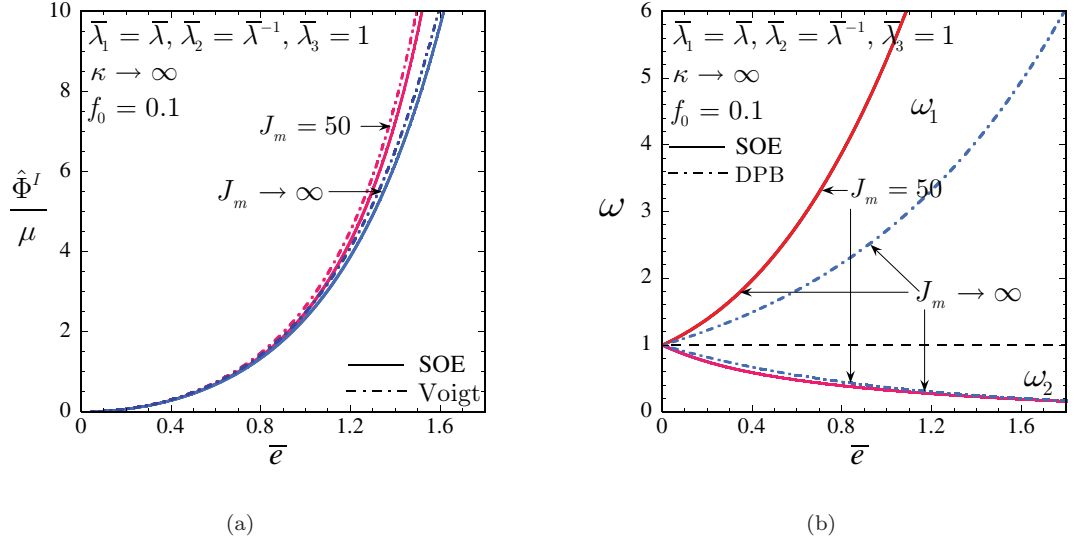


Figure 5.12: Effective response of a porous rubber with an incompressible, Gent matrix phase subjected to pure shear ($\bar{\lambda}_1 = \bar{\lambda}$, $\bar{\lambda}_2 = \bar{\lambda}^{-1}$, $\bar{\lambda}_3 = 1$), as a function of the logarithmic strain $\bar{e} = \ln \bar{\lambda}$. (a) The normalized effective stored-energy function $\hat{\Phi}^I/\mu$ as predicted by the second-order estimate (5.16) and the Voigt bound (5.7). (b) The evolution of the aspect ratios of the underlying pores, ω_1 and ω_2 . Part (b) also includes the aspect ratios as predicted by the DPB model (5.12).

5.2.2 Plane-strain loadings

Pure shear

In Figure 5.12, SOE predictions are given for the pure shear loading ($\bar{\lambda}_1 = \bar{\lambda}$, $\bar{\lambda}_2 = \bar{\lambda}^{-1}$, $\bar{\lambda}_3 = 1$) of a porous elastomer with incompressible Gent matrix phases. Results are shown for an initial porosity of $f_0 = 10\%$ and matrix lock-up parameters of $J_m = 50$ and $J_m \rightarrow \infty$, as a function of the logarithmic strain $\bar{e} = \ln \bar{\lambda}$. First, we note from Fig. 5.12(a) that the SOE predictions satisfy the rigorous Voigt upper bound (5.7). Recall that this bound is only helpful for isochoric deformations (*i.e.*, deformations with $\det \bar{\mathbf{F}} = 1$), like the one considered in this subsection, since it becomes unbounded otherwise. Recall as well that the DPB model (5.12) coincides exactly with the Voigt bound (5.7) in this case. In connection with the evolution of the microstructure, it should be remarked that the porosity does not evolve under pure shear deformations (*i.e.*, $f = f_0$). On the other hand, as shown by Fig. 5.12(b), the aspect ratios, ω_1 and ω_2 , of the underlying pores do evolve substantially with increasing strain. In particular ω_1 increases while ω_2 decreases with increasing \bar{e} . It is also interesting to observe that the evolution of the aspect ratios appears to be practically insensitive to the value of the matrix lock-up parameter J_m . For comparison purposes,

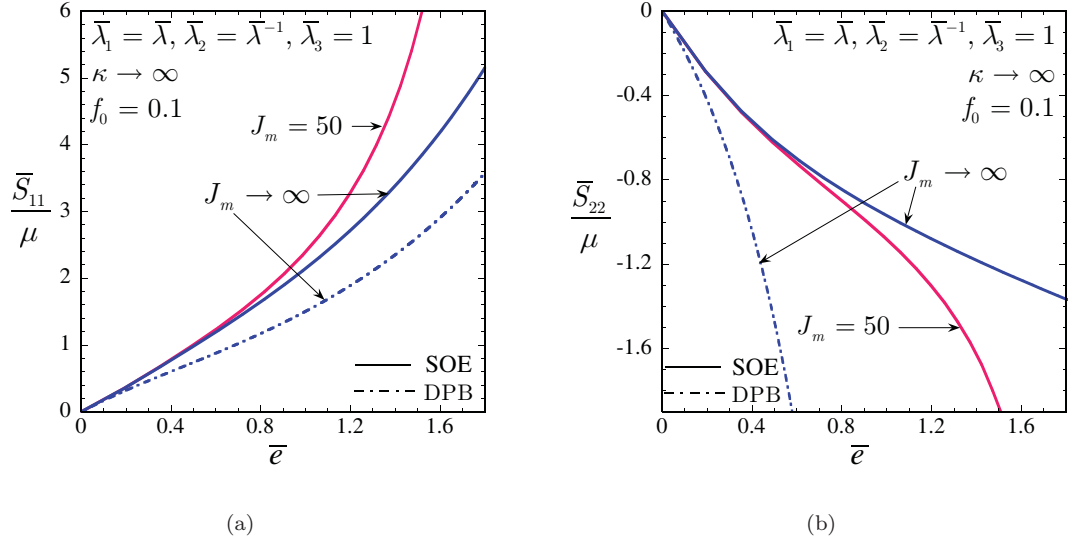


Figure 5.13: Effective response of a porous rubber with an incompressible Gent matrix phase subjected to pure shear ($\bar{\lambda}_1 = \bar{\lambda}$, $\bar{\lambda}_2 = \bar{\lambda}^{-1}$, $\bar{\lambda}_3 = 1$), as a function of the logarithmic strain $\bar{e} = \ln \bar{\lambda}$. (a) The normalized macroscopic stress \bar{S}_{11}/μ . (b) The normalized macroscopic stress \bar{S}_{22}/μ .

we have included in Fig. 5.12(b) the evolution of the aspect ratios ω_1 and ω_2 as predicted by the DPB model (5.12) for the case of $J_m \rightarrow \infty$. In this regard, it is noticed that the DPB result for ω_2 is very similar to the corresponding SOE prediction. On the other hand, the aspect ratio ω_1 , as computed from the DPB model, is largely below the SOE result. This has the direct implication that, in the direction of the applied tensile stretch $\bar{\lambda}_1 = \bar{\lambda}$, the DPB model should exhibit a weaker geometric stiffening—due to pore ovalization—than the SOE. By the same token, it should also exhibit a stronger geometric stiffening in the direction of the applied compressive stretch $\bar{\lambda}_2 = \bar{\lambda}^{-1}$. As a final point, it should be remarked that no loss of ellipticity is observed for any level of pure shear deformation from any of the models.

Figure 5.13 provides corresponding results for the normalized stress components: (a) \bar{S}_{11}/μ and (b) \bar{S}_{22}/μ as a function of the logarithmic strain $\bar{e} = \ln \bar{\lambda}$. SOE predictions are given for values of the matrix lock-up parameter of $J_m = 50$ and $J_m \rightarrow \infty$. DPB predictions are given only for $J_m \rightarrow \infty$. Fig. 5.13 clearly shows that the material parameter J_m has a strong effect on the behavior of the porous elastomer. This is not surprising since the response of the matrix phase is itself also highly dependent on J_m . Furthermore, we notice that both stress components exhibit substantial stiffening with the applied stretch. In this regard, we remark that (for $J_m \rightarrow \infty$) the

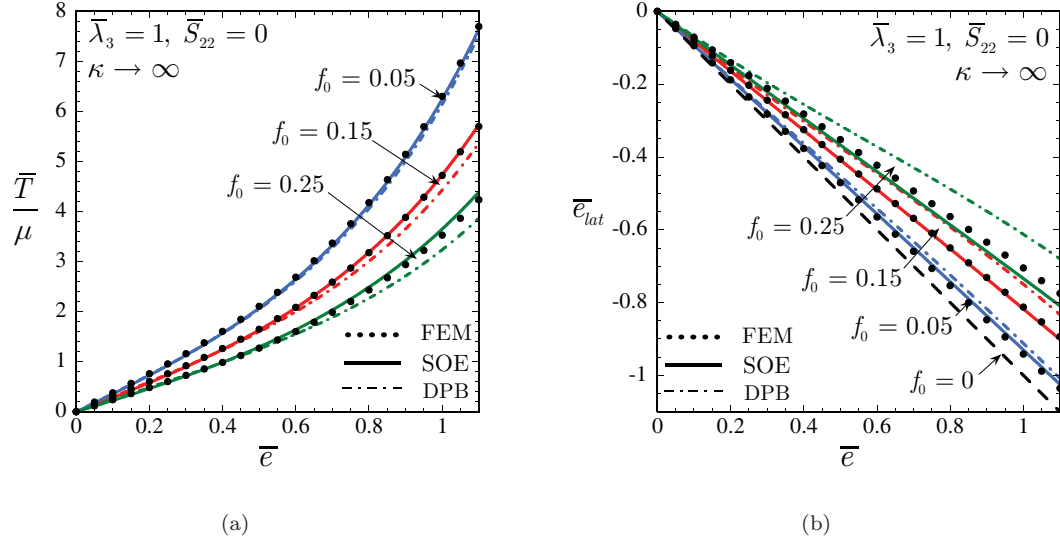


Figure 5.14: Effective response of a porous rubber subjected to plane-strain tension ($\bar{\lambda}_1 = \bar{\lambda} \geq 1$, $\bar{S}_{22} = \partial\hat{\Phi}^I/\partial\bar{\lambda}_2 = 0$, $\bar{\lambda}_3 = 1$), as a function of the logarithmic strain $\bar{e} = \ln\bar{\lambda}$. Comparisons between the SOE predictions, the Danielsson-Parks-Boyce model (DPB), and FEM results for a material with incompressible, Neo-Hookean matrix phase and various values of initial porosity f_0 . (a) The normalized macroscopic Cauchy stress $\bar{T}/\mu = \mu^{-1}(1/\bar{\lambda}_2)\partial\hat{\Phi}^I/\partial\bar{\lambda}_1$. (b) The lateral strain $\bar{e}_{lat} = \ln\bar{\lambda}_2$.

SOE prediction for the component \bar{S}_{11}/μ is much stiffer than the corresponding DPB estimate, while the opposite is true for the component \bar{S}_{22}/μ . This behavior is entirely consistent with the observations made in Fig. 5.12(b), where it was concluded that the pore ovalization predicted by the DPB model induces a stronger geometric softening (stiffening) in the direction of the tensile (compressive) stretch $\bar{\lambda}_1 = \bar{\lambda}$ ($\bar{\lambda}_2 = \bar{\lambda}^{-1}$) than the one predicted by the SOE.

In-plane uniaxial tension/compression

Figure 5.14 provides results for the overall response of a porous elastomer with incompressible Neo-Hookean matrix phase under plane-strain *tension* ($\bar{\lambda}_1 = \bar{\lambda} \geq 1$, $\bar{\lambda}_3 = 1$, $\bar{S}_{22} = \partial\hat{\Phi}^I/\partial\bar{\lambda}_2 = 0$). Results are shown for the second-order (5.16) and the DPB (5.12) estimates, and Finite Element (FEM) calculations (from Danielsson *et al.*, 2004) for initial porosities of 5, 15, and 25% as a function of the logarithmic strain $\bar{e} = \ln(\bar{\lambda})$. Part (a) shows the normalized macroscopic Cauchy stress $\bar{T}/\mu = \mu^{-1}(1/\bar{\lambda}_2)\partial\hat{\Phi}^I/\partial\bar{\lambda}_1$, and part (b), the associated lateral strain $\bar{e}_{lat} = \ln\bar{\lambda}_2$.

Before proceeding with the discussion of Fig. 5.14, it is necessary to make the following clarifications. First, the FEM results illustrated in Fig. 5.14 correspond to the effective response of

a multi-void cell model consisting of a random assembly of cubes that are either solid or contain an initially spherical void. (For further details on the cell model see Danielsson *et al.*, 2004.) The microstructure of this multi-void cell model is thus *monodisperse*, in contrast to the polydisperse microgeometry assumed by the SOE and the DPB models. Nevertheless, for the small and moderate values of porosity considered in the results shown in Fig. 5.14, the dispersion in the size of pores is not expected to be of critical importance on the overall response of the material. Second, it should be mentioned that the Cauchy stress $\bar{T}/\mu = \mu^{-1}(1/\bar{\lambda}_2)\partial\widehat{\Phi}^I/\partial\bar{\lambda}_1$, as opposed to the first Piola-Kirchhoff stress $\bar{S}/\mu = \mu^{-1}\partial\widehat{\Phi}^I/\partial\bar{\lambda}_1$, is shown in Fig. 5.14(a) for two reasons: the FEM results were originally provided for this variable in (Danielsson *et al.*, 2004), and it brings out more clearly the differences among the two compared estimates with the FEM results.

Figure 5.14 shows that the SOE predictions are in excellent agreement with the FEM calculations. Interestingly, the DPB model delivers estimates that are in very good agreement with the numerical calculations for the case of $f_0 = 5\%$, but, for larger initial porosities, the agreement between the DPB predictions and the FEM (and hence the SOE) results deteriorates noticeably, especially for larger initial porosities f_0 . It is also noted that the stress-strain curves in Fig. 5.14(a) exhibit a pronounced stiffening with increasing strain. With regard to Fig. 5.14(b), we notice that all three estimates indicate that the volume of the porous elastomer increases when the material is subjected to plane-strain tension, that is, $\bar{e} + \bar{e}_{lat} > 0$. (The line $\bar{e} + \bar{e}_{lat} = 0$, which corresponds to $f_0 = 0$, has been included in Fig. 5.14(b) for reference purposes.) Again, since the elastomeric matrix phase is incompressible, this has the direct implication that the porosity increases with the applied deformation.

Figure 5.15 provides analogous results to those shown in Fig. 5.14 for plane-strain *compression* ($\bar{\lambda}_1 = \bar{\lambda} \leq 1$, $\bar{\lambda}_3 = 1$, $\bar{S}_{22} = \partial\widehat{\Phi}^I/\partial\bar{\lambda}_2 = 0$). Unfortunately, no FEM results were reported in (Danielsson *et al.*, 2004) for this loading, and hence, attention is confined to the SOE and the DPB predictions. Fig. 5.15(a) shows that the predictions from the DPB model are much stiffer than the corresponding SOE results. This disparity, as it will be explained in more detail in the discussion of Fig. 5.16, is due to different predictions of the evolution of microstructure. Next, note that both models predict that the porous elastomer remains stable for all applied plane-strain compression. However, while the SOE predicts that the porosity will vanish at some finite compressive strain (indicated with the symbol “ \diamond ” in the plots), the DPB model predicts that zero porosity is never reached under plane-strain compression. We conclude by remarking from

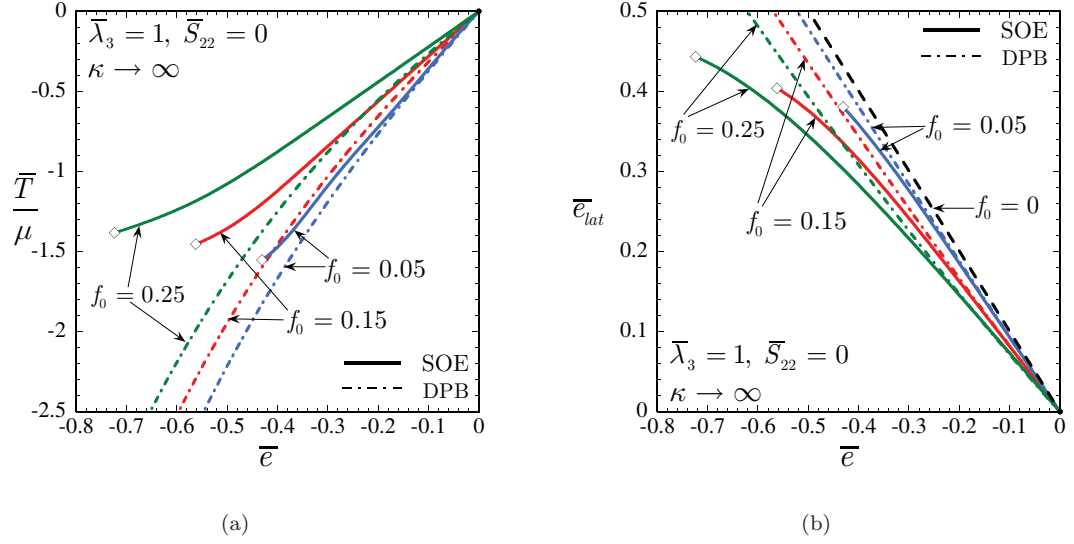


Figure 5.15: Effective response of a porous rubber subjected to plane-strain compression ($\bar{\lambda}_1 = \bar{\lambda} \leq 1$, $\bar{S}_{22} = \partial\hat{\Phi}^I/\partial\bar{\lambda}_2 = 0$, $\bar{\lambda}_3 = 1$), as a function of the logarithmic strain $\bar{e} = \ln \bar{\lambda}$. Comparisons between the SOE and the Danielsson-Parks-Boyce (DPB) predictions for a material with incompressible, Neo-Hookean matrix phase and various values of initial porosity f_0 . (a) The normalized macroscopic Cauchy stress $\bar{T}/\mu = \mu^{-1}(1/\bar{\lambda}_2)\partial\hat{\Phi}^I/\partial\bar{\lambda}_1$. (b) The lateral strain $\bar{e}_{lat} = \ln \bar{\lambda}_2$.

Fig. 5.15(b) that the volume of the porous elastomer decreases with the applied plane-strain compression, that is, $\bar{e} + \bar{e}_{lat} < 0$. (Similar to Fig. 5.14(b), the line $\bar{e} + \bar{e}_{lat} = 0$, denoting the response of the incompressible elastomeric matrix, has been included in Fig. 5.15(b) for references purposes.)

Figure 5.16 provides plots associated with the results shown in Fig. 5.14 and Fig. 5.15 for the effective behavior of a porous elastomer with incompressible Neo-Hookean matrix phase under plane-strain loading (*tension* and *compression*). Part (a) shows the evolution of the porosity f for initial porosities of $f_0 = 5, 15$, and 25% as a function of the applied strain $\bar{e} = \ln \bar{\lambda}$. Part (b) shows the evolution of the aspect ratios ω_1 and ω_2 for an initial porosity of $f_0 = 25\%$ as a function of the applied strain $\bar{e} = \ln \bar{\lambda}$. Fig. 5.16(a) shows that while the SOE predictions for the evolution of the porosity under plane-strain tension are in good agreement with the FEM calculations, the DPB predictions deviate significantly. Moreover, Fig. 5.16(a) illustrates explicitly the fact already revealed within the discussion of Fig. 5.14(b) and Fig. 5.15(b) that the porosity increases for plane-strain tension and decreases for plane-strain compression. In this regard, we note that the porosity predicted by the DPB model is always larger than the one predicted by the second-order

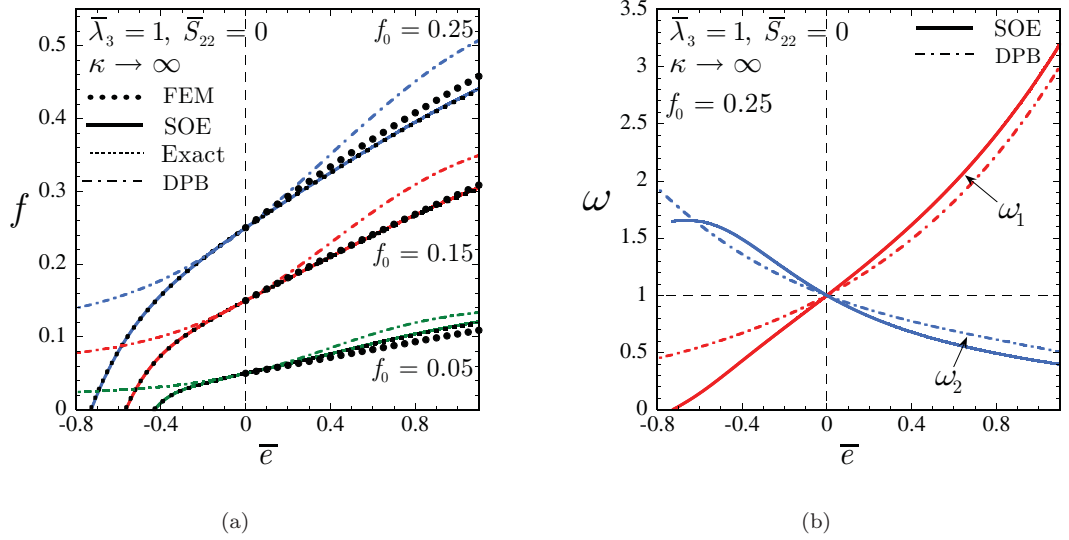


Figure 5.16: Plane-strain tension and compression ($\bar{\lambda}_1 = \bar{\lambda}$, $\bar{S}_{22} = \partial \hat{\Phi}^I / \partial \bar{\lambda}_2 = 0$, $\bar{\lambda}_3 = 1$) of a porous elastomer with incompressible, Neo-Hookean matrix phase with various values of initial porosity f_0 . Comparisons between the SOE and the Danielsson-Parks-Boyce (DPB) predictions for: (a) the evolution of porosity f , and (b) the evolution of the aspect ratios ω_1 and ω_2 .

estimate (5.16), which entails that for plane-strain tension ($\bar{e} > 0$) the DPB model predicts a larger geometric softening due to changes in porosity than the SOE, and, by the same token, a weaker geometric stiffening for plane-strain compression ($\bar{e} < 0$). Furthermore, as already remarked in Fig. 5.15, it is seen that under plane-strain compression the DPB porosity does not vanish at a finite strain as the SOE predicts, but instead, reaches a horizontal asymptote. To conclude with Fig. 5.16(a), we remark that the evolution of the porosity f , as determined from the second-order estimate (5.16), is in excellent agreement with the “exact” result, as computed from expression (5.21) (evaluated at the $\det \bar{\mathbf{F}}$ predicted by (5.16)). Turning now to Fig. 5.16(b), we notice that the aspect ratio ω_1 increases while ω_2 decreases for plane-strain tension. The opposite trend is observed for plane-strain compression. We also recognize that while the DPB predictions are similar to the SOE results for tension, they deviate significantly for compression. In this connection, note that the DPB prediction for ω_1 under plane-strain compression is largely above the corresponding SOE result, which is seen to vanish at some finite strain. In view of the fact that the decrease of ω_1 induces geometric softening in the present context, this strong disparity contributes to explain why the DPB predictions for the stress-strain relations in Fig. 5.15(a) are stiffer than the corresponding SOE results.

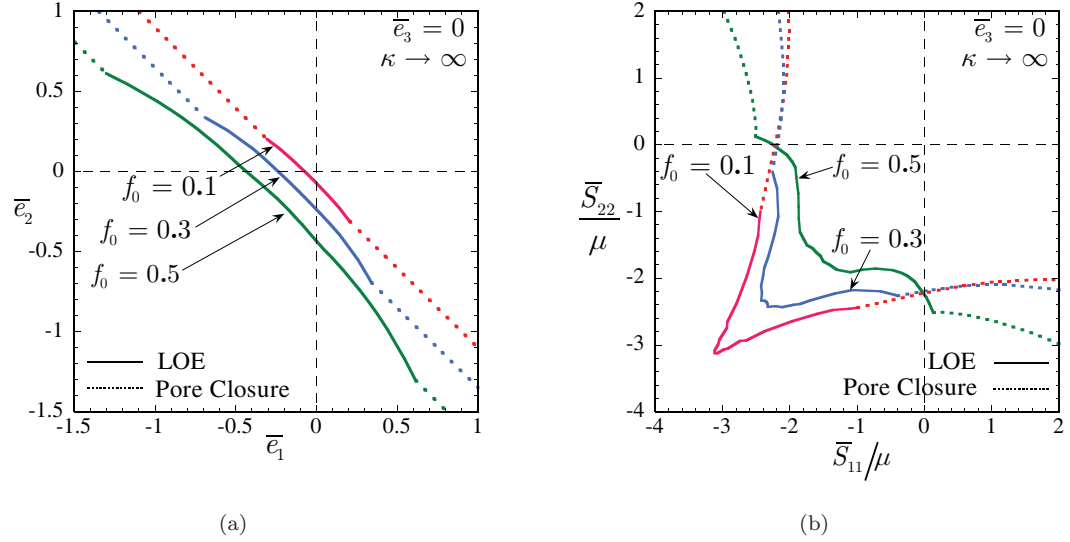


Figure 5.17: Macroscopic onset-of-failure surface, as determined by the loss of strong ellipticity of the second-order estimate (5.16), for a porous elastomer with incompressible, Neo-Hookean matrix phase and various values of initial porosity under plane-strain loading ($\bar{e}_3 = 0$). (a) Failure surface in strain space. (b) The corresponding failure surface in dimensionless stress space.

Macroscopic failure surfaces

Figure 5.17 shows the macroscopic failure surfaces, as determined by the loss of strong ellipticity of the second-order estimate (5.16), for a porous elastomer with incompressible, Neo-Hookean matrix phase and initial porosities of $f_0 = 10, 30$ and 50% under plane-strain loading ($\bar{e}_3 = 0$). Part (a) shows the results in strain space, and part (b), in stress space. For completeness, the boundary at which the porosity vanishes has also been included in Fig. 5.17.

Similar to Fig. 5.10(a) for axisymmetric loading, Fig. 5.17(a) shows that loss of strong ellipticity can only take place for volume-reducing deformations. More specifically, in the present context, the loci of points at which loss of strong ellipticity occurs satisfy the condition: $\ln(\det \bar{\mathbf{F}}) = \bar{e}_1 + \bar{e}_2 + \bar{e}_3 = \bar{e}_1 + \bar{e}_2 < 0$. Also in accord with Fig. 5.10(a), Fig. 5.17(a) depicts that Neo-Hookean porous elastomers subjected to plane-strain loadings improve their stability in strain space with increasing initial porosity. As a final remark, it is interesting to note that the results shown in Fig. 5.10(a) are qualitatively similar to those previously found for porous elastomers with 2D random, isotropic microstructures (see Figure 7 in Lopez-Pamies and Ponte Castañeda, 2004b). However, in quantitative terms, the 3D-microstructure material is more unstable (in strain space) than the 2D one, as loss of strong ellipticity occurs at smaller strains.

Consistent with all previous results, Fig. 5.17(b) shows that a necessary condition for loss of strong ellipticity to occur is the existence of a *compressive* component in the state of stress. In fact, note that for $f_0 < 0.5$ *both* components of the stress must be compressive. In this regard, it is emphasized that the corresponding stress \bar{S}_{33} (not shown in the figure) is positive. (Recall that the results correspond to plane-strain conditions, i.e., $\bar{e}_3 = 0$.) This is in accord with the results shown in Fig. 5.13(b) for axisymmetric loading, where loss of strong ellipticity could occur at states with two components of stress being compressive (with the other component being tensile). Moreover, it is observed that in stress space the porous elastomer is more unstable for larger values of the initial porosity, in accord with preceding results. The reasons for this behavior parallel those given in the context of Fig. 5.10 (for axisymmetric loading conditions).

5.3 Concluding remarks

In this chapter, we have made use of the framework developed in Chapter 2 to generate a homogenization-based constitutive model for the finite-deformation response of *isotropic* porous elastomers with *random* microstructures. In turn, we have made use of the proposed model to generate comprehensive predictions for the stress-strain relation, the evolution of microstructure, and the onset of macroscopic instabilities in Gent porous elastomers under a wide range of loading conditions and values of initial porosity.

In accord with the 2D porous elastomers studied in Chapters 3 and 4, the predictions generated in this chapter indicate that the evolution of the underlying microstructure has a significant effect on the mechanical response of isotropic porous elastomers. In particular, it has been observed that the decrease of porosity—induced by macroscopic, volume-reducing loadings—produces *geometric stiffening* of the effective incremental response of the material in the “direction” of the applied loading. At the same time—and rather interestingly—the decrease of porosity does also lead to the *geometric softening* of the effective incremental shear response of the material. Similarly, the change in shape of the underlying pores, as measured by the their average aspect ratios, has also been identified as a geometric mechanism that can produce stiffening of the effective incremental response of the porous elastomer in some directions, and softening in others.

An important consequence of the aforementioned softening mechanisms is that the “second-order” estimates for the effective behavior of porous elastomers can lose strong ellipticity, even

in the case when the underlying matrix phase material is taken to be strongly elliptic. Thus, in this work, loss of strong ellipticity has been found to occur under sufficiently large macroscopic, *compressive* stresses and strains. In other words, according to the predictions, the onset of macroscopic instabilities—as determined by loss of strong ellipticity—for the class of porous elastomers under consideration in this chapter is driven by the applied *compressive loading*. In this connection, it is worth remarking that the recent model of Danielsson *et al.* (2004), which is based on a generalization of the earlier Voigt bound (Ogden, 1978) and Hashin’s estimate (Hashin, 1985), is strongly elliptic for all deformations, and is thus unable to capture the expected development of instabilities under compressive loading.

Finally, the results generated in this chapter have been shown to be in good agreement with exact and numerical results available from the literature for special loading conditions, and generally improve on existing models for more general loading conditions. In particular—as already stated—the new model proposed here predicts the development of macroscopic instabilities for loading conditions where such instabilities are expected to occur from numerical simulations (Michel *et al.*, 2007), as well as from physical evidence (Kinney *et al.*, 2001; Gong and Kyriakides, 2005). This is in contrast with prior homogenization- and micromechanics-based models that fail to predict the development of such instabilities. Thus, although somewhat more difficult to implement than earlier homogenization estimates and micromechanics models, which make use of simpler trial fields and micromechanical hypotheses, the second-order method could prove to become a very useful tool in the development of accurate—but still computationally tractable—models for porous, as well as for other types of elastomeric composites.

5.4 Appendix I. Second-order estimates for isotropic porous elastomers with compressible matrix phases

In this appendix, we spell out the analysis corresponding to the computation of the second-order estimate (2.69) for the effective stored-energy function \widehat{W} of porous elastomers consisting of initially spherical, polydisperse, vacuous inclusions distributed randomly and isotropically (in the undeformed configuration) in a *compressible*, isotropic matrix phase characterized by the stored-energy function (5.1).

As a result of the restriction to pure stretch loadings (5.5), the modulus \mathbf{L} defined by expression (2.66) of the matrix phase in the linear comparison composite (LCC) reduces to $\mathbf{L} = \mathbf{L}^*$, where it is recalled that \mathbf{L}^* is orthotropic and possesses, at most, 9 independent components. In this work, we introduce further constraints among the components of \mathbf{L}^* in order to reduce them to 7 independent components, denoted by the parameters ℓ_α^* ($\alpha = 1, 2, \dots, 7$). Thus, the independent principal components of \mathbf{L}^* are chosen to be $L_{1111}^* = \ell_1^*$, $L_{2222}^* = \ell_2^*$, $L_{3333}^* = \ell_3^*$, $L_{1122}^* = \ell_4^*$, $L_{1133}^* = \ell_5^*$, $L_{2233}^* = \ell_6^*$, $L_{1212}^* = \ell_7^*$, while the other non-zero components

$$\begin{aligned}
 L_{2121}^* &= L_{1313}^* = L_{3131}^* = L_{2323}^* = L_{3232}^* = \ell_7^*, \\
 L_{1221}^* &= \sqrt{(\ell_1^* - \ell_7^*)(\ell_2^* - \ell_7^*)} - \ell_4^*, \\
 L_{1331}^* &= \sqrt{(\ell_1^* - \ell_7^*)(\ell_3^* - \ell_7^*)} - \ell_5^*, \\
 L_{2332}^* &= \sqrt{(\ell_2^* - \ell_7^*)(\ell_3^* - \ell_7^*)} - \ell_6^*,
 \end{aligned} \tag{5.30}$$

are dependent. The motivation for the constraints (5.30) is twofold:⁴ (i) relations (5.30) are consistent with the tangent modulus of Neo-Hookean materials; and (ii) conditions (5.30) simplify considerably the computations involved. It should be emphasized, however, that other choices are possible in principle.

Now, using the facts that $\overline{F} = \text{diag}(\overline{\lambda}_1, \overline{\lambda}_2, \overline{\lambda}_3)$ and $\mathbf{L} = \mathbf{L}^*$, it follows from (2.70) that the average deformation gradient in the matrix phase of the LCC, needed in the computation of \widehat{W} , is of the form $\overline{F}^{(1)} = \text{diag}(\overline{\lambda}_1^{(1)}, \overline{\lambda}_2^{(1)}, \overline{\lambda}_3^{(1)})$, where the average principal stretches $\overline{\lambda}_i^{(1)}$ ($i = 1, 2, 3$) in

⁴These conditions are the 3D version of (3.6).

the matrix phase are given by:

$$\begin{aligned}
\bar{\lambda}_1^{(1)} &= \bar{\lambda}_1 - f_0 E_{1111} [2\bar{g}_I \bar{\lambda}_1 + (\bar{h}_J + \kappa(\bar{J} - 1)) \bar{\lambda}_2 \bar{\lambda}_3] \\
&\quad - f_0 E_{1122} [2\bar{g}_I \bar{\lambda}_2 + (\bar{h}_J + \kappa(\bar{J} - 1)) \bar{\lambda}_1 \bar{\lambda}_3] \\
&\quad - f_0 E_{1133} [2\bar{g}_I \bar{\lambda}_3 + (\bar{h}_J + \kappa(\bar{J} - 1)) \bar{\lambda}_1 \bar{\lambda}_2], \\
\bar{\lambda}_2^{(1)} &= \bar{\lambda}_2 - f_0 E_{1122} [2\bar{g}_I \bar{\lambda}_1 + (\bar{h}_J + \kappa(\bar{J} - 1)) \bar{\lambda}_2 \bar{\lambda}_3] \\
&\quad - f_0 E_{2222} [2\bar{g}_I \bar{\lambda}_2 + (\bar{h}_J + \kappa(\bar{J} - 1)) \bar{\lambda}_1 \bar{\lambda}_3] \\
&\quad - f_0 E_{2233} [2\bar{g}_I \bar{\lambda}_3 + (\bar{h}_J + \kappa(\bar{J} - 1)) \bar{\lambda}_1 \bar{\lambda}_2], \\
\bar{\lambda}_3^{(1)} &= \bar{\lambda}_3 - f_0 E_{1133} [2\bar{g}_I \bar{\lambda}_1 + (\bar{h}_J + \kappa(\bar{J} - 1)) \bar{\lambda}_2 \bar{\lambda}_3] \\
&\quad - f_0 E_{2233} [2\bar{g}_I \bar{\lambda}_2 + (\bar{h}_J + \kappa(\bar{J} - 1)) \bar{\lambda}_1 \bar{\lambda}_3] \\
&\quad - f_0 E_{3333} [2\bar{g}_I \bar{\lambda}_3 + (\bar{h}_J + \kappa(\bar{J} - 1)) \bar{\lambda}_1 \bar{\lambda}_2]. \tag{5.31}
\end{aligned}$$

In these expressions, it is recalled that $\mathbf{E} = (\mathbf{P}^{-1} - (1 - f_0)\mathbf{L})^{-1}$, $\bar{g}_I = g_I(\bar{I})$, and $\bar{h}_J = h_J(\bar{J})$, with $\bar{I} = \bar{\lambda}_1^2 + \bar{\lambda}_2^2 + \bar{\lambda}_3^2$, $\bar{J} = \bar{\lambda}_1 \bar{\lambda}_2 \bar{\lambda}_3$. Note that relations (5.31) provide *explicit* expressions for the non-zero components of $\bar{\mathbf{F}}^{(1)}$ in terms of the applied loading, $\bar{\mathbf{F}}$, the initial porosity, f_0 , the constitutive functions, g , h , κ , of the elastomeric matrix phase, as well as of the independent components of \mathbf{L} , *i.e.*, ℓ_α^* ($\alpha = 1, 2, \dots, 7$).

Having determined $\bar{\mathbf{F}}^{(1)}$, we proceed next to compute the variable $\hat{\mathbf{F}}^{(1)}$, also needed in the computation of \widehat{W} . By again making use of the identity $\mathbf{L} = \mathbf{L}^*$, together with conditions (5.30), equations (2.72) can be seen to reduce to 7 nonlinear, algebraic equations for 7 combinations of the components of $\hat{\mathbf{F}}^{(1)}$, namely:

$$\begin{aligned}
(\hat{F}_{11}^{(1)} - \bar{\lambda}_1)^2 + 2f_1 \hat{F}_{12}^{(1)} \hat{F}_{21}^{(1)} + 2f_2 \hat{F}_{13}^{(1)} \hat{F}_{31}^{(1)} &= k_1, \\
(\hat{F}_{22}^{(1)} - \bar{\lambda}_2)^2 + \frac{1}{2f_1} \hat{F}_{12}^{(1)} \hat{F}_{21}^{(1)} + 2f_3 \hat{F}_{23}^{(1)} \hat{F}_{32}^{(1)} &= k_2, \\
(\hat{F}_{33}^{(1)} - \bar{\lambda}_3)^2 + \frac{1}{2f_2} \hat{F}_{13}^{(1)} \hat{F}_{31}^{(1)} + \frac{1}{2f_3} \hat{F}_{23}^{(1)} \hat{F}_{32}^{(1)} &= k_3, \\
(\hat{F}_{11}^{(1)} - \bar{\lambda}_1)(\hat{F}_{22}^{(1)} - \bar{\lambda}_2) - \hat{F}_{12}^{(1)} \hat{F}_{21}^{(1)} &= k_4/2, \\
(\hat{F}_{11}^{(1)} - \bar{\lambda}_1)(\hat{F}_{33}^{(1)} - \bar{\lambda}_3) - \hat{F}_{13}^{(1)} \hat{F}_{31}^{(1)} &= k_5/2, \\
(\hat{F}_{22}^{(1)} - \bar{\lambda}_2)(\hat{F}_{33}^{(1)} - \bar{\lambda}_3) - \hat{F}_{23}^{(1)} \hat{F}_{32}^{(1)} &= k_6/2, \\
(\hat{F}_{12}^{(1)})^2 + (\hat{F}_{21}^{(1)})^2 + (\hat{F}_{13}^{(1)})^2 + (\hat{F}_{31}^{(1)})^2 + (\hat{F}_{23}^{(1)})^2 + (\hat{F}_{32}^{(1)})^2 \\
+ 2f_4 \hat{F}_{12}^{(1)} \hat{F}_{21}^{(1)} + 2f_5 \hat{F}_{13}^{(1)} \hat{F}_{31}^{(1)} + 2f_6 \hat{F}_{23}^{(1)} \hat{F}_{32}^{(1)} &= k_7. \tag{5.32}
\end{aligned}$$

Here, $f_1 = \partial L_{1221}^*/\partial \ell_1^*$, $f_2 = \partial L_{1331}^*/\partial \ell_1^*$, $f_3 = \partial L_{2332}^*/\partial \ell_2^*$, $f_4 = \partial L_{1221}^*/\partial \ell_7^*$, $f_5 = \partial L_{1331}^*/\partial \ell_7^*$,

$f_6 = \partial L_{2332}^* / \partial \ell_7^*$, and

$$k_\alpha = \frac{1}{f_0} (\bar{\mathbf{F}} - \bar{\mathbf{F}}^{(1)}) \cdot \frac{\partial \mathbf{E}^{-1}}{\partial \ell_\alpha^*} (\bar{\mathbf{F}} - \bar{\mathbf{F}}^{(1)}) \quad (\alpha = 1, 2, \dots, 7). \quad (5.33)$$

It is not difficult to check that the nonlinear system of equations (5.32) may be solved *explicitly* to yield two distinct solutions for $x \doteq (\hat{F}_{11}^{(1)} - \bar{\lambda}_1)$, $y \doteq (\hat{F}_{22}^{(1)} - \bar{\lambda}_2)$, $z \doteq (\hat{F}_{33}^{(1)} - \bar{\lambda}_3)$ in terms of which the combinations $p_1 \doteq \hat{F}_{12}^{(1)} \hat{F}_{21}^{(1)}$, $p_2 \doteq \hat{F}_{13}^{(1)} \hat{F}_{31}^{(1)}$, $p_3 \doteq \hat{F}_{23}^{(1)} \hat{F}_{32}^{(1)}$, and $s \doteq (\hat{F}_{12}^{(1)})^2 + (\hat{F}_{21}^{(1)})^2 + (\hat{F}_{13}^{(1)})^2 + (\hat{F}_{31}^{(1)})^2 + (\hat{F}_{23}^{(1)})^2 + (\hat{F}_{32}^{(1)})^2$ may be uniquely determined. The two solutions for x , y , and z are as follows:

$$\begin{aligned} x &= (\hat{F}_{11}^{(1)} - \bar{\lambda}_1) = \pm \frac{(k_1 + f_1 k_4 + f_2 k_5) \sqrt{C_1 C_2}}{C_2 \sqrt{C_3}}, \\ y &= (\hat{F}_{22}^{(1)} - \bar{\lambda}_2) = \pm \frac{(k_4 + 4 f_1 (k_2 + f_3 k_6)) C_2}{2 \sqrt{C_1 C_2} \sqrt{C_3}}, \\ z &= (\hat{F}_{33}^{(1)} - \bar{\lambda}_3) = \pm \frac{(f_3 k_5 + f_2 (4 f_3 k_3 + k_6)) \sqrt{C_3}}{\sqrt{C_1 C_2}}, \end{aligned} \quad (5.34)$$

with $C_1 = f_2(4f_1k_2 + k_4) + 4f_1f_3^2(4f_2k_3 + k_5) + 2f_3(k_1 + f_1k_4 + f_2k_5 + 4f_1f_2k_6)$, $C_2 = f_2(4f_1k_2 + k_4 + 2f_2k_6) + 2f_3(k_1 + f_1k_4 + 2f_2(2f_2k_3 + k_5 + f_1k_6))$, $C_3 = k_1 + f_2k_5 + 2f_1(4f_2f_3k_3 + k_4 + f_3k_5 + f_2k_6) + 4f_1^2(k_2 + f_3k_6)$, where it must be emphasized that the positive (and negative) signs must be chosen to go together in the roots for x , y , and z . The corresponding final expressions for the remaining combinations read as:

$$\begin{aligned} p_1 &= xy - k_4/2, \quad p_2 = xz - k_5/2, \quad p_3 = yz - k_6/2, \quad \text{and} \\ s &= k_7 - 2(f_4p_1 + f_5p_2 + f_6p_3). \end{aligned} \quad (5.35)$$

At this point, it is important to emphasize that relations (5.34) and (5.35) provide *explicit* expressions for 7 combinations of the components of $\hat{\mathbf{F}}^{(1)}$ in terms of the applied loading $\bar{\mathbf{F}}$, the initial porosity f_0 , the constitutive functions g , h , κ of the elastomeric matrix phase, and the moduli ℓ_α^* ($\alpha = 1, 2, \dots, 7$). Note, however, that the variable $\hat{\mathbf{F}}^{(1)}$ has 9 components, so that two more relations would be needed to entirely characterize $\hat{\mathbf{F}}^{(1)}$, as it will be seen further below.

Each of the two distinct roots (5.34) for the combinations x , y , z , p_1 , p_2 , p_3 , s may be substituted in the generalized secant condition (2.65) to yield a system of 9 scalar equations for the 9 variables constituted by the 2 combinations of $\hat{\mathbf{F}}^{(1)}$: $p_4 = \hat{F}_{23}^{(1)} \hat{F}_{31}^{(1)} \hat{F}_{12}^{(1)}$, $p_5 = \hat{F}_{32}^{(1)} \hat{F}_{13}^{(1)} \hat{F}_{21}^{(1)}$, and the 7 moduli ℓ_α^* . Algebraic manipulation of the resulting system reveals that one equation is satisfied trivially,

and the remaining 8 equations may be cast in the following form:

$$\begin{aligned}
\ell_1^* x + \ell_4^* y + \ell_5^* z &= 2\hat{g}_I(x + \bar{\lambda}_1) + \left[\hat{h}_J + \kappa(\hat{J}^{(1)} - 1) \right] ((y + \bar{\lambda}_2)(z + \bar{\lambda}_3) - p_3) \\
&\quad - 2\bar{g}_I \bar{\lambda}_1 - (\bar{h}_J + \kappa(\bar{J} - 1)) \bar{\lambda}_2 \bar{\lambda}_3, \\
\ell_4^* x + \ell_2^* y + \ell_6^* z &= 2\hat{g}_I(y + \bar{\lambda}_2) + \left[\hat{h}_J + \kappa(\hat{J}^{(1)} - 1) \right] ((x + \bar{\lambda}_1)(z + \bar{\lambda}_3) - p_2) \\
&\quad - 2\bar{g}_I \bar{\lambda}_2 - (\bar{h}_J + \kappa(\bar{J} - 1)) \bar{\lambda}_1 \bar{\lambda}_3, \\
\ell_5^* x + \ell_6^* y + \ell_3^* z &= 2\hat{g}_I(z + \bar{\lambda}_3) + \left[\hat{h}_J + \kappa(\hat{J}^{(1)} - 1) \right] ((x + \bar{\lambda}_1)(y + \bar{\lambda}_2) - p_1) \\
&\quad - 2\bar{g}_I \bar{\lambda}_3 - (\bar{h}_J + \kappa(\bar{J} - 1)) \bar{\lambda}_1 \bar{\lambda}_2, \\
L_{1221}^* p_1 &= \left[\hat{h}_J + \kappa(\hat{J}^{(1)} - 1) \right] (p_4 - p_1(z + \bar{\lambda}_3)), \\
L_{1331}^* p_2 &= \left[\hat{h}_J + \kappa(\hat{J}^{(1)} - 1) \right] (p_4 - p_2(y + \bar{\lambda}_2)), \\
L_{2332}^* p_3 &= \left[\hat{h}_J + \kappa(\hat{J}^{(1)} - 1) \right] (p_4 - p_3(x + \bar{\lambda}_1)), \\
\ell_7^* &= 2\hat{g}_I,
\end{aligned} \tag{5.36}$$

and

$$p_4 = p_5. \tag{5.37}$$

In these relations, $\hat{g}_I = g_I(\hat{I}^{(1)})$, $\hat{h}_J = h_J(\hat{J}^{(1)})$, with

$$\begin{aligned}
\hat{I}^{(1)} &= \hat{\mathbf{F}}^{(1)} \cdot \hat{\mathbf{F}}^{(1)} = (x + \bar{\lambda}_1)^2 + (y + \bar{\lambda}_2)^2 + (z + \bar{\lambda}_3)^2 + s, \\
\hat{J}^{(1)} &= \det \hat{\mathbf{F}}^{(1)} \\
&= (x + \bar{\lambda}_1)(y + \bar{\lambda}_2)(z + \bar{\lambda}_3) - p_1(z + \bar{\lambda}_3) - p_2(y + \bar{\lambda}_2) - p_3(x + \bar{\lambda}_1) \\
&\quad + 2p_4,
\end{aligned} \tag{5.38}$$

and it is recalled that L_{1221}^* , L_{1331}^* , L_{2332}^* are given, respectively, by expressions (5.30)₂, (5.30)₃, (5.30)₄. The fact that one of the generalized secant equations (2.65) is satisfied trivially has the direct implication that $\hat{\mathbf{F}}^{(1)}$ enters the above equations only through 8 (instead of 9) traces, namely, x , y , z , p_1 , p_2 , p_3 , s , p_4 . As described below, these are the only traces needed in the computation of the second-order estimate (2.69) for \widehat{W} . Now, by recalling the definitions $p_1 = \hat{F}_{12}^{(1)} \hat{F}_{21}^{(1)}$, $p_2 = \hat{F}_{13}^{(1)} \hat{F}_{31}^{(1)}$, $p_3 = \hat{F}_{23}^{(1)} \hat{F}_{32}^{(1)}$, and $p_4 = \hat{F}_{23}^{(1)} \hat{F}_{31}^{(1)} \hat{F}_{12}^{(1)}$, $p_5 = \hat{F}_{32}^{(1)} \hat{F}_{13}^{(1)} \hat{F}_{21}^{(1)}$, it is seen that equation (5.37) can be solved in closed-form to render

$$p_4 = \pm \sqrt{p_1 p_2 p_3}. \tag{5.39}$$

Each of the two distinct roots (5.39) for p_4 may be substituted back in equations (5.36) to finally generate a closed system of 7 nonlinear, algebraic equations for the 7 independent moduli ℓ_α^* . These equations must be solved numerically.

Having computed from (5.36) the values of all 7 independent components of \mathbf{L} (*i.e.*, ℓ_α^*) for a given initial porosity (f_0), given material behavior (g, h, κ), and given loading ($\bar{\lambda}_1, \bar{\lambda}_2, \bar{\lambda}_3$), the values of the non-zero components of $\bar{\mathbf{F}}^{(1)}$ (*i.e.*, $\bar{\lambda}_1^{(1)}, \bar{\lambda}_2^{(1)}, \bar{\lambda}_3^{(1)}$) and the relevant combinations of $\hat{\mathbf{F}}^{(1)}$ (*i.e.*, $x, y, z, p_1, p_2, p_3, s, p_4$) may be readily determined using relations (5.31), (5.34), (5.35), and (5.39). In turn, these results can be used to compute the second-order estimate (2.69) for the effective stored-energy function \widehat{W} of isotropic porous elastomers. The final expression for \widehat{W} is given by (5.13) in the text.

In connection with these results, it is important to remark that there are 4 possible combinations of the roots introduced in (5.34) and (5.39), which lead to 4 different estimates for \widehat{W} . In the case when the bulk modulus of the material (at zero strain) κ is of the order of the shear modulus (at zero strain) μ , all 4 root combinations lead to very similar results for the effective stored-energy function \widehat{W} . However, when the bulk modulus is significantly larger than the shear modulus, *i.e.*, $\kappa \gg \mu$, the estimates produced by the 4 distinct combinations are very different. In fact, for $\kappa \gg \mu$, it will be shown in the next appendix that only one root combination generates physically meaningful estimates that are superior to the other three possibilities.

5.5 Appendix II. Second-order estimates for isotropic porous elastomers with incompressible matrix phases

In this appendix, we outline the derivation of the second-order estimate (2.69) for the effective stored-energy function \widehat{W}^I of porous elastomers consisting of initially spherical, polydisperse, vacuum inclusions distributed randomly and isotropically (in the undeformed configuration) in an *incompressible* matrix phase (5.1) with $\kappa = \infty$.

In the approach that follows, we start out with the results presented in Appendix I for the second-order estimate (5.13) for porous elastomers with *compressible* matrix phases and carry out the asymptotic analysis corresponding to the incompressible limit $\kappa \rightarrow \infty$. In this context, it is important to realize that 2 root combinations among the 4 possible ones described in Appendix I lead to estimates for \widehat{W} that become unbounded in the limit as $\kappa \rightarrow \infty$. More precisely, for $\bar{J} > 1$

($\bar{J} < 1$) the “positive” (+) (“negative” (-)) root in (5.34) results in estimates for \widehat{W} that blow up as $\kappa \rightarrow \infty$, regardless of the choice of roots for p_4 in expression (5.39). (For $\bar{J} = 1$ the asymptotic behavior of the roots is different and it will be addressed below.) These estimates suggest that a porous elastomer with an incompressible matrix phase would be itself incompressible, which is in contradiction with experimental evidence. Moreover, the 2 estimates associated with each of the roots in (5.39) for \widehat{W} that remain finite in the limit of incompressibility of the matrix phase are considerably different, in general. In order to discern which one of them is the better estimate, we make contact with the evolution of the microstructure. First, we recall that the evolution of porosity in porous elastomers with incompressible matrix phases can be computed *exactly* and the result is given by (5.21) in the text. In this regard, we note that the evolution of porosity associated with the 2 above finite estimates can be shown to be *exact* up to second order in the strain (*i.e.*, up to $(\bar{\lambda}_i - 1)^2$). However, for larger deformations, the porosities associated with these 2 roots differ significantly from each other with the choice $p_4 = \text{sign} \left((\bar{\lambda}_1^{(1)} - \bar{\lambda}_1) (\bar{\lambda}_2^{(1)} - \bar{\lambda}_2) (\bar{\lambda}_3^{(1)} - \bar{\lambda}_3) \right) \sqrt{p_1 p_2 p_3}$ in (5.39) leading to a better approximation to the exact result (5.21) than the alternative root. Thus, based on the above-presented physical arguments, there is only 1 root combination among the 4 possible choices that lead to physically meaningful, superior estimates in the limit as $\kappa \rightarrow \infty$, namely, for $\bar{J} < 1$ (for $\bar{J} > 1$), the “positive” (+) (“negative” (-)) root in (5.34) with the choice $p_4 = \text{sign} \left((\bar{\lambda}_1^{(1)} - \bar{\lambda}_1) (\bar{\lambda}_2^{(1)} - \bar{\lambda}_2) (\bar{\lambda}_3^{(1)} - \bar{\lambda}_3) \right) \sqrt{p_1 p_2 p_3}$ in (5.39). Regarding these combinations, it is important to make the following two remarks. First, both these combinations can be shown to generate estimates for deformations with $\bar{J} = 1$ that are superior to the other two alternatives. Moreover, the full numerical solution suggests that these two superior choices, (+) and (-) in (5.34) with the $p_4 = \text{sign} \left((\bar{\lambda}_1^{(1)} - \bar{\lambda}_1) (\bar{\lambda}_2^{(1)} - \bar{\lambda}_2) (\bar{\lambda}_3^{(1)} - \bar{\lambda}_3) \right) \sqrt{p_1 p_2 p_3}$ in (5.39), lead in fact to the same estimate for \widehat{W} when $\bar{J} = 1$. This is difficult to verify analytically, however, since the equations associated with the (+) root develop a singularity as $\kappa \rightarrow \infty$ when approaching $\bar{J} = 1$. Second, the asymptotic analysis associated with the superior root for deformations with $\bar{J} < 1$ leads exactly to the same expression for the effective stored-energy function \widehat{W}^I as the one obtained from the analysis associated with the superior root for deformations with $\bar{J} > 1$. In conclusion, the stored-energy function \widehat{W}^I can be written as a single expression valid for all values of $\bar{J} (> 0)$. Next, we sketch out the derivation of such expression.

Based on numerical evidence from the results for finite κ , an expansion for the unknowns in

this problem, *i.e.*, ℓ_α^* ($\alpha = 1, 2, \dots, 7$), is attempted in the limit as $\kappa \rightarrow \infty$ of the following form:

$$\begin{aligned}
\ell_1^* &= a_1 \Delta^{-1} + a_2 + a_3 \Delta + O(\Delta^2), \\
\ell_2^* &= b_1 \Delta^{-1} + b_2 + b_3 \Delta + O(\Delta^2), \\
\ell_3^* &= c_1 \Delta^{-1} + c_2 + c_3 \Delta + O(\Delta^2), \\
\ell_4^* &= d_1 \Delta^{-1} + d_2 + d_3 \Delta + O(\Delta^2), \\
\ell_5^* &= e_1 \Delta^{-1} + e_2 + e_3 \Delta + O(\Delta^2), \\
\ell_6^* &= m_1 \Delta^{-1} + m_2 + m_3 \Delta + O(\Delta^2), \\
\ell_7^* &= n_2 + n_3 \Delta + O(\Delta^2),
\end{aligned} \tag{5.40}$$

where $\Delta \doteq 1/\kappa$ is a small parameter and $a_1, a_2, a_3, b_1, b_2, b_3, c_1, c_2, c_3, d_1, d_2, d_3, e_1, e_2, e_3, m_1, m_2, m_3, n_2,$ and n_3 are unknown coefficients to be determined from the asymptotic analysis that follows. It proves useful to spell out the corresponding expansions of the constrained moduli $L_{1221}^*, L_{1331}^*, L_{2332}^*$, as well as those for (the non-zero components of $\bar{\mathbf{F}}^{(1)}$) $\bar{\lambda}_1^{(1)}, \bar{\lambda}_2^{(1)}, \bar{\lambda}_3^{(1)}$ and the combinations (of the components of $\hat{\mathbf{F}}^{(1)}$) $x, y, z, p_1, p_2, p_3, p_4,$ and s , in the limit as $\kappa \rightarrow \infty$. Thus, substituting expressions (5.40) in relations (5.30) for the components $L_{1221}^*, L_{1331}^*, L_{2332}^*$ can be shown to lead to the following expansions:

$$\begin{aligned}
L_{1221}^* &= \left(\sqrt{a_1 b_1} - d_1 \right) \Delta^{-1} + \frac{a_2 b_1 + a_1 b_2 - (a_1 + b_1) n_2}{2\sqrt{a_1 b_1}} - d_2 + O(\Delta), \\
L_{1331}^* &= \left(\sqrt{a_1 c_1} - e_1 \right) \Delta^{-1} + \frac{a_2 c_1 + a_1 c_2 - (a_1 + c_1) n_2}{2\sqrt{a_1 c_1}} - e_2 + O(\Delta), \\
L_{2332}^* &= \left(\sqrt{b_1 c_1} - m_1 \right) \Delta^{-1} + \frac{b_2 c_1 + b_1 c_2 - (b_1 + c_1) n_2}{2\sqrt{b_1 c_1}} - m_2 + O(\Delta).
\end{aligned} \tag{5.41}$$

Similarly, substituting (5.40) in relations (5.31) leads to:

$$\begin{aligned}
\bar{\lambda}_1^{(1)} &= \overset{\circ}{\lambda}_1^{(1)} + \overset{\surd}{\lambda}_1^{(1)} \Delta + O(\Delta^2), & \bar{\lambda}_2^{(1)} &= \overset{\circ}{\lambda}_2^{(1)} + \overset{\surd}{\lambda}_2^{(1)} \Delta + O(\Delta^2), \\
\bar{\lambda}_3^{(1)} &= \overset{\circ}{\lambda}_3^{(1)} + \overset{\surd}{\lambda}_3^{(1)} \Delta + O(\Delta^2).
\end{aligned} \tag{5.42}$$

The explicit form of the coefficients $\overset{\circ}{\lambda}_i^{(1)}, \overset{\surd}{\lambda}_i^{(1)}$ ($i = 1, 2, 3$) in these last expressions is too cumbersome to be included here. In any case, at this stage, it suffices to remark that they are known in terms of the coefficients $a_1, a_2, a_3, b_1, b_2, b_3, c_1, c_2, c_3, d_1, d_2, d_3, e_1, e_2, e_3, m_1, m_2, m_3, n_2,$ and n_3 introduced in (5.40). Finally, substituting (5.40) in relations (5.34), (5.35), and (in the

appropriate root of) (5.39) leads to:

$$\begin{aligned}
x &= x_1 + x_2\Delta + O(\Delta^2), \\
y &= y_1 + y_2\Delta + O(\Delta^2), \\
z &= z_1 + z_2\Delta + O(\Delta^2), \\
p_1 &= \mathring{p}_1 + \mathring{p}_1\Delta + O(\Delta^2), \\
p_2 &= \mathring{p}_2 + \mathring{p}_2\Delta + O(\Delta^2), \\
p_3 &= \mathring{p}_3 + \mathring{p}_3\Delta + O(\Delta^2), \\
p_4 &= \mathring{p}_4 + O(\Delta) = \text{sign} \left[(\overset{\circ}{\lambda}_1^{(1)} - \bar{\lambda}_1)(\overset{\circ}{\lambda}_2^{(1)} - \bar{\lambda}_2)(\overset{\circ}{\lambda}_3^{(1)} - \bar{\lambda}_3) \right] \sqrt{\mathring{p}_1\mathring{p}_2\mathring{p}_3} + O(\Delta), \\
s &= s_1 + O(\Delta),
\end{aligned} \tag{5.43}$$

where, similar to (5.42), the coefficients in these expressions are (known functions of the coefficients defined in (5.40)) too cumbersome to be included here. For later use, it is convenient to introduce the expansion of $\hat{J}^{(1)} = \det \hat{\mathbf{F}}^{(1)}$:

$$\hat{J}^{(1)} = \hat{J}_1^{(1)} + \hat{J}_2^{(1)}\Delta + O(\Delta^2), \tag{5.44}$$

where, making contact with (5.43), we note that $\hat{J}_1^{(1)} = (x_1 + \bar{\lambda}_1)(y_1 + \bar{\lambda}_2)(z_1 + \bar{\lambda}_3) - \mathring{p}_1(z_1 + \bar{\lambda}_3) - \mathring{p}_2(y_1 + \bar{\lambda}_2) - \mathring{p}_3(x_1 + \bar{\lambda}_1) + 2\mathring{p}_4$. In addition, it will also prove useful to introduce the following notation for the expansions of the derivatives of the constitutive functions g and h characterizing the elastomeric matrix phase in the limit as $\kappa \rightarrow \infty$:

$$\begin{aligned}
\hat{g}_I &= \hat{g}'_1 + \hat{g}'_2\Delta + O(\Delta^2), \\
\hat{h}_J &= \hat{h}'_1 + \hat{h}'_2\Delta + O(\Delta^2),
\end{aligned} \tag{5.45}$$

where it is recalled that $\hat{g}_I = g_I(\hat{I}^{(1)})$, $\hat{h}_J = h_J(\hat{J}^{(1)})$, and $\hat{I}^{(1)}$ and $\hat{J}^{(1)}$ are given by (5.38).

Next, by making use of expressions (5.40) through (5.45) in (5.36), a hierarchical system of equations is obtained for the unknown coefficients introduced in (5.40). The first set of equations, of order $O(\Delta^{-1})$, can be shown to yield the following non-trivial relations:

$$b_1 = \frac{\bar{\lambda}_1^2}{\lambda_2^2} a_1, \quad c_1 = \frac{\bar{\lambda}_1^2}{\lambda_3^2} a_1, \quad d_1 = \frac{\bar{\lambda}_1}{\lambda_2} a_1, \quad e_1 = \frac{\bar{\lambda}_1}{\lambda_3} a_1, \quad m_1 = \frac{\bar{\lambda}_1^2}{\lambda_2 \lambda_3} a_1, \tag{5.46}$$

and

$$\begin{aligned}
&(x_1 + \bar{\lambda}_1)(y_1 + \bar{\lambda}_2)(z_1 + \bar{\lambda}_3) - \mathring{p}_1(z_1 + \bar{\lambda}_3) - \mathring{p}_2(y_1 + \bar{\lambda}_2) - \mathring{p}_3(x_1 + \bar{\lambda}_1) \\
&+ 2\mathring{p}_4 = 1.
\end{aligned} \tag{5.47}$$

Note that equations (5.46) correspond actually to *explicit* expressions for the unknowns b_1 , c_1 , d_1 , e_1 , and m_1 in terms of the coefficient a_1 . On the other hand, equation (5.47)—which can also be written as $\hat{J}_1^{(1)} = 1$ —is an *implicit* equation that ultimately involves the coefficients a_1 , a_2 , b_2 , c_2 , d_2 , e_2 , m_2 , and n_2 . Now, by making use of (5.46) and (5.47), the second hierarchy of equations, of order $O(\Delta^0)$, can be shown to ultimately yield the following relations:

$$\begin{aligned}
a_2 x_1 + d_2 y_1 + e_2 z_1 + a_1 \left(x_2 + \frac{\bar{\lambda}_1}{\lambda_2} y_2 + \frac{\bar{\lambda}_1}{\lambda_3} z_2 \right) &= 2\hat{g}'_1 (x_1 + \bar{\lambda}_1) + \\
&\quad \left(\hat{h}'_1 + \hat{J}_2^{(1)} \right) \left[(y_1 + \bar{\lambda}_2)(z_1 + \bar{\lambda}_3) - \hat{p}_3^\circ \right] - 2\bar{g}_I \bar{\lambda}_1 - \bar{h}_J \bar{\lambda}_2 \bar{\lambda}_3, \\
d_2 x_1 + b_2 y_1 + m_2 z_1 + a_1 \frac{\bar{\lambda}_1}{\lambda_2} \left(x_2 + \frac{\bar{\lambda}_1}{\lambda_2} y_2 + \frac{\bar{\lambda}_1}{\lambda_3} z_2 \right) &= 2\hat{g}'_1 (y_1 + \bar{\lambda}_2) + \\
&\quad \left(\hat{h}'_1 + \hat{J}_2^{(1)} \right) \left[(x_1 + \bar{\lambda}_1)(z_1 + \bar{\lambda}_3) - \hat{p}_2^\circ \right] - 2\bar{g}_I \bar{\lambda}_2 - \bar{h}_J \bar{\lambda}_1 \bar{\lambda}_3, \\
e_2 x_1 + m_2 y_1 + c_2 z_1 + a_1 \frac{\bar{\lambda}_1}{\lambda_3} \left(x_2 + \frac{\bar{\lambda}_1}{\lambda_2} y_2 + \frac{\bar{\lambda}_1}{\lambda_3} z_2 \right) &= 2\hat{g}'_1 (z_1 + \bar{\lambda}_3) + \\
&\quad \left(\hat{h}'_1 + \hat{J}_2^{(1)} \right) \left[(x_1 + \bar{\lambda}_1)(y_1 + \bar{\lambda}_2) - \hat{p}_1^\circ \right] - 2\bar{g}_I \bar{\lambda}_3 - \bar{h}_J \bar{\lambda}_1 \bar{\lambda}_2, \\
\frac{1}{2} \left(\frac{\bar{\lambda}_1}{\lambda_2} a_2 + \frac{\bar{\lambda}_2}{\lambda_1} b_2 \right) - \frac{\bar{\lambda}_1^2 + \bar{\lambda}_2^2}{2\bar{\lambda}_1 \bar{\lambda}_2} n_2 - d_2 &= \left(\hat{h}'_1 + \hat{J}_2^{(1)} \right) \left[\frac{\hat{p}_4^\circ}{\hat{p}_1^\circ} - (z_1 + \bar{\lambda}_3) \right], \\
\frac{1}{2} \left(\frac{\bar{\lambda}_1}{\lambda_3} a_2 + \frac{\bar{\lambda}_3}{\lambda_1} c_2 \right) - \frac{\bar{\lambda}_1^2 + \bar{\lambda}_3^2}{2\bar{\lambda}_1 \bar{\lambda}_3} n_2 - e_2 &= \left(\hat{h}'_1 + \hat{J}_2^{(1)} \right) \left[\frac{\hat{p}_4^\circ}{\hat{p}_2^\circ} - (y_1 + \bar{\lambda}_2) \right], \\
n_2 &= 2\hat{g}'_1,
\end{aligned} \tag{5.48}$$

and

$$\hat{h}'_1 + \hat{J}_2^{(1)} = \left[\frac{\hat{p}_4^\circ}{\hat{p}_3^\circ} - (x_1 + \bar{\lambda}_1) \right]^{-1} \left(\frac{1}{2} \left(\frac{\bar{\lambda}_2}{\lambda_3} b_2 + \frac{\bar{\lambda}_3}{\lambda_2} c_2 \right) - \frac{\bar{\lambda}_2^2 + \bar{\lambda}_3^2}{2\bar{\lambda}_2 \bar{\lambda}_3} n_2 - m_2 \right). \tag{5.49}$$

Solving (5.49) for $\hat{J}_2^{(1)}$, the second term in the expansion (5.44), and substituting the result in equations (5.48), can be shown to ultimately lead to a system of 7 nonlinear equations—formed by Eqns. (5.47) and (5.48)—for the 7 unknowns:

$$\begin{aligned}
u_1 &\doteq a_1, & u_2 &\doteq n_2, & u_3 &\doteq \bar{\lambda}_1^{-2} b_2 - \bar{\lambda}_1^{-2} a_2, & u_4 &\doteq \bar{\lambda}_3^{-2} c_2 - \bar{\lambda}_1^{-2} a_2, \\
u_5 &\doteq \bar{\lambda}_2 d_2 - \bar{\lambda}_1 a_2, & u_6 &\doteq \bar{\lambda}_3 e_2 - \bar{\lambda}_1 a_2, & u_7 &\doteq \bar{\lambda}_2 m_2 - \bar{\lambda}_3 c_2.
\end{aligned} \tag{5.50}$$

Here, the primitive coefficients a_1 and n_2 have been relabelled as u_1 and u_2 , respectively, for consistency of notation.

At this point, it is important to recognize that knowledge of the 7 variables (5.50), as determined by the system of 7 equations (5.47)—(5.48), suffices to determine the leading-order terms (of the components of $\bar{\mathbf{F}}^{(1)}$ $\overset{\circ}{\lambda}_1^{(1)}$, $\overset{\circ}{\lambda}_2^{(1)}$, $\overset{\circ}{\lambda}_3^{(1)}$, in (5.42) and (of the combinations of the components of $\hat{\mathbf{F}}^{(1)}$) x_1 , y_1 , z_1 , $\overset{\circ}{p}_1$, $\overset{\circ}{p}_2$, $\overset{\circ}{p}_3$, $\overset{\circ}{p}_4$, and s_1 , in (5.43), as well as the second-order traces $\overset{\vee}{\lambda}_1^{(1)} \bar{\lambda}_2 \bar{\lambda}_3 + \overset{\vee}{\lambda}_2^{(1)} \bar{\lambda}_1 \bar{\lambda}_3 + \overset{\vee}{\lambda}_3^{(1)} \bar{\lambda}_1 \bar{\lambda}_2$ and $x_2 \bar{\lambda}_2 \bar{\lambda}_3 + y_2 \bar{\lambda}_1 \bar{\lambda}_3 + z_2 \bar{\lambda}_1 \bar{\lambda}_2$. The corresponding final expressions are too cumbersome to be written down here, however, they do satisfy certain interesting, simple relations which worth recording, namely:

$$\begin{aligned}
 x_1 &= \overset{\circ}{\lambda}_1^{(1)} + \bar{\lambda}_1, & y_1 &= \overset{\circ}{\lambda}_2^{(1)} + \bar{\lambda}_2, & z_1 &= \overset{\circ}{\lambda}_3^{(1)} + \bar{\lambda}_3, \\
 \overset{\circ}{p}_1 &= \frac{1}{f_0} \left(\overset{\circ}{\lambda}_1^{(1)} - \bar{\lambda}_1 \right) \left(\overset{\circ}{\lambda}_2^{(1)} - \bar{\lambda}_2 \right), & \overset{\circ}{p}_2 &= \frac{1}{f_0} \left(\overset{\circ}{\lambda}_1^{(1)} - \bar{\lambda}_1 \right) \left(\overset{\circ}{\lambda}_3^{(1)} - \bar{\lambda}_3 \right), \\
 \overset{\circ}{p}_3 &= \frac{1}{f_0} \left(\overset{\circ}{\lambda}_2^{(1)} - \bar{\lambda}_2 \right) \left(\overset{\circ}{\lambda}_3^{(1)} - \bar{\lambda}_3 \right), \\
 \overset{\vee}{\lambda}_1^{(1)} \bar{\lambda}_2 \bar{\lambda}_3 + \overset{\vee}{\lambda}_2^{(1)} \bar{\lambda}_1 \bar{\lambda}_3 + \overset{\vee}{\lambda}_3^{(1)} \bar{\lambda}_1 \bar{\lambda}_2 &= x_2 \bar{\lambda}_2 \bar{\lambda}_3 + y_2 \bar{\lambda}_1 \bar{\lambda}_3 + z_2 \bar{\lambda}_1 \bar{\lambda}_2.
 \end{aligned} \tag{5.51}$$

Finally, by making use of the above results, it can be shown that the leading-order term of the second-order estimate (5.13) in the limit of incompressibility is given by (5.16) in the text, where

$$\hat{I}^{(1)} = (x_1 + \bar{\lambda}_1)^2 + (y_1 + \bar{\lambda}_2)^2 + (z_1 + \bar{\lambda}_3)^2 + s_1. \tag{5.52}$$

In this relation, it should be emphasized again that the expressions for x_1 , y_1 , z_1 , and s_1 are known—but not shown here for their bulkiness—explicitly in terms of the applied loading, $\bar{\lambda}_1$, $\bar{\lambda}_2$, $\bar{\lambda}_3$, the initial porosity, f_0 , the constitutive function, g , and the 7 variables u_α , defined by (5.50), that are the solutions to the system of the 7 nonlinear, algebraic equations formed by (5.47) and (5.48).

Chapter 6

Hyperelastic laminates

This and the following chapter—in contrast to Chapters 3, 4, and 5, which have dealt with porous elastomers—are concerned with the application of the theoretical framework developed in Chapter 2 to *reinforced* elastomers. The present chapter deals with *reinforced* elastomers with laminate microstructures. In particular, the focus is on the evolution of the underlying microstructure and its connection with the overall stress-strain relation and the development of instabilities in these materials. More specifically, it is shown that the rotation of the layers—induced by the applied finite deformations—generates substantial geometric softening in the overall mechanical response of the composite. In addition, in spite of the fact that the local behavior is assumed to be strongly elliptic, the homogenized behavior of the laminate is found to lose strong ellipticity at sufficiently large deformations. To be precise, when the laminate is loaded in compression along the layers, a certain type of “kink-band” instability is detected corresponding to the material becoming infinitesimally soft to incremental shear deformations in the lamination direction.

Before proceeding with the development of the results, it is important to recall that laminates are one of the very few special microgeometries for which an *exact* solution may be computed (see, e.g., Triantafyllidis and Maker, 1985; Geymonat *et al.*, 1993; Triantafyllidis and Nestorvić, 2005). Such an *exact* solution is essentially constructed by setting piecewise-constant fields in the different layers and solving for the corresponding jump conditions. As it will be discussed in detail in this chapter, the second-order estimates recover such *exact* solution. That is, the results presented in this chapter correspond to *rigorous* estimates. As such, they will be useful in the context of the subsequent chapter for validating results for more general microgeometries (for which there are not exact solutions available).

6.1 Effective behavior of hyperelastic laminates

In this chapter, we study the problem of the effective behavior of two-phase, hyperelastic laminates with isotropic phases, characterized by the stored-energy functions $W^{(1)}$ and $W^{(2)}$, subjected to finite deformations. As already discussed in Section 2.4.2, a laminate is a limiting case of “particulate” microstructures (see Fig. 6.1), in which both phases play the roles of matrix and inclusion at the same time. In the analysis that follows, for consistency with earlier notation, we denote by “matrix” phase, the softest of the two layers, and by “inclusion” phase, the stiffest one.

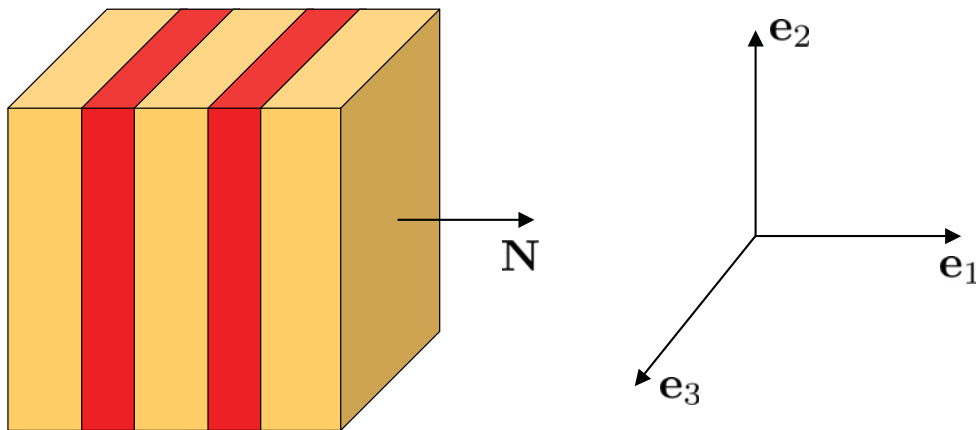


Figure 6.1: Reference configuration depiction of a laminate with lamination direction $\mathbf{N} = \mathbf{e}_1$ relative to the fixed laboratory frame of reference $\{\mathbf{e}_i\}$.

Of course, an *exact* solution for the effective behavior for the class of elastomeric laminates of interest in this chapter can be readily computed by assuming piecewise-constant fields in the different layers and solving for the corresponding jump conditions—exactly as is done in the context of linear elasticity. However, here, we will follow a different route. In particular, we will make use of the “tangent” second-order method of Ponte Castañeda and Tiberio (2000). This method will be shown to recover the exact solution with piecewise-constant fields in the phases. In addition, the use of this method will prove helpful to obtain further insight on the behavior of hyperelastic laminates. In this connection, it should be noted that the earlier tangent second-order method, as opposed to the new second-order method proposed in this work, is utilized here for mere computational simplicity, since both methods can be shown to lead exactly to the same estimates and provide the same insight for the special case of laminate microstructures. The reason for this agreement is that both—the tangent and the new—second-order methods are able to recover the exact result

whenever there are no field fluctuations within the given phases of the composite (see Ponte Castañeda, 1996 and Ponte Castañeda, 2002a for further details).

6.1.1 Tangent second-order homogenization estimates

In this subsection, for convenience and clarity, general expressions are provided for tangent second-order estimates for the effective behavior of two-phase elastomeric composites with general “particulate” microstructures. These general expressions are then utilized to generate rigorous estimates for the class of laminate microstructures of interest in this chapter.

Following Ponte Castañeda and Tiberio (2000) (see also Appendix IV in Chapter 2), the tangent second-order estimate for the effective stored-energy function \widehat{W} of two-phase elastomers consisting of inclusions, with given initial volume fraction c_0 and characterized by the isotropic stored-energy function $W^{(2)}$, in an elastomeric matrix phase with isotropic stored-energy function $W^{(1)}$, may be written as follows:

$$\begin{aligned} \widehat{W}(\bar{\mathbf{F}}) &= (1 - c_0) \left[W^{(1)}(\bar{\mathbf{F}}^{(1)}) + \frac{1}{2} \mathcal{S}^{(1)}(\bar{\mathbf{F}}^{(1)}) \cdot (\bar{\mathbf{F}} - \bar{\mathbf{F}}^{(1)}) \right] \\ &\quad + c_0 \left[W^{(2)}(\bar{\mathbf{F}}^{(2)}) + \frac{1}{2} \mathcal{S}^{(2)}(\bar{\mathbf{F}}^{(2)}) \cdot (\bar{\mathbf{F}} - \bar{\mathbf{F}}^{(2)}) \right]. \end{aligned} \quad (6.1)$$

In this expression, $\bar{\mathbf{F}}^{(1)}$ and $\bar{\mathbf{F}}^{(2)}$ denote, respectively, the average deformation gradients in the matrix and inclusion phases of a two-phase, “linear comparison composite” (LCC) with the *same microstructure*—in the undeformed configuration—as the original hyperelastic composite and with *local* stored-energy functions given by:

$$W_T^{(r)}(\mathbf{F}) = W^{(r)}(\bar{\mathbf{F}}^{(r)}) + \mathcal{S}^{(r)}(\bar{\mathbf{F}}^{(r)}) \cdot (\mathbf{F} - \bar{\mathbf{F}}^{(r)}) + \frac{1}{2} (\mathbf{F} - \bar{\mathbf{F}}^{(r)}) \cdot \mathcal{L}^{(r)}(\bar{\mathbf{F}}^{(r)}) (\mathbf{F} - \bar{\mathbf{F}}^{(r)}). \quad (6.2)$$

In the sequel, for ease of notation, the arguments of $\mathcal{S}^{(r)}$ and $\mathcal{L}^{(r)}$ will be omitted.

The variables $\bar{\mathbf{F}}^{(1)}$ and $\bar{\mathbf{F}}^{(2)}$ —needed in the computation of the tangent second-order estimate (6.1)—can be expediently computed from the effective stored-energy function \widehat{W}_T of the above-defined LCC. By making use of the general results developed in Section 2.4.2, such an *effective* stored-energy function can be written as follows

$$\widehat{W}_T(\bar{\mathbf{F}}) = \tilde{f} + \tilde{\mathbf{T}} \cdot \bar{\mathbf{F}} + \frac{1}{2} \bar{\mathbf{F}} \cdot \tilde{\mathbf{L}} \bar{\mathbf{F}}, \quad (6.3)$$

where $\tilde{f} = \bar{f} + \frac{1}{2} (\Delta \mathcal{L})^{-1} \Delta \mathbf{T} \cdot (\tilde{\mathbf{L}} - \bar{\mathcal{L}}) (\Delta \mathcal{L})^{-1} \Delta \mathbf{T}$, $\tilde{\mathbf{T}} = \bar{\mathbf{T}} + (\tilde{\mathbf{L}} - \bar{\mathcal{L}}) (\Delta \mathcal{L})^{-1} \Delta \mathbf{T}$ are *effective* quantities depending on the effective modulus tensor $\tilde{\mathbf{L}}$, which is specified further below. Also,

in these expressions, $f^{(r)} = W^{(r)}(\bar{\mathbf{F}}^{(r)}) - \mathbf{T}^{(r)} \cdot \bar{\mathbf{F}}^{(r)} - \frac{1}{2} \bar{\mathbf{F}}^{(r)} \cdot \mathcal{L}^{(r)} \bar{\mathbf{F}}^{(r)}$, $\mathbf{T}^{(r)} = \mathcal{S}^{(r)} - \mathcal{L}^{(r)} \bar{\mathbf{F}}^{(r)}$ ($r = 1, 2$), and $\Delta \mathcal{L} = \mathcal{L}^{(1)} - \mathcal{L}^{(2)}$, $\Delta \mathbf{T} = \mathbf{T}^{(1)} - \mathbf{T}^{(2)}$. Furthermore, $\bar{f} = (1 - c_0)f^{(1)} + c_0f^{(2)}$, $\bar{\mathbf{T}} = (1 - c_0)\mathbf{T}^{(1)} + c_0\mathbf{T}^{(2)}$, and $\bar{\mathcal{L}} = (1 - c_0)\mathcal{L}^{(1)} + c_0\mathcal{L}^{(2)}$. Finally, in the above relations, $\tilde{\mathbf{L}}$ is the effective modulus tensor of the two-phase, *linear-elastic* comparison composite with modulus tensors $\mathcal{L}^{(1)}$ and $\mathcal{L}^{(2)}$, and the same microstructure, in its undeformed configuration, as the *non-linear*, hyperelastic composite. As already discussed in Section 2.4.2, an accurate estimate for $\tilde{\mathbf{L}}$ for composites with “particulate” microstructures is the generalized estimate of the Hashin-Shtrikman (HS) type given by expression (2.55), and repeated here for convenience:

$$\tilde{\mathbf{L}} = \mathcal{L}^{(1)} + c_0 [(1 - c_0)\mathbf{P} - (\Delta \mathcal{L})^{-1}]^{-1}. \quad (6.4)$$

Recall that in this expression, the microstructural tensor \mathbf{P} serves to characterize the size, shape and orientation of the inclusions, as well as their spatial distribution. In passing, it should be noted that the estimate (6.4) is not only accurate for general “particulate” microgeometries, but it is actually *exact* for the class of laminate microstructures of interest in this chapter.

Having determined the relevant effective stored-energy function \widehat{W}_T for the auxiliary LCC problem, it follows from relations (2.60) that the phase average deformation gradients $\bar{\mathbf{F}}^{(1)}$ and $\bar{\mathbf{F}}^{(2)}$ can be readily computed from the tensorial equation:

$$\bar{\mathbf{F}} - \bar{\mathbf{F}}^{(1)} = \mathbf{P} \left[\mathcal{L}^{(1)} (\bar{\mathbf{F}} - \bar{\mathbf{F}}^{(1)}) + c_0 (\mathcal{S}^{(1)} - \mathcal{S}^{(2)}) \right], \quad (6.5)$$

and the global average condition:

$$\bar{\mathbf{F}}^{(2)} = \frac{1}{c_0} (\bar{\mathbf{F}} - (1 - c_0)\bar{\mathbf{F}}^{(1)}), \quad (6.6)$$

respectively. It is thus seen that for a given loading, as determined by $\bar{\mathbf{F}}$, and given microstructure, as determined by c_0 and \mathbf{P} , the computation of the tangent second-order estimate (6.1) for the effective stored-energy function of two-phase elastomeric composites with “particulate” microstructures ultimately amounts to solving the system of 9 nonlinear, scalar equations (6.5) for the 9 unknowns formed by the 9 components of $\bar{\mathbf{F}}^{(1)}$.

For the particular class of laminate microstructures of interest here, the microstructural tensor \mathbf{P} is given (in component form) by (see Section 2.4.2):

$$P_{ijkl} = K_{ik}^{-1} N_j N_l = (\mathcal{L}_{ipkq}^{(1)} N_p N_q)^{-1} N_j N_l, \quad (6.7)$$

where $K_{ik} = \mathcal{L}_{ipkq}^{(1)} N_p N_q$, the unit vector \mathbf{N} denotes the direction of lamination in the undeformed configuration (see Fig. 6.1), and indicial notation has been employed for clarity. Expression (6.7)

can now be substituted in equation (6.5) to yield the following system of equations for $\bar{\mathbf{F}}_{ij}^{(1)}$:

$$\bar{F}_{ij} - \bar{F}_{ij}^{(1)} = K_{ik}^{-1} \left[\mathcal{L}_{klpq}^{(1)} \left(\bar{F}_{pq} - \bar{F}_{pq}^{(1)} \right) N_l + c_0 \left(\mathcal{S}_{kl}^{(1)} - \mathcal{S}_{kl}^{(2)} \right) N_l \right] N_j. \quad (6.8)$$

At this point, it is convenient to recast equation (6.8) in a simpler form. To this end, it proves helpful to identify, without loss of generality, the direction of lamination \mathbf{N} with the laboratory basis vector \mathbf{e}_1 , namely, $\mathbf{N} = \mathbf{e}_1$ (see Fig. 6.1). In addition, for clarity of notation, it proves also helpful to define the unit vectors $\mathbf{N}^{\perp 2} \doteq \mathbf{e}_2$ and $\mathbf{N}^{\perp 3} \doteq \mathbf{e}_3$, such that $\mathbf{N}^{\perp 2} \cdot \mathbf{N} = \mathbf{N}^{\perp 3} \cdot \mathbf{N} = 0$. Having defined these variables, it is now easy to see that multiplying equation (6.8) with $N_j^{\perp 2}$ and $N_j^{\perp 3}$ leads to the following two relations:

$$\left[\bar{\mathbf{F}} - \bar{\mathbf{F}}^{(1)} \right] \mathbf{N}^{\perp 2} = \mathbf{0} \quad \text{and} \quad \left[\bar{\mathbf{F}} - \bar{\mathbf{F}}^{(1)} \right] \mathbf{N}^{\perp 3} = \mathbf{0}. \quad (6.9)$$

Note that conditions (6.9) are actually the *exact* jump conditions across the layer interfaces required to ensure continuity of the deformation vector field in the LCC. Further, an immediate implication of conditions (6.9) is that the average deformation gradient tensor $\bar{\mathbf{F}}^{(1)}$ is of the form:

$$\bar{\mathbf{F}}^{(1)} = \bar{\mathbf{F}} + \mathbf{a} \otimes \mathbf{N}, \quad (6.10)$$

where \mathbf{a} is, at this stage, an arbitrary vector (with three independent unknown components). In other words, conditions (6.9) constitute a system of 6 *linear*, algebraic equations for 6 components of the average deformation gradient tensor $\bar{\mathbf{F}}^{(1)}$. The remaining 3 components needed to completely specify $\bar{\mathbf{F}}^{(1)}$ must be determined from the 3 remaining equations in (6.8). To this end, use is made of (6.10) in (6.8) and the result multiplied with N_j . The resulting equation reads as follows:

$$a_i = K_{ik}^{-1} \left[\mathcal{L}_{klpq}^{(1)} N_l N_q a_p - c_0 \left(\mathcal{S}_{kl}^{(1)} - \mathcal{S}_{kl}^{(2)} \right) N_l \right]. \quad (6.11)$$

Next, by left-multiplying (6.11) with \mathbf{K} , the following equation is obtained:

$$K_{ij} a_j = \mathcal{L}_{imjn}^{(1)} N_m N_n a_j = \mathcal{L}_{ilpq}^{(1)} N_l N_q a_p - c_0 \left(\mathcal{S}_{il}^{(1)} - \mathcal{S}_{il}^{(2)} \right) N_l, \quad (6.12)$$

which after a trivial simplification can be finally rewritten as

$$\left[\mathcal{S}^{(1)} - \mathcal{S}^{(2)} \right] \mathbf{N} = \mathbf{0}. \quad (6.13)$$

Note that condition (6.13) constitutes precisely a system of 3 *nonlinear*, algebraic equations for the remaining 3 components of $\bar{\mathbf{F}}^{(1)}$. Note further that condition (6.13) is nothing more than the *exact* jump condition across the layer interfaces required to ensure static equilibrium in the LCC.

In summary, 6 out of the 9 scalar equations contained in (6.8) have been recast as a system of 6 *linear* equations, given by relations (6.9). These equations can be solved in closed form for 6 components of $\bar{\mathbf{F}}^{(1)}$. The remaining 3 equations in (6.8), which have been conveniently rewritten as (6.13), constitute a *closed* system of *nonlinear* equations for the remaining 3 components of $\bar{\mathbf{F}}^{(1)}$. In general, these 3 equations must be solved numerically, but depending on the particular forms of the stored-energy functions $W^{(1)}$ and $W^{(2)}$, possible simplifications might be carried out. Having computed the values of all the components of $\bar{\mathbf{F}}^{(1)}$ for a given $\bar{\mathbf{F}}$, the values of the components of $\bar{\mathbf{F}}^{(2)}$ can be readily determined using the global average condition (6.6). In turn, the tangent second-order estimate for the effective stored-energy function \widehat{W} of elastomeric laminates can then be computed, from expression (6.1), using these results. In this connection, it is important to recognize that the stored-energy function (6.1) simplifies eventually to

$$\widehat{W}(\bar{\mathbf{F}}) = (1 - c_0)W^{(1)}(\bar{\mathbf{F}}^{(1)}) + c_0W^{(2)}(\bar{\mathbf{F}}^{(2)}). \quad (6.14)$$

This is easy to see from the fact that $\bar{\mathbf{F}}^{(1)}$ (as well as $\bar{\mathbf{F}}^{(2)}$) is of the form (6.10) and the stress quantities $\mathcal{S}^{(1)}$ and $\mathcal{S}^{(2)}$ must satisfy condition (6.13).

The effective stress associated with the stored-energy function (6.14) is given by

$$\bar{\mathbf{S}} = \frac{\partial \widehat{W}}{\partial \bar{\mathbf{F}}} = (1 - c_0)\mathcal{S}^{(1)} \frac{\partial \bar{\mathbf{F}}^{(1)}}{\partial \bar{\mathbf{F}}} + c_0\mathcal{S}^{(2)} \frac{\partial \bar{\mathbf{F}}^{(2)}}{\partial \bar{\mathbf{F}}}, \quad (6.15)$$

which, upon use of the average condition (6.6) once again, may be rewritten as follows:

$$\bar{\mathbf{S}} = (1 - c_0) \left(\mathcal{S}^{(1)} - \mathcal{S}^{(2)} \right) \frac{\partial \bar{\mathbf{F}}^{(1)}}{\partial \bar{\mathbf{F}}} + \mathcal{S}^{(2)}. \quad (6.16)$$

Expression (6.16) can be simplified further by recognizing from (6.10) that the partial derivative of $\bar{\mathbf{F}}^{(1)}$ with respect to $\bar{\mathbf{F}}$ is of the form

$$\frac{\partial \bar{F}_{ij}^{(1)}}{\partial \bar{F}_{kl}} = \delta_{ik}\delta_{jl} + \frac{\partial a_i}{\partial \bar{F}_{kl}} N_j, \quad (6.17)$$

where δ_{ij} is the Kronecker delta, and indicial notation has been employed for clarity. It then follows immediately from (6.17) and (6.13) that the macroscopic stress can be ultimately written as:

$$\bar{\mathbf{S}} = (1 - c_0)\mathcal{S}^{(1)} + c_0\mathcal{S}^{(2)}. \quad (6.18)$$

From a computational point of view, it should be emphasized that expression (6.18) is significantly simpler than (6.16), since (6.18) depends only on the variable $\bar{\mathbf{F}}^{(1)}$ —which is defined by a set on

nonlinear algebraic equations—whereas (6.16) depends not only on $\bar{\mathbf{F}}^{(1)}$, but also on its partial derivative with respect to $\bar{\mathbf{F}}$.

At this stage, it is fitting to point out—and straightforward to see—that the tangent second-order estimates for the effective stored-energy function (6.14) and macroscopic stress (6.18) coincide identically with the *exact* results for the effective behavior of two-phase, hyperelastic laminates (with constant deformation gradients in the phases). Indeed, conditions (6.9) correspond to nothing more than the exact *jump conditions* across the layer interfaces required to ensure *continuity* of the *deformation vector field* in the hyperelastic composite. Similarly, condition (6.13) is nothing more than the exact *jump condition* across the layer interfaces required to ensure *static equilibrium*. In this regard, it is worth noticing that the linear comparison composite, defined by (6.2) and (6.3), is, actually, entirely equivalent to the nonlinear elastomeric composite.

Effective incremental modulus tensor $\hat{\mathcal{L}}$

For later use in the analysis of the macroscopic stability of elastomeric laminates, it proves now convenient to compute the effective incremental modulus tensor $\hat{\mathcal{L}}$ associated with the *exact* estimate (6.14). Thus, taking the partial derivative of $\bar{\mathbf{S}}$ in (6.18) with respect to the macroscopic deformation gradient $\bar{\mathbf{F}}$ and making use of (6.6) can be shown to lead to:

$$\hat{\mathcal{L}} = \frac{\partial^2 \widehat{W}}{\partial \bar{\mathbf{F}} \partial \bar{\mathbf{F}}} = (1 - c_0) \left(\mathcal{L}^{(1)} - \mathcal{L}^{(2)} \right) \frac{\partial \bar{\mathbf{F}}^{(1)}}{\partial \bar{\mathbf{F}}} + \mathcal{L}^{(2)}, \quad (6.19)$$

where it is recalled that $\mathcal{L}^{(r)} = \partial^2 W^{(r)}(\bar{\mathbf{F}}^{(r)}) / \partial \mathbf{F}^2$ denote the tangent moduli of the phases evaluated at the phase average deformation gradients. At this point, it is interesting to notice the parallel between expression (6.19) for the effective incremental modulus $\hat{\mathcal{L}}$, and expression (6.16) for the macroscopic stress $\bar{\mathbf{S}}$. Note, however, that in contrast to (6.16)—which could be ultimately rewritten as (6.18) by making use of the functional *form* of $\partial \bar{\mathbf{F}}^{(1)} / \partial \bar{\mathbf{F}}$ given by (6.17)—expression (6.19) requires knowledge of the entire explicit dependence—not only the functional form—of $\partial \bar{\mathbf{F}}^{(1)} / \partial \bar{\mathbf{F}}$ on $\bar{\mathbf{F}}^{(1)}$ in order to be simplified further. This is simply because the difference $(\mathcal{L}^{(1)} - \mathcal{L}^{(2)})$ —as opposed to $(\mathcal{S}^{(1)} - \mathcal{S}^{(2)})$ —need not satisfy any jump conditions.

Next, we generate an explicit expression for $\partial \bar{\mathbf{F}}^{(1)} / \partial \bar{\mathbf{F}}$ in terms of $\bar{\mathbf{F}}^{(1)}$. To this end, we first take the partial derivative of equations (6.9) and (6.13) with respect to $\bar{\mathbf{F}}$. The resulting equations

can be conveniently written (in component form) as follows:

$$\begin{aligned} \frac{\partial \bar{\mathbf{F}}_{ij}^{(1)}}{\partial \bar{\mathbf{F}}_{kl}} N_j^{\perp 2} &= \delta_{ik} \delta_{jl} N_j^{\perp 2}, \\ \frac{\partial \bar{\mathbf{F}}_{ij}^{(1)}}{\partial \bar{\mathbf{F}}_{kl}} N_j^{\perp 3} &= \delta_{ik} \delta_{jl} N_j^{\perp 3}, \\ \left(c_0 \mathcal{L}_{ijkl}^{(1)} - (1 - c_0) \mathcal{L}_{ijkl}^{(2)} \right) \frac{\partial \bar{\mathbf{F}}_{kl}^{(1)}}{\partial \bar{\mathbf{F}}_{mn}} N_j &= \mathcal{L}_{ijmn}^{(2)} N_j. \end{aligned} \quad (6.20)$$

Now, it is noted that relations (6.20) constitute a system of 81 *linear* equations for the 81 components of the fourth-order tensor $\partial \bar{\mathbf{F}}^{(1)} / \partial \bar{\mathbf{F}}$. (Of course, 36 out of these 81 equations are redundant since $\partial \bar{\mathbf{F}}^{(1)} / \partial \bar{\mathbf{F}}$ has major symmetry.) Finally, upon solving these equations, the following *explicit* expression for $\partial \bar{\mathbf{F}}^{(1)} / \partial \bar{\mathbf{F}}$ in terms of $\bar{\mathbf{F}}^{(1)}$ is obtained:

$$\frac{\partial \bar{\mathbf{F}}^{(1)}}{\partial \bar{\mathbf{F}}} = \frac{1}{1 - c_0} \mathcal{I} + \frac{c_0}{1 - c_0} \left(\mathcal{L}^{(1)} - \mathcal{L}^{(2)} \right)^{-1} \left[(1 - c_0) \mathbf{P} - \left(\mathcal{L}^{(1)} - \mathcal{L}^{(2)} \right)^{-1} \right]^{-1}, \quad (6.21)$$

where \mathcal{I} denotes the identity operator in the space of fourth-order tensors with major symmetry only (*i.e.*, $\mathcal{I}_{ijkl} = \delta_{ik} \delta_{jl}$), and it is recalled that \mathbf{P} is given by expression (6.7).

Having determined $\partial \bar{\mathbf{F}}^{(1)} / \partial \bar{\mathbf{F}}$, it is now straightforward to show that the effective incremental modulus (6.19) may be finally written as follows:

$$\hat{\mathcal{L}} = \mathcal{L}^{(1)} + c_0 \left[(1 - c_0) \mathbf{P} - \left(\mathcal{L}^{(1)} - \mathcal{L}^{(2)} \right)^{-1} \right]^{-1}. \quad (6.22)$$

In connection with expression (6.22), there are two remarks which worth recording. First, similar to the effective stored-energy function (6.14) and macroscopic stress (6.18), the computation of the incremental modulus tensor (6.22) amounts, plainly, to solving the 6 *linear* equations provided by conditions (6.9), together with the 3 *nonlinear* equations provided by condition (6.13), for the 9 components of $\bar{\mathbf{F}}^{(1)}$. Second, the incremental modulus tensor (6.22) coincides identically with the Hashin-Shtrikman estimate (6.4) for the effective modulus tensor of the relevant linear comparison composite. As already discussed in Section 2.6, the effective incremental modulus associated with the second-order estimate is not equal, in general, to the effective modulus of the auxiliary linear comparison composite (*i.e.*, $\hat{\mathcal{L}} \neq \tilde{\mathcal{L}}$). However, for the special case of laminate microstructures, the *linear* comparison composite, defined by (6.2) and (6.3), is exactly equivalent to the *nonlinear* composite and thus, $\hat{\mathcal{L}} = \tilde{\mathcal{L}}$.

6.1.2 Microstructure evolution

The previous subsection has provided rigorous estimates for the mechanical response of hyperelastic laminates subjected to finite deformations. In this subsection, in an attempt to gain further understanding on the effective behavior of these materials, we identify relevant microstructural variables and work out explicit expressions for their evolution along a given macroscopic loading path.

Recall from Section 2.5 that the appropriate microstructural variables for “particulate” microstructures are the current volume fraction, c , the current aspect ratios, ω_1, ω_2 , and the current orientation of the particles in the deformed configuration—as determined from the average deformation gradient in the “inclusion” phase $\bar{\mathbf{F}}^{(2)}$, by means of the tensor $\mathbf{Z} = \mathbf{Z}_0 \bar{\mathbf{F}}^{(2)-1}$ defined by expression (2.84). For the special class of laminate microstructures of interest here, $\mathbf{Z}_0 = \mathbf{N} \otimes \mathbf{N}$, so that the aspect ratios of the particles, ω_1, ω_2 , are initially unbounded, *i.e.*, the particles are really *layers* (see Section 2.4.2 for further details). As it will be seen more explicitly below, ω_1 and ω_2 remain also unbounded in the deformed configuration. Thus, in the context of laminates, there are only two relevant microstructural variables: (i) the current volume fraction c , and (ii) the current orientation of the layers in the deformed configuration. The former can be simply computed via

$$c = \frac{\det \bar{\mathbf{F}}^{(2)}}{\det \bar{\mathbf{F}}}. \quad (6.23)$$

The latter requires the consideration of the microstructural tensor $\mathbf{Z}^T \mathbf{Z}$, which in the present context is given by:

$$\mathbf{Z}^T \mathbf{Z} = \bar{\mathbf{F}}^{(2)-T} \mathbf{N} \otimes \bar{\mathbf{F}}^{(2)-T} \mathbf{N}. \quad (6.24)$$

Expression (6.24) clearly indicates that the symmetric, quadratic form $\mathbf{Z}^T \mathbf{Z}$ has two zero eigenvalues. This has the direct implication—already mentioned above—that the aspect ratios of the “particles”, ω_1, ω_2 , are unbounded in the deformed configuration. More importantly, expression (6.24) indicates that the direction of lamination \mathbf{N} in the undeformed configuration evolves into

$$\mathbf{n} = \|\bar{\mathbf{F}}^{(2)-T} \mathbf{N}\|^{-1} \bar{\mathbf{F}}^{(2)-T} \mathbf{N} \quad (6.25)$$

in the deformed configuration (see Fig. 6.2). This last relation is nothing more than Nanson’s formula. It essentially states that layer interfaces (with reference normal \mathbf{N}) are material surface elements that evolve as such. In connection with expression (6.25), it is also expedient to recognize that—by making use of the jump conditions (6.9) together with the average condition (6.6)—the

transpose of the inverse of $\bar{\mathbf{F}}^{(2)}$ can be written as follows:

$$\bar{\mathbf{F}}^{(2)-T} = \frac{c_0 - 1}{c_0 + (c_0 - 1)\bar{\mathbf{F}}^{-1}\mathbf{a} \cdot \mathbf{N}} \left[\frac{c_0}{c_0 - 1}\bar{\mathbf{F}}^{-T} + \left(\bar{\mathbf{F}}^{-1}\mathbf{a} \cdot \mathbf{N}\right)\bar{\mathbf{F}}^{-T} - \bar{\mathbf{F}}^{-T}\mathbf{N} \otimes \bar{\mathbf{F}}^{-1}\mathbf{a} \right]. \quad (6.26)$$

It is then a matter of straightforward algebra to conclude that expression (6.25) can be recast as the following *purely kinematical* relation:

$$\mathbf{n} = \|\bar{\mathbf{F}}^{-T}\mathbf{N}\|^{-1}\bar{\mathbf{F}}^{-T}\mathbf{N}. \quad (6.27)$$

That is, the evolution of the lamination direction along a given macroscopic loading path is entirely characterized by the macroscopic deformation gradient tensor $\bar{\mathbf{F}}$.

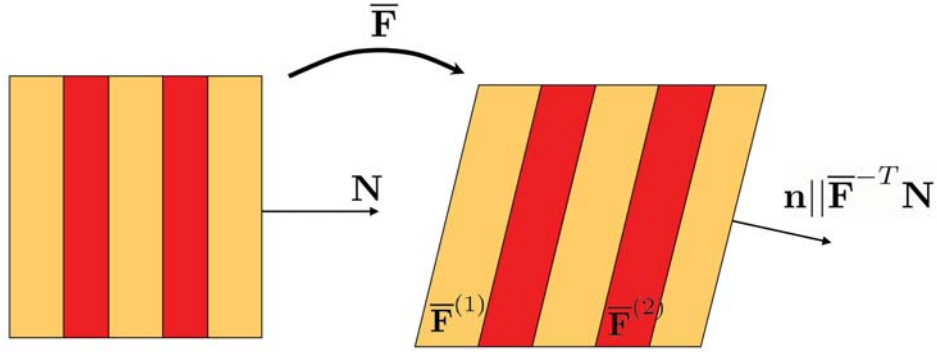


Figure 6.2: Schematic representation of the evolution of the direction of lamination along a loading path with macroscopic deformation gradient $\bar{\mathbf{F}}$.

6.2 Plane-strain loading of Neo-Hookean laminates

The results developed in the preceding section are general as far as the elastomeric phases, $W^{(1)}$ and $W^{(2)}$, and the loading conditions are concerned. In this section, attention is restricted to specific stored-energy functions for the phases, as well as to specific loading conditions, in order to illustrate—in a transparent manner—the effective behavior of hyperelastic laminates subjected to finite deformations. Of special interest is to bring out the effect of the *heterogeneity contrast* and *microstructure evolution* on the overall response and stability of these materials. Thus, attention will be restricted to Neo-Hookean stored-energy functions of the form

$$W^{(r)} = \frac{\mu^{(r)}}{2} (\mathbf{F} \cdot \mathbf{F} - 3) - \mu^{(r)} \ln(\det \mathbf{F}) + \left(\frac{\kappa^{(r)}}{2} - \frac{\mu^{(r)}}{3} \right) (\det \mathbf{F} - 1)^2, \quad (6.28)$$

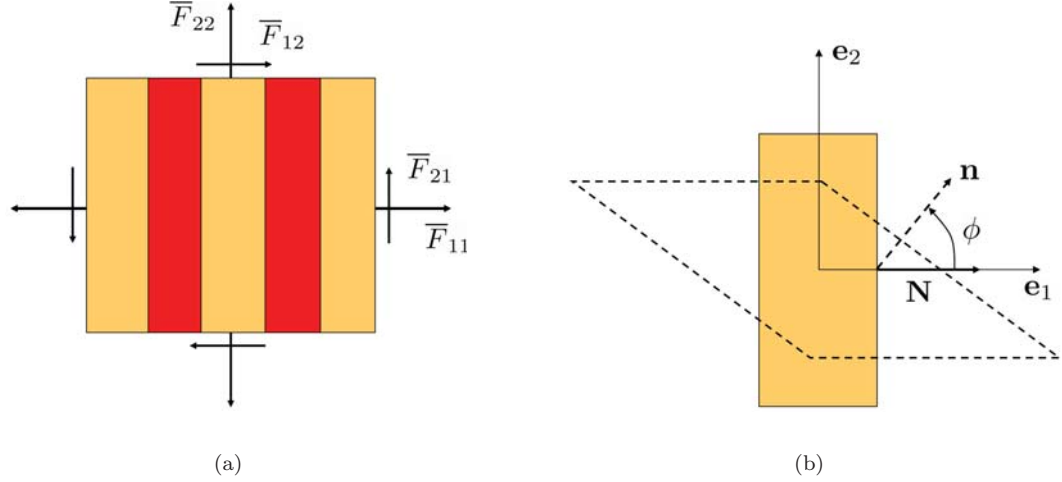


Figure 6.3: Schematic representation of: (a) the applied boundary conditions, and (b) the evolution of the lamination direction. In (b), the colored rectangle represents a typical layer with normal \mathbf{N} in the undeformed configuration; the dashed rectangle corresponds to the same layer in the deformed configuration, with current lamination direction \mathbf{n} .

where the material parameters $\mu^{(r)}$ and $\kappa^{(r)}$ denote, respectively, the shear and (three-dimensional) bulk moduli of phase r at zero strain. Furthermore, attention will be restricted to isochoric, plane-strain loading conditions of the form (see Fig. 6.3(a))

$$\bar{\mathbf{F}} = \bar{\mathbf{U}} = \begin{bmatrix} \cos \bar{\theta} & -\sin \bar{\theta} & 0 \\ \sin \bar{\theta} & \cos \bar{\theta} & 0 \\ 0 & 0 & 1 \end{bmatrix} \begin{bmatrix} \bar{\lambda} & 0 & 0 \\ 0 & \bar{\lambda}^{-1} & 0 \\ 0 & 0 & 1 \end{bmatrix} \begin{bmatrix} \cos \bar{\theta} & \sin \bar{\theta} & 0 \\ -\sin \bar{\theta} & \cos \bar{\theta} & 0 \\ 0 & 0 & 1 \end{bmatrix}, \quad (6.29)$$

where $\bar{\lambda}$ and $\bar{\lambda}^{-1}$ denote the in-plane principal stretches associated with $\bar{\mathbf{F}}$, while $\bar{\theta}$ characterizes the orientation (in the anticlockwise sense relative to the fixed laboratory frame of reference) of the in-plane Lagrangian principal axes.

The restriction (6.29) to macroscopic plane-strain deformations has the direct implication that the current direction of lamination in the deformed configuration, \mathbf{n} , as determined by expression (6.27), remains in the 1-2-plane (see Fig. 6.3(b)). In this connection, it proves expedient to introduce the scalar variable ϕ as the (in-plane) angle—measured in the anticlockwise sense—that characterizes the relative orientation of \mathbf{n} with respect to the lamination direction in the undeformed configuration \mathbf{N} (see Fig. 6.3(b)). More precisely, making use of (6.27) and (6.29),

$$\phi = \cos^{-1} \left[\frac{\sqrt{2} \left(\cos^2 \bar{\theta} + \bar{\lambda}^2 \sin^2 \bar{\theta} \right)}{\sqrt{1 + \bar{\lambda}^4 - (\bar{\lambda}^4 - 1) \cos 2\bar{\theta}}} \right]. \quad (6.30)$$

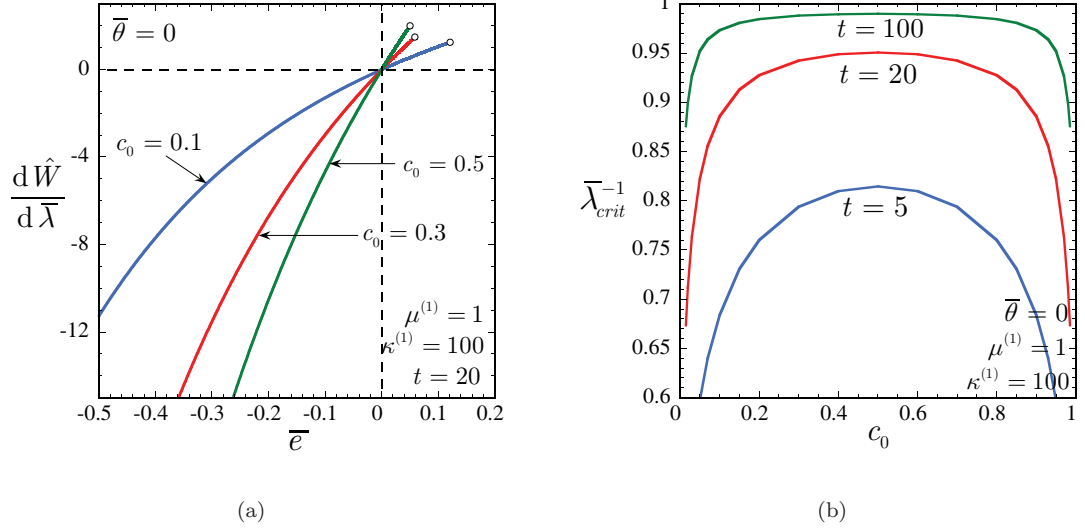


Figure 6.4: Effective behavior of a hyperelastic laminate with compressible Neo-Hookean phases subjected to aligned pure shear loading ($\bar{\theta} = 90^\circ$). (a) The macroscopic stress $d\hat{W}/d\bar{\lambda}$ for various values of initial volume fraction of the stiffer phase, c_0 , as a function of the logarithmic strain $\bar{\epsilon} = \ln \bar{\lambda}$. (b) The critical stretch, $\bar{\lambda}_{crit}$, at which the homogenized laminate loses strong ellipticity for various values of the contrast $t = \mu^{(2)}/\mu^{(1)} = \kappa^{(2)}/\kappa^{(1)}$, as a function of the initial volume fraction c_0 .

6.3 Results and discussion

In this section, results are provided for the in-plane effective behavior of elastomeric laminates with compressible Neo-Hookean phases characterized by stored-energy functions of the form (6.28), subjected to a wide range of loading conditions of the form (6.29). Results are given for $\mu^{(1)} = 1$, $\kappa^{(1)} = 100$, various values of heterogeneity contrast, $t = \mu^{(2)}/\mu^{(1)} = \kappa^{(2)}/\kappa^{(1)}$, and initial volume fraction, c_0 , of the stiffer phase (*i.e.*, phase 2). For clarity, the points at which loss of strong ellipticity is encountered are denoted with the symbol “o” in the plots.

6.3.1 Aligned pure shear

Figure 6.4 presents the effective behavior of a hyperelastic laminate with compressible Neo-Hookean phases subjected to aligned pure shear loading with $\bar{\theta} = 0$ in (6.29). Note that in this case, $\bar{\lambda} \geq 1$ in (6.29) corresponds to compression along the layers, and $\bar{\lambda} \leq 1$, to tension. Part (a) shows the effective stress $d\hat{W}/d\bar{\lambda}$ for a contrast of $t = \mu^{(2)}/\mu^{(1)} = \kappa^{(2)}/\kappa^{(1)} = 20$ and initial volume fractions of the stiffer phase of $c_0 = 10, 30, 50\%$, as a function of the logarithmic strain $\bar{\epsilon} = \ln \bar{\lambda}$. Part (b) shows the critical stretch, $\bar{\lambda}_{crit}^{-1}$, at which the homogenized response of the laminate loses strong

ellipticity for contrasts $t = 5, 20$, and 100 , as a function of the initial volume fraction c_0 .

It is observed from Figure 6.4(a) that the effective behavior of the hyperelastic laminate is harder for higher values of the initial volume fraction of the stiffer phase c_0 , as expected on physical grounds. More importantly, it is recognized from Figure 6.4(a) that the overall response of the elastomeric laminate under “tension” along the layers (*i.e.*, for $\bar{\lambda} \leq 1$) is radically different from its response under “compression” (*i.e.*, for $\bar{\lambda} \geq 1$). Indeed, under “tension,” the material is seen to remain stable for all applied deformations. On the other hand, under “compression,” the material becomes unstable through loss of strong ellipticity at relatively small values of strain. This is due to the vanishing of the effective incremental shear modulus $\widehat{\mathcal{L}}_{1212}$ and implies that the homogenized material may develop localized shear deformations in planar zones with normal—in the deformed configuration— \mathbf{e}_2 , and in the direction \mathbf{e}_1 (see Fig. 6.3). This behavior is consistent with the development of kink bands, which have been observed to appear in various types of stratified media (see, e.g., Kyriakides et al., 1995).

A key observation that should be made from Figure 6.4(b) is that, under pure shear “compression,” the elastomeric laminate becomes unstable at larger stretches $\bar{\lambda}_{crit}^{-1}$ (*i.e.*, smaller compressive strains) for higher values of the contrast t . In fact, it can be shown that $\bar{\lambda}_{crit}^{-1} \rightarrow 1$ as $t \rightarrow \infty$. That is, for the case when the stiffer layers are taken to be rigid (*i.e.*, for $t = \infty$), the laminate is already unstable at zero strain when subjected to pure shear compression. Of course, an elastomer reinforced with rigid layers is itself rigid under loading conditions that require deformation of the layers, such as aligned pure shear. The issue here is that in spite of being rigid, the material is actually unstable when subjected to aligned pure shear compression.

Figure 6.4(b) shows further that $\bar{\lambda}_{crit}^{-1} \rightarrow 0$ as $c_0 \rightarrow 0$. This is consistent with the fact that the elastomeric “matrix” phase of the material is strongly elliptic, so that in the absence of reinforcing phase (*i.e.*, for $c_0 = 0$) the material remains stable for all deformations. As the initial volume fraction of the stiffer layers c_0 is increased from zero, the critical stretch at which the material loses strong ellipticity $\bar{\lambda}_{crit}^{-1}$ increases monotonically up to $c_0 = 50\%$ at which $\bar{\lambda}_{crit}^{-1}$ reaches a maximum. After this point, further increase in c_0 results in the monotonic decrease of $\bar{\lambda}_{crit}^{-1}$. This behavior is simply due to the fact that the reinforcing phase—similar to the “matrix” phase—is strongly elliptic, so that in the limit as $c_0 \rightarrow 1$, $\bar{\lambda}_{crit}^{-1} \rightarrow 0$. In this connection, it should be noted that the results shown in Figure 6.4(b) for $\bar{\lambda}_{crit}^{-1}$ are completely symmetric about $c_0 = 50\%$, the point at which the material is most unstable. Finally, it should be pointed out that results similar

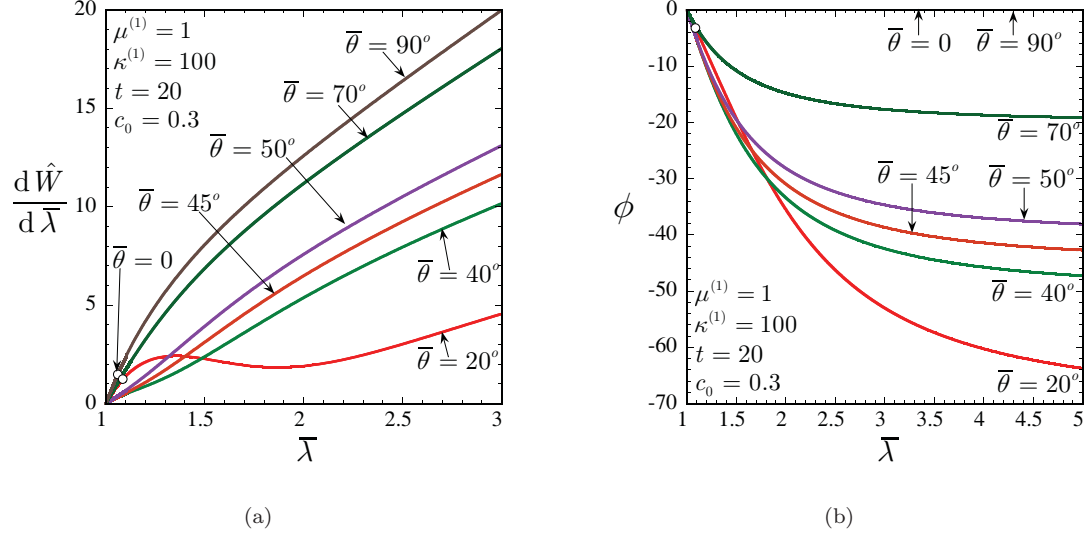


Figure 6.5: Effective behavior of a hyperelastic laminate subjected to pure shear loading at various angles $\bar{\theta}$ (in the *large* deformation regime). The results correspond to compressible Neo-Hookean phases with contrast $t = \mu^{(2)}/\mu^{(1)} = \kappa^{(2)}/\kappa^{(1)} = 20$, initial volume fraction of the stiffer phase $c_0 = 30\%$, and are shown as a function of the macroscopic stretch $\bar{\lambda}$. (a) The macroscopic stress $d\hat{W}/d\bar{\lambda}$. (b) The angle of rotation of layers ϕ .

to those shown in Figure 6.4(b) were first obtained by Triantafyllidis and Maker (1985).

6.3.2 Pure shear at an angle

Figure 6.5 provides plots for the effective behavior of Neo-Hookean laminates subjected to pure shear loading at the fixed angles $\bar{\theta} = 0, 20^\circ, 40^\circ, 45^\circ, 50^\circ, 70^\circ$, and 90° . Results are shown for a contrast of $t = \mu^{(2)}/\mu^{(1)} = \kappa^{(2)}/\kappa^{(1)} = 20$ and initial volume fraction of $c_0 = 30\%$, as a function of the macroscopic stretch $\bar{\lambda}$. Part (a) shows the effective stress $d\hat{W}/d\bar{\lambda}$, and part (b), the angle of rotation of the layers ϕ .

An important observation from Figure 6.5(a) is that for sufficiently large deformations, except for the case with $\bar{\theta} = 0$, the elastomeric laminate consistently shows a stiffer response for higher angles of loading, with the stiffest behavior being attained at $\bar{\theta} = 90^\circ$. The macroscopic stress for exactly $\bar{\theta} = 0$ —though slightly below—is essentially equal to that for $\bar{\theta} = 90^\circ$. In this connection, it is appropriate to remark that for the case of *incompressible* laminates, the effective stress-stretch relation for $\bar{\theta} = 0$ is exactly identical to that for $\bar{\theta} = 90^\circ$. In view of the relatively high values of the bulk moduli of both phases, $\kappa^{(1)} = 100$ and $\kappa^{(2)} = 20 \times 100 = 2000$, this explains the agreement between the $\bar{\theta} = 0$ and $\bar{\theta} = 90^\circ$ results shown in Figure 6.5. It is further noted from

Figure 6.5(a) that loss of strong ellipticity takes place only for the loadings with the two smallest angles: $\bar{\theta} = 0$ and $\bar{\theta} = 20^\circ$. Thus, it is seen that in spite of exhibiting practically identical stress-stretch relations, the behavior for the loadings with $\bar{\theta} = 0$ and $\bar{\theta} = 90^\circ$ are actually very different in terms of stability. Indeed, while the behavior for pure shear with $\bar{\theta} = 0$, which corresponds to *compression* along the layers, loses strong ellipticity, the behavior for pure shear with $\bar{\theta} = 90^\circ$, which corresponds to *tension* along the layers, remains stable for all applied deformations.

Figure 6.5(b) illustrates that the layers rotate clockwise (with respect to the fixed frame of reference) aligning themselves with the principal direction of tensile loading¹ (*i.e.*, $\phi \rightarrow \bar{\theta} - 90^\circ$ as $\bar{\lambda} \rightarrow \infty$), for all loadings, except at $\bar{\theta} = 0$, for which the layers do not rotate, but instead remain fixed for all applied stretches. That is, for *aligned* loadings, namely, $\bar{\theta} = 0$ and $\bar{\theta} = 90^\circ$, there is no evolution of the orientation of the layers. On the other hand, for *misaligned* loadings, the layers undergo a total rotation equal to the complementary angle of $\bar{\theta}$ as $\bar{\lambda} \rightarrow \infty$. Making contact with the stress-stretch relations displayed in Figure 6.5(a), this behavior suggests that the rotation of the layers is actually a *softening mechanism*, since, as shown by Figure 6.5, larger rotations correspond to softer overall stress-stretch relations. This point is corroborated in the context of the next figure.

Figure 6.6 provides plots for a blow up in the small deformation regime of the results shown in Figure 6.5. Figure 6.6 shows that loadings at complementary angles lead to identical effective responses in the small deformation regime, in accordance with the linear theory. In addition, it is observed from Figure 6.6(a) that—in the range from $\bar{\theta} = 0$ to $\bar{\theta} = 45^\circ$ —the effective stress-stretch relations in the small deformation regime are softer for larger angles of loading, attaining the softest response at $\bar{\theta} = 45^\circ$. As the deformation progresses in the finite deformation regime, the effective responses at complementary angles deviate from each other, due to the difference in the evolution of microstructure. Indeed, as already pointed out in the previous figure and as shown in Figure 6.6, larger layer rotation consistently leads to softer stress-stretch relations. It is thus concluded that the rotation of the layers, which depends critically on the loading conditions, is indeed a *softening mechanism*.

With regard to the above discussion, it is important to make the following remark. In view of the fact that smaller loading angles $\bar{\theta}$ lead to larger layer rotations, and hence, to softer effective responses of the laminate at large deformations, the softest response will be generated at $\bar{\theta} =$

¹This can be readily seen analytically by taking the limit $\bar{\lambda} \rightarrow \infty$ in the equation (6.30) for ϕ .

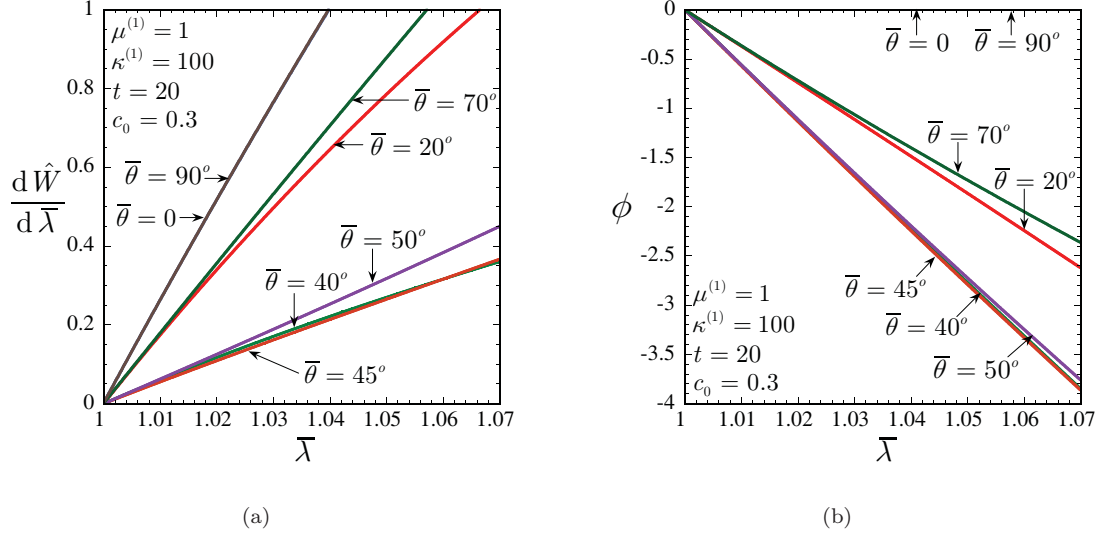


Figure 6.6: Effective behavior of a hyperelastic laminate subjected to pure shear loading at various angles $\bar{\theta}$ (in the *small* deformation regime). The results correspond to compressible Neo-Hookean phases with contrast $t = \mu^{(2)}/\mu^{(1)} = \kappa^{(2)}/\kappa^{(1)} = 20$, initial volume fraction of the stiffer phase $c_0 = 30\%$, and are shown as a function of the macroscopic stretch $\bar{\lambda}$. (a) The macroscopic stress $d\hat{W}/d\bar{\lambda}$. (b) The angle of rotation of layers ϕ .

$0+$ (*i.e.*, an infinitesimal misalignment from $\bar{\theta} = 0$). For such loading, the layers will undergo (essentially) a total rotation of $\phi = 90^\circ$. This is in contrast to the behavior at exactly $\bar{\theta} = 0$, for which there is not evolution of the layer orientation and the effective response of the laminate, together with the one at $\bar{\theta} = 90^\circ$, is the stiffest. This singularity at $\bar{\theta} = 0$ is entirely consistent with the emergence of kink-band-type instabilities discussed in the context of Figure 6.4 for *compressive* loadings along the layers.

Figure 6.7 illustrates the effects of the loading angle, $\bar{\theta}$, and the heterogeneity contrast, $t = \mu^{(2)}/\mu^{(1)} = \kappa^{(2)}/\kappa^{(1)}$, on the onset of instabilities in elastomeric laminates subjected to pure shear. Results are shown for Neo-Hookean phases with initial volume fraction of the stiffer phase of $c_0 = 30\%$. Part (a) shows the critical stretch, $\bar{\lambda}_{crit}$, at which the homogenized laminate loses strong ellipticity for contrasts of $t = 5, 20$, and 100 , as a function of the loading angle $\bar{\theta}$. Part (b) displays corresponding results for $\bar{\lambda}_{crit}$ for loading angles of $\bar{\theta} = 0, 10^\circ$, and 20° , as a function of the contrast t .

It is observed from Figure 6.7(a) that the laminate becomes more stable with increasing values of the loading angle $\bar{\theta}$. In fact, Figure 6.7(a) shows that there is a threshold (depending on the contrast t) in $\bar{\theta}$, beyond which the material remains stable for all applied deformations. Note

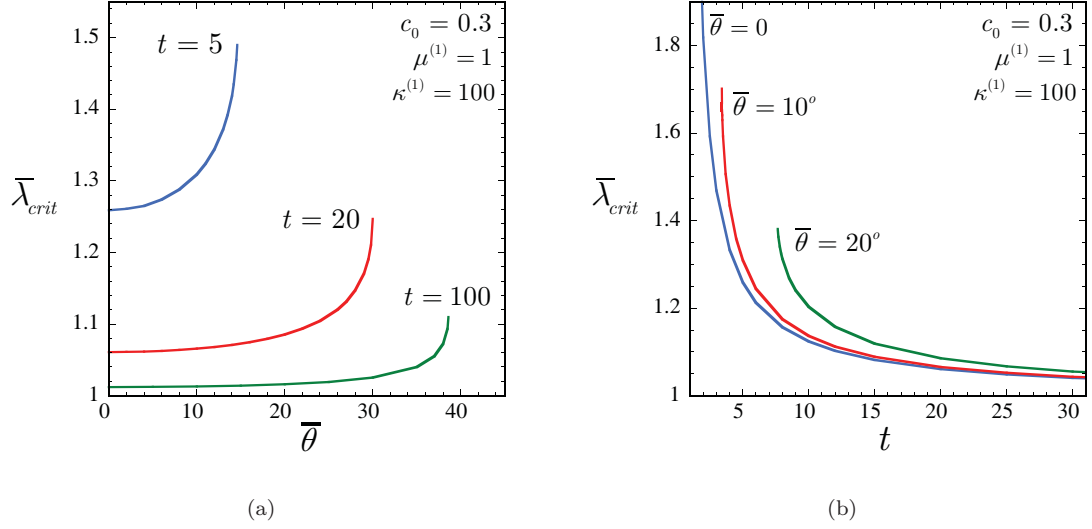


Figure 6.7: Pure shear loading of Neo-Hookean laminates. (a) The critical stretch, $\bar{\lambda}_{crit}$, at which loss of strong ellipticity takes place for various values of the contrast $t = \mu^{(2)}/\mu^{(1)} = \kappa^{(2)}/\kappa^{(1)}$, as a function of the loading angle $\bar{\theta}$. (b) The corresponding results for $\bar{\lambda}_{crit}$ for various values of the loading angle $\bar{\theta}$, as a function of the contrast t .

also that the laminate is more unstable for higher values of the contrast t . This dependence is more clearly illustrated by Figure 6.7(b). Interestingly, Figure 6.7(b) also shows that for aligned loadings (*i.e.*, for $\bar{\theta} = 0$), $\bar{\lambda}_{crit}$ has a vertical asymptote at $t = 1$. That is, under aligned pure shear loading with compression along the layers, the existence of even an infinitesimal heterogeneity contrast (*i.e.*, $t \neq 1$) between the layers will result in the material losing strong ellipticity at some finite stretch. Of course, at exactly $t = 1$ the laminate corresponds to a homogeneous strongly elliptic material, so that $\bar{\lambda}_{crit} = \infty$. For misaligned loadings, there are no vertical asymptotes, but, instead, there are thresholds (depending on $\bar{\theta}$) in t , beyond which the material remains stable for all applied deformations. Note further that for all three loading angles, $\bar{\theta} = 0, 10^\circ$, and 20° , $\bar{\lambda}_{crit} \rightarrow 1$ as $t \rightarrow \infty$, indicating that in the limiting case of rigid layers, the material loses strong ellipticity at zero strain. In summary, the above results indicate that *compressive* loading along the layers, together with *heterogeneity contrast* between the phases, are two major factors in the possible development of macroscopic instabilities in elastomeric laminates.

6.4 Concluding remarks

In this chapter, use has been made of the tangent second-order method of Ponte Castañeda and Tiberio (2000) to develop *exact* estimates for the effective behavior of hyperelastic laminates subjected to finite deformations. It is emphasized that the new second-order estimates proposed in this work reduce to the earlier tangent second-order method for the particular case of laminate microstructures, and that the latter has been utilized here for mere computational simplicity.

In this work, an explicit expression for the evolution of the orientation of the underlying layers in elastomeric laminates has been derived. Interestingly, this expression depends exclusively on the applied macroscopic deformation, and *not* on the constitutive behavior of the phases, nor on their volume fractions. Furthermore, it has been established that the rotation of the layers in elastomeric laminates subjected to finite deformations provides a *softening* mechanism on the overall behavior of these materials.

Another main result of this chapter is that elastomeric laminates may develop kink-band-type instabilities when subjected to sufficiently large compression along the underlying layers, provided that there is a sufficiently large heterogeneity contrast between them. The development of these instabilities have been related to the evolution of the microstructure, in particular, to the rotation of the layers.

Finally, it should be re-emphasized that the results presented in this chapter are *exact*. In this connection, they will be of great use in order to understand and validate the results presented in the next chapter, where more general microstructures—which include laminates as a limiting case—are considered.

Chapter 7

Reinforced elastomers: cylindrical fibers, random microstructure

This chapter is concerned with the effective behavior of fiber-reinforced elastomers. In particular, attention will be restricted to the in-plane response of an isotropic elastomer reinforced with aligned cylindrical fibers with elliptical cross-section. For the special case of rigid fibers and incompressible matrix phase, closed-form, analytical results are obtained. The results indicate—in accord with the findings of previous chapters—that the evolution of the microstructure has a dramatic effect on the effective response of the composite, and, in particular, on its stability. More specifically, it is found that the rotation of the fibers—induced by the applied finite deformations—generates significant geometric softening in the composite. Moreover, in spite of the fact that both the matrix and the fibers are assumed to be strongly elliptic, the homogenized behavior is found to lose strong ellipticity at sufficiently large deformations. In particular, when the reinforced elastomer is loaded in compression along the long, in-plane axis of the fibers, a certain type of “flopping” instability is detected, corresponding to the composite becoming infinitesimally soft to rotation of the fibers.

7.1 Plane-strain loading of fiber-reinforced, random elastomers

In this section, we study the problem of *plane-strain* deformations of fiber-reinforced elastomers where the cylindrical fibers, which are perpendicular to the plane of the deformation, are aligned in the \mathbf{e}_3 direction. Moreover, the fibers have an initial volume fraction c_0 and are taken to have

an initially elliptical cross section of aspect ratio ω_0 , and to be initially distributed with “elliptical symmetry,” involving equal aspect ratios and orientations for all the fibers, in the plane of deformation. For simplicity and without loss of generality, ω_0 will be taken greater than or equal to one in the development that follows. Note that the applied deformation $\bar{\mathbf{F}}$ here is entirely characterized by the 4 in-plane components: \bar{F}_{11} , \bar{F}_{22} , \bar{F}_{12} , and \bar{F}_{21} , since the out-of-plane components are known: $\bar{F}_{13} = \bar{F}_{23} = \bar{F}_{31} = \bar{F}_{32} = 0$, and $\bar{F}_{33} = 1$ (see Figure 7.1(a)).

Recalling the section on microstructure evolution from Chapter 2, the relevant microstructural variables, in the context of plane-strain loading for the type of fiber-reinforced elastomers considered here, are the *current* value of the volume fraction, c , the average in-plane aspect ratio, ω , and the average in-plane orientation of the fibers, ϕ . Figure 7.1(b) shows a schematic representation of the cross section in the plane of deformation of a typical fiber with the various microstructural variables. In this figure, the shaded ellipse represents the 1-2 cross section of a typical fiber with initial aspect ratio $\omega_0 = z_2^0/z_1^0$ in the *reference* configuration, with the rectangular Cartesian basis $\{\mathbf{e}_i\}$ denoting its principal directions. The dashed ellipse represents the 1-2 cross section of the same fiber in the *deformed* configuration. In this connection, the current average aspect ratio of the fiber is denoted by $\omega = z_2/z_1$ and the corresponding average principal directions are denoted by the rectangular Cartesian basis $\{\mathbf{e}'_i\}$, whose orientation relative to $\{\mathbf{e}_i\}$ is determined by the angle ϕ (which is measured in the anticlockwise sense). (Note that the initial orientation of the fibers corresponds to $\phi_0 = 0$.) For convenience, the basis $\{\mathbf{e}_i\}$ defining the principal direction of the inclusions in the reference configuration will be identified here with the fixed laboratory frame of reference. In the rest of this chapter, the components of any tensorial quantity will be referred to $\{\mathbf{e}_i\}$.

Following Section 2.1.3, the elastomeric matrix and fiber phases are taken to be characterized by (2D) isotropic stored-energy-functions of the form:

$$W^{(r)}(\mathbf{F}) = g^{(r)}(I) + h^{(r)}(J) + \frac{\kappa^{(r)} - \mu^{(r)}}{2} (J - 1)^2, \quad (7.1)$$

where it is recalled that $g^{(r)}$ and $h^{(r)}$ are material functions of their arguments: $I = \lambda_1^2 + \lambda_2^2$ and $J = \lambda_1\lambda_2$. Furthermore, the parameters $\mu^{(r)}$ and $\kappa^{(r)}$ denote the initial shear and in-plane bulk moduli of phase r , respectively. The analysis that follows will be carried out for general stored-energy functions of the form (7.1); however, for definiteness, results will be illustrated for Gent

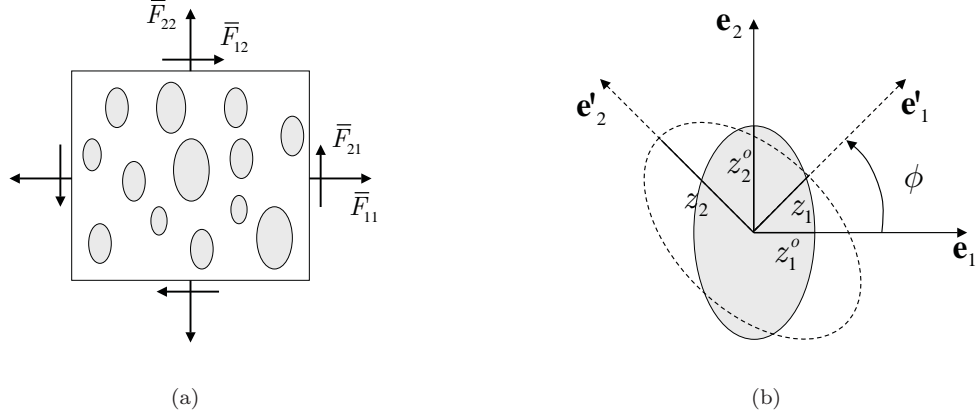


Figure 7.1: Schematic representation of the microstructure of a fiber-reinforced elastomer, depicting the applied loading and the various microstructural variables. (a) The 1-2 cross section of the composite together with the applied loading conditions. (b) The shaded ellipse represents the 1-2 cross section of a typical fiber with initial aspect ratio $\omega_0 = z_2^0/z_1^0$ in the reference configuration; the dashed ellipse corresponds to the 1-2 cross-section of the same fiber in the deformed configuration, with current aspect ratio $\omega = z_2/z_1$ and current orientation relative to the fixed laboratory frame given by ϕ .

materials with stored-energy function (3.2), repeated here for convenience:

$$W(\mathbf{F}) = -\frac{\mu J_m}{2} \ln \left[1 - \frac{I-2}{J_m} \right] - \mu \ln J + \left(\frac{\kappa - \mu}{2} - \frac{\mu}{J_m} \right) (J-1)^2, \quad (7.2)$$

Recall that in this expression, the parameter J_m is the limiting value for $I-2$ at which the material locks up. Recall as well that the stored-energy function (7.2) is *strongly elliptic* provided that $\mu > 0$, $J_m > 0$, and $\kappa > 2\mu/J_m + \mu$, which will be assumed here.

Next, making contact with the decompositions $\bar{\mathbf{F}} = \bar{\mathbf{R}}\bar{\mathbf{U}}$ and $\bar{\mathbf{U}} = \bar{\mathbf{Q}}\bar{\mathbf{D}}\bar{\mathbf{Q}}^T$ used in the context of expression (2.66), it is convenient for later use to introduce angles $\bar{\psi}$ and $\bar{\theta}$, serving to quantify the *macroscopic rotation* (or “continuum spin”) $\bar{\mathbf{R}}$, and the orientation (in the anticlockwise sense relative to the fixed laboratory frame) of the in-plane Lagrangian principal axes (or “loading angle”) $\bar{\mathbf{Q}}$, via the expressions:

$$\bar{\mathbf{R}} = \begin{bmatrix} \cos \bar{\psi} & -\sin \bar{\psi} \\ \sin \bar{\psi} & \cos \bar{\psi} \end{bmatrix} \quad \text{and} \quad \bar{\mathbf{Q}} = \begin{bmatrix} \cos \bar{\theta} & -\sin \bar{\theta} \\ \sin \bar{\theta} & \cos \bar{\theta} \end{bmatrix}. \quad (7.3)$$

The principal values of $\bar{\mathbf{U}}$ are, of course, the macroscopic principal stretches $\bar{\lambda}_1$ and $\bar{\lambda}_2$. Thus, the 4 independent loading parameters $\bar{\psi}$, $\bar{\theta}$, $\bar{\lambda}_1$ and $\bar{\lambda}_2$ are entirely equivalent to the 4 parameters \bar{F}_{11} , \bar{F}_{22} , \bar{F}_{12} , and \bar{F}_{21} .

Having specified the initial microstructure, the constitutive behavior of the matrix and fibers, and the applied loading conditions, we next compute the specialization of the second-order estimate (2.62) to the class of reinforced elastomers of interest in this chapter.

7.1.1 Second-order homogenization estimates: compliant fibers

Some of the algebraic manipulations that were utilized in the computation of the second-order estimate (2.69) for 2D periodic, porous elastomers in Chapter 4 prove equally helpful in the computation of the second-order estimate (2.62) for fiber-reinforced elastomers under *plane-strain* deformations. Thus, it suffices to consider the in-plane components of the modulus tensor $\mathbf{L}^{(1)}$ of the matrix phase of the linear comparison composite, which may be conveniently expressed as a matrix in $\mathfrak{R}^{4 \times 4}$:

$$\begin{bmatrix} L_{1111} & L_{1122} & L_{1112} & L_{1121} \\ L_{1122} & L_{2222} & L_{2212} & L_{2221} \\ L_{1112} & L_{2212} & L_{1212} & L_{1221} \\ L_{1121} & L_{2221} & L_{1221} & L_{2121} \end{bmatrix}, \quad (7.4)$$

where, for notational simplicity, the superscript ‘(1)’ has been suppressed for the components of $\mathbf{L}^{(1)}$, and use has been made of major symmetry (*i.e.*, $L_{ijkl} = L_{klij}$). Recalling that \mathbf{L}^* has been taken to be orthotropic, it follows that it may be written in the form:

$$\begin{bmatrix} L_{1111}^* & L_{1122} & 0 & 0 \\ L_{1122}^* & L_{2222}^* & 0 & 0 \\ 0 & 0 & L_{1212}^* & L_{1221}^* \\ 0 & 0 & L_{1221}^* & L_{2121}^* \end{bmatrix}. \quad (7.5)$$

Since $\overline{\mathbf{R}}$ and $\overline{\mathbf{Q}}$ can be readily computed from $\overline{\mathbf{F}}$, prescription (2.66) entails that $\mathbf{L}^{(1)}$ possesses 6 independent components, namely, $L_{1111}^*, L_{2222}^*, L_{1122}^*, L_{1212}^*, L_{2121}^*$, and L_{1221}^* . For the reasons already explained in preceding chapters, the following constraints are imposed among the components of (7.5):

$$L_{2121}^* = L_{1212}^*, \quad \text{and} \quad L_{1221}^* = \sqrt{(L_{1111}^* - L_{1212}^*)(L_{2222}^* - L_{1212}^*)} - L_{1122}^*. \quad (7.6)$$

Next, with the choice (2.66) for the modulus $\mathbf{L}^{(1)}$ of the matrix phase of the LCC, the conditions (7.6) for the components (7.5) of \mathbf{L}^* , and making use of the identifications $\ell_1^* = L_{1111}^*$, $\ell_2^* = L_{2222}^*$, $\ell_3^* = L_{1212}^*$, and $\ell_4^* = L_{1122}^*$, the equations (2.68) can be seen to reduce to 4 consistent equations

for the 4 components of $\hat{\mathbf{F}}^{(1)}$. These equations are more conveniently expressed in terms of the variable \mathbf{Y} :

$$\mathbf{Y} = \overline{\mathbf{Q}}^T \overline{\mathbf{R}}^T \left(\hat{\mathbf{F}}^{(1)} - \overline{\mathbf{F}} \right) \overline{\mathbf{Q}}, \quad (7.7)$$

which leads to the expressions:

$$\begin{aligned} (Y_{11})^2 + 2f_1 Y_{12} Y_{21} &= k_1, \\ (Y_{22})^2 + 2f_2 Y_{12} Y_{21} &= k_2, \\ (Y_{12})^2 + (Y_{21})^2 + 2f_3 Y_{12} Y_{21} &= k_3, \\ Y_{11} Y_{22} - Y_{12} Y_{21} &= k_4, \end{aligned} \quad (7.8)$$

where $f_1 = \partial L_{1221}^* / \partial L_{1111}^*$, $f_2 = \partial L_{1221}^* / \partial L_{2222}^*$, $f_3 = \partial L_{1221}^* / \partial L_{1212}^*$, and

$$\begin{aligned} k_1 &= \frac{c_0}{(1-c_0)^2} \left(\overline{\mathbf{D}} - \check{\mathbf{F}}^{(2)} \right) \cdot \frac{\partial \mathbf{E}^*}{\partial L_{1111}^*} \left(\overline{\mathbf{D}} - \check{\mathbf{F}}^{(2)} \right), \\ k_2 &= \frac{c_0}{(1-c_0)^2} \left(\overline{\mathbf{D}} - \check{\mathbf{F}}^{(2)} \right) \cdot \frac{\partial \mathbf{E}^*}{\partial L_{2222}^*} \left(\overline{\mathbf{D}} - \check{\mathbf{F}}^{(2)} \right), \\ k_3 &= \frac{c_0}{(1-c_0)^2} \left(\overline{\mathbf{D}} - \check{\mathbf{F}}^{(2)} \right) \cdot \frac{\partial \mathbf{E}^*}{\partial L_{1212}^*} \left(\overline{\mathbf{D}} - \check{\mathbf{F}}^{(2)} \right), \\ k_4 &= \frac{c_0}{2(1-c_0)^2} \left(\overline{\mathbf{D}} - \check{\mathbf{F}}^{(2)} \right) \cdot \frac{\partial \mathbf{E}^*}{\partial L_{1122}^*} \left(\overline{\mathbf{D}} - \check{\mathbf{F}}^{(2)} \right). \end{aligned} \quad (7.9)$$

In relations (7.9), $\check{\mathbf{F}}^{(2)} = \overline{\mathbf{Q}}^T \overline{\mathbf{R}}^T \overline{\mathbf{F}}^{(2)} \overline{\mathbf{Q}}$ and $\mathbf{E}^* = (\mathbf{P}^*)^{-1} - (1-c_0)\mathbf{L}^*$ with \mathbf{P}^* such that

$$P_{ijkl} = \overline{Q}_{rm} \overline{Q}_{jn} \overline{Q}_{sp} \overline{Q}_{lq} \overline{R}_{ir} \overline{R}_{ks} P_{mnpq}^*, \quad (7.10)$$

have been introduced for ease of notation. Moreover, the tensor \mathbf{P} in these expressions is given by (2.57), which can be integrated analytically. However, the final explicit expressions will not be included here for their bulkiness.

Equations (7.8) can be shown to yield two distinct solutions for Y_{11} and Y_{22} , in terms of which the combinations $Y_{12}Y_{21}$ and $Y_{12}^2 + Y_{21}^2$ may be determined. The two solutions read as follows:

$$\begin{aligned} Y_{11} &= \pm \frac{2f_1 k_4 + k_1}{\sqrt{4f_1^2 k_2 + 4f_1 k_4 + k_1}}, & Y_{22} &= \pm \frac{2f_1 k_2 + k_4}{\sqrt{4f_1^2 k_2 + 4f_1 k_4 + k_1}}, \\ Y_{12} Y_{21} &= Y_{11} Y_{22} - k_4, & Y_{12}^2 + Y_{21}^2 &= k_3 - 2f_3 Y_{12} Y_{21}, \end{aligned} \quad (7.11)$$

where it is emphasized that the positive (and negative) signs must be chosen to go together in the roots for Y_{11} and Y_{22} .

Next, using the relation $\hat{\mathbf{F}}^{(1)} = \overline{\mathbf{R}} \overline{\mathbf{Q}} \mathbf{Y} \overline{\mathbf{Q}}^T + \overline{\mathbf{F}}$, each of the two distinct roots for \mathbf{Y} may be substituted into expression (2.65). The resulting relation, together with expression (2.64),

form a system of 8 nonlinear algebraic equations for the 8 scalar unknowns $\overline{F}_{11}^{(2)}, \overline{F}_{22}^{(2)}, \overline{F}_{12}^{(2)}, \overline{F}_{21}^{(2)}$, $L_{1111}^*, L_{2222}^*, L_{1122}^*$, and L_{1212}^* , which must be solved numerically. It is worth mentioning that by exploiting the objectivity and isotropy of the stored-energy functions of the phases of the composite, the equations obtained from (2.65) and (2.64) may be finally cast into a rather simple form. Having computed the values of all the components of $\overline{\mathbf{F}}^{(2)}$ and $\mathbf{L}^{(1)}$ for a given initial fiber concentration c_0 and aspect ratio ω_0 , given material behavior $g^{(r)}, h^{(r)}$, and $\kappa^{(r)}$, and given loading $\overline{\mathbf{F}}$, the values of the components of $\overline{\mathbf{F}}^{(1)}$ and $\hat{\mathbf{F}}^{(1)}$ can be readily determined using relations (2.60)₁ together with (2.64) and (7.11), respectively. In turn, these results may be used to compute the second-order estimate (2.62) for the effective stored-energy function \widehat{W} of the fiber-reinforced elastomers. Also, the evolution of the microstructural variables c , ω , and ϕ may be determined from the estimate for $\overline{\mathbf{F}}^{(2)}$, by means of the tensor $\mathbf{Z} = \mathbf{Z}_0 \overline{\mathbf{F}}^{(2)-1}$, as discussed in Section 2.5. Thus, letting $\mathbf{Z}^T \mathbf{Z} = \mathbf{K} \mathbf{W} \mathbf{K}^T$, where \mathbf{W} is a diagonal tensor with components z_1^{-2} and z_2^{-2} , such that $\omega = z_2/z_1$, the orthogonal tensor \mathbf{K} defines the fiber-orientation angle ϕ (see Figure 7.1(b)) via the relation:

$$K = \begin{bmatrix} \cos \phi & -\sin \phi \\ \sin \phi & \cos \phi \end{bmatrix}. \quad (7.12)$$

In connection with these results, it is important to remark that the two above-mentioned roots lead to very similar results for the effective behavior of fiber-reinforced elastomers when both $\kappa^{(r)}$ ($r = 1, 2$) and ω_0 are finite (of the same order as $\mu^{(1)}$). However, in the limiting case when the microstructure approaches a simple laminate with compressible phases, *i.e.*, for $\omega_0 \gg 1$ with $\kappa^{(r)}$ and $\mu^{(1)}$ finite, there is *only one* root that is superior to the alternative choice, since only one root recovers the exact effective behavior of simple laminates. The choice of such root depends on the loading conditions. For instance, for aligned—with $\overline{\theta} = 0$ —loading conditions with $\overline{\lambda}_1 \geq 1$ ($\overline{\lambda}_1 \leq 1$), only the “positive” (“negative”) root recovers the exact behavior of simple laminates. On the other hand, for the case when the bulk modulus of the phases is large, and the aspect ratio of the fibers is finite, *i.e.*, for $\kappa^{(r)} \gg 1$ and ω_0 finite, it can be shown that only the “negative” root generates physically meaningful estimates—regardless of the loading conditions. (However, in the incompressible limit, $\kappa^{(r)} = \infty$, both roots recover the exact result for the laminate, $\omega_0 = \infty$.) Consequently, given that the primary interest here is in rubbers (which are known to be nearly incompressible) reinforced with fibers of finite aspect ratio, the “negative” root should be used in the computation of the second-order estimates for the effective behavior of fiber-reinforced elastomers.

7.1.2 Second-order homogenization estimates: rigid fibers

Compressible matrix

The computation of the second-order estimates (2.82) for the effective behavior of compressible elastomers reinforced with rigid fibers parallels that given in Section 7.1.1 for the elastomers reinforced by compliant fibers. Indeed, prescribing the same restrictions (7.6) for the modulus tensor $\mathbf{L}^{(1)}$ of the matrix phase of the linear comparison composite, equation (2.81) can be seen to provide 4 consistent equations for the 4 components of $\hat{\mathbf{F}}^{(1)}$. These equations have the same form (7.8) introduced in Section 7.1.1 in terms of the variable \mathbf{Y} , defined by relation (7.7), where now the corresponding $f_1, f_2, f_3, k_1, k_2, k_3, k_4$ are functions of $L_{1111}^*, L_{2222}^*, L_{1122}^*, L_{1212}^*, \bar{\mathbf{F}}, \bar{\mathbf{R}}^{(2)}$, as well as c_0, ω_0 , and the matrix constitutive functions, $g^{(1)}, h^{(1)}$, and $\kappa^{(1)}$. (Recall that for rigid fibers $\omega = \omega_0$.)

Next, each of the two distinct roots of equations (7.8) may be substituted into the generalized secant equation (2.65), using the expression $\hat{\mathbf{F}}^{(1)} = \bar{\mathbf{R}} \bar{\mathbf{Q}} \mathbf{Y} \bar{\mathbf{Q}}^T + \bar{\mathbf{F}}$. The resulting equation, together with the expression (2.79) for the orthogonal tensor $\bar{\mathbf{R}}^{(2)}$ characterizing the average rotation of the fibers ϕ (note that $\mathbf{K} = \bar{\mathbf{R}}^{(2)}$ in this case), form a system of 5 nonlinear algebraic equations for the 5 scalar unknowns $\phi, L_{1111}^*, L_{2222}^*, L_{1122}^*$, and L_{1212}^* , which must be solved numerically. Having computed the values of these variables, for given fiber concentration c_0 and aspect ratio ω , given matrix behavior, $g^{(1)}, h^{(1)}$, and $\kappa^{(1)}$, and given loading $\bar{\mathbf{F}}$, the values of the components of $\hat{\mathbf{F}}^{(1)}$ can be readily determined using relation (7.11). In turn, these results can be used to compute the second-order estimate (2.82) for the effective stored-energy function \widehat{W} of the rigidly reinforced elastomers. Finally, the same comments apply as in the previous subsection concerning the selection of the roots in expressions (7.7).

Incompressible matrix

The above expressions can be simplified considerably in the limit of incompressible behavior for the matrix phase, *i.e.*, $\kappa^{(1)} \rightarrow \infty$. In this context, it is recalled that the asymptotic behavior of the two above-mentioned “roots” is quite different for large values of $\kappa^{(1)}$. More specifically, in the limit $\kappa^{(1)} \rightarrow \infty$, the second-order estimates associated with the “negative” root can be shown (see Appendix I) to be consistent with the *exact* overall incompressibility constraint:

$$C(\bar{\mathbf{F}}) = \det \bar{\mathbf{F}} - 1 = 0, \quad (7.13)$$

whereas the estimates associated with the “positive” root lead to a different constraint, and are therefore inconsistent with the physics of the problem. Having clarified this point, it is noted that under plane-strain conditions the macroscopic incompressibility constraint (7.13) implies that the principal stretches can be written in the form $\bar{\lambda}_1 = \bar{\lambda}$ and $\bar{\lambda}_2 = 1/\bar{\lambda}$, where $\bar{\lambda} \geq 1$, so that there is only one loading parameter in this case (apart from the loading angle $\bar{\theta}$). It then follows (see Appendix I) that the second-order estimate (2.82), associated with the “negative” root, for the effective stored-energy function of an incompressible, isotropic elastomer reinforced with aligned, rigid fibers of elliptical cross section, in volume fraction $c = c_0$, and with aspect ratio $\omega = \omega_0$, ($\omega \geq 1$), reduces to:

$$\widehat{W}^I(\bar{\mathbf{F}}) = \widehat{W}^I(\bar{\mathbf{U}}) = \check{W}(\bar{\lambda}, \bar{\theta}) = (1 - c) g^{(1)}(\hat{I}^{(1)}), \quad (7.14)$$

where

$$\begin{aligned} \hat{I}^{(1)} = & \frac{c(1 + \bar{\lambda}^2)^2 + [1 + 2(c - 2)c\bar{\lambda}^2 + \bar{\lambda}^4]\omega + c(1 + \bar{\lambda}^2)^2\omega^2}{(1 - c)^2\bar{\lambda}^2\omega} \\ & - \frac{c(\bar{\lambda}^4 - 1)(\omega - 1)}{(1 - c)^2\bar{\lambda}^2\omega} \sin(\varphi) \sin(\varphi - 2\bar{\theta}) \\ & - \frac{2c(1 + \bar{\lambda}^2)(1 + \omega^2)}{(1 - c)^2\bar{\lambda}\omega} \cos(\varphi). \end{aligned} \quad (7.15)$$

In this relation, the angle φ is given by

$$\varphi = \phi - \bar{\psi}, \quad (7.16)$$

and satisfies the kinematical relation:

$$2\bar{\lambda}(1 + \omega^2) \sin(\varphi) - (\bar{\lambda}^2 - 1)(\omega^2 - 1) \sin[2(\varphi - \bar{\theta})] = 0. \quad (7.17)$$

Thus, the angle φ serves to describe the evolution of the particle orientation $\phi = \varphi + \bar{\psi}$, as a function of the loading parameters $\bar{\lambda}$ and $\bar{\theta}$, for a given value of the fiber aspect ratio ω , via the remarkably simple relation (7.17).

There are several important remarks that should be made in the context of expression (7.14) for the effective stored-energy function of the incompressible reinforced elastomer. First, this estimate linearizes properly, and therefore recovers the correct linearized moduli of the composite, in agreement with the Willis estimates for incompressible, rigidly reinforced, elastic materials, at small deformations. Second, this estimate can be seen to be consistent with *overall objectivity*,

$\widehat{W}^I(\overline{\mathbf{F}}) = \widehat{W}^I(\overline{\mathbf{U}})$, in view of the dependence on the rotation of the particles through the difference between the “macroscopic” rotation angle $\overline{\psi}$ and the “microstructural” rotation angle ϕ . This difference is what is known in plasticity as the “plastic spin.” Finally, it should be remarked that the stored-energy function (7.14) has been shown to satisfy the polyconvex, lower bound (Ponte Castañeda, 1989). For conciseness, the corresponding details will be omitted here. The Voigt upper bound (Ogden, 1978) becomes $+\infty$ in this context, so that it is trivially satisfied by (7.14).

There are also several interesting remarks that may be made on the context of expression (7.17) for the relevant microstructural variable, $\phi = \overline{\psi} + \varphi$, the average rotation angle of the fibers. (Recall that in this case the volume fraction, c , and aspect ratio, ω , of the fibers remain fixed, irrespectively of the applied deformation.) First, it is interesting to remark that the misalignment angle φ depends exclusively on the applied strain ($\overline{\lambda}$ and $\overline{\theta}$) and the shape of the fibers (ω), but *not* on the constitutive behavior of the matrix phase, nor on the volume fraction of fibers. Second, it can be shown from (7.17), that $\varphi \rightarrow \overline{\theta} - \pi/2$ as $\overline{\lambda} \rightarrow \infty$, for all $\overline{\theta} \in (0, \pi)$. That is, as $\overline{\lambda}$ increases, the fibers tend to orient themselves in such a way that their longest in-plane axes tend to become aligned with the tensile loading axis. Note that this behavior is in accord with the behavior of laminates presented in the preceding chapter. Further, for the special value of $\overline{\theta} = 0$, when the fibers are already (initially) aligned with the loading axes, the fibers do not rotate, but instead, remain fixed in orientation. In particular, this implies that the large-deformation behavior of φ has a discontinuity at $\overline{\theta} = 0$, corresponding to the situation when the fibers are aligned with the *compressive* axis, since in this case $\varphi \rightarrow -\pi/2$ ($\pi/2$) as $\overline{\lambda} \rightarrow \infty$, for $\overline{\theta} = 0 + (0-)$, but $\varphi = 0$, $\forall \overline{\lambda}$, for $\overline{\theta} = 0$. In the results section, this behavior will be related to the possible development of symmetry-breaking, macroscopic instabilities, for loading conditions involving compression along the long axes of the fibers.

Incompressible matrix: special cases

The second-order estimate (7.14) is valid for arbitrary fiber cross section. This includes two interesting extreme cases: $\omega \rightarrow \infty$, corresponding to a laminated material, and $\omega = 1$, corresponding to an isotropic distribution of circular fibers.

For the laminate case ($\omega \rightarrow \infty$), the stored-energy function (7.14) can be shown to become unbounded for all deformations except for simple shear “parallel” to the layers, *i.e.*, $\overline{\mathbf{F}} = \mathbf{I} + \overline{\gamma} \mathbf{e}_2 \otimes \mathbf{e}_1$, where $\overline{\gamma}$ is the amount of macroscopic shear. This is consistent with the fact that this type of

deformation is the only one that may be achieved without deforming the rigid phase. It is easy to show that for $\omega \rightarrow \infty$ and $\bar{\mathbf{F}} = \mathbf{I} + \bar{\gamma} \mathbf{e}_2 \otimes \mathbf{e}_1$, expression (7.15) reduces to:

$$\hat{I}^{(1)} = \frac{\bar{\gamma}^2}{(1-c)^2} + 2. \quad (7.18)$$

Also, in this case, as $\omega \rightarrow \infty$, equation (7.17) simplifies to:

$$2\bar{\lambda} \sin(\varphi) - (\bar{\lambda}^2 - 1) \sin[2(\varphi - \bar{\theta})] = 0. \quad (7.19)$$

Now, recalling that for the special case of laminates the effective behavior can be computed *exactly* by making use of the fact that the fields are constant in the phases, it is straightforward to show that the exact result for the effective stored-energy function of the type of laminates considered here is given by $\widehat{W}^I(\mathbf{U}) = (1-c)g^{(1)}(\bar{I}^{(1)})$, where $\bar{I}^{(1)}$ is the first invariant of the right Cauchy-Green deformation tensor associated with the *exact* average deformation gradient in the soft phase of the laminate, namely, $\bar{I}^{(1)} = \bar{\mathbf{F}}^{(1)} \cdot \bar{\mathbf{F}}^{(1)}$. Recognizing now that under simple shearing “parallel” to the layers the rotation of the rigid phase $\bar{\mathbf{R}}^{(2)} = \mathbf{I}$, the average deformation gradient in the soft phase may be computed exactly to yield $\bar{\mathbf{F}}^{(1)} = \mathbf{I} + \bar{\gamma}/(1-c) \mathbf{e}_2 \otimes \mathbf{e}_1$. Thus, it can be deduced that $\hat{I}^{(1)} = \bar{I}^{(1)}$, so that the second-order estimate (7.14) recovers the *exact* result in the limit as $\omega \rightarrow \infty$. It is also a matter of straightforward algebra to show that for $\bar{\mathbf{F}} = \mathbf{I} + \bar{\gamma} \mathbf{e}_2 \otimes \mathbf{e}_1$, expression (7.19) yields $\varphi = -\arcsin(\bar{\gamma}/\sqrt{4 + \bar{\gamma}^2}) = -\bar{\psi}$, so that the angle of rotation of the rigid phase as predicted by the second-order estimate reduces to the *exact* result $\phi = 0$.

On the other hand, for the isotropic case ($\omega = 1$), it is easy to show that $\hat{I}^{(1)}$ reduces to:

$$\hat{I}^{(1)} = \frac{1 + 2c - 4c\bar{\lambda} + 2c^2\bar{\lambda}^2 - 4c\bar{\lambda}^3 + (1 + 2c)\bar{\lambda}^4}{(1-c)^2\bar{\lambda}^2}. \quad (7.20)$$

Note that $\hat{I}^{(1)}$ depends on the principal stretch $\bar{\lambda}$ (but *not* on the loading angle $\bar{\theta}$), so that the corresponding stored-energy function (7.14) is *isotropic* (in the plane of deformation). There are, unfortunately, no exact results available for the effective behavior of isotropic, rigidly reinforced, incompressible elastomers to which to compare (7.20). But it is easy to see from (7.17) that the second-order estimates predict that φ should be exactly zero, so that the particles rotate precisely with the applied macroscopic rotation, *i.e.*, $\phi = \bar{\psi}$, which is entirely consistent with the in-plane isotropic symmetry of the reinforcement and its distribution.

We conclude this section by remarking that we are not aware of any results in the literature concerning the rotation of rigid fibers in (incompressible) hyperelastic materials under finite-deformation conditions. Thus, the relation (7.17), which appears to be physically consistent, at

least from low to moderate concentration of fibers, and remarkably simple in character, is the first of its type.

Application to rigidly reinforced, incompressible, Gent elastomers

In this subsection, for definiteness, we specialize the general result (7.14) to the particular case of rigidly reinforced, incompressible, Gent elastomers. Thus, making use of relations (7.2) and (7.14), the effective stored-energy function for incompressible Gent elastomers reinforced with aligned rigid fibers of elliptical cross section, with volume fraction c and aspect ratio ω , ($\omega \geq 1$), may be written as:

$$\widehat{W}^I(\bar{\mathbf{U}}) = (c-1) \frac{\mu^{(1)} J_m}{2} \ln \left[1 - \frac{\hat{I}^{(1)} - 2}{J_m} \right], \quad (7.21)$$

where $\hat{I}^{(1)}$ is given by (7.15). It then follows that the corresponding result for rigidly reinforced elastomers with incompressible Neo-Hookean matrix phases may be readily obtained upon taking the limit $J_m \rightarrow \infty$ in (7.21). The result reads as:

$$\widehat{W}^I(\bar{\mathbf{U}}) = (1-c) \frac{\mu^{(1)}}{2} (\hat{I}^{(1)} - 2). \quad (7.22)$$

The above expressions can be written more explicitly in the limit of in-plane isotropic symmetry of the reinforcement. In this context, $\hat{I}^{(1)}$ is given by (7.20) so that the expression (7.21) may be shown to reduce to:

$$\widehat{W}^I(\bar{\mathbf{U}}) = (c-1) \frac{\mu^{(1)} J_m}{2} \ln \left[1 - \frac{(\bar{\lambda} - 1)^2 \left[(\bar{\lambda} + 1)^2 + 2c(\bar{\lambda}^2 + 1) \right]}{J_m \bar{\lambda}^2 (1-c)^2} \right]. \quad (7.23)$$

Similarly, (7.22) reduces to:

$$\widehat{W}^I(\bar{\mathbf{U}}) = \frac{\mu^{(1)} (\bar{\lambda} - 1)^2 \left[(\bar{\lambda} + 1)^2 + 2c(\bar{\lambda}^2 + 1) \right]}{2\bar{\lambda}^2 (1-c)}. \quad (7.24)$$

It is interesting to note that the effective stored-energy function (7.21) for reinforced Gent elastomers locks up when the condition $\hat{I}^{(1)} = J_m + 2$ is satisfied. In order to get a representative notion of the behavior of this condition it is best to consider the simpler case of in-plane isotropic symmetry. For this case, it is straightforward to show that the stretch at which the material locks up is given by:

$$\bar{\lambda}_{lock} = p_1 + \sqrt{\frac{1}{2} + p_1^2 - p_2} + \sqrt{p_1 \left(2p_1 + \sqrt{2 + 4p_1^2 - 4p_2} \right) - p_2 - \frac{1}{2}}. \quad (7.25)$$

Here $p_1 = c/(1 + 2c)$ and $p_2 = (4c - 2 - (1 - c)^2 J_m)/(4 + 8c)$. For comparison purposes, it is noted that the associated matrix phase material locks up at:

$$\bar{\lambda}_{lock}^{matrix} = \frac{\sqrt{2 + J_m + \sqrt{J_m(4 + J_m)}}}{\sqrt{2}}. \quad (7.26)$$

It is not difficult to check from (7.25) that $\bar{\lambda}_{lock}$ is a monotonically decreasing function of c in the physical interval $c \in [0, 1]$, taking the values $\bar{\lambda}_{lock} = \bar{\lambda}_{lock}^{matrix}$ at $c = 0$ and $\bar{\lambda}_{lock} = 1$ at $c = 1$. In other words, reinforced Gent elastomers lock up at *smaller* finite stretches than the associated matrix phase materials. This is consistent with the fact that, on average, the deformation in the matrix phase of a rigidly reinforced material is larger than the macroscopic applied deformation (since the rigid phase does not deform), leading then to an overall smaller lock-up stretch.

As a final remark, it is noted that a result similar to (7.23) has been obtained (unpublished work) from an earlier version of the second-order estimate used in Lopez-Pamies and Ponte Castañeda (2004a) for the same type of Gent elastomeric composite. The two estimates, even though identical up to third order in the infinitesimal strain (*i.e.*, up to $O(\bar{\lambda} - 1)^3$), are significantly different for large values of the matrix lock-up parameter J_m and high concentration of fibers c , at large deformations. This disparity is due to the difference in the limiting lock-up behavior of both estimates as $J_m \rightarrow \infty$. Indeed, unlike expression (7.25), which becomes unbounded as $J_m \rightarrow \infty$, the lock-up stretch computed from the earlier second-order estimate yields $\bar{\lambda}_{lock} = 1/c$ as $J_m \rightarrow \infty$. In essence, both types of estimates indicate that the presence of rigid particles enhances the lock-up effect, which is physically expected. However, we believe that the new predictions may be more realistic for composites with *random* microstructures, for which the addition of rigid particles would enhance the lock-up effect, provided that it is already present in the matrix phase.

7.1.3 Loss of strong ellipticity

In this subsection, the specialization of the strong ellipticity condition (see Chapter 2, Section 2.6):

$$\widehat{K}_{ik} m_i m_k = \widehat{\mathcal{L}}_{ijkl} N_j N_l m_i m_k > 0 \quad (7.27)$$

for all $\mathbf{m} \otimes \mathbf{N} \neq \mathbf{0}$ with $\widehat{\mathcal{L}} = \partial^2 \widehat{W} / \partial \bar{\mathbf{F}}^2$, will be spelled out for the second-order estimates for the effective constitutive behavior of the *compressible* and *incompressible* reinforced elastomers developed in this section. To this end, and for simplicity in the incompressible case, it proves useful to choose the current configuration of the material as the reference state. Thus, recalling

that (Chadwick and Ogden, 1971) $\widehat{\mathcal{L}}_{ijkl} = \bar{J} \bar{\mathbf{F}}_{jr}^{-1} \bar{\mathbf{F}}_{ls}^{-1} \widehat{\mathcal{L}}_{irks}^c$, where the superscript ‘c’ denotes evaluation in the current configuration, the strong ellipticity condition (7.27) may be rewritten as:

$$\widehat{K}_{ik}^c m_i m_l = \widehat{\mathcal{L}}_{ijkl}^c n_j n_l m_i m_l > 0, \quad (7.28)$$

for all $\mathbf{n} \otimes \mathbf{m} \neq \mathbf{0}$. Here, $\widehat{K}_{ik}^c = \widehat{\mathcal{L}}_{ijkl}^c n_j n_l$ is the acoustic tensor corresponding to the situation when the current and reference configuration coincide, and use has been made of the fact that $\bar{J} > 0$. In this work, we are mainly interested in determining the boundary of the domain in deformation space, containing $\bar{\mathbf{F}} = \mathbf{I}$, at which strong ellipticity fails. (Recall that the type of reinforced elastomers considered here are characterized by strictly convex, and therefore strongly elliptic, effective stored-energy functions in the neighborhood of $\bar{\mathbf{F}} = \mathbf{I}$.) Then, it is clear that condition (7.28) will first cease to hold true away from $\bar{\mathbf{F}} = \mathbf{I}$ whenever the acoustic tensor $\widehat{\mathbf{K}}^c$ becomes singular. For plane-strain deformations, this amounts to the existence of real roots n_1/n_2 in the fourth-order polynomial equation:

$$\det \left[\widehat{\mathcal{L}}_{i1k1}^c \left(\frac{n_1}{n_2} \right)^2 + (\widehat{\mathcal{L}}_{i1k2}^c + \widehat{\mathcal{L}}_{i2k1}^c) \frac{n_1}{n_2} + \widehat{\mathcal{L}}_{i2k2}^c \right] = 0, \quad (7.29)$$

where n_1 and n_2 denote the direction cosines of the normal \mathbf{n} to the characteristic direction in the deformed configuration. Explicit (but cumbersome) conditions on the components of the incremental modulus $\widehat{\mathcal{L}}^c$ may be written down in order for the *quartic* equation (7.29) to possess complex roots. However, in general, it is simpler to determine the onset of loss of strong ellipticity by monitoring the four roots of (7.29), which are known in closed form, along the loading path of interest, and detecting at which point at least one of these 4 roots becomes real. Once the real roots n_1/n_2 are detected, they can be substituted in expression (7.28) in order to compute the associated eigenvectors \mathbf{m} corresponding to the zero eigenvalues of the acoustic tensor.

The loss-of-ellipticity condition (7.29) cannot be applied directly for *incompressible* reinforced elastomers. This is because the effective stored-energy function \widehat{W} becomes unbounded for all deformations not satisfying the *incompressibility constraint* $\det \bar{\mathbf{F}} = 1$, which implies that some of the components of the corresponding incremental modulus tensor $\widehat{\mathcal{L}}^c$ become unbounded as well. Consequently, the condition (7.29) must be suitably adapted for incompressible elastomers. Noting that the incompressibility constraint $\det \bar{\mathbf{F}} = 1$ implies that the vectors \mathbf{n} and \mathbf{m} in expression (7.28) must be such that $\mathbf{n} \cdot \mathbf{m} = \mathbf{0}$, it can be shown from (7.28) that, under plane-strain conditions, the loss of strong ellipticity is first attained away from $\bar{\mathbf{F}} = \mathbf{I}$, whenever the fourth-order polynomial

equation:

$$\begin{aligned} & \widehat{\mathcal{L}}_{2121}^c \left(\frac{n_1}{n_2} \right)^4 - 2 \left(\widehat{\mathcal{L}}_{1121}^c - \widehat{\mathcal{L}}_{2221}^c \right) \left(\frac{n_1}{n_2} \right)^3 + \left[\widehat{\mathcal{L}}_{1111}^c + \widehat{\mathcal{L}}_{2222}^c \right. \\ & \left. - 2 \left(\widehat{\mathcal{L}}_{1122}^c + \widehat{\mathcal{L}}_{1221}^c \right) \right] \left(\frac{n_1}{n_2} \right)^2 + 2 \left(\widehat{\mathcal{L}}_{1112}^c - \widehat{\mathcal{L}}_{2212}^c \right) \frac{n_1}{n_2} + \widehat{\mathcal{L}}_{1212}^c = 0 \end{aligned} \quad (7.30)$$

admits one or more real roots n_1/n_2 . It should be emphasized that the coefficients of the quartic equation (7.30), which correspond to projections of the acoustic tensor $\widehat{\mathbf{K}}^c$ onto the space of isochoric deformations, have finite values. Similar to the previous case of *compressible* materials, the loss of strong ellipticity of homogenized *incompressible* elastomers can be determined efficiently by monitoring the four roots of equation (7.30), which are available in closed-form, along the loading path of interest, and detecting at which point at least one of these 4 roots becomes real. For later use, it is helpful to record here the simplification of condition (7.30) for the situations in which the loading is aligned with the microstructure (*i.e.*, without loss of generality, for $\bar{\theta} = 0$ and $\bar{\theta} = \pi/2$). Then, the odd terms disappear and we are led to:

$$\widehat{\mathcal{L}}_{2121}^c \left(\frac{n_1}{n_2} \right)^4 + \left[\widehat{\mathcal{L}}_{1111}^c + \widehat{\mathcal{L}}_{2222}^c - 2 \left(\widehat{\mathcal{L}}_{1122}^c + \widehat{\mathcal{L}}_{1221}^c \right) \right] \left(\frac{n_1}{n_2} \right)^2 + \widehat{\mathcal{L}}_{1212}^c = 0. \quad (7.31)$$

Moreover, simple conditions (on the components of $\widehat{\mathcal{L}}^c$) may be written down in order for the fourth-order polynomial equation (7.31) to possess complex roots. Indeed, it is straightforward to show (see, e.g., Hill, 1979) that necessary and sufficient conditions for the quartic equation (7.31) to have complex roots are expressible as:

$$\begin{aligned} & \text{(i) } \widehat{\mathcal{L}}_{1212}^c > 0, \quad \text{(ii) } \widehat{\mathcal{L}}_{2121}^c > 0, \\ & \text{(iii) } \sqrt{\widehat{\mathcal{L}}_{1212}^c \widehat{\mathcal{L}}_{2121}^c} - \left(\widehat{\mathcal{L}}_{1122}^c + \widehat{\mathcal{L}}_{1221}^c \right) + \frac{\widehat{\mathcal{L}}_{1111}^c + \widehat{\mathcal{L}}_{2222}^c}{2} > 0. \end{aligned} \quad (7.32)$$

Thus, under aligned plane-strain deformations, loss of strong ellipticity of homogenized, incompressible, reinforced elastomers will first take place at the point at which one of the inequalities in (7.32) fails to hold true.

Finally, it should be mentioned that the traces of the effective incremental modulus $\widehat{\mathcal{L}}^c$ that appear in the above conditions for the loss of strong ellipticity of incompressible, rigidly reinforced elastomers under plane-strain deformations may be conveniently written in terms of the effective stored-energy function \check{W} , given by expression (7.14), and its first and second derivatives with respect to its arguments $\bar{\lambda}$ and $\bar{\theta}$. For brevity, the final expressions are not included here.

7.2 Results for plane-strain loading: random reinforced elastomers

This section presents results associated with the second-order estimates for general plane-strain loading of fiber-reinforced elastomers with Gent and Neo-Hookean phases. Results are given for $\mu^{(1)} = 1$ and various initial volume fractions, c_0 , and aspect ratios, ω_0 , of the fibers, and were computed up to the point at which the effective incremental moduli were found to lose strong ellipticity, or truncated at some sufficiently large strain if no such loss was found. For clarity, the points at which loss of strong ellipticity is encountered are denoted with the symbol “o” in the plots. The results and discussion for *pure shear* loading of (in-plane) isotropic (*i.e.*, $\omega = 1$), rigidly reinforced, incompressible, Neo-Hookean and Gent elastomers are presented first. They are followed by the results for *pure shear* loading of compressible and incompressible Gent and Neo-Hookean elastomers reinforced with fibers of elliptical cross section (*i.e.*, $\omega > 1$). Finally, results for *simple shear* of rigidly reinforced, incompressible, Neo-Hookean elastomers are discussed. The idea behind the choice of these results is to bring out the effect of the microstructure evolution, which depends critically on the boundary conditions, on the overall response and stability of the material.

7.2.1 Pure shear: circular rigid fibers and incompressible matrix

Figure 7.2 illustrates results for the effective behavior, as predicted by the second-order method, of an incompressible Neo-Hookean elastomer ($\kappa^{(1)} \rightarrow \infty$) reinforced with rigid fibers of circular cross section ($\omega = 1$) under pure shear loading ($\bar{\lambda}_1 = \bar{\lambda}_2^{-1} = \bar{\lambda}$). In particular, results are shown, as a function of the macroscopic stretch $\bar{\lambda}$, for: (a) the effective stored-energy function \widehat{W} , and (b) the associated stress $\bar{S} = d\widehat{W}/d\bar{\lambda}$, for fiber concentrations of 10, 20, and 30%. (Note that the closed-form expression for the effective (SOE) stored-energy function shown in Figure 7.2(a) is given by (7.24).) As stated above, there are no exact solutions for the effective behavior of isotropic, incompressible elastomers reinforced with a random, isotropic distribution of circular, rigid fibers to which to compare the results displayed in Figure 7.2. However, there is an exact result due to deBotton (2005) for the in-plane effective behavior of two-phase, transversely isotropic *sequentially laminated composites* with incompressible Neo-Hookean (matrix and inclusion) phases. Such an exact result (with rigid inclusion phase) has been included in Figure 7.2 for

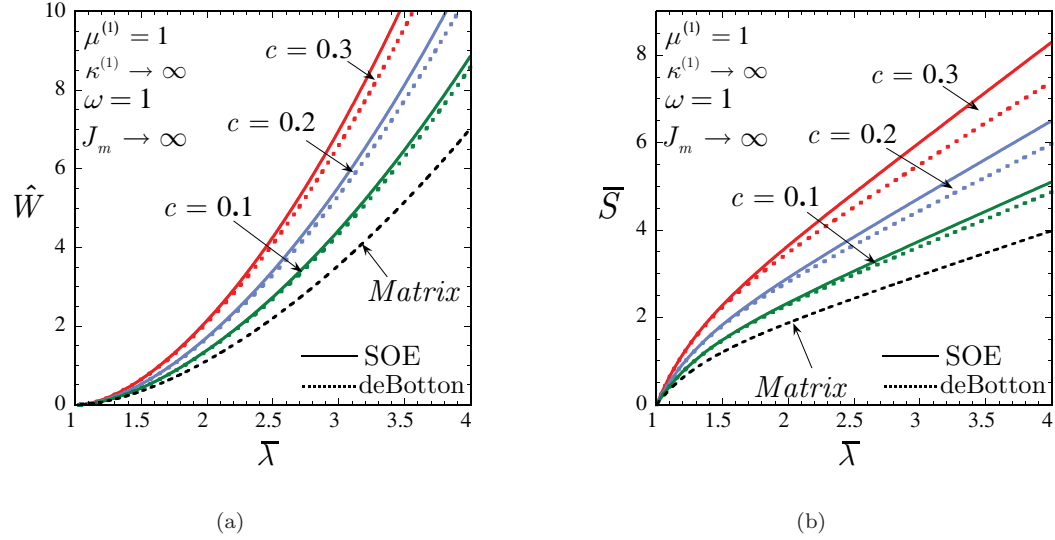


Figure 7.2: Effective response, as predicted by the second-order (SOE) and the exact result for sequentially laminated materials (deBotton), of a rigidly reinforced elastomer subjected to *pure shear* loading. The results correspond to an incompressible Neo-Hookean matrix phase and various values of the reinforcement concentration c , and are shown as a function of a the principal macroscopic stretch $\bar{\lambda}$. (a) The effective stored-energy function \hat{W} . (b) The corresponding stress $\bar{S} = d\hat{W}/d\bar{\lambda}$.

comparison purposes. It is observed that the agreement between the SOE and deBotton's results is good, especially for smaller volume fractions of the rigid phase. The agreement is also seen to improve for smaller values of the applied stretch. In fact, it can be shown that the second-order estimate (7.24) reduces identically to deBotton's result (see Eq. (56) in deBotton, 2005) up to third order in the strain (*i.e.*, up to $O((\bar{\lambda} - 1)^3)$). An interesting remark regarding the rather good agreement between the second-order estimate (7.24) and deBotton's result for *sequentially laminated composites* is now in order. Recall that the second-order estimate (7.24) has been developed for Neo-Hookean elastomers reinforced by circular, rigid fibers, as schematically depicted in Fig. 7.1(a). However—given that use has been made of the HS-type estimate (2.55) to solve the LCC auxiliary problem—expression (7.24) can also be reinterpreted as an estimate for the effective stored-energy function of isotropic, rigidly reinforced Neo-Hookean materials with other microstructures for which (2.55) is a good approximation (when the phases are taken to be linearly elastic). In this regard, it so happens that the *exact* overall modulus tensor of two-phase, linear composites with the sequentially laminated microstructure proposed by deBotton (2005) is precisely the HS-type estimate (2.55). Thus, expression (7.24) can be interpreted as the second-order estimate for the effective stored-energy function of rigidly reinforced Neo-Hookean elastomers with

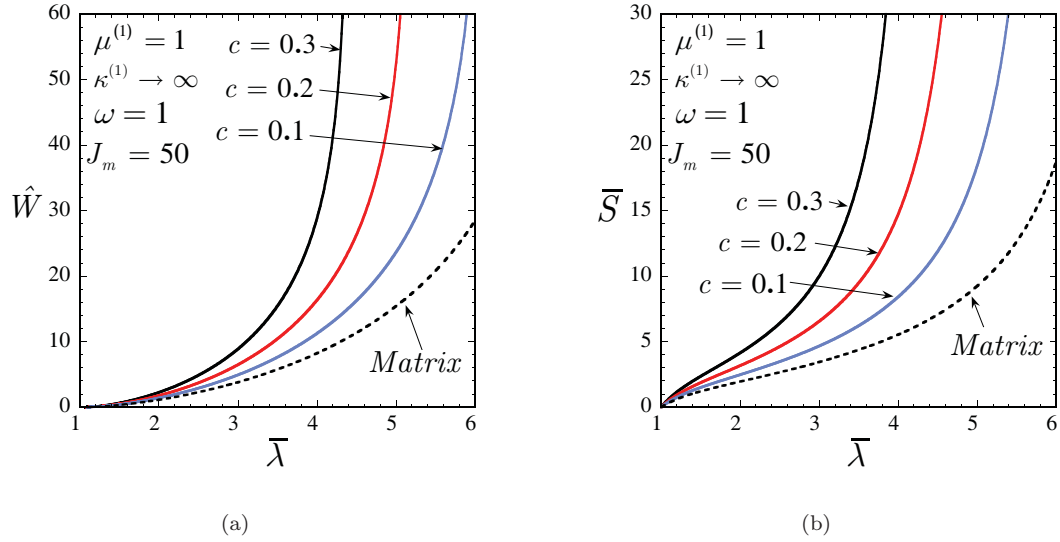


Figure 7.3: Second-order estimates for the effective behavior of elastomers reinforced with rigid fibers of circular cross section subjected to *pure shear* loading. The results correspond to an incompressible Gent matrix phase with given matrix lock-up parameter $J_m = 50$ and various values of the fiber concentration c , and are shown as a function of the principal macroscopic stretch $\bar{\lambda}$. (a) The effective stored-energy function \widehat{W} . (b) The corresponding stress $\bar{S} = d\widehat{W}/d\bar{\lambda}$.

the sequentially laminated microstructure of deBotton (2005). This explains the good agreement between the SOE and deBotton's results in Figure 7.2. To conclude this discussion, it is interesting to note that—given that for the sequentially laminated microstructure, the *homogenization step* in the second-order procedure is carried out exactly—the discrepancies between the SOE and deBotton's results illustrated in Figure 7.2 constitute a measure of the accuracy of the *linearization process* in the second-order method.

Figure 7.3 presents the effective behavior as predicted by the second-order method for an incompressible Gent¹ elastomer ($\kappa^{(1)} \rightarrow \infty$) reinforced with rigid fibers of circular cross section ($\omega = 1$) under pure shear loading ($\bar{\lambda}_1 = \bar{\lambda}_2^{-1} = \bar{\lambda}$). Results are shown for fiber concentrations of 10, 20 and 30%, and a value of the matrix lock-up parameter $J_m = 50$, as a function of the macroscopic stretch $\bar{\lambda}$. Part (a) shows the effective stored-energy function, and part (b), the associated stress $\bar{S} = d\widehat{W}/d\bar{\lambda}$. Note that the closed-form expression for the effective stored-energy function shown in Figure 7.3(a) is given by (7.23). A major observation that can be made from Figure 7.3 is the increasing reinforcement effect of the elastomeric matrix with the addition of rigid fibers, which is consistent with experimental observations. It is also interesting to remark that the stretch at

¹Unlike for Neo-Hookean composites, there are no exact results available for sequentially laminated composites with Gent phases.

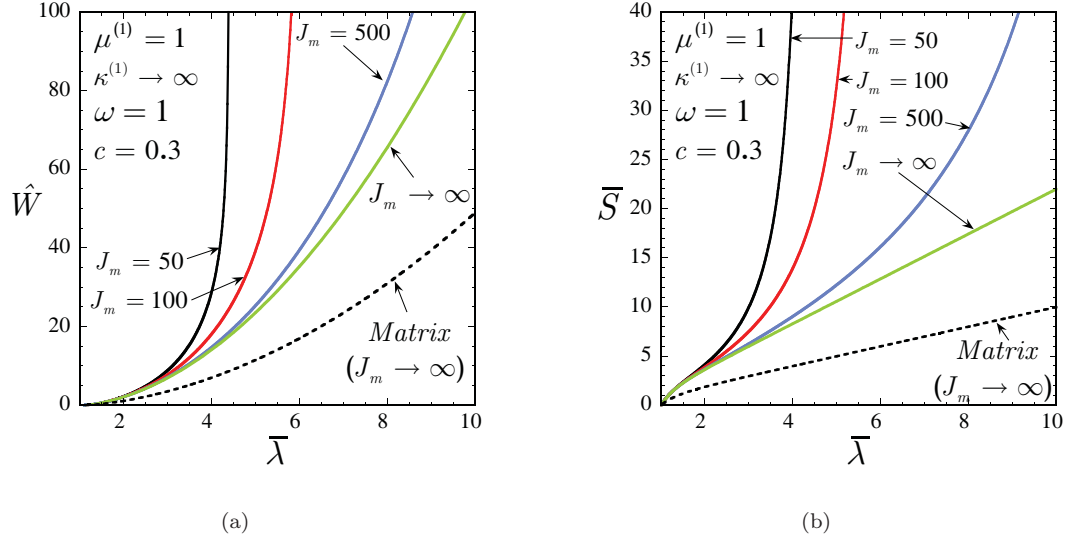


Figure 7.4: Second-order estimates for the effective behavior of elastomers reinforced with rigid fibers of circular cross section subjected to *pure shear* loading. The results correspond to an incompressible Gent matrix phase with $c = 30\%$ and various values of the matrix lock-up parameter J_m , and are shown as a function of the principal macroscopic stretch $\bar{\lambda}$. (a) The effective stored-energy function \widehat{W} . (b) The corresponding stress $\bar{S} = d\widehat{W}/d\bar{\lambda}$.

which the elastomeric composite locks up depends very strongly on the concentration of fibers. Indeed, it is observed that the composite locks up at smaller stretches with increasing values of c , as anticipated in the previous section.

Figure 7.4 shows corresponding plots for the effective behavior of an incompressible Gent elastomer reinforced with 30% of rigid fibers of circular cross section under pure shear loading for values of the matrix lock-up parameter $J_m = 50, 100, 500$, and $J_m \rightarrow \infty$, as a function of the macroscopic stretch $\bar{\lambda}$. Part (a) shows the effective stored-energy function, and part (b), the associated stress $\bar{S} = d\widehat{W}/d\bar{\lambda}$. It is observed from Figure 7.4 that the overall response of the reinforced elastomer is strongly dependent on the matrix lock-up parameter J_m , which is not surprising since the response of the matrix itself is also highly dependent on J_m . It is further noted from this figure that the second-order estimate for the effective behavior of a rigidly reinforced Neo-Hookean elastomer (*i.e.*, $J_m \rightarrow \infty$) does not exhibit lock-up at finite stretch, as already discussed in the context of equation (7.25). This is in contrast to the previous result obtained by Lopez-Pamies and Ponte Castañeda (2004a) with an earlier version of the second-order method, where lock-up was found to be attained at $\bar{\lambda} = 1/c$ for reinforced Neo-Hookean elastomers. For the reasons stated in Section 7.1.2, we believe that the new predictions are more accurate in the present context of

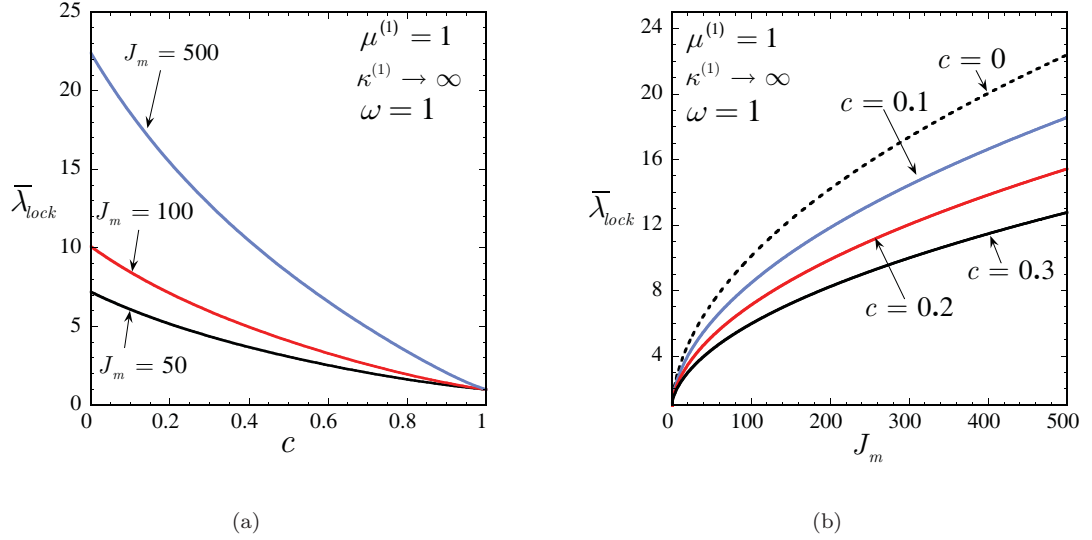


Figure 7.5: Second-order estimates for the macroscopic stretch $\bar{\lambda}_{lock}$ at which an (in-plane) isotropic rigidly reinforced incompressible Gent elastomer locks up. (a) $\bar{\lambda}_{lock}$ as a function of fiber concentration c for various values of the matrix lock-up parameter J_m . (b) $\bar{\lambda}_{lock}$ as a function of J_m for various values of c .

composites with *random* microstructures.

Figure 7.5 provides plots associated with the results shown in Figures 7.3 and 7.4 for the macroscopic stretch $\bar{\lambda}_{lock}$ at which a rigidly reinforced, incompressible, Gent elastomer locks up. Part (a) shows $\bar{\lambda}_{lock}$ for values of the matrix lock-up parameter $J_m = 50, 100$, and 500 , as a function of the fiber concentration c . Part (b) shows $\bar{\lambda}_{lock}$ for fiber concentrations of $0, 10, 20$, and 30% , as a function of J_m . Recall that the closed-form expression for the stretch $\bar{\lambda}_{lock}$ shown in Figure 7.5 is given by (7.25). The key point to be drawn from Figure 7.5 is that the elastomeric composite ($c > 0$) locks up at a smaller stretch than the corresponding matrix phase ($c = 0$). In fact, Figure 7.5(a) shows that $\bar{\lambda}_{lock}$ decreases monotonically from the lock-up of the matrix phase ($\bar{\lambda}_{lock} = \bar{\lambda}_{lock}^{matrix}$ at $c = 0$) to that of the rigid phase ($\bar{\lambda}_{lock} = 1$ at $c = 1$) with increasing c , as previously discussed. In addition, Figure 7.5(b) shows that the influence of the matrix lock-up parameter J_m on $\bar{\lambda}_{lock}$ weakens monotonically as J_m increases.

Finally, it is important to stress from the above results that (in-plane) isotropic ($\omega = 1$), rigidly reinforced, incompressible, Gent elastomers, which are strongly elliptic in the pure state, remain strongly elliptic for all deformations.

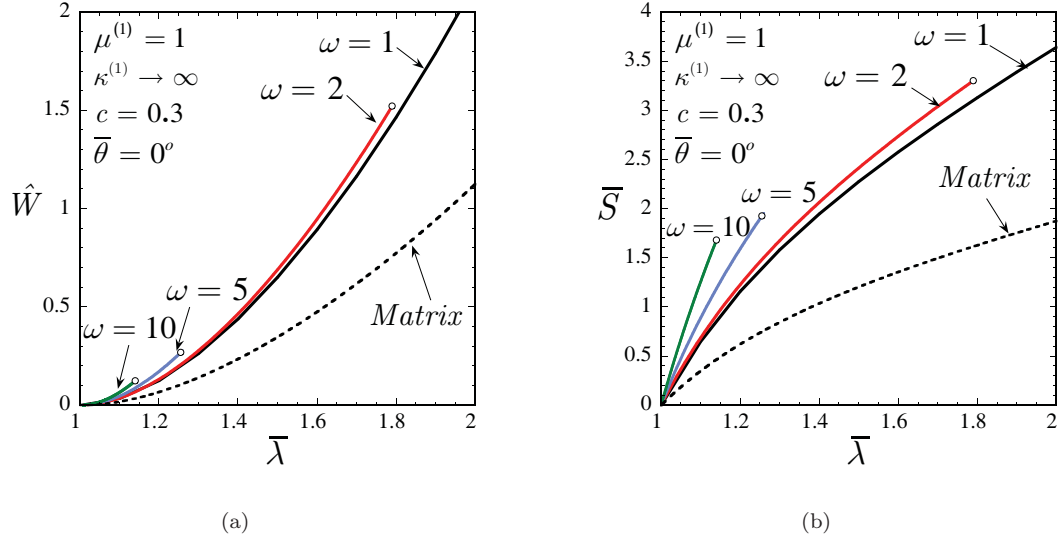


Figure 7.6: Second-order estimates for the effective behavior of rigidly reinforced elastomers subjected to aligned pure shear loading ($\bar{\theta} = 0^\circ$). The results correspond to an incompressible, Neo-Hookean matrix phase with given fiber concentration $c = 30\%$, and various values of the fiber aspect ratio ω , and are shown as a function of the principal macroscopic stretch $\bar{\lambda}$. (a) The effective stored-energy function \hat{W} . (b) The corresponding stress $\bar{S} = d\hat{W}/d\bar{\lambda}$.

7.2.2 Aligned pure shear: rigid fibers and incompressible matrix

Figure 7.6 presents the effective behavior as predicted by the second-order method for an incompressible, Neo-Hookean elastomer reinforced with rigid fibers of elliptical cross section under aligned pure shear loading with $\bar{\theta} = 0^\circ$, *i.e.*, compression along the longest in-plane axis of the fibers. Results are shown for fiber aspect ratios of 1, 2, 5, and 10, and fiber concentration of 30%, as a function of the macroscopic stretch $\bar{\lambda}$. Part (a) gives the effective stored-energy function, and part (b), the associated stress $\bar{S} = d\hat{W}/d\bar{\lambda}$. Note that the expression (7.22) for the effective stored-energy function shown in Figure 7.6(a) simplifies even further by recognizing, from (7.17), that for aligned pure shear loadings $\varphi = 0^\circ$. Also note that for this type of loading, the macroscopic rotation tensor $\bar{\mathbf{R}} = \mathbf{I}$, which together with the fact that $\varphi = 0^\circ$, implies that the fibers do not rotate, namely, $\phi = 0^\circ$. Similar to the case of pure shear loading of in-plane, isotropic, rigidly reinforced elastomers, the results shown in Figure 7.6 exhibit a significant reinforcement effect undergone by the elastomeric matrix with the addition of rigid fibers. The reinforcement is more pronounced for higher values of the aspect ratio. This is consistent with the fact that in the limit $\omega \rightarrow \infty$ (as the microstructure tends to a laminate) the material becomes rigid under the given loading conditions. Moreover, Figure 7.6 shows that the second-order method predicts loss of strong ellipticity of the

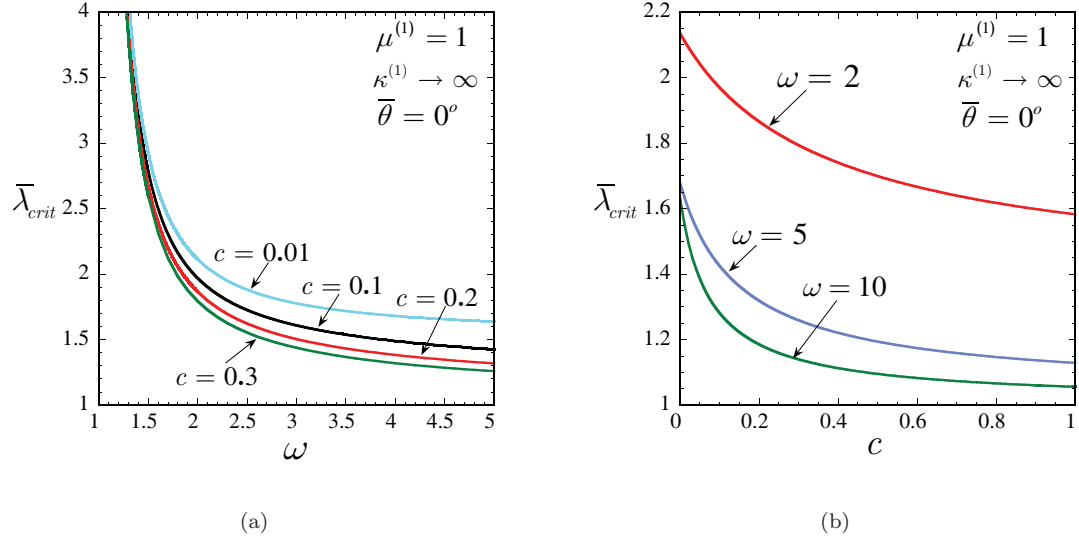


Figure 7.7: Aligned pure shear loading ($\bar{\theta} = 0^\circ$) of a rigidly reinforced, incompressible, Neo-Hookean elastomer. (a) The critical stretch $\bar{\lambda}_{crit}$ at which loss of strong ellipticity of the homogenized elastomer takes place for various fiber concentrations as a function of the aspect ratio of the fibers ω . (b) The critical stretch $\bar{\lambda}_{crit}$ for various aspect ratios as a function of the concentration of fibers c .

homogenized behavior of reinforced elastomers under aligned pure shear loading with $\bar{\theta} = 0^\circ$ for fiber aspect ratios $\omega > 1$. More particularly, it is observed that loss of strong ellipticity takes place at smaller stretches for higher ω . That is, under the type of deformation considered here, the composite stiffens, but also becomes more unstable with increasing values of the aspect ratio of the fibers.

Figure 7.7 provides plots associated with the results shown in Figure 7.6 for the critical stretch $\bar{\lambda}_{crit}$ at which the loss of strong ellipticity occurs for the homogenized behavior of rigidly reinforced, incompressible, Neo-Hookean elastomers. Part (a) shows $\bar{\lambda}_{crit}$ for concentration of fibers of 1, 10, 20, and 30%, as a function of the aspect ratio ω , and part (b), $\bar{\lambda}_{crit}$ for aspect ratios of 2, 5, and 10, as a function of the concentration of fibers c . It is seen from Figure 7.7(a) that, as already mentioned in the context of Figure 7.6, elastomers reinforced with fibers of higher aspect ratio lose strong ellipticity at smaller stretches. Another key point to be drawn from Figure 7.7(a) is that $\bar{\lambda}_{crit}$ has a vertical asymptote at $\omega = 1$. This entails that (in-plane) isotropic, rigidly reinforced, incompressible, Neo-Hookean elastomers remain strongly elliptic under all deformations, in agreement with the results shown in the preceding subsection. However, as soon as the isotropic symmetry is perturbed, the homogenized material loses strong ellipticity at some large, but finite, stretch. Note that $\bar{\lambda}_{crit} \rightarrow 1$ as $\omega \rightarrow \infty$, in agreement with the exact result for the corresponding

laminate. Also note that $\bar{\lambda}_{crit}$ is smaller for higher values of the concentration of fibers, so that reinforced elastomers with a higher content of fibers are more unstable. This point is more clearly illustrated by Figure 7.7(b). In addition, we remark from Figure 7.7(b) that $\bar{\lambda}_{crit}$ tends to a finite value as $c \rightarrow 0$. In this connection, recall that the Neo-Hookean elastomer utilized here for the matrix phase is a strongly elliptic material for all deformations. This implies that $\bar{\lambda}_{crit}$ has a singularity at $c = 0$, namely, $\bar{\lambda}_{crit} = \infty$ at $c = 0$, but $\bar{\lambda}_{crit} \rightarrow \bar{\lambda}_{crit}^0$ as $c \rightarrow 0$, where $0 < \bar{\lambda}_{crit}^0 < \infty$. Physically, this result suggests that the addition of even a small proportion of aligned, elliptical, rigid fibers can have a dramatic effect on the overall stability of an incompressible, strongly elliptic elastomer at some sufficiently large, but finite, compressive stretch along the longest in-plane axes of the fibers.

Finally, it is important to note that it was through failure of the condition (i) in (7.32) that strong ellipticity was systematically lost in the results shown in Figure 7.7. Within the context of condition (7.31), the fact of having the incremental effective modulus $\widehat{\mathcal{L}}_{1212}^c$ vanish implies that the normal to the characteristic direction in the deformed configuration is given by $\mathbf{n} = \mathbf{e}_2$, so that, by virtue of the incompressibility constraint, $\mathbf{m} = \mathbf{e}_1$. That is, the homogenized material may develop *localized shear* deformations in the plane determined by the normal \mathbf{e}_2 , and in the direction \mathbf{e}_1 . Making contact with the microstructure, the condition $\widehat{\mathcal{L}}_{1212}^c = 0$, under the given type of loading, would correspond to the possible *flopping* of the fibers, which is a physically plausible instability mechanism for these materials.

Figure 7.8 presents additional results for the critical stretch $\bar{\lambda}_{crit}$ for rigidly reinforced elastomers, with a fiber concentration of 30%, subjected to aligned pure shear loading with $\bar{\theta} = 0^\circ$, as a function of the aspect ratio ω . Part (a) gives results for incompressible, Gent elastomers with matrix lock-up parameters $J_m = 50$ and 100, and part (b), for compressible, Neo-Hookean elastomers with bulk moduli $\kappa^{(1)} = 11, 101$, and $\kappa^{(1)} \rightarrow \infty$. From Figure 7.8(a) it is discerned that the matrix lock-up parameter J_m has essentially no effect on the onset of loss of strong ellipticity of rigidly reinforced, incompressible, Gent elastomers. As a matter of fact, $\bar{\lambda}_{crit}$ is completely independent of J_m up to the point at which the material locks up. (Note that the stretch at which lock-up takes place has been included in 7.8(a) for reference purposes.) The main point that can be drawn from Figure 7.8(b) is that the loss of strong ellipticity of rigidly reinforced elastomers is very much dependent on the compressibility of the matrix phase. Indeed, it is found from this figure that

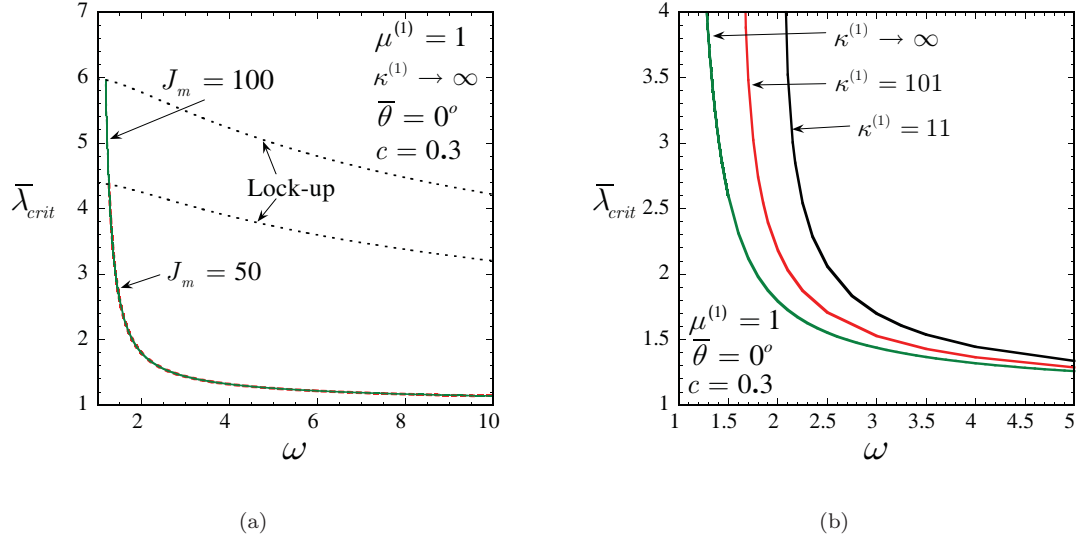


Figure 7.8: Aligned pure shear loading ($\bar{\theta} = 0^\circ$) of rigidly reinforced elastomers. (a) The critical stretch $\bar{\lambda}_{crit}$ at which loss of strong ellipticity of a rigidly reinforced, incompressible, Gent elastomer takes place for various values of the lock-up parameter J_m as a function of the aspect ratio of the fibers ω . (b) The corresponding critical stretch $\bar{\lambda}_{crit}$ for a rigidly reinforced, compressible, Neo-Hookean elastomer, at various values of the bulk modulus $\kappa^{(1)}$, as a function of the aspect ratio of the fibers ω .

rigidly reinforced, Neo-Hookean elastomers become more unstable with increasing incompressibility of the matrix phase (*i.e.*, for higher values of $\kappa^{(1)}$). This trend is consistent with the numerical results obtained by Triantafyllidis *et al.* (2006) for the loss of ellipticity of reinforced elastomers with *periodic* microstructures. It should be mentioned that, similar to the results shown in Figure 7.7, all the results for loss of strong ellipticity displayed in Figure 7.8 are due to the vanishing of the effective incremental shear modulus $\widehat{\mathcal{L}}_{1212}^c$, which, again, corresponds to a possible flopping-type instability.

7.2.3 Pure shear at an angle: rigid fibers and incompressible matrix

Figure 7.9 presents the effective behavior, as predicted by second-order estimate (7.22), for an incompressible, Neo-Hookean elastomer reinforced with rigid fibers of elliptical cross section under *pure shear* loading at the fixed angle $\bar{\theta} = 20^\circ$. Results are shown for a fiber concentration of 30% as a function of the macroscopic stretch $\bar{\lambda}$. Part (a) gives the effective stress $\bar{S} = d\widehat{W}/d\bar{\lambda}$ for fiber aspect ratios of $\omega = 1, 2, 5, 10$, and part (b), the average angle of rotation of the fibers ϕ , for fiber aspect ratios of $\omega = 1, 1.1, 1.5, 2, 5$, and $\omega \rightarrow \infty$. Note that for the given type of loading, the macroscopic rotation tensor $\bar{\mathbf{R}}$ is exactly equal to the identity so that the angle defined by

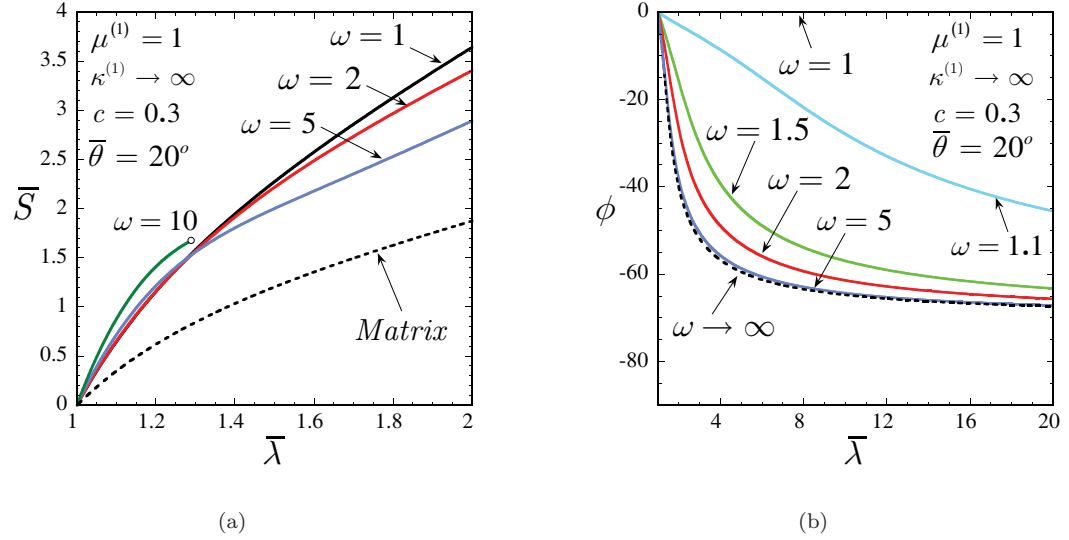


Figure 7.9: Second-order estimates for the effective behavior of rigidly reinforced elastomer subjected to pure shear loading at a fixed angle ($\bar{\theta} = 20^\circ$). The results correspond to an incompressible, Neo-Hookean, matrix phase with given fiber concentration $c = 30\%$, and various values of the fiber aspect ratio ω , and are shown as a function of the principal macroscopic stretch $\bar{\lambda}$. (a) The effective stress $\bar{S} = d\bar{W}/d\bar{\lambda}$. (b) The angle of rotation of the fibers ϕ .

equation (7.17), φ , corresponds to the angle of rotation of the fibers, namely, $\phi = \varphi$. Similar to the previous cases, Figure 7.9(a) shows a significant reinforcement effect of the matrix phase with the addition of rigid fibers. However, unlike the results for aligned pure shear loading with $\bar{\theta} = 0^\circ$, where higher values of the aspect ratio of the fibers were found to consistently provide a higher reinforcement effect, higher aspect ratios of the fibers lead here to a stiffer behavior of the composite only for small deformations, whereas for large stretches the opposite is true. Furthermore, only the elastomer with $\omega = 10$ in Figure 7.9(a) is found to lose strong ellipticity. This behavior is also different from what it was observed for aligned pure shear loading with $\bar{\theta} = 0^\circ$, where the break of isotropic symmetry (*i.e.*, $\omega > 1$) was shown to lead systematically to loss of strong ellipticity of the homogenized elastomer at some finite stretch. The above-mentioned disparities will be shown shortly to be linked to the evolution of the microstructure.

Figure 7.9(b) shows that circular fibers ($\omega = 1$) do not rotate under pure shear at a fixed angle, as previously discussed. On the other hand, elliptical fibers ($\omega > 1$) do rotate clockwise (with respect to the fixed frame of reference) under the present loading conditions, aligning their longest in-plane principal axes with the tensile axis, that is, for this case, $\varphi \rightarrow -70^\circ$ as $\bar{\lambda} \rightarrow \infty$. It is also interesting to observe that fibers with higher aspect ratio rotate faster. In this regard, it is noted

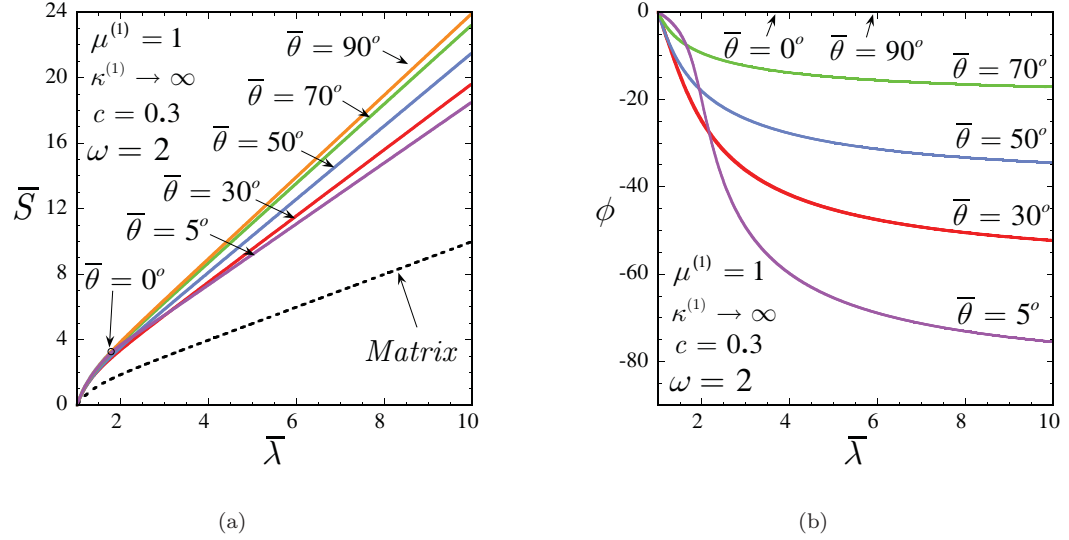


Figure 7.10: Second-order estimates for the effective behavior of rigidly reinforced elastomer subjected to pure shear loading at various angles $\bar{\theta}$ (in the large deformation regime). The results correspond to an incompressible, Neo-Hookean matrix phase with given fiber concentration $c = 30\%$ and aspect ratio $\omega = 2$, and are shown as a function of the principal macroscopic stretch $\bar{\lambda}$. (a) The effective stress $\bar{S} = d\widehat{W}/d\bar{\lambda}$. (b) The average angle of rotation of the fibers ϕ .

that the angle of rotation for the limiting case $\omega \rightarrow \infty$ has been included in Figure 7.9 for reference purposes. However, it must be recalled that the composite behaves rigidly for $\omega \rightarrow \infty$ under the given loading conditions. In view of the results for the overall constitutive response shown in Figure 7.9(a) and the evolution of the associated underlying microstructure shown in Figure 7.9(b), it is inferred that the rotation of the fibers constitutes, in the present context, a *softening* mechanism—in accord with the findings in Chapter 6 for laminate materials. Physically, the rigid rotations of the fibers serve to “accommodate” part of the applied macroscopic loading, which hinders the hardening of the matrix phase of the material. Given that fibers with larger aspect ratios rotate faster, they are able to “accommodate” a larger amount of the applied macroscopic deformation. This leads to a stronger softening effect which is consistent with the results shown in Figure 7.9(a) at large stretches.

Figure 7.10 provides plots for the effective behavior as predicted by the second-order method for an incompressible, Neo-Hookean elastomer reinforced with rigid fibers of elliptical cross section under pure shear loading at the fixed angles $\bar{\theta} = 0^\circ, 5^\circ, 30^\circ, 50^\circ, 70^\circ$, and 90° . Results are shown for a fiber aspect ratio of 2 and fiber concentration of 30%, as a function of the macroscopic stretch $\bar{\lambda}$. Part (a) shows the effective stress $\bar{S} = d\widehat{W}/d\bar{\lambda}$, and part (b), the average angle of rotation

of the fibers ϕ . As for the preceding results, $\bar{\mathbf{R}} = \mathbf{I}$, so that $\phi = \varphi$. A key observation that can be made from Figure 7.10(a), besides the clear reinforcement effect undergone by the matrix phase with the addition of rigid fibers, is that for large deformations, except for the case with $\bar{\theta} = 0^\circ$, the reinforced elastomer consistently shows a stiffer response for higher angles of loading, with the stiffest behavior being attained at $\bar{\theta} = 90^\circ$. For exactly $\bar{\theta} = 0^\circ$, the effective response coincides with that for $\bar{\theta} = 90^\circ$ for all stretches. This can be easily verified from (7.15) by noting, from (7.17), that for aligned loadings (*i.e.*, for $\bar{\theta} = 0^\circ$ and $\bar{\theta} = 90^\circ$) φ is exactly equal to 0° , as it has already been pointed out. It is further noted from Figure 7.10(a) that loss of strong ellipticity of the homogenized elastomer takes place for pure shear with $\bar{\theta} = 0^\circ$, which corresponds to *compression* along the longest in-plane axes of the fibers. On the other hand, for the pure shear loading with $\bar{\theta} = 90^\circ$, which corresponds to *tension* along the longest in-plane axes of the fibers, the homogenized elastomer does not lose strong ellipticity. This result might seem inconsistent at first. However, it should be recalled that the overall behavior of the material is anisotropic, and that even though the stress-stretch relations (in the loading direction) are identical for both pure shear deformations with $\bar{\theta} = 0^\circ$ and $\bar{\theta} = 90^\circ$, the corresponding incremental moduli are in fact different. In this regard, it is evoked that the loss of strong ellipticity of the homogenized elastomer under pure shear with $\bar{\theta} = 0^\circ$ is due to the fact that $\hat{\mathcal{L}}_{1212}^c = 0$ at $\bar{\lambda}_{crit}$, which physically is associated with a possible flopping instability of the fibers. On the other hand, for the case of $\bar{\theta} = 90^\circ$, the effective shear modulus $\hat{\mathcal{L}}_{1212}^c$ is not only positive, but it increases with the applied stretch.

Figure 7.10(b) shows that the elliptical fibers with $\omega = 2$ do rotate clockwise (with respect to the fixed frame of reference) aligning their longest in-plane principal axes with the principal direction of tensile loading (namely, $\phi \rightarrow \bar{\theta} - 90^\circ$ as $\bar{\lambda} \rightarrow \infty$), for all loadings, except at $\bar{\theta} = 0^\circ$, for which, again, the fibers do not rotate, but instead, remain fixed with their longest in-plane principal axes aligned with the principal direction of compressive loading. In essence, for aligned pure shear loadings (*i.e.*, $\bar{\theta} = 0^\circ$ and $\bar{\theta} = 90^\circ$) there is no evolution of the orientation of the fibers. On the contrary, for “misaligned” deformations, the fibers do undergo a total rotation equal to the complementary angle of $\bar{\theta}$ as $\bar{\lambda} \rightarrow \infty$, in agreement with the discussion of the large-deformation behavior of equation (7.17) in Section 7.1.2. This entails that reinforced elastomers deformed at smaller loading angles $\bar{\theta}$ are able to “accommodate” a larger portion of the applied macroscopic loading by rigid rotation of the underlying fibers, which has already been identified as a *softening*

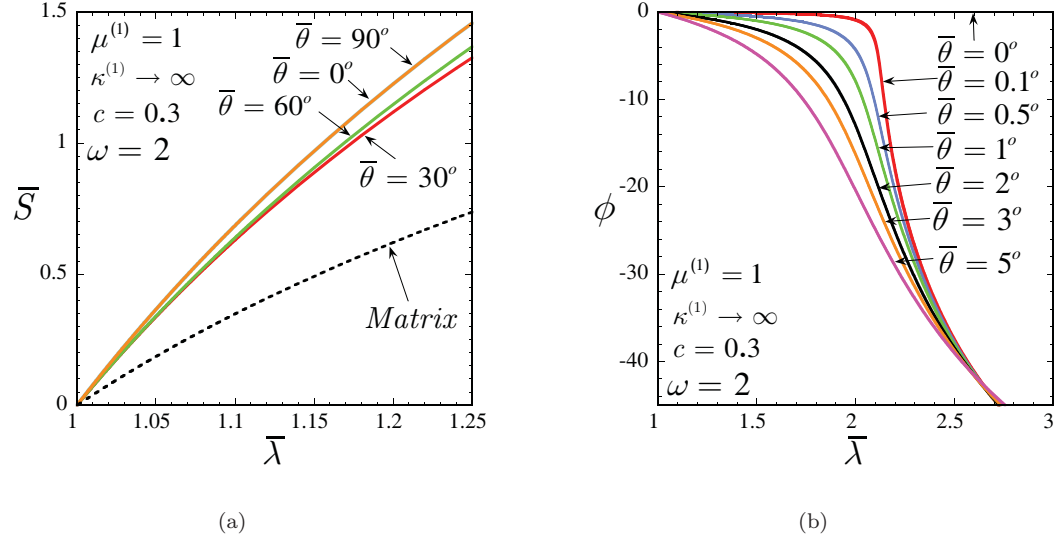


Figure 7.11: Second-order estimates for the effective behavior of rigidly reinforced elastomer subjected to pure shear loading at various angles $\bar{\theta}$ (in the small deformation regime). The results correspond to an incompressible, Neo-Hookean matrix phase with given fiber concentration $c = 30\%$ and aspect ratio $\omega = 2$, and are shown as a function of the principal macroscopic stretch $\bar{\lambda}$. (a) The effective stress $\bar{S} = d\bar{W}/d\bar{\lambda}$. (b) The average angle of rotation of the fibers ϕ .

mechanism. This is entirely consistent with the fact that the effective stress-stretch relations shown in Figure 7.10(a) are systematically stiffer for higher $\bar{\theta}$ (with the exception of $\bar{\theta} = 0^\circ$), in the finite-deformation regime.

Figure 7.11 provides plots for a blow up in the small deformation regime of some of the results shown in Figure 7.10. Figure 7.11(a) corresponds to a blow up of Figure 7.10(a) for the cases of $\bar{\theta} = 0^\circ, 30^\circ, 60^\circ$, and 90° . It can be seen from this figure that loadings at complementary angles produce an identical effective response of the material in the small deformation regime, in accordance with the linear theory. For sufficiently large deformations, the effective responses at complementary angles deviate from each other, due to the difference in the evolution of the microstructure, as already discussed. Figure 7.11(b) corresponds to a blow up of Figure 7.10(b) for the cases of $\bar{\theta} = 0^\circ$ and $\bar{\theta} = 5^\circ$ in which the results for $\bar{\theta} = 0.1^\circ, 0.5^\circ, 1^\circ, 2^\circ$, and 3° have been included in order to aid the discussion. In the previous section (as well as in some of the preceding results discussed in this section), it was observed that the fibers in the type of rigidly reinforced elastomers studied here do not rotate when subjected to pure shear deformations at exactly $\bar{\theta} = 0^\circ$. However, an infinitesimal misalignment of this loading angle was shown to result into a 90° rotation of the fibers as the applied stretch $\bar{\lambda}$ was increased. In this connection, Figure 7.11(b) clearly shows

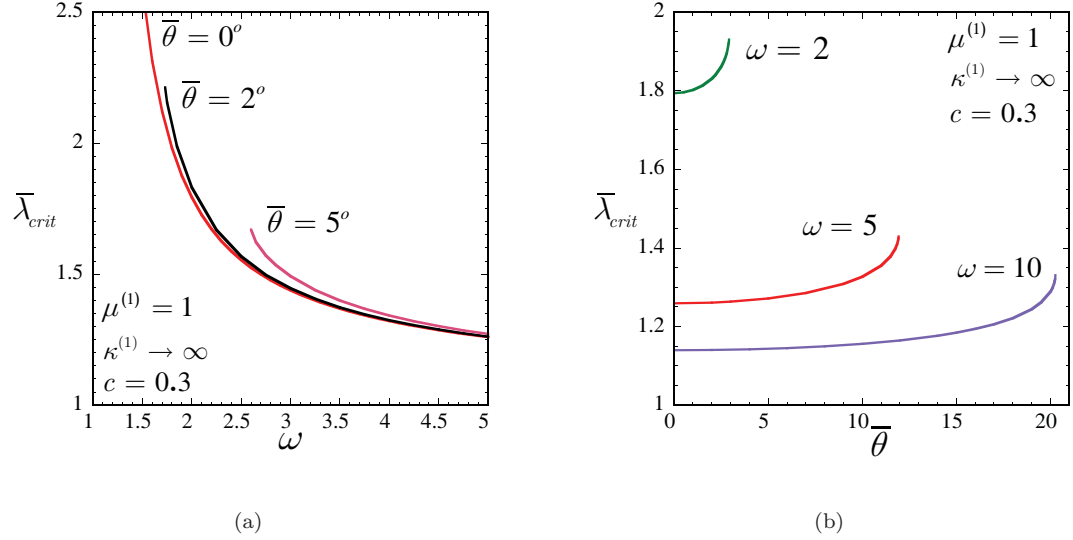


Figure 7.12: Pure shear loading of rigidly reinforced elastomers. (a) The critical stretch $\bar{\lambda}_{crit}$ at which loss of strong ellipticity of a rigidly reinforced, incompressible, Neo-Hookean elastomer takes place for various loading angles $\bar{\theta}$, as a function of the aspect ratio of the fibers ω . (b) The corresponding results for $\bar{\lambda}_{crit}$ for various values of the aspect ratio of the fiber as a function of the angle of loading $\bar{\theta}$.

that loadings at small angles $\bar{\theta}$ can lead to large rotations of the fibers. Interestingly, this figure shows that for relatively small loading angles $\bar{\theta}$, the corresponding rotation of the fibers develops a highly nonlinear evolution as a function of the applied macroscopic stretch $\bar{\lambda}$. Indeed, as $\bar{\theta}$ approaches 0° , ϕ remains small initially as $\bar{\lambda}$ increases up to certain finite stretch at which it undergoes a dramatic increase. In essence, by making use of the established fact that larger fiber rotations potentially lead to a softer overall constitutive response, it is seen that a slight misalignment (about $\bar{\theta} = 0^\circ$) in the applied loading can result into a drastically different, much softer, effective response of the material at large deformations. This is entirely consistent with the emergence of flopping-type instabilities at $\theta = 0^\circ$.

Figure 7.12 shows the effect of the loading angle $\bar{\theta}$ on the critical stretch $\bar{\lambda}_{crit}$ for rigidly reinforced, incompressible, Neo-Hookean elastomers subjected to pure shear. Results are shown for a fiber concentration of 30%. Part (a) gives $\bar{\lambda}_{crit}$ for loading angles of $\bar{\theta} = 0^\circ, 2^\circ$, and 5° , as a function of the fiber aspect ratio ω , and part (b), $\bar{\lambda}_{crit}$ for fiber aspect ratios of 2, 5, and 10, as a function of $\bar{\theta}$. An important observation that can be made from Figure 7.12(a) is that, irrespectively of the loading angle, elastomers reinforced with fibers of higher aspect ratio are more unstable. Note also that unlike the $\bar{\lambda}_{crit}$ for $\bar{\theta} = 0^\circ$ which exhibits a vertical asymptote at $\omega = 1$, the $\bar{\lambda}_{crit}$ for misaligned loadings (*i.e.*, $\bar{\theta} \neq 0^\circ$) reaches a maximum finite value at a certain

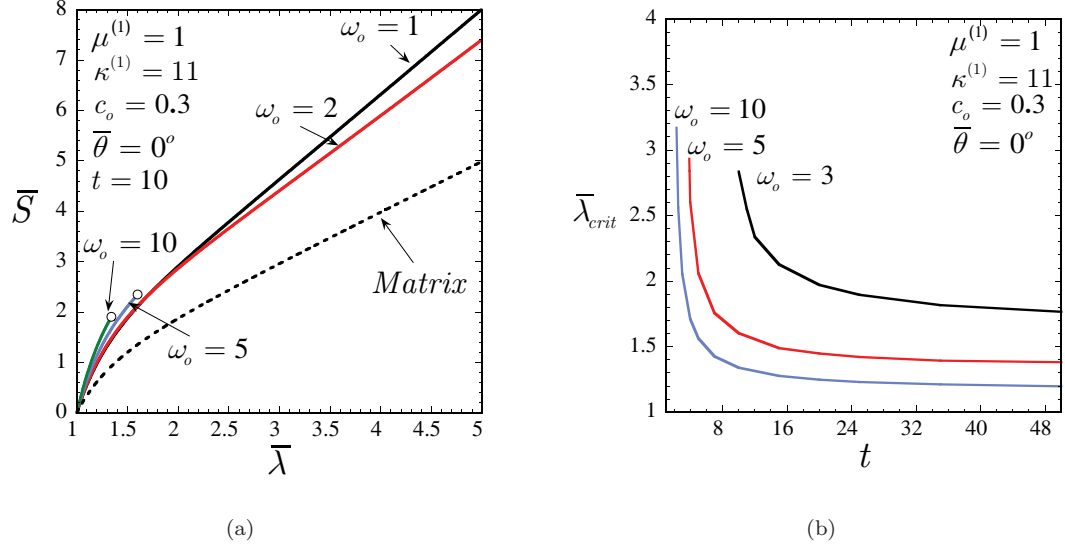


Figure 7.13: Second-order estimates for the effective behavior of reinforced elastomers subjected to aligned pure shear loading ($\bar{\theta} = 0^\circ$). The results correspond to a compressible, Neo-Hookean matrix reinforced with an initial volume fraction of 30% of stiffer, Neo-Hookean fibers of initially elliptical cross section. (a) The effective stress $\bar{S} = d\bar{W}/d\bar{\lambda}$ for contrasts of $t = \mu^{(2)}/\mu^{(1)} = \kappa^{(2)}/\kappa^{(1)} = 10$ and various aspect ratios, as a function of the applied stretch $\bar{\lambda}$. (b) The critical stretch $\bar{\lambda}_{crit}$ at which loss of strong ellipticity of the homogenized reinforced elastomer takes place for various fiber aspect ratios, as a function of the contrast t .

$\omega > 1$ beyond which no loss of ellipticity is detected. It is further noted from this figure that the homogenized material becomes unstable at larger stretches with increasing values of the loading angle. This point is more clearly illustrated by Figure 7.12(b). In fact, Figure 7.12(b) shows that beyond a certain threshold (depending on the aspect ratio ω) in $\bar{\theta}$, the homogenized elastomer does not lose strong ellipticity. Physically, the results shown in Figure 7.12 for rigidly reinforced, incompressible elastomers indicate that the *compressive* component of the applied loading along the longest in-plane axes of the fibers, together with the fiber *aspect ratio*, are the two major elements governing the macroscopic stability of the material. Indeed, the higher the aspect ratio and the higher the compressive deformation along the longest in-plane axes of the fibers, the more unstable the material is.

7.2.4 Aligned pure shear: compliant fibers and compressible matrix

Figure 7.13 presents the effective behavior as predicted by the second-order method for a compressible, Neo-Hookean elastomer reinforced with stiffer Neo-Hookean fibers of initially elliptical cross

section under aligned pure shear loading with $\bar{\theta} = 0^\circ$. The fibers and the matrix are characterized by Neo-Hookean stored-energy functions such that $\mu^{(2)}/\mu^{(1)} = \kappa^{(2)}/\kappa^{(1)} = t$, with t denoting the contrast. Results are shown for an initial fiber concentration of $c_0 = 30\%$. Part (a) shows the effective stress $\bar{S} = d\widehat{W}/d\bar{\lambda}$ for a contrast of $t = 10$ and initial fiber aspect ratios of $\omega_0 = 1, 2, 5$, and 10 , as a function of the macroscopic stretch $\bar{\lambda}$, and part (b), the critical stretch $\bar{\lambda}_{crit}$ at which the homogenized elastomer loses strong ellipticity for initial fiber aspect ratios of $\omega_0 = 3, 5$, and 10 , as a function of the contrast t . First, note the parallel between Figure 7.13(a) and 7.6(b). (Recall that the fibers were taken to be *rigid* in Figure 7.6(b).) Observe that the results shown in Figure 7.13(a) exhibit a significant reinforcement effect with the addition of stiffer fibers, but less pronounced than that one observed in Figure 7.6(b). Also, unlike the results shown in Figure 7.6(b), where higher values of the aspect ratio of the fibers consistently led to a stiffer overall behavior, higher aspect ratios of the fibers lead here to a stiffer overall behavior of the material only for small deformations, whereas the opposite is true for large stretches. Furthermore, unlike the results shown in Figure 7.6(b), where loss of strong ellipticity of the homogenized elastomer was always detected at some finite stretch for any aspect ratio $\omega > 1$, the results shown in Figure 7.13(a) are found to lose ellipticity only for sufficiently large initial aspect ratios ($\omega_0 = 5$ and 10). These discrepancies will be shown to be connected with the evolution of the microstructure. In Figure 7.13(b), it is seen that, under the given loading conditions, the type of reinforced elastomers considered here become more unstable with increasing stiffness of the fibers. In fact, for small values of ω , loss of strong ellipticity is detected only for sufficiently large values of t . This figure also shows that, similar to the results for *rigidly* reinforced elastomers, higher initial fiber aspect ratios lead to a more unstable overall behavior. Finally, it should be remarked that the loss of strong ellipticity shown in Figure 7.13(b) is due to the vanishing of the effective shear modulus $\widehat{\mathcal{L}}_{1212}^c$ in condition (7.29), corresponding, once again, to the possible “flopping” of the fibers.

Figure 7.14 provides plots associated with the results shown in Figure 7.13(a) for the evolution of the underlying microstructure in compressible, Neo-Hookean elastomers reinforced with stiffer Neo-Hookean fibers of contrast $t = 10$. Results are shown for an initial fiber volume fraction of $c_0 = 30\%$, and initial fiber aspect ratios of $\omega_0 = 1, 2, 5$, and 10 , as a function of the applied stretch $\bar{\lambda}$. Part (a) shows the evolution of the volume fraction of the fibers c , and (b), the evolution of the aspect ratio ω . It is evident from Figure 7.14(a) that the volume fraction of the fibers does not change significantly under aligned pure shear deformations, irrespectively of the initial aspect

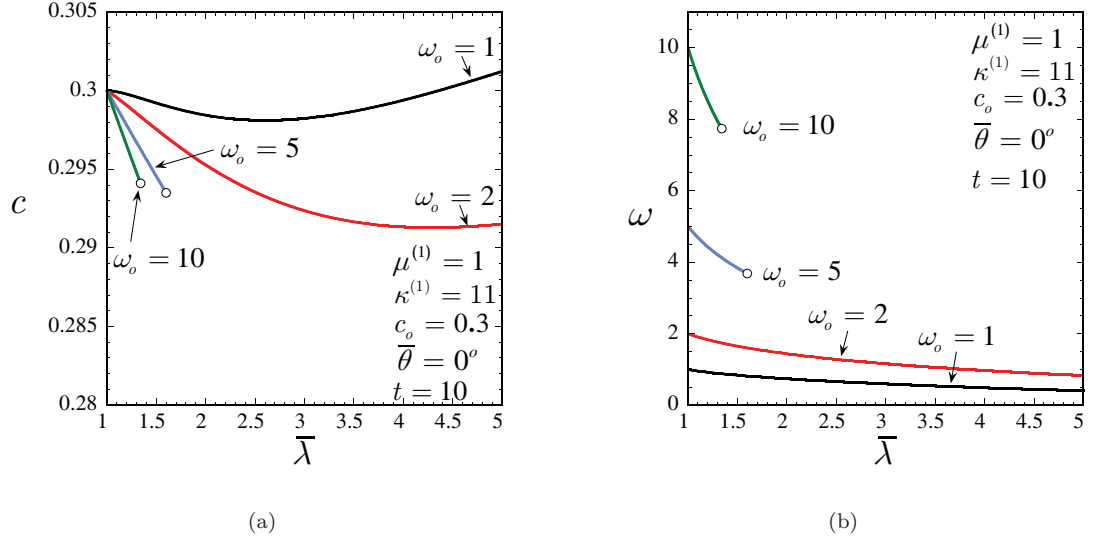


Figure 7.14: Aligned pure shear loading ($\bar{\theta} = 0^\circ$) of a compressible, Neo-Hookean elastomer reinforced with stiffer Neo-Hookean fibers of initially elliptical cross section. Results are shown for a contrast of $t = \mu^{(2)}/\mu^{(1)} = \kappa^{(2)}/\kappa^{(1)} = 10$, various initial fiber aspect ratios, and initial fiber concentration of 30%, as a function of the applied stretch $\bar{\lambda}$. (a) The evolution of the volume fraction of the fibers. (b) The evolution of the aspect ratio of the fibers.

ratio of the fibers. This result is due to the facts that the macroscopic deformation applied here is isochoric, and that both, the matrix and the fibers, were taken to be fairly incompressible (*i.e.*, $\kappa^{(1)} = 11$ and $\kappa^{(2)} = 110$). More insightful are the results shown in Figure 7.14(b), where it is seen that the aspect ratio of the fibers decreases significantly as a function of the macroscopic applied stretch $\bar{\lambda}$, as it might be expected on physical grounds since compression is being applied along the longest in-plane axes of the fibers. It is also worthwhile to remark from this figure that aspect ratios with a higher initial value exhibit a higher rate of decrease as a function of $\bar{\lambda}$. Recall now that the amount of *compressive* loading along the longest in-plane axes of the fibers, together with the fiber *aspect ratio*, have been established to be the two major elements governing the macroscopic instabilities of the type of *rigidly* reinforced elastomers of interest in this work. This statement holds true more generally for elastomers reinforced with stiffer fibers of finite stiffness. In this regard, it is relevant to remark that for the cases shown in Figure 7.14(b) the microstructure evolves into a more stable configuration, as the aspect ratio of the fibers decreases with increasing $\bar{\lambda}$. In particular, note that for the case of $\omega_o = 2$, the current aspect ratio ω evolves into values smaller than unity for sufficiently large stretches. Once $\omega < 1$, the longest axes of the fibers become aligned with the principal direction of tensile loading, a configuration

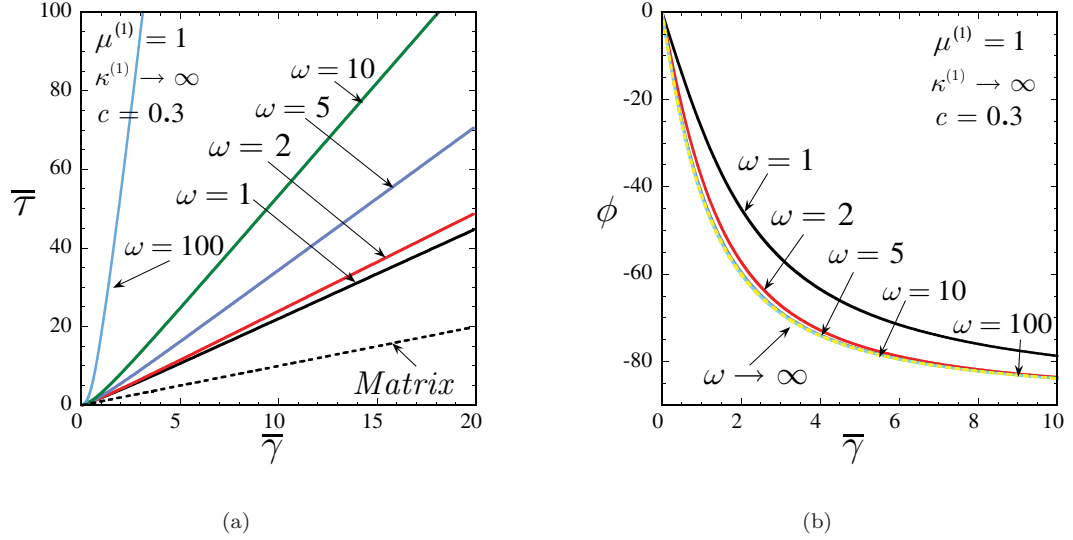


Figure 7.15: Second-order estimates for the effective behavior of rigidly reinforced elastomers subjected to simple shear “perpendicular” to the fibers. The results correspond to an incompressible, Neo-Hookean, matrix phase with fiber concentration $c = 30\%$ and various values of the fiber aspect ratio ω , and are shown as a function of the applied macroscopic shear $\bar{\gamma}$. (a) The effective stress $\bar{\tau} = d\widehat{W}/d\bar{\gamma}$. (b) The average angle of rotation of the fibers ϕ .

for which the material remains strongly elliptic. This is in contrast to the results presented in Figure 7.6(b) for *rigid* fibers with $\omega = 2$, which were found to admit loss of strong ellipticity at finite stretch. Evidently, in this latter case, the aspect ratio of the rigid fibers remained fixed along the deformation path, thus constraining the microstructure from evolving into a more stable configuration. Note that for the cases of $\omega_0 = 5$ and $\omega_0 = 10$ in Figure 7.14(b) loss of strong ellipticity takes place before the current aspect ratio reaches 1.

7.2.5 Simple shear: rigid fibers and incompressible matrix

Figure 7.15 presents second-order estimates for the effective behavior of an incompressible, Neo-Hookean elastomer reinforced with rigid fibers of elliptical cross section under simple shear loading “perpendicular” to the fibers, *i.e.*, $\bar{\mathbf{F}} = \mathbf{I} + \bar{\gamma} \mathbf{e}_1 \otimes \mathbf{e}_2$. Results are shown for fiber aspect ratios of 1, 2, 5, 10, and 100, and fiber concentration of 30%, as a function of the applied macroscopic shear $\bar{\gamma}$. Part (a) shows the effective stress $\bar{\tau} = d\widehat{W}/d\bar{\gamma}$, and (b), the average angle of rotation of the fibers ϕ . Note that in this case the applied macroscopic rotation tensor is given by $\bar{\mathbf{R}} = 1/\sqrt{4 + \bar{\gamma}^2}(2(\mathbf{e}_1 \otimes \mathbf{e}_1 + \mathbf{e}_2 \otimes \mathbf{e}_2) + \bar{\gamma}(\mathbf{e}_1 \otimes \mathbf{e}_2 - \mathbf{e}_2 \otimes \mathbf{e}_1))$ so that $\bar{\psi} = -\arcsin(\bar{\gamma}/\sqrt{4 + \bar{\gamma}^2})$. It is observed from Figure 7.15(a) that, similar to all previous cases, the addition of rigid fibers into

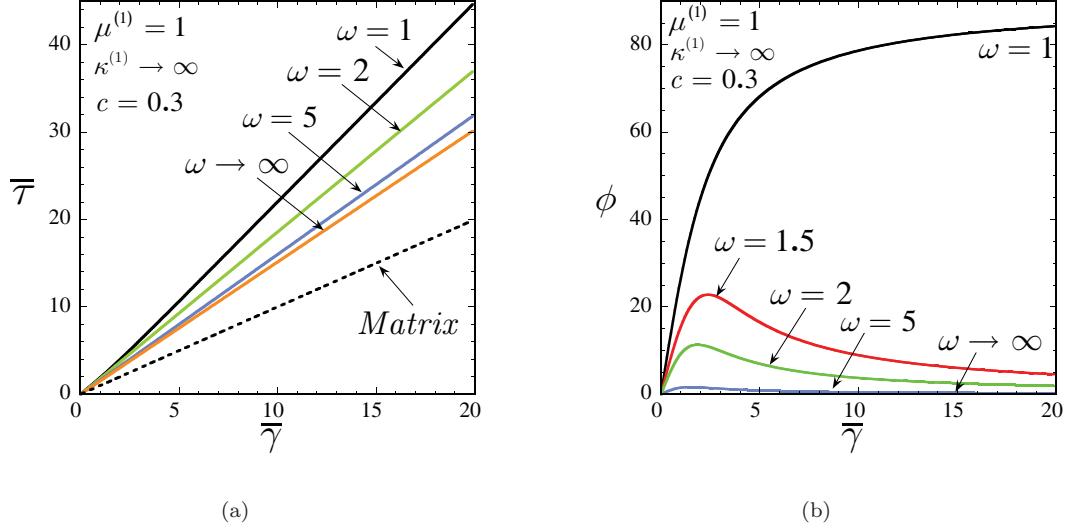


Figure 7.16: Second-order estimates for the effective behavior of rigidly reinforced elastomers subjected to simple shear “parallel” to the fibers. The results correspond to an incompressible Neo-Hookean matrix phase with fiber concentration $c = 30\%$ and various values of the fiber aspect ratio ω , and are shown as a function of the applied macroscopic shear $\bar{\gamma}$. (a) The effective stress $\bar{\tau} = d\widehat{W}/d\bar{\gamma}$. (b) The average angle of rotation of the fibers ϕ .

the elastomeric matrix produces a significant reinforcement effect on the overall response of the material. Furthermore, this reinforcement effect becomes more pronounced for higher values of the fiber aspect ratio. This is consistent with the fact that in the limit $\omega \rightarrow \infty$ (as the microstructure tends to a simple laminate) the material becomes rigid under simple shear “perpendicular” to the fibers. Figure 7.15(b) shows that all fibers, irrespectively of their aspect ratio, undergo a monotonic clockwise rotation (relative to the fixed frame of reference) with $\phi \rightarrow -90^\circ$ as $\bar{\gamma} \rightarrow \infty$, tending to align their longest in-plane axes with the principal tensile direction of the right stretch tensor $\bar{\mathbf{U}}$. As it was the case for pure shear at a fixed angle, fibers with higher aspect ratio rotate faster. In this regard, it is noted that the result for $\omega \rightarrow \infty$ has been included in Figure 7.15(b) only for reference purposes. (Recall that the material behaves rigidly in this limit under the present loading conditions.) Finally, it is interesting to remark that no loss of strong ellipticity was found to take place in these materials under the given loading conditions.

Figure 7.16 presents similar results for simple shear loading “parallel” to the fibers, *i.e.*, $\bar{\mathbf{F}} = \mathbf{I} + \bar{\gamma} \mathbf{e}_2 \otimes \mathbf{e}_1$. In this case, the applied macroscopic rotation tensor is given by $\bar{\mathbf{R}} = 1/\sqrt{4 + \bar{\gamma}^2}(2(\mathbf{e}_1 \otimes \mathbf{e}_1 + \mathbf{e}_2 \otimes \mathbf{e}_2) + \bar{\gamma}(\mathbf{e}_2 \otimes \mathbf{e}_1 - \mathbf{e}_1 \otimes \mathbf{e}_2))$ so that $\bar{\psi} = \arcsin(\bar{\gamma}/\sqrt{4 + \bar{\gamma}^2})$. Similar to Figure 7.15(a), the results presented in Figure 7.16(a) show a reinforcement effect with the addition of rigid

fibers. However, unlike Figure 7.15(a), Figure 7.16(a) shows that this reinforcement effect is more pronounced for lower values of the fiber aspect ratio. Indeed, it is seen that the reinforcement effect decreases monotonically with increasing aspect ratio, attaining the stiffest behavior at $\omega = 1$, and the softest one at $\omega \rightarrow \infty$. (Recall that simple shear “parallel” to the fibers is the *only* admissible deformation for $\omega \rightarrow \infty$ in the context of *rigid* fibers.) Interestingly, this is exactly the same trend followed in the infinitesimal strain regime, where higher fiber aspect ratios lead to softer overall responses of the material. Figure 7.16(b) shows that circular fibers rotate with the applied macroscopic rotation, that is, $\phi = \bar{\psi}$, and hence they undergo an anticlockwise monotonic rotation (relative to the fixed frame of reference) with $\phi \rightarrow 90^\circ$ as $\bar{\gamma} \rightarrow \infty$. On the other hand, elliptical fibers initially rotate anticlockwise, reaching a maximum value at certain shear $\bar{\gamma}$ after which they rotate clockwise asymptotically tending to 0° , thus aligning their longest in-plane axes with the principal tensile direction of the right stretch tensor $\bar{\mathbf{U}}$. Note that $\phi = 0^\circ$ for all $\bar{\gamma}$ for the limiting case $\omega \rightarrow \infty$, in agreement with the exact result (for a laminate). Finally, akin to simple shearing “perpendicular” to the fibers, no loss of strong ellipticity was found to take place in these materials under the given conditions.

7.3 Concluding remarks

In this chapter, *analytical* estimates have been derived for the in-plane effective behavior, the microstructure evolution, and the onset of macroscopic instabilities in fiber-reinforced elastomers with *random* microstructures subjected to finite deformations, by making use of the framework developed in Chapter 2.

A major result of this work is the strong influence of the evolution of the microstructure on the overall behavior of reinforced elastomers. Indeed, in the specific context of elastomers reinforced with *rigid* fibers (of elliptical cross section), the rotation (in the plane of the deformation) of the fibers when the composite is subjected to finite stretches has been identified as a potential *softening* mechanism. Physically, the fibers can “accommodate” some of the applied macroscopic deformation through rigid rotations, tending to align themselves with the tensile loading axis, which induces softer modes of deformation in the matrix phase. As a consequence, the overall response of the composite under loadings that promote large rotations of the underlying fibers tend to be much softer than those associated with loadings inducing smaller rotations (or no rotations at all).

Perhaps more significantly, the microstructure evolution not only has implications for the effective behavior, but also for the overall stability of the composite. In this regard, it has been shown that loss of strong ellipticity, corresponding to the possible development of shear-band type instabilities at a macroscopic length scale, can take place in strongly elliptic elastomers reinforced with *stiff* fibers (of elliptical cross section) at physically realistic levels of deformation. The underlying microscopic mechanism driving these macroscopic instabilities has been identified with the possible “flopping” of the fibers, due to a sufficiently large *compressive* component of the applied deformation along the long (in-plane) axes of the fibers. More specifically, in spite of the randomness, the assumed “elliptical symmetry” of the microstructure exhibits a preferred microstructural orientation. Thus, the “flopping” of the fibers provides a *symmetry breaking* mechanism leading to the possible development of a macroscopic instability. Indeed, in the limit as the fibers (and their two-point correlation function) are taken to be circular, so that the composite becomes isotropic, no loss of strong ellipticity is detected, as there are no symmetries to be broken.

Another important conclusion of this work is that the addition of rigid inclusions in an elastomer enhances the “lock-up” effect in the material due to the stretching of the polymer chains, provided that it is already present in the matrix phase. From the continuum point of view, this is consistent with the fact that, on average, the deformation in the matrix phase of a rigidly reinforced material is larger than the applied macroscopic deformation (since the rigid phase does not deform), leading then to a smaller overall lock-up stretch. Physically, the effect of introducing rigid inclusions into an elastomer would make the polymeric chains wrap around the particles, which would be consistent with a smaller overall lock-up stretch upon deformation of the composite.

7.4 Appendix I. Incompressibility limit for rigidly reinforced elastomers: cylindrical fibers

In this appendix, we sketch out the asymptotic analysis corresponding to the *incompressible* limit associated with the second-order estimate (2.82) for elastomers with *isotropic* matrix phases of the form (7.1) reinforced with *rigid* fibers of volume fraction c and aspect ratio ω . As already discussed in the main body of text, only one of the two possible roots associated with the second-order estimates developed in this work provides physically sound results. Hence, only the limit associated with this root is presented here. It must be emphasized that the results generated by the following asymptotic analysis have been checked to be in agreement with the full numerical solution.

Based on numerical evidence from the results for finite $\kappa^{(1)}$, an expansion for the unknowns (*i.e.*, L_{1111}^* , L_{2222}^* , L_{1122}^* , L_{1212}^* , and ϕ) in this problem is attempted in the limit as $\kappa^{(1)} \rightarrow \infty$ of the following form:

$$\begin{aligned}
L_{1111}^* &= a_1 \Delta^{-1/3} + a_2 + a_3 \Delta^{1/3} + O(\Delta^{2/3}), \\
L_{2222}^* &= b_1 \Delta^{-1/3} + b_2 + b_3 \Delta^{1/3} + O(\Delta^{2/3}), \\
L_{1122}^* &= d_1 \Delta^{-1/3} + d_2 + d_3 \Delta^{1/3} + O(\Delta^{2/3}), \\
L_{1212}^* &= e_2 + e_3 \Delta^{1/3} + e_4 \Delta^{2/3} + O(\Delta), \\
\phi &= \phi_o + \phi_1 \Delta^{1/3} + O(\Delta^{2/3}),
\end{aligned} \tag{7.33}$$

where $\Delta = 1/\kappa^{(1)}$ is a small parameter and $a_1, a_2, a_3, b_1, b_2, b_3, d_1, d_2, d_3, e_2, e_3, e_4, \phi_o$, and ϕ_1 are unknown coefficients to be determined from the asymptotic analysis that follows. It will prove useful to spell out the corresponding expansions for the constrained components L_{2121}^* and L_{1221}^* , as well as those for the components of $\mathbf{Y} = \overline{\mathbf{Q}}^T \overline{\mathbf{R}}^T \left(\hat{\mathbf{F}}^{(1)} - \overline{\mathbf{F}} \right) \overline{\mathbf{Q}}$, in the limit as $\kappa^{(1)} \rightarrow \infty$. Thus, introducing (7.33) in relations (7.6) for the components L_{2121}^* and L_{1221}^* can be shown to lead to the following expansions:

$$\begin{aligned}
L_{2121}^* &= e_2 + e_3 \Delta^{1/3} + O(\Delta^{2/3}), \\
L_{1221}^* &= \left(\sqrt{a_1 b_1} - d_1 \right) \Delta^{-1/3} + \frac{a_2 b_1 + a_1 b_2 - (a_1 + b_1) e_2}{2\sqrt{a_1 b_1}} - d_2 + O(\Delta^{1/3}).
\end{aligned} \tag{7.34}$$

Similarly, introducing (7.33) in relations (7.11) for the components of \mathbf{Y} leads to:

$$\begin{aligned}
Y_{11} &= x_1 + x_2\Delta^{1/3} + x_3\Delta^{2/3} + x_4\Delta + O(\Delta^{4/3}), \\
Y_{22} &= y_1 + y_2\Delta^{1/3} + y_3\Delta^{2/3} + y_4\Delta + O(\Delta^{4/3}), \\
Y_{12}Y_{21} &= p_1 + p_2\Delta^{1/3} + p_3\Delta^{2/3} + p_4\Delta + O(\Delta^{4/3}), \\
Y_{12}^2 + Y_{21}^2 &= s_1 + O(\Delta^{1/3}).
\end{aligned} \tag{7.35}$$

The explicit form of the coefficients in these expressions are too cumbersome to be included here. In any case, at this stage, it suffices to note that they are known in terms of the variables introduced in (7.33) (and higher-order correcting terms). In connection with the relations (7.35), it is necessary to remark that the asymptotic expressions for the combinations $Y_{12}Y_{21}$ and $Y_{12}^2 + Y_{21}^2$ have been specified, instead of those for the independent components Y_{12} and Y_{21} , since, as discussed in the main body of the text, they are the relevant variables in this problem. For later use, it will also prove helpful to introduce the notation for the expansions of the constitutive function $g^{(1)}$ characterizing the matrix phase in the limit $\kappa^{(1)} \rightarrow \infty$:

$$\begin{aligned}
g^{(1)}(\hat{I}^{(1)}) &= \hat{g} = \hat{g}_o + \hat{g}_1\Delta^{1/3} + \hat{g}_2\Delta^{2/3} + O(\Delta), \\
g_I^{(1)}(\hat{I}^{(1)}) &= \hat{g}_I = \hat{g}'_o + \hat{g}'_1\Delta^{1/3} + \hat{g}'_2\Delta^{2/3} + O(\Delta), \\
g^{(1)}(\bar{I}) &= \bar{g}, \\
g_I^{(1)}(\bar{I}) &= \bar{g}_I,
\end{aligned} \tag{7.36}$$

where $\hat{I}^{(1)} = \hat{\mathbf{F}}^{(1)} \cdot \hat{\mathbf{F}}^{(1)}$, $\hat{J}^{(1)} = \det \hat{\mathbf{F}}^{(1)}$, and appropriate smoothness has been assumed for $g^{(1)}$. Analogous expressions are defined for the material function $h^{(1)}$.

Now, by introducing expressions (7.33)–(7.36) in the generalized secant equation (2.65), as well as in the equation (2.79) for the rigid rotation of the fibers, a hierarchical system of equations is obtained for the unknown coefficients in (7.33) and higher-order correcting terms. Thus, the equations of first order $O(\Delta^{-1})$ can be shown to yield the following relations:

$$\bar{J} = \bar{\lambda}_1\bar{\lambda}_2 = 1, \quad \bar{\lambda}_2x_1 + \bar{\lambda}_1y_1 + x_1y_1 - p_1 = 0, \quad e_2 = 2\hat{g}'_o. \tag{7.37}$$

Here, it is important to remark that condition (7.37)₁ is nothing more than the *exact* incompressibility constraint (7.13) specialized to plane-strain deformations. Moreover, it is noted that conditions (7.37)₂ and (7.37)₃ establish relations among the unknowns $a_1, a_2, b_1, b_2, d_1, d_2, e_2$, and ϕ_o . Next, by making use of (7.37), the equations of second order $O(\Delta^{-2/3})$ can be shown to

ultimately render the conditions:

$$\bar{\lambda}_2 x_2 + \bar{\lambda}_1 y_2 + x_1 y_2 + x_2 y_1 - p_2 = 0, \quad e_3 = 2\hat{g}'_1, \quad (7.38)$$

which establish further relations among $a_1, a_2, a_3, b_1, b_2, b_3, d_1, d_2, d_3, e_2, e_3$, and ϕ_o . Making use now of (7.37) and (7.38) in the equations of third order $O(\Delta^{-1/3})$ gives:

$$\begin{aligned} b_1 &= \bar{\lambda}_1^4 a_1, \\ y_1 \bar{\lambda}_1^4 a_1 + x_1 \bar{\lambda}_1^2 a_1 + \bar{\lambda}_1 (\bar{\lambda}_1^2 a_1 - d_1) &= 0, \\ \bar{\lambda}_2 x_3 + \bar{\lambda}_1 y_3 + x_1 y_3 + y_1 x_3 + x_2 y_2 - p_3 &= d_1 - \bar{\lambda}_1^2 a_1, \\ e_4 &= 2\hat{g}'_2, \\ \phi_o &= \varphi + \bar{\psi}, \end{aligned} \quad (7.39)$$

where

$$\cos \varphi = \frac{(c-1)d_1}{c\bar{\lambda}_1(1+\bar{\lambda}_1^2)a_1} + \frac{(1+c)\bar{\lambda}_1}{c(1+\bar{\lambda}_1^2)}, \quad (7.40)$$

and $\bar{\psi}$ denotes the angle associated with the macroscopic rotation tensor $\bar{\mathbf{R}}$.

Finally, with the help of relations (7.37) through (7.40), the equations of fourth order $O(\Delta)$ can be shown to yield:

$$\begin{aligned} b_2 - \bar{\lambda}_1^4 a_2 &= \frac{2(1-\bar{\lambda}_1^4)}{d_1 - \bar{\lambda}_1^2 a_1} \left(d_1 \hat{g}'_o + a_1 (\hat{g}'_o - 2\bar{g}_I) \bar{\lambda}_1^2 \right), \\ 2a_1^2 \bar{\lambda}_1^4 (a_1 \bar{\lambda}_1^2 - d_1) (\bar{\lambda}_2 x_2 + \bar{\lambda}_1 y_2) - d_1^2 (a_2 - 2\hat{g}'_o) \bar{\lambda}_1^2 \\ &\quad - 2a_1^2 \bar{\lambda}_1 \left[d_2 \bar{\lambda}_1^3 + 2(\hat{g}'_o - \bar{g}_I) (\bar{\lambda}_1^5 + x_1 (\bar{\lambda}_1^4 - 1)) + \mu^{(1)} \bar{\lambda}_1^3 \right] \\ &\quad + 2a_1 d_1 \left[\bar{g}'_I (2 - 4\bar{\lambda}_1^4) + 2\hat{g}'_o (\bar{\lambda}_1^4 - 1) + \bar{\lambda}_1^2 (d_2 + a_2 \bar{\lambda}_1^2 + \mu^{(1)}) \right] = 0, \\ \bar{\lambda}_2 x_4 + \bar{\lambda}_1 y_4 + x_1 y_4 + y_1 x_4 + x_2 y_3 + x_3 y_2 - p_4 &= d_2 + \mu^{(1)} \\ &\quad - 2^{-1} \bar{\lambda}_1^{-2} \left(b_2 + a_2 \bar{\lambda}_1^4 - 2\hat{g}'_o (\bar{\lambda}_1^4 + 1) \right), \\ e_5 &= 2\hat{g}'_3, \\ \cos \phi_1 &= G(a_1, d_1, a_2, d_2) \sin \phi_o, \end{aligned} \quad (7.41)$$

where G is (a known function of its arguments) too cumbersome to be included here, and use has been made of the facts that $\hat{h}_o = \bar{h} = 0$ and $\hat{h}'_o = \bar{h}_J = -\mu^{(1)}$.

Although the above system of algebraic, nonlinear equations is not closed (*i.e.*, there are more unknowns than equations), it is possible to solve for the appropriate combinations of coefficients

introduced in (7.33), which allows the determination of the leading order term of ϕ , as well as the leading order term of the components of \mathbf{Y} in the limit $\kappa^{(1)} \rightarrow \infty$. The results read as follows:

$$\phi_o = \varphi + \bar{\psi}, \quad (7.42)$$

$$\begin{aligned} x_1 &= \frac{c}{1-c} (\bar{\lambda} - \cos \varphi), \\ y_1 &= \frac{c}{1-c} (\bar{\lambda}^{-1} - \cos \varphi), \\ p_1 &= \frac{c}{\bar{\lambda}(1-c)^2} \left((2-c)\bar{\lambda} - (\bar{\lambda}^2 + 1) \cos \varphi + c\bar{\lambda} \cos^2 \varphi \right), \\ s_1 &= \frac{c}{2\omega(1-c)^2 \bar{\lambda}^2} \left[-4(1 + (\omega - 1)\omega) (\bar{\lambda} + \bar{\lambda}^3) \cos(\varphi) \right. \\ &\quad \left. + 2 \left(\omega(c-4)\bar{\lambda}^2 + (1 + \bar{\lambda}^2)^2 + \omega^2(1 + \bar{\lambda}^2)^2 - \omega c \bar{\lambda}^2 \cos(2\varphi) \right) \right. \\ &\quad \left. - 2(\omega^2 - 1) (\bar{\lambda}^4 - 1) \cos(2\bar{\theta}) \sin(\varphi)^2 \right. \\ &\quad \left. + (\omega^2 - 1) (\bar{\lambda}^4 - 1) \sin(2\bar{\theta}) \sin(2\varphi) \right], \end{aligned} \quad (7.43)$$

respectively, where the angle φ satisfies expression (7.17) given in the text. Here, $\bar{\lambda} = \bar{\lambda}_1 = \bar{\lambda}_2^{-1}$, and $\bar{\theta}$ denotes the orientation of the in-plane principal axes of $\bar{\mathbf{U}}$ in agreement with the notation employed in Section 7.1.2.

Finally, it is straightforward to show that the leading order term of the expansion of the second-order estimate (2.82) in the limit of incompressibility may be ultimately written in terms of the leading order term of ϕ (7.42) and \mathbf{Y} (7.43). The final explicit expression is given by (7.14) in the text.

Chapter 8

Reinforced elastomers: cylindrical fibers, periodic microstructure

This objective of this chapter is to develop, by means of the second-order homogenization method, a constitutive model for the mechanical behavior of elastomers reinforced with aligned cylindrical fibers subjected to finite deformations. Specific results are generated for the case when the matrix and fiber materials are characterized by generalized Neo-Hookean solids, and the distribution of the fibers is periodic. In particular, model predictions are provided and analyzed for fiber-reinforced elastomers with Gent phases and square and hexagonal fiber distributions, subjected to a wide variety of three-dimensional loading conditions. It is found that for compressive loadings in the fiber direction, the derived constitutive model may lose strong ellipticity, indicating the possible development of macroscopic instabilities that may lead to kink band formation. The onset of shear band-type instabilities is also detected for certain in-plane modes of deformation. Furthermore, the subtle influence of the distribution, volume fraction, and stiffness of the fibers on the effective behavior and onset of macroscopic instabilities in these materials is investigated thoroughly.

8.1 Overall behavior of periodic, fiber-reinforced elastomers

In this chapter, we make use of the second-order estimate (2.62) to develop a homogenization-based constitutive model for the effective mechanical response of fiber-reinforced elastomers with periodic microstructures. Following Section 2.1.3, for relative simplicity, the elastomeric matrix

phase and the fiber are taken to be characterized by stored-energy functions of the form:

$$W^{(r)}(\mathbf{F}) = \Phi^{(r)}(\lambda_1, \lambda_2, \lambda_3) = g^{(r)}(I) + h^{(r)}(J) + \frac{\kappa^{(r)}}{2}(J-1)^2 \quad (8.1)$$

($r = 1, 2$), where it is recalled that $I \equiv I_1 = \text{tr} \mathbf{C} = \mathbf{F} \cdot \mathbf{F} = \lambda_1^2 + \lambda_2^2 + \lambda_3^2$, $J = \sqrt{\det \mathbf{C}} = \det \mathbf{F} = \lambda_1 \lambda_2 \lambda_3$ are, respectively, the first and third fundamental invariants of the right Cauchy-Green deformation tensor $\mathbf{C} = \mathbf{F}^T \mathbf{F}$, with λ_i ($i = 1, 2, 3$) denoting the principal stretches associated with \mathbf{F} . Further, $\kappa^{(r)}$ denotes the three-dimensional bulk modulus at zero strain of phase r , and $g^{(r)}$ and $h^{(r)}$ are twice-differentiable material functions that satisfy the following relations: $g^{(r)}(3) = h^{(r)}(1) = 0$, $g_I^{(r)}(3) = \mu^{(r)}/2$, $h_J^{(r)}(1) = -\mu^{(r)}$, and $4g_{II}^{(r)}(3) + h_{JJ}^{(r)}(1) = \mu^{(r)}/3$. Here, $\mu^{(r)}$ denotes the shear modulus at zero strain of phase r , and the subscripts I and J indicate differentiation with respect to these invariants. Note that when the above conditions are satisfied, the stored-energy function (8.1) linearizes properly, in the sense that $W^{(r)}(\mathbf{F}) = (1/2)(\kappa^{(r)} - 2/3\mu^{(r)})(\text{tr} \boldsymbol{\varepsilon})^2 + \mu^{(r)} \text{tr} \boldsymbol{\varepsilon}^2 + o(\boldsymbol{\varepsilon}^3)$, where $\boldsymbol{\varepsilon}$ is the infinitesimal strain tensor, as $\mathbf{F} \rightarrow \mathbf{I}$. Furthermore, note that to recover incompressible behavior in (8.1), it suffices to make the parameter $\kappa^{(r)}$ tend to infinity (in which case $W^{(r)}(\mathbf{F}) = g^{(r)}(I)$ together with the incompressibility constraint $J = 1$).

Within the context of the material model (8.1), it is worth recalling that by requiring $g^{(r)}(I)$ and $h^{(r)}(J) + \frac{\kappa^{(r)}}{2}(J-1)^2$ to be strictly convex functions of their arguments, the stored-energy function (8.1) is strongly elliptic. This constitutive hypothesis, which will be adopted here, guarantees that no localized deformations will develop within the given elastomeric matrix and fiber phases, in accord with experimental evidence for “neat” rubber-like solids. Note also that the stored-energy function (8.1) is an extension of the so-called generalized Neo-Hookean (or I_1 -based) materials to account for compressibility that includes constitutive models widely used in the literature. The analysis that follows will be carried out for stored-energy functions of the general form (8.1). However, for definiteness, specific results will be presented and discussed for fiber-reinforced elastomers with Gent (Gent, 1996) matrix and fiber phases:

$$W^{(r)}(\mathbf{F}) = -\frac{J_m^{(r)} \mu^{(r)}}{2} \ln \left[1 - \frac{I-3}{J_m^{(r)}} \right] - \mu^{(r)} \ln J + \left(\frac{\kappa^{(r)}}{2} - \frac{J_m^{(r)} + 3}{3 J_m^{(r)}} \mu^{(r)} \right) (J-1)^2. \quad (8.2)$$

In this material model, the parameter $J_m^{(r)}$ indicates the limiting value for $I-3$ at which the elastomer locks up. Note that the stored-energy function (8.2) is strongly elliptic for all deformations provided that $\mu^{(r)} > 0$, $J_m^{(r)} > 0$, and $\kappa^{(r)} > 2\mu^{(r)}/J_m^{(r)} + 2/3\mu^{(r)}$, which will be assumed here. Note further that upon taking the limit $J_m^{(r)} \rightarrow \infty$ in (8.2), the Gent material reduces to the compressible Neo-Hookean solid.

8.1.1 Voigt bound

Before proceeding with the computation of the second-order estimate, it proves useful, for comparison purposes, to write down the Voigt upper bound (Ogden, 1978) for hyperelastic composites. Thus, when specialized to fiber-reinforced elastomers with initial volume fraction of fibers c_0 and (matrix and fiber) phases of the form (8.1), this rigorous upper bound leads to:

$$\widehat{W}(\overline{\mathbf{F}}) = (1 - c_0) \left[g^{(1)}(\overline{I}) + h^{(1)}(\overline{J}) \right] + c_0 \left[g^{(2)}(\overline{I}) + h^{(2)}(\overline{J}) \right] + \frac{(1 - c_0)\kappa^{(1)} + c_0\kappa^{(2)}}{2} (\overline{J} - 1)^2, \quad (8.3)$$

where $\overline{I} = \overline{\mathbf{F}} \cdot \overline{\mathbf{F}} = \overline{\lambda}_1^2 + \overline{\lambda}_2^2 + \overline{\lambda}_3^2$ and $\overline{J} = \det \overline{\mathbf{F}} = \overline{\lambda}_1 \overline{\lambda}_2 \overline{\lambda}_3$ stand for, respectively, the first and third invariants associated with the macroscopic deformation gradient tensor $\overline{\mathbf{F}}$. Note that the bound (8.3) depends only on the initial volume fraction of the fibers, c_0 , and contains no dependence on higher-order statistical information about the microstructure. This limitation can be readily recognized in the present context from the fact that the stored-energy function (8.3) is *isotropic*, while the exact overall behavior of the fiber-reinforced elastomers of interest in this work is obviously *orthotropic*. Moreover, it is interesting to remark that the Voigt bound (8.3) remains strongly elliptic for all deformations $\overline{\mathbf{F}}$, provided that $g^{(r)}(\overline{I})$ and $h^{(r)}(\overline{J}) + \frac{\kappa^{(r)}}{2}(\overline{J} - 1)^2$ ($r = 1, 2$) are strictly convex functions of their arguments, which has been assumed here.

8.1.2 Second-order homogenization estimates

In this subsection, we spell out the main steps in the computation of the second-order estimate (2.62) for the effective stored-energy function \widehat{W} of elastomers, characterized by stored-energy functions of the form (8.1), reinforced with monodisperse, initially circular, aligned cylindrical fibers—also characterized by potentials of the form (8.1)—distributed periodically in: a) square and b) hexagonal arrangements in the undeformed configuration, as depicted in Fig. 8.1.

In order to carry out the computation for the second-order estimate (2.62) for the above-specified class of elastomeric composites, the precise form of the modulus tensor \mathbf{L}^* , introduced in expression (2.66), needs to be spelled out. In this regard, recall first that \mathbf{L}^* is orthotropic with respect to the laboratory frame of reference $\{\mathbf{e}_i\}$ and has at most 9 independent components (*i.e.*, ℓ_α^*). In this work, for simplicity, we introduce further constraints among the components of \mathbf{L}^* in order to reduce them to 7 independent components. Thus, following Chapter 5, the independent principal components of \mathbf{L}^* are chosen to be $L_{1111}^* = \ell_1^*$, $L_{2222}^* = \ell_2^*$, $L_{3333}^* = \ell_3^*$, $L_{1122}^* = \ell_4^*$,

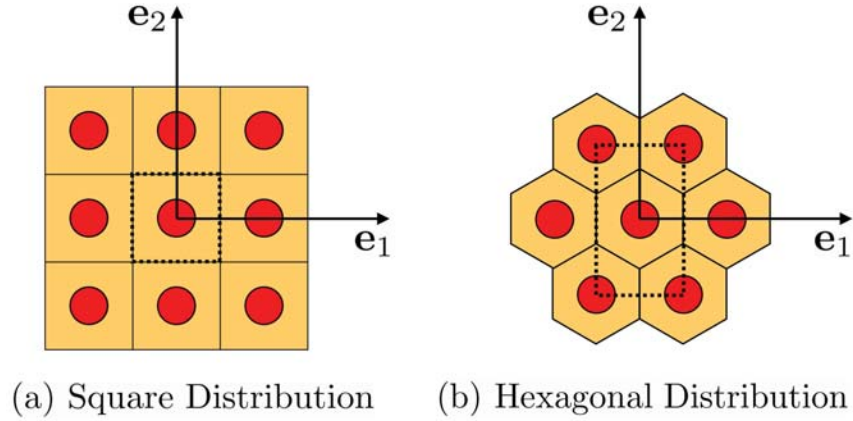


Figure 8.1: Undeformed configuration depiction of: (a) periodic square and (b) periodic hexagonal arrangement of circular fibers.

$L_{1133}^* = \ell_5^*$, $L_{2233}^* = \ell_6^*$, $L_{1212}^* = \ell_7^*$, while the other non-zero components

$$\begin{aligned}
 L_{2121}^* &= L_{1313}^* = L_{3131}^* = L_{2323}^* = L_{3232}^* = \ell_7^*, \\
 L_{1221}^* &= \sqrt{(\ell_1^* - \ell_7^*)(\ell_2^* - \ell_7^*)} - \ell_4^*, \\
 L_{1331}^* &= \sqrt{(\ell_1^* - \ell_7^*)(\ell_3^* - \ell_7^*)} - \ell_5^*, \\
 L_{2332}^* &= \sqrt{(\ell_2^* - \ell_7^*)(\ell_3^* - \ell_7^*)} - \ell_6^*,
 \end{aligned} \tag{8.4}$$

are dependent. The motivation for the constraints (8.4) is twofold: (i) relations (8.4) are consistent with the tangent modulus of Neo-Hookean materials;¹ and (ii) conditions (8.4) simplify considerably the computations involved. It should be emphasized, however, that other choices are possible in principle.

Having specified the functional form of \mathbf{L}^* , and hence that of $\mathbf{L}^{(1)}$ via (2.66), we proceed next to compute the variable $\hat{\mathbf{F}}^{(1)}$, needed in the computation of the second-order estimate (2.62) for \widehat{W} . In this connection, we recognize that equations (2.68) reduce to 7 nonlinear, algebraic equations for 7 combinations of the components of $\hat{\mathbf{F}}^{(1)}$. These equations—as it will become more clear further below—are more conveniently expressed in terms of the variable \mathbf{Y} :

$$\mathbf{Y} = \overline{\mathbf{Q}}^T \overline{\mathbf{R}}^T (\hat{\mathbf{F}}^{(1)} - \overline{\mathbf{F}}) \overline{\mathbf{Q}} \tag{8.5}$$

¹In fact, conditions (8.4)₁ are consistent with tangent moduli of any isotropic stored-energy function of the general form (8.1).

which leads to the expressions:

$$\begin{aligned}
Y_{11}^2 + 2f_1 Y_{12}Y_{21} + 2f_2 Y_{13}Y_{31} &= \frac{2}{1-c_0} \frac{\partial \widehat{W}_T}{\partial \ell_1^*} \doteq k_1 \quad , \\
Y_{22}^2 + \frac{1}{2f_1} Y_{12}Y_{21} + 2f_3 Y_{23}Y_{32} &= \frac{2}{1-c_0} \frac{\partial \widehat{W}_T}{\partial \ell_2^*} \doteq k_2 \quad , \\
Y_{33}^2 + \frac{1}{2f_2} Y_{13}Y_{31} + \frac{1}{2f_3} Y_{23}Y_{32} &= \frac{2}{1-c_0} \frac{\partial \widehat{W}_T}{\partial \ell_3^*} \doteq k_3 \quad , \\
Y_{11}Y_{22} - Y_{12}Y_{21} &= \frac{1}{1-c_0} \frac{\partial \widehat{W}_T}{\partial \ell_4^*} \doteq \frac{k_4}{2} \quad , \\
Y_{11}Y_{33} - Y_{13}Y_{31} &= \frac{1}{1-c_0} \frac{\partial \widehat{W}_T}{\partial \ell_5^*} \doteq \frac{k_5}{2} \quad , \\
Y_{22}Y_{33} - Y_{23}Y_{32} &= \frac{1}{1-c_0} \frac{\partial \widehat{W}_T}{\partial \ell_6^*} \doteq \frac{k_6}{2} \quad , \\
Y_{12}^2 + Y_{21}^2 + Y_{13}^2 + Y_{31}^2 + Y_{23}^2 + Y_{32}^2 + 2f_4 Y_{12}Y_{21} + 2f_5 Y_{13}Y_{31} \\
+ 2f_6 Y_{23}Y_{32} &= \frac{2}{1-c_0} \frac{\partial \widehat{W}_T}{\partial \ell_7^*} \doteq k_7 \quad .
\end{aligned} \tag{8.6}$$

Here, $f_1 = \partial L_{1221}^*/\partial \ell_1^*$, $f_2 = \partial L_{1331}^*/\partial \ell_1^*$, $f_3 = \partial L_{2332}^*/\partial \ell_2^*$, $f_4 = \partial L_{1221}^*/\partial \ell_7^*$, $f_5 = \partial L_{1331}^*/\partial \ell_7^*$, $f_6 = \partial L_{2332}^*/\partial \ell_7^*$, and

$$k_I = -\frac{c_0}{(1-c_0)} (\overline{\mathbf{F}} - \overline{\mathbf{F}}^{(2)}) \cdot \frac{\partial \mathbf{L}^{(1)}}{\partial \ell_\alpha^*} (\overline{\mathbf{F}} - \overline{\mathbf{F}}^{(2)}) - c_0 \mathbf{E} \cdot \frac{\partial \mathbf{P}}{\partial \ell_\alpha^*} \mathbf{E} \tag{8.7}$$

($\alpha = 1, 2, \dots, 7$), where $\mathbf{E} = \mathbf{L}^{(1)}(\overline{\mathbf{F}} - \overline{\mathbf{F}}^{(2)}) - \mathcal{S}^{(1)}(\overline{\mathbf{F}}) + \mathcal{S}^{(2)}(\overline{\mathbf{F}}^{(2)})$ has been introduced for convenience, and it is remarked that the explicit expressions for the tensor \mathbf{P} for the two types of periodic microstructures considered here are given in Appendix I. It is not difficult to check that—though nonlinear—equations (8.6) may be solved *explicitly* to yield two distinct solutions for Y_{11} , Y_{22} , Y_{33} in terms of which the combinations $p_1 \doteq Y_{12}Y_{21}$, $p_2 \doteq Y_{13}Y_{31}$, $p_3 \doteq Y_{23}Y_{32}$, and $s \doteq Y_{12}^2 + Y_{21}^2 + Y_{13}^2 + Y_{31}^2 + Y_{23}^2 + Y_{32}^2$ may be uniquely determined. The two solutions for Y_{11} , Y_{22} , and Y_{33} are as follows:

$$\begin{aligned}
Y_{11} &= \pm \frac{(k_1 + f_1 k_4 + f_2 k_5) \sqrt{C_1 C_2}}{C_2 \sqrt{C_3}}, \\
Y_{22} &= \pm \frac{(k_4 + 4f_1(k_2 + f_3 k_6)) C_2}{2 \sqrt{C_1 C_2} \sqrt{C_3}}, \\
Y_{33} &= \pm \frac{(f_3 k_5 + f_2(4f_3 k_3 + k_6)) \sqrt{C_3}}{\sqrt{C_1 C_2}},
\end{aligned} \tag{8.8}$$

with $C_1 = f_2(4f_1 k_2 + k_4) + 4f_1 f_3^2(4f_2 k_3 + k_5) + 2f_3(k_1 + f_1 k_4 + f_2 k_5 + 4f_1 f_2 k_6)$, $C_2 = f_2(4f_1 k_2 + k_4 + 2f_2 k_6) + 2f_3(k_1 + f_1 k_4 + 2f_2(2f_2 k_3 + k_5 + f_1 k_6))$, $C_3 = k_1 + f_2 k_5 + 2f_1(4f_2 f_3 k_3 + k_4 + f_3 k_5 +$

$f_2k_6) + 4f_1^2(k_2 + f_3k_6)$, where it must be emphasized that the positive (and negative) signs must be chosen to go together in the roots for Y_{11} , Y_{22} , and Y_{33} . The corresponding final expressions for the remaining combinations read as:

$$\begin{aligned} p_1 &= Y_{11}Y_{22} - k_4/2, & p_2 &= Y_{11}Y_{33} - k_5/2, & p_3 &= Y_{22}Y_{33} - k_6/2, & \text{and} \\ s &= k_7 - 2(f_4p_1 + f_5p_2 + f_6p_3). \end{aligned} \quad (8.9)$$

At this point, it is expedient to make a few remarks regarding expressions (8.8) and (8.9). First, it is important to emphasize that these relations provide *explicit* expressions for 7 combinations of the components of $\hat{\mathbf{F}}^{(1)}$ in terms of the applied loading $\bar{\mathbf{F}}$, the constitutive functions $g^{(r)}$, $h^{(r)}$, $\kappa^{(r)}$ ($r = 1, 2$), the initial volume fraction of fibers c_0 , as well as the moduli ℓ_α^* ($\alpha = 1, 2, \dots, 7$) and the phase average deformation gradient in the fiber phase of the linear comparison composite $\bar{\mathbf{F}}^{(2)}$. Note, however, that the tensorial variable $\hat{\mathbf{F}}^{(1)}$ has 9 components, so that two more relations are required to entirely characterize $\hat{\mathbf{F}}^{(1)}$, as discussed below.

Next, making use of each of the two distinct roots (8.8) for the combinations Y_{11} , Y_{22} , Y_{33} , p_1 , p_2 , p_3 , s in the generalized secant condition (2.65) can be shown to lead to a system of 9 scalar equations for the 9 unknowns constituted by the 2 combinations of $\hat{\mathbf{F}}^{(1)}$: $p_4 = Y_{23}Y_{31}Y_{12}$, $p_5 = Y_{32}Y_{13}Y_{21}$, and the 7 moduli ℓ_α^* . From algebraic manipulation of the resulting system, it can be seen that one such equation is satisfied trivially, and the remaining 8 equations may be cast in the following expedient manner:

$$\begin{aligned} \ell_1^*Y_{11} + \ell_4^*Y_{22} + \ell_5^*Y_{33} &= 2\hat{g}_I^{(1)}(Y_{11} + \bar{\lambda}_1) + \left[\hat{h}_J^{(1)} + \kappa^{(1)}(\hat{J}^{(1)} - 1) \right] \\ &\times ((Y_{22} + \bar{\lambda}_2)(Y_{33} + \bar{\lambda}_3) - p_3) - 2\bar{g}_I^{(1)}\bar{\lambda}_1 - \left(\bar{h}_J^{(1)} + \kappa^{(1)}(\bar{J} - 1) \right) \bar{\lambda}_2\bar{\lambda}_3, \\ \ell_4^*Y_{11} + \ell_2^*Y_{22} + \ell_6^*Y_{33} &= 2\hat{g}_I^{(1)}(Y_{22} + \bar{\lambda}_2) + \left[\hat{h}_J^{(1)} + \kappa^{(1)}(\hat{J}^{(1)} - 1) \right] \\ &\times ((Y_{11} + \bar{\lambda}_1)(Y_{33} + \bar{\lambda}_3) - p_2) - 2\bar{g}_I^{(1)}\bar{\lambda}_2 - \left(\bar{h}_J^{(1)} + \kappa^{(1)}(\bar{J} - 1) \right) \bar{\lambda}_1\bar{\lambda}_3, \\ \ell_5^*Y_{11} + \ell_6^*Y_{22} + \ell_3^*Y_{33} &= 2\hat{g}_I^{(1)}(Y_{33} + \bar{\lambda}_3) + \left[\hat{h}_J^{(1)} + \kappa^{(1)}(\hat{J}^{(1)} - 1) \right] \\ &\times ((Y_{11} + \bar{\lambda}_1)(Y_{22} + \bar{\lambda}_2) - p_1) - 2\bar{g}_I^{(1)}\bar{\lambda}_3 - \left(\bar{h}_J^{(1)} + \kappa^{(1)}(\bar{J} - 1) \right) \bar{\lambda}_1\bar{\lambda}_2, \\ L_{1221}^*p_1 &= \left[\hat{h}_J^{(1)} + \kappa^{(1)}(\hat{J}^{(1)} - 1) \right] (p_4 - p_1(Y_{33} + \bar{\lambda}_3)), \\ L_{1331}^*p_2 &= \left[\hat{h}_J^{(1)} + \kappa^{(1)}(\hat{J}^{(1)} - 1) \right] (p_4 - p_2(Y_{22} + \bar{\lambda}_2)), \\ L_{2332}^*p_3 &= \left[\hat{h}_J^{(1)} + \kappa^{(1)}(\hat{J}^{(1)} - 1) \right] (p_4 - p_3(Y_{11} + \bar{\lambda}_1)), \\ \ell_7^* &= 2\hat{g}_I^{(1)}, \end{aligned} \quad (8.10)$$

and

$$p_4 = p_5, \quad (8.11)$$

where $\bar{g}^{(1)} = g^{(1)}(\bar{I})$, $\bar{h}^{(1)} = h^{(1)}(\bar{J})$, $\hat{g}_I^{(1)} = g_I^{(1)}(\hat{I}^{(1)})$, $\hat{h}_J^{(1)} = h_J^{(1)}(\hat{J}^{(1)})$ have been introduced for ease of notation, with

$$\begin{aligned} \hat{I}^{(1)} = \hat{\mathbf{F}}^{(1)} \cdot \hat{\mathbf{F}}^{(1)} &= (\mathbf{Y} + \bar{\mathbf{D}}) \cdot (\mathbf{Y} + \bar{\mathbf{D}}) \\ &= (Y_{11} + \bar{\lambda}_1)^2 + (Y_{22} + \bar{\lambda}_2)^2 + (Y_{33} + \bar{\lambda}_3)^2 + s, \end{aligned} \quad (8.12)$$

$$\begin{aligned} \hat{J}^{(1)} = \det \hat{\mathbf{F}}^{(1)} &= \det(\mathbf{Y} + \bar{\mathbf{D}}) = (Y_{11} + \bar{\lambda}_1)(Y_{22} + \bar{\lambda}_2)(Y_{33} + \bar{\lambda}_3) \\ &- p_1(Y_{33} + \bar{\lambda}_3) - p_2(Y_{22} + \bar{\lambda}_2) - p_3(Y_{11} + \bar{\lambda}_1) + 2p_4. \end{aligned} \quad (8.13)$$

A direct implication of the fact that one of the generalized secant equations (2.65) is satisfied trivially is that the components of $\hat{\mathbf{F}}^{(1)}$ enter the above framework exclusively through 8—as opposed to 9—distinct combinations, namely: Y_{11} , Y_{22} , Y_{33} , p_1 , p_2 , p_3 , p_4 , and s . As described below, these are the only combinations needed in the computation of the second-order estimate (2.62) for \widehat{W} . Having clarified this point, we remark next that—by recalling the definitions $p_1 = Y_{12}Y_{21}$, $p_2 = Y_{13}Y_{31}$, $p_3 = Y_{23}Y_{32}$, $p_4 = Y_{23}Y_{31}Y_{12}$, and $p_5 = Y_{32}Y_{13}Y_{21}$ —equation (8.11) can be solved in closed form to render:

$$p_4 = \pm \sqrt{p_1 p_2 p_3}. \quad (8.14)$$

Now, each of the two roots in (8.14) can be substituted back in (8.10) to generate a system of 7 equations for the 7 moduli ℓ_α^* . Note that—since \mathbf{Y} depends directly on $\bar{\mathbf{F}}^{(2)}$ —the resulting equations depend directly on the variable $\bar{\mathbf{F}}^{(2)}$, which must be determined from equation (2.64), recalled here for convenience:

$$\bar{\mathbf{F}}^{(2)} = \bar{\mathbf{F}} + (1 - c_0)\mathbf{P} \left[\mathcal{S}^{(1)}(\bar{\mathbf{F}}) - \mathcal{S}^{(2)}(\bar{\mathbf{F}}^{(2)}) - \mathbf{L}^{(1)}(\bar{\mathbf{F}} - \bar{\mathbf{F}}^{(2)}) \right]. \quad (8.15)$$

In short, relations (8.10) and (8.15) are seen to constitute a closed system of (7+9=)16 scalar, coupled, algebraic equations for the 16 scalar unknowns formed by the 7 moduli ℓ_α^* and the 9 components of $\bar{\mathbf{F}}^{(2)}$. In general, these equations must be solved numerically.

Having computed from (8.10) and (8.15) the values of the 7 independent components of $\mathbf{L}^{(1)}$ (i.e., ℓ_α^*) and the 9 components of $\bar{\mathbf{F}}^{(2)}$ for a given loading, $\bar{\mathbf{F}}$, given matrix and fiber behavior, $g^{(r)}$, $h^{(r)}$, $\kappa^{(r)}$ ($r = 1, 2$), and given initial volume fraction of fibers, c_0 , the values of the components of $\bar{\mathbf{F}}^{(1)}$ and the relevant combinations of $\hat{\mathbf{F}}^{(1)}$ (i.e., Y_{11} , Y_{22} , Y_{33} , p_1 , p_2 , p_3 , s , p_4) may be readily determined using relations (2.60)₁, (8.8), (8.9), and (8.14). In turn, these results can be used

to compute the second-order estimate (2.62) for the effective stored-energy function \widehat{W} of fiber-reinforced elastomers. The final expression for \widehat{W} may be written as follows:

$$\begin{aligned} \widehat{W}(\overline{\mathbf{F}}) &= (1 - c_0) \left[g^{(1)}(\hat{I}^{(1)}) + h^{(1)}(\hat{J}^{(1)}) + \frac{\kappa^{(1)}}{2}(\hat{J}^{(1)} - 1)^2 \right] \\ &\quad + c_0 \left[g^{(2)}(\overline{I}^{(2)}) + h^{(2)}(\overline{J}^{(2)}) + \frac{\kappa^{(2)}}{2}(\overline{J}^{(2)} - 1)^2 \right] \\ &\quad - (1 - c_0) \mathcal{S}^{(1)}(\overline{\mathbf{D}}) \cdot \left(\mathbf{Y} + \overline{\mathbf{D}} - \overline{\mathbf{Q}}^T \overline{\mathbf{R}}^T \overline{\mathbf{F}}^{(1)} \overline{\mathbf{Q}} \right), \end{aligned} \quad (8.16)$$

where $\overline{I}^{(2)} = \overline{\mathbf{F}}^{(2)} \cdot \overline{\mathbf{F}}^{(2)}$ and $\overline{J}^{(2)} = \det \overline{\mathbf{F}}^{(2)}$ have been introduced for convenience.

We conclude this subsection by making the following three practical remarks. First, it is important to emphasize that the second-order estimate (8.16) can be shown to be *objective* and *orthotropic*, in accord with the appropriate *exact* result (2.12). Second, it should be noted that the effective stored-energy function (8.16) does indeed depend—as pointed out above—on the variable $\hat{\mathbf{F}}^{(1)}$ only through the 8 combinations Y_{11} , Y_{22} , Y_{33} , p_1 , p_2 , p_3 , p_4 , and s . Moreover, it is important to point out that there are 4 possible combinations of the roots introduced in (8.8) and (8.14), which lead to 4 different estimates for \widehat{W} . In the case when the bulk moduli (at zero strain) of the matrix and fibers, $\kappa^{(1)}$ and $\kappa^{(2)}$, are of the order of the shear moduli (at zero strain), $\mu^{(1)}$ and $\mu^{(2)}$, all 4 root combinations lead to very similar results for the effective stored-energy function \widehat{W} . However, when the bulk moduli are significantly larger than the shear moduli—namely, when the composite is nearly incompressible—the estimates produced by the 4 distinct combinations are very different. In fact, in this case, it can be shown that only 1 root combination generates physically meaningful estimates relative to the other 3 possibilities. More precisely, for $\kappa^{(r)} \gg \mu^{(s)}$ ($r, s = 1, 2$), the “negative” (–) root in (8.8), together with the choice $p_4 = \text{sign} \left((\overline{F}_{11}^{(1)*} - \overline{\lambda}_1)(\overline{F}_{22}^{(1)*} - \overline{\lambda}_2)(\overline{F}_{33}^{(1)*} - \overline{\lambda}_3) \right) \sqrt{p_1 p_2 p_3}$, where $\overline{\mathbf{F}}^{(1)*} = \overline{\mathbf{Q}}^T \overline{\mathbf{R}}^T \overline{\mathbf{F}}^{(1)} \overline{\mathbf{Q}}$, in (8.11) leads to estimates that are superior to the other 3 alternatives. Given that rubber-like materials are (in general) fairly incompressible, this is the root combination that should be selected to compute the second-order estimate (8.16) for fiber-reinforced elastomers.

Generalized plane-strain loading

The second-order estimate (8.16) is valid for general macroscopic deformations $\overline{\mathbf{F}}$. In the following section, we will be particularly interested in *generalized plane-strain* macroscopic deformations of the form:

$$\overline{\mathbf{F}} = \overline{F}_{11} \mathbf{e}_1 \otimes \mathbf{e}_1 + \overline{F}_{12} \mathbf{e}_1 \otimes \mathbf{e}_2 + \overline{F}_{21} \mathbf{e}_2 \otimes \mathbf{e}_1 + \overline{F}_{22} \mathbf{e}_2 \otimes \mathbf{e}_2 + \overline{\lambda}_3 \mathbf{e}_3 \otimes \mathbf{e}_3. \quad (8.17)$$

For this type of loading conditions, the computation of (8.16) simplifies substantially. More specifically, for macroscopic loadings of the form (8.17), it is easy to check that 5 out of the 9 scalar equations in (8.15) are satisfied identically by the choices:

$$\overline{F}_{33}^{(2)} = \overline{\lambda}_3 \quad \text{and} \quad \overline{F}_{13}^{(2)} = \overline{F}_{31}^{(2)} = \overline{F}_{23}^{(2)} = \overline{F}_{32}^{(2)} = 0, \quad (8.18)$$

while the remaining 4 equations for the 4 in-plane components $\overline{F}_{11}^{(2)}, \overline{F}_{22}^{(2)}, \overline{F}_{12}^{(2)}, \overline{F}_{21}^{(2)}$ are given by:

$$\overline{F}_{\Sigma\Theta}^{(2)} = \overline{F}_{\Sigma\Theta} + (1 - c_0)P_{\Sigma\Theta\Gamma\Delta} \left[\mathcal{S}_{\Gamma\Delta}^{(1)}(\overline{\mathbf{F}}) - \mathcal{S}_{\Gamma\Delta}^{(2)}(\overline{\mathbf{F}}^{(2)}) - L_{\Gamma\Delta\Upsilon\Lambda}^{(1)}(\overline{F}_{\Upsilon\Lambda} - \overline{F}_{\Upsilon\Lambda}^{(2)}) \right]. \quad (8.19)$$

Here, capital Greek indices range from 1 to 2, and it is important to note, for later use, that equations (8.19) depend on \mathbf{L}^* only through the moduli $\ell_1^*, \ell_2^*, \ell_4^*$, and ℓ_7^* .

Next, under conditions (8.17), $k_3 = k_5 = k_6 = 0$ in (8.7), so that expressions (8.8), (8.9), and (8.14) reduce to:

$$Y_{11} = \pm \frac{k_1 + 2f_1k_4}{\sqrt{k_1 + 4f_1(f_1k_2 + k_4)}}, \quad Y_{22} = \pm \frac{2f_1k_2 + k_4}{\sqrt{k_1 + 4f_1(f_1k_2 + k_4)}}, \quad Y_{33} = 0, \quad (8.20)$$

and

$$p_1 = Y_{11}Y_{22} - k_4/2, \quad s = k_7 - 2f_4p_1, \quad p_2 = p_3 = p_4 = 0. \quad (8.21)$$

Note that—similar to equations (8.19)—expressions (8.20) and (8.21) also depend on \mathbf{L}^* only through the moduli $\ell_1^*, \ell_2^*, \ell_4^*$, and ℓ_7^* .

Finally, making use of the above simplifications, it is straightforward to see that 2 out of the 7 scalar equations in (8.10) are satisfied trivially, while the remaining 5 nontrivial equations reduce to:

$$\begin{aligned} \ell_1^*Y_{11} + \ell_4^*Y_{22} &= 2\hat{g}_I^{(1)}(Y_{11} + \overline{\lambda}_1) + \left[\hat{h}_J^{(1)} + \kappa^{(1)}(\hat{J}^{(1)} - 1) \right] (Y_{22} + \overline{\lambda}_2)\overline{\lambda}_3 \\ &\quad - 2\overline{g}_I^{(1)}\overline{\lambda}_1 - \left[\overline{h}_J^{(1)} + \kappa^{(1)}(\overline{J} - 1) \right] \overline{\lambda}_2\overline{\lambda}_3, \\ \ell_4^*Y_{11} + \ell_2^*Y_{22} &= 2\hat{g}_I^{(1)}(Y_{22} + \overline{\lambda}_2) + \left[\hat{h}_J^{(1)} + \kappa^{(1)}(\hat{J}^{(1)} - 1) \right] (Y_{11} + \overline{\lambda}_1)\overline{\lambda}_3 \\ &\quad - 2\overline{g}_I^{(1)}\overline{\lambda}_2 - \left[\overline{h}_J^{(1)} + \kappa^{(1)}(\overline{J} - 1) \right] \overline{\lambda}_1\overline{\lambda}_3, \\ L_{1221}^* &= - \left[\hat{h}_J^{(1)} + \kappa^{(1)}(\hat{J}^{(1)} - 1) \right] \overline{\lambda}_3, \\ \ell_7^* &= 2\hat{g}_I^{(1)}, \end{aligned} \quad (8.22)$$

and

$$\begin{aligned} \ell_5^*Y_{11} + \ell_6^*Y_{22} &= 2\hat{g}_I^{(1)}\overline{\lambda}_3 + \left[\hat{h}_J^{(1)} + \kappa^{(1)}(\hat{J}^{(1)} - 1) \right] \\ &\times ((Y_{11} + \overline{\lambda}_1)(Y_{22} + \overline{\lambda}_2) - p_1) - 2\overline{g}_I^{(1)}\overline{\lambda}_3 - \left(\overline{h}_J^{(1)} + \kappa^{(1)}(\overline{J} - 1) \right) \overline{\lambda}_1\overline{\lambda}_2. \end{aligned} \quad (8.23)$$

To summarize, relations (8.19) and (8.22) constitute a *closed* system of 8 coupled, algebraic equations for the 4 in-plane components $\overline{F}_{11}^{(2)}, \overline{F}_{22}^{(2)}, \overline{F}_{12}^{(2)}, \overline{F}_{21}^{(2)}$ and the 4 moduli $\ell_1^*, \ell_2^*, \ell_4^*$, and ℓ_7^* . Knowledge of these variables, together with the explicit relations (8.18), (8.20), (8.21), suffices to compute the second-order estimate (8.16) for \widehat{W} for generalized plane-strain deformations (8.17). As a final remark, it is interesting to note that equation (8.23), which establishes a connection between the moduli ℓ_5^*, ℓ_6^* and the in-plane variables $\overline{F}_{11}^{(2)}, \overline{F}_{22}^{(2)}, \overline{F}_{12}^{(2)}, \overline{F}_{21}^{(2)}, \ell_1^*, \ell_2^*, \ell_4^*$, and ℓ_7^* , does not intervene in the computation of \widehat{W} .

8.2 Results and discussion

In this section, the second-order estimate (8.16) is used to study the effective stress-strain response and the macroscopic stability of Gent elastomers reinforced with monodisperse, initially circular, cylindrical Gent fibers aligned in the \mathbf{e}_3 axis and distributed periodically with square (*SA*) and hexagonal (*HA*) arrangements in the \mathbf{e}_1 – \mathbf{e}_2 plane in the undeformed configuration (see Fig. 8.1). Results are given for compressible Gent (matrix and fiber) phases with lock-up parameters $J_m^{(1)} = J_m^{(2)} = J_m = 100$, and are computed up to the point at which either the effective incremental modulus, $\widehat{\mathcal{L}} = \partial^2 \widehat{W} / \partial \overline{\mathbf{F}}^2$, is found to lose strong ellipticity—according to condition (2.89)—or fiber contact is detected (see Section 2.5.1 for details on the estimation of fiber-contact within the HS-type approximation (2.55) for the LCC). If neither of these phenomena occurs, the results are truncated at some sufficiently large value of the deformation. For clarity, the points at which the homogenized material loses strong ellipticity are denoted with the symbol “o” in the figures, whereas the symbol “•” is utilized to indicate contact between fibers.

The results presented in this section are organized as follows. First, we present and discuss the response of fiber-reinforced elastomers subjected to *axisymmetric shear*. These results are followed by the effective response of fiber-reinforced elastomers subjected to *in-plane pure* and *simple shear*. We finish this section by providing results for *out-of-plane pure shear*. The motivation behind the selection of these results is to provide an overall understanding of the effective response of fiber-reinforced elastomers under out-of-plane, in-plane, and coupled in-plane and out-of-plane modes of deformation, while illustrating the intimate connection between the effective behavior and macroscopic stability of these materials with the evolution of the underlying microstructure.

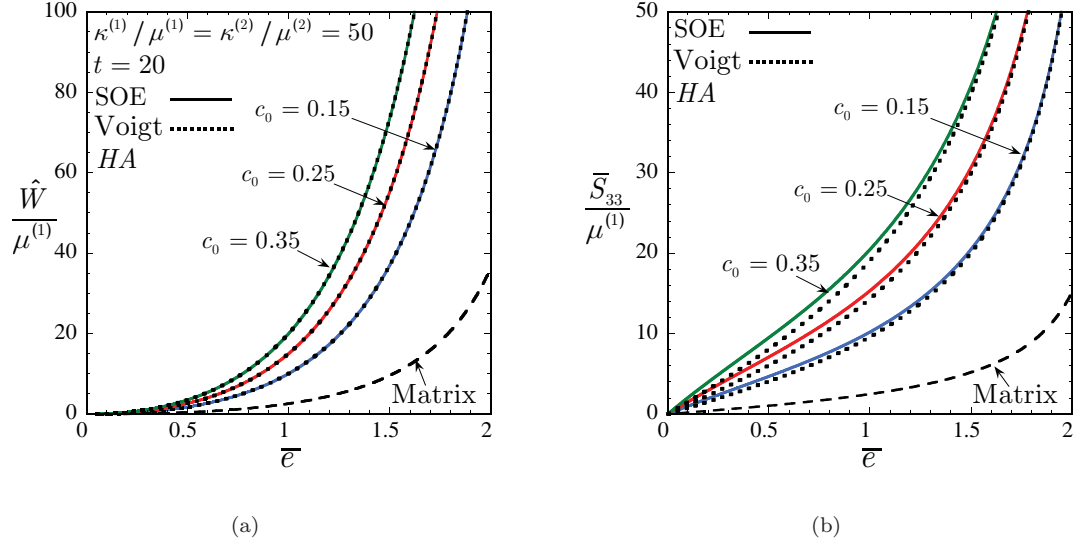


Figure 8.2: Effective response, as predicted by the second-order estimate (SOE) and the Voigt bound, of a fiber-reinforced elastomer subjected to “tensile” axisymmetric shear: $\bar{\mathbf{F}} = \bar{\lambda}_1 \mathbf{e}_1 \otimes \mathbf{e}_1 + \bar{\lambda}_2 \mathbf{e}_2 \otimes \mathbf{e}_2 + \bar{\lambda}_3 \mathbf{e}_3 \otimes \mathbf{e}_3$ with $\bar{\lambda}_3 = \bar{\lambda} \geq 1$ and $\bar{\lambda}_1 = \bar{\lambda}_2 = \bar{\lambda}^{-1/2}$. The results correspond to Gent phases with compressibility ratios $\kappa^{(1)}/\mu^{(1)} = \kappa^{(2)}/\mu^{(2)} = 50$, contrast $t = \mu^{(2)}/\mu^{(1)} = 20$, and various values of initial volume fraction of fibers c_0 , and are shown as a function of the logarithmic strain $\bar{e} = \ln \bar{\lambda}$. (a) The normalized effective stored-energy function $\widehat{W}/\mu^{(1)}$. (b) The normalized stress component $\bar{S}_{33}/\mu^{(1)} = (1/\mu^{(1)})\partial\widehat{W}/\partial\bar{F}_{33}$.

8.2.1 Axisymmetric shear

Figures 8.2 and 8.3 present the effective behavior, as predicted by the second-order estimate (8.16) (denoted by SOE in the plots) and the Voigt bound (8.3), for a compressible Gent matrix reinforced with an initially periodic hexagonal distribution (HA) of Gent fibers under axisymmetric shear deformation: $\bar{\mathbf{F}} = \bar{\lambda}_1 \mathbf{e}_1 \otimes \mathbf{e}_1 + \bar{\lambda}_2 \mathbf{e}_2 \otimes \mathbf{e}_2 + \bar{\lambda}_3 \mathbf{e}_3 \otimes \mathbf{e}_3$ with $\bar{\lambda}_3 = \bar{\lambda}$ and $\bar{\lambda}_1 = \bar{\lambda}_2 = \bar{\lambda}^{-1/2}$. Fig. 8.2 illustrates results for tension in the fiber direction (i.e., $\bar{\lambda} \geq 1$) and Fig. 8.3, for compression (i.e., $\bar{\lambda} \leq 1$). In particular, results are shown for compressibility ratios $\kappa^{(1)}/\mu^{(1)} = \kappa^{(2)}/\mu^{(2)} = 50$, shear contrast $t = \mu^{(2)}/\mu^{(1)} = 20$, and initial volume fractions of fibers $c_0 = 15, 25$ and 35%, as a function of the logarithmic strain $\bar{e} = \ln \bar{\lambda}$. Parts (a) show the normalized effective stored-energy function $\widehat{W}/\mu^{(1)}$, and parts (b), the normalized stress in the fiber direction $\bar{S}_{33}/\mu^{(1)} = (1/\mu^{(1)})\partial\widehat{W}/\partial\bar{F}_{33}$.

It is observed from both figures, Figs. 8.2 and 8.3, that the effective behavior of the fiber-reinforced elastomer is stiffer for higher values of the initial volume fraction of fibers c_0 , as expected on physical grounds. In this connection, note that the behavior of the composite (i.e., $c_0 > 0$) is much stiffer than that of the matrix material (i.e., $c_0 = 0$). Moreover, it is interesting to remark

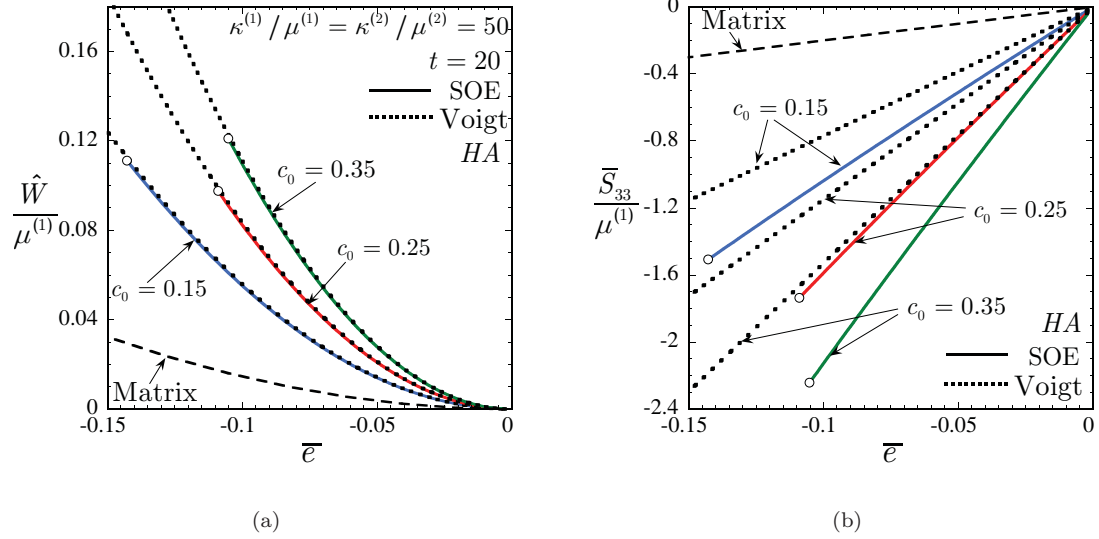


Figure 8.3: Effective response of a fiber-reinforced elastomer subjected to “compressive” axisymmetric shear: $\bar{\mathbf{F}} = \bar{\lambda}_1 \mathbf{e}_1 \otimes \mathbf{e}_1 + \bar{\lambda}_2 \mathbf{e}_2 \otimes \mathbf{e}_2 + \bar{\lambda}_3 \mathbf{e}_3 \otimes \mathbf{e}_3$ with $\bar{\lambda}_3 = \bar{\lambda} \leq 1$ and $\bar{\lambda}_1 = \bar{\lambda}_2 = \bar{\lambda}^{-1/2}$. The results correspond to Gent phases with compressibility ratios $\kappa^{(1)}/\mu^{(1)} = \kappa^{(2)}/\mu^{(2)} = 50$, contrast $t = \mu^{(2)}/\mu^{(1)} = 20$, and various values of initial volume fraction of fibers c_0 , and are shown as a function of the logarithmic strain $\bar{e} = \ln \bar{\lambda}$. (a) The normalized effective stored-energy function $\widehat{W}/\mu^{(1)}$. (b) The normalized stress component $\bar{S}_{33}/\mu^{(1)} = (1/\mu^{(1)})\partial\widehat{W}/\partial\bar{F}_{33}$.

from Figs. 8.2(a) and 8.3(a) that the second-order estimates—though strictly below—are practically indistinguishable from the Voigt bound. In this regard, it is fitting to recall that for the case of *applied* axisymmetric shear of fiber-reinforced elastomers with *incompressible, isotropic* matrix phase and *incompressible, isotropic* fibers, the Voigt bound can be shown to be an *exact* result for the effective stored-energy function \widehat{W} , regardless of the shape, orientation, and distribution of the fibers in the transverse plane (e.g., here, the \mathbf{e}_1 – \mathbf{e}_2 plane). In view of the relatively high values of the bulk moduli of the matrix phase, $\kappa^{(1)}/\mu^{(1)} = 50$, and the fibers, $\kappa^{(2)}/\mu^{(1)} = 1000$, this suggests that the Voigt bound—and hence the second-order estimates—shown in Figs. 8.2(a) and 8.3(a) are actually very good approximations to the corresponding exact results. Parenthetically, it is also appropriate to record here that, under axisymmetric shear (and only in this case), the second-order estimate (8.16) can be shown to reduce to the Voigt bound (8.3) in the limit of overall incompressibility of the material (i.e., $\kappa^{(1)} \rightarrow \infty$ and $\kappa^{(2)} \rightarrow \infty$), thus recovering the exact result. Next, it is recognized from Figs. 8.2 and 8.3 that—according to the SOE results—the overall response of the fiber-reinforced elastomer under axisymmetric tension is radically different from its response

under axisymmetric compression. Indeed, under axisymmetric tension, the material stiffens until it eventually locks up at an approximate strain of $\bar{\epsilon} = 2.3$ (irrespective of the initial volume fraction of fibers c_0). On the other hand, under axisymmetric compression, the material stiffens monotonically, but it also becomes unstable—through loss of strong ellipticity—at relatively small values of strain. More specifically, all the results shown in Fig. 8.3 lose strong ellipticity because of the vanishing of the effective incremental shear moduli $\widehat{\mathcal{L}}_{1313}$ and $\widehat{\mathcal{L}}_{2323}$. This implies that the homogenized material may develop *localized shear deformations* in planar zones with normal—in the deformed configuration— $\mathbf{n} = \mathbf{e}_3$, and in the directions $\mathbf{m} \in \text{Span}\{\mathbf{e}_1, \mathbf{e}_2\}$. This response is rather subtle and merits further explanation. When subjected to axisymmetric compression, as shown by Fig. 8.3(b), the fiber-reinforced elastomer *stiffens*—due to the constitutive stiffening of the matrix phase and the fibers—in the “direction” of the applied loading (i.e., $\widehat{\mathcal{L}}_{3333}$ increases with the applied stretch). However, its overall incremental shear response (perpendicular to the direction of the fibers) *softens* to the point that the material loses strong ellipticity at some finite stretch (at which $\widehat{\mathcal{L}}_{1313} = \widehat{\mathcal{L}}_{2323} = 0$). This remarkable behavior predicted by the second-order estimate (and *not* by the Voigt bound, as explained in more detail below) is in agreement with experimental evidence (see, for instance, Hsu *et al.*, 1998), where the observed failure mode in fiber-reinforced composites subjected to compressive deformation in the fiber direction leads to kink band type instabilities.

We conclude the discussion of Figs. 8.2 and 8.3 by making the following two remarks. First, it is important to note that in spite of being a very good estimate for the effective stored-energy function \widehat{W} of fiber-reinforced elastomers subjected to axisymmetric shear (provided that the bulk moduli of the matrix phase, $\kappa^{(1)}$, and the fibers, $\kappa^{(2)}$, are sufficiently large), the Voigt bound remains strongly elliptic *for all* applied deformations, in disagreement with physical evidence (and with the second-order predictions). This can be readily checked by realizing that the Voigt bound (8.3), which is essentially the arithmetic average of the local behavior of the matrix phase and the fibers, is a strictly polyconvex function of the applied deformation gradient $\overline{\mathbf{F}}$ and hence strongly elliptic, as already pointed out in Section 8.1.1. Second, the corresponding stress-strain results for a *periodic square* distribution of fibers are essentially identical to those illustrated in Figs. 8.2 and 8.3 for the periodic hexagonal distribution. This is to be expected since the Voigt bound for \widehat{W} , which agrees with the second-order estimates in the context of Figs. 8.2 and 8.3, is a *microstructure independent* result (i.e., it only depends on the volume fraction of the phases).

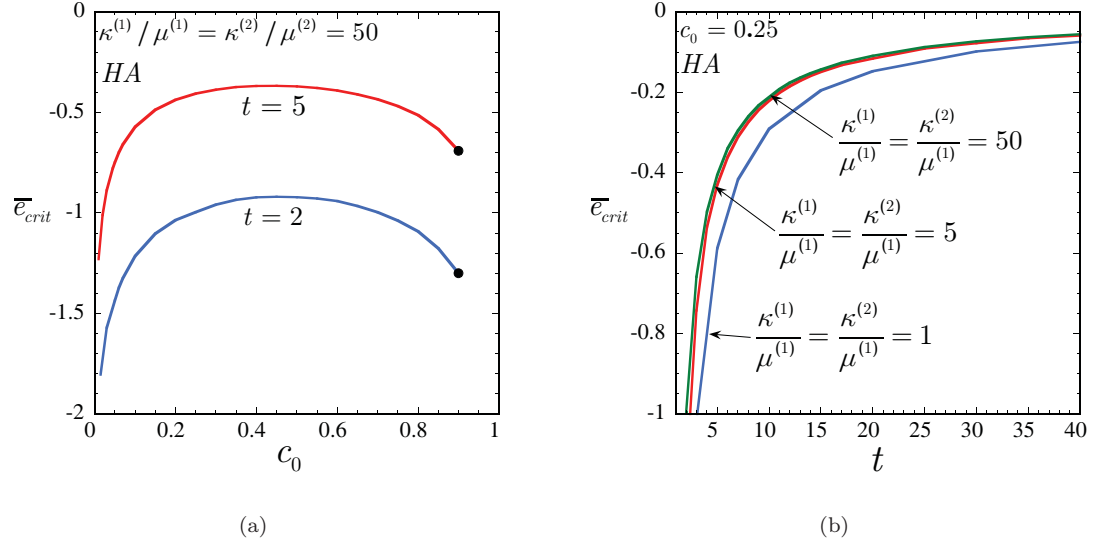


Figure 8.4: Axisymmetric shear ($\bar{\mathbf{F}} = \bar{\lambda}^{-1/2} \mathbf{e}_1 \otimes \mathbf{e}_1 + \bar{\lambda}^{-1/2} \mathbf{e}_2 \otimes \mathbf{e}_2 + \bar{\lambda} \mathbf{e}_3 \otimes \mathbf{e}_3$) of a Gent elastomer reinforced with aligned, cylindrical Gent fibers distributed periodically in a hexagonal arrangement (HA). (a) The critical strain $\bar{\epsilon}_{crit} = \ln \bar{\lambda}_{crit}$ at which the homogenized fiber-reinforced elastomer loses strong ellipticity for two values of the contrast $t = \mu^{(2)}/\mu^{(1)}$, as a function of the initial volume fraction of fibers c_0 . (b) The critical strain $\bar{\epsilon}_{crit}$ for various values of the compressibility ratios $\kappa^{(1)}/\mu^{(1)} = \kappa^{(2)}/\mu^{(1)}$, as a function of the contrast t .

Figure 8.4 provides plots associated with the results shown in Fig. 8.3 for the critical strain, $\bar{\epsilon}_{crit} = \ln \bar{\lambda}_{crit}$, at which the homogenized response of the fiber-reinforced elastomer loses strong ellipticity for: (a) contrasts $t = \mu^{(2)}/\mu^{(1)} = 2$ and 5, and compressibility ratios $\kappa^{(1)}/\mu^{(1)} = \kappa^{(2)}/\mu^{(2)} = 50$, as a function of the initial volume fraction of fibers c_0 ; and (b) compressibility ratios $\kappa^{(1)}/\mu^{(1)} = \kappa^{(2)}/\mu^{(1)} = 1, 5$, and 50, and fiber volume fraction $c_0 = 25\%$, as a function of the contrast t . A key observation that should be made from Fig. 8.4 is that, under axisymmetric shear compression, the fiber-reinforced elastomer becomes unstable at smaller compressive strains $\bar{\epsilon}_{crit}$ for higher values of the contrast t . In fact, it can be shown that $\bar{\epsilon}_{crit} \rightarrow 0$ as $t \rightarrow \infty$. That is, for the case when the fibers are taken to be rigid (i.e., for $t = \infty$), the fiber-reinforced elastomer is already unstable at zero strain when subjected to axisymmetric shear compression. Of course, an elastomer reinforced with rigid fibers is itself rigid under loading conditions that require deformation of the fibers. The issue here is that in spite of being rigid (in the principal solution), the material is actually unstable when subjected to axisymmetric shear compression along the fiber direction.

Figure 8.4(a) shows that $\bar{\epsilon}_{crit} \rightarrow -\infty$ as $c_0 \rightarrow 0$. This is consistent with the fact that the elastomeric matrix phase of the material is strongly elliptic, so that in the absence of fibers (i.e.,

for $c_0 = 0$) the material remains stable for all deformations. As the initial volume fraction of fibers c_0 is increased from zero, the critical strain at which the material loses strong ellipticity \bar{e}_{crit} increases monotonically up to a certain $c_0 < 50\%$ at which \bar{e}_{crit} reaches a maximum. After this point, further increase in c_0 results in a monotonic decrease of \bar{e}_{crit} . This behavior can be easily explained by recognizing that the fibers are strongly elliptic, so that in the limit as $c_0 \rightarrow 1$, \bar{e}_{crit} is expected to become unbounded. Note, however, that the limiting value $c_0 = 1$ cannot be actually reached, since for the periodic hexagonal distribution of fibers under consideration here, fiber contact takes place (in the undeformed configuration) at $c_0 = \pi/(2\sqrt{3}) \approx 91\%$, as indicated in Fig. 8.4(a) by the symbol “•.” Finally, it is interesting to note that the inverted “U-shape” of the loss of strong ellipticity curves shown in Fig. 8.4(a) is reminiscent of the corresponding *exact* result for two-phase laminates (Triantafyllidis and Maker, 1985), which have been considered by various authors as 2D models for fiber-reinforced materials (see, e.g., Triantafyllidis and Maker, 1985, and Kyriakides et al., 1995).

Figure 8.4(b) shows that the homogenized response of the fiber-reinforced elastomer loses strong ellipticity at smaller critical strains \bar{e}_{crit} for higher values of the bulk moduli of the elastomeric matrix phase, $\kappa^{(1)}$, and of the fibers, $\kappa^{(2)}$. That is, in strain space, the less compressible the more unstable the material is. Interestingly, this trend has also been observed in other material systems (see, e.g., Triantafyllidis *et al.*, 2006; Lopez-Pamies and Ponte Castañeda, 2006b; Michel *et al.*, 2007).

Finally, it is fitting to mention that the corresponding results for a periodic square distribution of fibers are essentially identical to those illustrated in Fig. 8.4 for the periodic hexagonal distribution, with the exception that the onset of fiber contact in Fig. 8.4(a) would then take place at $c_0 = \pi/4 \approx 79\%$, as opposed to $c_0 = \pi/(2\sqrt{3}) \approx 91\%$. This result, together with the observations made from Figs. 8.2 and 8.3, suggest that not only the overall stress-strain relation, but also the macroscopic stability of fiber-reinforced elastomers subjected to axisymmetric shear are controlled mainly by the *contrast* between the elastomeric matrix phase and the fibers and their respective *volume fractions*, and *not* so much by the in-plane fiber distribution.

8.2.2 In-plane pure shear

Figure 8.5 provides plots for the effective behavior of Gent elastomers reinforced with periodic square (*SA*) and hexagonal (*HA*) distributions of Gent fibers for in-plane pure shear loading. More

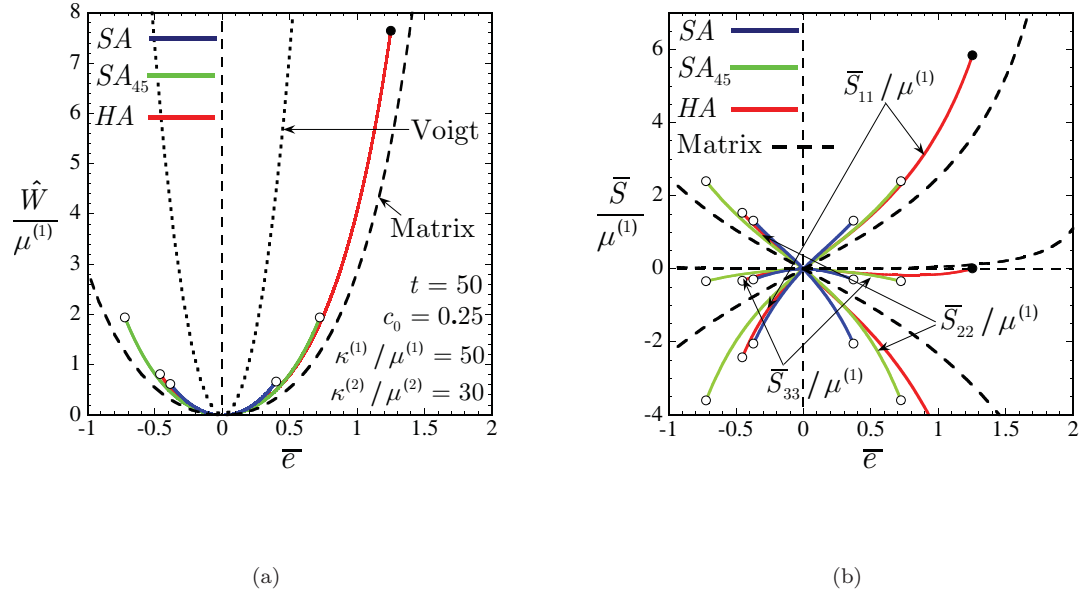


Figure 8.5: In-plane pure shear (aligned $\bar{\mathbf{F}} = \bar{\lambda} \mathbf{e}_1 \otimes \mathbf{e}_1 + \bar{\lambda}^{-1} \mathbf{e}_2 \otimes \mathbf{e}_2 + \mathbf{e}_3 \otimes \mathbf{e}_3$ and at a 45° angle $\bar{\mathbf{F}} = (\bar{\lambda} + \bar{\lambda}^{-1})/2(\mathbf{e}_1 \otimes \mathbf{e}_1 + \mathbf{e}_2 \otimes \mathbf{e}_2) + (\bar{\lambda} - \bar{\lambda}^{-1})/2(\mathbf{e}_1 \otimes \mathbf{e}_2 + \mathbf{e}_2 \otimes \mathbf{e}_1) + \mathbf{e}_3 \otimes \mathbf{e}_3$) of a fiber-reinforced elastomer. The results, which are given for periodic square (SA and SA₄₅) and hexagonal (HA) arrangement of fibers, correspond to Gent phases with compressibility ratios $\kappa^{(1)}/\mu^{(1)} = 50$ and $\kappa^{(2)}/\mu^{(2)} = 30$, contrast $t = \mu^{(2)}/\mu^{(1)} = 50$, and fiber volume fraction $c_0 = 25\%$, and are shown as a function of the logarithmic strain $\bar{e} = \ln \bar{\lambda}$. (a) The normalized effective stored-energy function $\widehat{W}/\mu^{(1)}$. (b) The normalized stress components $\bar{S}_{11}/\mu^{(1)}$, $\bar{S}_{22}/\mu^{(1)}$, $\bar{S}_{33}/\mu^{(1)}$ written with respect to the macroscopic Lagrangian principal axes.

specifically, for both distributions, results are presented for pure shear loading aligned with the principal axes of the microstructure $\{\mathbf{e}_i\}$ (later referred to as pure shear in the $[1,0,0]$ direction): $\bar{\mathbf{F}} = \bar{\lambda}_1 \mathbf{e}_1 \otimes \mathbf{e}_1 + \bar{\lambda}_2 \mathbf{e}_2 \otimes \mathbf{e}_2 + \bar{\lambda}_3 \mathbf{e}_3 \otimes \mathbf{e}_3$ with $\bar{\lambda}_1 = \bar{\lambda}$, $\bar{\lambda}_2 = \bar{\lambda}^{-1}$, and $\bar{\lambda}_3 = 1$ (see Fig. 8.1). For the SA distribution, results are also presented for pure shear loading oriented at 45° with respect to $\{\mathbf{e}_i\}$ (later referred to as pure shear in the $[1,1,0]$ direction): $\bar{\mathbf{F}} = (\bar{\lambda} + \bar{\lambda}^{-1})/2(\mathbf{e}_1 \otimes \mathbf{e}_1 + \mathbf{e}_2 \otimes \mathbf{e}_2) + (\bar{\lambda} - \bar{\lambda}^{-1})/2(\mathbf{e}_1 \otimes \mathbf{e}_2 + \mathbf{e}_2 \otimes \mathbf{e}_1) + \mathbf{e}_3 \otimes \mathbf{e}_3$ (see Fig. 8.1). (Note that this last loading is denoted by SA₄₅ in the plots.) Results are given for compressibility ratios $\kappa^{(1)}/\mu^{(1)} = 50$ and $\kappa^{(2)}/\mu^{(2)} = 30$, contrast $t = \mu^{(2)}/\mu^{(1)} = 50$, and fiber volume fraction $c_0 = 25\%$, as function of the logarithmic strain $\bar{e} = \ln \bar{\lambda}$. Part (a) shows the normalized effective stored-energy function $\widehat{W}/\mu^{(1)}$ and part (b), the normalized non-zero stress components $\bar{S}_{11}/\mu^{(1)}$, $\bar{S}_{22}/\mu^{(1)}$, $\bar{S}_{33}/\mu^{(1)}$ written with respect to the macroscopic Lagrangian principal axes—denoted here by $\{\mathbf{u}_i\}$. In this connection, note that for pure shear loading in the $[1,0,0]$ direction: $\mathbf{u}_i = \mathbf{e}_i$ ($i = 1, 2, 3$); while for pure shear loading in the $[1,1,0]$ direction: $\mathbf{u}_1 = \sqrt{2}/2(\mathbf{e}_1 + \mathbf{e}_2)$, $\mathbf{u}_2 = \sqrt{2}/2(\mathbf{e}_2 - \mathbf{e}_1)$, $\mathbf{u}_3 = \mathbf{e}_3$.

First, we remark from Fig. 8.5(a) that the second-order estimates are well below the rigorous Voigt upper bound. This result is consistent with the fact that, under the in-plane loading conditions considered in Fig. 8.5, the Voigt bound—unlike the second-order estimates and in contradiction with physical evidence—becomes infinite as the fibers tend to become rigid. The fibers considered in Fig. 8.5 are not exactly rigid, but the relatively high contrast of $t = 50$ between the matrix phase and the fibers already reveals the asymptotic character of the Voigt bound as $t \rightarrow \infty$. Fig. 8.5(a) also shows that the effective behavior of the fiber-reinforced material is stiffer than that of the matrix phase, as expected on physical grounds. Another important observation from Fig. 8.5(a) is the overall anisotropic response of the composite, which is entirely due to the anisotropic initial arrangement of the fibers. More precisely, the overall behavior of the reinforced elastomer with the square arrangement of fibers (see Fig. 8.1(a)) is seen to be different for pure shear loading in the $[1,0,0]$ direction (SA) than in the direction $[1,1,0]$ (SA_{45}). In particular, the $[1,0,0]$ results appear to be stiffer. This interesting behavior will be explained below, within the context of Fig. 8.5(b). Furthermore, as a consequence of the overall, in-plane, square symmetry of the material, we also note that the results for tension (i.e., for $\bar{\epsilon} \geq 0$) are indistinguishable from those for compression (i.e., for $\bar{\epsilon} \leq 0$). In contrast, for the hexagonal arrangement (HA) of fibers (see Fig. 8.1(b)), the effective behavior of the reinforced elastomer is different for tension ($\bar{\epsilon} \geq 0$) than for compression ($\bar{\epsilon} \leq 0$).

Before proceeding with the discussion of the stress-strain results illustrated in Fig. 8.5(b), it proves helpful to make the following remark. Under the present in-plane loading conditions, the two major underlying mechanisms governing the overall response of the fiber-reinforced elastomers are: the *constitutive stiffening/softening* of the matrix phase with increasing strain, and the *geometric stiffening/softening* effects due to the evolution of the *distribution* of the fibers. The constitutive and geometric effects due to the straining and the evolution of the volume fraction, shape, and orientation of the fibers are negligible. This is because the fibers—which are 50 times stiffer than the matrix phase—remain essentially undeformed along the entire deformation process.

For tensile loadings ($\bar{\epsilon} \geq 0$), Fig. 8.5(b) illustrates that for all three cases, SA , SA_{45} , and HA , the in-plane stress component $\bar{S}_{11}/\mu^{(1)}$ increases monotonically with increasing strain. The other in-plane stress component, $\bar{S}_{22}/\mu^{(1)}$, is seen to decrease monotonically with increasing $\bar{\epsilon}$, but at a much more rapid rate than $\bar{S}_{11}/\mu^{(1)}$. This disparity is consistent with the fact that, in the direction of the Lagrangian principal axis \mathbf{u}_1 —in which tension is applied—the fibers get farther apart as

the deformation progresses, whereas in the direction of the Lagrangian principal axis \mathbf{u}_2 —in which compression is applied—they get closer. The former mechanism induces *geometric* softening on the material and the latter, stiffening. Note that this mechanism is also consistent with the fact that the *SA* results are stiffer than the *SA*₄₅ ones, since at any given value of the applied strain $\bar{\epsilon}$, the fibers are closer to one another in the $[1, 0, 0]$ direction than in the direction $[1, 1, 0]$. In addition, it is interesting to note from Fig. 8.5(b) that a considerably large—but smaller than $\bar{S}_{22}/\mu^{(1)}$ —compressive stress $\bar{S}_{33}/\mu^{(1)}$ develops in the fiber direction as the strain increases. Note that analogous comments apply to the results for compressive loading ($\bar{\epsilon} \leq 0$).

Finally, we remark from Fig. 8.5 that the material with the square arrangement of fibers becomes unstable—through loss of strong ellipticity—under both types of pure shear conditions (*SA* and *SA*₄₅), with the *SA* results losing strong ellipticity at smaller strains. On the other hand, the material with the hexagonal distribution of fibers is seen to lose strong ellipticity only under compression ($\bar{\epsilon} \leq 0$), whereas fiber contact is detected under tension ($\bar{\epsilon} \geq 0$) before any macroscopic instability takes place. Interestingly, for all the above-mentioned cases in which macroscopic instabilities do develop, strong ellipticity is consistently lost due to the vanishing of the incremental shear response perpendicular to the direction of maximum applied compressive strain. For instance, for the *SA* and *HA* cases with $\bar{\epsilon} \leq 0$, strong ellipticity is lost due to the vanishing of $\widehat{\mathcal{L}}_{2121}$, while for the *SA* case with $\bar{\epsilon} \geq 0$, strong ellipticity is lost due to the vanishing of $\widehat{\mathcal{L}}_{1212}$. This means that, under in-plane pure shear loading, the homogenized fiber-reinforced elastomer may develop *localized shear* deformations in planar zones with normal in the deformed configuration \mathbf{n} , given by the macroscopic Lagrangian principal axis associated with the smallest principal stretch (i.e., the maximum compressive strain), and in the in-plane direction perpendicular to such axis. Making contact now with the microstructure, it is interesting to note that the normal \mathbf{n} corresponds actually to the in-plane direction in which neighboring fibers are closest. This behavior, which is somewhat similar to the one observed for axisymmetric compression, is rather subtle. Indeed, when subjected to in-plane pure shear loading, the overall response of the fiber-reinforced elastomer *stiffens*—as a consequence, partly, of the reinforcing fibers coming closer—in the direction of the maximum applied compressive strain, \mathbf{n} . However, its overall incremental shear response perpendicular to \mathbf{n} *softens* to the point that the material may become macroscopically unstable at some finite stretch. To conclude the discussion of Fig. 8.5, it should be mentioned that this remarkable behavior predicted by the second-order estimate (8.16) is in agreement with

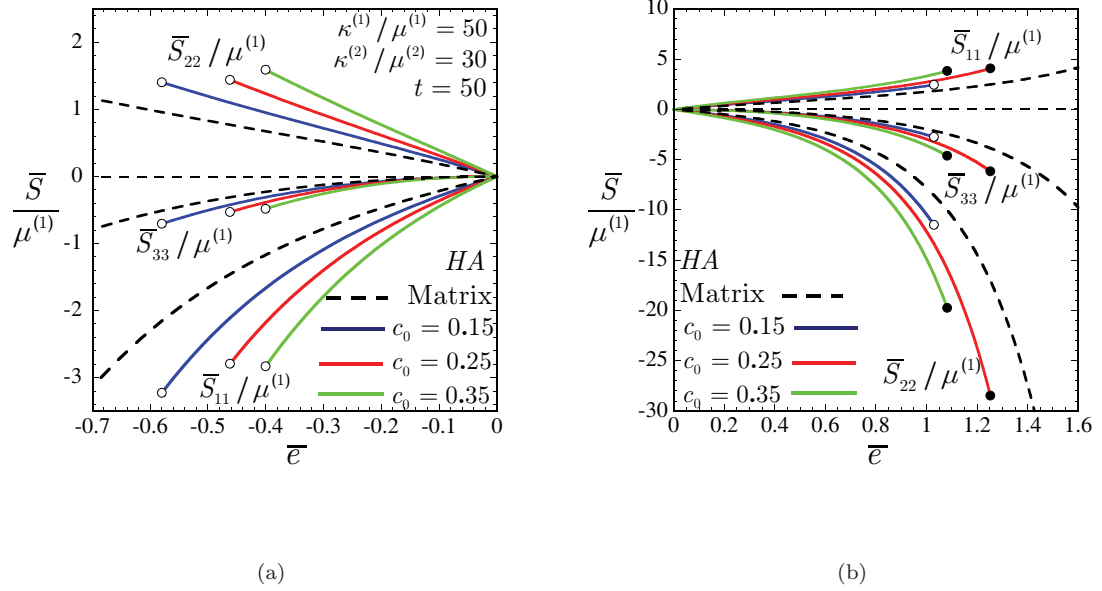


Figure 8.6: In-plane aligned pure shear ($\bar{\mathbf{F}} = \bar{\lambda} \mathbf{e}_1 \otimes \mathbf{e}_1 + \bar{\lambda}^{-1} \mathbf{e}_2 \otimes \mathbf{e}_2 + \mathbf{e}_3 \otimes \mathbf{e}_3$) of a fiber-reinforced Gent elastomer with an initially hexagonal arrangement (HA) of fibers. The results correspond to compressibility ratios $\kappa^{(1)}/\mu^{(1)} = 50$, $\kappa^{(2)}/\mu^{(2)} = 30$, contrast $t = \mu^{(2)}/\mu^{(1)} = 50$, and initial volume fractions $c_0 = 15, 25$ and 35%. The normalized stress components $\bar{S}_{11}/\mu^{(1)}$, $\bar{S}_{22}/\mu^{(1)}$, $\bar{S}_{33}/\mu^{(1)}$ for: (a) pure shear compression $\bar{e} \leq 0$, and (b) pure shear tension $\bar{e} \geq 0$.

the recent numerical (F.E.M.) results of Triantafyllidis *et al.* (2006) for the in-plane behavior of fiber-reinforced elastomers.

Figures 8.6 and 8.7 illustrate the influence of the initial volume fraction of fibers, c_0 , and the shear contrast, $t = \mu^{(2)}/\mu^{(1)}$, on the effective stress-strain relation of fiber-reinforced elastomers with Gent (matrix and fiber phases) subjected to pure shear loading conditions. For conciseness, results are provided for *aligned* pure shear loading ($\bar{\mathbf{F}} = \bar{\lambda} \mathbf{e}_1 \otimes \mathbf{e}_1 + \bar{\lambda}^{-1} \mathbf{e}_2 \otimes \mathbf{e}_2 + \mathbf{e}_3 \otimes \mathbf{e}_3$) and an initially hexagonal distribution (HA) of fibers. However, it should be emphasized that the results presented in Figs. 8.6 and 8.7 are similar to those obtained for “misaligned” pure shear loadings, as well as for different initial fiber distributions.

Figure 8.6 displays results for the normalized effective stress components $\bar{S}_{11}/\mu^{(1)}$, $\bar{S}_{22}/\mu^{(1)}$, $\bar{S}_{33}/\mu^{(1)}$ for fiber-reinforced Gent elastomers with compressibility ratios $\kappa^{(1)}/\mu^{(1)} = 50$, $\kappa^{(2)}/\mu^{(2)} = 30$, contrast $t = \mu^{(2)}/\mu^{(1)} = 50$, and initial volume fractions $c_0 = 15, 25$, and 35%, as a function of the logarithmic strain $\bar{e} = \ln \bar{\lambda}$. Part (a) shows results for aligned pure shear compression ($\bar{e} \leq 0$), and part (b), for aligned pure shear tension ($\bar{e} \geq 0$). The increase of the initial volume fraction of fibers c_0 can be seen to have three major effects on the effective stress-strain relation of the

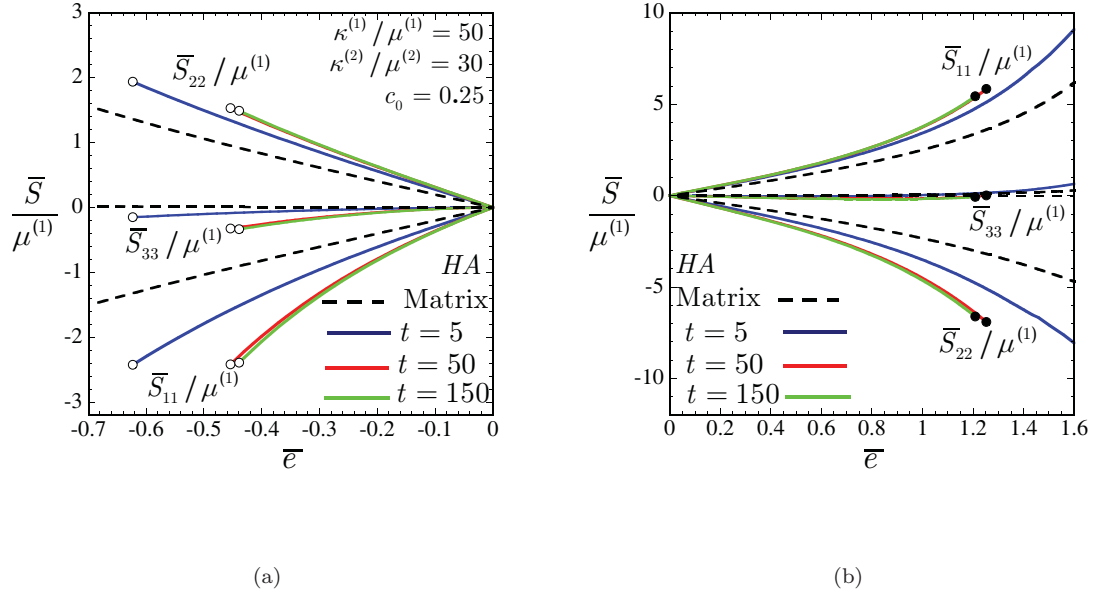


Figure 8.7: In-plane aligned pure shear ($\bar{\mathbf{F}} = \bar{\lambda} \mathbf{e}_1 \otimes \mathbf{e}_1 + \bar{\lambda}^{-1} \mathbf{e}_2 \otimes \mathbf{e}_2 + \mathbf{e}_3 \otimes \mathbf{e}_3$) of a fiber-reinforced Gent elastomer with an initially hexagonal arrangement (HA) of fibers. The results correspond to compressibility ratios $\kappa^{(1)}/\mu^{(1)} = 50$, $\kappa^{(2)}/\mu^{(2)} = 30$, initial volume fraction $c_0 = 0.25$ and shear contrasts $t = \mu^{(2)}/\mu^{(1)} = 5, 50, 150$. The normalized stress components $\bar{S}_{11}/\mu^{(1)}$, $\bar{S}_{22}/\mu^{(1)}$, $\bar{S}_{33}/\mu^{(1)}$ for: (a) pure shear compression $\bar{e} \leq 0$, and (b) pure shear tension $\bar{e} \geq 0$.

reinforced elastomer. First, the overall behavior of the material is stiffer. Second, in spite of the fact that the material is stiffer, it is also less stable, as loss of strong ellipticity occurs at smaller strains. Finally, fiber contact is also seen to occur at smaller finite strains. All these three effects are consistent with the fact that increasing the volume fraction of the fibers corresponds effectively to increasing the relative size of the *reinforcing* inclusions in the material. Indeed, “bigger” stiffer fibers are expected to lead to an overall stiffer behavior. Further, “bigger” fibers imply that neighboring fibers are closer to one another. Thus, according to preceding discussions, closer fibers lead to *softer* effective incremental shear moduli, which, in turn, lead to smaller critical strains at loss of strong ellipticity. Moreover, closer fibers clearly lead to smaller macroscopic strains at fiber contact.

Figure 8.7 displays corresponding results for fiber-reinforced Gent elastomers with compressibility ratios $\kappa^{(1)}/\mu^{(1)} = 50$, $\kappa^{(2)}/\mu^{(2)} = 30$, initial volume fraction $c_0 = 0.25$ and shear contrasts $t = \mu^{(2)}/\mu^{(1)} = 5, 50, 150$, as a function of the logarithmic strain $\bar{e} = \ln \bar{\lambda}$. Part (a) shows results for aligned pure shear compression ($\bar{e} \leq 0$), and part (b), for aligned pure shear tension ($\bar{e} \geq 0$). As expected on physical grounds, increasing the shear contrast t is seen to lead to an overall stiffer

behavior of the composite. In addition, and similar to increasing fiber volume fraction, increasing the shear contrast t is seen to lead to smaller critical strains at which loss of strong ellipticity and fiber contact take place. These trends are a direct consequence of the fact that by increasing t , the average deformation in the matrix phase increases—and, by the same token, the average deformation in fibers decreases. As a result, neighboring fibers get closer leading—as explained above—to the onset of instabilities and fiber contact at smaller strains.

Figure 8.8 illustrates the influence of the initial distribution of fibers (SA vs. HA), initial fiber volume fraction, c_0 , and shear contrast, $t = \mu^{(2)}/\mu^{(1)}$, on the onset of macroscopic instabilities in fiber-reinforced Gent elastomers. In particular, SA and HA results are shown for *aligned* pure shear loading $\bar{\mathbf{F}} = \bar{\lambda}\mathbf{e}_1 \otimes \mathbf{e}_1 + \bar{\lambda}^{-1}\mathbf{e}_2 \otimes \mathbf{e}_2 + \mathbf{e}_3 \otimes \mathbf{e}_3$, compressibility ratios $\kappa^{(1)}/\mu^{(1)} = 5$, $\kappa^{(2)}/\mu^{(2)} = 3$ and $\kappa^{(1)}/\mu^{(1)} = 50$, $\kappa^{(2)}/\mu^{(2)} = 30$, for: (a) the critical strain, $\bar{e}_{crit} = \ln \bar{\lambda}_{crit}$, at which the composite loses strong ellipticity for contrast $t = 50$, as a function of the initial fiber volume fraction c_0 ; and (b) \bar{e}_{crit} for initial volume fraction $c_0 = 0.25$, as a function of the contrast t . It is clear from Fig. 8.8 that the initial distribution of fibers plays a major role in the development of macroscopic instabilities. More precisely, it is observed that the material with initially square distribution (SA) of fibers is more unstable (in strain space) than that one with hexagonal distribution (HA). Interestingly, this trend has also been observed in porous elastomers (Michel *et al.*, 2007). Furthermore, similar to the axisymmetric shear results shown in Fig. 8.4(b), Fig. 8.8 illustrates that for in-plane pure shear, fiber-reinforced elastomers with higher bulk moduli, $\kappa^{(1)}$ and $\kappa^{(2)}$, are more unstable.

Figure 8.8(a) shows that the critical strain \bar{e}_{crit} is a monotonically increasing function of the initial fiber volume fraction c_0 . In the dilute limit (i.e., $c_0 \rightarrow 0$), $\bar{e}_{crit} \rightarrow -\infty$, since the elastomeric matrix is strongly elliptic. Moreover, in this limit, it is interesting to observe that the results for the square (SA) and hexagonal (HA) distributions of fibers become practically indistinguishable. This implies that as $c_0 \rightarrow 0$, the fibers do not interact with each other, and hence their initial distribution becomes irrelevant. Note further from Fig. 8.8(a) that for sufficiently large values of c_0 , fiber contact (denoted with the symbol “•” in the plots) precedes loss of strong ellipticity.

Figure 8.8(b) shows that \bar{e}_{crit} increases monotonically as a function of the contrast $t = \mu^{(2)}/\mu^{(1)}$. In the limit of small contrast (i.e., $t \rightarrow 1$), $\bar{e}_{crit} \rightarrow -\infty$, so that the material remains strongly elliptic for all deformations. On the other hand, in the limit as the fibers are taken to be rigid (i.e., $t \rightarrow \infty$), the critical strain at which the material loses strong ellipticity tends to a finite, non-zero

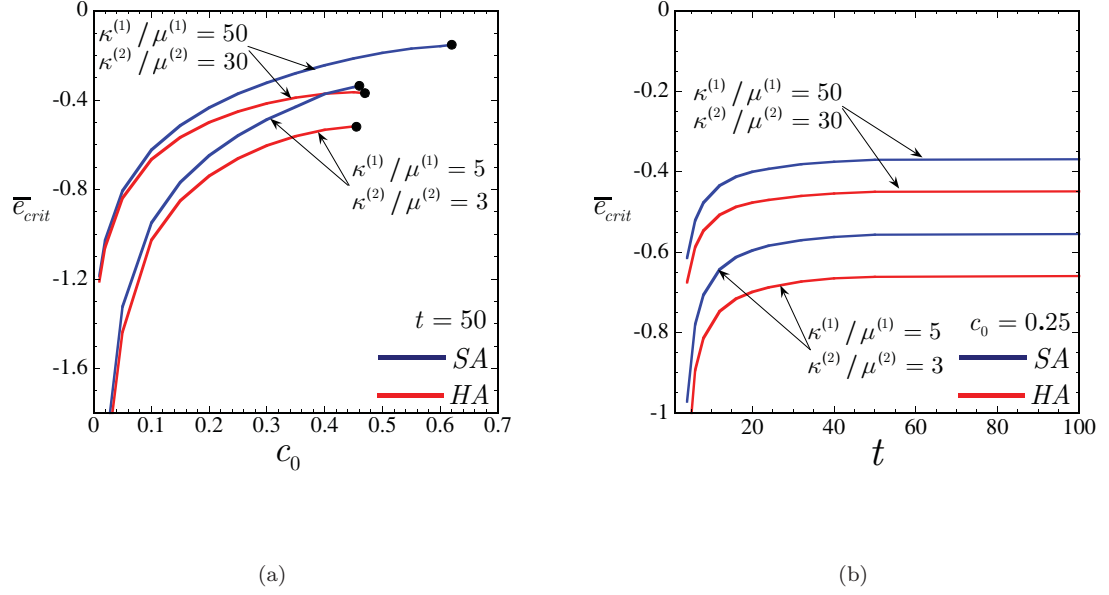


Figure 8.8: In-plane aligned pure shear ($\bar{\mathbf{F}} = \bar{\lambda} \mathbf{e}_1 \otimes \mathbf{e}_1 + \bar{\lambda}^{-1} \mathbf{e}_2 \otimes \mathbf{e}_2 + \mathbf{e}_3 \otimes \mathbf{e}_3$) of fiber-reinforced Gent elastomers with initially square (SA) and hexagonal (HA) arrangements of fibers. (a) The critical strain $\bar{e}_{crit} = \ln \bar{\lambda}_{crit}$ at which the homogenized fiber-reinforced elastomer loses strong ellipticity, as a function of the initial volume fraction of fibers c_0 . (b) The critical strain \bar{e}_{crit} as a function of the shear contrast $t = \mu^{(2)}/\mu^{(1)}$. The results are given for various values of compressibility ratios $\kappa^{(1)}/\mu^{(1)}$ and $\kappa^{(2)}/\mu^{(2)}$.

asymptotic value \bar{e}_{crit}^∞ . This is unlike the behavior illustrated in Fig. 8.4(b) for axisymmetric shear, where $\bar{e}_{crit} \rightarrow 0$ in the limit as $t \rightarrow \infty$. The key difference between these two loading conditions is as follows. For axisymmetric shear and large t , the effective stored-energy function (8.16) can be shown to be of the form $\widehat{W} = \widehat{W}_t t + O(t^0)$. On the other hand, for in-plane pure shear and large t , $\widehat{W} = \widehat{W}_0 + O(t^{-1})$. In other words, for axisymmetric shear, the overall behavior of the material becomes rigid when the fibers are taken to be rigid, and as a result, $\bar{e}_{crit} \rightarrow 0$ in the limit as $t \rightarrow \infty$. On the contrary, for in-plane pure shear, the effective stored-energy function \widehat{W} does not become unbounded when the fibers are taken to be rigid, but instead, it tends to some finite limiting behavior \widehat{W}_0 , so that \bar{e}_{crit}^∞ needs not be zero.

In short, the results illustrated in Figs. 8.5–8.8 reveal that the overall behavior of fiber-reinforced elastomers subjected to in-plane pure shear deformations depends very critically on the initial *distribution* and *volume fraction* of the fibers. The dependence on the *contrast* between the elastomeric matrix and fibers, as measured by t , is very significant from small to moderate values of t . For relatively large contrasts (e.g., here, $t > 50$), the behavior of the composite tends to that of elastomers with rigid fibers, and hence, it becomes virtually insensitive to further changes in t .

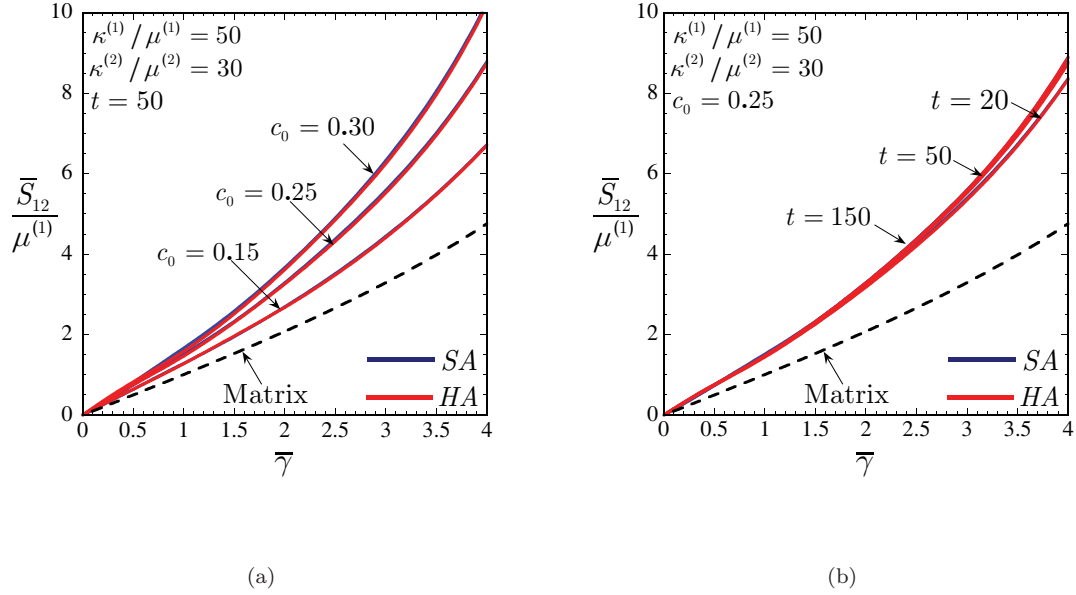


Figure 8.9: In-plane simple shear ($\bar{\mathbf{F}} = \mathbf{e}_1 \otimes \mathbf{e}_1 + \mathbf{e}_2 \otimes \mathbf{e}_2 + \mathbf{e}_3 \otimes \mathbf{e}_3 + \bar{\gamma} \mathbf{e}_1 \otimes \mathbf{e}_2$) of a fiber-reinforced elastomer. The results, which are given for periodic square (SA) and hexagonal (HA) distributions of fibers, correspond to Gent phases with compressibility ratios $\kappa^{(1)}/\mu^{(1)} = 50$ and $\kappa^{(2)}/\mu^{(2)} = 30$. The normalized effective shear stress $\bar{S}_{12}/\mu^{(1)} = (1/\mu^{(1)})\partial\widehat{W}/\partial\bar{\gamma}$, as a function of the amount of shear $\bar{\gamma}$ for: (a) contrast $t = \mu^{(2)}/\mu^{(1)} = 50$ and various initial volume fractions c_0 , and (b) for initial volume fraction $c_0 = 25\%$ and various values of the contrast t .

This is unlike the behavior observed for axisymmetric shear deformations (Figs. 8.2–8.4), where the dependence on t was critical in the entire physical range $1 \leq t \leq \infty$, and the dependence on the fiber distribution was practically negligible.

8.2.3 In-plane simple shear

Figure 8.9 displays results, as predicted by the second-order estimate (8.16), for the effective behavior of fiber-reinforced Gent elastomers subjected to in-plane simple shear: $\bar{\mathbf{F}} = \mathbf{e}_1 \otimes \mathbf{e}_1 + \mathbf{e}_2 \otimes \mathbf{e}_2 + \mathbf{e}_3 \otimes \mathbf{e}_3 + \bar{\gamma} \mathbf{e}_1 \otimes \mathbf{e}_2$ with $\bar{\gamma}$ denoting the amount of shear. In particular, results are shown for initially square (SA) and hexagonal (HA) distributions of fibers and compressibility ratios $\kappa^{(1)}/\mu^{(1)} = 50$ and $\kappa^{(2)}/\mu^{(2)} = 30$. Part (a) shows the normalized shear stress $\bar{S}_{12}/\mu^{(1)} = (1/\mu^{(1)})\partial\widehat{W}/\partial\bar{\gamma}$ for initial volume fractions of fibers $c_0 = 15, 25, 30\%$ and fixed contrast $t = \mu^{(2)}/\mu^{(1)} = 50$, as a function of the amount of shear $\bar{\gamma}$. Part (b) shows the normalized shear stress $\bar{S}_{12}/\mu^{(1)}$ for contrasts $t = 20, 50, 150$ and fixed initial volume fraction $c_0 = 25\%$, as a function of $\bar{\gamma}$. In accord with the results considered in the preceding subsections, Fig. 8.9(a) shows that

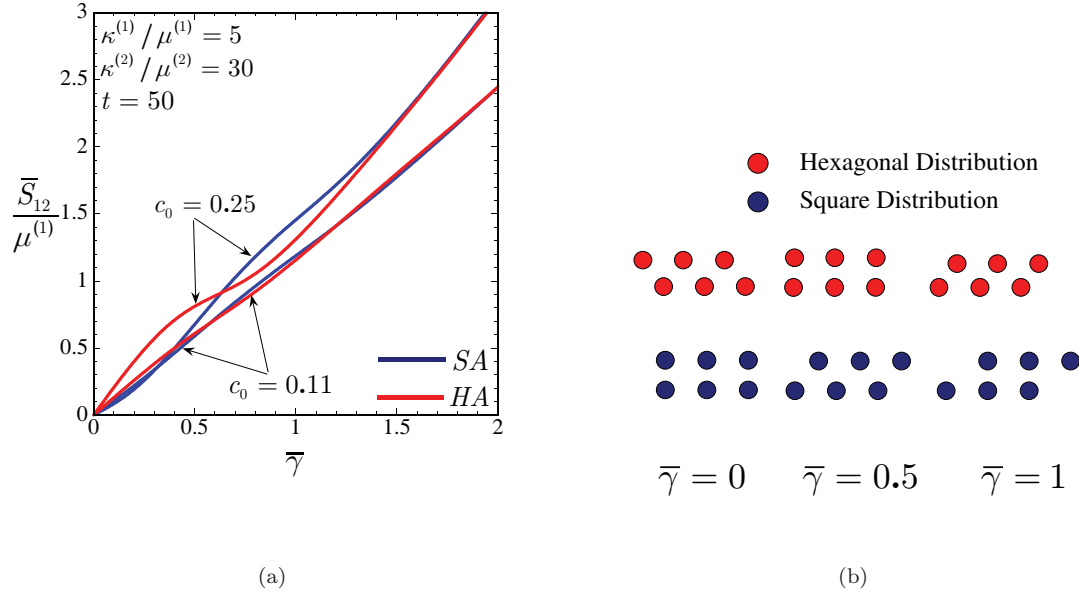


Figure 8.10: In-plane pre-compressed simple shear ($\bar{\mathbf{F}} = \mathbf{e}_1 \otimes \mathbf{e}_1 + 3/5\mathbf{e}_2 \otimes \mathbf{e}_2 + \mathbf{e}_3 \otimes \mathbf{e}_3 + \bar{\gamma}\mathbf{e}_1 \otimes \mathbf{e}_2$) of a fiber-reinforced elastomer. The results, which are given for periodic square (*SA*) and hexagonal (*HA*) distributions of fibers, correspond to Gent phases with compressibility ratios $\kappa^{(1)}/\mu^{(1)} = 5$ and $\kappa^{(2)}/\mu^{(2)} = 30$, contrast $t = 50$, and initial volume fraction of fibers $c_0 = 11$ and 25%. (a) The normalized effective shear stress $\bar{S}_{12}/\mu^{(1)} = (1/\mu^{(1)})\partial\widehat{W}/\partial\bar{\gamma}$, as a function of the applied amount of shear $\bar{\gamma}$. (b) Schematic representation of the evolution of the distribution of fibers upon loading.

the effective behavior of the fiber-reinforced elastomer is stiffer for higher values of c_0 . Similarly, Fig. 8.9(b) shows that the behavior of the composite is stiffer for higher values of the contrast t . Note, however, that the effect of increasing t is rather weak. Again, this is because the asymptotic behavior of \widehat{W} for in-plane deformations and large t is of the form: $\widehat{W} = \widehat{W}_0 + O(t^{-1})$, as discussed in the previous section. Finally, it is interesting to remark that the effect of the initial distribution of fibers (i.e., *SA* vs. *HA*) on the effective behavior of the composite under in-plane simple shear is negligible at the initial volume fractions of fibers considered. This point is investigated further in the context of the next figure.

Figure 8.10 illustrates results for the effective behavior of fiber-reinforced Gent elastomers, with square (*SA*) and hexagonal (*HA*) fiber distributions, subjected to in-plane *pre-compressed* simple shear: $\bar{\mathbf{F}} = \mathbf{e}_1 \otimes \mathbf{e}_1 + 3/5\mathbf{e}_2 \otimes \mathbf{e}_2 + \mathbf{e}_3 \otimes \mathbf{e}_3 + \bar{\gamma}\mathbf{e}_1 \otimes \mathbf{e}_2$. This type of loading condition, which has already been considered by Lahellec *et al.* (2004) in a somewhat different context, serves to bring out neatly the influence of the initial, as well as evolving, distribution of fibers on the macroscopic behavior of the composite. Part (a) shows the normalized shear stress $\bar{S}_{12}/\mu^{(1)} = (1/\mu^{(1)})\partial\widehat{W}/\partial\bar{\gamma}$ as a function of the amount of shear $\bar{\gamma}$ for compressibility ratios $\kappa^{(1)}/\mu^{(1)} = 5$, $\kappa^{(2)}/\mu^{(2)} = 30$,

contrast $t = \mu^{(2)}/\mu^{(1)} = 50$, and initial fiber concentrations $c_0 = 11$ and 25%. Part (b) depicts an schematic representation of the evolution of the fiber distribution along the loading process for both initial arrangement of fibers.

A key observation from Fig. 8.10(a) is the oscillations exhibited by the macroscopic stress-strain response of the material for both initial (square and hexagonal) distributions of fibers. These oscillations are a direct consequence of the evolution of the microstructure. More specifically, the oscillations are caused by the evolution of the *distribution* of the fibers, which alternates from configurations where the fibers are aligned with other fibers to configurations where the fibers are aligned between two other fibers, as illustrated by Fig. 8.10(b). Note that the oscillations are more pronounced for higher values of initial volume fraction, as a consequence of the stronger interactions between the fibers. Note further that for sufficiently large deformations $\bar{\gamma}$, the oscillations die out. In order to understand this behavior, it should be recalled that besides the evolution of the distribution of the fibers, there is another mechanism that governs the overall behavior of the material under in-plane deformations, namely, the constitutive stiffening of the matrix phase due to the straining. For large $\bar{\gamma}$, the matrix *constitutive* stiffening dominates, and the *geometric* effect due to the evolution of the fiber distribution becomes negligible, hence explaining the apparent disappearance of oscillations for large $\bar{\gamma}$ in Fig. 8.10(a).

No loss of strong ellipticity was detected for any of the results shown in Figs. 8.9 and 8.10. However, it should be mentioned that by sufficiently increasing the pre-compressed strain in the \mathbf{e}_2 direction (e.g., from $2/5 = 0.4$ to 0.5) would lead to loss of strong ellipticity at some finite value of the amount of shear $\bar{\gamma}$. Interestingly, the mechanism by which fiber-reinforced elastomers lose strong ellipticity when subjected to in-plane pre-compressed simple shear is entirely analogous to that one detected for in-plane pure shear. Namely, loss of strong ellipticity occurs by the vanishing of the effective incremental shear modulus perpendicular to the direction in which neighboring fibers are closest to each other.

8.2.4 Out-of-plane pure shear

Figure 8.11 and 8.12 present the effective behavior, as predicted by the second-order estimate (8.16), of Gent elastomers reinforced with periodic square (*SA*) and hexagonal (*HA*) distributions of Gent fibers subjected to out-of-plane pure shear: $\bar{\mathbf{F}} = \bar{\lambda}_1 \mathbf{e}_1 \otimes \mathbf{e}_1 + \bar{\lambda}_2 \mathbf{e}_2 \otimes \mathbf{e}_2 + \bar{\lambda}_3 \mathbf{e}_3 \otimes \mathbf{e}_3$ with $\bar{\lambda}_3 = \bar{\lambda}$, $\bar{\lambda}_1 = \bar{\lambda}^{-1}$, and $\bar{\lambda}_2 = 1$. Fig. 8.11 illustrates results for tension in the fiber direction

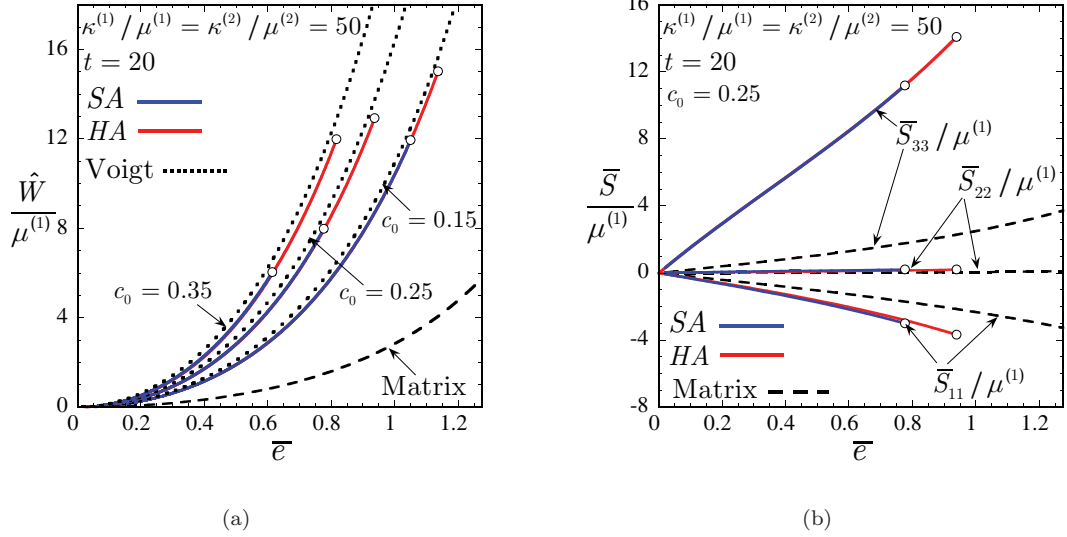


Figure 8.11: Effective response of Gent fiber-reinforced elastomers subjected to “tensile” out-of-plane pure shear: $\bar{\mathbf{F}} = \bar{\lambda}_1 \mathbf{e}_1 \otimes \mathbf{e}_1 + \bar{\lambda}_2 \mathbf{e}_2 \otimes \mathbf{e}_2 + \bar{\lambda}_3 \mathbf{e}_3 \otimes \mathbf{e}_3$ with $\bar{\lambda}_3 = \bar{\lambda} \geq 1$, $\bar{\lambda}_1 = \bar{\lambda}^{-1}$, and $\bar{\lambda}_2 = 1$. Results are shown for compressibility ratios $\kappa^{(1)}/\mu^{(1)} = \kappa^{(2)}/\mu^{(2)} = 50$, contrast $t = \mu^{(2)}/\mu^{(1)} = 20$, and various values of initial volume fraction of fibers c_0 , as a function of the logarithmic strain $\bar{e} = \ln \bar{\lambda}$. (a) The normalized effective stored-energy function $\widehat{W}/\mu^{(1)}$. (b) The normalized stress components $\bar{S}_{11}/\mu^{(1)}$, $\bar{S}_{22}/\mu^{(1)}$, $\bar{S}_{33}/\mu^{(1)}$.

(i.e., $\bar{\lambda} \geq 1$) and Fig. 8.12, for compression (i.e., $\bar{\lambda} \leq 1$). In particular, results are shown for compressibility ratios $\kappa^{(1)}/\mu^{(1)} = \kappa^{(2)}/\mu^{(2)} = 50$ and contrast $t = \mu^{(2)}/\mu^{(1)} = 20$, as a function of the logarithmic strain $\bar{e} = \ln \bar{\lambda}$. Parts (a) show the normalized effective stored-energy function $\widehat{W}/\mu^{(1)}$ for initial volume fractions of fibers $c_0 = 15, 25, 35\%$, and parts (b), the normalized stress components $\bar{S}_{11}/\mu^{(1)}$, $\bar{S}_{22}/\mu^{(1)}$, $\bar{S}_{33}/\mu^{(1)}$ for $c_0 = 25\%$.

In accord with the preceding subsections, Figs. 8.11 and 8.12 show that the effective behavior of the fiber-reinforced elastomer is stiffer for higher values of c_0 . Consistent with previous results, it is also seen that the second-order estimates satisfy the rigorous Voigt bound. Moreover, it is important to remark that the results displayed in Figs. 8.11 and 8.12 indicate that the effective behavior of the fiber-reinforced elastomer—as measured by the effective stored-energy function \widehat{W} and macroscopic stress $\bar{\mathbf{S}}$ —for out-of-plane pure shear deformations depends very weakly on the initial distribution of fibers (since the SA and HA results are very much identical). This behavior is in precise agreement with the results found for axisymmetric shear deformations, which were discussed in the context of Figs. 8.2 and 8.3. In this regard, as for axisymmetric shear deformations, the independence on fiber distribution in the present context can be understood by recognizing

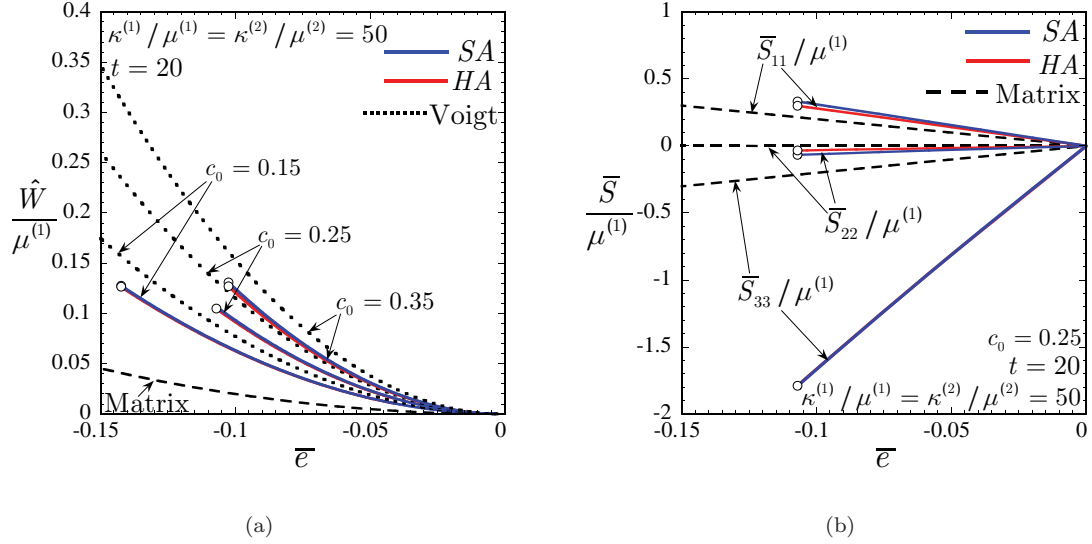


Figure 8.12: Effective response of Gent fiber-reinforced elastomers subjected to “compressive” out-of-plane pure shear: $\bar{\mathbf{F}} = \bar{\lambda}_1 \mathbf{e}_1 \otimes \mathbf{e}_1 + \bar{\lambda}_2 \mathbf{e}_2 \otimes \mathbf{e}_2 + \bar{\lambda}_3 \mathbf{e}_3 \otimes \mathbf{e}_3$ with $\bar{\lambda}_3 = \bar{\lambda} \leq 1$, $\bar{\lambda}_1 = \bar{\lambda}^{-1}$, and $\bar{\lambda}_2 = 1$. Results are shown for compressibility ratios $\kappa^{(1)}/\mu^{(1)} = \kappa^{(2)}/\mu^{(2)} = 50$, contrast $t = \mu^{(2)}/\mu^{(1)} = 20$, and various values of initial volume fraction of fibers c_0 , as a function of the logarithmic strain $\bar{e} = \ln \bar{\lambda}$. (a) The normalized effective stored-energy function $\widehat{W}/\mu^{(1)}$. (b) The normalized stress components $\bar{S}_{11}/\mu^{(1)}$, $\bar{S}_{22}/\mu^{(1)}$, $\bar{S}_{33}/\mu^{(1)}$.

that out-of-plane pure shear is a *fiber-dominated* mode of deformation. That is, under out-of-plane pure shear, the local strain in the fibers—which are much stiffer than the matrix phase—is comparable to the strain in the elastomeric matrix, and, as a consequence, the effective stored-energy function \widehat{W} and macroscopic stress $\bar{\mathbf{S}}$ are controlled primarily by the *contrast* (t) and the fiber *volume fraction* (c_0), and *not* so much by the fiber distribution. Interestingly, this is not true for the effective incremental modulus tensor $\widehat{\mathcal{L}}$ —which measures the macroscopic stability of the homogenized material—as discussed next.

Figure 8.11 shows that fiber-reinforced elastomers with *SA* and *HA* fiber distributions become unstable—through loss of strong ellipticity—at finite values of deformation when subjected to out-of-plane pure shear with *tension* in the fiber direction. Note, however, that materials with the *SA* distribution lose strong ellipticity at smaller strains than those with the *HA* arrangement of fibers. Interestingly, all the *SA* and *HA* results displayed in Fig. 8.11 lose strong ellipticity because of the vanishing of the incremental, *in-plane*, shear modulus $\widehat{\mathcal{L}}_{2121}$. Making contact with the evolution of the microstructure, this failure mechanism—which is exactly the same as the one encountered for *in-plane* pure and simple shear deformations—is caused by the fact that neighboring fibers get

closer to each other with the increasing applied deformation. Thus, as for the in-plane deformations discussed in the preceding subsection, the onset of macroscopic instabilities for out-of-plane pure shear with tension in the fiber direction depends critically on the overall incremental *in-plane* behavior of the composite, and hence, on the *in-plane* distribution of fibers.

Similar to Fig. 8.11, Fig. 8.12 shows that fiber-reinforced elastomers with *SA* and *HA* fiber distributions also lose strong ellipticity when subjected to out-of-plane pure shear with *compression* in the fiber direction. In this case, loss of strong ellipticity takes place because of the vanishing of the effective incremental shear modulus $\widehat{\mathcal{L}}_{1313}$. This failure mode—similar to the one encountered for axisymmetric shear compression—is consistent with the development of kink band type instabilities in the fiber-reinforced composite. Note that because of the failure mode is *fiber-dominated* (i.e., $\widehat{\mathcal{L}}_{1313} = 0$), the critical strains at which the homogenized material loses strong ellipticity are very much independent of the in-plane fiber distribution.

8.3 Concluding remarks

In this chapter, we have derived a homogenization-based constitutive model for the overall mechanical behavior of elastomers reinforced with aligned cylindrical fibers subjected to large deformations, by means of the second-order homogenization method proposed in Chapter 2. Although this method applies more generally, in this work, for relative simplicity, it has been applied to materials with generalized Neo-Hookean (matrix and fiber) phases and periodic distribution of fibers. Explicit results have been computed and discussed for fiber-reinforced compressible Gent elastomers with square and hexagonal distribution of fibers subjected to *out-of-plane*, *in-plane* and coupled *in-plane* and *out-of-plane* loading conditions.

By incorporating finer details about the initial microstructural information, such as the fiber shape, orientation, and distribution, the proposed model exhibits orthotropic material symmetry distinguishing between *fiber-* and *matrix-* dominated modes of deformation. Indeed, as illustrated through various representative results, loading conditions that involve deformation in the fiber direction lead to much stiffer model responses than those that do not induce fiber deformation. In this connection, it has been shown that for fiber-dominated modes, the behavior of the fiber-reinforced elastomers—as predicted by the second-order method—is controlled primarily by the *contrast* between the (matrix and fiber) phases and the fiber *volume fraction*. On the other hand,

for matrix-dominated modes of deformation, the overall material behavior is controlled by the in-plane *distribution* and *volume fraction* of the fibers—provided that the fibers are sufficiently stiffer than the elastomeric matrix phase.

Similar to other elastomeric systems subjected to finite deformations (see Chapters 3–7), the predictions generated in this chapter indicate that the evolution of the underlying microstructure has a very significant and subtle effect on the mechanical response of fiber-reinforced elastomers. In this case, it has been observed that the evolution of the *distribution* of the fibers produces significant geometric stiffening/softening of the effective response of these materials. In particular, it has been observed that when neighboring fibers get closer together (farther apart) in a given direction, the effective incremental response of the material stiffens (softens) in that same direction. At the same time—and more importantly—neighboring fibers getting closer (farther) in a given direction do also lead to the softening (stiffening) of the effective incremental shear response of the material perpendicular to that direction. This latter behavior has been shown to have strong consequences for the macroscopic stability of fiber-reinforced elastomers.

Finally, it is important to emphasize that a major strength of the proposed constitutive model is that it can lose strong ellipticity—even in the case when the underlying matrix phase material and fibers are taken to be strongly elliptic—for loading conditions for which macroscopic instabilities are expected to occur from physical evidence (Kyriakides et al., 1995) and numerical simulations (Triantafyllidis *et al.*, 2006). More remarkably, the specific failure modes by which the estimate loses strong ellipticity depend very critically on the applied loading conditions. Thus, for *out-of-plane* loading conditions with compressive deformation in the fiber direction, the constitutive model loses strong ellipticity in a way that is consistent with the possible development of kink-band-type instabilities. On the other hand, for *in-plane* loading conditions, as well as for mixed *in-plane* and *out-of-plane* conditions with tensile deformation in the fiber direction, the constitutive model loses strong ellipticity in a way that is consistent with the breaking of the symmetries of the underlying, highly ordered, periodic microstructure.

8.4 Appendix I. The microstructural tensor \mathbf{P}

In this appendix, we provide explicit expressions for the components of the microstructural tensor \mathbf{P} , which serves to characterize the two types of microstructures, in the reference configuration, considered in this chapter: a) periodic square, and b) periodic hexagonal arrangements of monodisperse, aligned cylindrical fibers with initially circular cross section (see Fig. 8.1 in the main body of the text).

Periodic Square Distribution

For the periodic square distribution, the expression (2.59) for \mathbf{P} specializes to:

$$P_{ijkl} = \frac{1}{\pi(1-c_0)} \sum_{\substack{p=-\infty \\ -\{p=q=0\}}}^{+\infty} \sum_{q=-\infty}^{+\infty} \left(L_{imkn}^{(1)} \xi_m \xi_n \right)^{-1} \xi_j \xi_l \frac{J_1^2 \left(2\sqrt{\pi c_0} \sqrt{p^2 + q^2} \right)}{p^2 + q^2}, \quad (8.24)$$

where $\xi_1 = p$, $\xi_2 = q$, and $J_1(\cdot)$ is the Bessel function of first kind.

Periodic Hexagonal Distribution

For the periodic hexagonal distribution, the expression (2.59) for \mathbf{P} specializes to:

$$P_{ijkl} = \frac{\sqrt{3}}{2\pi(1-c_0)} \sum_{\substack{p=-\infty \\ -\{p=q=0\}}}^{+\infty} \sum_{q=-\infty}^{+\infty} \left(L_{imkn}^{(1)} \xi_m \xi_n \right)^{-1} \xi_j \xi_l \frac{J_1^2 \left(\frac{2^{3/2}}{3^{1/4}} \sqrt{\pi c_0} \sqrt{p^2 - pq + q^2} \right)}{p^2 - pq + q^2}, \quad (8.25)$$

where $\xi_1 = p$, $\xi_2 = \sqrt{3}/3(2q - p)$.

Chapter 9

Closure

In this thesis, an analytical, nonlinear homogenization framework has been developed for elastomeric composites subjected to finite deformations. The framework has the ability to account for the initial stiffness, volume fraction, shape, orientation, and distribution of the phases in a given elastomeric composite, as well as for the *evolution* of these parameters along a given macroscopic loading path. This last feature is essential in order to endow the framework with the ability to predict the possible development of macroscopic instabilities in finite deformations.

The proposed theory is based on an appropriate extension of the “second-order” homogenization method developed by Ponte Castañeda (2002a) in the context of viscoplastic composites. The key idea of this method is the construction of variational principles making use of the notion of a “linear comparison composite.” This construction ultimately allows to convert available *linear* homogenization estimates into estimates for the *nonlinear* response of elastomeric composites. An important point to emphasize here is that, in spite of the fact that the homogenization is carried out at the level of a *linear* comparison composite, the method has the capability to account for the *nonlinear kinematics* inherent in finite elasticity. Thus, for instance, the method can be ensured to satisfy overall *objectivity* requirements.

Motivated by most applications of interest, special attention has been given to elastomers with “particulate” microstructures and isotropic phases. In particular, general expressions have been derived for the effective stored-energy function and the microstructure evolution of two-phase composites consisting of *ellipsoidal* isotropic particles distributed either *randomly* or *periodically* in a compressible isotropic elastomer. Note that the use of ellipsoidal particles includes—as limiting cases—spherical particles, cylindrical fibers, as well as laminates. Within this class of composite elastomers, further specialization of the general expressions have been provided for the cases when

the particles are either *vacuous* or *rigid*. These idealizations—useful to model actual porous and reinforced elastomers—simplify considerably the computation of the estimates. In particular, it is found that for the rigid case, the deformation of the particles reduces to a pure rigid rotation, as expected on physical grounds. This remarkable result exemplifies once again that even though the method makes use of a linear comparison composite to carry out the homogenization process, it does so taking into account the *nonlinear kinematics* involved in the actual behavior of composite elastomers.

The theoretical framework developed in this thesis has been employed to generate estimates for the effective stress-strain relation, microstructure evolution, and macroscopic onset-of-failure surfaces—as determined by the loss of strong ellipticity of the homogenized behavior (Geymonat *et al.*, 1993)—for various classes of porous and reinforced elastomers. These applications have been discussed in Chapters 3 through 8. To be precise, Chapters 3 through 5 have dealt with porous elastomers, while Chapters 6, 7, and 8 have dealt with reinforced elastomers. Next, we summarize the main findings in these chapters.

Chapter 3 has addressed the problem of the in-plane effective behavior of *porous* elastomers consisting of aligned cylindrical voids distributed *randomly* and *isotropically* in an isotropic, strongly elliptic matrix phase. One of the main results of this chapter was that the second-order estimates proposed in this work are superior to the “earlier” tangent second-order estimates of Ponte Castañeda and Tiberio (2000). The most distinctive difference was the fact that the new—unlike the earlier tangent—second-order estimates were shown to recover the exact evolution of the porosity in the case when the matrix phase of the porous elastomer was taken to be incompressible. In terms of effective behavior, the second-order estimates were shown to satisfy the Voigt bound¹ as well as to be in very good agreement with the exact result available for hydrostatic loading. More remarkably, the second-order estimates were found to admit loss of strong ellipticity under sufficiently large compressive deformations, in spite of the fact that the elastomeric matrix phase was taken to be strongly elliptic. The reasons for this behavior were linked to the evolution of the microstructure. In particular, it was observed that the decrease of porosity—induced by compressive loading—led to the softening of the effective incremental shear moduli of the composite, which, in turn, led (in some cases) to the loss of strong ellipticity of the porous elastomer.

¹Recall that for the case when the matrix phase is incompressible, the Voigt bound is only non-trivial for isochoric deformations.

Chapter 4 has also addressed the problem of the in-plane effective behavior of porous elastomers consisting of aligned cylindrical voids in an isotropic, strongly elliptic matrix phase, but the distribution of the voids was taken to be *periodic*—as opposed to *random*, like in Chapter 3. One of the main aims of Chapter 4 was to carry out comprehensive comparisons between second-order estimates and FEM calculations available for periodic microstructures. In this regard, the second-order estimates were shown to deliver remarkably accurate results not only for the effective stress-strain relation of porous elastomers, but more generally, for the evolution of the underlying microstructure, as well as for the onset of macroscopic instabilities in these materials. Another important result of this chapter was that the initial distribution of voids did not have a significant influence on the effective stress-strain relation of porous elastomers. However, it did play a major role in the development of macroscopic instabilities in these materials. In particular, it was shown that as the distribution of the pores tended to be more random and isotropic, the porous elastomer tended to be relatively more stable. In this connection, it should be re-emphasized that in the limit as the distribution of the pores is completely *random* and *isotropic*, the development of macroscopic instabilities does not vanish, but, instead, it persists, as discussed in Chapter 3.

In contrast to Chapters 3 and 4—where two-dimensional (2D) model problems were studied to gain insight on the behavior of porous elastomers, as well as to establish the accuracy of the second-order method—the main objective of Chapter 5 was to develop homogenization-based constitutive models for porous elastomers with more realistic, three-dimensional (3D) microstructures. Thus, the type of porous elastomers considered in Chapter 5 were made up of initially spherical, polydisperse, vacuous inclusions distributed randomly and isotropically—in the undeformed configuration—in a compressible, and incompressible, isotropic elastomeric matrix. This microstructure—though idealized—could be considered as a fair approximation to actual microstructures in actual porous elastomers. One of the strengths of the second-order estimates derived in Chapter 5 was their relative simplicity. Indeed, in spite of incorporating fine microstructural information, the estimates reduced to solving a system of 7 nonlinear, algebraic equations. In addition, the estimates derived in Chapter 5 were shown to be in good agreement with exact and numerical results available from the literature for special loading conditions. For more general conditions, however, the second-order estimates were seen to be drastically different from existing models. In particular, similar to their 2D counterparts discussed in Chapter 3, the proposed

estimates were found to admit loss of strong ellipticity for loading conditions where such instabilities were expected to occur from experimental evidence (*i.e.*, mostly for *compressive* loadings). This was in contrast with all existing (micromechanics- and homogenization-based) models, which failed to lose strong ellipticity, and, instead, remained stable for all applied loading conditions. The reasons for this result, once again, were discussed to be essentially due to the ability of the second-order method to capture more accurately the subtle influence of the evolution of the microstructure on the mechanical response of elastomeric composites.

Chapter 6 has dealt with the effective behavior of *reinforced* elastomers with layered microstructures. The motivation to consider such special class of microgeometries was twofold. First, *exact* estimates could be computed quasi-analytically, which allowed to gain precious insight on the effective behavior of reinforced elastomers subjected to finite deformations. Second, there was a practical interest to generate a preliminary understanding of the overall behavior of block copolymers with layered microstructures. The main result of this chapter was to establish that the rotation of the underlying layers—induced by the applied finite deformations—generated substantial geometric softening in the overall mechanical response of laminates. Moreover, in spite of the fact that, locally, the material was assumed to be strongly elliptic, the homogenized behavior of the laminate was found to lose strong ellipticity at sufficiently large deformations. In particular, when the laminate was loaded in compression along the layers, a certain type of “kink-band” instability was detected corresponding to the material becoming infinitesimally soft to incremental shear deformations in the lamination direction.

Chapter 7 was concerned with the in-plane effective behavior of elastomers reinforced with aligned cylindrical fibers of initially elliptical cross section. Further, the fibers were distributed randomly with elliptical symmetry in the undeformed configuration. A major result of this chapter was the strong influence of the evolution of the microstructure on the overall behavior of reinforced elastomers. Indeed, in the specific context of elastomers reinforced with *rigid* fibers (of elliptical cross section), the rotation (in the plane of the deformation) of the fibers when the composite was subjected to finite stretches was identified as a potential *softening* mechanism, in accord with the findings of Chapter 6 (for laminates). Physically, the fibers could “accommodate” some of the applied macroscopic deformation through rigid rotations, hence inducing softer modes of deformation in the matrix phase. In addition, the microstructure evolution not only had implications for the effective behavior, but also for the overall stability of the composite. In this regard, it was

shown that loss of strong ellipticity could take place in strongly elliptic elastomers reinforced with *stiff* fibers (of elliptical cross section) at physically realistic levels of deformation. The underlying microscopic mechanism driving these macroscopic instabilities was identified with the possible “flopping” of the fibers, due to a sufficiently large *compressive* component of the applied deformation along the long (in-plane) axes of the fibers. More specifically, in spite of the randomness, the assumed “elliptical symmetry” of the microstructure exhibited a preferred microstructural orientation. Thus, the “flopping” of the fibers provided a *symmetry breaking* mechanism leading to the possible development of a macroscopic instability. Indeed, in the limit as the fibers (and their two-point correlation function) were taken to be circular, so that the composite became isotropic, no loss of strong ellipticity was detected, as there were no symmetries to be broken.

Finally, Chapter 8 was devoted to the development of a homogenization-based constitutive model for elastomers reinforced with aligned cylindrical fibers subjected to finite deformations. In contrast to Chapter 7—where attention was restricted to the *in-plane* effective behavior of *random*, fiber-reinforced elastomers—Chapter 8 dealt with the effective behavior of fiber-reinforced elastomers with *periodic* microstructures subjected to general, three-dimensional, finite deformations. The motivations to consider such type of material systems were to generate a constitutive model for typical fiber-reinforced elastomeric structures, such as rubber tires, as well as to develop a preliminary understanding of the overall behavior of block copolymers with cylindrical microstructures. One of the important features of the model derived in Chapter 8 is that—by incorporating finer details about the initial microstructural information, such as the fiber shape, orientation, and distribution—it exhibited orthotropic material symmetry distinguishing between *fiber-* and *matrix-* dominated modes of deformation. In addition, it was shown via representative model predictions that the evolution of the *distribution* of the fibers generated significant geometric stiffening/softening of the effective response of fiber-reinforced elastomers. In particular, it was established that when neighboring fibers got closer together (farther apart) in a given direction, the effective incremental response of the material stiffened (softened) in that same direction. At the same time—and more importantly—neighboring fibers getting closer (farther) in a given direction did also lead to the softening (stiffening) of the effective incremental shear response of the material perpendicular to that direction. Furthermore—and similar to the findings in previous chapters—the proposed constitutive model lost strong ellipticity for loading conditions for which macroscopic instabilities were expected to occur from experimental observations and numerical simulations.

More remarkably, the specific failure modes by which the estimate lost strong ellipticity depended very critically on the applied loading conditions, in agreement with physical evidence.

In summary, all the elastomeric systems studied in this thesis have revealed that there is a very important and subtle interplay between the evolution of the underlying microstructure and the overall behavior and stability of elastomeric composites. Moreover, it has been shown that the second-order method proposed in this work is powerful enough as to capture this interplay in order to deliver accurate estimates not only for the effective stress-strain relation, but also for the microstructure evolution, as well as for the onset of macroscopic instabilities of elastomeric composites subjected to finite deformations. In addition to its accuracy, the second-order method has been shown to ultimately lead to remarkably simple estimates, which could be easily implemented in standard finite element packages for solving structural problems of interest.

At this stage, it is important to make a few remarks regarding future directions in connection with the results presented in this work. First of all, it should be recalled that in this thesis the mechanical behavior of “neat” elastomers has been approximated as purely elastic. While this might be a good approximation for certain ranges of loading-rate conditions and temperatures, more elaborated approximations should be assumed in general. Indeed, elastomers are known to exhibit hysteretic effects, as well as rate and temperature dependence (Bergström and Boyce, 1998; Khan and Lopez-Pamies, 2002) that may be of great importance for certain applications. A future objective, then, would be to develop a homogenization framework to model the *viscoelastic* response of elastomeric composites under large deformations.

Another important effect that has not been addressed in this thesis is that of *interphases*. It is well known (see, e.g., Ramier, 2004) that the actual mechanical behavior of reinforced elastomers is strongly dependent on the reinforcement/matrix interaction. For instance, the stress-stretch response of a synthetic rubber reinforced with untreated silica particles may differ by as much as 100% (in the finite deformation regime) from the response of the same synthetic rubber reinforced with silica that has been treated on the surface (Ramier, 2004). Accordingly, it is crucial to take into account the essential features characterizing the “interphase” between the reinforcement and the elastomeric matrix in order to generate robust constitutive models for reinforced elastomers. Additionally, the study of such interphases may offer fundamental insight related to other problems of increasing interest such as damage, and more importantly, polymer nanocomposites, where interphases play a major role.

Following up on the previous paragraph, a problem of increasing interest is that of the multi-functional behavior of *polymer nanocomposites*. Ever since the late 1980's, numerous experimental studies have established that a significant enhancement of the mechanical, thermal, electrical, optical, and other physical properties in polymer-matrix nanocomposites is achievable for special choices of the microstructure, even for small amounts of inhomogeneities (Bockstaller *et al.*, 2005). For instance, certain nylon-silicate nanocomposites have been shown to exhibit a 50% increase in the modulus and the tensile strength, together with a 100% increase in the heat distortion temperature, with only 5% volume fraction of the nanophase (Lagashetty and Venkataraman, 2005). Rubber-ferrite nanocomposites have proved as very promising materials for flexible magnets, microwave absorbers, pressure/photo sensors, as well as for other applications (Lagashetty and Venkataraman, 2005). Not surprisingly, all of these multi-functional phenomena are highly dependent on the microstructure. It seems, thus, that polymer nanocomposites are a fertile soil for developing efficient modeling tools—in the spirit of the ones developed in this thesis—with the capability not only to predict the behavior of these materials, but also to determine the specific microstructures that lead to selected target properties.

Finally, it would also be of interest to consider the problems of semicrystalline polymers, block-copolymers with polydomains, liquid-crystal elastomers, shape-memory polymers, and soft biological tissues. It is believed that the ideas developed in this thesis could be used as the foundation for the modeling of such complex material systems in an efficient manner.

Appendix A

Second-order homogenization estimates incorporating field fluctuations in finite elasticity¹

O. Lopez-Pamies and P. Ponte Castañeda

Department of Mechanical Engineering and Applied Mechanics
University of Pennsylvania, Philadelphia, PA 19104-6315, U.S.A.

Dedicated to Ray Ogden on the occasion of his 60th birthday

Abstract—This paper presents the application of a recently proposed “second-order” homogenization method (Ponte Castañeda 2002; *J. Mech. Phys. Solids* **50**, 737) to the estimation of the effective behavior of hyperelastic composites subjected to *finite* deformations. The key idea is to introduce an optimally chosen “linear comparison composite,” which can then be used to convert available homogenization estimates for linear composites directly into new estimates for the nonlinear hyperelastic composites. More precisely, the method makes use of “generalized” secant moduli that are intermediate between the standard “secant” and “tangent” moduli of the nonlinear phases,

¹This Appendix, as presented, has been published in Lopez-Pamies and Ponte Castañeda, 2004a.

and that depend not only on the averages, or first moments of the fields in the phases, but also on the second moments of the field fluctuations, or phase covariance tensors. The use of the method is illustrated in the context of carbon-black-filled, and fiber-reinforced elastomers, and estimates analogous to the well-known Hashin-Shtrikman and self-consistent estimates for linear-elastic composites are generated. The new estimates are compared with corresponding estimates using an earlier version of the method (Ponte Castañeda and Tiberio 2000; *J. Mech. Phys. Solids* **48**, 1389) neglecting the use of fluctuations, and the new results are found to be superior. In particular, the new estimates, unlike the earlier ones, are found to satisfy a rigorous bound, and to give more realistic predictions in the important limit of incompressible behavior.

A.1 Hyperelastic composites and effective behavior

The objective of this paper is to develop estimates for the effective behavior of hyperelastic composite materials subjected to *finite deformations*. The materials are made up of N different (homogeneous) phases, which are assumed to be distributed randomly in a specimen occupying a volume Ω_0 in the reference configuration. Furthermore, the size of the typical inhomogeneity (e.g., particle, void, crystal) is much smaller than the size of the specimen and the scale of variation of the loading conditions. The constitutive behavior of the phases is characterized by stored energies $W^{(r)}$ ($r = 1, \dots, N$) that are *nonconvex* functions of the deformation gradient \mathbf{F} . The local energy function of the composite may be written

$$W(\mathbf{X}, \mathbf{F}) = \sum_{r=1}^N \chi^{(r)}(\mathbf{X}) W^{(r)}(\mathbf{F}), \quad (\text{A.1})$$

where the functions $\chi^{(r)}$ are equal to 1 if the position vector \mathbf{X} is inside phase r (i.e., $\mathbf{X} \in \Omega_0^{(r)}$) and zero otherwise. The stored-energy functions of the phases are, of course, assumed to be *objective* in the sense that $W^{(r)}(\mathbf{Q}\mathbf{F}) = W^{(r)}(\mathbf{F})$ for all proper orthogonal \mathbf{Q} and arbitrary deformation gradients \mathbf{F} . Making use of the polar decomposition $\mathbf{F} = \mathbf{R}\mathbf{U}$, where \mathbf{U} is the right stretch tensor and \mathbf{R} is the rotation tensor, it follows, in particular, that $W^{(r)}(\mathbf{F}) = W^{(r)}(\mathbf{U})$.

The local or microscopic constitutive relation for the material is given by

$$\mathbf{S} = \frac{\partial W}{\partial \mathbf{F}}(\mathbf{X}, \mathbf{F}), \quad (\text{A.2})$$

where \mathbf{S} denotes the first Piola-Kirchhoff stress tensor. Note that sufficient smoothness has been

assumed for W in \mathbf{F} and that \mathbf{F} is required to satisfy the *material impenetrability* condition: $\det \mathbf{F}(\mathbf{X}) > 0$ for \mathbf{X} in Ω_0 . For example, this condition would be satisfied for incompressible materials, where $\det \mathbf{F}$ is required to be exactly 1. For more details on hyperelastic materials, refer to the monograph by Ogden (1984).

Following the works of Hill (1972), Hill and Rice (1973) and Ogden (1974), the *effective stored-energy function* of the composite is defined by

$$\widetilde{W}(\overline{\mathbf{F}}) = \inf_{\mathbf{F} \in \mathcal{K}(\overline{\mathbf{F}})} \langle W(\mathbf{X}, \mathbf{F}) \rangle = \inf_{\mathbf{F} \in \mathcal{K}(\overline{\mathbf{F}})} \sum_{r=1}^N c^{(r)} \langle W^{(r)}(\mathbf{F}) \rangle^{(r)}, \tag{A.3}$$

where \mathcal{K} denotes the set of admissible deformation gradients:

$$\mathcal{K}(\overline{\mathbf{F}}) = \{ \mathbf{F} \mid \mathbf{x} = \boldsymbol{\chi}(\mathbf{X}) \text{ with } \mathbf{F} = \text{Grad} \boldsymbol{\chi}, \det \mathbf{F} > 0 \text{ in } \Omega_0, \mathbf{x} = \overline{\mathbf{F}} \mathbf{X} \text{ on } \partial \Omega_0 \}. \tag{A.4}$$

Above, the symbols $\langle \cdot \rangle$ and $\langle \cdot \rangle^{(r)}$ have been introduced to denote volume averages over the composite (Ω_0) and over phase r ($\Omega_0^{(r)}$), respectively, so that the scalars $c^{(r)} = \langle \chi^{(r)} \rangle$ serve to denote the volume fractions of the given phases.

It is noted that \widetilde{W} physically corresponds to the average elastic energy that is stored in the composite when it is subjected to an affine displacement boundary condition with prescribed average deformation gradient $\langle \mathbf{F} \rangle = \overline{\mathbf{F}}$. Furthermore, it can be easily shown that \widetilde{W} is objective, that is, $\widetilde{W}(\overline{\mathbf{F}}) = \widetilde{W}(\overline{\mathbf{U}})$, where $\overline{\mathbf{U}}$ is the macroscopic right stretch tensor in the polar decomposition of the macroscopic deformation gradient $\overline{\mathbf{F}} = \overline{\mathbf{R}} \overline{\mathbf{U}}$, with $\overline{\mathbf{R}}$ denoting the macroscopic rotation tensor.

The usefulness of the definition (A.3) derives from the fact that the *average stress*, defined by $\overline{\mathbf{S}} = \langle \mathbf{S} \rangle$, can be shown to be related to the average deformation gradient $\overline{\mathbf{F}}$ via the relation

$$\overline{\mathbf{S}} = \frac{\partial \widetilde{W}}{\partial \overline{\mathbf{F}}}, \tag{A.5}$$

where, again, sufficient smoothness must be assumed for \widetilde{W} . This is the effective or macroscopic constitutive relation for the nonlinear elastic composite. Of course, the average stress and deformation gradient must satisfy macroscopic equilibrium and compatibility. In particular, the macroscopic rotational balance equation $\overline{\mathbf{S}} \overline{\mathbf{F}}^T = \overline{\mathbf{F}} \overline{\mathbf{S}}^T$ must be satisfied (Hill, 1972).

It is further recalled that under the hypotheses of *polyconvexity* of W , together with suitable growth conditions for W , the infimum in relation (A.3) defining \widetilde{W} is known (Ball, 1977) to be attained when the field \mathbf{x} is assumed to be in a suitable functional space. Ogden (1978) proposed alternative constitutive hypotheses on W ensuring the existence of extremum principles of potential

and complementary energy in finite elasticity. More precise definitions of the effective energy \widetilde{W} are available at least for *periodic* microstructures (Müller 1987; Braides 1985). Such definitions generalize the classical definition of the effective energy for periodic media with convex energies (Marcellini, 1978), by allowing for possible interactions between unit cells, essentially by taking an infimum over the set of all possible combinations of units cells. Physically, this corresponds to accounting for the possibility of the development of instabilities in the composite at sufficiently high deformation. In practice, however, the definition (A.3) should provide an adequate measure of the effective behavior up to the point at which instabilities develop (see Geymonat *et al.*, 1993). Note that \widetilde{W} is essentially the quasiconvexification (or relaxation) of W .

The focus here will be in the characterization of the effective behavior of composites made up of *rubber elastic* phases. Given objectivity, isotropy then implies that the stored-energy functions of the phases can be written as symmetric functions of the principal stretches $\lambda_1, \lambda_2, \lambda_3$ (*i.e.*, the principal values of \mathbf{U}), so that $W^{(r)}(\mathbf{F}) = \Phi^{(r)}(\lambda_1, \lambda_2, \lambda_3) = \Phi^{(r)}(\lambda_2, \lambda_1, \lambda_3)$, etc. A fairly general class of such stored-energy functions, which has been found to give good agreement with experimental data for rubberlike materials, was proposed by Ogden (1972). Although the methods developed in this paper will apply more generally, for simplicity, the attention here will be focused on *polyconvex* energy functions of the type

$$W(\mathbf{F}) = f(\mathbf{F}) + g(J), \quad (\text{A.6})$$

where $J = \det \mathbf{F} = \lambda_1 \lambda_2 \lambda_3$, and f and g are taken to be *convex* functions of the tensor \mathbf{F} and the scalar variable $J > 0$, respectively. A simple, special case of this general class of materials, which will be considered in some detail below is given by the *compressible* Neo-Hookean material with stored-energy function of the form:

$$W(\mathbf{F}) = \frac{\mu}{2} (\lambda_1^2 + \lambda_2^2 + \lambda_3^2 - 3) + \frac{\mu'}{2} (J - 1)^2 - \mu \ln J. \quad (\text{A.7})$$

where the parameters $\mu > 0$ and $\mu' > 0$ denote the standard Lamé moduli. Note that $W(\mathbf{F}) \sim (1/2)\mu'(\text{tr}\boldsymbol{\varepsilon})^2 + \mu\text{tr}\boldsymbol{\varepsilon}^2$, where $\boldsymbol{\varepsilon}$ is the infinitesimal strain tensor, as $\mathbf{F} \rightarrow \mathbf{I}$, so that the stored-energy function (A.7) linearizes properly. In addition, the limit as $\mu' \rightarrow \infty$ in relation (A.7) corresponds to incompressible behavior ($J \rightarrow 1$).

The objective of this work then becomes to obtain estimates for the effective stored-energy function \widetilde{W} of hyperelastic composites subjected to finite deformations. This is an extremely difficult problem, because it amounts to solving a set of highly nonlinear partial differential equations

with random coefficients. As a consequence, there are precious few *analytical* estimates for \widetilde{W} . Ogden (1978) noted that use of the trial field $\mathbf{F} = \overline{\mathbf{F}}$ in the definition (A.3) for \widetilde{W} leads to an upper bound analogous to the well-known Voigt upper bound in linear elasticity. Also, under appropriate hypotheses on W ensuring the existence of a principle of minimum complementary energy, Ogden (1978) also proposed a generalization of the Reuss lower bound. However, the required constitutive hypothesis is too strong to include materials such as the compressible Neo-Hookean material defined by relation (A.7). For this reason, Ponte Castañeda (1989) proposed an alternative generalization of the Reuss lower bound, exploiting the polyconvexity hypothesis. For polyconvex materials of the type (A.6), this lower bound takes the form:

$$\widetilde{W}(\overline{\mathbf{F}}) \geq \widetilde{W}_{PC}(\overline{\mathbf{F}}) \doteq (\overline{f^*})^*(\overline{\mathbf{F}}) + (\overline{g^*})^*(\det \overline{\mathbf{F}}). \quad (\text{A.8})$$

Thus, the bound \widetilde{W}_{PC} reduces to the polyconvex envelope (Dacorogna, 1989) of the function W , given by relation (A.6), when the special case of a homogeneous material is considered. Note that, due to the lack of convexity of the function W , this lower bound is much sharper (see Ponte Castañeda, 1989) than the bound that would be obtained by means of the standard Legendre-Fenchel transform applied directly to the function W , which would lead to a bound of the type $(\overline{W^*})^*(\overline{\mathbf{F}})$.

There are also numerous empirically based, and *ad hoc* estimates for various special cases, including the case of rigidly reinforced rubbers (see (Mullins and Tobin, 1965; Treloar, 1975; Meinecke and Taftaf, 1988; Govindjee and Simo, 1991; Bergström and Boyce, 1999)). Our aim here is to develop a general class of *analytical estimates* that are based on homogenization theory and that are applicable to large classes of composite systems, including rigidly reinforced rubbers, porous elastomers and other heterogeneous elastomeric systems, such as nematic elastomers and block copolymers. Such estimates should allow for the incorporation of statistical information beyond the phase volume fractions, thus allowing for a more precise characterization of the influence of microstructure on effective behavior. Some progress along these lines has been made recently (Ponte Castañeda and Tiberio, 2000; Lahellec *et al.*, 2004) with the extension of an earlier version of the “second-order” nonlinear homogenization technique (Ponte Castañeda, 1996) to finite elasticity.

A.2 The second-order variational procedure

Our proposal for generating homogenization estimates in finite elasticity is based on an appropriate extension of the “second-order” homogenization procedure that has been recently developed by Ponte Castañeda (2001; 2002a) in the context of nonlinear dielectrics and viscous composites with convex, nonlinear potentials. This new method is in turn a generalization of the “linear comparison” variational method of Ponte Castañeda (1991) in a way that incorporates many of the desirable features of an earlier version of the second-order method (Ponte Castañeda, 1996; Ponte Castañeda and Willis, 1999), including the fact that the estimates generated should be exact to second order in the heterogeneity contrast (Suquet and Ponte Castañeda, 1993). It is relevant to mention in this context that earlier works (e.g., Talbot & Willis, 1985; Ponte Castañeda 1991) delivered bounds that are exact *only to first order* in the contrast. Next we give a brief description of the proposed method.

Following (Ponte Castañeda, 1996), define a *comparison* linear “thermoelastic” composite with potential:

$$W_0(\mathbf{X}, \mathbf{F}) = \sum_{r=1}^N \chi^{(r)}(\mathbf{X}) W_0^{(r)}(\mathbf{F}), \quad (\text{A.9})$$

where the quadratic functions $W_0^{(r)}$ correspond to second-order Taylor approximations of the nonlinear stored-energy functions $W^{(r)}$ about certain uniform reference deformations $\mathbf{F}^{(r)}$:

$$W_0^{(r)}(\mathbf{F}) = W^{(r)}(\mathbf{F}^{(r)}) + \mathbf{S}^{(r)}(\mathbf{F}^{(r)}) \cdot (\mathbf{F} - \mathbf{F}^{(r)}) + \frac{1}{2}(\mathbf{F} - \mathbf{F}^{(r)}) \cdot \mathbf{L}_0^{(r)}(\mathbf{F} - \mathbf{F}^{(r)}). \quad (\text{A.10})$$

Here $\mathbf{S}^{(r)} = \partial W^{(r)} / \partial \mathbf{F}$, and $\mathbf{L}_0^{(r)}$ is a positive definite, constant tensor to be determined later. Then, $\mathbf{S} = \mathbf{S}^{(r)}(\mathbf{F}^{(r)}) + \mathbf{L}_0^{(r)}(\mathbf{F} - \mathbf{F}^{(r)})$ is the stress associated with \mathbf{F} in phase r of the linear comparison composite. Note that the nonlinear stored-energy functions $W^{(r)}$ can then be *approximated* as:

$$W^{(r)}(\mathbf{F}) = W_0^{(r)}(\mathbf{F}) + V^{(r)}(\mathbf{F}^{(r)}, \mathbf{L}_0^{(r)}). \quad (\text{A.11})$$

where the $V^{(r)}$ are “error” functions defined by:

$$V^{(r)}(\mathbf{F}^{(r)}, \mathbf{L}_0^{(r)}) = \underset{\hat{\mathbf{F}}^{(r)}}{\text{stat}} \left[W^{(r)}(\hat{\mathbf{F}}^{(r)}) - W_0^{(r)}(\hat{\mathbf{F}}^{(r)}) \right]. \quad (\text{A.12})$$

In these expressions, the optimization operation *stat* with respect to a variable means differentiation with respect to that variable and setting the result equal to zero to generate an expression for the optimal value of the variable.

For later use, let

$$\widetilde{W}_0(\overline{\mathbf{F}}; \mathbf{F}^{(s)}, \mathbf{L}_0^{(s)}) = \min_{\mathbf{F} \in \mathcal{K}} \langle W_0(\mathbf{X}, \mathbf{F}) \rangle = \min_{\mathbf{F} \in \mathcal{K}} \sum_{r=1}^N c^{(r)} \langle W_0^{(r)}(\mathbf{F}) \rangle^{(r)} \quad (\text{A.13})$$

be the effective free-energy density associated with the *fictitious* linear thermoelastic composite, which has the same microstructure as the original nonlinear elastic composite. To see this more explicitly (see, for example, Willis, 1981), note that the Euler-Lagrange equations of the variational problem for \widetilde{W}_0 are

$$\nabla \cdot (\mathbf{L}_0 \nabla \mathbf{x} - \mathbf{T}) = \mathbf{0} \quad \text{in } \Omega, \quad \mathbf{x} = \overline{\mathbf{F}} \mathbf{X} \quad \text{on } \partial\Omega, \quad (\text{A.14})$$

where \mathbf{L}_0 is the elasticity tensor of the linear comparison composite with free energy (A.10), \mathbf{T} denotes a suitably defined thermal stress tensor, and where the temperature and heat capacity at constant strain are taken to be unity and zero, respectively. Note that this fictitious linear thermoelastic problem is one involving, in general, non-symmetric “stress” and “strain” measures, so that suitable generalizations of the classical thermoelastic analyses are required (Ponte Castañeda and Tiberio, 2000). In particular, estimates of the self-consistent and Hashin-Shtrikman types may be obtained by appropriate extension of the corresponding methods for linear-elastic composites (Laws, 1973; Willis, 1981).

Using relations (A.11), averaging the resulting expression for W over Ω_0 , minimizing over \mathbf{F} in \mathcal{K} and optimizing over tensors $\mathbf{F}^{(s)}$ and $\mathbf{L}_0^{(s)}$, it follows that (Ponte Castañeda, 2002a):

$$\widetilde{W}(\overline{\mathbf{F}}) = \operatorname{stat}_{\mathbf{F}^{(s)}, \mathbf{L}_0^{(s)}} \left\{ \widetilde{W}_0(\overline{\mathbf{F}}; \mathbf{F}^{(s)}, \mathbf{L}_0^{(s)}) + \sum_{r=1}^N c^{(r)} V^{(r)}(\mathbf{F}^{(r)}, \mathbf{L}_0^{(r)}) \right\}, \quad (\text{A.15})$$

where the $V^{(r)}$ and \widetilde{W}_0 are defined by relations (A.12) and (A.13), respectively. Here it has been assumed that the resulting optimal values of $\mathbf{F}^{(s)}$ and $\mathbf{L}_0^{(s)}$ are such that the linear comparisons problem (A.13) is well posed.

It is easy to verify that formally setting the tensors $\mathbf{F}^{(s)}$ identically equal to zero leads to estimates of the type first proposed in (Ponte Castañeda, 1991) for materials with convex energy functions. In order to do better, it is necessary to consider the definition of the functions $V^{(r)}$ above in more detail. First note that optimizing with respect to the variables $\widehat{\mathbf{F}}^{(r)}$ in (A.12) leads to the relations:

$$\mathbf{S}^{(r)}(\widehat{\mathbf{F}}^{(r)}) - \mathbf{S}^{(r)}(\mathbf{F}^{(r)}) = \mathbf{L}_0^{(r)}(\widehat{\mathbf{F}}^{(r)} - \mathbf{F}^{(r)}), \quad (\text{A.16})$$

where again sufficient smoothness has been assumed for the $W^{(r)}$. This condition has a nice physical interpretation as depicted in the one-dimensional sketch shown in Figure A.1a: it corresponds to

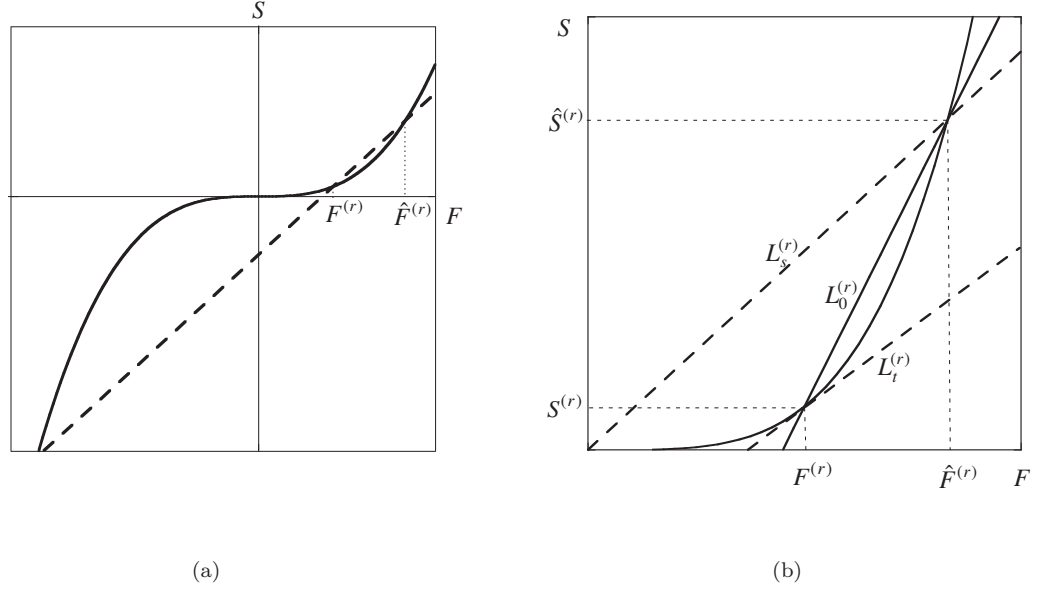


Figure A.1: (a) Sketch of the *nonlinear* constitutive relation (continuous stress S vs. stretch F curve) and of its *linear approximation* (dashed line). (b) Schematic comparison of the “secant” ($\mathbf{L}_s^{(r)}$), “tangent” ($\mathbf{L}_t^{(r)}$) and new “generalized secant” ($\mathbf{L}_0^{(r)}$) approximations.

a *linear approximation* to the nonlinear constitutive relation for the elastic material in phase r interpolating between the deformations $\mathbf{F}^{(r)}$ and $\hat{\mathbf{F}}^{(r)}$. Note that this condition does not have a unique solution, and appropriate choices must be made for the relevant variables. Indeed, as illustrated in Figure A.1a, there are 3 stationary points (the 3 points where the dashed, straight line intersects the continuous nonlinear curve), which lead to three different types of approximations. Thus, as illustrated in Figure A.1b, the “secant” approximation is obtained by setting $\mathbf{F}^{(r)} = \mathbf{0}$, while the “tangent” approximation is obtained by letting $\hat{\mathbf{F}}^{(r)}$ tend to $\mathbf{F}^{(r)}$. On the other hand, when $\hat{\mathbf{F}}^{(r)} \neq \mathbf{F}^{(r)}$ and $\mathbf{F}^{(r)} \neq \mathbf{0}$, a new type of approximation is obtained, which has been referred to (Ponte Castañeda, 2002a) as a “generalized secant” approximation.

Under the assumption that $\hat{\mathbf{F}}^{(r)} \neq \mathbf{F}^{(r)}$, consideration of the optimality conditions with respect to the variables $\mathbf{F}^{(r)}$ and $\mathbf{L}_0^{(r)}$ in expression (A.15) formally leads to the following prescriptions:

$$\mathbf{F}^{(r)} = \langle \mathbf{F} \rangle^{(r)} \doteq \bar{\mathbf{F}}^{(r)}, \quad (\text{A.17})$$

and

$$(\hat{\mathbf{F}}^{(r)} - \bar{\mathbf{F}}^{(r)}) \otimes (\hat{\mathbf{F}}^{(r)} - \bar{\mathbf{F}}^{(r)}) = \langle (\mathbf{F} - \bar{\mathbf{F}}^{(r)}) \otimes (\mathbf{F} - \bar{\mathbf{F}}^{(r)}) \rangle^{(r)} \doteq \mathbf{C}_{\mathbf{F}}^{(r)}, \quad (\text{A.18})$$

where use has been made of the relation:

$$\mathbf{C}_{\mathbf{F}}^{(r)} = \frac{2}{c^{(r)}} \frac{\partial \widetilde{W}_0}{\partial \mathbf{L}_0^{(r)}}. \quad (\text{A.19})$$

In the first relation, the symbol $\overline{\mathbf{F}}^{(r)}$ has been used to denote the phase averages of the deformation field $\langle \mathbf{F} \rangle^{(r)}$. Thus, the reference deformations $\mathbf{F}^{(r)}$ have been identified with the *phase averages* or *first moments* of the deformation field $\overline{\mathbf{F}}^{(r)}$. In the second relation, the symbol $\mathbf{C}_{\mathbf{F}}^{(r)}$ have been introduced to denote the *covariance tensor* of the *deformation fluctuations* in phase r (e.g., Bobeth & Diener, 1987). Therefore, the variables $\hat{\mathbf{F}}^{(r)}$ have been associated with the second moments of the deformation field in the phases.

In connection with the above prescriptions, it is necessary to make the following clarifications. Concerning the prescription (A.17), it should be noted that relation (A.17) only makes stationary with respect to $\mathbf{F}^{(r)}$ the terms arising from the linear comparison energy \widetilde{W}_0 . In other words, there are additional terms arising from the functions $V^{(r)}$, which have been neglected, for simplicity. Concerning the prescription (A.18), it needs to be emphasized that it is not possible to satisfy conditions (A.18) in full generality. This is due to the fact that the left-hand of relation (A.18) is a fourth-order tensor of rank 1, whereas the right-hand side is generally of full rank. This means that only certain components (or traces) of these expressions can be enforced. This point will be discussed in more detail in the context of the specific examples considered in the applications section. Generally speaking, the optimal choice of the variables $\mathbf{F}^{(r)}$ and $\mathbf{L}_0^{(r)}$ is still an open problem. However, it is known at least in the context of plasticity (Ponte Castañeda, 2002b) that conditions (A.17) and appropriate traces of (A.18) lead to accurate estimates for the effective behavior. This suggests that even if the prescriptions (A.17) and (A.18) are not strictly optimal, they are still probably not far from optimal.

It follows from the above prescriptions that the secant-type condition (A.16) specializes to:

$$\frac{\partial W^{(r)}}{\partial \mathbf{F}}(\hat{\mathbf{F}}^{(r)}) - \frac{\partial W^{(r)}}{\partial \mathbf{F}}(\overline{\mathbf{F}}^{(r)}) = \mathbf{L}_0^{(r)}(\hat{\mathbf{F}}^{(r)} - \overline{\mathbf{F}}^{(r)}), \quad (\text{A.20})$$

and that the expression (A.15) for the effective potential of the hyperelastic composite reduces to:

$$\widetilde{W}(\overline{\mathbf{F}}) = \sum_{r=1}^N c^{(r)} \left[W^{(r)}(\hat{\mathbf{F}}^{(r)}) - \frac{\partial W^{(r)}}{\partial \mathbf{F}}(\overline{\mathbf{F}}^{(r)}) \cdot (\hat{\mathbf{F}}^{(r)} - \overline{\mathbf{F}}^{(r)}) \right]. \quad (\text{A.21})$$

In summary, the estimate (A.21) has been generated. Like the earlier “second-order” estimates (Ponte Castañeda, 1996), it depends on the phase averages $\overline{\mathbf{F}}^{(r)}$ of the deformation field

in a suitably defined linear “thermoelastic” comparison composite, subject to the self-consistent prescription (A.17) on the reference variables $\mathbf{F}^{(r)}$. However, the new prescription (A.20) for the comparison moduli $\mathbf{L}_0^{(r)}$ is different from earlier *ad hoc* choices, being somewhat intermediate between the “secant” (Ponte Castañeda, 1991) and the “tangent” conditions (Ponte Castañeda, 1996). In addition, the new estimate depends directly on the variables $\hat{\mathbf{F}}^{(r)}$, which, in turn, depend on (appropriate traces of) the “second moments” of the *fluctuations* $\mathbf{C}_{\mathbf{F}}^{(r)}$ of the deformation field in the phases of the linear comparison composite, as specified by the prescription (A.18). Furthermore, like the earlier “second-order” estimates, they are exact to second-order in the heterogeneity contrast (Suquet and Ponte Castañeda, 1993).

It is remarked finally that the linear comparison problem (A.13) that needs to be considered for the determination of the phase averages $\bar{\mathbf{F}}^{(r)}$ and fluctuations $\mathbf{C}_{\mathbf{F}}^{(r)}$ needed in expression (A.21) for \widetilde{W} is precisely the same that was considered by Ponte Castañeda and Tiberio, 2000 in the earlier version of the second-order method. These authors provided expressions of the Hashin-Shtrikman and self-consistent types (Willis, 1981) for the average deformations $\bar{\mathbf{F}}^{(r)}$ in the generalized N -phase “thermoelastic” composites (A.10), from which corresponding estimates may be generated for the corresponding effective stored-energy functions \widetilde{W}_0 , and, in turn, for the fluctuations $\mathbf{C}_{\mathbf{F}}^{(r)}$ via (A.19). For brevity, the relevant general expressions will not be repeated here, and only the appropriate specialized versions of the results will be quoted in the applications sections for the special case of rigidly reinforced systems.

A.3 Application to particle-reinforced elastomers

The second-order estimate (A.21) for the effective stored-energy function of hyperelastic composites applies for N -phase systems, including, with a suitable reinterpretation, polycrystalline aggregates of anisotropic phases. In this section, the special case of isotropic rigidly reinforced rubbers is considered. This case has already been considered using the earlier version of the second-order method (Ponte Castañeda and Tiberio, 2000) and these earlier results will be used here as a reference. Thus, the focus will be on two-phase composites consisting of rigid, spherical inclusions distributed isotropically with volume fraction $c^{(2)} = c$ in a hyperelastic matrix with energy function $W^{(1)} = W$, such that the composite is statistically isotropic in the undeformed configuration.

Because of the objectivity of \widetilde{W} , it suffices to consider macroscopic stretch loading histories

(*i.e.*, $\bar{\mathbf{F}} = \bar{\mathbf{U}}$; $\bar{\mathbf{R}} = \mathbf{I}$). Because of the spherical (isotropic) symmetry of the reinforcement and its distribution, it is expected (Ponte Castañeda and Tiberio, 2000) that the average rotation tensor of the rigid phase is the identity, so that the average deformation gradient in the inclusion phase is also equal to the identity (*i.e.*, $\bar{\mathbf{F}}^{(2)} = \mathbf{I}$). It then follows trivially that the average deformation gradient in the hyperelastic phase is given by:

$$\bar{\mathbf{F}}^{(1)} = \frac{1}{1-c} (\bar{\mathbf{U}} - c\mathbf{I}). \quad (\text{A.22})$$

Note that $\bar{\mathbf{F}}^{(1)} = \bar{\mathbf{U}}^{(1)}$, so it is convenient to define the principal stretches associated with $\bar{\mathbf{U}}^{(1)}$ via $\bar{\lambda}_i^{(1)} = (\bar{\lambda}_i - c)/(1-c)$ ($i = 1, 2, 3$), where $\bar{\lambda}_i$ ($i = 1, 2, 3$) are the principal stretches associated with $\bar{\mathbf{U}}$. The above result would still be expected to apply, up to the onset of some possible instability, even if the shape or distribution (see Ponte Castañeda and Willis, 1995) of the rigid phase were not spherical, provided that their symmetry axes were aligned with the principal directions of $\bar{\mathbf{U}}$. Otherwise, the reinforcement would undergo an average rigid rotation $\bar{\mathbf{R}}^{(2)}$, which would have to be determined from the full homogenization procedure described in the earlier sections of this paper. This would, of course, make the treatment of such cases more complicated. However, such more general analyses should lead to the result that $\bar{\mathbf{F}}^{(2)} = \bar{\mathbf{R}}^{(2)} = \mathbf{I}$ for the special case considered here where the reinforcement is isotropically distributed. Lahellec (2004) has pursued this more general approach in the analogous context of a two-phase, periodic composite loaded symmetrically. (The case of rigid fibers was approximated by taking the contrast to be sufficiently large.)

A.3.1 Lower bounds

Before proceeding with the second-order estimates, the above-mentioned “polyconvex” lower bounds of Ponte Castañeda (1989) will be specialized here for later reference. Note that the classical Voigt upper bound is infinite in this case. It can be shown that specialization of the bound (A.8) to an isotropic rigidly reinforced elastomer with a compressible Neo-Hookean matrix (A.7) leads to:

$$\widetilde{W}_{PC}(\bar{\mathbf{U}}) = (1-c) \left[\frac{\mu}{2} (\bar{\mathbf{F}}^{(1)} \cdot \bar{\mathbf{F}}^{(1)} - 3) + \frac{\mu'}{2} \left(\frac{\bar{J}-1}{1-c} \right)^2 - \mu \ln \left(\frac{\bar{J}-c}{1-c} \right) \right], \quad (\text{A.23})$$

where μ, μ' are the Lamé moduli of the elastic phase, $\bar{\mathbf{F}}^{(1)}$ is given by (A.22), and $\bar{J} = \bar{\lambda}_1 \bar{\lambda}_2 \bar{\lambda}_3$. In the derivation of this result, it has been assumed that the stored energy $W^{(2)}$ of the rigid phase is infinite unless $\bar{\mathbf{F}}^{(2)} = \mathbf{I}$, in which case it is zero. This assumption is consistent with the hypothesis that due to the isotropy of the rigid particles and their distribution, the particles do not rotate.

In the incompressible limit, $\mu' \rightarrow \infty$ the above lower bound reduces to $\widetilde{W}_{PC}^I(\overline{\mathbf{U}}) = \widetilde{\Phi}_{PC}^I(\overline{\lambda}_1, \overline{\lambda}_2, \overline{\lambda}_3)$, where

$$\widetilde{\Phi}_{PC}^I(\overline{\lambda}_1, \overline{\lambda}_2, \overline{\lambda}_3) = (1-c) \frac{\mu}{2} \left[\left(\frac{\overline{\lambda}_1 - c}{1-c} \right)^2 + \left(\frac{\overline{\lambda}_2 - c}{1-c} \right)^2 + \left(\frac{\overline{\lambda}_3 - c}{1-c} \right)^2 - 3 \right], \quad (\text{A.24})$$

whenever $\overline{J} = \overline{\lambda}_1 \overline{\lambda}_2 \overline{\lambda}_3 = 1$ (and ∞ otherwise). Note that this bound is, therefore, consistent with the ‘‘exact’’ incompressibility constraint

$$g_E(\overline{\lambda}_1, \overline{\lambda}_2, \overline{\lambda}_3) = \overline{\lambda}_1 \overline{\lambda}_2 \overline{\lambda}_3 - 1 = 0, \quad (\text{A.25})$$

expected on physical grounds (i.e., a composite with an incompressible matrix and rigid inclusions should be incompressible). However, this bound does not linearize properly, i.e., it does not reduce to the classical Reuss lower bound for infinitesimal deformations. In spite of this fact, this bound will prove to be useful below in checking the validity of the new second-order estimates to be developed next.

A.3.2 Second-order estimates

For the above-defined class of rigidly reinforced elastomers, the second-order estimate (A.21) reduces to

$$\widetilde{W}(\overline{\mathbf{U}}) = (1-c) \left[W(\hat{\mathbf{F}}^{(1)}) - \frac{\partial W}{\partial \mathbf{F}}(\overline{\mathbf{F}}^{(1)}) \cdot (\hat{\mathbf{F}}^{(1)} - \overline{\mathbf{F}}^{(1)}) \right], \quad (\text{A.26})$$

where $\overline{\mathbf{F}}^{(1)}$ has already been specified in (A.22). It remains to determine the variable $\hat{\mathbf{F}}^{(1)}$, as well as the modulus tensor \mathbf{L}_0 of the matrix phase in the linear comparison composite, which can be achieved by means of the relation

$$\frac{\partial W}{\partial \mathbf{F}}(\hat{\mathbf{F}}^{(1)}) - \frac{\partial W}{\partial \mathbf{F}}(\overline{\mathbf{F}}^{(1)}) = \mathbf{L}_0(\hat{\mathbf{F}}^{(1)} - \overline{\mathbf{F}}^{(1)}), \quad (\text{A.27})$$

together with suitably chosen traces of the relation

$$(\hat{\mathbf{F}}^{(1)} - \overline{\mathbf{F}}^{(1)}) \otimes (\hat{\mathbf{F}}^{(1)} - \overline{\mathbf{F}}^{(1)}) = \mathbf{C}_{\mathbf{F}}^{(1)}. \quad (\text{A.28})$$

In this last relation,

$$\mathbf{C}_{\mathbf{F}}^{(1)} = \frac{2}{1-c} \frac{\partial \widetilde{W}_0}{\partial \mathbf{L}_0} \quad (\text{A.29})$$

is the covariance of the fluctuations in the matrix phase of the linear comparison composite, with effective stored energy function given by:

$$\widetilde{W}_0(\overline{\mathbf{U}}) = (1-c)W(\overline{\mathbf{F}}^{(1)}) + \frac{1}{2}(\overline{\mathbf{U}} - \mathbf{I}) \cdot \left(\widetilde{\mathbf{L}}_0 - \frac{1}{1-c} \mathbf{L}_0 \right) (\overline{\mathbf{U}} - \mathbf{I}). \quad (\text{A.30})$$

This last relation has been generated by making use of a generalization of Levin’s relation (Levin, 1967) for two-phase *thermoelastic* composites (see also (Ponte Castañeda and Tiberio, 2000)), letting phase 2 have the energy function:

$$W^{(2)}(\mathbf{F}) = \frac{1}{2}\mu_0^{(2)}(\mathbf{F} - \mathbf{I}) \cdot (\mathbf{F} - \mathbf{I}), \tag{A.31}$$

and taking the limit as $\mu_0^{(2)} \rightarrow \infty$ in the free energy expression (A.13). Again, note that the above form for $W^{(2)}$ is consistent with the requirement that $\overline{\mathbf{F}}^{(2)}$ should tend to \mathbf{I} in the limit as $\mu_0^{(2)} \rightarrow \infty$. In expression (A.30), $\widetilde{\mathbf{L}}_0$ thus denotes the effective modulus tensor of a two-phase, *linear-elastic* comparison composite consisting of a distribution of rigid inclusions with volume fraction c in a matrix with elastic modulus \mathbf{L}_0 and the *same* microstructure as the nonlinear elastic composite (in its undeformed configuration).

It is emphasized that the above estimate for \widetilde{W} is actually valid for *any* estimate for the effective modulus tensor $\widetilde{\mathbf{L}}_0$ of the linear comparison composite. For example, use can be made of the following *isotropic* Hashin-Shtrikman and self-consistent estimates for $\widetilde{\mathbf{L}}_0$:

$$\begin{cases} \mathbf{L}_0 + \frac{c}{1-c}\mathbf{P}^{-1} & HS, \\ \mathbf{L}_0 + c\widetilde{\mathbf{P}}^{-1} & SC. \end{cases} \tag{A.32}$$

where \mathbf{P} and $\widetilde{\mathbf{P}}$ are obtained by setting $\mathbf{L}^{(0)}$ equal to \mathbf{L}_0 and $\widetilde{\mathbf{L}}_0$, respectively, in the expression:

$$\mathbf{P}^{(0)} = \frac{1}{4\pi} \int_{|\boldsymbol{\xi}|=1} \mathbf{H}^{(0)}(\boldsymbol{\xi}) dS, \tag{A.33}$$

with $K_{ik}^{(0)} = L_{ijkh}^{(0)}\xi_j\xi_h$, $\mathbf{N}^{(0)} = \mathbf{K}^{(0)-1}$, $H_{ijkh}^{(0)}(\boldsymbol{\xi}) = N_{ik}^{(0)}\xi_j\xi_h$.

While fairly explicit, the above results, in general, require the computation of the tensor \mathbf{P} (or $\widetilde{\mathbf{P}}$), which depends on the anisotropy of \mathbf{L}_0 (or $\widetilde{\mathbf{L}}_0$). In turn, the anisotropy of these tensors depends on the functional form of the stored-energy function W and the loading configuration, as determined by $\overline{\mathbf{F}} = \overline{\mathbf{U}}$. In addition, the derivatives of the tensor \mathbf{P} with respect to \mathbf{L}_0 are needed in the characterization of the fluctuations $\mathbf{C}_{\mathbf{F}}^{(1)}$, which requires further computations. In this work, which presents the first application of the (improved version of the) second-order method to finite elasticity, a simple, yet illustrative example, where the computation of the \mathbf{P} tensor and its derivatives is simple, will be worked out in detail. Thus, estimates of the Hashin-Shtrikman type will be derived for *plane strain* loading of a *two-dimensional* fiber-reinforced composite. More general situations, including *uniaxial* and *shear* loading of *three-dimensional* particle-reinforced composites, and types of estimates will be presented elsewhere.

However, before specializing to the two-dimensional fiber-reinforced composite, it is noted here that when used together with the Reuss estimate for the effective modulus tensor ($\tilde{\mathbf{L}}_0 = (1 - c)^{-1}\mathbf{L}_0$), the second-order method yields the explicit result:

$$\tilde{W}(\bar{\mathbf{U}}) = (1 - c)W \left[\frac{1}{1 - c} (\bar{\mathbf{U}} - c\mathbf{I}) \right] \doteq \tilde{W}_R(\bar{\mathbf{U}}). \quad (\text{A.34})$$

This estimate agrees exactly with the corresponding estimate generated using the earlier version of the second-order method without fluctuations (Ponte Castañeda and Tiberio, 2000). This is a direct consequence of the fact that the fluctuations in the Reuss theory are identically zero, so that there are no differences between the earlier and newer versions of the second-order theory. As already known (Ponte Castañeda and Tiberio, 2000), the Reuss estimate (A.34) is not necessarily a lower bound, except for small deformations, when the above result reduces (exactly to second order in the infinitesimal strain) to the classical Reuss lower bound. It is interesting to note that the estimate (A.34) was first obtained by Govindjee and Simo (1991) by different means.

When the Reuss estimate (A.34) is specialized to a *compressible* Neo-Hookean matrix phase with W given by the relation (A.7), it specializes to:

$$\tilde{W}_R(\bar{\mathbf{U}}) = (1 - c) \left[\frac{\mu}{2} (\bar{\mathbf{F}}^{(1)} \cdot \bar{\mathbf{F}}^{(1)} - 3) + \frac{\mu'}{2} (\bar{J}^{(1)} - 1)^2 - \mu \ln (\bar{J}^{(1)}) \right], \quad (\text{A.35})$$

where μ, μ' are the Lamé moduli of the elastic phase, $\bar{\mathbf{F}}^{(1)}$ is given by (A.22), and $\bar{J}^{(1)} = \bar{\lambda}_1^{(1)} \bar{\lambda}_2^{(1)} \bar{\lambda}_3^{(1)}$ (with $\bar{\lambda}_i^{(1)} = (\bar{\lambda}_i - c)/(1 - c)$).

It is interesting to remark that the Reuss estimate (A.35) differs from the lower bound (A.23) only through the terms that depend on the determinant. It can be shown that this estimate *violates* the bound (A.23) for certain loadings. For example, for loadings such that $\bar{J}^{(1)} = 1$, it can be verified that the Reuss estimate (A.35) actually lies below the bound (A.23).

From the result (A.35) it is possible to generate the corresponding result for an *incompressible* Neo-Hookean matrix phase by considering the limit as μ' tends to infinity. The result may be written in the form $\tilde{W}_R^I(\bar{\mathbf{U}}) = \tilde{\Phi}_R^I(\bar{\lambda}_1, \bar{\lambda}_2, \bar{\lambda}_3)$, where:

$$\tilde{\Phi}_R^I(\bar{\lambda}_1, \bar{\lambda}_2, \bar{\lambda}_3) = (1 - c) \frac{\mu}{2} \left[\left(\frac{\bar{\lambda}_1 - c}{1 - c} \right)^2 + \left(\frac{\bar{\lambda}_2 - c}{1 - c} \right)^2 + \left(\frac{\bar{\lambda}_3 - c}{1 - c} \right)^2 - 3 \right]. \quad (\text{A.36})$$

In this expression, the principal stretches $\bar{\lambda}_i$ are required to satisfy the “approximate” incompressibility constraint $\bar{J}^{(1)} = 1$, which can be written as

$$g_A(\bar{\lambda}_1, \bar{\lambda}_2, \bar{\lambda}_3) = \left(\frac{\bar{\lambda}_1 - c}{1 - c} \right) \left(\frac{\bar{\lambda}_2 - c}{1 - c} \right) \left(\frac{\bar{\lambda}_3 - c}{1 - c} \right) - 1 = 0. \quad (\text{A.37})$$

While exact to second-order in the infinitesimal strain, this “approximate” macroscopic incompressibility constraint is not identical to the “exact” constraint (A.25). Note that, because of this, the incompressible Reuss estimate (A.36) is really different from the incompressible polyconvex bound (A.24).

Thus, it appears that at least for the Reuss-type estimate, where the fluctuations are ignored, the second-order method yields predictions that are inaccurate in the incompressible limit and have been shown to violate a rigorous bound more generally. Within the context of the *earlier* second-order theory, it was found that even for estimates of the Hashin-Shtrikman type, the incompressible limit was troublesome, and direct application of the theory led to the same “approximate” macroscopic incompressibility constraint (A.37). For this reason, an “alternate” approach (see also (Lahellec *et al.*, 2004) for yet a third approach) was proposed in reference (Ponte Castañeda and Tiberio, 2000) to avoid this limitation of the earlier version of the second-order theory. This approach consisted in evaluating the compressible term proportional to μ' directly. For later reference, the result of this “alternate” approach is recalled here:

$$\tilde{\Phi}_R^A(\bar{\lambda}_1, \bar{\lambda}_2, \bar{\lambda}_3) = (1-c)\frac{\mu}{2} \left[\left(\frac{\bar{\lambda}_1 - c}{1-c} \right)^2 + \left(\frac{\bar{\lambda}_2 - c}{1-c} \right)^2 + \left(\frac{\bar{\lambda}_3 - c}{1-c} \right)^2 - 3 - 2 \ln \left(\bar{J}^{(1)} \right) \right], \quad (\text{A.38})$$

where the logarithmic term arises because the exact constraint (A.25) must be enforced (and therefore $\bar{J}^{(1)} = (\bar{\lambda}_1 - c)(\bar{\lambda}_2 - c)(\bar{\lambda}_3 - c)/(1-c)^3$ is not necessarily equal to 1).

Naturally, the hope is that the *new* version of the second-order theory, incorporating field fluctuations, should lead to better predictions, which should not only yield the “exact” incompressibility constraint in the limit of an incompressible matrix phase, but should also *not* violate any known bounds. This expectation will be explored in the next section in the context of the fiber-reinforced example mentioned earlier.

A.4 Plane strain loading of transversely isotropic, fiber-reinforced Neo-Hookean composites

A.4.1 Formulation

In this section, plane strain deformations of a fiber-reinforced composite are considered where the rigid fibers, which are perpendicular to the plane of the deformation, are aligned in the x_3 direction. The distribution of the reinforcement in the transverse plane is isotropic, so that the hypotheses

that were made in the derivation of relation (A.26) for \widetilde{W} carry over to this special case, with an appropriate (two-dimensional) modification of the relevant \mathbf{P} tensor in the relevant expressions for $\widetilde{\mathbf{L}}_0$. Here, for simplicity, estimates of the Hashin-Shtrikman (HS) type (A.32)₁ will be determined for the special case of a Neo-Hookean matrix phase with stored-energy function given by (A.7). The applied deformation $\overline{\mathbf{F}} = \overline{\mathbf{U}}$ in this case is entirely characterized by the two in-plane principal stretches $\bar{\lambda}_1$ and $\bar{\lambda}_2$, the out-of-plane principal stretch $\bar{\lambda}_3$ being identically 1.

Because of the transverse isotropy of the microstructure and the orthogonal symmetry of the loading condition, it is reasonable to assume that the linear comparison problem of relevance here will also exhibit orthotropic symmetry, with the symmetry axes aligned with the applied loading $\overline{\mathbf{F}} = \overline{\mathbf{U}}$. For plane strain conditions, it suffices to consider the in-plane components of a general deformation tensor \mathbf{F} relative to the symmetry axes, which for convenience will be written as a vector in \mathcal{R}^4 :

$$[F_{11} \quad F_{22} \quad F_{12} \quad F_{21}]^T. \quad (\text{A.39})$$

The modulus tensor \mathbf{L}_0 of the linear comparison composite, which is expected to also exhibit orthotropic symmetry, will correspondingly be expressed as a matrix in $\mathcal{R}^{4 \times 4}$:

$$\begin{bmatrix} L_{1111}^* & L_{1122} & 0 & 0 \\ L_{1122}^* & L_{2222}^* & 0 & 0 \\ 0 & 0 & L_{1212}^* & L_{1221}^* \\ 0 & 0 & L_{1221}^* & L_{2121}^* \end{bmatrix}. \quad (\text{A.40})$$

where the diagonal symmetry of the tensor \mathbf{L}_0 has been used (i.e., $L_{ijkl} = L_{klij}$).

Now, given the above assumptions, the tensor $\hat{\mathbf{F}}^{(1)}$ is seen to have at most 4 independent components ($\hat{F}_{11}^{(1)}, \hat{F}_{22}^{(1)}, \hat{F}_{12}^{(1)}, \hat{F}_{21}^{(1)}$), which must be extracted from relation (A.28). This suggests that the tensor \mathbf{L}_0 should have at most 4 independent components, with respect to which \widetilde{W}_0 should be differentiated to generate 4 relations for the 4 components of $\hat{\mathbf{F}}^{(1)}$ using relation (A.29). Carrying this program out would, in effect, fix the traces of relation (A.28) to be considered. At the present time, it is not clear what the best choice for the components of \mathbf{L}_0 (and, therefore, for the traces of (A.28)) should be. Here, use will be made of the following prescriptions:

$$L_{1212} = L_{2121}, \quad \text{and} \quad L_{1221} + L_{1122} = \sqrt{(L_{1111} - L_{1212})(L_{2222} - L_{1212})}, \quad (\text{A.41})$$

which reduce the components of the \mathbf{L}_0 to only 4 independent ones ($L_{1111}, L_{2222}, L_{1122}, L_{1212}$). The motivations for these choices are: (i) they are consistent with those satisfied by the components of

the tangent modulus of a Neo-Hookean material, expressed relative to the symmetry axes; and (ii) they simplify considerably the expressions for the tensor \mathbf{P} (in fact, they lead to simple analytical results for all components, which are spelled out in Appendix A).

With these additional hypotheses, the equations (A.28) to (A.30), together with equations (A.32)₁ for the Hashin-Shtrikman estimate for $\tilde{\mathbf{L}}_0$, can be used to generate 4 equations for the 4 components of $\hat{\mathbf{F}}^{(1)}$, which are of the form:

$$\begin{aligned} \left(\hat{F}_{11}^{(1)} - \bar{F}_{11}^{(1)}\right)^2 + 2f_1 \hat{F}_{12}^{(1)} \hat{F}_{21}^{(1)} &= k_1 \\ \left(\hat{F}_{22}^{(1)} - \bar{F}_{22}^{(1)}\right)^2 + 2f_2 \hat{F}_{12}^{(1)} \hat{F}_{21}^{(1)} &= k_2 \\ \left(\hat{F}_{12}^{(1)}\right)^2 + \left(\hat{F}_{21}^{(1)}\right)^2 + 2f_3 \hat{F}_{12}^{(1)} \hat{F}_{21}^{(1)} &= k_3 \\ \left(\hat{F}_{11}^{(1)} - \bar{F}_{11}^{(1)}\right) \left(\hat{F}_{22}^{(1)} - \bar{F}_{22}^{(1)}\right) - \hat{F}_{12}^{(1)} \hat{F}_{21}^{(1)} &= k_4, \end{aligned} \quad (\text{A.42})$$

where $f_1, f_2, f_3, k_1, k_2, k_3, k_4$ are functions of the components of \mathbf{L}_0 (or, more precisely, of the 3 ratios L_{1111}/L_{2222} , L_{1122}/L_{2222} , and L_{1212}/L_{2222}), as well as of the deformation $\bar{\mathbf{F}}$ and the fiber concentration c . These equations can be shown to have only two distinct solutions for $\hat{F}_{11}^{(1)}$ and $\hat{F}_{22}^{(1)}$, in terms of which $\hat{F}_{12}^{(1)}$ and $\hat{F}_{21}^{(1)}$ may be computed. Note that there are 4 possible solutions for these last two variables (this is because only the combinations $\hat{F}_{12}^{(1)} \hat{F}_{21}^{(1)}$ and $\left(\hat{F}_{12}^{(1)}\right)^2 + \left(\hat{F}_{21}^{(1)}\right)^2$ can be determined uniquely from these equations), but for a given root for $\hat{F}_{11}^{(1)}$ and $\hat{F}_{22}^{(1)}$, they all give the same predictions for the energy, so that they are all essentially identical. For completeness, it is noted that the two roots for $\hat{F}_{11}^{(1)}$ and $\hat{F}_{22}^{(1)}$ are given by:

$$\hat{F}_{11}^{(1)} - \bar{F}_{11}^{(1)} = \pm \frac{2f_1 k_4 + k_1}{\sqrt{4f_1 2k_2 + 4f_1 k_4 + k_1}}, \quad \hat{F}_{22}^{(1)} - \bar{F}_{22}^{(1)} = \pm \frac{2f_1 k_2 + k_4}{\sqrt{4f_1 2k_2 + 4f_1 k_4 + k_1}}, \quad (\text{A.43})$$

where it is emphasized that the positive (and negative) signs in the roots for $\hat{F}_{11}^{(1)}$ and $\hat{F}_{22}^{(1)}$ go together.

Finally, for each of the two essentially distinct roots for the components of $\hat{\mathbf{F}}^{(1)}$ in terms of the 4 independent components of \mathbf{L}_0 , two sets of 4 additional equations are generated for L_{1111} , L_{2222} , L_{1122} , and L_{1212} from the generalized secant conditions (A.27). Now, for the particular case of the Neo-Hookean potential (A.7), one of these equations can be solved exactly for L_{1212} , giving the result $L_{1212} = \mu$. The remaining 3 equations must be solved numerically. Having computed the values of all the components of \mathbf{L}_0 for a given fiber volume fraction c , given material parameters (μ and μ'), and given loading ($\bar{\lambda}_1$ and $\bar{\lambda}_2$), the values of the components of $\hat{\mathbf{F}}^{(1)}$ can be computed using relations (A.43). Then, these results may be used together with the expression (A.22) for

$\bar{\mathbf{F}}^{(1)}$ to compute the effective stored-energy function \widetilde{W} for the rigidly reinforced composite using relation (A.26).

Some illustrative results will be presented in the next subsection and compared with earlier results and bounds. However, before doing this, the incompressible limit ($\mu' \rightarrow \infty$) of the effective stored energy is considered here. (Note that for actual rubbers $\mu'/\mu \approx 10^4$.) In this context, it is important to note that the above two distinct roots have very different asymptotic behaviors in the limit as μ' increases. The main distinguishing feature of the solutions associated with the two roots (A.43) of the equations (A.42) is that for one root, which is labeled the “positive” (+) root, $\hat{J}^{(1)} = \det \hat{\mathbf{F}}^{(1)} \geq \bar{J}^{(1)} = \det \bar{\mathbf{F}}^{(1)}$, while for the other, labeled the “negative” (−) root, the opposite is true.

For the negative-root solution, it can be shown that consideration of the incompressible limit of the energy for \widetilde{W} leads to the “approximate” incompressibility constraint (A.37), in agreement with the corresponding limit obtained from the earlier version of the “second-order” theory (not incorporating field fluctuations). Because of this negative feature, and for reasons that will be detailed in the next subsection on results, this solution will not be pursued further here.

On the other hand, for the positive-root solution, it can be shown that the incompressible limit of \widetilde{W} is consistent with the “exact” incompressibility constraint (A.25), and therefore consistent with the expected physics of the problem. The mathematical limit is a bit unusual in that some of the components of \mathbf{L}_0 (i.e., $L_{1111}, L_{1122}, L_{2222}$) become unbounded at *finite* values of μ' , depending on μ , the loading level and the particle concentration. Further details are given in Appendix B, but the final result for the effective stored-energy function of the rigidly reinforced composite with a Neo-Hookean matrix phase may be written:

$$\begin{aligned} \tilde{\Phi}_{HS}^I(\bar{\lambda}_1, \bar{\lambda}_2) = & \tilde{\Phi}_R^I(\bar{\lambda}_1, \bar{\lambda}_2) + \frac{\mu}{2} \frac{c}{(1-c)} \left[\frac{(\bar{\lambda}_2 - c)(\bar{\lambda}_1 - 1)^2}{(\bar{\lambda}_1 - c)} + \frac{(\bar{\lambda}_1 - c)(\bar{\lambda}_2 - 1)^2}{(\bar{\lambda}_2 - c)} \right. \\ & \left. + (\bar{\lambda}_1 - \bar{\lambda}_2)^2 \right], \end{aligned} \quad (\text{A.44})$$

where $\tilde{\Phi}_R^I$ is given by expression (A.36) with $\bar{\lambda}_3 = 1$, and it is emphasized that the exact incompressibility constraint (A.25) is satisfied. This result should be compared with the corresponding result (cf. eqn. (46) in (Ponte Castañeda and Tiberio, 2000)) from the earlier version of the second-order procedure (without fluctuations), which, unlike (A.44), is inconsistent with the exact incompressibility constraint (A.25).

In the next section, comparisons will be made with the “alternate” version (see Appendix of

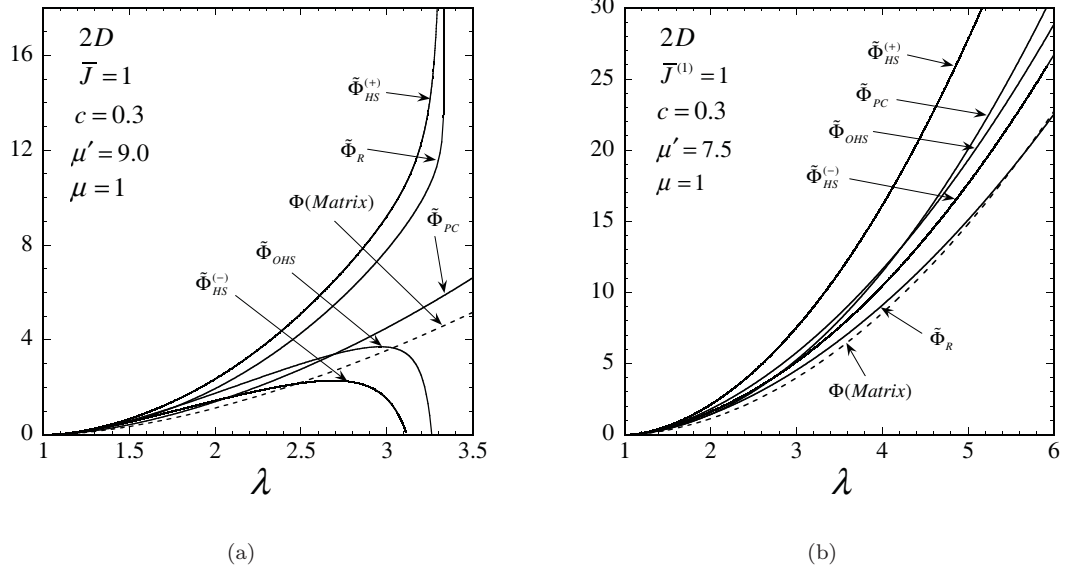


Figure A.2: New second-order and other estimates and bounds for the effective stored energy of a *compressible* Neo-Hookean rubber reinforced with a fixed concentration ($c = 0.3$) of aligned rigid fibers, as functions of the applied stretch λ . (a) Pure shear loading with $\bar{\lambda}_1 = \lambda$ and $\bar{\lambda}_2 = 1/\lambda$; and (b) loading with $\bar{\lambda}_1 = \lambda$ and $\bar{\lambda}_2$ such that $\bar{J}^{(1)} = 1$. The labels $\tilde{\Phi}_{HS}^{(+)}$ and $\tilde{\Phi}_{HS}^{(-)}$ correspond to the “positive” and “negative” roots of the new Hashin-Shtrikman second-order estimates, and the labels $\tilde{\Phi}_{OHS}$, $\tilde{\Phi}_R$, and $\tilde{\Phi}_{PC}$ correspond respectively to the old version (Ponte Castañeda and Tiberio, 2000) of the second-order HS estimates, the Reuss estimate and the polyconvex lower bound, respectively.

(Ponte Castañeda and Tiberio, 2000)) of the old second-order estimate, which also leads to the exact incompressibility constraint, and is given by:

$$\tilde{\Phi}_{OHS}^A(\bar{\lambda}_1, \bar{\lambda}_2) = \tilde{\Phi}_R^A(\bar{\lambda}_1, \bar{\lambda}_2) + \frac{\mu}{2} \left(\frac{c}{1-c} \right) \left[1 + \frac{(1-c)^2}{(\bar{\lambda}_1 - c)(\bar{\lambda}_2 - c)} \right] \left[(\bar{\lambda}_1 - 1)^2 + (\bar{\lambda}_2 - 1)^2 \right]. \quad (\text{A.45})$$

where $\tilde{\Phi}_R^A$ is given by expression (A.38). Briefly, this estimate was generated by applying the old second-order method to only part of the energy, the additional terms being evaluated by other means. This required certain manipulations that were difficult to justify. The new estimate (A.44), on the other hand, is generated directly from the improved version of the second-order method, without the need of additional assumptions.

A.4.2 Results

Figure A.2 provides a comparison of the new second-order estimates of the HS type with earlier estimates and bounds for a *compressible* Neo-Hookean matrix phase with given moduli μ , and μ' , reinforced with $c = 0.30$ rigid fibers. Results are shown as function of the applied stretch

λ for two different types of loading: (a) pure shear with $\bar{\lambda}_1 = \lambda$ and $\bar{\lambda}_2 = 1/\lambda$, which satisfies the exact overall incompressibility constraint $\bar{J} = \det \bar{\mathbf{F}} = 1$; and (b) $\bar{\lambda}_1 = \lambda$ and $\bar{\lambda}_2$ chosen such that the “approximate” overall incompressibility constraint $\bar{J}^{(1)} = \det \bar{\mathbf{F}}^{(1)} = 1$ is satisfied. (It is emphasized that the composite is compressible and therefore should be able to accommodate both types of deformation conditions.) For completeness, both “roots” are shown for the new second-order estimates, respectively labelled $\tilde{\Phi}_{HS}^{(+)}$ and $\tilde{\Phi}_{HS}^{(-)}$ for the above-defined “positive-root” and “negative-root” solutions. They are compared against the polyconvex *lower* bound (A.23), denoted $\tilde{\Phi}_{PC}$, the Reuss estimate (A.35), denoted $\tilde{\Phi}_R$, and the old version (Ponte Castañeda and Tiberio, 2000) of the second-order HS estimates, labelled $\tilde{\Phi}_{OHS}$. The energy function of the matrix phase is also shown in dashed lines for reference.

The main observation that can be made from Figure A.2(a) is that while the new “positive-root” estimate $\tilde{\Phi}_{HS}^{(+)}$ satisfies the polyconvex lower bound $\tilde{\Phi}_{PC}$, both the “negative-root” estimate $\tilde{\Phi}_{HS}^{(-)}$ and the old second-order estimate $\tilde{\Phi}_{OHS}$ violate this bound at sufficiently large stretches λ . In fact, it can be seen from this figure that both $\tilde{\Phi}_{HS}^{(-)}$ and $\tilde{\Phi}_{OHS}$ have a seemingly unphysical behavior since they become lower than the matrix energy for sufficiently large stretches. This anomalous behavior for $\tilde{\Phi}_{HS}^{(-)}$ and $\tilde{\Phi}_{OHS}$ can be seen to be consistent with the above-mentioned observations that they both lead to overall incompressibility constraints that are inconsistent with the imposed deformation (i.e., pure shear). Even though the matrix phase is compressible, the value of μ' in this case ($\mu' = 9$) is sufficiently large to show the effect of the incompressible limit of these estimates, which again is inconsistent with the applied loading in this case. The implication of all of this is that the “positive-root” estimate $\tilde{\Phi}_{HS}^{(+)}$ must be superior to both the “negative-root” estimate $\tilde{\Phi}_{HS}^{(-)}$ and the old second-order estimate $\tilde{\Phi}_{OHS}$, at least for nearly incompressible behavior for the matrix phase.

However, as shown in Figure A.2(b), the “positive-root” estimate $\tilde{\Phi}_{HS}^{(+)}$ also does better than the other two HS-type estimates when an overall loading condition is imposed that is consistent with the “approximate” incompressibility constraint ($\bar{J}^{(1)} = \det \bar{\mathbf{F}}^{(1)} = 1$), so that the “negative-root” estimate $\tilde{\Phi}_{HS}^{(-)}$ and the old second-order estimate $\tilde{\Phi}_{OHS}$ would not be expected to blow up in the incompressible limit. (Note that $\mu' = 7.5$ in this case, which is also a relatively large value.) This figure also shows that the Reuss estimate (identical for the new and old second-order theories because of the lack of fluctuations) violates the bound in this case.

Putting these observations together with the earlier observations concerning the incompressible

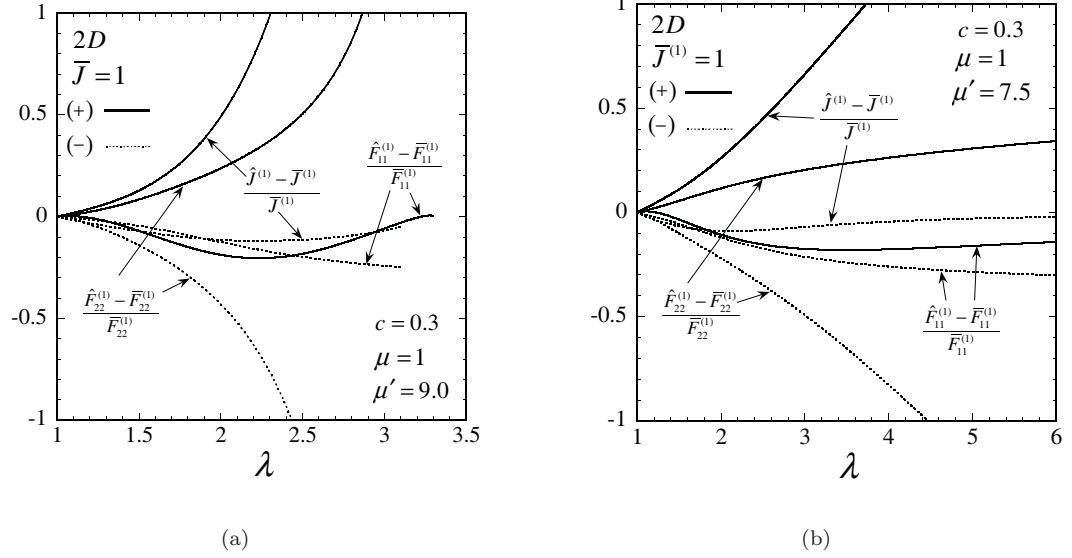


Figure A.3: Plots of the phase fluctuation measures $\hat{F}_{11}^{(1)} - \bar{F}_{11}^{(1)}$, $\hat{F}_{22}^{(1)} - \bar{F}_{22}^{(1)}$ and $\hat{J}^{(1)} - \bar{J}^{(1)}$, versus the stretch λ for the same reinforced, compressible, Neo-Hookean rubbers considered in the context of Figure A.2. (a) Pure shear loading with $\bar{\lambda}_1 = \lambda$ and $\bar{\lambda}_2 = 1/\lambda$; and (b) loading with $\bar{\lambda}_1 = \lambda$ and $\bar{\lambda}_2$ such that $\bar{J}^{(1)} = 1$.

limits, the unescapable conclusion is that the “positive-root” estimate $\tilde{\Phi}_{HS}^{(+)}$ must be superior to the “negative-root” estimate $\tilde{\Phi}_{HS}^{(-)}$, as well as to the old second-order estimate $\tilde{\Phi}_{OHS}$. Therefore, the new theory with fluctuations has been demonstrated to have the capability to give much improved predictions in finite elasticity, at least relative to the earlier theory (Ponte Castañeda and Tiberio, 2000).

In Figures A.3, the new second-order predictions for the variables $\hat{F}_{11}^{(1)} - \bar{F}_{11}^{(1)}$ and $\hat{F}_{22}^{(1)} - \bar{F}_{22}^{(1)}$, as well as for the variable $\hat{J}^{(1)} - \bar{J}^{(1)}$, appropriately normalized by the corresponding phase averages, are given for compressible Neo-Hookean rubbers reinforced by $c = 0.3$ of rigid particles. Both the predictions of the “positive” and “negative” roots are shown for completeness. Figure A.3(a) and (b) give results for the two loadings identified in the context of Figure A.2: (a) pure shear with $\bar{\lambda}_1 = \lambda$ and $\bar{\lambda}_2 = 1/\lambda$, and (b) $\bar{\lambda}_1 = \lambda$ and $\bar{\lambda}_2$ chosen such that $\bar{J}^{(1)} = 1$. Although the variables $\hat{F}_{11}^{(1)} - \bar{F}_{11}^{(1)}$ and $\hat{F}_{22}^{(1)} - \bar{F}_{22}^{(1)}$ cannot be identified exactly with the fluctuations of the deformation fields F_{11} and F_{22} over the matrix phase (because of the complex interactions among the various components of the deformation field arising from the selected traces of relation (A.28)), they do provide some measure of the fluctuations of the deformation field in the matrix. The main observation in the context of these plots is that $\hat{J}^{(1)} > \bar{J}^{(1)}$ for the positive root, which is

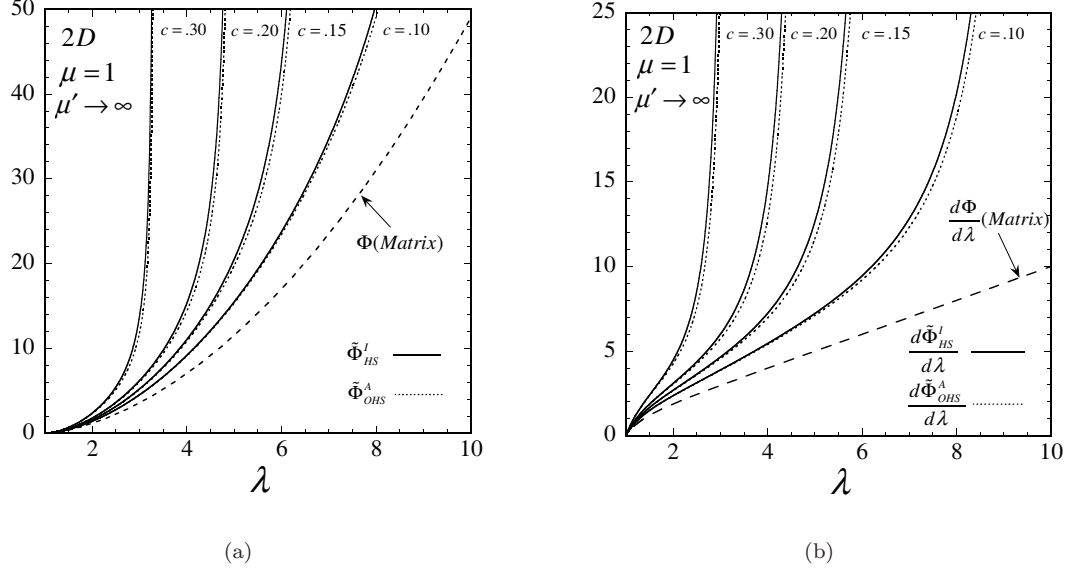


Figure A.4: Plots of the new (positive-root only) and old second-order predictions for the effective response of an *incompressible* Neo-Hookean rubber reinforced with various concentrations c of aligned rigid fibers, and loaded in pure shear with $\bar{\lambda}_1 = \lambda$ and $\bar{\lambda}_2 = 1/\lambda$. (a) The stored-energy functions $\tilde{\Phi}_{HS}^I$ and $\tilde{\Phi}_{OHS}^A$; and (b) the corresponding stresses $S = d\tilde{\Phi}_{HS}^I/d\lambda$ and $d\tilde{\Phi}_{OHS}^A/d\lambda$, both as functions of the applied stretch λ .

physically more appealing than $\hat{J}^{(1)} < \bar{J}^{(1)}$ for the negative root. In addition, it appears that there are considerable differences between the two roots, for a given loading, and between the predictions of the same root, for the two different loadings, which is consistent with the observations already made in the context of the energies.

In Figures A.4, plots are given for the new second-order estimates (“positive root” only) for the stored-energy function $\tilde{\Phi}_{HS}^I$ and corresponding stress $S = d\tilde{\Phi}_{HS}^I/d\lambda$, as functions of the applied stretch λ , for an *incompressible* Neo-Hookean material reinforced by rigid fibers at various concentration c , subjected to pure shear $\bar{\lambda}_1 = \lambda$ and $\bar{\lambda}_2 = 1/\lambda$. These new second-order results were obtained by making use of the explicit expression (A.44) and are compared with the “alternate” form of the earlier version (Ponte Castañeda and Tiberio, 2000) of the second-order theory, as given by expression (A.45) and shown in dotted lines. First of all, note that the behavior of the composite is quite different from that of the Neo-Hookean matrix phase in that it becomes much stiffer as the applied stretch $\bar{\lambda}$ tends to $1/c$, where the composite is found to lock up (i.e., the energy and the stress blow up). This is an interesting feature that was already predicted by the earlier version of the theory (Ponte Castañeda and Tiberio, 2000) and is confirmed by the more

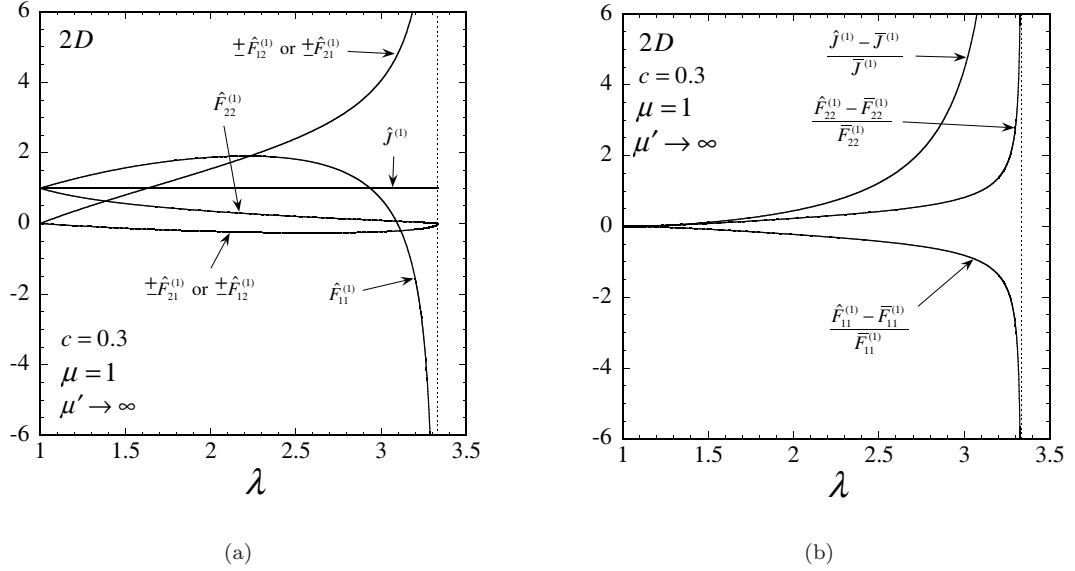


Figure A.5: Plots of the phase fluctuations variable $\hat{\mathbf{F}}^{(1)}$ versus the stretch λ for an *incompressible* Neo-Hookean rubber reinforced with $c = 0.3$ concentration of aligned rigid fibers, and loaded in pure shear with $\bar{\lambda}_1 = \lambda$ and $\bar{\lambda}_2 = 1/\lambda$. (a) The four non-zero components of $\hat{\mathbf{F}}^{(1)}$, as well as $\hat{j}^{(1)}$; and (b) the normalized field fluctuations variables $\hat{F}_{11}^{(1)} - \bar{F}_{11}^{(1)}$, $\hat{F}_{22}^{(1)} - \bar{F}_{22}^{(1)}$ and $\hat{j}^{(1)} - \bar{j}^{(1)}$.

accurate results arising from the improved theory incorporating fluctuations. It is also interesting to remark that the predictions of the new second-order theory are in fact very close to the corresponding predictions of the “alternate” version of the old second-order theory. The fact that these two estimates, which have been generated by very different methods, are quite close may suggest that the predictions generated are fairly accurate in this case. In turn, this similarity in the predictions of the two theories is consistent with the expectation that the most significant nonlinearities giving rise to large fluctuations are associated with the strongly nonlinear incompressibility constraint. The fact that the fluctuations are not used in the old second-order theory is compensated in its “alternate” version by the exact computation of the terms associated with the determinant constraint. The new second-order theory, using fluctuations, is robust enough to handle the incompressibility constraint directly (without the need of any special treatment for the determinant terms in the energy expression).

Finally, in Figures A.5, plots are given for the variables $\hat{F}_{11}^{(1)}$, $\hat{F}_{22}^{(1)}$, $\hat{F}_{12}^{(1)}$ and $\hat{F}_{21}^{(1)}$ for the incompressible Neo-Hookean rubber reinforced with $c = 0.3$ of rigid fibers. Figure A.5(a) gives the raw values of these variables, which demonstrate that $\hat{J}^{(1)} = 1$, a feature that was critical in the asymptotic solution for nearly incompressible behavior, as shown in Appendix B. As can be

deduced from equations (A.42), the basic variables in the analysis are $\hat{F}_{11}^{(1)} - \bar{F}_{11}^{(1)}$ and $\hat{F}_{22}^{(1)} - \bar{F}_{22}^{(1)}$, and the combinations $\hat{F}_{12}^{(1)} \hat{F}_{21}^{(1)}$ and $\left(\hat{F}_{12}^{(1)}\right)^2 + \left(\hat{F}_{21}^{(1)}\right)^2$. These combinations of variables allow the determination of the effective energy and associated stress in a unique manner, but do not allow the unique determination of the variables $\hat{F}_{12}^{(1)}$ and $\hat{F}_{21}^{(1)}$ themselves. This is the reason for the multiple labels on these curves. Figure A.5(b) gives plots of the variables $\hat{F}_{11}^{(1)} - \bar{F}_{11}^{(1)}$ and $\hat{F}_{22}^{(1)} - \bar{F}_{22}^{(1)}$, normalized by the corresponding phase averages. Although these variables cannot be identified exactly with the fluctuations of the deformation fields F_{11} and F_{22} over the matrix phase (because of the complex interactions among the various components of the deformation field arising from the selected traces of relation (A.28)), they do provide some measure of the fluctuations of the deformation field in the matrix. With the given normalizations, it is seen that these fluctuation variables preserve the symmetry of the loading (pure shear) and increase with increasing stretch, blowing up at $\bar{\lambda} = 1/c$. A scalar measure of the fluctuations, which also incorporates dependence on the variables $\hat{F}_{12}^{(1)}$ and $\hat{F}_{21}^{(1)}$, is provided by $\hat{J}^{(1)} - \bar{J}^{(1)}$. This variable also suggests that the fluctuations, suitably normalized by $\bar{J}^{(1)}$, increase with λ from zero at $\lambda = 1$ to $\lambda = 1/c$, when it blows up.

A.5 Concluding remarks

In this paper, the recently proposed “second-order” homogenization method (Ponte Castañeda, 2002a) has been extended to finite elasticity and applied to estimate the macroscopic response of particle- and fiber-reinforced elastomers subjected to large deformations. The resulting predictions appear to be quite good, exhibiting two qualitative features of special note.

First, the predicted constitutive behavior for rigidly reinforced composites with *incompressible* Neo-Hookean matrix phases turn out to be incompressible in an overall sense. Simple as this requirement may be from the physical point of view, it is a non-trivial mathematical result due to the strong nonlinearities associated with the incompressibility of the matrix phase ($\det \mathbf{F} = 1$). In fact, it is known that an earlier version of the method (Ponte Castañeda and Tiberio, 2000), which neglected the use of the field fluctuations, led to predictions for the overall response of such rigidly reinforced incompressible elastomers that were not consistent with the overall incompressibility constraint, except in the limit of small deformations. The fact that the new second-order estimates are consistent with the overall incompressibility constraint for arbitrarily large deformations is an

accomplishment for the theory, and serves to provide further evidence that the fluctuations are essential in generating accurate estimates for the effective behavior of nonlinear composites, in general, especially when such fluctuations are expected to be significant.

Second, the predictions for the effective response of such incompressible elastomers is found to exhibit a curious “lock-up” phenomenon at a finite stretch, even when the matrix behavior is assumed to allow arbitrarily large stretches. This interesting feature, which had already been observed in the context of the earlier version of the theory (Ponte Castañeda and Tiberio, 2000), can only be explained in terms of the evolution of the microstructure produced by finite changes in geometry, and serves to provide further evidence of the strength of the second-order homogenization methods in terms of capturing the effects of these additional nonlinearities in the field equations. A curious consequence of this lock-up phenomenon is the fact that the overall stress-strain relations for these materials exhibit a familiar “S” shape, even for relatively small concentrations of the rigid particles. This is in spite of the fact that the matrix phase, taken to be Neo-Hookean, does not have such a shape.

Acknowledgments

This work was supported by NSF grant DMS-0204617.

Appendix A

In this appendix, the in-plane components of the tensor \mathbf{P} associated with the orthotropic modulus tensor \mathbf{L}_0 , given by expression (A.40) and subjected to constraints (A.41), are computed for the special case of cylindrical inclusions with circular cross section. In this case, the general expression (A.33) for \mathbf{P} reduces to:

$$\mathbf{P} = \frac{1}{2\pi} \int_{\xi_1^2 + \xi_2^2 = 1} H_{ijkl}(\xi_1, \xi_2, \xi_3 = 0) dS, \quad (\text{A.46})$$

where it has been assumed that the fibers are aligned in the x_3 direction (note that the “surface” integral is evaluated over the unit circle).

Now, using the change of variables defined by $\xi_1 = \cos(\theta)$ and $\xi_2 = \sin(\theta)$, it follows that the non-vanishing (in-plane) components of \mathbf{P} can be expressed as:

$$\begin{aligned} P_{1111} &= \frac{1}{2\pi} \int_0^{2\pi} \frac{K_{22} \cos^2(\theta)}{\det \mathbf{K}} d\theta = \frac{1 + \frac{L_{2222}}{L_{1212}} + 2\sqrt{\frac{L_{2222}}{L_{1111}}}}{2L_{1111} \left(1 + \sqrt{\frac{L_{2222}}{L_{1111}}}\right)^2} \\ P_{2222} &= \frac{1}{2\pi} \int_0^{2\pi} \frac{K_{11} \sin^2(\theta)}{\det \mathbf{K}} d\theta = \frac{1 + \frac{L_{1111}}{L_{1212}} + 2\sqrt{\frac{L_{1111}}{L_{2222}}}}{2L_{1111} \left(1 + \sqrt{\frac{L_{2222}}{L_{1111}}}\right)^2} \end{aligned}$$

$$\begin{aligned}
P_{1122} &= \frac{1}{2\pi} \int_0^{2\pi} \frac{-K_{12} \cos(\theta) \sin(\theta)}{\det \mathbf{K}} d\theta = \frac{-(L_{1221} + L_{1122})}{2L_{1111}L_{1212} \left(1 + \sqrt{\frac{L_{2222}}{L_{1111}}}\right)^2} \\
P_{1212} &= \frac{1}{2\pi} \int_0^{2\pi} \frac{K_{22} \sin^2(\theta)}{\det \mathbf{K}} d\theta = \frac{1 + \frac{L_{2222}}{L_{1212}} + 2\frac{L_{2222}}{L_{1212}} \sqrt{\frac{L_{1111}}{L_{2222}}}}{2L_{1111} \left(1 + \sqrt{\frac{L_{2222}}{L_{1111}}}\right)^2} \\
P_{2121} &= \frac{1}{2\pi} \int_0^{2\pi} \frac{K_{11} \cos^2(\theta)}{\det \mathbf{K}} d\theta = \frac{1 + \frac{L_{1111}}{L_{1212}} + 2\frac{L_{1111}}{L_{1212}} \sqrt{\frac{L_{2222}}{L_{1111}}}}{2L_{1111} \left(1 + \sqrt{\frac{L_{2222}}{L_{1111}}}\right)^2} \\
P_{1221} &= P_{1122}.
\end{aligned} \tag{A.47}$$

Note that the tensor \mathbf{P} exhibits both major symmetry, $P_{ijkl} = P_{klij}$, as well as orthotropic symmetry, consistent with similar requirements for \mathbf{L}_0 . Also note that, due to the symmetry of the modulus tensor \mathbf{L}_0 and the type of loading considered in this paper (*i.e.*, $\bar{\mathbf{F}} = \bar{\mathbf{U}}$; $\bar{\mathbf{R}} = \mathbf{I}$), the only relevant components that enter in the homogenization process are P_{1111} , P_{2222} , and P_{1122} . The other components have been included in this appendix for completeness.

Appendix B

In this appendix, additional details are presented on the incompressible limit associated with the “positive” root of the new second-order method applied to a Neo-Hookean-type material reinforced with rigid fibers. The asymptotic solution resulting from this heuristic derivation has been checked to give good agreement with the full numerical solution.

This limit is a bit unusual in the sense that some of the components of the modulus tensor \mathbf{L}_0 become unbounded at a finite value, μ^* , of the Lamé modulus μ' of the elastomeric matrix, which depends on the loading, material parameters, and fiber concentration. Thus, motivated by the numerical solution for general μ' , an expansion is attempted in the limit as $\mu' \rightarrow \mu^*$ of the following form:

$$\begin{aligned}
L_{2222} &= \frac{1}{\Delta} \\
L_{1111} &= \frac{a_1}{\Delta} + a_2 + O(\Delta) \\
L_{1122} &= \frac{b_1}{\Delta} + b_2 + O(\Delta) \\
L_{1212} &= \frac{c_1}{\Delta} + c_2 + O(\Delta) \\
L_{1221} &= \frac{d_1}{\Delta} + d_2 + O(\Delta),
\end{aligned} \tag{A.48}$$

where, by definition, $\Delta = 1/L_{2222}$ is a small parameter and $a_1, b_1, c_1, d_1, a_2, b_2, c_2$, and d_2 are unknown coefficients (more precisely, they are ratios between the components of \mathbf{L}_0) that ultimately

depend on the applied loading, the material parameters, and the fiber concentration.

Now, as already mentioned earlier, the constraint (A.41)₁, together with the generalized secant conditions (A.27), can be shown to lead to the exact result that $L_{1212} = \mu$. In turn, the constraint (A.41)₂ can be used to solve for L_{1221} in terms of the other components of \mathbf{L} . Because of these facts, the following simplifications are obtained:

$$c_1 = 0, \quad c_2 = \mu, \quad d_1 = \sqrt{a_1} - b_1 \quad \text{and} \quad d_2 = \frac{a_2 - \mu(a_1 + 1)}{2\sqrt{a_1}} - b_2. \quad (\text{A.49})$$

Next, using the relations (A.48) and (A.49), the general expressions (A.43) for the (“positive” root) components of $\hat{\mathbf{F}}^{(1)} - \bar{\mathbf{F}}^{(1)}$ lead to expansions of the type:

$$\begin{aligned} \hat{F}_{11}^{(1)} &- \bar{F}_{11}^{(1)} = x_1(a_1) + x_2(a_1, a_2)\Delta + O(\Delta^2) \\ \hat{F}_{22}^{(1)} &- \bar{F}_{22}^{(1)} = y_1(a_1) + y_2(a_1, a_2)\Delta + O(\Delta^2) \\ \hat{F}_{12}^{(1)} &= u_1(a_1) + u_2(a_1, a_2)\Delta + O(\Delta^2) \\ \hat{F}_{21}^{(1)} &= v_1(a_1) + v_2(a_1, a_2)\Delta + O(\Delta^2). \end{aligned} \quad (\text{A.50})$$

The explicit form of the coefficients in these expansions is too cumbersome to be included here. Instead, only the unknown arguments upon which they depend have been specified. For instance, note that the leading term of all the components of $\hat{\mathbf{F}}^{(1)} - \bar{\mathbf{F}}^{(1)}$ depend solely on a_1 .

At this point, expressions (A.48) and (A.50) can be introduced into the three reduced (*i.e.*, using $L_{1212} = \mu$) generalized secant conditions to obtain a hierarchical system of equations. The leading order terms $O(\Delta^{-1})$ of these equations are given by

$$a_1 x_1 + b_1 y_1 = 0, \quad b_1 x_1 + y_1 = 0, \quad \sqrt{a_1} - b_1 = 0, \quad (\text{A.51})$$

where the arguments of x_1 and y_1 have been omitted for brevity. Note that setting the determinant associated with expressions (A.51)₁ and (A.51)₂ to zero implies (A.51)₃. Furthermore, it can be shown that the equation system (A.51) can be trivially satisfied by x_1 and y_1 (*i.e.*, $y_1 = -\sqrt{a_1}x_1$). In summary, the terms of order $O(\Delta^{-1})$ yield only one new condition, namely that, $b_1 = \sqrt{a_1}$.

After some simplification, the terms of order $O(\Delta^0)$ in the generalized secant equations can be

shown to reduce to:

$$\begin{aligned}
\frac{\sqrt{c}\mu(1+b_1)|(\bar{\lambda}_2-1)-b_1(\bar{\lambda}_1-1)|}{\sqrt{2}(1-c)a_1^{1/4}} &= -\frac{\bar{\lambda}_2^{(1)}}{\hat{j}^{(1)}}\mu + \frac{\mu}{\bar{\lambda}_1^{(1)}} + \mu^*\bar{\lambda}_2^{(1)}\left(\hat{j}^{(1)} - \bar{J}^{(1)}\right) \\
\frac{\sqrt{c}\mu(1+b_1)|(\bar{\lambda}_2-1)-b_1(\bar{\lambda}_1-1)|}{\sqrt{2}(1-c)a_1^{3/4}} &= -\frac{\bar{\lambda}_1^{(1)}}{\hat{j}^{(1)}}\mu + \frac{\mu}{\bar{\lambda}_2^{(1)}} + \mu^*\bar{\lambda}_1^{(1)}\left(\hat{j}^{(1)} - \bar{J}^{(1)}\right) \\
b_2 = \frac{a_2 - \mu(a_1 + 1)}{2\sqrt{a_1}} + \mu^*\left(\hat{j}^{(1)} - 1\right) &- \frac{\mu}{\hat{j}^{(1)}}, \tag{A.52}
\end{aligned}$$

where $\hat{j}^{(1)} = (x_1 + \bar{\lambda}_1^{(1)})(y_1 + \bar{\lambda}_2^{(1)}) - u_1 v_1$, which depends exclusively on a_1 , is the first term in the expansion of $\hat{J}^{(1)}$ (i.e., $\hat{J}^{(1)} = \hat{j}^{(1)} + O(\Delta)$). It is noted now that (A.52)₁ and (A.52)₂ constitute a system of two equations for the two unknowns a_1 and μ^* (with b_1 being known in terms of a_1). Furthermore, equation (A.52)₃ establishes a relationship between a_2 and b_2 in an analogous manner to the relationship established between a_1 and b_1 by (A.51)₃. This structure suggests that the coefficients a_i and b_i ($i=1,2,3,\dots$), along with the corrections to μ^* , could be determined from the generalized secant equations of order $O(\Delta^{i-1})$ (although this will not be pursued here).

Returning to the problem involving a_1 and μ^* , it is easy to show from (A.52)₁ and (A.52)₂ that

$$a_1 = \left(\frac{\bar{\lambda}_2^{(1)}}{\bar{\lambda}_1^{(1)}}\right)^2 \quad \text{and} \quad \mu^* = \frac{\frac{\sqrt{c}\mu(1+\sqrt{a_1})|(\bar{\lambda}_2-1)-\sqrt{a_1}(\bar{\lambda}_1-1)|}{\sqrt{2}(1-c)a_1^{1/4}} + \frac{\bar{\lambda}_2^{(1)}}{\hat{j}^{(1)}}\mu - \frac{\mu}{\bar{\lambda}_1^{(1)}}}{\bar{\lambda}_2^{(1)}\left(\hat{j}^{(1)} - \bar{J}^{(1)}\right)}. \tag{A.53}$$

The results given by expressions (A.53) suffice to characterize—through (A.49) and (A.51)—the leading order terms of the components of \mathbf{L}_0 and $\hat{\mathbf{F}}^{(1)} - \bar{\mathbf{F}}^{(1)}$, as well as the value of μ^* .

Next, the limit $\mu' \rightarrow \infty$ is considered in the context of expression (A.26) for the effective stored energy function of the rigidly reinforced, Neo-Hookean, elastomer. In this connection, it is important to note that the required expression for $\hat{\mathbf{F}}^{(1)}$ does not change for values of μ' greater than μ^* . ($\bar{\mathbf{F}}^{(1)}$ is, of course, also independent of μ' .) This means that for sufficiently large values of μ' , the effective stored energy function takes the form:

$$\widetilde{W}(\bar{\mathbf{U}}) = \mu'g(\bar{\lambda}_1, \bar{\lambda}_2) + \tilde{\Phi}(\bar{\lambda}_1, \bar{\lambda}_2), \tag{A.54}$$

where it is emphasized that $\tilde{\Phi}$ is independent of μ' , and

$$g(\bar{\lambda}_1, \bar{\lambda}_2) = \frac{1}{2}\left(\hat{j}^{(1)} - 1\right)^2 - \left(\bar{J}^{(1)} - 1\right)\left[\hat{j}^{(1)} - \frac{\bar{\lambda}_1\bar{\lambda}_2 - c}{1-c}\right] = 0. \tag{A.55}$$

As already discussed in the body of the text, consideration of the limit as $\mu' \rightarrow \infty$ leads to the overall incompressibility constraint given by $g(\bar{\lambda}_1, \bar{\lambda}_2) = 0$. On the other hand, using (A.53)₁, it

follows from the definition of $\hat{j}^{(1)}$ that

$$\hat{j}^{(1)} = \frac{\bar{\lambda}_1 \bar{\lambda}_2 - c}{1 - c}, \tag{A.56}$$

which, together with (A.55), can be shown to lead to the condition

$$\bar{J} = \bar{\lambda}_1 \bar{\lambda}_2 = 1, \tag{A.57}$$

which is nothing more than the “exact” incompressibility constraint (A.25), specialized to plane strain conditions. With this condition, the effective stored energy function for the *incompressible*, rigidly reinforced, Neo-Hookean elastomer is generated from the left-over terms, labelled $\tilde{\Phi}$ in expression (A.54). The resulting explicit expression is given by (A.44).

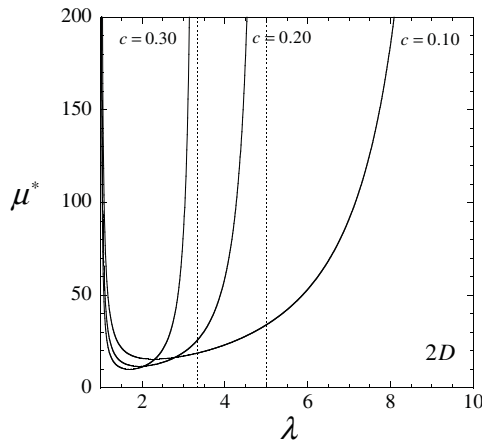


Figure A.6: Plot of μ^* as a function of the stretch λ for various concentrations c of aligned rigid fibers under pure shear loading $\bar{\lambda}_1 = \lambda$ and $\bar{\lambda}_2 = 1/\lambda$.

It is interesting to remark that the new version of the second-order method predicts incompressible overall behavior even for rigidly reinforced Neo-Hookean rubbers that have sufficiently high (but not necessarily infinite) values of μ' (i.e., for $\mu' \geq \mu^*$). This type of prediction, although perhaps not strictly correct, is probably very accurate. Physically, this is related to the fact that the overall incompressibility of the composite is expected to increase with increasing values of the volume fraction of the rigid fibers in the compressible elastomeric matrix. Figure (A.6) shows the limiting values μ^* at which the second-order method predicts the onset of incompressible behavior as a function of the deformation for various concentrations c of rigid fibers. Note that $\mu^* \rightarrow \infty$ as $\lambda \rightarrow 1$ and $\lambda \rightarrow 1/c$. This asymptotic behavior is consistent with the full numerical solution as well as with small-strain linearization conditions.

For completeness, the expressions for the leading order terms in the expansions of $\hat{F}_{11}^{(1)} - \bar{F}_{11}^{(1)}$ and $\hat{F}_{22}^{(1)} - \bar{F}_{22}^{(1)}$, from which the corresponding expressions for $\hat{F}_{12}^{(1)}$ and $\hat{F}_{21}^{(1)}$ can be readily determined (recall that $\hat{J}^{(1)} = 1$), are given by:

$$\begin{aligned} \hat{F}_{11}^{(1)} - \bar{F}_{11}^{(1)} &= \frac{\sqrt{c} \left[\left(\frac{\bar{\lambda}_2^{(1)}}{\bar{\lambda}_1^{(1)}} \right)^2 (\bar{\lambda}_1 - 1)^2 - (\bar{\lambda}_2 - 1)^2 \right]}{\sqrt{2}(1-c) \left[\left(\frac{\bar{\lambda}_2^{(1)}}{\bar{\lambda}_1^{(1)}} \right)^{1/2} + \left(\frac{\bar{\lambda}_2^{(1)}}{\bar{\lambda}_1^{(1)}} \right)^{3/2} \right] \left| (\bar{\lambda}_2 - 1) - \frac{\bar{\lambda}_2^{(1)}}{\bar{\lambda}_1^{(1)}} (\bar{\lambda}_1 - 1) \right|}} \\ \hat{F}_{22}^{(1)} - \bar{F}_{22}^{(1)} &= \frac{-\sqrt{c} \left(\frac{\bar{\lambda}_2^{(1)}}{\bar{\lambda}_1^{(1)}} \right) \left[\left(\frac{\bar{\lambda}_2^{(1)}}{\bar{\lambda}_1^{(1)}} \right)^2 (\bar{\lambda}_1 - 1)^2 - (\bar{\lambda}_2 - 1)^2 \right]}{\sqrt{2}(1-c) \left[\left(\frac{\bar{\lambda}_2^{(1)}}{\bar{\lambda}_1^{(1)}} \right)^{1/2} + \left(\frac{\bar{\lambda}_2^{(1)}}{\bar{\lambda}_1^{(1)}} \right)^{3/2} \right] \left| (\bar{\lambda}_2 - 1) - \frac{\bar{\lambda}_2^{(1)}}{\bar{\lambda}_1^{(1)}} (\bar{\lambda}_1 - 1) \right|}}. \end{aligned} \tag{A.58}$$

References

- Abeyaratne, R., Triantafyllidis, N., 1984. An investigation of localization in a porous elastic material using homogenization theory. *Journal of Applied Mechanics* 51, 481–486.
- Acerbi, E., Fusco, N., 1984. Semicontinuity problems in the calculus of variations. *Archive for Rational Mechanics and Analysis* 86, 125–145.
- Arruda, E.M., Boyce, M.C., 1993. A three-dimensional constitutive model for the large stretch behavior of rubber elastic materials. *Journal of the Mechanics and Physics of Solids* 41, 389–412.
- Ball, J.M., 1977. Convexity conditions and existence theorems in nonlinear elasticity. *Archive for Rational Mechanics and Analysis* 63, 337–403.
- Ball, J.M., 1982. Discontinuous equilibrium solutions and cavitation in nonlinear elasticity. *Philosophical Transactions of the Royal Society of London, Series A*, 306, 557–611.
- Ball, J.M., 2002. Some open problems in elasticity. In *Geometry, Mechanics, and Dynamics*, 3–59, Springer, New York.
- Ball, J.M., Murat, F., 1984. $W^{1,p}$ -quasiconvexity and variational problems for multiple integrals. *Journal of Functional Analysis* 58, 225–253.
- Beju, I., 1971. Theorems on existence, uniqueness and stability of the solution of the place boundary-value problem, in statics, for hyperelastic materials. *Archive for Rational Mechanics and Analysis* 42, 1–23.
- Bergström, J.S., Boyce, M.C., 1998. Constitutive modeling of the large strain time-dependent behavior of elastomers. *Journal of the Mechanics and Physics of Solids* 46, 931–954.
- Bergström, J.S., Boyce, M.C., 1999. Mechanical behavior of particle-filled elastomers. *Rubber Chemistry and Technology* 69, 781–785.
- Bischoff, E.J., Arruda, E.M., Grosh, K., 2002. A microstructurally based orthotropic hyperelastic constitutive law. *Journal of Applied Mechanics* 69, 570–579.
- Blatz, P.J., Ko, W.L., 1962. Application of finite elasticity theory to the deformation of rubbery materials. *Transactions of the Society of Rheology* 6, 223–251.

- Bloch, F., 1928. Über die Quantenmechanik der Elektronen in Kristallgittern. *Z. Physik* 52, 555–599.
- Bobeth, M., Diener, G., 1987. Static elastic and thermoelastic field fluctuations in multiphase composites. *Journal of the Mechanics and Physics of Solids* 35, 137–149.
- Bockstaller, M.R., Mickiewicz, R.A., Thomas, E.L., 2005. Block copolymer nanocomposites: perspectives for tailored functional nanomaterials. *Advanced Materials* 17, 1331–1349.
- Braides, A., 1985. Homogenization of some almost periodic coercive functionals. *Rendiconti della Accademia Nazionale delle Scienze detta dei XL* 9, 313–322.
- Brun, M., Lopez-Pamies, O., Ponte Castañeda, P., 2007. Homogenization estimates for fiber-reinforced elastomers with periodic microstructures. *International Journal of Solids and Structures*, submitted for publication.
- Chadwick, P., 1976. *Continuum Mechanics: Concise Theory and Problems*. George Allen and Unwin Ltd., London.
- Chadwick, P., Ogden, R., 1971. On the definition of elastic moduli. *Archive for Rational Mechanics and Analysis* 44, 41–53.
- Cohen, Y., Albalak, R. J., Dair, B. J., Capel, M. S., Thomas, E. L., 2000. Deformation of oriented lamellar block copolymer films. *Macromolecules* 33, 6502–6516.
- Dacorogna, B., 1989. *Direct Methods in the Calculus of Variations*. Oxford University Press, Oxford.
- Dacorogna, B., 2001. Necessary and sufficient conditions for strong ellipticity of isotropic functions in any dimension. *Discrete and Continuous Dynamical Systems—Series B*, 1, 257–263.
- Dair, B. J., Honeker, C. C., Alward, D. B., Avgeropoulos, A., Hadjichristidis, N., Fetters, L. J., Capel, M., Thomas, E. L., 1999. Mechanical properties and deformation behavior of the double gyroid phase in unoriented thermoplastic elastomers. *Macromolecules* 32, 8145–8152.
- Danielsson, M., Parks, D.M., Boyce, M.C., 2004. Constitutive modeling of porous hyperelastic materials. *Mechanics of Materials* 36, 347–358.
- deBotton, G., 2005. Transversely isotropic sequentially laminated composites in finite elasticity. *Journal of the Mechanics and Physics of Solids* 53, 1334–1361.

- deBotton, G., Hariton, I., Socolsky, E. A., 2006. Neo-Hookean fiber-reinforced composites in finite elasticity. *Journal of the Mechanics and Physics of Solids* 54, 533–559.
- Eshelby, J.D., 1957. The determination of the elastic field of an ellipsoidal inclusion and related problems. *Proceedings of the Royal Society of London A* 241, 376–396.
- Feng, W., Christensen, R. M., 1982. Nonlinear deformation of elastomeric foams. *International Journal of Non-Linear Mechanics* 17, 335–367.
- Gent, A. N., 1996. A new constitutive relation for rubber. *Rubber Chemistry and Technology* 69, 59–61.
- Gent, A. N., Thomas, A. G., 1959. The deformation of foamed elastic materials. *Journal of Applied Polymer Science* 1, 107–113.
- Geymonat, G., Müller, S., Triantafyllidis, N., 1993. Homogenization of nonlinearly elastic materials, microscopic bifurcation and macroscopic loss of rank-one convexity. *Archive for Rational Mechanics and Analysis* 122, 231–290.
- Gibson, L. J., Ashby, M. F., 1997. *Cellular Solids*. Cambridge University Press, Cambridge, UK.
- Gong, L., Kyriakides, S., 2005. Compressive response of open-cell foams. Part II: Initiation and evolution of crushing. *International Journal of Solids and Structures* 42, 1381–1399.
- Govindjee, S., 1997. An evaluation of strain amplification concepts via Monte Carlo simulations of an ideal composite. *Rubber Chemistry and Technology* 70, 25–37.
- Govindjee, S., Simo, J., 1991. A Micromechanically based continuum damage model for carbon black-filled rubbers incorporating Mullins' effect. *Journal of the Mechanics and Physics of Solids* 39, 87–112.
- Guo, Z.Y., Peng, X.Q., Moran, B., 2006. A composites-based hyperelastic constitutive model for soft tissue with application to the human annulus fibrosus. *Journal of the Mechanics and Physics of Solids* 54, 1952–1971.
- Gurson, A. L., 1977. Continuum theory of ductile rupture by void nucleation and growth: Part I—Yield criteria and flow rules for porous ductile media. *Journal of Engineering Materials and Technology* 99, 2–15.

Hashin, Z., 1962. The elastic moduli of heterogeneous materials. *Journal of Applied Mechanics* 29, 143–150.

Hashin, Z., 1985. Large isotropic elastic deformation of composites and porous media. *International Journal of Solids and Structures* 21, 711–720.

He, Q.C., Le Quang, H., Feng, Z.Q., 2006. Exact results for the homogenization of elastic fiber-reinforced solids at finite strain. *Journal of Elasticity* 21, 153–177.

Herve, E., Stolz, C., Zaoui, A., 1991. On Hashin's composite spheres assemblage. *Comptes Rendus Mecanique* 313, 857–862.

Hill, R., 1957. On the uniqueness and stability in the theory of finite strain. *Journal of the Mechanics and Physics of Solids* 5, 229–241.

Hill, R., 1972. On constitutive macro-variables for heterogeneous solids at finite strain. *Proceedings of the Royal Society of London A* 326, 131–147.

Hill, R., 1979. On the theory of plane strain in finitely deformed compressible materials. *Mathematical Proceedings of the Cambridge Philosophical Society* 86, 161–178.

Hill, R., Rice, J.R., 1973. Elastic potentials and the structure of inelastic constitutive laws. *SIAM Journal on Applied Mathematics* 25, 448–461.

Holzapfel, G.A., Gasser, T.C., Ogden, R.W., 2000. A new constitutive framework for arterial wall mechanics and a comparative study of material models. *Journal of Elasticity* 61, 1–48.

Honeker, C. C., Thomas, E. L., 1996. Impact of morphological orientation in determining mechanical properties in triblock copolymers. *Chemistry of Materials* 8, 1702–1714.

Honeker, C. C., Thomas, E. L., Albalak, R. J., Hadjuk, D. A., Gruner, S. M., Capel, M. C., 2000. Perpendicular deformation of a near-single crystal triblock copolymer with a cylindrical morphology. 1. Synchrotron SAXS. *Macromolecules* 33, 9395–9406.

Horgan, C.O., Saccomandi, G., 2005. A new constitutive theory for fiber-reinforced incompressible nonlinearly elastic solids. *Journal of the Mechanics and Physics of Solids* 53, 1985–2015.

Hou, H.-S., Abeyaratne, R., 1992. Cavitation in elastic and elastic-plastic solids. *Journal of the Mechanics and Physics of Solids* 40, 571–592.

- Hsu, S.-Y., Vogler, T. J., Kyriakides, S., 1998. Compressive strength predictions for fiber composites. *Journal of Applied Mechanics* 65, 7–16.
- Kailasam, M., Ponte Castañeda, P., 1998. A general constitutive theory for linear and nonlinear particulate media with microstructure evolution. *Journal of the Mechanics and Physics of Solids* 46, 427–465.
- Kailasam, M., Ponte Castañeda, P., Willis, J.R., 1997. The effect of particle size, shape distribution and their evolution on the constitutive response of nonlinearly viscous composites: I. Theory. *Philosophical Transactions of the Royal Society of London A* 355, 1835–1852.
- Khan, A.S., Lopez-Pamies, O., 2002. Time and temperature dependent response and relaxation of a soft polymer. *International Journal of Plasticity* 18, 1359–1372.
- Kinney, J. H., Marshall, G. W., Marshall, S. J., Haupt, D. L., 2001. Three-dimensional imaging of large compressive deformations in elastomeric foams. *Journal of Applied Polymer Science* 80, 1746–1755.
- Kittel, C. 1968. *Introduction to solid state physics*, John Wiley & Sons, Inc., New York.
- Knowles, J. K., Sternberg, E., 1975. On the ellipticity of the equations of nonlinear elastostatics for a special material. *Journal of Elasticity* 5, 341–361.
- Knowles, J. K. and Sternberg, E., 1977. On the failure of ellipticity of the equations for finite elastostatic plane strain. *Archive for Rational Mechanics and Analysis* 63, 321–336.
- Kyriakides, S., Arseculeratne, R., Perry, E. J., Liechti, K. M. 1995. On the compressive failure of fiber reinforced composites. *International Journal of Solids and Structures* 32, 689–738.
- Lagashetty, A., Venkataraman, A., 2005. Polymer Nanocomposites. *Resonance* July 2005, 49–60.
- Lahellec, N., Mazerolle, F., Michel, J.-C., 2004. Second-order estimate of the macroscopic behavior of periodic hyperelastic composites: theory and experimental validation. *Journal of the Mechanics and Physics of Solids* 52, 27–49.
- Laws, N., 1973. On the thermostatics of composite materials. *Journal of the Mechanics and Physics of Solids* 21, 9–17.
- Levin, V. M., 1967. Thermal expansion coefficients of heterogeneous materials, *Mekhanika Tverdogo Tela* 2, 88–94.

Levin, V.A., Lokhin, V.V., Zingerman, K.M., 2000. Effective elastic properties of porous materials with randomly dispersed pores: Finite deformations. *Journal of Applied Mechanics* 67, 667–670.

Lopez-Pamies, O., Ponte Castañeda, P., 2003. Second-order estimates for the large deformation response of particle-reinforced rubber. *Comptes Rendus Mecanique* 331, 1–8.

Lopez-Pamies, O., Ponte Castañeda, P., 2004a. Second-order homogenization estimates incorporating field fluctuations in finite elasticity. *Mathematics and Mechanics of Solids* 9, 243–270.

Lopez-Pamies, O., Ponte Castañeda, P., 2004b. Second-order estimates for the macroscopic response and loss of ellipticity in porous rubbers at large deformations. *Journal of Elasticity* 76, 247–287.

Lopez-Pamies, O., Ponte Castañeda, P., 2006a. On the overall behavior, microstructure evolution, and macroscopic stability in reinforced rubbers at large deformations. I—Theory. *Journal of the Mechanics and Physics of Solids* 54, 807–830.

Lopez-Pamies, O., Ponte Castañeda, P., 2006b. On the overall behavior, microstructure evolution, and macroscopic stability in reinforced rubbers at large deformations. II—Application to cylindrical fibers. *Journal of the Mechanics and Physics of Solids* 54, 831–863.

Lopez-Pamies, O., Ponte Castañeda, P., 2007a. Homogenization-based constitutive models for porous elastomers and implications for macroscopic instabilities: I—Analysis. *Journal of the Mechanics and Physics of Solids*, submitted for publication.

Lopez-Pamies, O., Ponte Castañeda, P., 2007b. Homogenization-based constitutive models for porous elastomers and implications for macroscopic instabilities: II—Results. *Journal of the Mechanics and Physics of Solids*, submitted publication.

Lopez-Pamies, O., Ponte Castañeda, P., 2007c. Macroscopic behavior and microstructure evolution in composite elastomers with layered microstructures. In preparation.

Marcellini, P., 1978. Periodic solutions and homogenization of nonlinear variational problems. *Annali di Matematica Pura ed Applicata* 4, 139–152.

Mark, J. E., Erman, B., Eirich, F. R., 2005. *The science and technology of rubber*. Elsevier Academic Press.

- Marsden, J. E., Hughes, T. J. R., 1983. *Mathematical Foundations of Elasticity*. Prentice-Hall Inc., Englewood Cliffs, N. J.
- Meinecke, E.A., Taftaf, M. I., 1988. Effect of carbon-black on the mechanical properties of elastomers. *Rubber Chemistry and Technology* 61, 534–547.
- Merodio, J., Ogden, R.W., 2005. Mechanical response of fiber-reinforced incompressible nonlinearly elastic solids. *International Journal of Non-Linear Mechanics* 40, 213–227.
- Michel, J.-C., Lopez-Pamies, O., Ponte Castañeda, P., Triantafyllidis, N., 2007. Microscopic and macroscopic instabilities in finitely strained porous elastomers. *Journal of the Mechanics and Physics of Solids*. In press.
- Milton, G.W., 2002. *The theory of composites*. Cambridge Monographs on Applied and Computational Mathematics, vol. 6. Cambridge University Press, Cambridge.
- Morrey, C. B., 1952. Quasi-convexity and the lower semicontinuity of multiple integrals. *Pacific Journal of Mathematics* 2, 25–53.
- Müller, S., 1987. Homogenization of nonconvex integral functionals and cellular elastic materials. *Archive for Rational Mechanics and Analysis* 99, 189–212.
- Mullins, L., Tobin, N. R., 1965. Stress softening in rubber vulcanizates. Part I. Use of strain amplification factor to describe the elastic behavior of filler-reinforced vulcanized rubber. *Journal of Applied Polymer Science* 99, 189–212.
- Nemat-Nasser, S., Iwakuma, T., and Hejazi, M., 1982. On composites with periodic structure. *Mechanics of Materials* 1, 239–267.
- Ogden, R., 1972. Large deformation isotropic elasticity: on the correlation of experiment and theory for compressible rubberlike solids. *Proceedings of the Royal Society of London A*, 328, 567–583.
- Ogden, R., 1974. On the overall moduli of non-linear elastic composites. *Journal of the Mechanics and Physics of Solids* 22, 541–553.
- Ogden, R., 1978. Extremum principles in non-linear elasticity and their application to composites—I Theory. *International Journal of Solids and Structures* 14, 265–282.
- Ogden, R., 1984. *Non-linear elastic deformations*. Ellis Horwood Ltd., Chichester, England.

- O'Rourke, J.P., Ingber, M.S., Weiser, M.W., 1997. The effective elastic constants of solids containing spherical inclusions. *Journal of Composite Materials* 31, 910–934.
- Ponte Castañeda, P., 1989. The overall constitutive behavior of nonlinearly elastic composites. *Proceedings of the Royal Society of London A* 422, 147–171.
- Ponte Castañeda, P., 1991. The effective mechanical properties of nonlinear isotropic composites. *Journal of the Mechanics and Physics of Solids* 39, 45–71.
- Ponte Castañeda, P., 1996. Exact second-order estimates for the effective mechanical properties of nonlinear composite materials. *Journal of the Mechanics and Physics of Solids* 44, 827–862.
- Ponte Castañeda, P., 2001. Second-order theory for nonlinear dielectric composites incorporating field fluctuations. *Physical Review B* 64, 214205–1–14.
- Ponte Castañeda, P., 2002a. Second-order homogenization estimates for nonlinear composites incorporating field fluctuations. I. Theory. *Journal of the Mechanics and Physics of Solids* 50, 737–757.
- Ponte Castañeda, P., 2002b. Second-order homogenization estimates for nonlinear composites incorporating field fluctuations. II. Applications. *Journal of the Mechanics and Physics of Solids* 50, 759–782.
- Ponte Castañeda, P., Willis, J. R., 1995. The effect of spatial distribution on the effective behavior of composite materials and cracked media. *Journal of the Mechanics and Physics of Solids* 43, 1919–1951.
- Ponte Castañeda, P., Suquet, P., 1998. Nonlinear composites. *Advances in Applied Mechanics* 34, 171–302.
- Ponte Castañeda, P., Willis, J. R., 1999. Variational second-order estimates for nonlinear composites. *Proceedings of the Royal Society of London A* 455, 1799–1812.
- Ponte Castañeda, P., Tiberio, E., 2000. A second-order homogenization procedure in finite elasticity and applications to black-filled elastomers. *Journal of the Mechanics and Physics of Solids* 48, 1389–1411.
- Prasman, E., Thomas, E. L., 1998. High-strain tensile deformation of a sphere-forming triblock copolymer/mineral oil. *Journal of Polymer Science: Part B: Polymer Physics* 36, 1625–1636.

- Qiu, G.Y., Pence, T.J., 1997. Remarks on the behavior of simple directionally reinforced incompressible nonlinearly elastic solids. *Journal of Elasticity* 49, 1–30.
- Ramier, J., 2004. *Comportement mécanique d'élastomères chargés, influence de l'adhésion charge-polymère, influence de la morphologie*. Ph. D. Dissertation, Institut National des Science Appliquées de Lyon.
- Reuss, A., 1929. Be rechnung der fließgrenze von mikhkristallen. *Zeitschrift für Angewandte Mathematik und Mechanik* 9, 49–58.
- Silhavy, M., 1999. On isotropic rank one convex functions. *Proceedings of the Royal Society of Edinburgh* 129A, 1081–1105.
- Simpson, H.C., Spector, S.J., 1983. On copositive matrices and strong ellipticity for isotropic materials. *Archive for Rational Mechanics and Analysis* 84, 55–68.
- Spencer, A.J.M., 1972. *Deformations of fibre-reinforced materials*. Oxford University Press, Oxford.
- Spencer, A.J.M., 1984. *Continuum theory of the mechanics of fibre-reinforced composites*. Springer, Wein, New York.
- Suquet, P., 1990. A simplified method for the prediction of homogenized elastic properties of composites with periodic structure. *Comptes Rendus Mecanique* 311, 769–774.
- Suquet, P., Ponte Castañeda, P., 1993. Small-contrast perturbation expansions for the effective properties of nonlinear composites. *Comptes Rendus Mecanique* 317, 1515–1522.
- Talbot, D. R. S., Willis, J. R., 1985. Variational principles for inhomogeneous nonlinear media. *IMA Journal of Applied Mathematics* 35, 39–54.
- Treloar, L.R., 1975. *The Physics of Rubber Elasticity*. Oxford University Press, Oxford.
- Triantafyllidis, N., Abeyaratne, R.C., 1983. Instability of a finitely deformed fiber-reinforced elastic material. *Journal of Applied Mechanics* 50, 149–156.
- Triantafyllidis, N., Maker, B.N., 1985. On the comparison between microscopic and macroscopic instability mechanisms in a class of fiber-reinforced composites. *Journal of Applied Mechanics* 52, 794–800.
- Triantafyllidis, N., Bardenhagen, S. G., 1996. The influence of scale size on the stability of periodic

solids and the role of associated higher order gradient continuum models. *Journal of the Mechanics and Physics of Solids* 44, 1891–1928.

Triantafyllidis, N., Nestorvić, N., 2005. Onset of failure in finitely strained layered composites subjected to combined normal and shear strain. *Journal of the Mechanics and Physics of Solids* 52, 941–974.

Triantafyllidis, N., Nestorvić, M.D., Schraad, M.W., 2006. Failure surfaces for finitely strained two-phase periodic solids under general in-plane loading. *Journal of Applied Mechanics* 73, 505–515.

Voigt, W., 1889. Ueber die beziehung zwischen den beiden elasticitätsconstanten isotroper körper. *Annalen der Physik* 274, 573–587.

Wang, A.S.D., Ertepinar, A., 1972. Stability and vibrations of elastic thick-walled cylindrical and spherical shells subjected to pressure. *International Journal of Non-Linear Mechanics* 7, 539–555.

Wesolowski, Z., 1967. Stability of elastic thick-wall spherical shell loaded by external pressure. *Archiwum Mechaniki Stosowanej* 19, 3–23.

Willis, J.R., 1977. Bounds and self-consistent estimates for the overall moduli of anisotropic composites. *Journal of the Mechanics and Physics of Solids* 25, 185–202.

Willis, J.R., 1981. Variational and related methods for the overall properties of composites. *Advances in Applied Mechanics* 21, 1–78.

Willis, J.R., 1982. Elasticity theory of composites. *Mechanics of Solids*, 653–686.

Willis, J.R., 2000. The overall response of nonlinear composite media. *European Journal of Mechanics A/Solids* 19, S165–S184.

Yeoh, O. H., 1993. Some forms of the strain energy function for rubber. *Rubber Chemistry and Technology* 66, 754–771.

Zee, L., Sternberg, E., 1983. Ordinary and strong ellipticity in the equilibrium theory of incompressible hyperelastic solids. *Archive for Rational Mechanics and Analysis* 83, 53–90.